TRANSPORTATION RESEARCH

RECORD

No. 1307

Pavement Design, Management, and Performance

Pavement Analysis, Design, Rehabilitation, and Environmental Factors 1991



A peer-reviewed publication of the Transportation Research Board

TRANSPORTATION RESEARCH BOARD
NATIONAL RESEARCH COUNCIL
WASHINGTON, D.C. 1991

Transportation Research Record 1307
Price: $51.00

Subscriber Category
IIB pavement design, management, and performance

TRB Publications Staff
Director of Publications: Nancy A. Ackerman
Senior Editor: Naomi C. Kassabian
Associate Editor: Alison G. Tobias
Assistant Editors: Luanne Crayton, Norman Solomon
Graphics Coordinator: Diane L. Snell
Production Coordinator: Karen S. Waugh
Office Manager: Phyllis D. Barber
Production Assistant: Betty L. Hawkins

Printed in the United States of America

Library of Congress Cataloging-in-Publication Data
National Research Council. Transportation Research Board.

Pavement analysis, design, rehabilitation, and environmental factors.
p. cm.—(Transportation research record, ISSN 0361-1981 ; no. 1307)
ISBN 0-309-05117-7
1. Pavements—Performance. 2. Pavements—Cracking. 3. Pavements, Concrete—Cracking. 4. Pavements—Testing. I. National Research Council (U.S.). Transportation Research Board. II. Series:
Transportation research record ; 1307.
TE7.H5 no. 1307
[TE251.5]
388 s—dc20
[625.8] 91-32361
CIP

Sponsorship of Transportation Research Record 1307

GROUP 2—DESIGN AND CONSTRUCTION OF TRANSPORTATION FACILITIES
Chairman: Raymond A. Forsyth, Sacramento, California

Pavement Management Section
Chairman: R. G. Hicks, Oregon State University

Committee on Rigid Pavement Design
Chairman: Walter P. Kilareski, Department of Civil Engineering, Penn State University
Don R. Alexander, Ernest J. Barenberg, Brian T. Bock, Kathleen Theresa Hall, Amir N. Hanna, John E. Hunt, Michael P. Jones, Starr D. Kohn, Roger Larson, Jo A. Lary, Richard A. McComb, B. Frank McCullough, Theodore L. Neff, Mauricio R. Poblete, Gary Wayne Sharpe, Shiraz D. Tayabji, Mang Tia, James H. Woodstrom, William A. Yrjanson, John P. Zaniewski, Terrence L. Zoller, Dan G. Zollinger

Committee on Flexible Pavement Design
Chairman: Joe P. Mahoney, Department of Civil Engineering, University of Washington
Secretary: Chris A. Bell, Department of Civil Engineering, Oregon State University
Douglas I. Anderson, Uno Arebratt, Jacques Bonnot, Elton R. Brown, James L. Brown, Stephen F. Brown, George R. Cochran, N. F. Coetzee, David C. Esch, C. R. Freeme, Wilbur Charles Greer, Jr., Jerry J. Hajek, Newton Jackson, W. N. Lofroos, Kenneth H. McGhee, Carl L. Monismith, William A. Nokes, John L. Rice, James A. Scherocman, Peter Sebaaly, James A. Sherwood, James F. Shook, Herbert F. Southgate, T. Paul Teng, Marshall R. Thompson, Harry H. Ulery, Jr.

Committee on Pavement Rehabilitation
Chairman: David E. Newcomb, University of Minnesota
Secretary: Richard W. May, Asphalt Institute
Paul Autret, Michael C. Belangie, Thomas L. Boswell, James L. Brown, Martin L. Cawley, Denis E. Donnelly, Wade L. Gramling, Joseph B. Hannon, Don M. Harriott, Ira J. Huddleston, Thomas J. Kazmierowski, Walter P. Kilareski, Aramis Lopez, Jr., Joe P. Mahoney, William G. Miley, Louis G. O'Brien, Roger C. Olson, Gary Wayne Sharpe, James F. Shook, Eugene L. Skok, Jr., Mary Stroup-Gardiner, R. N. Stubstad, Shiraz D. Tayabji, Robert L. White

Geology and Properties of Earth Materials Section
Chairman: Robert D. Holtz, University of Washington, Department of Civil Engineering

Committee on Frost Action
Chairman: Thomas C. Kinney, University of Alaska—Fairbanks
Kenneth O. Anderson, Richard L. Berg, Frederick M. Boyce, Edwin J. Chamberlain, George R. Cochran, Barry J. Dempsey, Denis E. Donnelly, David C. Esch, Wilbur M. Haas, Neil F. Hawks, Larry K. Heinig, Ira J. Huddleston, Newton Jackson, Ronald H. Jones, Hiroshi Kubo, C. William Lovell, Joe P. Mahoney, Melvin W. Morgan, Mary Rutherford, John A. Shuster, Ted S. Vinson, Chen Xiaobai, Qiang Zhu

Committee on Environmental Factors Except Frost
Chairman: Robert L. Lytton, Texas A&M University
Samuel H. Carpenter, Fu Hua Chen, Koon Meng Chua, Judith B. Corley, Barry J. Dempsey, Gary L. Fitts, Donald G. Fohs, Donald J. Janssen, Lawrence D. Johnson, Amos Komornik, Joseph Massucco, Said Ossama Mazen, R. Gordon McKeen, Thomas M. Petry, Miguel Picornell, Rogel H. Prysock, Albert C. Ruckman, Larry A. Scofield, Malcolm L. Steinberg, Jacob Uzan, Gdalyah Wiseman

Frank R. McCullagh and G. P. Jayaprakash, Transportation Research Board staff

Sponsorship is indicated by a footnote at the end of each paper. The organizational units, officers, and members are as of December 31, 1990.

Transportation Research Record 1307

Contents

Foreword vii

Truck Tire Characteristics and Asphalt Concrete Pavement Rutting 1
Harry A. Smith

Rational Look at Truck Axle Weight 8
Michael S. Mamlouk

Model Tests for Moving-Load Effects on Pavements 20
Raj Siddharthan, A. Anooshehpoor, and Jon A. Epps

Twenty-Year Study of Asphalt Rubber Pavements in Phoenix, Arizona 29
Equbalali Charania, Joe O. Cano, and Russell H. Schnormeier

Distributions of Strain Components and Work Within Flexible Pavement Structures 39
Herbert F. Southgate

Performance of Flexible Pavements 51
James Mark Matthews and B. B. Pandey

Evaluation of Louisiana Experimental Base Project with VESYS 63
William O. Hadley

Relating Creep Testing to Rutting of Asphalt Concrete Mixes 75
Vernon J. Marks, Roderick W. Monroe, and John F. Adam

Application of ASTM E1049-85 in Calculating Load Equivalence Factors from In Situ Strains 82
T. Papagiannakis, A. Oancea, N. Ali, J. Chan, and A. T. Bergan

A Reliable Resilient Modulus Testing System 90
Rafael F. Pezo, Dong-Soo Kim, Kenneth H. Stokoe II, and William R. Hudson

Evaluation of Two-Layer Pavements Using Dimensional Analysis 99
Lutfi Raad and Lyla K. Marhamo

Permanent Deformation for Flexible Airfield Pavement Design 111
Samuel Hanthequeste Cardoso and Matthew W. Witczak

Comparison and Reanalysis of AASHO Road Test Rigid Pavement Data 122
W. Ronald Hudson, Michael T. McNerney, and Terry Dossey

Behavior of a Rigid Pavement Under Moving Dynamic Loads 129
Muhammad A. Nasim, Steven M. Karamihas, Thomas D. Gillespie, Will Hansen, and David Cebon

Development and Application of Randomness Index for Continuously Reinforced Concrete Pavement 136
Young-Chan Suh, B. Frank McCullough, and Kenneth D. Hankins

Field-Calibrated Mechanistic-Empirical Models for Jointed Concrete Pavements 143
Michael I. Darter, Kurt D. Smith, and David G. Peshkin

Model of Slab Cracking for Portland Cement Concrete Pavements 154
M. Poblete, P. Ceza, J. David, R. Espinosa, A. García, and J. Gónzalez

Factors Affecting Deterioration of Transverse Cracks in Jointed Reinforced Concrete Pavements 162
Zafar I. Raja and Mark B. Snyder

California Experience with Cracking and Seating of Concrete Pavements 169
Gordon K. Wells, Joseph B. Hannon, and Nelson H. Predoehl

Performance of Asphalt Concrete Resurfacing of Jointed Reinforced Concrete Pavement on the Illinois Interstate Highway System 180
Kathleen T. Hall, Michael I. Darter, and James P. Hall

Crack and Seat Performance 188
Keun-Wook Yi

Crack Monitoring System for Cracked and Seated PCC Pavements 194
Nader Tabatabaee and Peter Sebaaly

Concrete Pavement Rehabilitation and Overlay: Ontario's Experience 201
Thomas J. Kazmierowski and Harry J. Sturm

Theoretical Implications of the AASHTO 1986 Nondestructive Testing Method 2 for Pavement Evaluation 211
Anastasios M. Ioannides

Case Studies in Rehabilitation Strategy Development 221
Michael I. Darter and Kathleen T. Hall

Life-Cycle Cost Analysis of Ohio Pavement Rehabilitation Demonstration Projects 234
Chhote L. Saraf, James C. Kennedy, Jr., Kamran Majidzadeh, and S. William Dudley

Concrete Slabs Stabilized by Subsealing: A Performance Report 243
Shie-Shin Wu

Analysis of Three Concrete Restoration Techniques 249
B. F. McCullough, David W. Fowler, James R. Lundy, and Brock E. Hoskins

Development of Drainage Coefficients for the 1986 AASHTO Guide for Design of Pavement Structures 256
Stephen B. Seeds and R. Gary Hicks

Temperature and Suction Profiles Beneath Highway Pavements: Computed and Measured 268
D. E. Pufahl and R. L. Lytton

ABRIDGMENT 277
Wave Model of Mat Foundation Movement on Expansive Clays
L. D. Johnson and A. L. Branch, Jr.

Simulation of Climatic and Vegetation Effects on Pavements on Expansive Clays 281
M. Picornell and Mohd Asri B. Abd Rahim

Measuring Negative Pore Water Pressures in a Freezing Environment 291
D. G. Fredlund, J. K. Gan, and H. Rahardjo

Field Testing of a Model for Water Flow and Heat Transport in Variably Saturated, Variably Frozen Soil 300
Xia Xu, John L. Nieber, John M. Baker, and David E. Newcomb

Effect of a Geotextile on Water Migration and Frost Heave in a Large-Scale Test Basin 309
Sally A. Shoop and Karen S. Henry

Foreword

Smith reviewed the literature and found that truck tire pressure can influence pavement rutting but is not the primary cause and that improvements in asphalt concrete (AC) mix design offer the best potential for minimizing rutting. Mamlouk discussed the effect of dynamic loading on pavement and enhancements to weigh-in-motion devices to represent the actual dynamic load spectrum. Siddharthan et al. performed tests on foam rubber pavement models and found that moving load vertical displacement is affected by the speed of the moving load.

Charania et al. presented a 20-year historical survey of asphalt-rubber pavements performance in Phoenix, Arizona. Southgate determined that under the inside edge of either dual tire is the location along the centerline of the axle of the maximum strain energy density in the pavement. He also reported on shear values as they relate to pavement depth. Matthews and Pandey investigated the life of full-depth granular pavements in India and developed a flexible pavement life regression equation using the rut depth and subgrade vertical strain values. Hadley used the VESYS IIIA computer program to predict the performance of the Louisiana Experimental Base Project and found that it can predict PSI values and fatigue cracking over a short period of time.

Marks et al. evaluated the correlation between rut depth and resilient modulus or creep resistance. Papagiannakis et al. provided a comparative overview of the methods used for calculating mechanistic load equivalency factors; however, the comparison was not conclusive and could not verify the best methods for describing the fatigue cycle caused in asphalt concrete by multiple axle loads. Pezo et al. examined the SHRP modification to the 1986 AASHTO resilient modulus test procedures for determining the properties of roadbed soil and pavement components.

Raad and Marhamo applied dimensional analysis to develop solutions for critical response parameters using linear elastic theory. Discussed is the power of dimensional analysis in providing representative, simple engineering solutions for a wide range of pavement variables, which become significant because of the extensive experimental and analytical data now available. Cardoso and Witczak presented a methodology developed to predict flexible airfield pavement deformation in Brazil with emphasis on the utilization of lateritic gravel. A good overall comparison in design life prediction with the FAA approach was obtained.

Hudson et al. reviewed three computer analyses of the AASHO Road Test for rigid pavements and their resultant pavement performance equations. Nasim et al. described computer programs developed for calculating strain histories in rigid pavements under heavy truck traffic and their capabilities and limitations. Suh et al. discussed the development, use, and application of a Randomness Index for transverse cracks in continuously reinforced concrete pavements. Darter et al. discussed the development of field-calibrated mechanistic-empirical models for key performance indicators for jointed concrete pavements.

Poblete et al. developed a predictive model of slab cracking for Chile's portland concrete cement (PCC) pavements. Raja and Snyder presented a synthesis of factors that may reduce aggregate interlock load transfer on cracked jointed reinforced concrete pavements and the relative effect of these factors on transverse crack deterioration.

Wells et al. reported on the experience of the California Department of Transportation with cracking and seating of PCC pavement before placement of an AC overlay and concluded that the strategy is beneficial in preventing or retarding reflection cracking in the AC overlays. Hall et al. reported on the survival of 213 AC overlays of jointed reinforced concrete pavements and showed that thick overlays lasted substantially longer and carried substantially more traffic than thin overlays on D-cracked and non-D-cracked pavements. Non-D-cracked pavement overlays outperformed D-cracked pavement overlays. Yi described New Mexico's experience with the crack and seat of PCC pavement before AC overlay and found that the strategy used in conjunction with a paving fabric is effective at reducing reflection cracking.

Tabatabaee and Sebaaly developed an inexpensive simple mechanical gauge to monitor the movement of crack or joint openings in PCC structures, and overlaid and PCC pavements, and they report on its performance. Kazmierowski and Sturm discussed the before and after rehabilitation performance of a PCC pavement in terms of load transfer efficiencies, pavement edge deflections, roughness, skid resistance, pavement condition, cracking, noise level, traffic, and surface texture. Ioannides traced the derivation of the AASHTO 86 NDT-Method 2 equations and highlighted a number of theoretical shortcomings. Ioannides also makes recommendations for the gradual elimination of statistical/empirical constructs.

Darter and Hall presented case studies in the rehabilitation strategy and demonstrated that restoration is the most cost-effective alternative for pavements that are structurally adequate and do not have concrete durability problems. Saraf et al. illustrated the use of the suitable life-cycle cost analysis procedure to compare five rehabilitation techniques on eight projects. Adjustments were made to compare the techniques on an equitable basis; the results indicated that this procedure was a reasonable method. Wu reported on North Carolina's investigation of subsealing of concrete slabs to correct slab movement and pumping. He determined that none of the void detection techniques used produced compatible data and that subsealing can cause performance problems if not handled properly. McCullough et al. described three concrete pavement restoration techniques and evaluated their field performance.

Seeds and Hicks described the mechanistic-empirical methodology that was applied to develop the procedure for considering the effects of drainage in the AASHTO Guide pavement structural design process. Pufahl and Lytton developed a computer model that computes the temperature and suction profiles beneath highway pavements or other similar covered areas throughout a specified time period. The theory and comparisons of computed and measured values of temperature and suction are presented. Johnson and Branch discussed the assessment of pavement and structural damage caused by soil differential movement through the use of wave pattern foundation movement modeling.

Picornell and Abd Rahim described a simplified model to simulate the infiltration of rainfall through the soil crack fabric and the removal of soil moisture by soil evaporation and plant transpiration along the side of a pavement. Fredlund et al. discuss the possibility of using devices available for suction measurements in unfrozen, unsaturated soils for the measurement of negative pure water pressure under freezing conditions. The theory of freezing soil and thermal properties of soil are also presented. Xu et al. evaluated the simultaneous heat and water model with measured values for soils located in Minnesota and found that the predicted frost depth and temperature profile agree well with measured field data, whereas agreement with liquid soil water content was fair. Shoop and Henry examined the effect of needle-punched polyester geotextile on moisture migration and frost heave during freezing and thawing in a large test basin and determined that if a geotextile is used in frost-susceptible soil, proper drainage and the correct fabric type must be used to prevent increased frost heave.

Truck Tire Characteristics and Asphalt Concrete Pavement Rutting

HARRY A. SMITH

Increased truck tire inflation pressures have been perceived as a major contributor to premature wheelpath rutting of asphalt concrete (AC) pavements. Consequently, a critical evaluation was conducted of available information pertaining to heavy-vehicle tire inflation pressures and related characteristics as they influence AC pavement performance, particularly premature wheelpath rutting. However, the collection, review, and evaluation of literature and information extended into the larger subject area of vehicle-tire-pavement interaction A large number of documents plus personal interviews and discussions were reviewed to provide the basis for the critical evaluation. The essential findings are that (a) recent increases in truck tire inflation pressures are not the primary cause of premature AC pavement rutting, (b) high tire-pavement contact pressures can influence wheelpath rutting of AC surface courses, (c) improvements in AC mix design offer the best potential for minimizing wheelpath rutting, and (d) the wide variations in vehicle-tire configurations significantly influence AC pavement performance.

Increases in truck tire pressures over the past 20 years have been perceived by many in the highway industry as contributing to reduced pavement performance of America's highways, particularly premature wheelpath rutting of asphalt concrete (AC) surfaces. In 1985 AASHTO approved a resolution that, among other things, objected to the introduction of higher-pressure truck tires, and subsequently established the Task Force on High Pressure Truck Tires (*1*). On February 12 and 13, 1987, a workshop on high-pressure truck tires was conducted in Austin, Texas (*2*). At the workshop it was indicated that the tire pressure problem interacts with such other factors as vehicle design, wheel loads, pavement design, and quality of pavement construction. The consensus was that tire pressure is merely one component of the issue of larger truck sizes and weights. There is a more general need for an improved understanding of the basic vehicle-tire-pavement interaction. Many of the information needs concerning this interaction are being addressed by current and planned research in NCHRP, FHWA, and Strategic Highway Research Program (SHRP) activities. Consequently, an immediate need exists for a critical assessment of available research and experience to determine what information can be implemented and the existence of any remaining information gaps.

At the request of the AASHTO Joint Task Force on Pavements, an NCHRP project, Critical Assessment of Tire Pressure Research, was conducted with objectives being (a) to identify and critically evaluate previous and ongoing research pertaining to truck tire pressures and pavement performance, (b) to determine potential impacts of developments in the truck and tire industries on the subject, and (c) to identify information gaps and research needs.

3320 Lauriston Place, Fairfax, Va. 22031. Current affiliation: Pavement Consultancy Services, Law Engineering, Inc., 12240 Indian Creek Court, Beltsville, Md. 20705-1242.

PROBLEM SCOPE

All vehicle loads must be transmitted from the vehicle body through the suspension systems and tires to the pavement surface, where they are then distributed through the pavement structure to the subgrade soils. Determination of the unit loads expected to be applied to the pavement surface would be simple if the loads were static and the tires had no structural characteristics. However, such is not the case, and tire contact pressures are not uniform. The magnitude and significance of this contact pressure nonuniformity have not been absolutely documented and are discussed in detail in the following paragraphs.

A major concern of the highway community in recent years has been the occurrence of premature wheelpath rutting in AC pavements. Because of substantial evidence that operating tire pressures of heavy trucks have been increasing, the higher tire pressures have been perceived as contributing to pavement rutting. This perception has generated considerable research on documentation of actual operating tire pressures, influence of tire type on pressures, relationships between tire inflation pressures and tire-pavement contact pressures, and distribution of contact pressures within the contact area. Because pavement rutting can be controlled both by reducing tire-pavement contact pressures and by increasing resistance to the contact pressures through improved AC mix design, research and other developments have occurred in the mix design area.

In 1984 the Subcommittee on Materials of the Western Association of Highway and Transportation Officials (WASHTO) held a conference on asphalt pavement rutting because some agencies considered rutting one of their most pressing issues. After the conference, a report (*3*) was issued dealing primarily with the material and construction aspects of the problem. The report contained recommendations on mix design, construction procedures, selection of aggregates and asphalt materials, and the need for performance type specifications.

Many recommendations in the WASHTO report were incorporated into an FHWA Technical Advisory (*4*). This publication recognizes that implementation of available knowledge and experience in such areas as materials selection, mix design, plant operation, and construction procedures can pro-

duce high-quality AC pavements that will minimize premature wheelpath rutting.

In 1987 the AASHTO Highway Subcommittee on Construction conducted a survey on the pavement rutting problem. Of 62 responses, 52 (84 percent) were of the opinion that rutting of AC pavements is a major (or significant) type of distress on their highway system, and 54 (93 percent) expressed the opinion that heavy-truck tire pressures was a major cause of rutting. Subsequently, the AASHTO Joint Task Force on Rutting was formed to follow up on the survey and its results. A report was submitted to the Standing Committee on Highways at the 1988 AASHTO meeting (*5*).

Although increased axle loads, traffic volumes, and tire pressures have contributed to the pavement rutting problem, the AASHTO joint task force believed that other factors within the control of highway agencies have contributed to the problem and that asphalt pavement rutting can be minimized when such pavements are properly designed, built, and maintained. Even in areas where rutting is not perceived as a serious problem, improved mix design and construction controls could reduce development of distress and increase pavement life (*5–9*).

TIRE TYPES AND PRESSURES

Until recent years, there appears to have been little interest and concern about the tire factor in the tire-pavement interaction system. Even with the increased research activity, this factor is the least understood and most controversial aspect of the problem. Some analytical studies (*10*) indicate that contact pressures can be as much as four times tire inflation pressures at localized spots in the contact area, but the actual existence and significance of such localized pressures on pavement performance have not been verified. The gross loads applied to tires, and tire selection and design in relation to those loads, influence contact pressure distribution. In an effort to control wheel loads in relation to tire type and size, 28 states currently regulate load per inch of tire width. Eighteen states limit the load to 600 lb/in. of width. The most significant concern to be resolved may be the determination of realistic tire contact pressures for pavement design purposes.

At the time of the AASHO road test, the primary tire type was bias ply with a cold inflation pressure of 75 psi. In the intervening 30 years the prevalent tire type has changed to radial-ply design, and increased axle loads have resulted in the selection of tires with recommended cold pressures of 85 to 105 psi. Actual field measurements of truck tire inflation pressures indicate an average of about 100 psi, but information on tire sizes and temperatures at the time of measurement is generally not available (*11–16*). Although the averages are about as expected, inflation pressures above the average—with highs up to 150 psi—were often recorded. The excessive tire pressures may also have been associated with gross wheel overloads. The heat generated during operation of the vehicle over the road results in a hot-tire inflation pressure of 5 to 15 psi above the cold-tire inflation pressure.

Most of the earlier studies of tire-pavement interaction were of the analytical type and involved various assumptions. AC pavement prediction models based on limiting tensile strain at the bottom of the AC layer were generally used. Rutting was often evaluated on the basis of compressive stresses at the base or subgrade surface. In some cases, tire-pavement contact pressure distribution within the contact area was estimated to have localized peaks of as much as four times the inflation pressure (*10*).

Recent research (*17*) has provided more realistic information on actual tire-pavement contact pressures under a variety of conditions. Carefully instrumented experimental studies by Goodyear Tire and Rubber Company (*18*) indicate that increasing inflation pressure at constant load shifts the point of maximum contact pressure to the center region of the contact area, whereas increasing tire load at constant inflation pressure shifts the point of maximum contact pressure toward the perimeter (see Figure 1). The Goodyear experimental work also showed that the maximum contact pressure levels for three tire types were about 1.5 to 2 times the inflation pressure (see Table 1).

Although several research reports have described analytical methods for evaluating the influence of tire type and tire

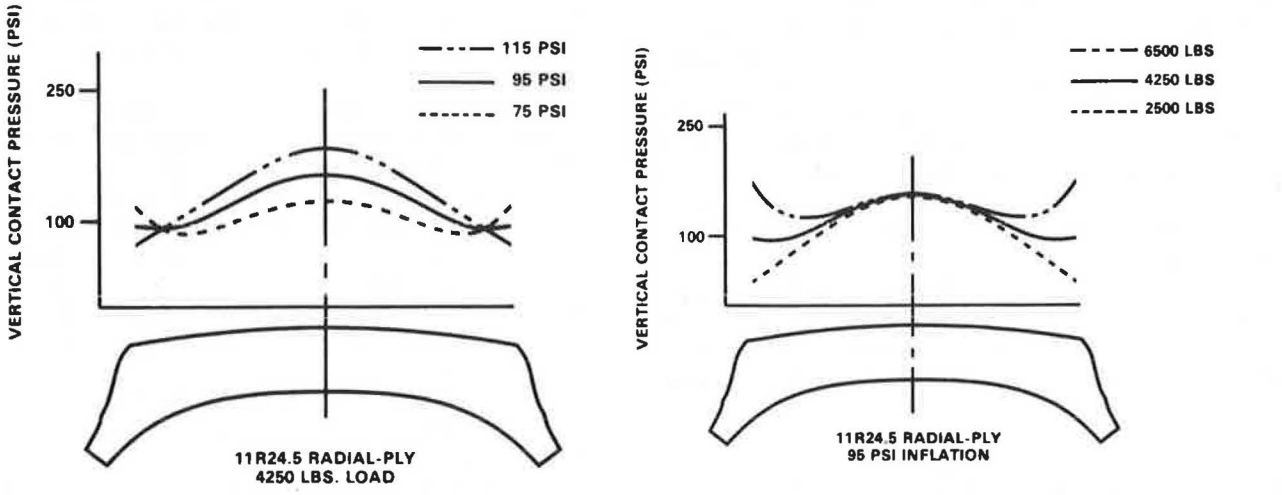


FIGURE 1 Effect of tire pressure and load on point of maximum contact pressure (*23*).

TABLE 1 RATIO OF MAXIMUM CONTACT PRESSURE TO INFLATION (*23*)

	INFLATION (psi)	MAXIMUM CONTACT PRESSURE (M.C.P.) (psi)	RATIO (M.C.P.) TO INFLATION
11-24.5	65	117	1.8
4250 lbs. LOAD	75	114	1.5
	95	118	1.2
11r24.5	75	122	1.6
4250 lbs. LOAD	95	152	1.6
	115	182	1.6
385/65R22.5	100	200	2.0
8500 lbs. LOAD	120	226	1.9
	140	252	1.8

inflation pressures on pavement performance, a study recently completed by FHWA (*19*) provides the most complete and documented analysis of relationships among wheel loads, tire types, and tire pressures on two AC pavements. The study was conducted at the full-scale pavement testing facility at the Turner-Fairbanks Highway Research Center in McLean, Virginia, using the Accelerated Loading Facility (ALF) testing machine. Loads were applied by one-half of a dual-tire, single-axle assembly and ranged from 9,400 to 22,500 lb. Bias- and radial-ply tires at cold inflation pressures of 76, 108, and 140 psi were used, making over 500,000 passes during the pavement performance evaluation. The effects of wheel load, tire type, and tire inflation pressure were evaluated in terms of measured responses (deflections and strains), pavement rutting and cracking, and changes in pavement materials after the traffic loading. Tire-pavement contact pressure distribution was not measured.

The project report (*19*) for this comprehensive research study includes much meaningful information. The following are of special significance:

- For the dual-tire wheel assembly loads, tire pressures, pavement sections, and climatic conditions studied, the effect of load was greater than that of tire pressure. The measured pavement responses doubled for an increase in load from 9,400 to 19,000 lb, whereas increasing the tire inflation pressure from 76 to 140 psi resulted in less than a 10 percent increase in measured response (see Figure 2).
- The combination of high tire pressure, high temperature, and thin pavement was extremely damaging.

From a technical standpoint, tire inflation pressure alone does not appear to be a major contributing factor in premature rutting. Inflation pressure only roughly influences contact pressures at the pavement surface. As wheel loads are increased, inflation pressures and contact pressures will of necessity increase. Although AC pavements can be designed and built to perform satisfactorily under current load and contact pressure conditions, realistic contact pressure limits must be established for the future.

The overriding concern from a pavement standpoint is the potentially damaging influence from the use of wide-base (super

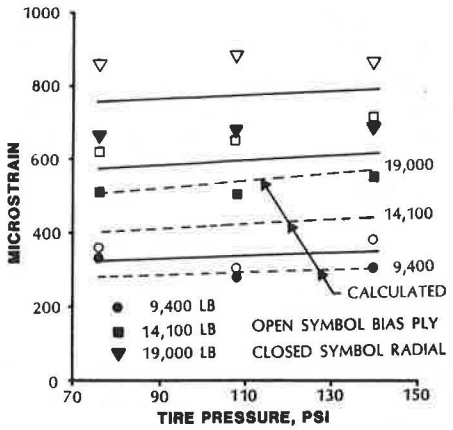


FIGURE 2 Effects of load and tire pressure on strain at bottom of asphalt layer for Lane 2.

single) tires as a replacement for dual-tire configurations on the heavy-truck fleet in the United States. Currently, only a limited amount of actual experience and documented research exist on the subject.

Findings of a number of theoretical and experimental studies, (*20–23*) agree that wide-base single tires cause greater pavement damage than conventional dual tires at comparable axle loads by an average factor of about 1.5. The various computed equivalencies depend on pavement structure, assumed distress relationships, tire size and type, tire inflation pressure, and procedures for determining tire-pavement contact pressures. For example, Sharp et al. (*20*) conducted an experimental study in Australia to evaluate the relative damaging effects of single, tandem, and triple axles with conventional dual and wide-base single tires. The tires were 11.00R22.5 and 18.00R22.5, inflated to 100 psi cold. Tire contact areas were measured, but uniform contact pressures were assumed. Deflection testing took place at two sites, one with conventional AC and the other with a seal coat over granular base. Regression equations were developed between deflection ratios and corresponding loads. Different axle loads were considered equivalent if they induced identical deflection ratios. The findings were as follows:

- Wide-base single tires produced greater pavement deflections than conventional dual tires for comparable loads.
- For a single axle, a load of 13,000 lb on wide-base single tires was considered equivalent to a load of 18,000 lb on conventional dual tires. (The damage factor ratio was 1.38.)
- For tandem-axle groups, a load of 24,300 lb on wide-base single tires was considered equivalent to a load of 29,900 lb on conventional dual tires. (The damage factor ratio was 1.23.)
- For triaxle groups, a load of 37,600 lb on wide-base single tires was considered equivalent to a load of 40,700 lb on conventional dual tires. (The damage factor ratio was only 1.08.)

Significant experimental work on the influence of tire type on AC pavement performance has also been conducted in Finland at the Technical Research Center, Road and Traffic Laboratory (*21*). The measurements were made by pressure cells and strain gauges installed in two AC pavement test sections in the Virttaa test track. Recent research included the comparison of two dual-tire assemblies and three wide-base single tire assemblies, all with three different axle loads and three tire pressures. Uneven tire loads within the dual assemblies were simulated with inflation pressure differences. The following tire assemblies were used:

1. 12R22.5 duals,
2. 265/70R19.5 duals,
3. 445/65R22.5 wide-base single,
4. 385/65R22.5 wide-base single, and
5. 350/75R22.5 wide-base single.

The diameter of the second assembly is 20 percent less than that of the first assembly, and the tires are slightly narrower, to permit a lower trailer platform. Strain and deflection measurements were converted to equivalent axle passes by fatigue failure criteria, with a 10-t single axle load on dual 12R22.5 tire assemblies as the reference. Some of the conclusions are as follows:

- Damaging power for all tire assemblies is influenced to the greatest extent by axle loads.
- When distribution of load is equalized between tires, the least damaging assembly is the conventional dual 12R22.5 followed by the smaller dual and the wide-base single tire assemblies. The narrower wide-base single tires were as much as four times more damaging than the reference assembly.
- Contact pressure is greatest in the center of all radial tires tested. Maximum contact pressures were not available.

The uneven load distribution between dual tires was simulated in a series of measurements with one tire inflated to 72.5 psi and the other to 145 psi. This pressure just about doubled the damaging power of the dual assembly.

A recent study (*22*) of the effect of the tire pressure and tire type on flexible pavement response conducted at the Pennsylvania Transportation Institute included the measurement of tire-pavement contact pressures and the use of the actual pressure distributions in mechanistic models to predict the responses of flexible pavements under various loading conditions. Tire types tested were 11–22.5 bias, 11R22.5 radial, and 385/65R22.5 wide-base single at inflation pressures of 75 to 145 psi. Contact pressure distributions were all nonuniform, with a maximum of 1.75 times inflation pressures and the maximum occurring along the center rib for all three tire types. As axle loads were increased, the portion carried on the outer tread of radials increased and the ratio of maximum to minimum contact pressure decreased. The more significant results of the analytical portion of the study are as follows:

- Magnitude of the axle load is the predominant factor for all variations in pavement response for the tire types, inflation pressures, and pavement thicknesses investigated (see Figure 3).
- The wide-base single tire produced the maximum tensile strains and compressive stresses under all combinations of axle loads and layer thicknesses.

Extensive literature reviews on vehicle-tire-pavement interaction have been conducted by Papagiannakis et al. (*23*) for the Canadian Ministry of Transportation and Communications and by Cebon (*24*) of the University of Cambridge, England. Their observations and findings are generally consistent with those described.

Investigations of AC pavement rutting and the influence of suspension systems on dynamic loading of pavements have been conducted for the Federal Minister of Transport in Germany (*25,26*). Of particular significance is the finding that, for the conditions of the test (a hot summer day), wheelpath rutting was the result of deformation flow (shear) within the AC rather than consolidation. Carpenter and Freeman (*9*) of the University of Illinois question the use of vertical stress to characterize AC mixtures with regard to resistance to wheelpath rutting, particularly for AC overlays on rigid surfaces.

CONCLUSIONS

A substantial research effort aimed at determining more realistic loadings to use in pavement design was conducted by

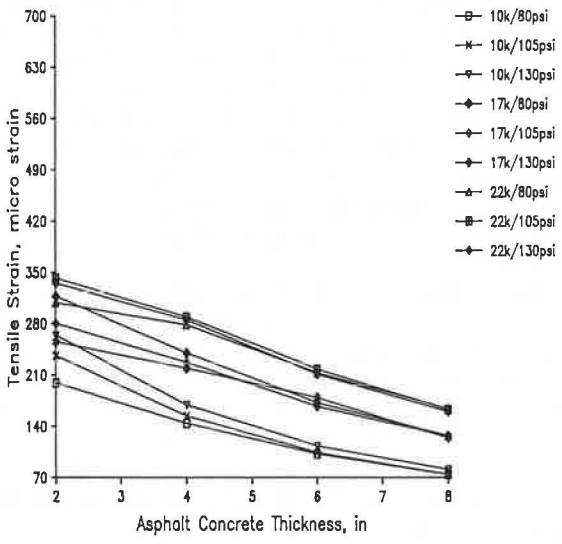


FIGURE 3 Effect of tire pressure and load on tensile strain at bottom of asphalt layer for dual radial tires (*27*).

the Roads and Transportation Association of Canada in 1984–1986 (*27,28*). Field testing involved 13 instrumented flexible pavement sections at various locations in Canada, as well as several combinations of axle loadings and configurations. Vehicles were also instrumented to record dynamic load for different suspension types and road roughness. Measurements of surface deflections and tensile strains at the bottom of the AC were used to determine load equivalencies for various vehicle configurations. Bump-induced dynamic loads were 130 to 200 percent of the static loads for one bump (see Figure 4); with multiple bumps that caused whole body oscillation (bounce), estimated load equivalency factors were 6.5 to 12.5 times the magnitude of predicted equivalency factors for smooth pavements.

Indications are that the technical tools and information will be available shortly to optimize vehicle-pavement interaction and to produce the most cost-effective and efficient movement of goods and services over highways. Recognizing the progress being made toward optimization, current and future research activities should be coordinated in a manner that will ensure the most effective results. An initial step in this direction could be expansion of tire pressure research to include a critical assessment of heavy vehicle–pavement interaction. A major requirement for eventual accomplishment of efficient movement of goods and services is continued communication among the drivers, vehicle truck operators, and highway industry personnel to develop realistic policy for use of the information to produce the desired optimization.

Although increased axle loads and traffic volumes have contributed to asphalt pavement rutting, research and experience provide the basis for minimizing premature rutting in the future, assuming vehicle configurations, tire types, and paving materials do not change drastically. In addition, current research should provide the means for optimizing AC pavement mix design and vehicle configurations that will substantially improve pavement performance in the future. A major requirement for producing this improvement is the determination of realistic tire-pavement contact pressures that can be accommodated by both the highway paving and tire manufacturing industries. Although no indication is currently available concerning realistic and attainable contact pressures, it is recognized that 350-psi tire pressures are successfully accommodated by airfield pavements. The NCHRP and SHRP research in progress will provide the tools for working toward this optimization.

SUMMARY

A brief summary of the study findings, identified information gaps, and research needs follows:

Essential Findings

Tire Inflation Pressures

Increases in tire inflation pressures are not the primary cause of premature AC wheelpath rutting. Tire inflation pressures are only one of the components of the issue of larger truck sizes and weights. Although average truck tire inflation pressures have increased about 20 psi over the past 30 years, research indicates that these increases significantly influence the performance only of thin asphalt pavements. In the opinion of experienced materials and pavement engineers in the western states, where premature rutting is considered most prominent, long-lasting and good-performing AC pavement can be designed and built using currently available materials and technology to withstand wheel loads and tire inflation pressures generally being used at the present time.

Tire-Pavement Contact Pressures

High tire-pavement contact pressures can influence AC pavement wheelpath rutting. Although tire inflation pressures, interacting with wheel loads, do influence tire-pavement contact pressures, the two are not equal. Contact pressures are not uniform within a tire-pavement contact area and are influenced substantially by tire type and design. This condition

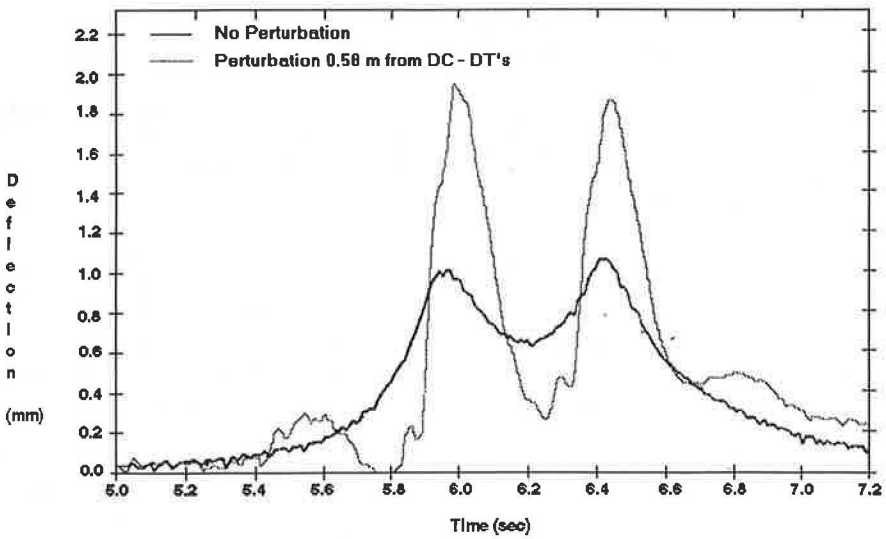


FIGURE 4 Typical deflection response under tandem axles (*21*).

can result in maximum contact pressures being as high as double the inflation pressure. AC pavement analysis and design procedures should consider properly determined maximum tire-pavement contact pressures rather than tire inflation pressures.

Variations in Vehicle-Tire Configurations

The number of variations in vehicle-tire configurations has increased and will likely continue to do so. All of the following factors affect pavement performance to varying degrees:

- Number of axles;
- Load per axle;
- Axle spacing and configuration;
- Load per inch of width of tire;
- Tire type, size, and configuration;
- Tire contact pressure (maximum and distribution);
- Tire diameter; and
- Suspension system.

With regard to load per inch of width, 18 states currently limit the load per wheel to 600 lb/in. of tire width. This approach is applicable regardless of the number or type of tires per axle. The use of wide-base single tires may provide benefits or, as some research indicates, cause increased pavement deterioration. When used to replace narrower tires on the front steering axles of heavy trucks such as concrete mixers, these tires are likely to result in reduced contact pressures. When used to replace a conventional dual-tire assembly without reducing the axle load, research indicates that they increase pavement damage. The optimization of the vehicle-tire-pavement system could result in the identification of an appropriate use for this type of tire.

Information Gaps

Realistic Tire-Pavement Contact Pressures

Although significant progress has been made in recent years in the areas of AC mix design and construction control, which has reduced the potential for premature rutting, changes in heavy-vehicle components and configurations could result in further increases in contact pressures. On the other hand, anticipated improvements in asphalt cement and asphalt-aggregate mixtures technology from SHRP could result in the ability to produce AC pavements capable of performing satisfactorily under increased tire-pavement contact pressures. It is essential to establish realistic maximum limits for tire-pavement contact pressures for which AC pavements can be designed and built using readily available materials and generally accepted construction technology, not only to minimize pavement deterioration now but also to provide the critical link to vehicle-tire-pavement optimization in the future.

Optimization of Vehicle-Pavement Design

Information and tools are being developed by recently completed, in-progress, and programmed research that could lead to accomplishment of the ultimate objective of optimizing the vehicle-tire-pavement system to provide the most efficient movement of goods and services.

Research Needs

Determine Realistic Tire-Pavement Contact Pressures

Advances in AC mix design, specifically NCHRP and SHRP asphalt research activities, will provide promising tools for determining realistic maximum limits for tire-pavement contact pressures based on laboratory testing of available materials. The need is for application of these tools by follow-on research to determine realistic contact pressures. Identification of such limits should be used during optimization of vehicle-tire-pavement design. The tire industry in particular should be encouraged to consider these realistic limits during tire design. A means to regulate compliance with established criteria must also be found.

No current or programmed research by NCHRP, SHRP, or FHWA appears to respond directly to this needed research. AASHTO should support an NCHRP study with the objective of determining realistic tire-pavement contact pressures.

Critical Assessment of Vehicle-Tire-Pavement Research

This is an opportune time to advance the optimization of vehicle-tire-pavement design based on the extensive research being conducted worldwide on pavement design and performance, the influence of vehicle dynamics on pavements, and various vehicle components and configurations. Because of the interactions among the various factors, a critical review and an assessment of all research activities are needed to encourage the necessary interaction and to identify any gaps in the information being developed.

Continuous oversight and coordination of the various research activities should be provided in some form either by AASHTO, TRB, or FHWA staff, or by a research project.

Public Agency Vehicle Configuration Policy

As research reveals information leading toward optimization of vehicle-tire-pavement design to maximize highway transport productivity and minimize pavement and vehicle wear, there will be an increasing need for highway agency policy decisions. Some of these decisions may be required in the near future, before completion of all research. For example, wide-base or super single tires are already being used in other countries as a replacement for dual-tire assemblies and have been observed in this country. These tires are being used rather extensively on the front steering axles of concrete mixers and other heavy trucks that frequently operate off paved roads. The trend toward pounds per inch of tire width as a regulatory tool could alleviate the immediate problem but is not likely to resolve the issue in the long term. There is a need for policy actions to effectively control the use of these tires. The vehicle-tire-pavement optimization activities will determine their ultimate acceptability.

AASHTO should be constantly aware of policy considerations resulting from the extensive amount of vehicle-tire-pavement research and worldwide trends and should appoint a committee or task force to monitor developments and to act on policy concerns as they arise.

In summary, the extensive amount of research and experience on tire-pavement interaction adequately addresses most of the concerns about pavement rutting and tire pressures. The substantial switch from bias-ply to radial truck tire design has generally been beneficial to pavement performance.

The most prominent need is the determination of realistic tire-pavement contact pressures to avoid future pavement deterioration as loads and vehicle configurations change. Although beyond the original scope of the study, the tire-pavement problem is one component of the issue of larger truck configurations, sizes, and weights. Consequently, the ultimate need is for optimization of pavement and vehicle design to provide improved trucking productivity while minimizing adverse impacts on pavements. Because of the extensive current and planned research in this area, the primary action required is the coordination of these activities, particularly between the pavement and vehicle industries.

ACKNOWLEDGMENT

The previous paragraphs contain essential portions of a report prepared under an NCHRP project for the AASHTO Standing Committee on Highways, Task 36, Critical Assessment of Tire Pressure Research.

REFERENCES

1. J. Friedenrich. The AASHTO Task Force on High Pressure Truck Tires. Presented at 2nd International Conference on Pavement Management, Ontario, Canada, 1988.
2. *Proc., Symposium/Workshop on High Pressure Truck Tires*, AASHTO, Washington D.C., Feb. 1987.
3. U. B. Betenson et al. *Asphalt Pavement Rutting in Western States*. Western Association of State Highway and Transportation Officials, 1984.
4. *Asphalt Concrete Mix Design and Field Control*. FHWA Technical Advisory 5040.27. FHWA, U.S. Department of Transportation, 1988.
5. *Report of AASHTO Joint Task Force on Rutting*. AASHTO, Washington, D.C., 1988.
6. F. N. Finn and K. Nair. *NCHRP Report 195: Minimizing Premature Cracking of Asphaltic Concrete Pavements*. TRB, National Research Council, Washington, D.C., 1978.
7. R. A. Jimenez and D. A. DaDeppo. *Asphaltic Concrete Mix Design Evaluation*. University of Arizona, Tucson, 1986.
8. R. D. Pavlovich, T. S. Schuler, R. G. McKeen, and M. Eliassi. *Investigation of Mathematical Models for Asphalt Pavement Rutting*. New Mexico Engineering Research Institute, Albuquerque, 1987.
9. S. M. Carpenter and T. J. Freeman. Characterizing Premature Deformation in Asphalt Concrete Placed over Portland Cement Concrete Pavements. In *Transportation Research Record 1070*, TRB, National Research Council, Washington, D.C., 1986.
10. J. T. Tielking. Finite Element Tire Model. Presented at FHWA Load Equivalency Workshop, Turner-Fairbank Highway Research Center, McLean, Va., 1988.
11. P. H. DeCabooter. *Wisconsin Truck Tire Study*. Wisconsin Department of Transportation, Madison, 1988.
12. C. Bartholomew. *Truck Tire Pressures in Colorado*. University of Colorado, Denver, 1989.
13. D. R. Middleton, E. L. Roberts, and T. Chira-Chavala. Measurement and Analysis of Truck Tire Pressures on Texas Highways. In *Transportation Research Record 1070*, TRB, National Research Council, Washington, D.C. 1986.
14. P. Josephson and H. Svensson. *Tyre Pressure in Heavy Vehicle Tyres*. Chalmers University of Technology, Sweden, 1985.
15. H. Stuit. *Tire Pressures and Temperatures of Heavy Danish Lorries*. National Road Laboratory, Denmark, 1988.
16. R. B. Clark. Tires, Pressures and Pavements. Presented at SAE Truck and Bus Meeting, Charlotte, N.C., SAE, Warrendale, Pa., 1989.
17. K. M. Marshek, H. H. Chen, R. B. Connell, and W. R. Hudson. Experimental Determination of Pressure Distribution of Truck Tire-Pavement Contact. In *Transportation Research Record 1070*, TRB, National Research Council, Washington, D.C., 1986.
18. P. Yap. *A Comparative Study of the Effect of Truck Tire Types on Road Contact Pressures*. Paper 881846. SAE, Warrendale, Pa., 1988.
19. R. Bonaquist, R. Surdahl, and W. Mogawer. *Pavement Testing Facility—Effects of Tire Pressure on Flexible Pavement Responses and Performance*. Report FHWA-RD-89-123. FHWA, U.S. Department of Transportation, Aug. 1989.
20. K. G. Sharp, P. E. Sweatman, and D. W. Potter. *A Comparative Study of the Effects of Wide Base Single and Dual Tires on Rebound Pavement Deflection*. Australian Road Research Board, Australia, 1986.
21. M. Huhtala, J. Pihlajamäki, and M. Pienmäki. Effects of Tires and Tire Pressures on Road Pavements. In *Transportation Research Record 1227*, TRB, National Research Council, Washington, D.C., 1989, pp. 107–114.
22. P. Sebaaly and N. Tabatabaee. Effect of Tire Pressure and Type on Response of Flexible Pavement. In *Transportation Research Record 1227*, TRB, National Research Council, Washington, D.C., 1989, pp. 115–127.
23. A. T. Papagiannakis and R. C. G. Haas. *Wide-Base Truck Tires: Industry Trends and State of the Knowledge of Their Impact on Pavements*. Ministry of Transportation and Communications, Ontario, Canada, 1986.
24. D. Cebon. *Vehicle-Generated Road Damage: A Review*. Cambridge University, Cambridge, England, 1989.
25. I. J. Eisenmann et al. *Effects of Constructional Design of Commercial Vehicles on the Stress in Road Pavement*. Federal Minister of Transport, Germany, 1984.
26. J. Eisenmann and A. Hilmer. *Influence of Wheel Load and Inflation Pressure on the Rutting Effect of Asphalt Pavements—Experimental and Theoretical Investigations*. Federal Minister of Transportation, Germany, 1986.
27. J. T. Christison. *Pavement Response to Heavy Vehicle Test Program: Part 2—Load Equivalency Factors*. In *Vehicle Weights and Dimensions Study*, Vol. 9, Roads and Transportation Association of Canada, Ottawa, 1986.
28. J. T. Christison and J. H. F. Woodrooffe. *Pavement Response to Bump Induced Axle Loads: Experimental Findings*. In *Vehicle Weights and Dimensions Study*, Vol. 10, Roads and Transportation Association of Canada, Ottawa, 1986.

Publication of this paper sponsored by Committee on Flexible Pavement Design.

Rational Look at Truck Axle Weight

MICHAEL S. MAMLOUK

The load applied by trucks on pavement varies instantaneously due to road roughness, truck speed, suspension type, tire pressure, and other factors. The instantaneous actual (dynamic) load fluctuates above and below the static weight, and the difference can be significant. Current weigh-in-motion (WIM) devices provide a snapshot of the dynamic load spectrum. These measurements can be improved by using multisensor devices to better represent the actual wheel load distribution. The larger the number of sensors in a WIM device, the larger the accuracy in representing the dynamic load spectrum. Multisensor WIM devices can be used to estimate both the mean and the standard deviation of the dynamic wheel forces applied by the tires on the pavement. A larger number of sensors is required to accurately estimate the standard deviation than the number required to accurately estimate the mean. Also, the chance of underestimating the actual standard deviation is larger than that of overestimating the actual standard deviation. Because pavement performance is affected more by dynamic loads than by static loads, dynamic loads could be better used to control the legal load limit, taxation, penalties, and pavement design and analysis. Further research is needed to provide proper implementation procedures and to separate the dynamic forces caused by truck and road factors.

The pavement design process requires a large amount of input data, including traffic characteristics, material properties, and environmental conditions. The crux of the problem is how to analyze these data to determine optimum layer thicknesses so that the pavement will last for a specified design life without excessive failure. One of the important areas of analysis is to evaluate how the pavement is affected by the application of wheel loads under various conditions—a problem that has not been fully resolved.

The load applied by trucks on the pavement structure is dynamic, which means that it varies from one instant of time to another, as shown in Figure 1 (*1*). Figure 1 shows that the instantaneous wheel force of a walking beam suspension truck, for example, could vary from 25 to 175 percent of the static wheel load at a speed of 50 mph on a medium-roughness road. Other studies (*2,3*) show that the dynamic forces applied by moving truck wheels have typical root mean square amplitudes of 10 to 30 percent of the static wheel loads. The fluctuation of the dynamic wheel load above and below the static weight is affected by road roughness, truck speed, suspension type, tire type, tire pressure, tire condition (bald or new), load center of gravity, and frame and axle configuration. For example, two axles having the same static weight but different suspension types, tire types, tire pressures, speeds, or pavement roughness will affect the pavement differently.

Forces on the pavement applied by vehicles in motion have a different character than those produced by stationary vehicles. The interaction between moving vehicles and pavement is a complex process that has not been fully understood or addressed either by highway engineers or by vehicle manufacturers.

The conventional practice of weighing trucks is to obtain the static weights of various axles. This static axle load is currently being used for pavement analysis and design, truck taxation and fining, fund allocation for road maintenance, and pavement management. In recent years the weigh-in-motion (WIM) technique has been used by most states in an attempt to obtain axle weights in a more comprehensive, simpler, and faster way than the static technique. However, there is a great concern among highway engineers because the WIM devices do not duplicate the static weight. Also, under the same conditions the same WIM device does not even record the same weight; thus, the results are not repeatable.

Results of recent research related to vehicle-pavement interaction are reviewed, and some issues crucial to the pavement and truck community are discussed. A new, accurate, and precise concept of how truck axles could be weighed and analyzed is proposed. The justification and potential use of the new method of axle weighing in pavement design, road maintenance, budget allocation, and truck taxation are addressed.

DYNAMIC MOVEMENTS OF TRUCKS

The characteristics of heavy vehicles that are of greatest interest to pavement performance include suspension and axle configuration, tire type and pressure, axle load, and vehicle speed. These vehicle characteristics have significantly changed since the AASHO road test, which developed the relationship between truck traffic and pavement wear and formed the basis for the pavement design and truck weight regulations currently used in many states. These changes in heavy-vehicle characteristics made the current methods of pavement design obsolete or biased. The main reason for this problem is the empirical nature of these design methods, which are valid only under the original conditions and are not accurately adaptable to changes in these conditions.

A heavy truck is complex from the standpoint of dynamics. The mass of the truck can be broken down into a sprung mass and an unsprung mass (*4*). The sprung mass includes body, frame, powertrain, payload, and driver. The unsprung mass includes axles, spindles, brakes, wheels, and tires. Both sprung and unsprung masses bounce and contribute independently to the composite dynamic pavement load, although the bouncing of the sprung mass is much greater than that of the unsprung mass. The total load imparted to the pavement by a

College of Engineering and Applied Sciences, Arizona State University, Tempe, Ariz. 85287–6306.

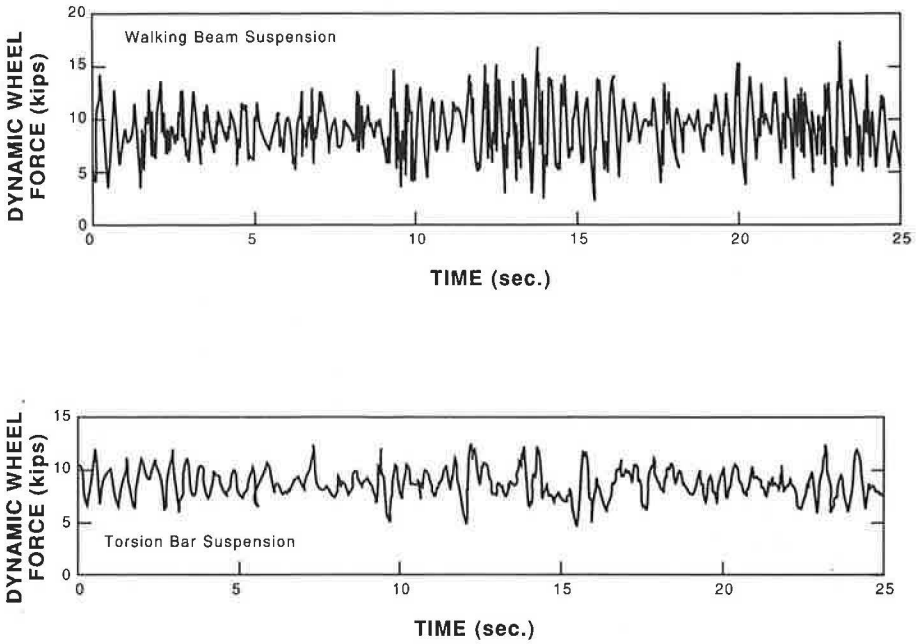


FIGURE 1 Typical instantaneous dynamic wheel force at 50-mph speed for medium road roughness (*1*).

moving vehicle is the sum of the static load or weight of the vehicle and the forces generated by the vertical movements of both sprung and unsprung masses. The force generated on the pavement is related to the vertical movement according to Newton's second law (force = mass × acceleration). Additional impact forces are also generated when tires lose pavement contact.

Figure 2 shows various movements of the sprung and unsprung masses of the truck. The sprung (suspended) mass develops three types of motion: bounce, pitch, and roll. The bounce is a simple up-and-down motion of the entire mass, whereas the pitch is an out-of-phase fore-and-aft bounce. The roll, which is relatively small, is an out-of-phase side-to-side bounce. In general, these motions are coupled, and an impulse at the front or rear wheels excites them. The motions occur at the natural frequency of the system, which is the frequency with which the system oscillates in the absence of external forces. The natural frequency of bounce oscillation for a heavy-duty vehicle at rated loads is about 1 to 2 Hz, whereas body pitch typically occurs at 6 to 7 Hz. These natural frequencies increase as the suspended mass is reduced by payload removal (*4*).

The unsprung mass also exhibits oscillatory behavior, but at a natural frequency that is somewhat higher than that of the sprung mass. In the case of a single axle suspension, two types of motion occur. The axle may bounce up and down, with its centerline parallel to the ground, or the axle ends may bounce out of phase with each other (tramp). In the case of a tandem axle suspension, a third vibration mode of interaxle pitch is possible. In this mode, the tire force is cyclically shifted fore and aft between the two axles. The presence of this interaxle pitch requires a coupling mechanism between the two axles. The natural frequency of axle bounce and interaxle pitching is in the range of 10 to 12 Hz. The extent to which these interaxle vibration modes predominate, or exist at all, is a function of the design of the suspension system (*4*).

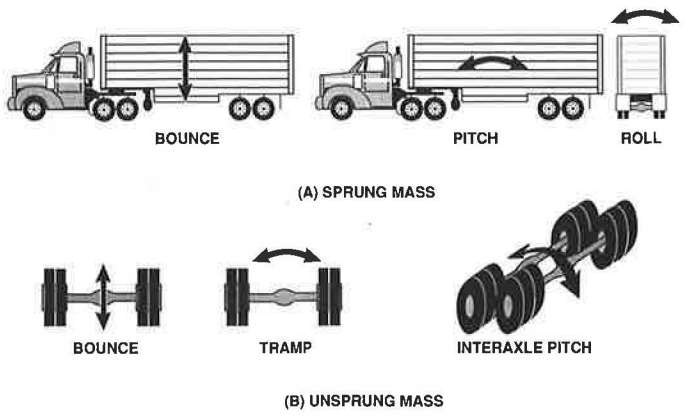


FIGURE 2 Movements of the sprung and unsprung masses.

SUSPENSION CHARACTERISTICS AND TYPES

The suspension is the mechanical system by which the axles of a truck or trailer are mounted on the vehicle chassis. The suspension is designed to achieve optimum load-carrying capacity, durability, stability and control, and ride quality, under service conditions that are determined by overall vehicle design, drive train and tire characteristics, cargo and operational usage, and road conditions (*5*). These design objectives are not necessarily optimum conditions for road performance. The following paragraphs discuss specific properties and types of suspension systems.

The suspension system consists essentially of a spring mechanism and a damping system. The springs are components of the suspension intended to absorb the energy of the vehicles' bumping over road surface irregularities. Several types of springs are used in truck suspensions. Steel leaf springs and air bags are the most popular. Flexible beams, torsion bars, and rubber and rubber-steel composite blocks are other common types. On the other hand, the damping system may include shock absorbers or other devices designed to dissipate (damp) the bouncing vibrations of the vehicle and springs, as well as rods, bars, or beams intended to transfer loads between adjacent axles and to stabilize the truck and trailer. Load transfer and dynamic behavior (vibrations and damping) are key to how axle suspensions influence pavement wear. These components work with the springs to give a suspension the operating qualities that make it suitable for particular uses.

A number of approaches have been developed over the years for meeting the diverse performance requirements of tandem and triaxle suspensions of heavy-duty trucks. These approaches can be grouped into four design categories that are representative of virtually all current production: the walking beam, the leaf spring, the air suspension, and the torsion bar. Different suspensions affect pavement performance differently, according to the way the load is transmitted to the truck axles. Also, the same suspension type can affect the pavement differently depending on whether it is a prime mover (tractor) suspension or a trailer suspension. This difference is caused by the tractive force produced between the tires of the tractor suspension and the pavement surface, which can transfer part of the load from one axle to the other. The following paragraphs summarize the main features of various suspension types and how they affect pavement (*4*).

Walking Beam Suspension

The walking beam suspension, shown in Figure 3a, is favored for its roll resistance, off-road performance, and equalization effectiveness and comprises a large, though diminishing, portion of the overall tandem suspension population. The dynamic pavement loading activity of the walking beam can be described as moderate to high over smooth and slightly rough roads and high over very rough roads. The walking beam suspension exhibits the largest dynamic loading of the four suspension types. Because there is so little damping at the walking beam, oscillation amplitudes can become high if road inputs are encountered at the natural frequency of interaxle pitch.

Leaf Spring Suspension (Four- and Six-Spring)

The leaf spring suspension is the most common heavy-duty suspension for on-highway vehicles, primarily due to its low cost, low weight, and low maintenance requirements (see Figure 3b). These features make the leaf spring particularly popular for use on trailers and converter dollies. For the most part, the behavior of the leaf spring is indicative of the behavior of any single-leaf suspension, such as that used almost universally as the front-axle suspension of heavy-duty vehicles.

The dynamic pavement loading activity of the leaf spring suspension can be described as moderate over most roads and is generally acknowledged to represent an improvement over the activity level of the walking beam suspension. The leaf spring suspension was the type used in the AASHO road test.

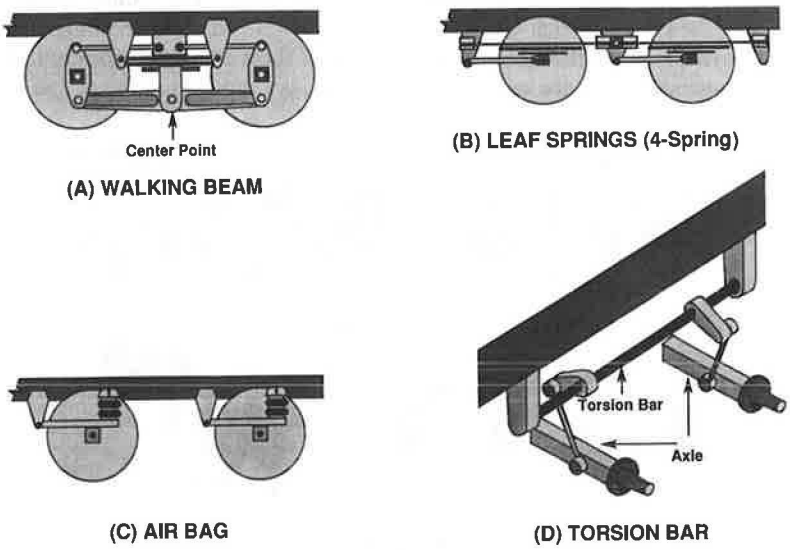


FIGURE 3 Common suspension types.

Air Suspension (Air Bag)

Although the air suspension, shown in Figure 3c, is often more expensive than the other suspension types, it has become increasingly popular in recent years because of its smooth ride and the protection afforded the cargo. The air suspension generally exhibits the least amount of dynamic loading activity of the four suspension types.

Torsion-Bar Suspension

The torsion-bar suspension, shown in Figure 3d, is used primarily in the western United States and Australia. Typically priced slightly higher than the four spring, the lightweight torsion-bar suspension generally provides the best ride offered by a mechanical suspension. However, it is not commonly used, principally because of its frequent lubrication requirements and high rebuild cost. Dynamic activity of the torsion bar is low to moderate and is generally acknowledged to be considerably lower than that of the four spring.

The percent shares of various suspension types on new trucks in the United States are presented in Table 1 (*5*).

TIRE TYPES AND PRESSURE

The tires used in the AASHO road test were predominately bias ply inflated to 75 to 80 psi cold inflation pressure, which was the standard practice and manufacturer's specification at the time. Currently, radial tires are common on heavy trucks, with typical pressures of 100 psi. Also, new tire designs, such as low-profile tires and wide-base single tires to replace dual tires, are gaining acceptance.

Tires are constructed with several layers of rubber and fiber. Older designs used natural or synthetic fiber cord wrapped on an angle with respect to the tire tread (i.e., on the bias). In radial tires, the ply is wrapped perpendicular to the tread direction. Both bias and radial tires may be reinforced with fiber belts of steel, glass, or other material wrapped generally parallel with the tread direction. Bias-ply tires accounted for almost the entire U.S. tire market until the 1970s, when European experience with improved wear, fuel economy, and road hazard resistance of radial tires began to have an impact (*6*).

A rapidly growing share of the tire market for long-haul highway trucks is being met by the newer low-profile tires, which have smaller diameters than regular tires. The main advantage of low-profile tires may be the reduction in vehicle height and the associated increase in trailer cubic capacity.

TABLE 1 PERCENT SHARES OF VARIOUS SUSPENSION TYPES ON NEW TRUCKS IN THE UNITED STATES

SUSPENSION TYPE	TRACTORS	TRAILERS
Walking Beam	15-25	<2
Leaf Spring	55-70	>80
Air Bag	15-20	10-15
Other	2-4	Nil

Some manufacturers have introduced single wide-base tires (super singles) to be used in place of dual tires or when higher loads are to be carried. The main advantage of wide-base tires is the improved fuel economy. Most wide-base tires in the United States are used on front drive axles of heavy hauler vehicles.

Tire inflation pressures maintain the tire's design profile and thus proper road contact under vehicle loading. Vehicle operations with improper tire pressures lead to excessive tire wear, particularly with radial tires, and influence vehicle handling characteristics. Too low a pressure at a particular load causes the tire to flatten out more and, in turn, causes added flexure and heat buildup in operation. Too high a pressure reduces contact area and stiffens the tire, increasing the risk of skidding and loss of breaking ability.

Higher tire pressure produces greater stress at the surface of the pavement, and highway engineers suspect that this effect is sometimes implicated in problems with wheelpath rutting on flexible pavement. Other characteristics of tires also influence the distribution of forces under the tires and, thus, may affect pavement wear.

VEHICLE-PAVEMENT INTERACTION

Knowledge of the interaction between trucks and roads is insufficient to provide the clear understanding needed to develop a completely mechanistic pavement design method. Over the years, the trucking community has supported basic research leading to the development of mechanistic models for truck dynamic behavior. Although much of this effort has focused on handling a braking behavior, the models provide a foundation for prediction of pavement loading produced by trucks (*7*).

Current mechanistic practice for pavement analysis and design oversimplifies the vehicle-pavement interaction process. In general, a constant-magnitude static wheel load is imposed on a multilayered elastic pavement system, and such critical responses as stresses and strains are computed. These critical responses are further related to pavement life using some empirical relations. Although this method of pavement analysis and design is much more sophisticated than purely empirical design approaches, the vehicle-pavement relationship is still considered a one-way relationship in which vehicles affect pavement but pavement does not affect vehicles.

Pavements and vehicles impose forces on each other through a process of progressive deterioration of the pavement surface because of applied loads. This pavement deterioration leads to excitation of axle suspensions and results in greater dynamic loads on the pavement surface. The process, therefore, is an accelerating one in which variations in pavement condition and vehicle load reinforce each other through time, becoming more significant as the pavement deteriorates further. Because this reciprocal imposition of forces is influenced both by pavement characteristics and by vehicle characteristics, both of these factors must be considered in a dynamic, or time-dependent, environment, along with other contributing factors, such as vehicle speed, in predicting the accumulation of pavement damage. The implication of this interactive process is that preservation of highway infrastructure can be managed not only through changes in pavement design, construc-

tion, maintenance, rehabilitation, and reconstruction, but also through control of vehicle dynamic loads by improving the characteristics of vehicles (*8*).

The study of vehicle-pavement interaction requires the following basic elements (*7*):

1. A mechanistic truck dynamic model that computes the dynamic vehicle loads applied on the pavement as a function of pavement roughness and vehicle characteristics.
2. A mechanistic pavement dynamic model that computes the dynamic pavement responses as a function of the dynamic vehicle loads and pavement geometric and material properties; and
3. A pavement deterioration model that relates the pavement responses to pavement damage.

The process can be simplified by developing a truck equivalency formula, which combines various truck properties that, in turn, can be related to pavement damage by an equivalent damage formula. Currently, an NCHRP project (*9*) is being performed to investigate these issues.

The term "dynamic load" indicates variable loading with time. A true dynamic model should also consider the inertia of the object. This principle can be applied to vehicles as well as to the pavement structure. In other words, there is a difference between the dynamic modeling of vehicles and that of pavements. A dynamic vehicle model could be used with a static pavement model or vice versa. An accurate analysis of the effect of vehicles on pavement should consider the dynamic response both of vehicles and of pavement as well as their interactions, such a model does not currently exist.

EFFECT OF ROUGHNESS, SPEED, AND TIRE PRESSURE ON DYNAMIC FORCE FOR VARIOUS SUSPENSIONS

A limited number of studies (*1*,*4*,*10*,*11*) have been performed to evaluate the dynamic force generated by various suspension types on the pavement surface. Two approaches can be used to measure the wheel dynamic force. The first approach is to attach sensors to the pavement surface in the wheelpath and to measure the actual load applied on the pavement. The shortcoming of this approach, however, is that the wheel force varies from one instant to another. Therefore, each pavement sensor does not provide a good representation of the variable load applied on the pavement surface but records a snapshot of the wheel load spectrum. The second approach for measuring the wheel dynamic force is to attach sensors to the truck axles. Although the latter method provides continuous recording of the dynamic force applied on the axle, the force is not the exact same force that is applied on the pavement surface. The difference between the axle force and the pavement force is a function of the stiffness of the tires, which introduces yet another element of dynamic load measurement variability.

A study to evaluate dynamic pavement loading characteristics was conducted by Sweatman (*1*). The study was sponsored by the Australian Road Research Board in response to a recommendation by the National Association of Australian State Road Authorities (NAASRA). In the study, a wheel force transducer was used to measure dynamic wheel loads in two- and three-axle groups for speeds ranging between 25 and 50 mph over road surfaces ranging from as-new construction to those exceeding the maximum desirable tolerable roughness. The effects of tire inflation pressure and axle group load were taken into account. All tires used in the study were tubeless, radial dual tires. A factorial experimental design was used to determine the dynamic loading expressed as a form of coefficient of variation, termed the "dynamic load coefficient" (DLC). Nine suspension types were tested, including five tandem drive axle suspensions and four trailer suspensions (two tandem groups and two triaxle groups). In addition to the DLC, the load-sharing performance of each suspension (or how uniformly the load is shared by various axles within the suspension group) was examined. Two replicate tests were performed for each factor combination.

In Sweatman's study (*1*), roughness was measured by the NAASRA roughness meter (*12*), which operates by summing positive rear-axle-to-body displacements in a standard station sedan traversing the road at traffic speed. Roughness is expressed in arbitrary units of counts per kilometer (or counts per mile).

Data extracted from the Sweatman study (*1*) were reanalyzed and plotted in Figures 4–7 to show the effect of road roughness, vehicle speed, and tire pressure on the dynamic force for various suspension types. The four figures show the response of a walking beam drive tandem axle, a leaf spring trailer axle, an air bag trailer tandem axle, and a torsion-bar drive tandem axle, respectively. The dynamic force on the pavement surface is expressed in terms of the DLC. The DLC is defined as the standard deviation of the wheel force distribution divided by the overall mean wheel force. Of course, the larger the variability of the dynamic force applied on the pavement, the larger the DLC.

As shown in the figures, the variability of the wheel force (DLC) increases with increasing road roughness and truck speed. However, changing the tire pressure from 70 to 100 psi did not significantly change the DLC value in most cases. A comparison of the four figures shows that the walking beam suspension has the largest dynamic load effect of the suspension types.

WEIGH-IN-MOTION

There are many variations of products on the market for weighing of highway vehicles in motion, offered by as many as 10 different vendors. Current technologies include strain gauge load cells, strain gauges on a beam, strain gauge bending plates, capacitance pads, capacitance strips and piezoelectric cables and films. Each of these is currently being tested or is in actual use; as of 1988, 46 states had or have had WIM systems. The technology has been developed for more than 40 years in the United States, and enhancements will probably continue for many years.

A great concern indicated by various highway agencies is that the WIM devices are not accurate enough because they do not duplicate the static weight (*13–15*). Also, the devices do not record the same weight under the same conditions; thus, the results are not repeatable.

According to the previous discussion on vehicle dynamics, the problem is not the accuracy of the WIM devices but, rather, how to interpret the WIM results. When a truck wheel

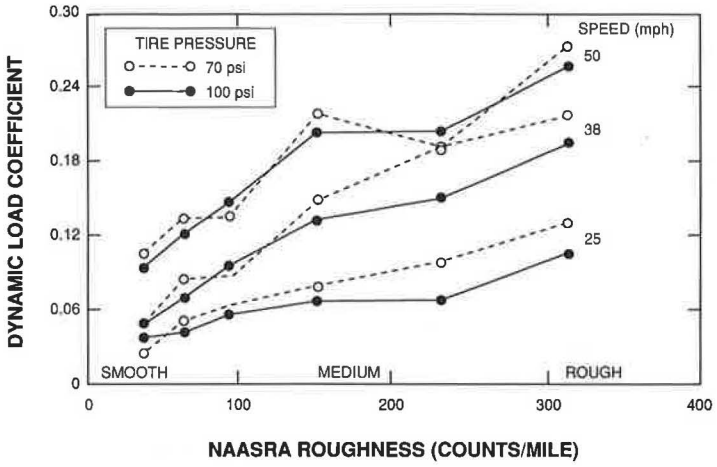


FIGURE 4 Effect of roughness, speed, and tire pressure on the dynamic load coefficient of walking beam suspension (*1*).

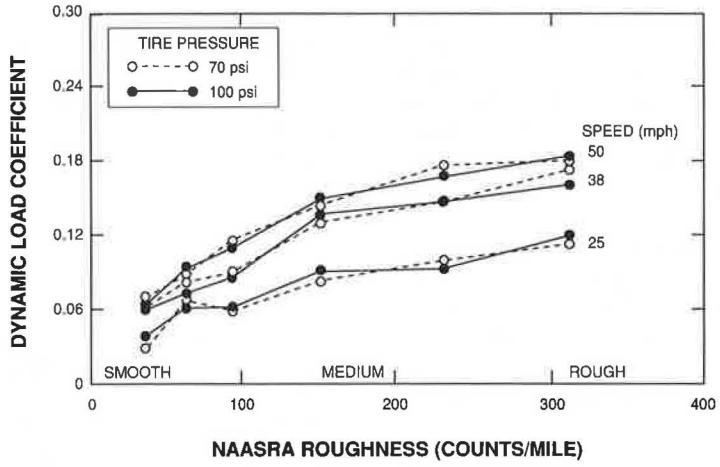


FIGURE 5 Effect of roughness, speed, and tire pressure on the dynamic load coefficient of leaf spring suspension (*1*).

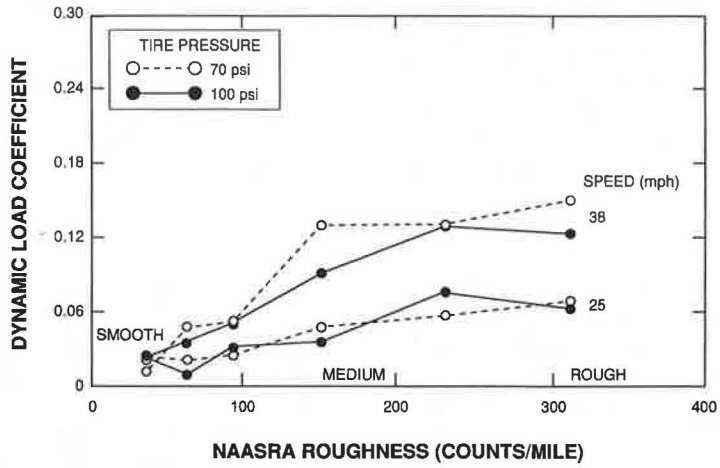


FIGURE 6 Effect of roughness, speed, and tire pressure on the dynamic load coefficient of air bag suspension (*1*).

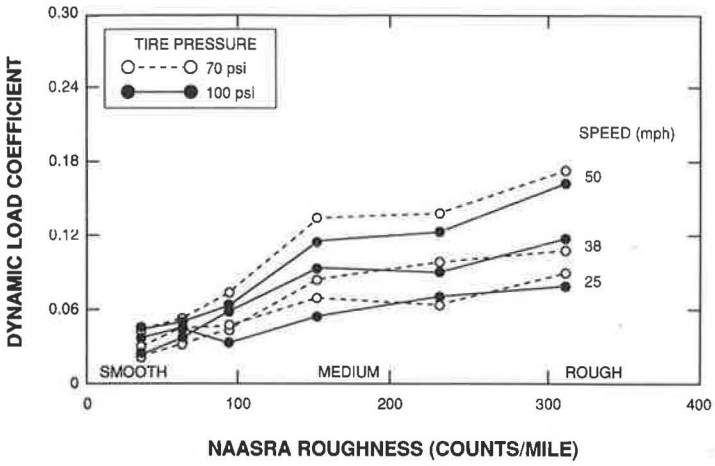


FIGURE 7 Effect of roughness, speed, and tire pressure on the dynamic load coefficient of torsion-bar suspension (*1*).

passes over any point on the pavement surface, this point feels a certain instantaneous dynamic force. Because the dynamic force applied by the truck wheel on the pavement surface varies instantaneously above and below the static weight, it would be a coincidence if the constant static and the variable dynamic readings matched. Therefore, the WIM device records the actual dynamic force that is applied at that instant of time, which is generally different than the static weight. This instantaneous force could be at the peak, at the lowest point, or at any point in between.

Of course, there could be some device errors, as with any other device. However, it is believed that most of the inconsistencies in results obtained by WIM devices are due to the dynamic effect. Thus, the difference between the WIM results and the static weight should not be viewed as error or inaccuracy but, rather, as the difference between dynamic and static effects.

MULTISENSOR WIM DEVICE

In order to measure the dynamic weight or to estimate the static weight from the dynamic weight, a multisensor device can be used rather than a single-sensor device. These sensors will obviously record different weights for the same moving wheel. If the number of these sensors is large enough, the average value of various sensor readings will usually give a good estimate of the static wheel weight. Also, the variance of various sensor readings will provide a good estimate of the variance of the dynamic forces. However, some deviations might result due to the effect of traction forces between tires and pavement and due to the effect of the geometry of the truck frame.

Glover (*16*) performed numerical simulation of multisensor WIM outputs with a variety of spacing arrangements. He concluded that a WIM System with nine evenly spaced sensors could yield a good estimate of the static load. Cebon (*17*) performed theoretical analysis and concluded that a WIM device with three evenly spaced sensors could provide a reasonable estimate of the static load. He indicated that the average value of the three sensor outputs provides reasonable accuracy for a wide range of speeds an dynamic loading frequencies. With such an arrangement, the theoretical coefficient of variation of the difference between static and dynamic weights can be reduced to 30 to 50 percent of the difference for a single-sensor WIM system. On the basis of the Cebon study (*17*), a portable WIM pad with three equally spaced capacitive strip transducers is being developed by Golden River Ltd. in the United Kingdom (*18*).

A NEW MULTISENSOR WIM APPROACH

Up to the present time, the objective of highway engineers has been obtaining an accurate static axle or wheel weight. This static weight is currently being used to enforce the legal load limit and to provide a basis for pavement analysis, truck taxation, penalty, and other truck regulations. Even the multisensor WIM concept proposed by Glover (*16*) and Cebon (*17*) is based on improving the WIM results to get values close to the static weight.

It should be realized, however, that the pavement does not "feel" the static weight of moving wheels but, rather, the instantaneous dynamic force. Thus, the rate of pavement deterioration is more correlated to the dynamic weight than the static weight. For example, two axles having the same static weight but different speeds or different suspension types, or driven on pavements with different roughnesses, will affect the pavement differently. The difference in effect increases with increasing truck speed and pavement roughness and varies with suspension type.

A new approach is suggested in which a multisensor WIM device is used to capture the dynamic force distribution generated by the truck wheel rather than averaging the dynamic readings to estimate the static weight. Also, the legal load limit, taxation, and penalties, as well as pavement design and analysis, could be a function of the dynamic wheel forces actually applied on the pavement rather than the static weight.

One of the difficulties of this new approach, however, is the separation between the dynamic effect caused by the truck due to such factors as the truck's static weight, suspension type, speed, and tire pressure and the dynamic effect caused

by the road roughness. Although pavement design, equivalency factors, and pavement performance analysis should consider both truck and pavement factors, truck taxation and penalties should be based on truck factors only. For example, truck companies cannot be penalized if the highway agency does not properly maintain the road. One possible solution to this problem is to develop adjustment factors for different road roughnesses and to base the truck taxation and penalties on a standard or typical pavement roughness.

To obtain the optimum number of sensors in a multisensor WIM device, statistical analysis of dynamic loading data could be performed. The objective of the statistical analysis is to compute the number of sensors required in a multisensor device to represent the dynamic wheel forces within a specified tolerable error with a reasonable confidence level. Of course, the larger the number of sensors, the more closely the dynamic forces can be represented. In other words, the larger the sample size, the more the population can be represented. On the other hand, the larger the number of sensors, the more expensive the WIM device.

Two statistical approaches can be used to compute the minimum number of sensors needed in a WIM device to represent various dynamic forces accurately. The first approach is to limit the maximum error in estimating the mean of the dynamic forces, whereas the second approach is to limit the maximum error in estimating the standard deviation of the dynamic forces. If the objective is to accurately estimate the static weight from the dynamic forces, only the first approach is needed. However, if the objective is to accurately represent various dynamic activities of the truck, both approaches are needed.

In this analysis, the dynamic forces of the truck are assumed to be normally distributed. In order to estimate the maximum amount of error in predicting the mean of the dynamic forces that corresponds to a certain number of WIM sensors, the following inequality can be used:

$$-\frac{sz_\alpha}{n^{1/2}} \leq \mu - \bar{x} \leq +\frac{sz_\alpha}{n^{1/2}} \tag{1}$$

where

μ = mean of the population of the dynamic forces (actual mean);
$\bar{x}$ = mean of the sample of the dynamic forces (estimated mean);
s = standard deviation of the sample of the dynamic forces (estimated standard deviation);
n = sample size (number of WIM sensors);
z_α = standardized normal deviate, which is a function of the desired confidence level; and
$100\ (1 - \alpha)$ = confidence level.

To estimate the maximum amount of error in predicting the standard deviation of the dynamic forces that corresponds to a certain number of WIM sensors, it can be assumed that the term $(n - 1)s^2/\sigma^2$ follows a X^2 distribution with $(n - 1)$ degrees of freedom. It follows that

$$s\left[\frac{(n-1)}{X_U^2}\right]^{1/2} \leq \sigma \leq s\left[\frac{(n-1)}{X_L^2}\right]^{1/2} \tag{2}$$

which implies that the ratio σ/s can be estimated as follows:

$$\left[\frac{(n-1)}{X_U^2}\right]^{1/2} \leq \frac{\sigma}{s} \leq \left[\frac{(n-1)}{X_L^2}\right]^{1/2} \tag{3}$$

where

σ = standard deviation of the population of the dynamic forces (actual standard deviation) and
X_U^2 and X_L^2 = upper and lower percentage points of the X^2 distribution, respectively, which are functions of the desired confidence level and degrees of freedom $(n - 1)$.

Data reported by Sweatman (*1*) have been used to estimate the optimum number of WIM sensors. Sweatman measured the dynamic wheel forces for different suspension types, truck speeds, tire pressures, and road roughnesses but did not explicitly report the means and standard deviations of various dynamic forces. Instead, two data parameters are reported: the DLC and the load sharing coefficient (LSC). The LSC was obtained by dividing the mean value for each wheel force distribution by the static wheel load (assuming equal load distribution between the wheels in the group). Thus, the LSC indicates the variations between the measured mean wheel force and its expected or desired value and is given by the following (*1*):

$$\text{LSC} = \frac{2n\bar{x}}{Mg} \tag{4}$$

where

n = number of axles in the group,
$\bar{x}$ = mean wheel force,
M = axle group mass, and
g = gravitational acceleration.

Using the LSC data reported by Sweatman (*1*), the mean wheel forces were computed according to Equation 4. Furthermore, the DLC is given by the following:

$$\text{DLC} = \frac{s}{\bar{X}} \tag{5}$$

where

s = standard deviation of the wheel force distribution and
$\bar{X}$ = overall mean wheel force (average of $\bar{x}$).

Equation 5 was used to compute the standard deviation of the dynamic wheel forces from the DLC and the overall mean wheel force ($\bar{X}$) values obtained in Equation 4.

Although data are provided by Sweatman (*1*) for both tandem and tridem axles, only tandem axles were used in the present study. Using Equation 1, the error in estimating the mean of the dynamic wheel forces associated with different numbers of WIM sensors was computed for four tandem-axle suspension types. Table 2 presents the error in estimating the means of the dynamic wheel loads for various numbers of sensors for 100-psi tire pressure at 95 percent confidence level. Figures 8–11 show the same results graphically for the walking

TABLE 2 MAXIMUM ERROR IN ESTIMATING THE MEAN OF THE DYNAMIC WHEEL LOAD FOR VARIOUS NUMBERS OF SENSORS FOR 100-psi TIRE PRESSURE AT 95 PERCENT CONFIDENCE LEVEL

SUSPENSION	ROUGHNESS*	SPEED (MPH)	ERROR(KIPS) FOR NO. OF SENSORS **				
			1	3	5	7	9
WALKING BEAM	Low	25	0.5	0.3	0.2	0.2	0.2
		50	1.2	0.7	0.6	0.5	0.4
	High	25	1.4	0.8	0.6	0.5	0.5
		50	3.4	1.9	1.5	1.3	1.1
LEAF SPRING	Low	25	0.5	0.3	0.2	0.2	0.2
		50	0.9	0.5	0.4	0.3	0.3
	High	25	1.7	1.0	0.8	0.6	0.6
		50	2.6	1.5	1.2	1.0	0.9
AIR BAG	Low	25	0.3	0.2	0.1	0.1	0.1
		50	–	–	–	–	–
	High	25	0.9	0.5	0.4	0.3	-.3
		50	–	–	–	–	–
TORSION BAR	Low	25	0.6	0.3	0.3	0.2	0.2
		50	0.7	0.4	0.3	0.3	0.2
	High	25	1.4	0.8	0.6	0.5	0.5
		50	2.7	1.6	1.2	1.0	0.9

*Low and high correspond to NAASRA roughness meter readings of 35 and 312 counts/mile, respectively.

**All errors are positive or negative.

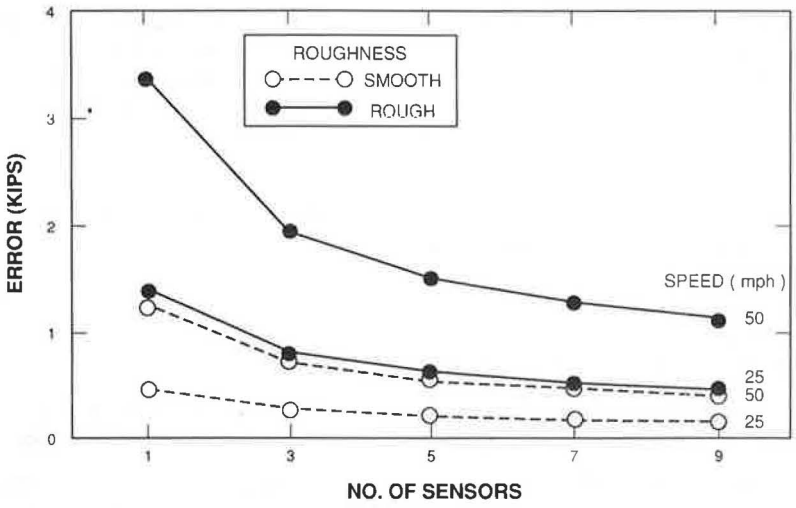


FIGURE 8 Maximum error in estimating the mean of the dynamic wheel load for walking beam suspension for 100-psi tire pressure at 95 percent confidence level.

beam, leaf spring, air bag, and torsion-bar suspensions, respectively.

Figures 8–11 show that the maximum error in estimating the mean of the dynamic wheel force decreases with an increase in the number of sensors. This conclusion is valid for various suspension types, roughnesses, and speeds. The largest reduction in error in estimating the mean of dynamic forces is obtained by increasing the number of sensors from one to three. Increasing the number of sensors more than three does not considerably reduce the error. For example, for the walking beam suspension, high roughness, and 50-mph speed, the maximum error for one, three, five, seven, and nine sensors decreases from ±3.4 to ±1.9 to ±1.5 to ±1.3 to ±1.1 kips, respectively.

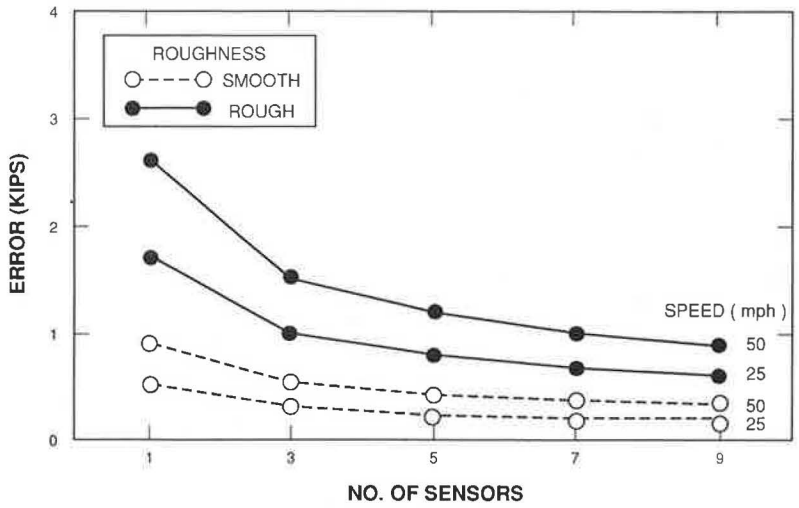


FIGURE 9 Maximum error in estimating the mean of the dynamic wheel load for leaf spring suspension for 100-psi tire pressure at 95 percent confidence level.

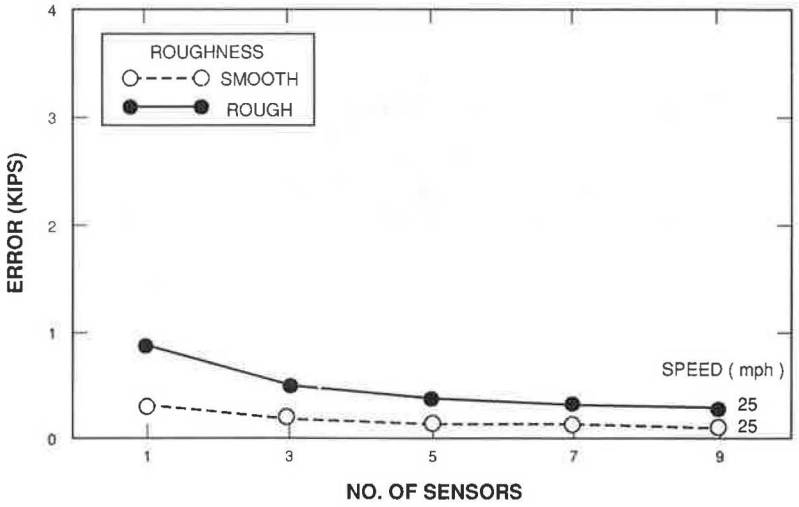


FIGURE 10 Maximum error in estimating the mean of the dynamic wheel load for air bag suspension for 100-psi tire pressure at 95 percent confidence level.

Figures 8–11 also show that the maximum error in estimating the mean of the dynamic wheel load using a specific number of sensors varies with roughness, speed, and suspension type. As expected, this error increases with increasing roughness or speed, or both. The air bag suspension results in the smallest maximum error even at high speeds because of its small dynamic movements.

Using Equation 3, the maximum and minimum ratios between the actual standard deviation (σ) and the measured standard deviation were completed for various numbers of sensors at a 95 percent confidence level, as presented in Table 3. The minimum and maximum ratios are not reciprocals. Also, these ratios are the same for different suspension types, roughnesses, and speeds because they are not affected by the actual means or standard deviations. Figure 12 shows the ratios between the actual and estimated standard deviations for various numbers of sensors at a confidence level of 95 percent.

In Table 3 and Figure 12, when the number of sensors in a WIM device increases, the actual and estimated (measured) standard deviations approach each other more closely. For example, when the number of sensors is three, the ratio between the actual and estimated standard deviations varies between 58 and 442 percent, whereas this ratio varies between 72 and 171 percent when the number of sensors is nine. However, increasing the number of sensors by more than five does not considerably reduce the error in estimating the standard deviation. Also, the upper limit of the actual and estimated standard deviations is farther than one from the lower limit. This difference indicates that, when using a specific number of sensors, the chance of underestimating the actual standard deviation is larger than the chance of overestimating the actual standard deviation.

Comparing Figure 12 with Figures 8–11, the errors in estimating the standard deviation are larger than the errors in estimating the mean for the same number of sensors. This

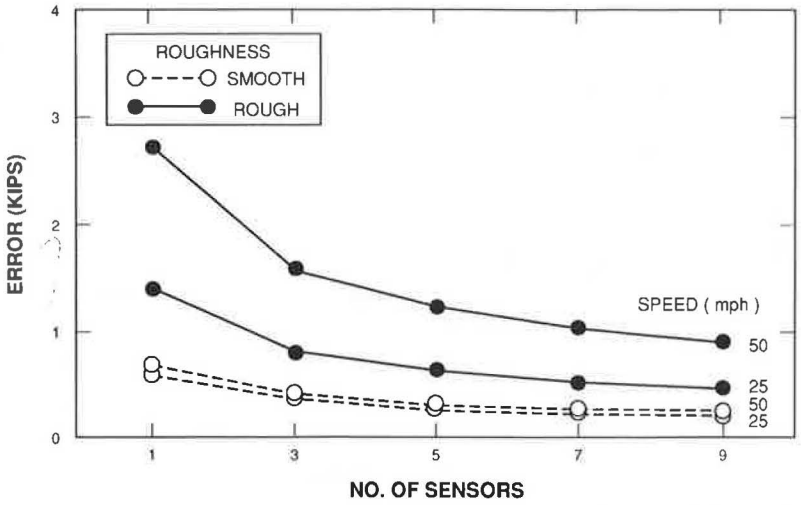


FIGURE 11 Maximum error in estimating the mean of the dynamic wheel load for torsion-bar suspension for 100-psi tire pressure at 95 percent confidence level.

TABLE 3 MAXIMUM ERROR IN ESTIMATING THE STANDARD DEVIATION OF THE DYNAMIC WHEEL LOAD AT 95 PERCENT CONFIDENCE LEVEL

NO. OF SENSORS	ACTUAL/ESTIMATED STANDARD DEVIATIONS	
	MINIMUM	MAXIMUM
1	N/A*	N/A
3	0.58	4.42
5	0.65	2.37
7	0.69	1.92
9	0.72	1.71

*N/A = not applicable

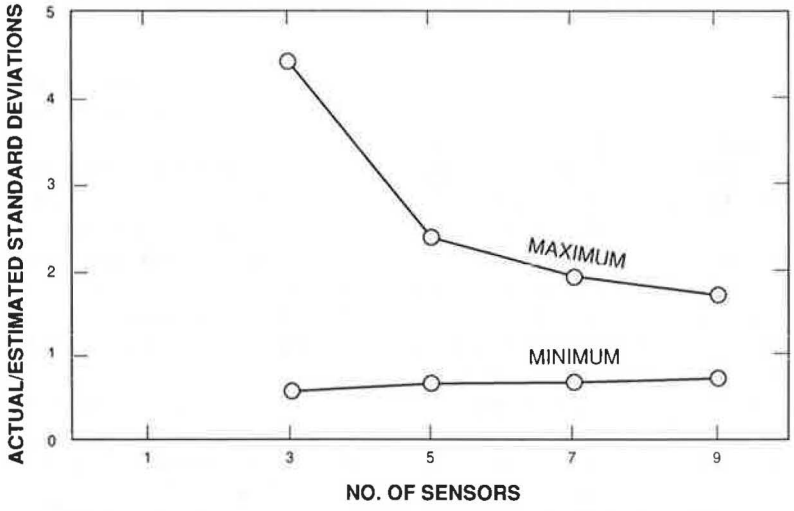


FIGURE 12 Maximum error in estimating the standard deviation of the dynamic wheel load at 95 percent confidence level.

finding means that a larger number of sensors is required in a WIM device to accurately estimate the standard deviation than the number required to accurately estimate the mean.

WHEEL VERSUS AXLE DYNAMIC LOADS

The wheel load is defined here as a dual wheel on one side of an axle. All data reported have been for tandem axles. The extrapolation of the dynamic axle weight from the dynamic wheel weight is not straightforward due to the dynamic movements of the sprung and unsprung masses reported previously (see Figure 2). In cases with only vertical bounce of sprung and unsprung masses, the instantaneous dynamic weight of a single axle is double the dynamic wheel weight at the same instant of time, assuming that the wheels at the two ends of the axle have equal static weights. However, if the sprung mass is rolling or the unsprung mass is subjected to tramp movement, or both, the instantaneous weights of wheels on the two sides of the axle are different. By the same token, the pitch movement of the sprung and unsprung masses changes the instantaneous weights between the axles. Moreover, the summation of the weights of all wheels at the same instant of time does not necessarily equal the gross weight of the truck, because of various movements of sprung and unsprung masses.

SUMMARY AND CONCLUSIONS

The load applied by trucks on the pavement structure varies from one instant of time to another. This variation in the dynamic load is largely affected by road roughness, truck speed, and suspension type and to some extent by tire pressure. For example, previous studies indicate that the instantaneous truck wheel load can vary from 25 to 175 percent of the static wheel load for walking beam suspension at 50 mph on medium-roughness roads.

WIM devices provide weights different than the static weight because of the instantaneous variations in the dynamic weight. Current WIM devices are one-sensor devices that provide a snapshot of the dynamic load spectrum. Thus, they do not fully represent the dynamic activity of the vehicle wheel load. Multisensor WIM devices are more capable of representing the actual wheel load distribution. The larger the number of sensors in a WIM device, the larger the accuracy in representing the dynamic load spectrum. Multisensor WIM devices can be used to estimate both the mean and the standard deviation of the dynamic wheel forces applied by the tires on the pavement. A larger number of sensors is required to accurately estimate the standard deviation than the number required to accurately estimate the mean. Also, the chance of underestimating the actual standard deviation is larger than that of overestimating the actual standard deviation.

Pavement performance is affected by dynamic loads more than by static loads. It is therefore recommended that the legal load limit, taxation, and penalties, as well as pavement design and analysis, could be better controlled in terms of the dynamic wheel forces actually applied on the pavement rather than the static weight. The dynamic wheel forces can be represented by the average and the standard deviation of the dynamic forces. Also, FHWA could have more influence on truck manufacturing with regard to suspension type and other vehicle characteristics to ensure slow pavement deterioration. These suggestions, however, need further refinement and research to provide the proper implementation procedure and to separate the dynamic forces caused by truck factors and road factors.

REFERENCES

1. P. F. Sweatman. *A Study of Dynamic Wheel Forces in Axle Group Suspensions of Heavy Vehicles*. Special Report 27. Australian Road Research Board, Australia, June 1983.
2. C. G. B. Mitchell and L. Gycnes. Dynamic Pavement Loads Measured for a Variety of Truck Suspensions. *Proc., 2nd International Conference on Heavy Vehicle Weights and Dimensions*, Kelowna, British Columbia, June 1989.
3. J. H. F. Woodrooffe, P. A. LeBlanc, and K. R. LePiane. Effects of Suspension Variations on the Dynamic Wheel Loads of a Heavy Articulated Highway Vehicle. In *Vehicle Weights and Dimension Study*, Vol. 11, Conroad Transportation Research Corporation, Canada, 1986.
4. *Effect of Heavy Suspension Design on Dynamic Pavement Loading*. Western Highway Institute, San Bruno, Calif., June 1989.
5. J. R. Morris. *Effect of Heavy Vehicle Characteristics on Pavement Response and Performance—Phase I*. Prepared for NCHRP, TRB, National Research Council, Washington, D.C., Aug. 1987 (rev. Dec. 1987).
6. M. Wisla. Trends for Tires. *Fleet Equipment*, Vol. 13, No. 2, Feb. 1987.
7. T. D. Gillespie. Modeling Truck Dynamic Loads. Presented at FHWA Load Equivalency Workshop, McLean, Va., Sept. 1988.
8. E. J. Barenberg. Role of Instrumented Pavements in Establishing Load Equivalencies. Presented at FHWA Load Equivalency Workshop, McLean, Va., Sept. 1988.
9. *Effects of Heavy Vehicle Characteristics on Pavement Response and Performance—Phase II*. Proposal for NCHRP Project 1-25(1). University of Michigan, Ann Arbor, Feb. 1988.
10. J. B. Sousa et al. Effects of Dynamic Loads on Performance of Asphalt Concrete Pavements. In *Transportation Research Record 1207*, TRB, National Research Council, Washington, D.C., 1988.
11. T. Papagiannakis et al. Effects of Dynamic Loads on Flexible Pavements. In *Transportation Research Record 1207*, TRB, National Research Council, Washington, D.C., 1988.
12. J. Stevenson. *A Study of the Economics of Road Vehicle Limits: Pavements*. NAASRA ERVL Study Team Report T4. National Association of Australian State Road Authorities, Australia, 1976.
13. P. Davies and F. Sommerville. Calibration and Accuracy Testing of Weigh-in-Motion Systems. In *Transportation Research Record 1123*, TRB, National Research Council, Washington, D.C., 1987.
14. B. Izadmehr and C. E. Lee. Accuracy and Tolerances of Weight-in-Motion Systems. In *Transportation Research Record 1123*, TRB, National Research Council, Washington, D.C., 1987.
15. B. Izadmehr and C. E. Lee. On-Site Calibration of Weigh-in-Motion Systems. In *Transportation Research Record 1123*, TRB, National Research Council, Washington, D.C., 1987.
16. M. H. Glover. *Weighing Axles in Motion with a Multiple Sensor System*. Working Paper WP VED/88/50. Transport and Road Research Laboratory, Crowthorne, England, 1988.
17. D. Cebon. Design of Multiple-Sensor Weigh-in-Motion Systems. *Proc., International Conference of Mechanical Engineering*, Part D, August 1989.
18. D. Cebon and C. D. Winkler. Multiple-Sensor Weigh-in-Motion: Theory and Experiments. Presented at 70th Annual Meeting of the Transportation Research Board, Washington, D.C., 1991.

Publication of this paper sponsored by Committee on Flexible Pavement Design.

Model Tests for Moving-Load Effects on Pavements

RAJ SIDDHARTHAN, A. ANOOSHEHPOOR, AND JON A. EPPS

Three-layer foam rubber models were subjected to moving loads at different speeds. The response is reported in terms of displacements in three pavement sections, representing both thin and thick surface layers and bottom layers. The model tests provided high-quality data against which the validity of different numerical codes that can model moving-load effects on the pavement can be verified. The recorded response reveals that the shape of the vertical displacement pulse is substantially affected by the speed of the moving load. Among the three models tested, the most inflexible model indicated that the amplitude of the response is unaffected by the speed of the moving load. With more flexible models, a substantial reduction in displacement amplitude occurs for points located deeper below the surface. A close examination of the vertical displacement pulse shape suggests that the pulse is much narrower than that given by a Haversine function.

Emphasis in pavement design practice has been shifting in recent years from the use of empirical design approaches to more rational means of determining the structural requirements of pavements. The new design guidelines proposed by agencies such as AASHTO reflect this shift. These more rational methods are often referred to as mechanistic design procedures, in which pavement performance is estimated on the basis of fundamental properties of the pavement layers. The widely used pavement performance models, such as fatigue cracking of asphalt concrete and rutting, require a knowledge of stresses and strains induced by the vehicular loading on the pavement (*1–3*).

Pavement stresses and strains are often computed using layered elastic pavement material properties (*4,5*). In the last decade or so, more rational pavement material characterization models have been proposed (*6–8*). These approaches consider stress-dependent material properties and the effects of the development of failure conditions in the unbound materials. However, all of these models represent vehicular loading as static loading. The vehicular loading is essentially dynamic; therefore, dynamic effects such as inertia and resonance can be important.

Full-scale pavement testing and in situ instrumentation have received considerable attention in the past. Recently, a study has been completed under a contract from FHWA (*9*). Similar studies can provide such information as (a) in-situ pavement response to verify mathematical models, (b) mechanistic design procedures for pavement design, and (c) an estimate of in situ material properties under a variety of environmental and loading conditions. Though such studies provide valuable results, they are expensive and time-consuming.

Response results obtained by subjecting three-layer foam rubber models (representing a typical pavement section) to a moving load are presented. The main aim of this model test is to obtain a data base that can be used to verify mathematical models that predict pavement response to moving loads. Foam rubber models have been used successfully in engineering studies of soil-structure interaction, topographical effects during seismic excitation, and fault plane rupture propagation. Foam rubber (polyurethane) is inexpensive and lightweight and exhibits a considerable range in density and stiffness. The advantages of using foam rubber for the modeling of pavement structures are presented in the following section.

University of Nevada, Reno, Nev. 89557-0030.

USEFULNESS OF PHYSICAL MODEL STUDIES

Although a more rational material characterization is being adopted, the loading conditions currently modeled are not representative. The moving vehicular load is represented as a static axisymmetric load. As a vehicle approaches a point in a pavement, that point experiences an increase in vertical stress, which reaches a maximum when the wheel is directly over the point and then decreases as the vehicle moves away. The vertical stress variation depends mainly on the speed of the vehicle, its tire pressure, and the pavement layer properties. Instrumented road tests reveal that typical vehicle-induced vertical stress pulses (dynamic) are bell shaped and have a duration of around 120 msec for a vehicle traveling at 50 mph (*9–11*).

Physical modeling has been used to study numerous engineering problems. A physical model acts as an analog that automatically accounts for such factors as the diffraction, reflection, refraction, and conversion of waves (e.g., conversion of SV-wave to P-wave at boundaries) when waves created by the moving load interact with the different layers. It is necessary to make a number of assumptions in all analytical and numerical codes when studying the pavement response to a moving load. The factors mentioned are not all adequately modeled in these codes. However, the validity of the available codes can be verified using the results obtained from the model tests. The study of physical models can also lead to physical insights that may not be evident from computer modeling or theoretical calculations. Other benefits from physical modeling include (a) the ability to model a complex layering pattern and such boundary conditions as approach fills in bridges and (b) the three-dimensional effects that can reveal such phenomena as unexpected resonances and coupling.

In principle, the induced dynamic loads from a moving vehicle can be simulated using the finite element method. However, such an approach will, without doubt, be involved and time-consuming. In finite element studies, the boundaries have to be defined sufficiently far away from the region of interest, and the discretization (especially in the case of the

moving load) should be very fine. Recently, Siddharthan (*12*) proposed a new method of analysis to study the response of horizontally layered medium to traveling surface pressure loads. This computationally efficient method is based on an existing methodology for the study of deposits subjected to offshore wave loading (*13*). In this analytical method, the layers are treated as a continuum that extends to infinity in the lateral direction. The rigid bottom layer can be located at a finite depth from the surface. The response data obtained from the model study reported here can be used to verify the applicability of this method of analysis and the finite element method. Such verification studies can be undertaken relative either to the model itself or to the corresponding prototype.

Full-scale testing on instrumented pavements can yield a wealth of pavement response data. However, the recorded response will be the net effect of a variety of factors, such as pavement layer thicknesses, vehicle speeds, types of tire design, tire pressures, and environmental conditions. Furthermore, the influence of material properties of unbound materials (nonlinear, stress-dependent) as well as the viscoelastic properties of the asphalt concrete will also be present. In other words, it is impossible in such studies to isolate the effects of one factor (e.g., the vehicular load moving at different speeds). Such a task is achieved in the model test described here. The foam rubber exhibits linear elastic material properties in the range of stresses used in the test, and surface loading is simulated using a long cylinder that can be moved at different speeds. This loading provides a good representation of plane strain conditions under the cylinder. Therefore, a two-dimensional plane strain model is sufficient to predict the model response. If a moving circular load is used to simulate loading, a complete three-dimensional finite element model involving an exorbitantly larger computational cost is necessary.

The light weight and low rigidity of foam rubber lead to modeling frequencies in the audio range, whereas with more rigid materials, the frequencies are often in the megahertz range. Because it is soft, foam rubber can be cut and shaped easily. The bonding of different foam rubber layers can be accomplished with rubber contact cement. The attenuation properties of foam rubber correspond to a quality factor Q of about 10 (damping coefficient of 5 percent), which is comparable to the Q values expected for earth materials near the surface.

A number of seismic response studies have reported using foam rubber. Such studies include (a) wave propagation resulting from stick-slip fault movement (*14*), (b) sedimentary basin and topographical effects on earthquake wave propagation (*15*), (c) behavior of the Pacoima Dam during the 1971 San Fernando earthquake (*16*), and (d) seismic behavior of a one-quarter power plant that was constructed in Taiwan and has been excited by earthquakes (*17*). These studies have clearly demonstrated the usefulness of foam rubber in the modeling of layers of different stiffnesses and in dynamic problems.

DESCRIPTION OF THE MODEL TESTS

Model Construction

Typical pavement sections have three layers: asphalt concrete, granular base, and subgrade. The stiffness and density of these layers vary. Figure 1 shows three pavement layer models constructed using foam rubber. The surface and bottom layers are the stiffest and softest, respectively. The layer thicknesses and properties of the layers are presented in Table 1. The three foam rubber materials were selected such that the stiffness and density ratios between the layers represent typical field pavement layer values. Model 1 was constructed by gluing together the three foam rubber blocks in thicknesses of 4.0, 10.2, and 51.0 cm. The glue (rubber contact cement) leaves a strong but flexible glue line. The foam layer thickness ratios for the three models are typical of different pavement sections. In the plan, the layers form a 2.5-m × 2-m rectangle. The three layers rest on a rigid concrete floor.

Model 2 was constructed by gluing an additional 2.5-cm surface layer thickness to Model 1. Finally, Model 3 was obtained by gluing an additional 50 cm of the bottom layer to Model 2.

Instrumentation and Loading

Figure 2 shows an isometric view of the model resting on the floor. In all tests, the models were instrumented to measure displacement at three points, referred to as A1, B2, and A3. Points A1 and A3 are located along Section A-A in the surface and bottom layers, respectively. Point B2 lies along Section B-B and is located in the middle layer. The displacement recording setup uses small light-emitting diodes (LEDs), which have to be monitored through detectors. Additional information on the recording system is presented subsequently. The space required for the detectors along Section A-A did not permit the location of an LED in the middle layer. Thus, the LEDs were located within the foam rubber along the centerline of the moving path. This placement was achieved by coring out small pieces of foam rubber at Locations A1, B2, and A3 and gluing LEDs to the interior of the model.

The displacement at any LED location can be measured using two-axis optical position-sensing detectors that are focused on the LED embedded in the foam. The sensor (PIN-SC/40 by United Detector Technology, Inc.) is a square of photovoltaic material, approximately 2.5 mm on each side,

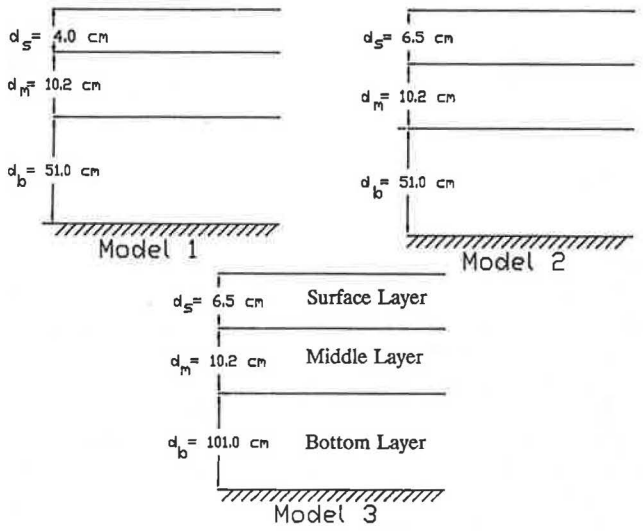


FIGURE 1 Three foam rubber models.

TABLE 1 MODEL LAYER THICKNESSES AND PROPERTIES

		Surface Layer	Middle Layer	Bottom Layer
Layer Thickness (cm)	Model 1	4.0	10.2	51.0
	Model 2	6.5	10.2	51.0
	Model 3	6.5	10.2	101.0
Layer Stiffness (kN/m^2) (Young's Modulus)		348.9	47.9	9.5
Layer Density (kg/m^3)		24.0	17.6	16.0
Poisson's Ratio		0.4	0.4	0.4

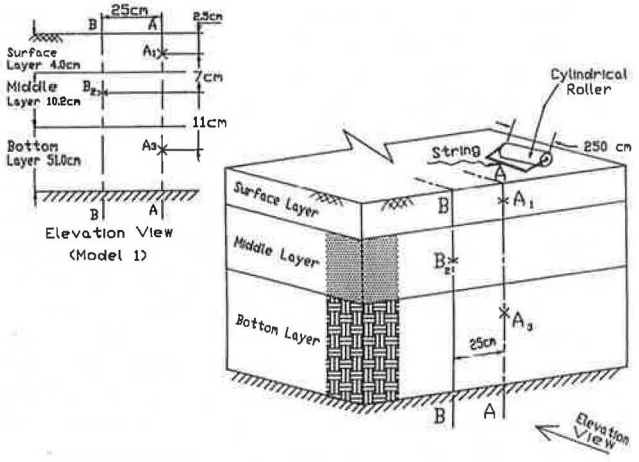


FIGURE 2 View showing instrumentation (Model 1).

to which five leads are attached—one to the center and one to each of the four sides. This sensor provides a continuous output as the LED location moves from the initial focus point to either direction along each of the two perpendicular axes. The size and shape of the LED image are not critical as long as the image remains on the active surface of the detector. Differential amplifiers are connected to sensor leads, and they provide the horizontal X and vertical Y displacement outputs that are recorded on a transient digitizer. The gain of the amplifiers is about 500, and it is independent of the frequency up to a value of 10 kHz.

The data-logging system consists of a Compaq computer, a Tecmar Labmaster analog-to-digital (A/D) converter, and an 8087 coprocessor to increase the speed of math calculations. The system is capable of recording transient signals on up to eight channels. The records are converted to 12-bit digital words and may be sampled at rates of $17/n$ Khz, where n equals the number of channels. After every test, the results can be displayed graphically, and the records can be stored on floppy disks for future analysis.

The signal-to-noise ratio varies with the intensity of the LEDs and the distance between the LED and the sensor. One way to reduce the noise is to use high-intensity LEDs. The LEDs used in the study are among the brightest; however, the sensing devices have a large impedance and, thus, can pick up noise caused by other electronic devices in the laboratory. Four pole Butterworth (low-pass, dc-coupled) filters with a cutoff frequency of about 750 Hz were introduced between the output of the amplifiers and the input of the A/D converter. More details on the instrumentation and calibration of the recording system are presented by Anooshehpoor (*18*). The instrumentation was found to be capable of measuring displacement to within approximately 0.13 mm.

The moving load is simulated using a hollow, cylindrical steel drum, identical to the one used in the Vialit test (*19,20*). The Vialit test has been proposed to study the adhesiveness of asphalt cement in the retention of chip seal aggregate. The drum is 25 cm in diameter and 25 cm in length and has a handle by which it can be rolled or pulled. The exterior surface of the cylinder is covered with a smooth canvas. The weight of the cylinder can be increased by filling the hollow portion with sand or water. As explained in the following section, the horizontal displacement response of the model is small compared with the vertical response. To increase the signal-to-noise ratio (especially the horizontal displacement), it was necessary to have a substantial weight for the cylinder. However, this requirement was not considered a problem because the model is linear and, thus, displacements corresponding to lower loads could be obtained using linearity. The total weight of the cylinder is 14.44 kg, and the contact area it makes on the top layer is 38 × 250 mm, giving a uniform contact pressure of approximately 14.9 kN/m^2.

No attempt was made to run the tests at a specified speed. Tests were carried out over three ranges of speed: slow, medium, and fast. The speed between any two tests in a given

range was not identical. The speed of rolling was estimated from the time it took the cylinder to travel between Section A-A and Section B-B.

RESULTS OF THE MODEL TESTS

The responses recorded were the Y displacements at A1, B2, and A3 and the X displacement at B2. The typical measured responses in Model 1 at Points A1 (vertical displacement) and B2 (horizontal displacement) for a slow speed of rolling are shown in Figures 3a and 3b, respectively. The speed of rolling was 41.7 cm/sec. As expected, the vertical responses displayed a pulse shape. On the other hand, the horizontal displacement response was quite small and was significantly affected by the noise. Consequently, the horizontal displacement results should be viewed with skepticism. The discussion of the results only considers the vertical response. For comparison, the vertical response at three different speeds is shown in Figure 4 for Point A1. The response histories have been shifted along the time axis so that they appear together. The medium and fast speeds are approximately 73.5 and 138.9 cm/sec, respectively.

The figures reveal that the shape of the pulse is substantially affected by the speed of rolling. The rate of displacement increases with the speed; at the fast speed, the pulse is essentially a sharp spike. The duration of the pulse, t_f (see Figure 3a), is directly influenced by the speed of rolling. The time during which the roller remains directly above the point of measurement is much smaller for the fast speed. Correspondingly, the pulse width is also smaller for this case. The amplitude of the vertical response does not seem to be affected for slow and medium speeds. The trend is a reduction in amplitude as the speed of rolling increases. The reduction at A1 at fast speed compared with the value at slow speed is within 10 percent. For the higher speed, the response is substantially smaller than the corresponding values at slower speeds, especially in the bottom layer (A3). The reduction at A3 is as much as 36 percent. The amplitude and duration of the pulse obtained with all models are presented in Table 2. Altogether, there are three models (Model 1, Model 2, and Model 3) and three tests (three different speeds), giving a total of nine tests. An estimation of the duration of the pulse for the horizontal response was not possible.

The amplitude of vertical displacement is substantially reduced when an additional surface layer is added (Model 2) and increases when an additional bottom layer is included

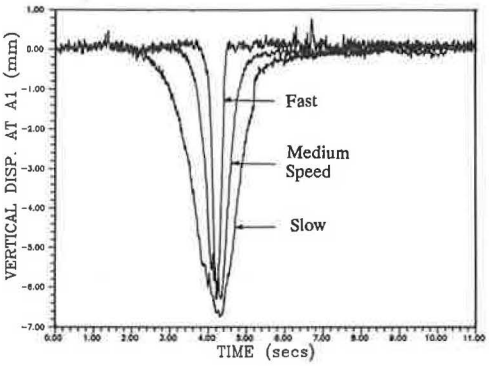


FIGURE 4 Vertical displacement of Model 1 at A1 for all three speeds.

(Model 3). For Model 2, in which a thick surface layer is present, there is virtually no change in displacement at different speeds of rolling. However, for Model 3, in which the flexibility of the model is increased with the addition of a piece to the bottom layer, the influence of speed can again be seen. In Model 3, the reduction in displacement between the fast and slow speeds of rolling is within about 8 percent at Point A1.

Dynamic effects such as inertia and damping are present due to the dynamic loading conditions generated by the moving load. When the speed of movement is very slow, static loading conditions prevail. Therefore, a change in the response associated with the change in the speed of rolling is a measure of the dynamic effects. Among the three models tested, Model 2 is the stiffest. In this model, the amplitude of the vertical displacement is unaffected by the speed of rolling. On the other hand, the influence of dynamic loading is present with the other, more flexible models.

The vertical displacement histories for A1 at all speeds of rolling for Models 2 and 3 are shown in Figures 5a and 5b, respectively. Figure 5a reveals that, although the amplitude is unaffected by the speed of rolling, the pulse shape appears to be different. At higher speeds, the pulse shape is squeezed to reflect the shorter duration of the load pavement above the point of interest. A more detailed discussion of the pulse shape is presented subsequently.

Figure 6 shows the vertical displacement response recorded at A1 for all three models at the slow speed of rolling. This figure can lead to a wrong interpretation that the pulse shape for Model 3 is substantially different from that of the other

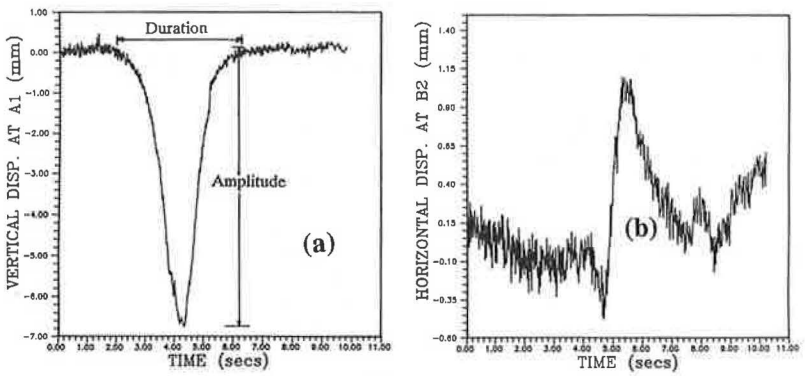


FIGURE 3 Typical response of Model 1 for slow speed: (a) vertical displacement at A1; (b) horizontal displacement at B2.

TABLE 2 RESULTS FOR ALL MODEL TESTS

MODEL #	TEST #	SPEED OF ROLLING (cm/s)	DISPLACEMENT COMPONENT	AMPLITUDE (mm)	PULSE DURATION t_f (secs.)
Model 1	Test 1	41.7 (slow)	Vertical at A1	6.9	4.2
			Vertical at B2	6.6	4.0
			Vertical at A3	3.9	4.2
			Horizontal at B2	1.0	---
Model 1	Test 2	73.5 (medium)	Vertical at A1	6.6	2.0
			Vertical at B2	6.3	1.9
			Vertical at A3	3.7	1.9
			Horizontal at B2	0.7	---
Model 1	Test 3	138.9 (fast)	Vertical at A1	6.2	0.9
			Vertical at B2	6.1	1.0
			Vertical at A3	2.5	1.0
			Horizontal at B2	1.1	---
Model 2	Test 4	41.7 (slow)	Vertical at A1	4.4	4.3
			Vertical at B2	3.4	4.2
			Vertical at A3	2.2	4.0
			Horizontal at B2	1.4	---
Model 2	Test 5	65.8 (medium)	Vertical at A1	4.3	3.0
			Vertical at B2	3.4	2.5
			Vertical at A3	2.3	3.3
			Horizontal at B2	1.4	---
Model 2	Test 6	104.2 (fast)	Vertical at A1	4.2	1.6
			Vertical at B2	3.4	1.7
			Vertical at A3	2.2	1.8
			Horizontal at B2	1.5	---
Model 3	Test 7	29.8 (slow)	Vertical at A1	6.8	6.7
			Vertical at B2	6.1	6.2
			Vertical at A3	4.8	6.1
			Horizontal at B2	0.7	---
Model 3	Test 8	78.1 (medium)	Vertical at A1	6.6	2.6
			Vertical at B2	6.0	2.6
			Vertical at A3	4.8	2.8
			Horizontal at B2	0.9	---
Model 3	Test 9	113.6 (fast)	Vertical at A1	6.3	1.8
			Vertical at B2	5.8	1.9
			Vertical at A3	4.8	1.8
			Horizontal at B2	1.1	---

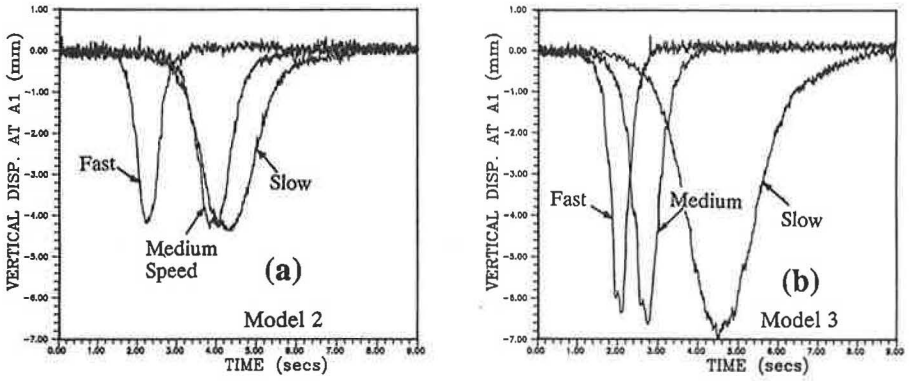


FIGURE 5 Vertical displacement of A1 for (a) Model 2 and (b) Model 3.

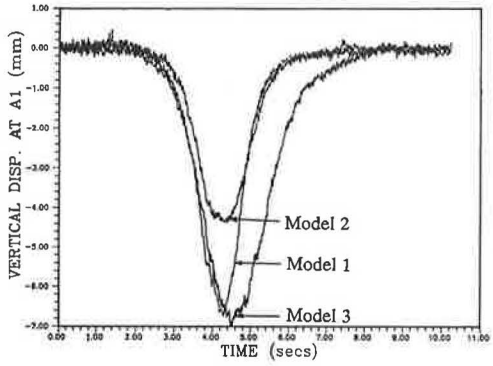


FIGURE 6 Vertical displacement at A1 for all models at slow speed.

models. The speed of rolling for Model 3 (Test 7, Table 2) is much lower than the speeds associated with the other models.

APPLICATION OF THE MODEL TESTS

As discussed previously, the results obtained with the laboratory models can be used to validate numerical and analytical procedures. On the other hand, the results can also be converted to prototype scale using the well-established dimensional analysis procedure (*21–23*). The converted results can then be used to interpret prototype behavior.

The first step in the dimensional analysis procedure is to form a number of dimensionless quantities. The dimensionless quantities used are (a) the ratio of displacement to layer thickness, u/d; (b) Poisson's ratio, ν; (c) the ratio of Young's modulus to the applied wheel pressure, E/Q; (d) the quantity $\rho V^2/E$, in which ρ is the mass density and V is the velocity of the moving load; and (e) the quantity Vt_f/d, where t_f is the duration of the pulse.

According to the model laws, the dimensionless parameters for the prototype and the model can be compared. Selecting the representative ratios of 4, 8,900, and 100 between the prototype and the model for the thickness, Young's modulus, and mass density, respectively, the following relationships between the prototype (p) and the model (m) result:

$$V_p/V_m = 9.43 \quad (1)$$

$$t_p/t_m = 0.424 \quad (2)$$

$$Q_p/Q_m = 8{,}900 \quad (3)$$

$$u_p/u_m = 4.0 \quad (4)$$

Values of layer thicknesses and properties in the prototype scale are presented in Table 3. Because the layer thickness ratio between the prototype and the model is 4.0, the loaded area in the prototype is 152 × 1000 mm. The velocity of rolling in the model tests varied from 29.8 to 138.9 cm/sec. From Equation 1, this value corresponds to a prototype velocity ranging from 2.81 to 13.1 m/sec. In the model, the contact pressure is 14.9 kN/m^2; therefore, from Equation 3, the prototype contact pressure is 132.6 MN/m^2. The tire pressure for highway vehicles is much less, typically varying between 0.62 and 0.83 MN/m^2 (*3,24*). For a high signal-to-noise ratio, a high contact pressure was necessary in the model. Using the principle of linearity and Equation 4 relative to a representative prototype tire pressure of 0.75 MN/m^2, the prototype displacement is computed from

$$u_p = \left(\frac{0.75}{132.6}\right)(4)u_m = 0.023u_m \quad (5)$$

Using Equations 1, 2, and 5, model variables such as the speed of rolling, duration of pulse, and displacement can be converted into a corresponding prototype response. The prototype response values at A1 are presented in Table 4. The table presents the duration (pulse width) at half the amplitude value (t_h) as well as the ratio t_h/t_f.

The amplitude of the vertical displacements is on the order of 0.1 millimeter for the prototype pavement sections, a level that a field deflection measuring device should be able to handle. A discussion on the relative amplitudes of the vertical displacements between the different pavement sections has already been presented. The measured prototype duration of the pulse (t_f) varies between 0.38 and 2.84 sec (see Table 4). Field measurements have indicated that the typical duration is about 0.120 sec for a vehicle traveling at 22.4 m/sec (50 mph) (*9,10*). If an inversely proportional variation between the speed and the duration of the pulse is assumed, the duration of the pulse should vary between 0.21 and 0.96 sec for the range of speeds considered in the test. The measured duration is somewhat higher than that recorded in the field, probably because the load amplitude and the loaded area for the prototype and the field situations differ. Higher contact pressures used to improve the signal-to-noise ratio and plane

TABLE 3 PROTOTYPE LAYER THICKNESSES

		Surface Layer	Middle Layer	Bottom Layer
Layer Thickness (cm)	Prototype 1	16.0	40.8	204.0
	Prototype 2	26.0	40.8	204.0
	Prototype 3	26.0	40.8	404.0
Layer Stiffness (10^4kN/m^2) (Young's Modulus)		310.5	42.6	8.5
Layer Density (kg/m^3)		2400	1760	1600
Poisson's Ratio		0.4	0.4	0.4

strain conditions simulated in the model will, of course, result in a higher pulse duration. Furthermore, the properties of the pavement layers can also affect the field-measured duration.

The ratio t_h/t_f can provide information on the shape of the displacement pulse. If a Haversine function is assumed for the variation between the vertical displacement and time, the t_h/t_f ratio will be 0.5. The Haversine function is widely used to describe the stress pulse-duration curve caused by traffic loading (AASHTO T274-82). The ratio t_h/t_f in the tests varies between 0.29 and 0.37 (see Table 4), which indicates that the load-duration relationship is much narrower (in time scale) than that given by the Haversine function. This result has some practical significance. The current procedures for estimating the resilient modulus of soils (AASHTO T274-82) and asphalt concrete propose applying a Haversine load-duration relationship. Although the shape of the load-duration variation may not be very important for soils, it may be important for asphalt concrete because it exhibits a strong strain rate dependency.

CONCLUSIONS

Pavement response results for moving loads have been discussed in terms of displacements measured in three laboratory models constructed using foam rubber. Foam rubber is inexpensive and lightweight and can be easily cut into different shapes. The moving load is simulated by rolling a long cylinder across the surface of the model at different speeds. Such model studies can be viewed as an alternative to a much more expensive, full-scale field testing program. The model tests provide high-quality data against which the predictive capability of different numerical codes could be checked. The prototype response obtained from model tests on the basis of modeling laws have also been presented. Three different models representing both thin and thick surface and bottom layers were used in the study.

The model's displacement response was measured using LEDs mounted along the centerline of the wheelpath. The movements of the LEDs caused by the moving load were monitored by position sense detectors, which provided a continuous output yielding the locations of the LEDs about two perpendicular axes.

The recorded response reveals that the shape of the vertical displacement pulse is substantially affected by the speed of the moving load. The displacement response can reveal the characteristics of the load that created the displacement. For a fast speed of rolling, the pulse is essentially a sharp spike. Among the three models tested. the most inflexible model showed that the vertical displacement amplitude is unaffected by the speed of the moving load. However, the other two more flexible models exhibited lower amplitudes with faster rolling speeds. The reduction in amplitude can be substantial for points located deeper below the surface. Apart from the amplitude, the duration of the pulse is significantly governed by the speed of the moving load. The duration of the pulse, which can be used to interpret loading rate, is important for asphalt concrete because it exhibits viscoelastic material properties.

The measured duration of the pulse in prototype response varies between 0.38 and 2.84 sec, which is somewhat longer than considered typical for pavements. The difference can be attributed to the pavement layer material properties and to the difference in loading characterization. The investigation of the vertical displacement pulse shape suggests that the pulse is much narrower than that given by a Haversine function.

Finally, the model tests yield a data base for pavement response but only for the simple case of the layer geometries and loading conditions considered. Additional research is suggested and should include studies involving nonuniform con-

TABLE 4 RESPONSE AT A1 IN PROTOTYPE

PROTOTYPE #	TEST #	SPEED OF ROLLING (m/s)	DISPLACEMENT AMPLITUDE (mm)	DURATION t_f (secs.)	DURATION AT HALF AMPLITUDE t_h (secs.)	t_h/t_f
	Test 1	3.9	0.159	1.78	0.55	0.31
Prototype 1	Test 2	6.9	0.152	0.85	0.25	0.29
	Test 3	13.1	0.143	0.38	0.13	0.34
	Test 4	3.9	0.101	1.82	0.64	0.35
Prototype 2	Test 5	6.2	0.099	1.27	0.42	0.33
	Test 6	9.8	0.097	0.68	0.25	0.37
	Test 7	2.8	0.156	2.84	0.85	0.30
Prototype 3	Test 8	7.4	0.152	1.10	0.34	0.31
	Test 9	10.7	0.145	0.76	0.21	0.31

tact pressures, sloping layers, and more representative axle configurations.

ACKNOWLEDGMENT

This study was funded by a National Science Foundation grant. The support is gratefully acknowledged.

REFERENCES

1. R. G. Hicks and F. Finn. Prediction of Pavement Performance from Calculated Stress and Strain at San Diego Test Road. *Proc., Association of Asphalt Paving Technologists*, 1974.
2. *Research and Development of the Asphalt Institute's Thickness Design Manual*, 9th ed. Research Report 82-2. Asphalt Institute, College Park, Md., Aug. 1982.
3. O. K. Kim, C. A. Bell, and J. E. Wilson. Effect of Increased Truck Tire Pressure on Asphalt Concrete Pavement. *Journal of Transportation Engineering, ASCE*, Vol. 115, No. 4, July 1989, pp. 329–350.
4. G. Alborn. *ELSYM5, Computer Program for Determining Stresses and Deformations in a Five-Layer Elastic System*. Institute of Transportation and Traffic Engineering, University of California, Berkeley, 1972.
5. Computer Program BISAR. In *User's Manual* (abbreviated version). Koninklijke/Shell Laboratorium, Amsterdam, The Netherlands, July 1972.
6. L. Raad and J. L. Figueroa. Load Response of Transportation Support Systems. *Journal of Transportation Engineering, ASCE*, Vol. 106, No. TE2, Jan. 1980, pp. 111–128.
7. M. R. Thompson. *ILLI-PAVE, User's Manual*. Transportation Facilities Group, Department of Civil Engineering, University of Illinois, Nov. 1982.
8. R. S. Harichandran, M. S. Yeh, and G. Y. Baladi. MICH-PAVE: A Nonlinear Finite Element Program for the Analysis of Flexible Pavements. Presented at 69th Annual Meeting of the Transportation Research Board, Washington, D.C., Jan. 1990.
9. P. Sebaaly, N. Tabatabaee, and T. Scullion. *In Situ Instrumentation for Resilient Moduli Measurements*. Pennsylvania Transportation Institute, University Park; FHWA, U.S. Department of Transportation, Jan. 1988.
10. B. Sebaaly, T. G. Davis, and M. S. Mamlouk. Dynamics of Falling Weight Deflectometer. *Journal of Transportation Engineering, ASCE*, Vol. 111, Nov. 1985, pp. 618–632.
11. M. S. Hoffman and M. R. Thompson. Comparative Study of Selected Nondestructive Testing Devices. In *Transportation Research Record 852*, TRB, National Research Council, Washington, D.C., 1982, pp. 42–51.
12. R. Siddharthan and R. Fashbaugh. *Response of Layered Deposits to Traveling Surface Waves*. National Science Foundation, Washington, D.C., March 1990.
13. R. Siddharthan. Wave Induced Displacements in Seafloor Sands. *International Journal of Numerical and Analytical Methods in Geomechanics*, Vol. 11, No. 2, March–April 1987, pp. 155–170.
14. J. N. Brune. Earthquake Modeling by Stick-Slip Along Pre-Cut Surfaces in Stressed Foam Rubber. *Bulletin of the Seismological Society of America*, Vol. 63, 1973, pp. 2105–2119.
15. J. L. King and J. N. Brune. Modeling the Seismic Response of Sedimentary Basins. *Bulletin of the Seismological Society of America*, Vol. 71, 1981, pp. 1469–1487.
16. A. Anooshehpoor and J. N. Brune. Foam Rubber Modeling of Topographic and Dam Interaction Effects at Pacoima Dam. *Bulletin of the Seismological Society of America*, Vol. 79, No. 5, Oct. 1989. pp. 1347–1360.
17. A. Anooshehpoor, J. N. Brune, and R. H. Loveberg. *Foam Rubber Modeling of Seismic Site Effects and Soil-Structure Interaction*. Final Report. Electric Power Research Institute, July 1989.
18. A. Anooshehpoor. *Foam Rubber Model Studies of Problems in Seismology and Earthquake Engineering*, Ph.D. dissertation. University of California, San Diego, 1988.
19. J. Boudrealt. Adhesiveness Study by Vialit Testing. *Proc. Canadian Technical Asphalt Association, Annual Meeting*, Saskatoon, Saskatchewan, Canada, 1984.
20. J. Brossel. Adhesiveness Study of Bonding Materials and Aggregates Used in Road Surfacing. *Bulletin de Liaison de Laboratories*, Le Laboratoire Central des Ponts et Chaussees, Paris, France, 1963.
21. E. Buckingham. On Physically Similar Systems—Illustrations of the Use of Dimensional Equations. *Physical Review*, Vol. 4, No. 4, 1914. pp. 345–376.
22. P. W. Bridgman. *Dimensional Analysis*. Yale University Press, New Haven, Conn., 1943.
23. L. I. Sedov. *Similarity and Dimensional Methods in Mechanics*. Academy Press, New York, 1959.
24. D. R. Middleton, F. L. Roberts, and T. Chira-Chavala. Measuremetns and Analysis of Truck Tire Pressures on Texas Highways. In *Transportation Research Record 1070*, National Research Council, Washington, D.C., 1986, pp. 1–8.

Publication of this paper sponsored by Committee on Flexible Pavement Design.

Twenty-Year Study of Asphalt Rubber Pavements in Phoenix, Arizona

EQUBALALI CHARANIA, JOE O. CANO, AND RUSSELL H. SCHNORMEIER

The details of asphalt rubber application on city streets pioneered by the city of Phoenix, Arizona, since the mid-1960s are outlined. Problems encountered in the early use of this material are noted. Various guidelines and specifications developed by the city for the successful use of asphalt rubber are summarized. Viscosity of asphalt cement with and without an asphalt rubber seal was determined, and the importance of these results on the aging phenomenon are discussed. Many of the city's original streets with asphalt rubber application were not evaluated because they have been reconstructed. The remaining streets were inspected, and the pavement conditions for each were observed. Detailed observations of all the street pavements are summarized, and the important findings from this 20-year historical survey of asphalt rubber pavements are discussed. Conclusions on the use and advantages of asphalt rubber as a maintenance treatment for the city's streets are noted. In spite of the advantages and good engineering characteristics of asphalt rubber chip seal, there was mounting public opposition to its continued use because loose chips caused damage to cars. The city therefore developed a special asphalt rubber hot mix. This alternative surface treatment has proven to be as effective and reliable as asphalt rubber chip seals. Details of the design of this mix and its advantages are discussed in depth.

The city of Phoenix, Arizona, has an extensive network of streets with more than 550 mi of major streets and 3,500 mi of collector and residential streets. These streets are constantly monitored, and appropriate maintenance and rehabilitation are provided on a routine basis through a pavement management system. In the mid-1960s, the city of Phoenix pioneered the use of asphalt rubber chip seal. Asphalt rubber is a mixture of 75 to 80 percent hot asphalt cement and 20 to 25 percent ground recycled tire rubber, mixed at a temperature of 300°F to 400°F to cause a reaction. A small amount of additive is added to the mixture to improve its flow characteristics for spray application.

EARLY USE

The earliest application of asphalt rubber was in 1964, followed by more extensive field testing at Sky Harbor International Airport taxiways in 1965. Success and experience of using asphalt rubber at the airport led to its routine use on city streets. A number of terms used in relation to pavements and rehabilitation are summarized in a later section. Phoenix has used asphalt rubber in two types of surface treatments: (a) stress absorbing membrane (SAM), in which a hot asphalt rubber chip seal is applied to the distressed cracked surface, and (b) stress absorbing membrane interlayer (SAMI), in which hot asphalt rubber chip seal is applied to the surface, followed by a 1½- to 2-in. asphalt concrete (AC) overlay. SAMIs were generally used in major streets with a great number of utility cuts in addition to extensive cracking. Asphalt rubber application has allowed the city to incorporate existing pavements that have been evaluated as structurally inadequate, resulting in substantial savings.

One of the earliest applications of asphalt rubber chip seal was placed on Indian School Road from Central Avenue to 7th Street in 1971. The surface of the pavement was in poor condition and was badly cracked. Application of an asphalt rubber chip seal was a temporary measure to prevent the street from complete deterioration and failure. It was then scheduled for total reconstruction in 2 years. However, the street has performed satisfactorily with little maintenance for the past 19 years. The current condition of the street is shown in Figure 1. The traffic count on this street has increased from 30,000 average daily traffic (ADT) in 1971 to 60,000 ADT in 1990. This section will be totally reconstructed in 1991. Another application was on the I-17 frontage road and offramp at Van Buren Street in December 1968. This pavement was removed because of the major interchange improvements for I-10 and I-17 in 1989. A SAM consisting of hot asphalt rubber followed by an application of hot precoated ⅜-in. aggregate was used at this site. Diluents were not used in the asphalt rubber seal. The 1967 surface was scheduled to be replaced; however, the asphalt rubber seal saved it for 21 years.

Since 1967, this treatment has been applied to more than 3,000 lane-mi in Phoenix in addition to the main runway at Sky Harbor International Airport, lake liners, and lagoon ponds.

The principal problem encountered early in the asphalt rubber construction was chip loss in low- or nontraffic areas. Some bleeding and loss of the asphalt rubber resulted. The problem was solved by increasing the asphalt rubber application and by applying a flush coat to the seal in a timely manner. A flush coat is recommended when ⅜-in chip seal is used.

With this extensive use of asphalt rubber chip seal over a span of almost 30 years, the city has developed considerable experience in the use of this method (*1–4*).

GUIDELINES AND SPECIFICATIONS FOR USE OF ASPHALT RUBBER CHIP SEAL

The following guidelines and specifications have been developed for the use and application of asphalt rubber chip seal on city streets:

E. Charania and J. O. Cano, Street Transportation Department, City of Phoenix, 1034 E. Madison Street, Phoenix, Ariz. 85034. R. H. Schnormeier, Russ' ENCORP, 810 E. Camelback Road, Suite A4, Phoenix, Ariz. 85014.

- Asphalt rubber is produced with 80 percent hot asphalt cement and 20 percent coarse ground recycled tire rubber, mixed at a temperature of 300°F to 400°F.
- Aggregates used are ⅜- or ¼-in. nominal and are hot precoated.
- Asphalt rubber is generally applied at a rate of 0.6 gal/yd^2.
- Hot precoated chips are applied at a rate of 37 to 40 lb/yd^2.

The chip seal produced a unique paving material with superior engineering properties. The main advantage of the asphalt rubber treatment has been virtually complete cessation of surface maintenance for 12 years, except for utility cuts. Cracks have not reflected through the seal on aged pavements. Continued observations of treated streets confirm the significant advantage of this method in preventing reflective cracking. Long-term studies have indicated that cracks less than 0.25 in. wide generally do not reflect through the seal for 8 years and, in some cases, for as many as 12 years. For the occasional cases in which reflection cracking occurred, there was no spalling or deterioration into potholes.

Transverse cracking has not been totally stopped by asphalt rubber SAM or SAMI. However, secondary cracking that normally radiates off a primary transverse crack does not normally occur. Secondary cracking usually causes potholes at major cracks.

The greatest advantage in stopping reflective cracking has been in alligator-type cracks and shrinkage cracks. Any crack greater than 0.3 in. should be prepared and filled.

VISCOSITY

Another unique advantage of asphalt rubber is that it does not bleed in hot weather or crack in cold because its viscosity is much less temperature-dependent than that of asphalt cement. Asphalt rubber has a 35° to 50° higher softening point than standard asphalt. When using asphalt rubber, the choice of base asphalt may be reduced by one to two grades to improve the cold properties of the asphalt rubber mix.

Observations of viscosity-time relationships at the Sky Harbor Airport are shown in Figure 2. The asphalt viscosity graph reflects the apparent trends for the two asphalts on the basis of the average of five samples taken between 1972 and 1985. The section with conventional asphalt was rehabilitated with reclamite 3 years after it was placed, which affected the viscosity of the asphalt (see Figure 2). The literature (*5*) indicates that a logarithmic relationship exists between viscosity and time for nonrubberized asphalt. The viscosity should approach an upper level as oxidation progresses and its volatiles are removed. From these observations, viscosity of asphalt cement with an asphalt rubber seal has exhibited no increase. In the same period, the nonrubberized sealed asphalts increased in viscosity more than 20-fold.



FIGURE 1 Condition of Indian School Road after 19 years.

Effects of the asphalt rubber seal on the aging phenomenon also become apparent from various observations. The asphalt rubber layer acts as a sealant, preventing the loss and reaction of the asphalt's more volatile components. This sealing action preserves the viscosity of the pavement and maintains much of the flexibility of the treated surface.

An earlier study (*4*) also indicated that sealed concrete retains its original properties for 12 years or more.

Although hardening of regular asphalt with time is well documented, the hardening, or lack of it, for asphalt rubber–sealed asphalt is the important result of this study. The asphalt rubber–sealed AC has exhibited no appreciable increase in viscosity after 13 years. As mentioned, in the same period the nonrubberized asphalt has increased in viscosity over 20-fold. With such well-maintained viscosity, the durability of the surface is greatly increased. The reduction in oxidation an aging has been proven by the longer life of asphalt rubber applications. Hot AC mixtures with crumb rubber placed since 1972 have shown major reductions in aging. The 3,000 lane-mi of SAMs in Phoenix have retarded aging to extend the pavement life by a factor of 2 to 3.

ECONOMICS OF ASPHALT-RUBBER

Economics must be considered when deciding whether or not to apply asphalt rubber. The cost of asphalt rubber in 1971 was three times the cost of conventional chip seal. Today the actual cost of the asphalt rubber is approximately two times that of conventional chip seal.

Asphalt rubber chip seals have performed well in Phoenix for 20 years over soundly cracked pavements. It was found that 12 to 15 years of maintenance-free life can be expected from asphalt rubber seals. Normal life expectancy using the conventional chip seal over very poor pavement is about 2 years, and more than 6 to 7 years over reasonably sound pavements. Asphalt rubber about doubles the life of the pavement and reduces maintenance. Thus, over a 12-year period, asphalt rubber costs will equal conventional chip costs.

OBSERVATIONS OF ASPHALT-RUBBER PAVEMENTS

Almost 70 percent of the streets studied in the previous report (*4*) were not evaluated this time because these streets have been reconstructed. The remaining 30 percent of the pavements were inspected and their conditions noted. The complete observations of the pavement conditions of these streets

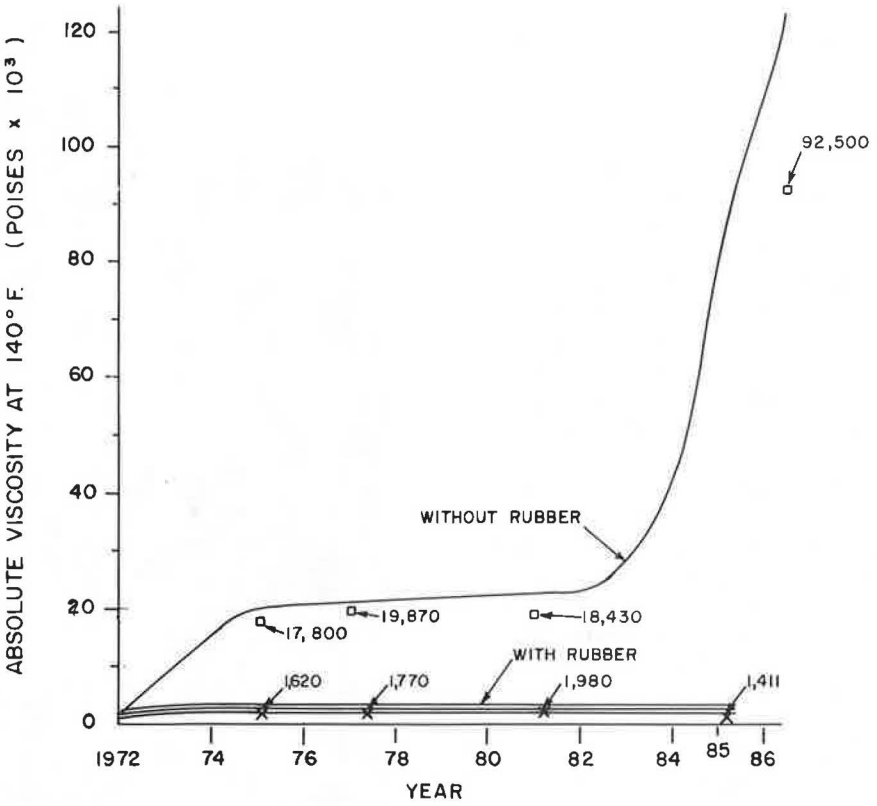


FIGURE 2 Absolute viscosity versus time for Phoenix Sky Harbor Airport asphalts.

are available from the authors, but the highlights are shown here in the appendix. The important findings drawn from these observations are as follows:

- Most of the street pavements inspected showed severe cracking and fatigue failures over the years. The pavements had suffered deterioration due to traffic, weather, and age. In most cases, there were signs of rubber that was still elastic, but at other locations the rubber had become dry.
- Inspections of the subgrade at a number of locations revealed no sign of soil-cement. It appeared that cement was either washed out or in some way chemically altered, because the materials showed no cohesion or strength. Also, shrinkage cracks reflected in all cases after 15 years.
- Chip loss was observed from pavements at various locations, including both low- and heavy-traffic areas. As observed earlier, asphalt rubber loses its flexibility with time and does not retain the chips. Chip loss on a typical street edge is shown in Figure 3.
- Cracking caused by fatigue-type failure, characterized by alligator cracking followed by potholes in the original pavement, was stopped for 15 years due to the use of asphalt-rubber chip seal. Although asphalt rubber cannot bridge wide cracks, it reduces crack width and prevents spalling at the edges for 10 to 12 years. However, recent observations indicate that there is complete deterioration after 20 years. In some cases, wide cracks that were almost 1-in. deep occurred when using the cement-stabilized soil base concept.
- The continuing effect of asphalt rubber on the aging phenomenon could not be evaluated because the pavements placed at Sky Harbor Airport have been reconstructed to meet the FAA geometric design.
- After 20 years, an estimated 20 percent of the asphalt rubber seal (SAM) still remains and is still functioning.
- Several miles of pavements received a standard seal coat (mini-SAM) between the 12th and 16th years.
- A few miles were overlaid with a standard hot AC on a SAMI after 8 years or more as a SAM.
- Several projects held the existing street in place up to 20 years until reconstruction could be accomplished.



FIGURE 3 Chip loss on street edge.

- Samples taken after 17 years indicate a very flexible surface as compared with the standard hard, brittle surfacing after 6 years.
- As indicated in the 15-year study by Schnormeier (*4*), cracking developed about 12 to 15 years after application. At 15 years, little or no secondary cracking had developed. Secondary cracking did develop on most streets after 15 years, causing some potholes. Many of the cracked surfaces were reflected soil-cement base shrinkage cracks.
- The survey indicated that the surface needed a rejuvenation by a fog seal, reclamite, or some rejuvenating sealer. The 52nd Street project is a good example of obtaining three or four times the pavement life with timely treatment.
- The soil-cement base designs have developed large (1½-in.) transverse cracks and some longitudinal cracks that the asphalt rubber has not stopped.
- Many of the original SAM applications are currently being overlaid with 1 in. of asphalt rubber hot mix.
- The design comparison on 13th Street and Camelback illustrates the life expectancy of asphalt rubber. The street was constructed in 1974 and butted against a street constructed in 1972. The 1974 construction was 4½ in. of soil cement, 1½-in. of AC, and SAM. The 1972 section was 6 in. of aggregate base with 2 in. of AC. The 1974 construction was less than half the cost of the 1972 section. The asphalt rubber SAM has not cracked after 17 years, whereas the aggregate asphalt section exhibits 99 percent cracking. The boundary between the two sections is shown in Figure 4.
- Pavements with high traffic volumes performed better than those with low traffic volumes. It appears that traffic helped keep the pavement sealed and slowed the rate of deterioration.

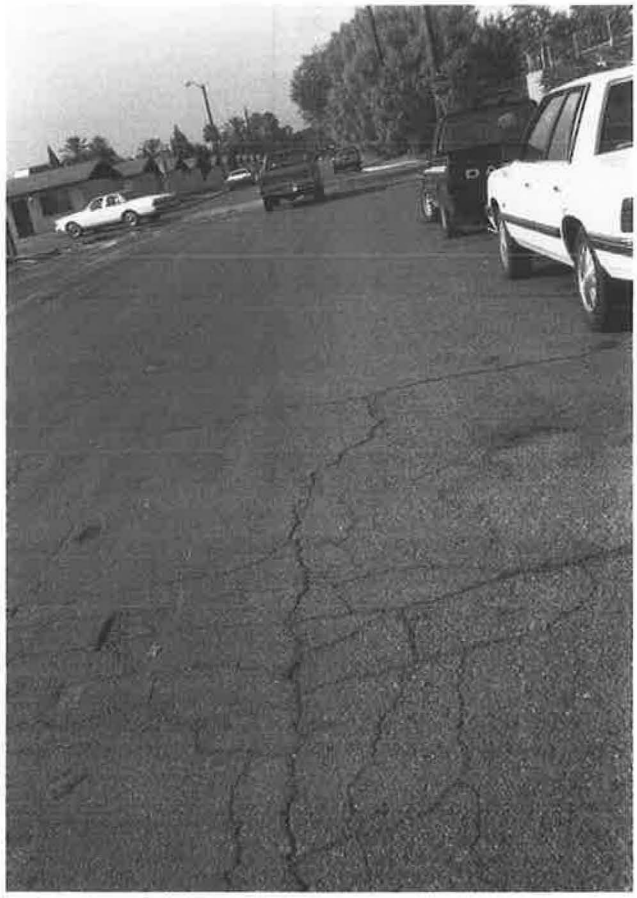


FIGURE 4 Boundary between two sections on 13th Street and Camelback.

CONCLUSIONS ON USE AND ADVANTAGES OF ASPHALT RUBBER

Chip seals have been a dependable maintenance treatment for Phoenix streets. They have added extra life to the pavements and enabled the city to delay reconstruction of streets. Asphalt rubber seal coats—SAMs and SAMIs—have given the pavement management system a number of advantages, as summarized:

- The seals retard reflective cracking in paving materials with less than 0.25-in. cracks for 8 to 12 years.
- They stop secondary cracking up to 15 years.
- They retard spalling of AC around potholes and larger cracks.
- They waterproof the structure to obtain maximum stability.
- They seal and preserve the in-place original quality of asphalt cement and the asphalt concrete.
- They considerably reduce maintenance due to the factors just mentioned.
- They seal the subgrade to minimize volume changes that take place because of moisture changes.
- They serve as a stress-absorbing interlayer to reduce future maintenance.
- They function as an excellent crack-filling material and joint sealer.
- They last 2 to 2½ times longer than most standard seals in Phoenix. If preventive seals were applied at proper times, the seals would last 2 to 5 times longer.
- Rubber particles separate from asphalt cement because the rubber absorbs the light fraction, causing it to lose flexibility and requiring maintenance. If another asphalt rubber seal, fog seal, or rejuvenation seal is applied at the proper time, the pavement life can be extended by the type of reseal selected.

Despite the successful use of asphalt rubber, it must be used with careful consideration of the pavement's structural condition, size of cracks, and intended use, as well as the absorption properties of the asphalt material. Although asphalt rubber does absorb pavement stresses and does seal, it docs not stop cracking or failures in the existing pavement or subgrade. The cracks are still present; however, they do not come to the surface to cause problems. When used as a SAMI, the minimum overlay thickness should be 1½ in. to prevent reflection.

PROBLEMS WITH CHIP SEAL

Despite the sound engineering properties, economic advantages, and success of chip seals, the public suffered consid-

erable aggravation by the inconvenience of the chip seal process. In addition, loose chips were often scattered by the leading cars, resulting in a number of shattered windshields and unhappy motorists.

Due to mounting public pressure, the Phoenix City Council directed the Street Transportation Department to discontinue the use of chip seals. Thus, the city was forced to develop an alternative surface treatment that was as economical and reliable as the chip seal.

DESIGN OF MIX

As an alternative to chip seals, the Street Transportation Department developed a special asphalt rubber hot mix (*6*). The mix was designed with a gap gradation to incorporate a large amount of asphalt rubber binder. Gradation limits of the mix are shown in Figure 5, together with the line of maximum density. Details of the rubber in the mix are available from the authors.

The use of asphalt rubber mix with 10 percent asphalt-rubber binder was chosen on the basis of the authors' experience with tests on mixes with as much as 13 percent asphalt rubber binder in 1985. The concept was to design a mix with a high asphalt rubber content and large voids, as much as 24 percent, in the mineral aggregate (VMA). This procedure results in a dense mix that would seal the badly cracked pavements and prevent moisture from getting into the subgrade. The stability of the mix was obtained from the aggregate interlock.

In order to examine the effects of light- and heavy-traffic conditions, both a 100-blow and a 75-blow Marshall were run on mixes with asphalt concrete binder of 8.5 and 9 percent. The results of various parameters are presented in Table 1. The modulus of the mix is a function of stability and flow. The values in Table 1 indicate that the mixes have low stability and high flows, resulting in low values of the modulus. Thus, the mix behaves as elastic material.

During the initial paving, the asphalt mix began to be picked up on tires because of the nature and physical properties of the mix. To keep the temperature of the rubber mix down so that it would start to stabilize, a water truck had been used to spray the pavement. By spraying the pavement, the water actually stripped the tack coat in those areas that were deficient in asphalt thickness (less than ½ in. in some cases). Thus, small sections of asphalt came up. It was proposed that the contractor spread sand on the pavement to stabilize the mix, which worked well. A chip spreader was used to disperse the sand at the rate of 2 to 3 lb/yd^2.

From field and laboratory tests, it was decided that 8 percent asphalt rubber binder was suitable for streets with heavy traffic and 9 percent asphalt rubber binder was appropriate for streets with light traffic. Furthermore, to prevent rubber from sticking to tires, it is necessary to spread sand over the overlay areas when the ambient temperatures exceeded 100°F.

ADVANTAGES OF ASPHALT RUBBER HOT MIX

Approximately 3,000 t of recycled tire rubber was used in the 600 lane-mi of asphalt rubber–concrete overlaid during the past 2 years. This process required grinding of about 600,000 old tires and helped eliminate the waste disposal problems that would have otherwise occurred. The use of old tires in the mix helped in preventing pollution and maintaining a good quality environment. Since 1971, Phoenix has paved almost 3,600 lane-mi using almost 3.6 million scrap tires.

It is anticipated that the new mix overlay will be more durable and will perform better than the chip seal because asphalt rubber retards oxidation and deterioration of the

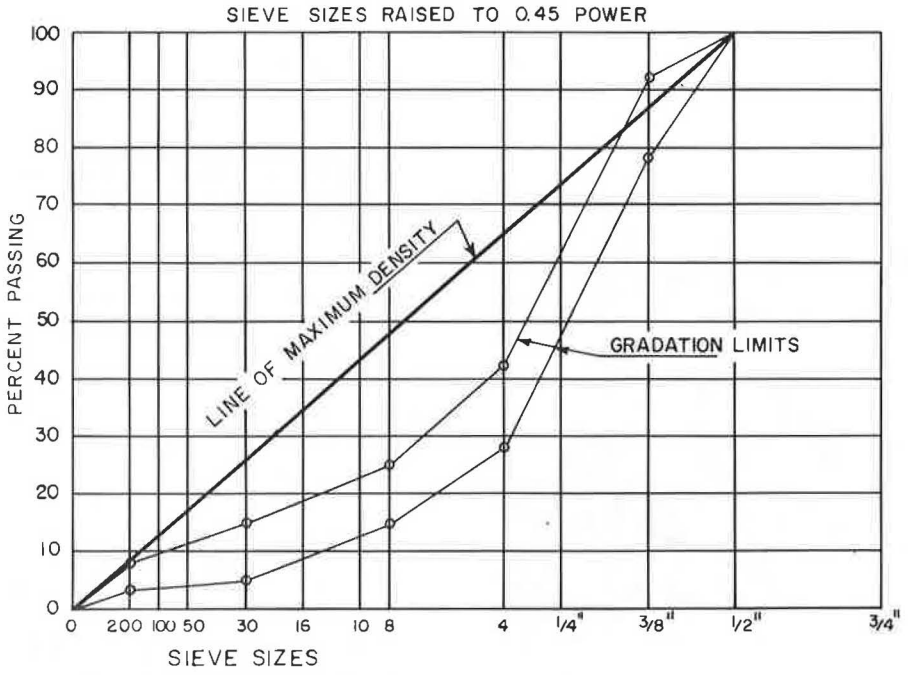


FIGURE 5 Asphalt rubber surface course mix gradation limits.

TABLE 1 DESIGN PARAMETERS FOR ASPHALT RUBBER MIX

	Marshall 75 Blows		Marshall 100 Blows	
% AC	8.5%	9.0%	8.5%	9.0%
% Aggregate Voids	23.3	24.2	22.4	23.6
% Voids in Comp. Mix	5.2	5.1	4.0	4.3
Unit Weight	138.8	137.8	140.3	138.8
Stability	955	1082	998	1176
Flow	19	22	21	22

pavement. On the basis of the performance of the test sections, it can be concluded that a 1-in. asphalt rubber–concrete overlay will resist cracks from reflecting through the existing worn out pavement.

The skid resistance of the surface is not reduced by rubber. There are significant improvements in two other areas. First, the surface provides a much improved riding surface. Second, there is a marked decrease in traffic noise. Reports from residents near a major street overlaid with this mix confirm this observation.

A photograph showing the typical condition of the street being overlaid with asphalt rubber hot mix is shown in Figure 6.

GLOSSARY

Asphalt-rubber: a blend of asphalt cement, reclaimed tire rubber, and certain additives in which the rubber component is at least 15 percent, by weight, of the total blend and has reacted in the hot asphalt cement sufficiently to cause swelling of the rubber particles.

Asphalt rubber chip seal: application of hot asphalt rubber followed by an application of hot precoated ¼-in. (6.3-mm) nominal, or ⅜-in. (9.5-mm) nominal, aggregate.



FIGURE 6 Overlay with asphalt rubber hot mix: condition before overlay (*left*); completed half (*right*).

Standard or conventional chip seal: application of hot asphalt cement (AC-20 or AC-40) followed by an application of hot precoated ¼- or ⅜-in. nominal aggregated.

Flush seal: application of emulsified asphalt mixed 50–50 with water and applied at 0.1 to 0.2 gal/yd² (0.45 to 0.91 L/m²).

Stress-absorbing membrane (SAM): application of hot asphalt rubber chip seal to a distressed surface.

Stress-absorbing membrane interlayer (SAMI): application of a hot asphalt rubber chip seal to a distressed surface followed by an AC overlay.

Mini-SAMI: application of a hot asphalt rubber chip seal to a surface followed by the application of a conventional chip seal.

Asphalt rubber gap-graded concrete (ARC): gap-graded asphalt rubber hot mix that incorporates a high asphalt rubber content and large voids in the mineral aggregate, placed with standard lay-down equipment and rollers.

Reflective crack: any crack that has developed in the pavement and has passed through the overlay.

APPENDIX

Twenty-Year Historical Survey of Pavement Conditions

WESTWOOD NEIGHBORHOOD IMPROVEMENT DISTRICT, CONTRACTOR—BENTSON (CONSTRUCTED 1972)

West half of 24th Avenue from Thomas Road to alley south of Pinchot Avenue (0.285 mi)

1976: Good surface; good texture; asphalt concrete slippage on soil-cement on south end.

1979: Slippage has healed; some longitudinal cracks at Earll Drive; shrinkage cracks that have developed in untreated area stop at rubber treatment; good surface and texture.

1985: Pavement resealed (mini-SAMI); good condition.

1990: 1986 standard chip; severe cracking; new treatment required.

23rd Avenue from Thomas Road to Catalina Drive and east half of 23rd Avenue to Avalon Drive (0.201 mi)
1976: Good surface texture; some slippage on south end.
1979: Some soil-cement cracks have developed; slippage has healed; good condition.
1985: Resealed (mini-SAMI); soil-cement cracks reflected.
1990: Severe cracking; rubber has lost elasticity; oxidized; needs rehabilitation.

24th Avenue from Indian School Road to Grand Canal (0.268 mi)
1976: Severe chip loss from 23rd Drive to the Grand Canal; slippage of asphalt concrete surface on cement-treated soil at Indianola Avenue and Indian School Road intersection.
1979: Slippage areas have been patched and have stabilized; severe chip loss has stabilized; slight loss continues.
1985: Resealed (mini-SAMI); good condition.
1990: Fair to good condition; some cracking.

Indianola Avenue from Black Canyon Highway to 24th Avenue (0.121 mi)
1976: Good textured seal; asphalt concrete slippage on soil-cement by Mardian Construction Co. parking lot exit.
1979: Slippage has stabilized; good texture and surface.
1985: Soil-cement cracks have reflected through; some shrinkage cracking; texture remains good.
1990: 1986 standard chip seal; good condition.

Fairmont Avenue from 24th Avenue to Grand Canal (0.10 mi)
1976: Good textured seal; asphalt concrete slippage on soil-cement severe at 24th Avenue and 23rd Drive.
1979: Slippage still severe; areas have been patched; beginning to stabilize.
1985: Patched areas have slipped; same condition as 1979.
1990: 1986 standard chip seal; severe cracking; rubber still flexible; needs rehabilitation.

Glenrosa Avenue from Black Canyon Highway to 23rd Avenue (0.23 mi)
1976: Good surface texture; some chip loss from oil drippings on cracks; some slippage of asphalt concrete on soil-cement at 23rd Avenue. Portions of asphalt concrete cracked by reflection from soil-cement base before rubber seal in 1972; these cracks did not come through asphalt-rubber seal.
1979: Good surface texture; slippage has healed; still no cracks through asphalt-rubber seal.
1985: Surface has been resealed (mini-SAMI); major construction on both sides by developers; original pavement good.
1990: Some cracking; newer pavement on north side without rubber is more cracked; scheduled for ARC overlay in late 1990.

Turney Avenue from 23rd Avenue to 22nd Drive (0.067 mi)
1976: Good condition and texture; some chip loss next to curb.
1979: Same condition.
1985: Reconstruction for new development.
1990: Severely cracked; needs reconstruction; scheduled for ARC overlay in late 1990.

22nd Drive from Turney Avenue to Campbell Avenue (0.127 mi)
1976: Good condition and texture.
1979: Some raveling; 10 percent chip loss.
1985: Reconstruction for new development.
1990: New on east side; west side severely cracked; needs reconstruction; scheduled for ARC overlay in late 1990.

South side of Turney Avenue from 21st Avenue west approximately 300 ft (0.057 mi)
1976: Severe chip loss, up to 90 percent in areas; pavement shows reflective cracks from soil-cement.
1979: Street has been resealed with standard chip seal; cracks through the reseal.
1985: Reconstructed for new development.
1990: Scheduled for ARC overlay in late 1990.

South side of Turney Avenue from 20th Drive to 19th Avenue (0.188 mi)
1976: 25 percent chip loss on south side; asphalt concrete slippage on soil-cement at 19th Avenue with some reflective cracks.
1979: Resealed; cracks showing on north side after seal; no cracks showing in rubber treatment; good surface texture; slippage has healed; only a few cracks showing.
1985: Fewer cracks on south side; same condition as 1979.
1990: Scheduled for ARC overlay in late 1990.

20th Avenue from Turney Avenue south to dead end (0.10 mi)
1976: 75 percent chip loss; appears to be insufficient asphalt-rubber; 30 percent chip embedment; some cracks developing.
1979: Same condition with cracking in chip loss areas; needs resealing.
1985: Resealed surface looks very good.
1990: Scheduled for ARC overlay in late 1990.

Highland Avenue from 23rd Avenue to 23rd Drive (0.054 mi)
1976: Okay with good texture.
1979: Loss of chip at dead end area; little or no traffic.
1985: Surface has cracked and has developed potholes; major construction areas for new development.
1990: Severely cracked; needs rehabilitation; scheduled for fabric and 1½-in. overlay in late 1990.

23rd Avenue from Highland Avenue to Pierson Avenue (0.10 mi)
1976: Varied 10 to 20 percent chip loss; fair to good texture surface; not much traffic.
1979: Still raveling; some cracking; needs reseal or flush coat.
1985: Resealed (mini-SAMI); good condition.
1990: Rubber SAM (double) in 1986; good condition; some cracks.

Pierson Avenue from 23rd Drive to 23rd Avenue (0.05 mi)
1976: Raveling at corners and parking areas.
1979: Continues to ravel in same areas.
1985: Trench work has caused need for resealing; very good condition.
1990: Good condition; some cracks; scheduled for fabric and 1¼-in. overlay in late 1990.

Pierson Avenue from 23rd Drive to 22nd Avenue (0.134 mi)
1976: 10 to 20 percent chip loss; fair to good textured surface; severe slippage of asphalt concrete on soil-cement in entire area; some patching in slippage areas.
1979: Chip loss continues; slippage areas have been patched and have stabilized; new slippage developing.
1985: Slippage has stopped; new construction on portions for development; good condition.
1990: Severely cracked; some wide cracks; scheduled for ARC overlay in late 1990.

East half of 26th Avenue from Pierson Avenue to Highland Avenue (0.121 mi)
1976: Chip loss in parking lane; fair to good textured surface.
1979: Same condition with a few cracks.
1985: Same condition.
1990: Scheduled for ARC overlay in late 1990.

Coolidge Street from Black Canyon Highway west to dead end (0.20 mi)
1976: 40 percent chip; not much traffic.
1979: Same condition; needs to be resealed.
1985: Surface resealed (mini-SAMI); good condition.
1990: Very low or no traffic; severely cracked; loss of chips; alligator cracks; completely stripped; scheduled for ARC overlay in late 1990.

North half of Hazelwood Avenue from Black Canyon Highway west to dead end (0.008 mi)
1976: Okay; good surface; has a shallow chip embedment; 10 to 15 percent chip loss; needed to be flushed after construction.
1979: Same condition; needs reseal because of new construction in area; essentially no crack reflection in asphalt-rubber originating from underlaying soil-cement base wherever chips remained in place.
1985: Surface resealed because of construction; cement-treated soil shrinkage cracks have reflected through almost all rubber applications except in highly traveled areas.
1990: Scheduled for ARC overlay in late 1990.

ST. FRANCIS NEIGHBORHOOD IMPROVEMENT DISTRICT, BOUNDED BY 7TH TO 16TH STREET, INDIAN SCHOOL TO CAMELBACK ROAD, CONTRACTOR—TANNER (CONSTRUCTED 1974)

11th Street from Meadowbrook Avenue to Campbell Avenue (0.12 mi)
1979: Good condition.
1985: Good condition; new construction on west side.
1990: Standard chip seal in late 1985.

Minnezona Avenue from 9th Street to 7th Street (0.18 mi)
1976: 20 percent chip loss; severe loss near 7th Street.
1979: Same condition.
1985: Over 50 percent chip loss; needs resealing.
1990: Standard chip seal in 1988.

8th Place from Grand Canal to Highland Avenue (0.22 mi)
1976: Some chip loss with cracking near post office.
1979: Same condition.
1985: Severe chip loss south of Minnezona; large soil-cement shrinkage cracks; no secondary cracking.
1990: Standard chip seal in 1985.

8th Street from Grand Canal to Meadowbrook Avenue (0.07 mi)
1979: Same condition.
1985: 30 percent chip loss to Minnezona; 80 percent loss to Canal; no traffic for kneading surface.
1990: Standard chip seal in 1985.

8th Place from Camelback Road to Pierson Street (0.12 mi)
1979: New construction on east side; rubber seal okay.
1985: New construction due to development.
1990: Standard chip seal in 1985.

Pierson Street from 8th Place to 10th Street (0.05 mi)
1976: Roped surface.
1979: Surface has smoothed out; condition has stabilized.
1985: Good condition.
1990: Standard chip seal in 1985.

10th Street from Pierson Street to Highland Avenue (0.12 mi)
1976: 40 to 50 percent chip loss early; roped surface that has been resealed.
1979: Same condition.
1985: Fair condition; severe cracking needs reseal with rubber.
1990: Poor condition; severe cracking; chip lost; standard chip in 1985.

Highland Avenue from 7th Street to 15th Street (0.87 mi)
1976: 10 to 40 percent chip loss early; some areas have been resealed; chip loss problem in shaded areas.
1979: Same condition; no cracks.
1985: Same condition from 10th to 15th; poor condition 7th to 10th; several cracks; severe raveling at intersection.
1990: Resurfaced; standard chip seal in 1985.

15th Street from Meadowbrook Avenue to Highland Avenue (0.13 mi)
1976: Small early chip loss; good surface remaining.
1979: Very good condition.
1985: Same condition; some raveling at driveways; no cracks.
1990: No seal coat; same condition; some cracks and raveling at driveway.

14th Place from Meadowbrook Avenue to Highland Avenue (0.12 mi)
1979: Good condition.
1985: Small reflective cracking; good condition.
1990: Original rubber surface; some cracking and chip loss.

Pierson Street from 14th to 12th Street (0.25 mi)
1976: Okay except for embedded chips causing a black surface; some slippage of asphalt concrete on soil-cement at 12th Street.
1979: Fair condition with about 40 percent chip loss in parking area.

1985: Fair condition; little or no cracks.
1990: Original asphalt-rubber surface; some cracking and chip loss; considerable chip loss in parking lane.

13th Street from Pierson Street to Highland Avenue (0.12 mi)
1976: Roping has worked out in center area; roping severe and remains the same as placed in 1974 in parking areas; looks like a bleeding pavement.
1979: Pavement has stabilized; no cracks; roping is smoothing out; bleeding not a problem.
1985: Very good condition on north end with very heavy traffic; overall good surface with little cracking.
1990: Original asphalt-rubber surface in fair condition; some cracking and roping.

14th Street from Campbell Avenue to Glenrosa Avenue (0.24 mi)
1976: Chip loss at construction joint; good surface.
1979: Very good condition.
1985: Same condition.
1990: No seal coat; surface in fair to poor condition.

Deveonshire Avenue from 12th Street to Longview Avenue (0.12 mi)
1976: 20 to 30 percent chip loss.
1979: Same condition.
1985: Pavement resealed; very good condition.
1990: Nothing done; no seal coat; no maintenance for past 16 years; fair surface.

Minnezona Avenue from 12th to 13th Street (0.13 mi)
1976: Considerable chip loss in shaded areas.
1979: Very good condition.
1985: Good condition; some soil-cement crack reflection.
1990: Nothing done; no seal coat; fair surface.

Elm Street from 13th to 12th Street (0.012 mi)
1976: 20 percent chip loss.
1979: Same condition; no cracks.
1985: More chip loss on outside edges; no cracks.
1990: Nothing done; no seal coat; good to fair surface.

STREET MAINTENANCE, CONTRACTOR—BENTSON (CONSTRUCTED 1971)

52nd Street from Van Buren to Roosevelt Street (0.5 mi)
1976: Alligator cracking in center portion with some chip loss; texture good; area has little or no subgrade support with high water table; very high pavement deflections under traffic.
1979: Severe alligator cracking over entire project; very weak subgrade with very high deflection.
1985: 1983 rubber chipped again; no cracks; very good surface.
1990: Rubber chip seal in 1983; very good condition after 19 years.

STREET MAINTENANCE, CONTRACTOR—TANNER (CONSTRUCTED 1973)

Buckeye Road from Central Avenue to 3rd Street (0.2 mi)
1976: Some cracking; overall condition good.
1979: Some large shrinkage cracking; some alligator cracking at Central Avenue; good condition.
1985: 1982 asphalt rubber reseal; good surface; poor ride.
1990: Severe cracking; needs rehabilitation.

Thomas Road from 19th Avenue to 12th Street, 10-ft strip, both sides (2.5 mi)
1976: Some chip loss on inside edge; good texture; comparing existing pavement in center portions, asphalt rubber has stopped cracking.
1979: Asphalt rubber portion in very good condition considering preexisting conditions; standard area in center severely cracked and needs maintenance.
1985: Fair condition with nothing being done since 1973 from 19th Avenue to 7th Avenue; 7th Avenue to 17th Street overlaid in 1983.
1990: Severely cracked in non-asphalt-rubber area; reconstruction summer of 1990.

52nd Street from Thomas Road to McDowell Road (1.0 mi)
1976: Some chip loss in southbound lane with alligator cracking on north end.
1979: Same condition.
1985: Rubber sealed again in 1983; very good condition.
1990: Fair to good condition.

52nd Street from Roosevelt Street to entrance of Motorola (0.30 mi)
1976: Alligator cracking in center portion with chip loss; traffic indicates very large deflection on soft subgrade.
1979: Entire area has alligator cracks with very high deflections; pavement has not developed potholes due to rubber particle properties.
1985: Rubber sealed again in 1983; excellent condition.
1990: Fair to good condition.

SPECIAL PROJECTS FOR STREET MAINTENANCE, ASPHALT-RUBBER ON PRIMED SUBGRADE OF NATURAL SOIL, CONTRACTOR—CITY OF PHOENIX (CONSTRUCTED 1970)

55th Avenue from Claredon Avenue to 600 ft north on east half only (0.1 mi)
1976: Very good condition except for two potholes on east side of street (*1*).
1979: Total street resealed in 1976 with standard chip seal, making the surface a mini-SAMI. West half cracked; east half not cracked. East half in good condition with some depressions from subgrade conditions. Rubber molded to depressions. The 1-ft overlap on the conventional pavement has stopped cracks. Treated berm has deteriorated, causing potholes on east edge.

1985: After 15 years of use and some additions by new development, pavement is failing because of lack of subgrade support; pavement should be reconstructed or overlaid with another asphalt rubber chip seal.
1986: Nominal chip seal.

It is of interest that the potholes mentioned stood unrepaired for several years and showed little tendency to expand into the roadway, which they would most certainly have done in a conventional light surface treatment over a clay loam soil (plasticity index 18, passing #200 sieve, 80 percent). Procedure definitely has promise for low-traffic-volume roads. Traffic count on street is 4,500 average daily traffic (ADT).
1990: Alligator-cracked surface; little or no surface movement; good surface after 21 years.

SPECIAL PROJECT, CONTRACTOR—TANNER (CONSTRUCTED 1971)

Indian School Road from Central Avenue to 7th Street (0.75 mi)
1973: Very good condition; excellent surface; 25,000 veh/day.
1976: Good condition; some chip loss at intersections; 30,000 veh/day.
1979: Fair condition with cracks; very good texture; Central Avenue intersection 75 percent raveled away; 37,000 veh/day.
1985: 1981 resealed (mini-SAMI); very good condition with 48,000 ADT; unable to find manholes; rubber sealed system.
1990: No reseals; pavement has cracked but doing well; 1991 planned reconstruction.

REFERENCES

1. R. H. Schnormeier. Use of Asphalt-Rubber on Low-Cost, Low-Volume Streets. In *Special Report 160: Low Volume Roads*, TRB, National Research Council, Washington, D.C., 1975.
2. R. H. Schnormeier. *Eleven Year Pavement Condition History of Asphalt-Rubber Seal in Phoenix, Arizona*. ASTM Publication 724. ASTM, Philadelphia, Pa., Dec. 1979.
3. R. H. Schnormeier. Use of Asphalt-Rubber on Low-Cost, Low-Volume Street: A Review After 13 Years. In *Transportation Research Record 898*, TRB, National Research Council, Washington, D.C., 1983.
4. R. H. Schnormeier. *Fifteen Year Pavement Condition History of Asphalt-Rubber Membranes in Phoenix, Arizona*. TRB, National Research Council, Washington, D.C., 1985.
5. R. F. Coons and P. H. Wright. An Investigation of the Hardening of Asphalt Recovered from Pavements of Various Ages. *Proc., Association of Asphalt Paving Technologists*, Vol. 37, 1968.
6. J. O. Cano and E. Charania. The Phoenix Experience Using Asphalt-Rubber. *Proc., National Seminar on Asphalt-Rubber*, Kansas City, Mo., Oct. 1989.

Publication of this paper sponsored by Committee on Flexible Pavement Design.

Distributions of Strain Components and Work Within Flexible Pavement Structures

HERBERT F. SOUTHGATE

An investigation was made to determine the location along the centerline of the axle of the maximum strain energy density, or work, in the pavement as defined by classical physics. The location is under the inside edge of either dual tire. The most influential strain was the shear component. The distribution of shear strains and stresses with depth through the full-depth asphaltic concrete and into the subgrade was investigated. Using Simpson's rule for an even number of increments, or using the trapezoidal rule, allows the summation of strain energy density to be calculated at various depths. The sum of work throughout the pavement structure provides a greater insight to the behavior of the pavement because all components of strain, or stress, are considered and the variation throughout the depth may be large according to the location within the tire print. The sum of strain energy density is much greater under the edge of the dual tire than under the center of the dual tire, yet the magnitude of the strain energy density at the bottom of the asphaltic concrete may be nearly identical. For an 18-kip, four-tired, single axle load, the depth of maximum shear is approximately 35 to 40 percent of the thickness from the surface downward for a maximum pavement thickness of approximately 8 in.; thereafter the depth of maximum shear moves toward the surface as thickness increases. An investigation of shear stress indicated that the maximum value was approximately 67 psi due to an 18-kip single axle load and tire contact pressure of 80 psi within a 4-in. full-depth asphaltic concrete pavement. Investigation of three pavements indicated shear flow could be seen as deep as 6 in. below the surface. From the stress analyses presented, the stress at the 6-in. depth would be approximately 25 psi. An established critical value for the shear stress of asphaltic concrete is not known.

The first purpose of this investigation was to determine the locations within the pavement structure showing the greatest response to wheel loads, as evidenced by stresses and strains (*1*). A second purpose was to study patterns of strain or stress under limited conditions of eight thicknesses of full-depth asphaltic concrete having an elastic modulus of 480 ksi (compatible with the modulus assigned to Kentucky thickness design curves) on a California bearing ratio (CBR) 5 subgrade (modulus of elasticity of 7,500 psi). The imposed limitations were selected to permit development of behavioral patterns suitable for comparison and understanding of the individual strain or stress components and of their interactions through strain energy density. These analyses are not intended to provide specific numerical answers covering all situations but may provide values for future analyses of a broader list of variables, such as other subgrade moduli, asphaltic concrete moduli, multilayer pavements, magnitudes of load, tire footprints subdivided into small individual areas with variable load and contact pressures, and tire and axle configurations.

Kentucky Transportation Center, College of Engineering, University of Kentucky, Lexington, Ky. 40506-0043.

The Chevron *N*-layer computer program (Michelow, unpublished) has been modified (*2*) to accept multiple tire loads located within an *X-Y* grid. Superposition principles have been incorporated so the effects of a single load or multiple loads can be calculated at specified locations. Strain energy density is the internal resistance within the body at a specific location that is equal to effects of the external force on the body. Equations to calculate the strain energy density at a specified location within a three-dimensional space incorporate a combination of input parameters, strains, and stresses calculated within the computer program.

Calculation of the total work caused by the external force requires a triple integration of the calculated strain energy density within the body, or the summation of the strain energy density calculated at every point within the body. Such an effort is too massive and expensive to be realistically possible. Reasonable approximations can be made using Simpson's rule to sum the calculated strain energy densities at specified depths for a specific set of *X-Y* coordinates. Irwin (*3*) has related strain energy with fracture energy using the same equation.

PATTERNS OF WORK

Figure 1 shows the calculated strain energy density at 1-in. increments for thicknesses of 4, 8, and 12 in. of full-depth asphaltic concrete on a CBR 5 subgrade—a resilient modulus of 7,500 psi. The three curves for each thickness represent the inside edge of the tire, the center of the tire, and the point midway between the inside edge and the center. The area under the curve indicates the distribution of work through the pavement structure. These patterns raise the question, "Where is the location of maximum work as a function of the locations of the imposed loads?"

LOCATION OF MAXIMUM STRAIN ENERGY DENSITY

An investigation was made to determine the internal work at specified locations. Figure 2 shows patterns of work as a function of location along the centerline of a two-tired single axle load of 18 kips on 8 in. of full-depth asphaltic concrete on a CBR 5 subgrade corresponding to a resilient modulus of 7,500 psi. The work is a summation of the strain energy density using Simpson's rule. It is summed separately for the asphaltic concrete thickness and for 8 in. into the subgrade; these values are then combined to obtain the total work at that location from the top of the asphaltic concrete through the top 8 in.

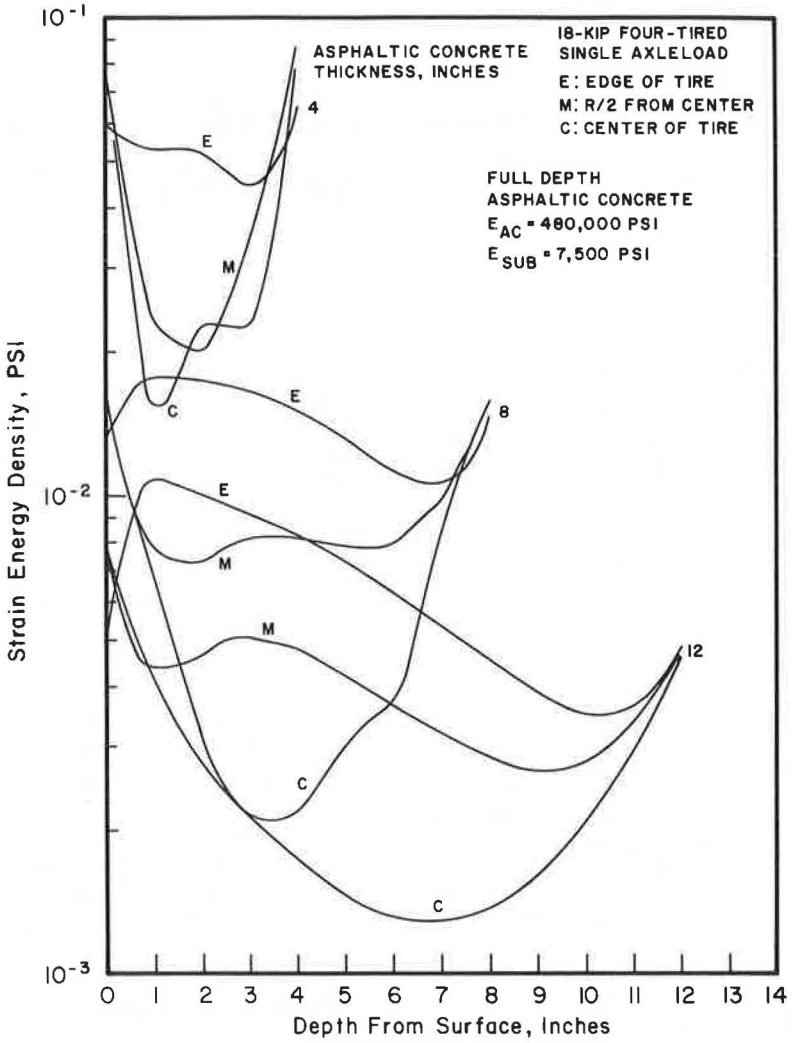


FIGURE 1 Distribution of strain energy density as a function of depth for 4, 8, and 12 in. of full-depth asphaltic concrete at center of tire, edge of tire, and midway between center and edge.

of the subgrade. Note the changes in patterns of work with increasing thickness of asphaltic concrete. The maximum work is always located under the edge of the loaded area.

Figure 3 shows patterns of work for the same structure and axle load except that four equally loaded areas replace the two areas used to obtain Figure 2. The locations of maximum accumulated work are still under the edge of the loaded areas, but the maximum has shifted to the inside edges of the dual areas.

As shown in Figure 4, there appears to be a family of curves relating strain energy density at specific depths as a function of thickness of asphaltic concrete. Figure 5 shows a sensitivity analysis (using Simpson's rule) of the accumulated strain energy density versus thickness of asphaltic concrete for locations corresponding to the edge of the tire, the center of the tire, and midway between the edge and center. The effect of adding a layer of dense-graded aggregate varying from 0 to 8 in. as a layer beneath the asphaltic concrete causes a relatively minor reduction of accumulated strain energy density within the asphaltic concrete layer.

INFLUENCE OF VARIOUS COMPONENTS OF STRAIN

Figures 1–3, particularly Figure 1, prompt the question, "Which one component or components of strain cause the wide variation in strain energy density under the same loaded area?" Figures 6–8 show the distributions of strains through 4, 8, and 12 in. of asphaltic concrete, respectively, caused by an 18-kip, four-tired, single axle load. The distributions are shown for each component of strain for locations at the edge, at the center, and midway between the edge and center of the tire. The XX component is in the plane of the pavement surface, perpendicular to the centerline of the axle. Component YY also is in the plane of the pavement surface and is parallel to the centerline of the axle. Component ZZ is perpendicular to the centerline of the axle and increases with increasing pavement depth. In Figure 6, the XX strain at the bottom of the asphaltic concrete is relatively high. Also, there is almost no difference in pattern or magnitude for the three different answer locations within the tire contact area. The same can

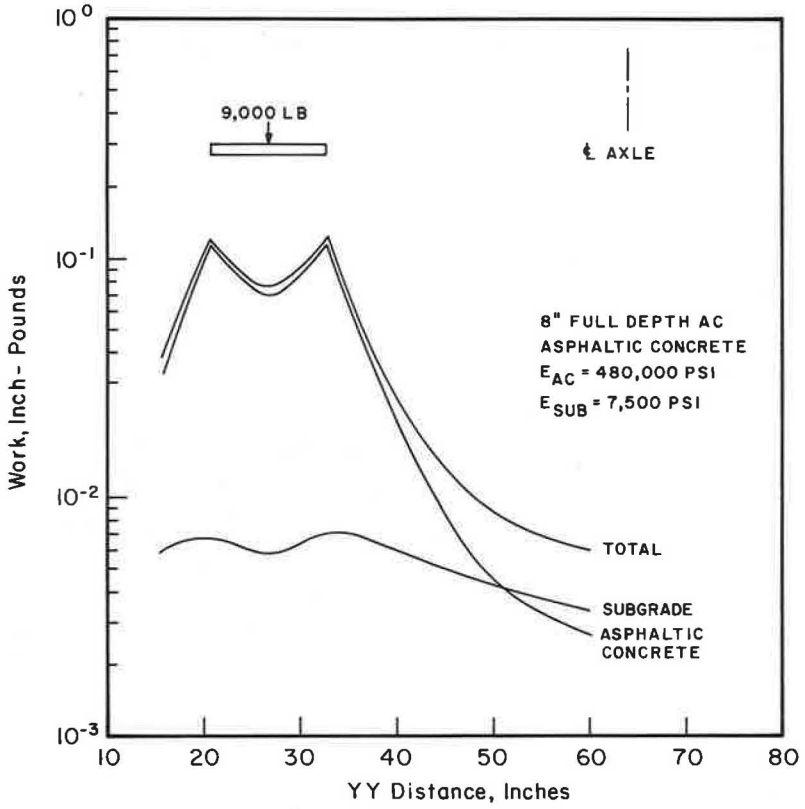


FIGURE 2 Distribution of work for an 8-in. full-depth asphaltic concrete pavement versus location along centerline of the axle for a two-tired 18-kip axle load.

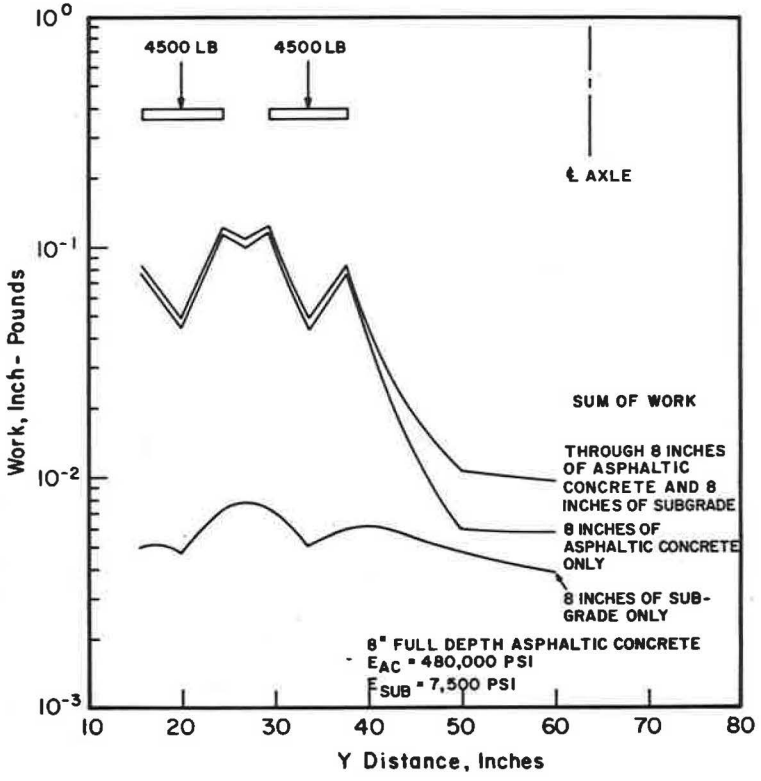


FIGURE 3 Distribution of work for an 8-in. full-depth asphaltic concrete pavement versus location along the centerline of the axle for a four-tired 18-kip axle load.

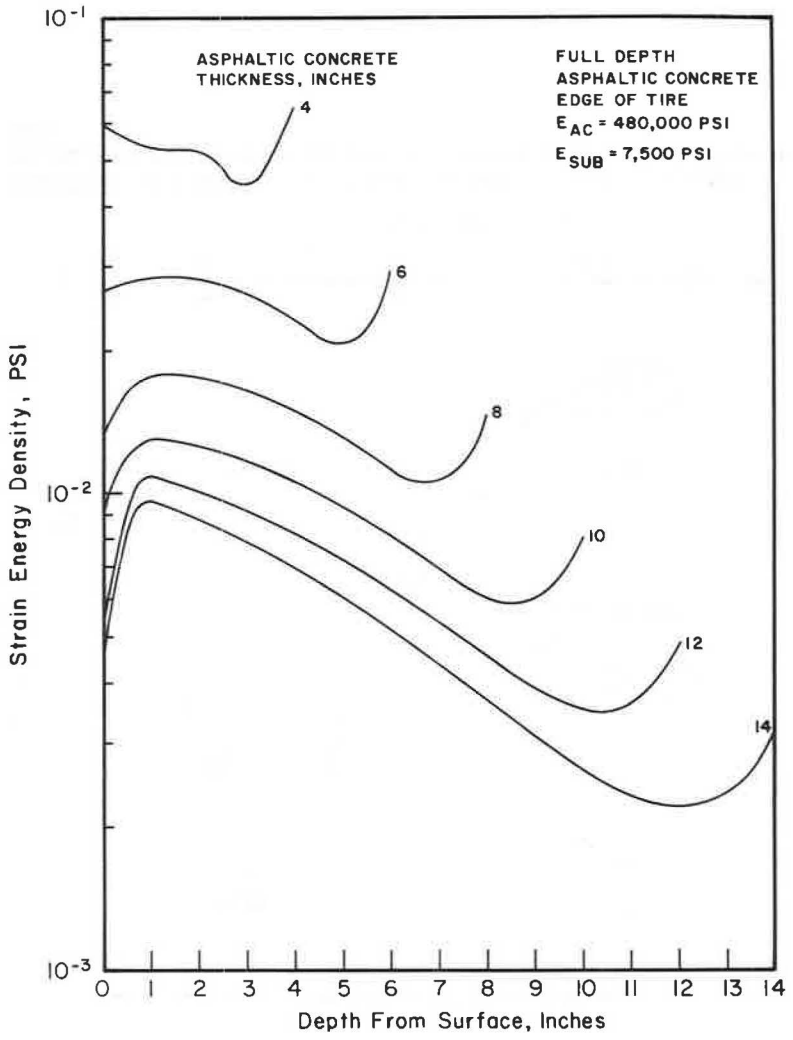


FIGURE 4 Distribution of strain energy density under the inside edge of dual tires of a four-tired, 18-kip, single axle load for various thicknesses of full-depth asphaltic concrete.

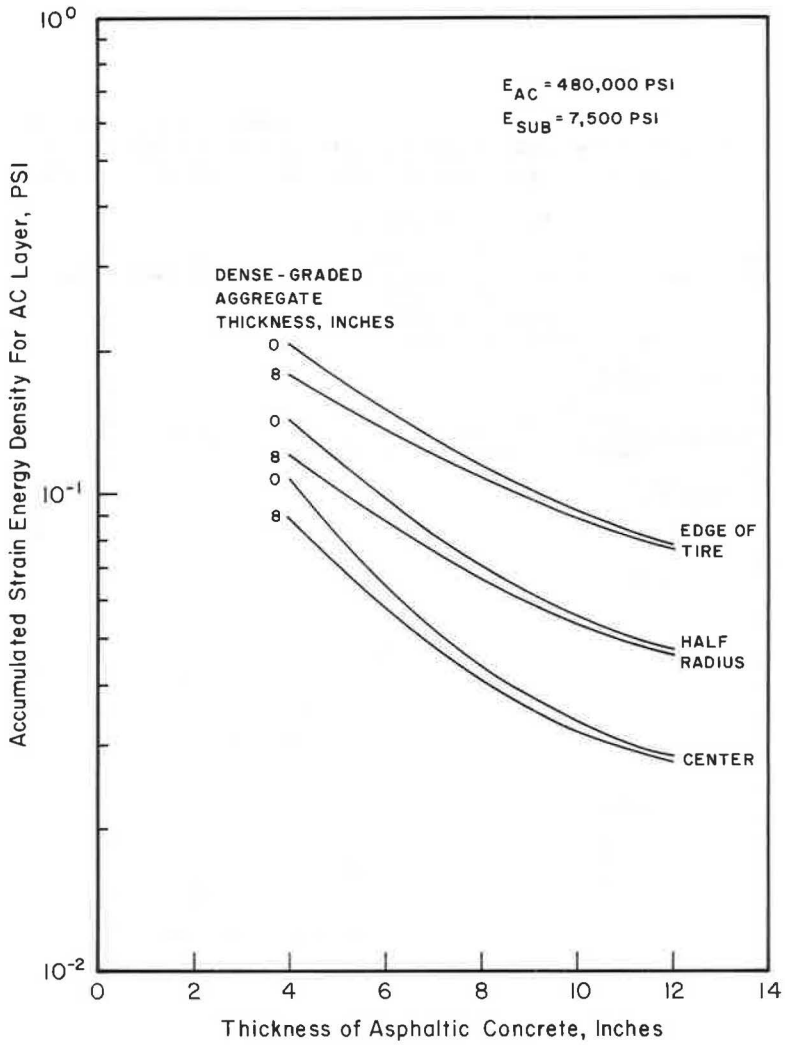


FIGURE 5 Accumulated strain energy density as a function of thickness of dense-graded aggregate base for various asphaltic concrete layer thicknesses.

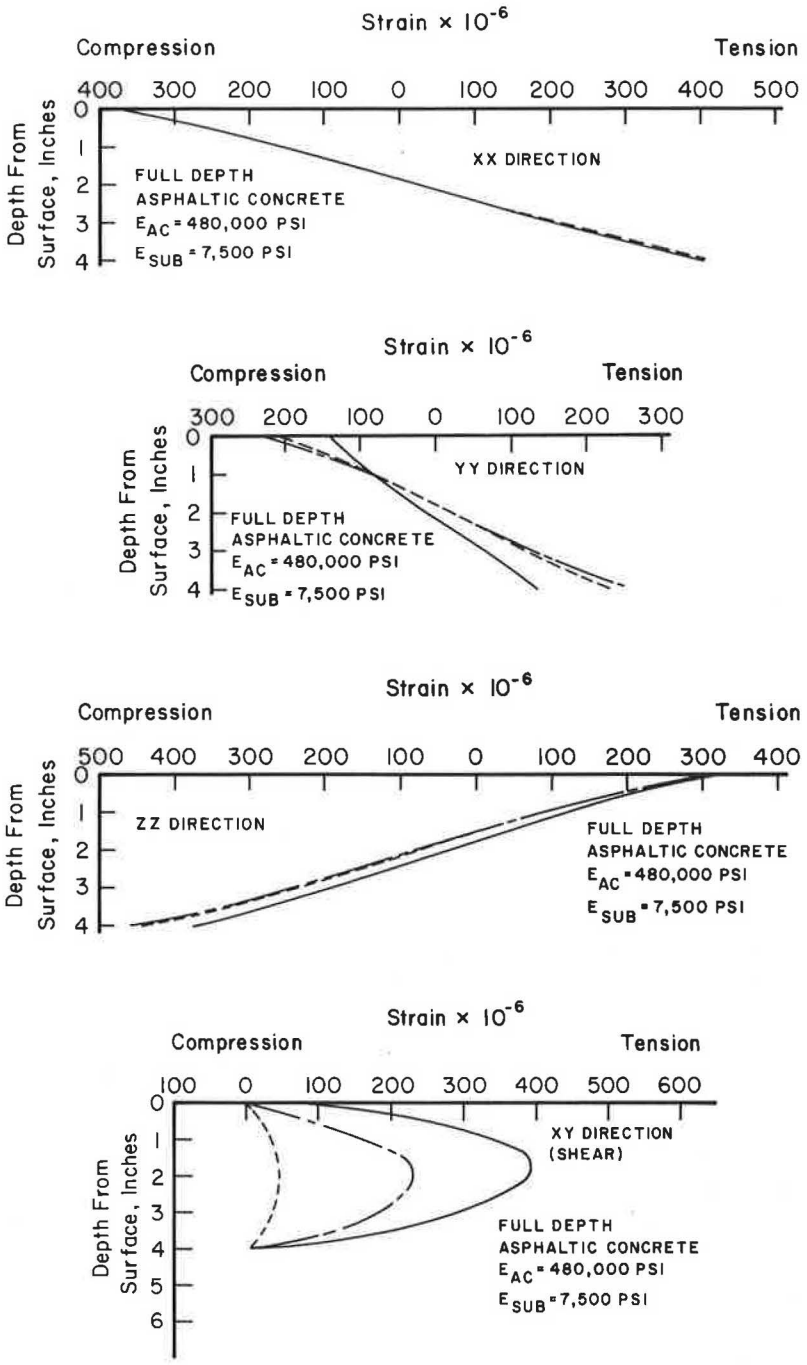


FIGURE 6 Distribution of strains from surface through 4 in. of full-depth asphaltic concrete under an 18-kip four-tired, single-axle load (solid line is at edge of tire; short dashed line is at center of tire; line with short and long dashes is at 1/2 radius).

be said for the YY and ZZ components. The magnitude of the shear (XY) component is highly dependent on the answer location within the tire contact area. The shear (XY) component for each loaded area is zero at the center of that area and appears to be a maximum at the edge of the area. There is a residual effect of shear at the center of the area due to other loaded areas. However, the magnitude of shear varies greatly with depth within the asphaltic concrete and with location within the loaded area. Therefore, the shear component is the major factor influencing the variations in distributions of strain energy density for the asphaltic concrete illustrated in Figure 1. The same comments are true for Figures 7 and 8 except that the magnitudes of the strains are decreasing and the angularity of strain versus depth increases with increasing thickness of asphaltic concrete.

Figures 9–11 show the variations in each strain component for thicknesses of 4, 8, and 12 in. of full-depth asphaltic concrete at locations corresponding to the inside edge of a dual

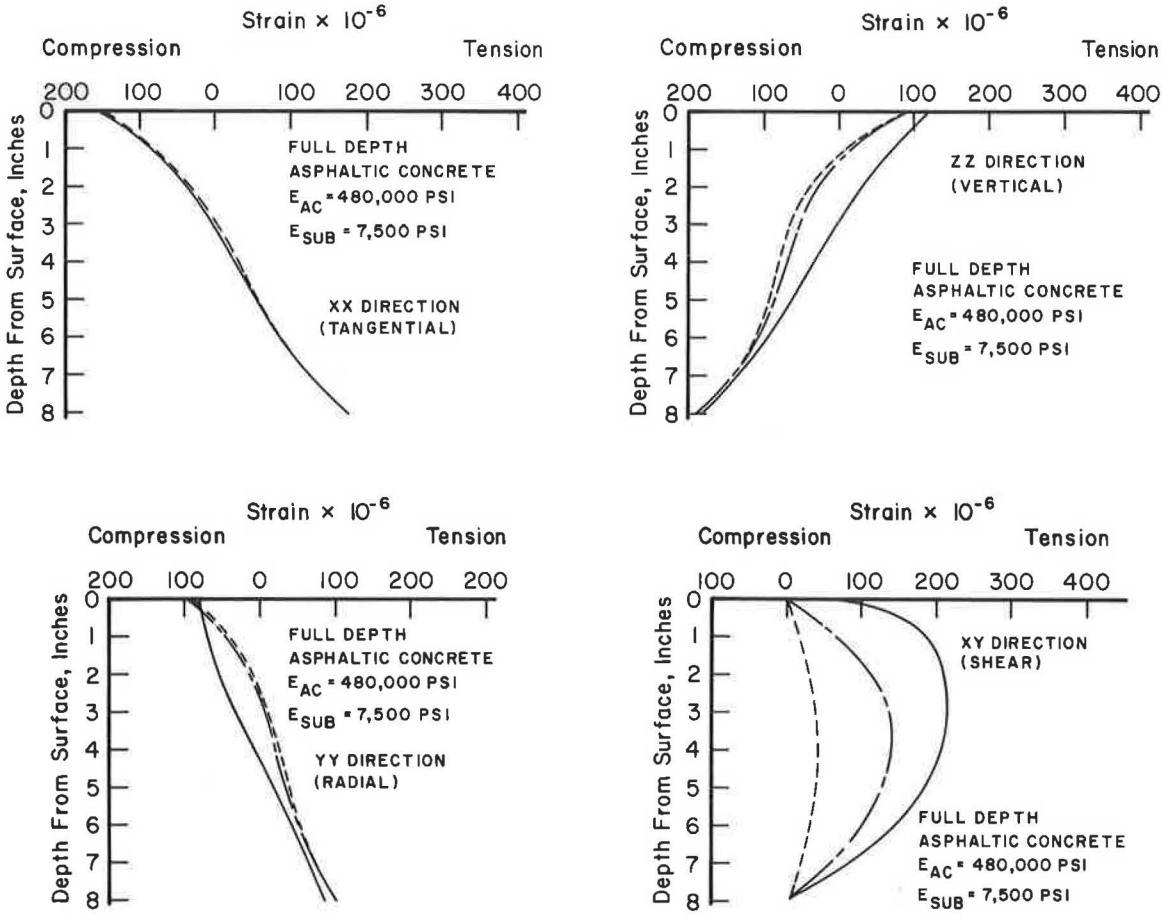


FIGURE 7 Distribution of strains from surface through 8 in. of full-depth asphaltic concrete under an 18-kip, four-tired, single-axle load (solid line is at edge of tire; short dashed line is at center of tire; line with short and long dashes is at 1/2 radius).

tire. Each figure also illustrates the complexity of the XX component's being in compression then progressively changing to tension while the YY component is exactly the opposite, the ZZ component is always in compression, and the XY component is always in tension but varies from nearly zero at the interfaces to a much higher value near the center of the asphalt layer. Figures 12–15 show the family of strain distributions with depth for various thicknesses of full-depth asphaltic concrete (XX, YY, ZZ, and XY, respectively). Figure 15 indicates that the depth at which the maximum shear strain occurs varies with the thickness of the asphaltic concrete. The variation of depth at maximum shear versus pavement thickness is shown in Figure 16. For an 18-kip single-axle load, the maximum shear for pavements up to 8.5 in. of full-depth asphaltic concrete occurs at a depth below the surface corresponding to approximately 35 to 40 percent of the layer thickness. For example, the maximum shear for a 6-in. pavement occurs 2.5 in. below the surface. For 8.5 in. (216 mm), the depth is 3 in. below the surface. Figure 16 also indicates that, for an 18-kip (80-kN) single axle load, the maximum shear will occur no deeper than 3 in. below the surface even when the pavement thickness exceeds 8.5 in. Just because the maximum shear force will occur no deeper than 3 in. does not mean that the asphalt will not experience shear flow below 3 in. If the maximum tolerable shear strain corresponds to a shear force less than the maximum shear force, shear flow will occur below the surface until the depth corresponding to the tolerable shear strain is reached. The maximum lateral displacement of aggregate particles probably should coincide with the depth at which the maximum shear strain (or force) occurs. Lesser movement of particles should take place at deeper depths until the material can withstand the shear force. This phenomenon has been observed and is discussed in a later section.

STRESS ANALYSIS

To determine the shear strength required of the asphaltic concrete mix to resist shear flow, Figures 17 and 18 show the results of analyses using stress components instead of strain components. These two figures are similar to Figures 15 and 16. Figure 17 shows the distribution of shear stress with depth of full-depth asphaltic concrete caused by a four-tired, 18-kip, single-axle load; the stress pattern is similar to the strain pattern shown in Figure 15. Close inspection of Figure 17 shows that the depth of maximum shear stress is the same as that for shear strain for the same pavement thickness. Thus,

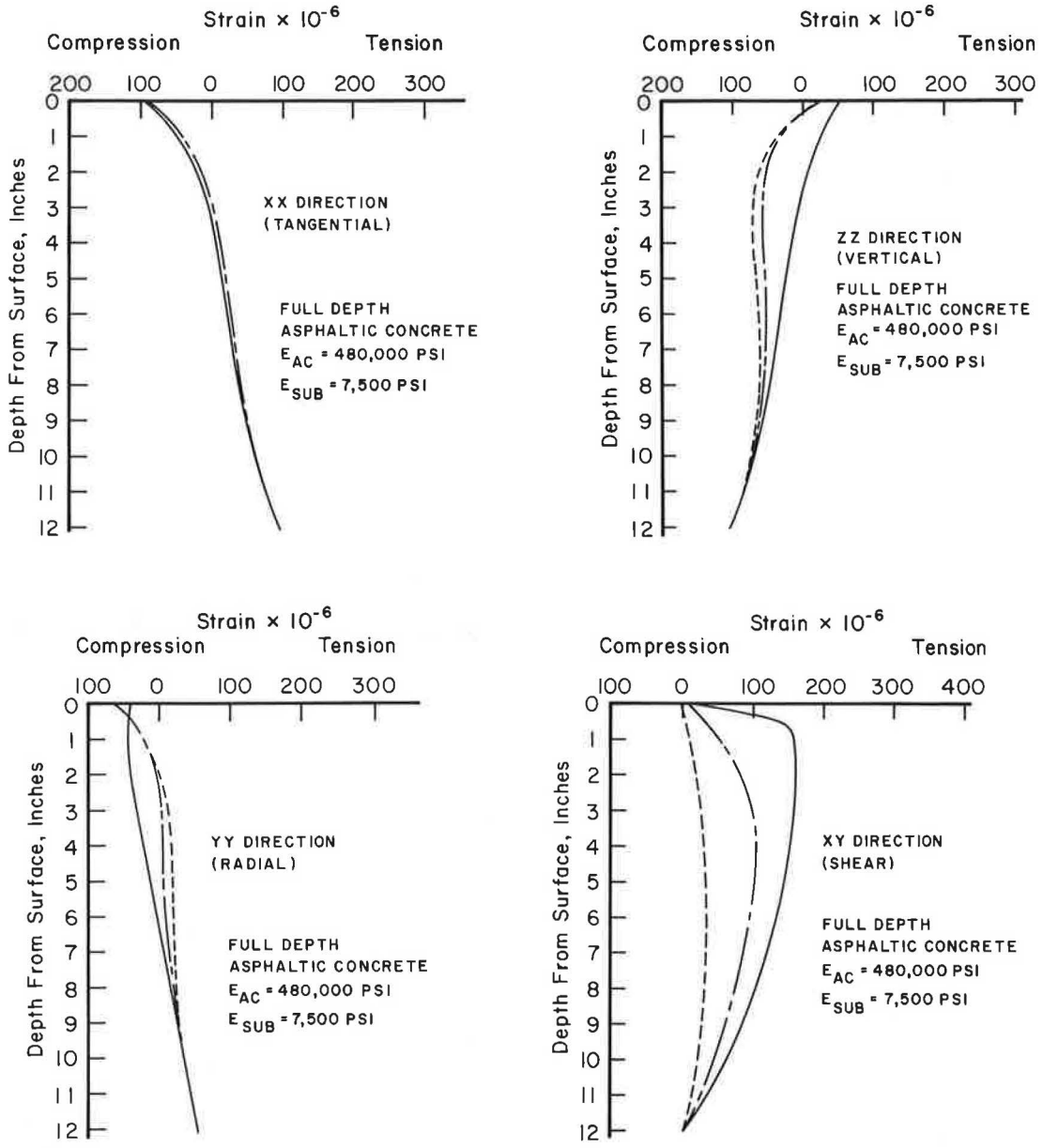


FIGURE 8 Distribution of strains from surface through 12 in. of full-depth asphaltic concrete under an 18-kip, four-tired, single-axle load (solid line is at edge of tire; short dashed line is at center of tire; line with short and long dashes is at 1/2 radius).

Figure 16 is applicable either for shear strain or for shear stress. Figure 18 shows the maximum stress as a function of thickness of asphaltic concrete.

IMPLICATIONS FOR COMPOSITE PAVEMENTS

These analyses illustrate some significant impacts for asphaltic concrete overlays. Because shear stresses and strains reach a maximum within the top 40 percent of the asphaltic concrete layer, rehabilitation of older pavements having two or more overlays may require a different strategy. Kentucky's surface mix has the lowest modulus compared with that of binder and base mixes. When a new overlay is constructed, the older courses of surface mix become the zones of increased shear stress and strain. Aggregate particles may be reoriented by traffic until they are parallel to the pavement surface. Tack coats are necessary to ensure bonding of the new overlay to the existing pavement. However, the combination of an initially weaker modulus and parallel aggregate orientation coupled with a tack coat leads to potentially weak zones with regard to shear resistance. Therefore, milling the old surface mixes and replacing that thickness with new material or reclaimed asphaltic concrete, or both, should be considered. For older pavements, initial milling and overlay costs may be considerably higher. However, benefits would include the removal of material already susceptible to lateral displacement (contributing to rutting) and placement of one lift having

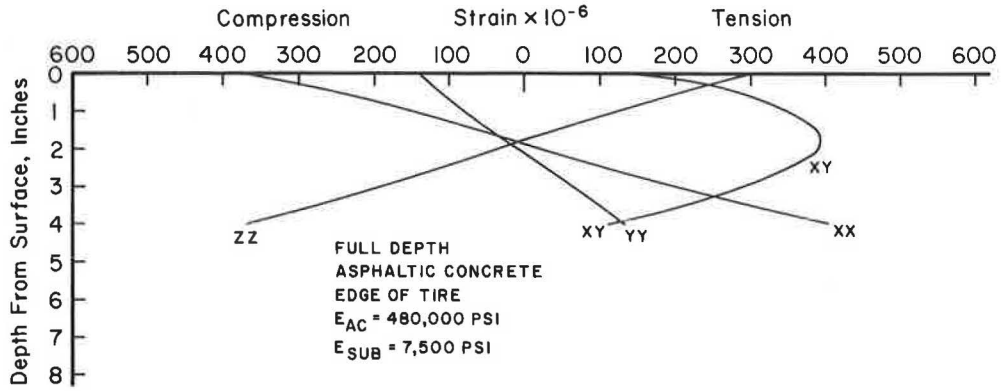


FIGURE 9 Distribution of all strain components from surface through 4 in. of full-depth asphaltic concrete under an 18-kip, four-tired, single-axle load.

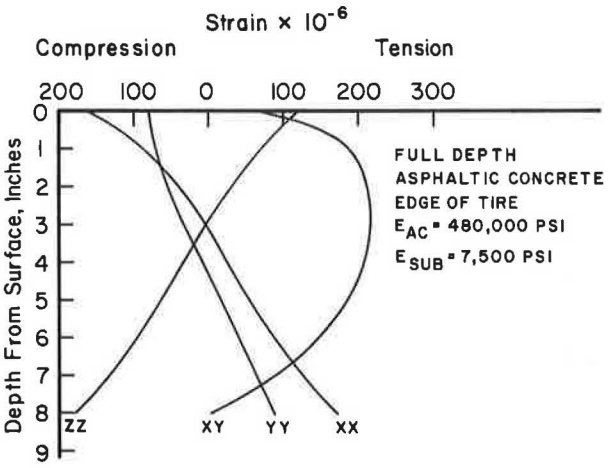


FIGURE 10 Distribution of all strain components from surface through 8 in. of full-depth asphaltic concrete under an 18-kip, four-tired, single-axle load.

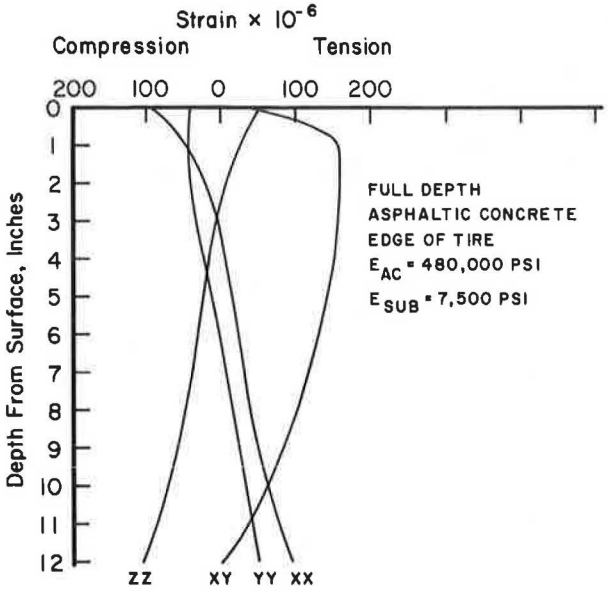


FIGURE 11 Distribution of all strain components from surface through 12 in. of full-depth asphaltic concrete under an 18-kip, four-tired, single-axle load.

better aggregate interlocking and increased resistance to rutting. These benefits should result for lifts up to 3.5 or 4 in. If the milled thickness exceeds 4 in., consideration should be given to constructing a minimum thickness as a leveling course on top of the remaining original pavement and then constructing a 3-in. lift followed by the final surfacing course.

An alternative might be to consider the development of an asphalt mix having a coarser gradation with a top size of 1.5 or 2 in. The larger aggregate gradation may provide more stability and resistance to shear flow. Kentucky has developed a so-called "big-stone mix" that has a top size of 2.5 in. for use in pavements subjected to very heavy loads. For the same period of time, preliminary results indicate that rutting (shear flow) in the big-stone mix is less than half that for conventional mixes (1-in. top size) subjected to relatively the same volume of heavy loadings. Considering the general rule that the minimum lift thickness corresponds to approximately twice the size of the largest aggregate in the gradation, lift thicknesses greater than 3 in. might become feasible.

A composite pavement cross section consisting of 4 in. of asphaltic concrete on 10 in. of portland cement concrete was analyzed. Distribution of stresses and strains differed considerably from the normal pattern for flexible pavements in which stresses and strains dissipate with increasing depth. Analyses indicated that higher shear stresses and strains may occur at the flexible-rigid interface than near the surface and become more pronounced with increasing tire contact pressure. The rigid layer beneath the flexible layer contributes reactionary stresses and strains within the flexible layer. Increased tire contact pressure and axle loads may cause lateral displacement of the asphaltic concrete, resulting in surface rutting. Such phenomena suggest that some pavement failures may be based on shear and other factors rather than on fatigue criteria alone.

OBSERVATIONS

A 17-in. full-depth asphaltic concrete pavement was trenched in 1980 or 1981. A visual inspection showed shear flow from the surface to approximately the 6-in. depth. Within approximately the top 3 in. (the zone of maximum shear), nearly all aggregates were parallel to the pavement surface and appeared to be separated by a thin layer of asphalt cement—

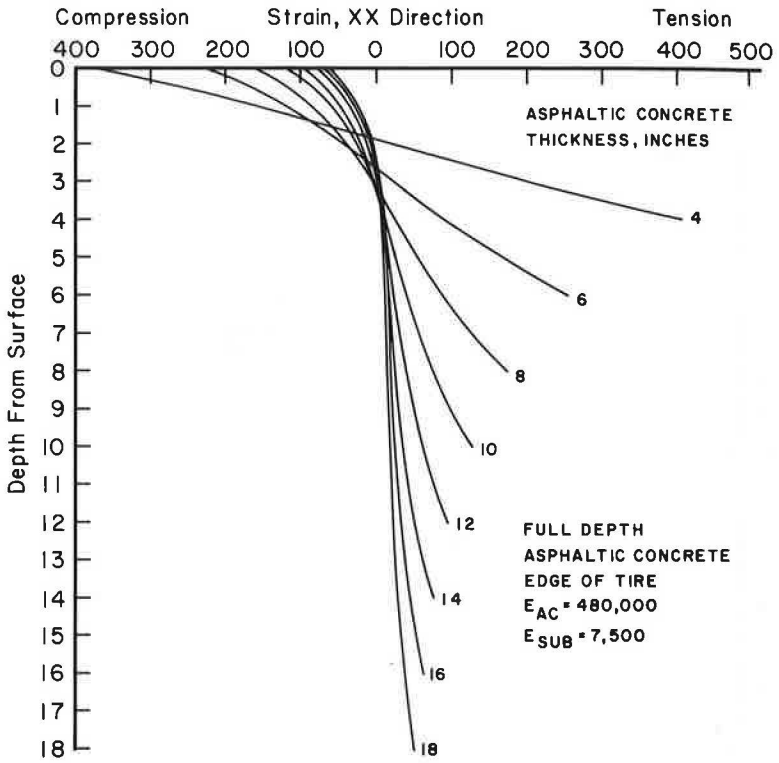


FIGURE 12 Distribution of strain in XX (tangential) direction from surface through various thicknesses of full-depth asphaltic concrete under an 18-kip, four-tired, single-axle load.

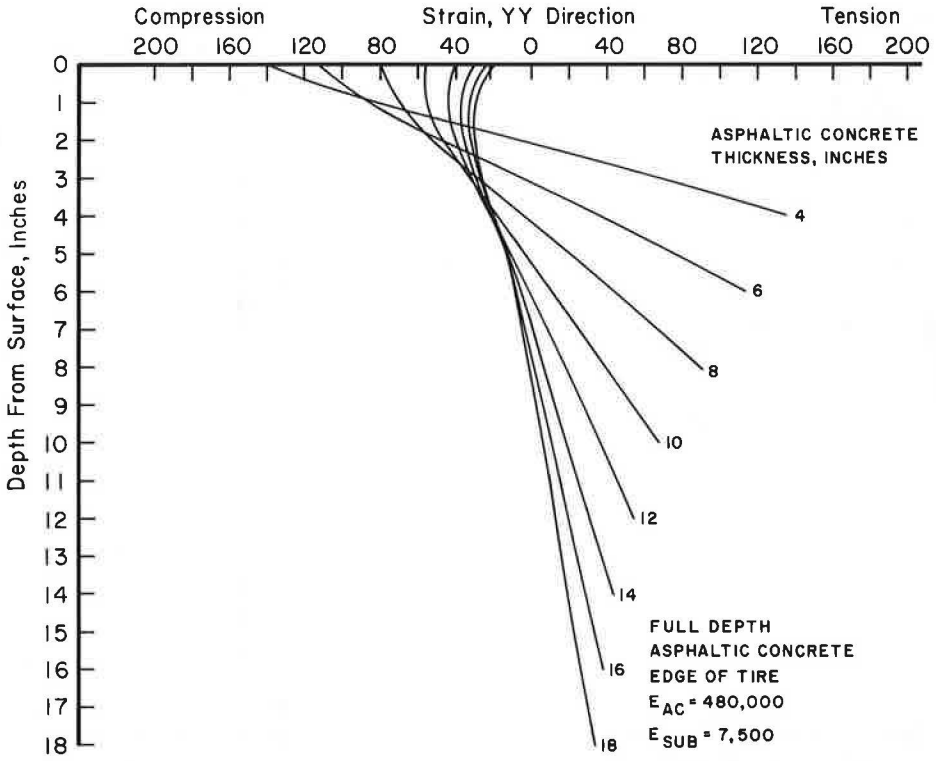


FIGURE 13 Distribution of strain in YY (radial) direction from surface through various thicknesses of full-depth asphaltic concrete under an 18-kip, four-tired, single-axle load.

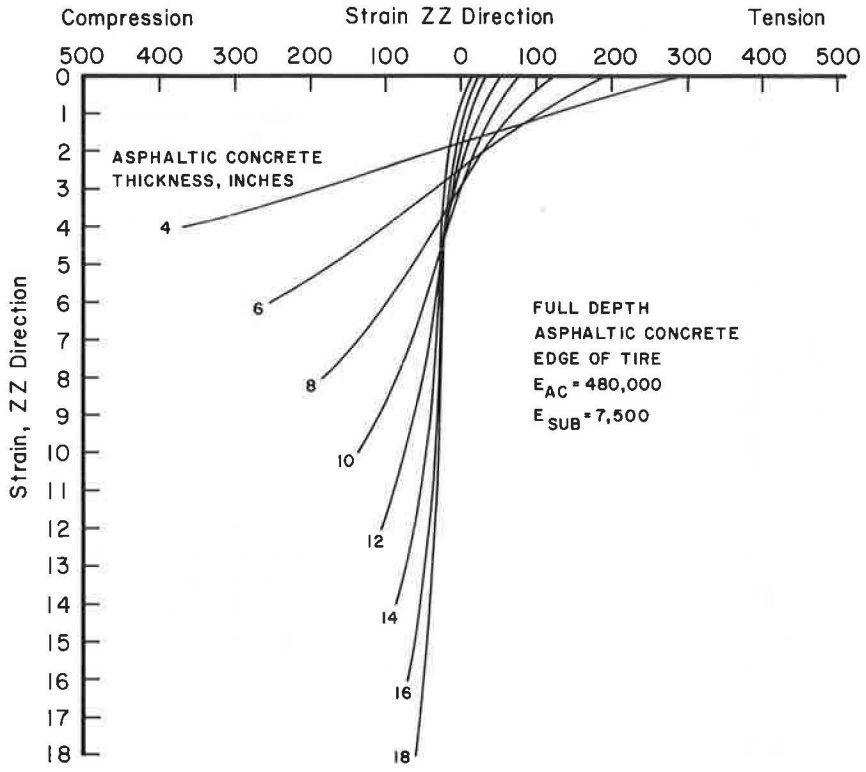


FIGURE 14 Distribution of strain in ZZ (vertical) direction from surface through various thicknesses of full-depth asphaltic concrete under an 18-kip, four-tired, single-axle load.

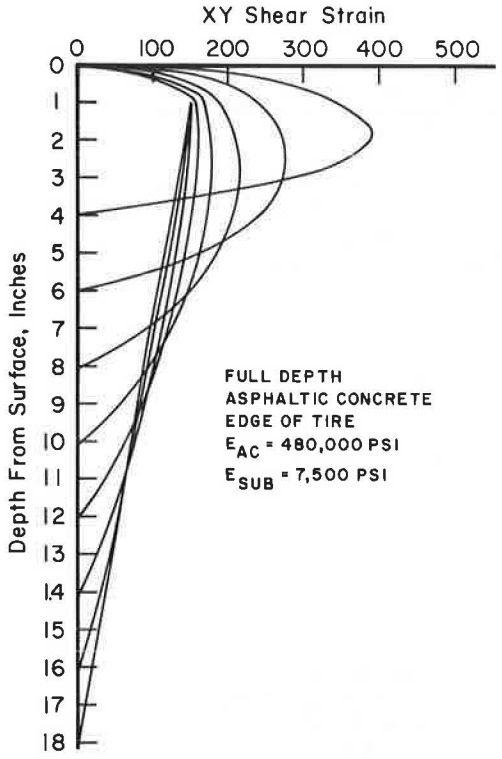


FIGURE 15 Distribution of strain in XY (shear) direction from surface through various thicknesses of full-depth asphaltic concrete under an 18-kip, four-tired, single-axle load.

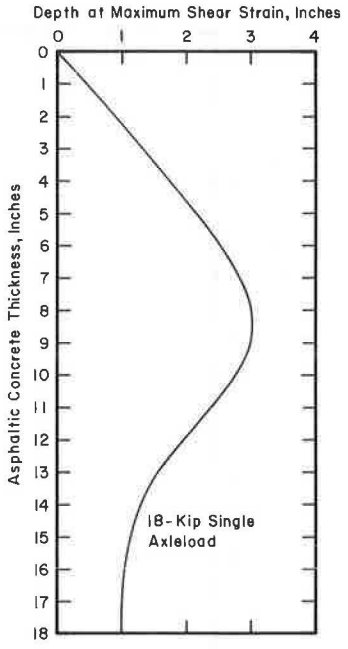


FIGURE 16 Depth of maximum shear strain under an 18-kip, four-tired, single axle load versus thickness of full-depth asphaltic concrete.

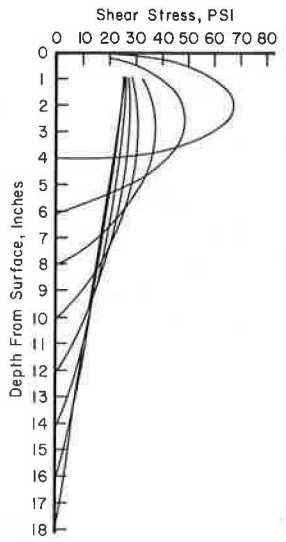


FIGURE 17 Distribution of shear stresses under an 18-kip, four-tired, single axle load from surface to bottom of various thicknesses of full-depth asphaltic concrete.

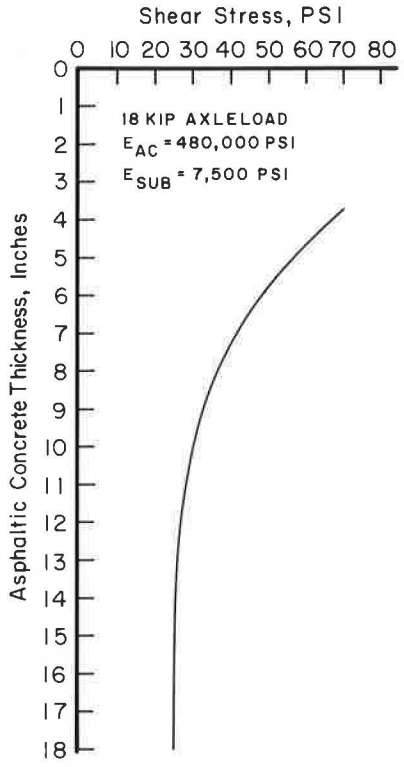


FIGURE 18 Distribution of maximum shear stress under an 18-kip, four-tired, single-axle load versus thickness of full-depth asphaltic concrete.

similar to a sandwich. The 1.25-in. surface mix had been reduced to approximately 0.5 in. in the wheel track and was nearly 2.5 in. thick between wheel tracks. Thus, material had been moved laterally by shear-flow action. At each of two construction interfaces, the long axes were parallel to the construction surface for the layer below. Between the 3- and 6-in. depths, the orientation of the aggregates became more random with increasing depth from the surface. Below the 6-in. depth, the aggregates were randomly oriented to each other except at layer interfaces, as should be expected, and no shear flow was evident below that depth. Compaction equipment had turned the long axis of the aggregate particles parallel to the surface.

The same observation was noted when two 18-in. full-depth asphaltic concrete pavements were trenched on another route. On another pavement consisting of 7.5 in. of asphaltic concrete on 12 in. of crushed stone aggregate, there was a slight indentation at the top of the aggregate base. However, the indentation was so slight that it may have been caused by construction equipment during paving of the bottom layer of asphaltic concrete. The same shear-flow action was observed in the asphaltic concrete at this site as seen at the full-depth asphaltic concrete pavement sites. Orientation of the aggregates was nearly random at the bottom of the 7.5 in. of asphaltic concrete.

CORRELATION OF THEORY AND OBSERVATION

Shear is most likely to occur wherever the shear resistance is the least. One inherent zone of potential weakness to shear forces is at interfaces of construction lifts. At such interfaces, the roller may turn the top layer of aggregates in the lower lift parallel to the surface. Therefore, the aggregates at the bottom of the upper layer have the least opportunity of interlocking with the top aggregates of the layer below. Lift thicknesses can be determined easily by examining cores in which the long axis of too many of the aggregate particles are parallel to the interface. Typical lift thicknesses constructed in Kentucky consist of 0.75 to 1 in. of surface mix, 1.5 to 2 in. of binder mix, and 2 to 2.5 in. of base mix. Thus, for a 6- or 8-in. asphaltic concrete pavement, maximum shear will occur at the 2.5- or 3-in. depth, respectively—right where a construction plane produces the least aggregate interlock. Thus, shear flow should be expected where aggregate interlock is the least.

For the pavements that were trenched, shear flow was observed down to the 6-in. depth. Figure 17 shows that the shear stress at the 6-in. depth for these pavements would be approximately 25 psi. A shear stress of 25 psi might be a safe level or might be excessively high for asphaltic concrete pavements. The tolerable shear stress level for asphaltic concrete is not known at this time. a value of 25 psi might be safe for asphaltic concrete modulus of 480 ksi but might change as the modulus changes.

SUMMARY

Following are the most important findings of these sensitivity analyses:

1. Sensitivity analyses indicate that the maximum-strain energy density occurs under the edge of the tire closest to the other tire in a dual tire arrangement.

2. For a given thickness of asphaltic concrete, the distribution of any one of the three principal strains or stresses varies slightly with location within the tire contact area.

3. Shear is the strain or stress component that exhibits the most variation throughout the thickness of the asphaltic concrete and is primarily a function of the location within the tire contact area. The maximum variation occurs under the edge of the tire closest to the adjacent dual tire.

4. The depth of maximum shear is a function of the thickness of the asphaltic concrete layer. For thicknesses up to approximately 8.5 in., that depth is approximately equal to 35 to 40 percent of the thickness of asphaltic concrete. For greater thicknesses, the depth of maximum shear appears to move up toward the surface and might become asymptotic at approximately the 1-in. depth. These values are appropriate for a four-tired, 18-kip, single axle load and would vary for other magnitudes of load and configurations of tires and axles.

RECOMMENDATIONS

1. Consideration should be given to any or all of the following:

- Increasing the shear resistance of the binder mix,
- Eliminating the binder-mix layer and replacing it with a base-mix layer, and
- Developing a coarser mix for use immediately below the wearing course.

2. Consideration might be given to the placement of a 1-in. surface-mix layer on a minimum of a 3-in. layer of a high shear–resistant mix to eliminate a construction interface in the zone of maximum shear.

3. Pavements having two or more overlays of surface mix that are candidates for another overlay might be considered for milling all previous surface mixes and placing one layer of base mix followed by a surface mix to eliminate material already weakened by shear flow.

4. In-place pavements exhibit distresses that indicate shear failures within the asphaltic concrete layers. Research is under way to determine shear parameters of hollow cylindrical specimens of asphaltic concrete (*4*). Critical values for shear stresses or strains are not known at this time. Torsional testing of solid specimens may provide insight, but development of higher-capacity equipment than is currently available is necessary. Future research may provide critical values of stresses as well as guidance for use in design of new pavements and rehabilitation strategies.

ACKNOWLEDGMENTS

The financial support provided by the Kentucky Transportation Cabinet and FHWA is gratefully acknowledged.

REFERENCES

1. H. F. Southgate and R. C. Deen. *Distributions of Strain Components and Work Within Flexible Pavement Structures*. Research Report UKTRP-86-21. Kentucky Transportation Research Program, University of Kentucky, Lexington, Sept. 1986.
2. H. F. Southgate, R. C. Deen, and J. G. Mayes. Strain Energy Analysis of Pavement Designs for Heavy Trucks. In *Transportation Research Record 949*, TRB, National Research Council, Washington, D.C., 1981.
3. L. H. Irwin. Use of Fracture Energy as a Fatigue Failure Criterion. *Proc., Association of Asphalt Paving Technologists*, Minneapolis, Minn., Vol. 46, 1977, pp. 41–63.
4. J. B. Sousa and C. L. Monismith. Dynamic Response of Paving Materials. In *Transportation Research Record 1136*, TRB, National Research Council, Washington, D.C., 1987.

Publication of this paper sponsored by Committee on Flexible Pavement Design.

Performance of Flexible Pavements

JAMES MARK MATTHEWS AND B. B. PANDEY

An investigation was conducted to determine the life period of full-depth granular pavements in India. Benkelman beam deflections, rutting, cracking, and patching were measured on different test sections to calculate the performance of the pavements. A repeated-load-test apparatus was fabricated in the laboratory for testing the subgrade soils and water-bound macadam base to determine the elastic moduli under repeated triaxial stress conditions. A finite element computer program was developed to determine the stresses and strains in pavement layers and to correlate the pavement performance and the critical stress and strain values. The pavement surface deflections measured by Benkelman beam are in close agreement with the values predicted by the computer program. From the repeated-load-test results, relationships were found between (a) the resilient modulus and the lateral pressure and (b) the resilient modulus and the sum of principal stresses. The equation developed for predicting the rut depth from the Benkelman beam deflection data is in close agreement with that developed in the AASHO road test. The rut depth was also related to the gravel surfacing depth and the cumulative axles. Finally, a regression equation for finding the lives of flexible pavements was established using the rut depth and subgrade vertical strain values.

Highway engineers have been constantly working toward developing a rational method to estimate the life of a given pavement through full-scale road tests, model studies, laboratory experiments, and theoretical analysis. Unlike steel and concrete, whose structural properties are well defined, the behavior of crushed rock, water-bound macadam (WBM), and other granular materials is extremely complex and was little understood until about 30 years ago. Since then slow progress has been made in the development of a rational method to find the relationship between the life period of pavements and the design of constituent layers.

Flexible pavement methods are still empirical or semiempirical, on the basis of past experience with similar subgrades, pavement materials, and traffic loads. These methods are satisfactory as long as the materials, traffic loading conditions, and layer thicknesses do not differ from those for which the methods were developed. Because of considerable increase in frequency and intensity of axle loads and the use of new pavement materials, the semiempirical design methods are no longer adequate.

The focus here is on the study of the performance of WBM pavements and the laboratory evaluation of properties of the pavement materials to predict the serviceable life of a granular pavement in India.

James Mark Matthews, Richmond Field Station, Institute of Transportation Studies, University of California, Berkeley, Calif. 94720. Current affiliation: Department of Civil Engineering, Temple University, 12th and Norris Streets, Philadelphia, Pa. 19122. B. B. Pandey, Indian Institute of Technology, Kharagpur, 721 302, WB, India.

DEVELOPMENT OF FINITE ELEMENT ANALYSIS

A computer program known as RAOPAVE was developed by idealizing the flexible pavement into a finite element continuum. The analysis was carried out for a single wheel load of 40,131 (9,000 lb) distributed over a circular area of 152-mm radius with a tire pressure of 0.55 MPa (80 psi).

Idealization

In this investigation a layered pavement system was idealized as an axisymmetric solid with finite boundaries in both radial and axial directions, as shown in Figure 1. The axisymmetric body was then divided into a set of ring elements, rectangular in section and connected along their nodal circles. The finite elements are actually complete rings in the circumferential direction, and the nodal points at which they are connected are circular lines in plan view. Because of axisymmetry, the three-dimensional problem reduces to a two-dimensional case similar to a plane strain problem. Tensile stresses and strains were taken to be positive, and compressive stresses and strains negative. For each element the four nodal points were numbered in the clockwise direction. Each node has two degrees of freedom.

Displacement Functions

The two displacement components in a solid continuum varied as complicated functions of position. A number of approaches, including power series and Fourier series expansions, have been proposed by several researchers (*1,2*) to represent the behavior of displacement components inside each element. Because of the assumptions made about these functions, the accuracy of the answer increases as the element size decreases. For this investigation, the displacement functions inside each element were approximated by the following:

$$u(r,z) = b_1 + b_2r' + b_3z' + b_4r'z' \quad (1)$$

$$v(r,z) = b_5 + b_6r' + b_7z' + b_8r'z' \quad (2)$$

where for each element the local coordinate system r',z' was used, which has its origin at the center of each element.

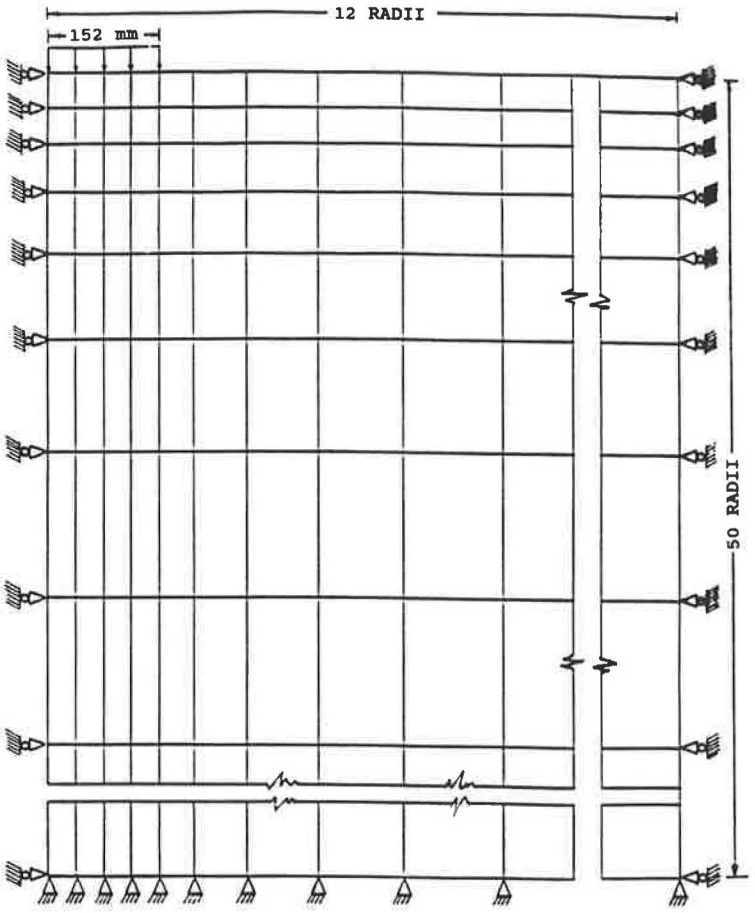


FIGURE 1 Finite element idealization.

Global Stiffness

The stiffnesses of all elements were assembled to obtain the total stiffness for the system. The required assembly was accomplished by using the element-node table and displacement-code number array. Because the system stiffness matrix comes out to be banded and symmetric, it is assembled in half-band form. A consistent load vector was formulated using the principle of virtual work (*3*).

Boundary Conditions

Nodal points on the vertical boundary at a distance of 12 radii from the center and on the centerline were constrained from radial movement; those on the bottom boundary were not allowed to move vertically or horizontally. The bottom boundary was fixed at a depth of 50 radii in accordance with the findings of Duncan et al. (*4*).

Verification of Elastic Finite Element Analysis

The validity of the finite element computer program was established by comparing the results with those of Ahlvin and Ulery (*5*). The vertical and radial stresses along the centerline of the load, as shown in Figures 2 and 3, respectively, and at a radial distance of 0.752 radii (from the centerline of the load) obtained by the program, were compared with those obtained by the elastic half-space analysis after Ahlvin and Ulery. The deflections and stresses computed by this program agree closely with those obtained from the elastic half-space analysis. A detailed printout of the computer program is provided by Tangella (*6*). Several other elastic multilayered computer programs (e.g., ELSYM, BISAR, ILLIPAVE, and FEPAVE) are available for the structural analysis of a pavement, and any of them also can be used. However, the finite element method using the principle of stress transfer developed by Zienkiewicz et al. (*2*) is suitable for eliminating the tensile stresses in unbound granular layers. This work is beyond the scope of the present study and has been done elsewhere (*7*).

EXPERIMENTAL SETUP

The schematic diagram of the experimental setup for repeated load triaxial tests is shown in Figure 4. The details of this setup and its mode of working are given by Tangella (*6*) and Tangella and Pandey (*8*).

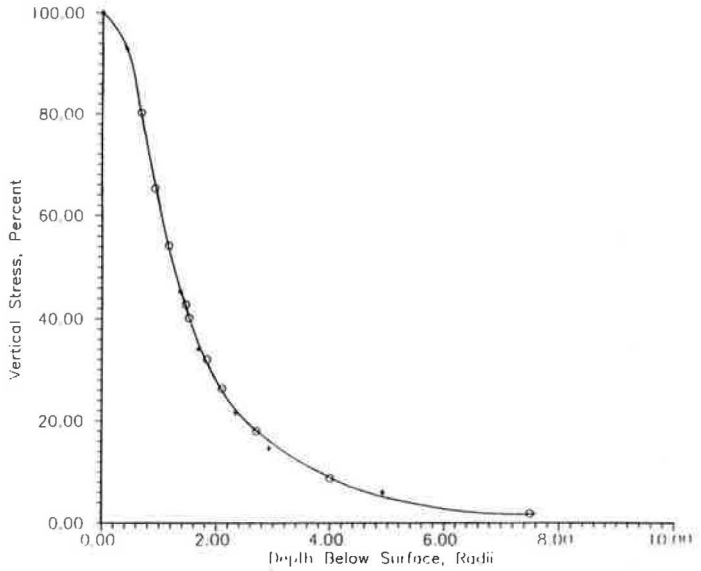


FIGURE 2 Comparison between vertical stresses of RAOPAVE (*open circles*) and elastic half-space analysis (at centerline of load) (*closed circles*).

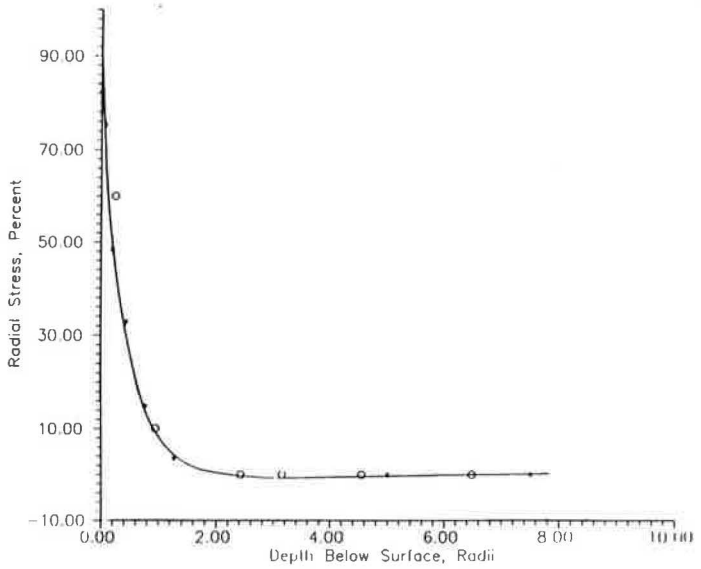


FIGURE 3 Comparison between radial stresses of RAOPAVE (*open circles*) and elastic half-space analysis (at centerline of load) (*closed circles*).

Repeated-Load Experiments

Specimens 100 mm in diameter and 200 mm in height were cast using the soil samples brought from the subgrades of the field test sections. The field bulk density was calculated for each test section at the maximum in-situ moisture content for each of the four seasons. The samples were cast to the field density at the highest value of the in situ moisture content. Trials were made, varying the number of layers and the number of blows, using the standard Proctor hammer (of 24.44 N weight and 300-mm fall) to compact the soil to the fixed volume. The variation in the moisture content of the specimen was kept within 0.2 percent.

Initially, 10 load repetitions were applied to condition the specimen. After 1,000 repetitions, for a given deviatoric stress and for each set of lateral pressures, the load cell and linear variable differential transformer (LVDT) pulses were recorded for about 30 load repetitions. The process was continued until all sets of deviatoric stresses were recorded. Strict control was exercised in casting the specimens at the in situ moisture content and field density. Figure 5 shows the repeatability of two experiments. Deviatoric stresses ranging

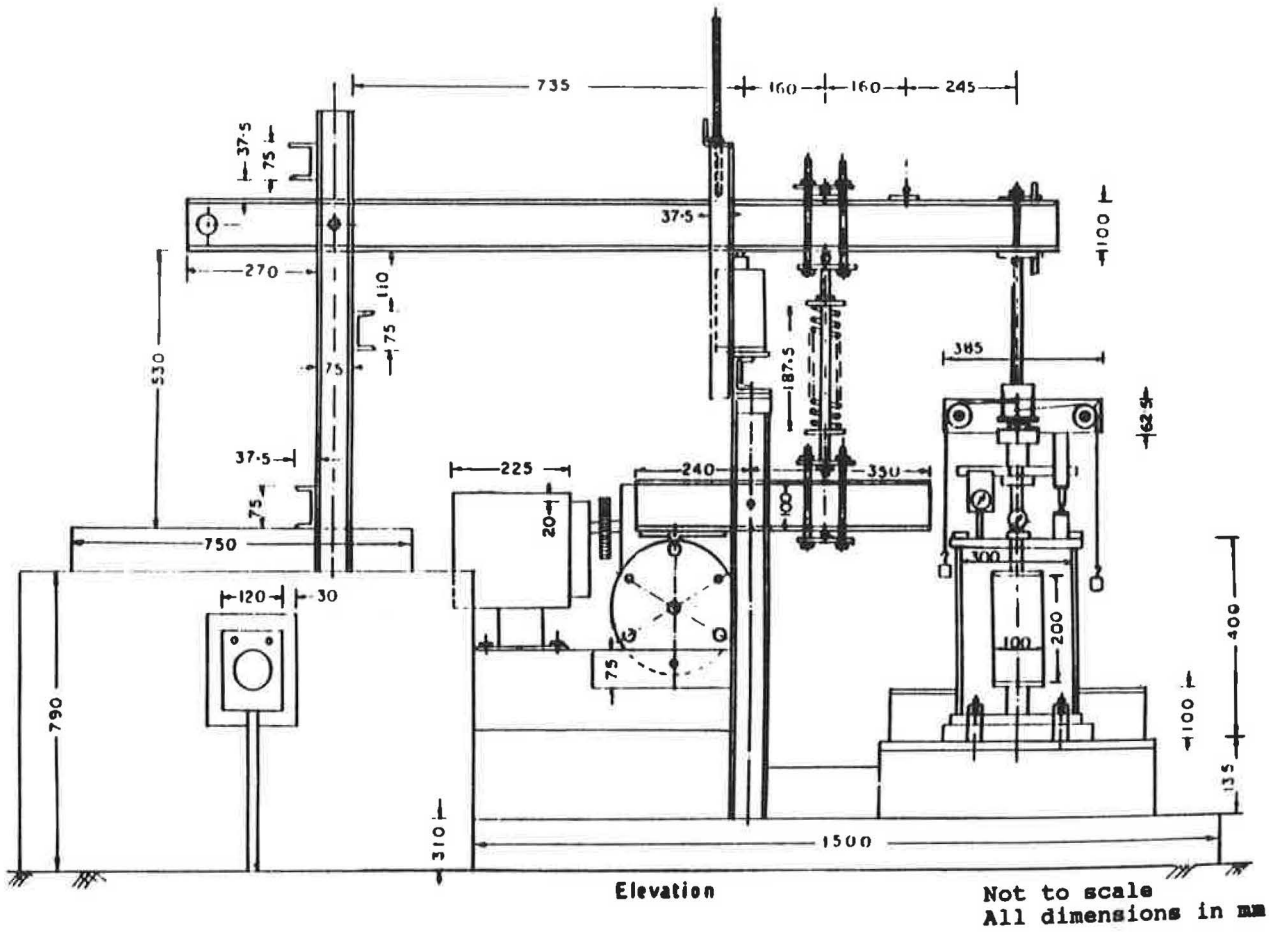


FIGURE 4 Experimental setup.

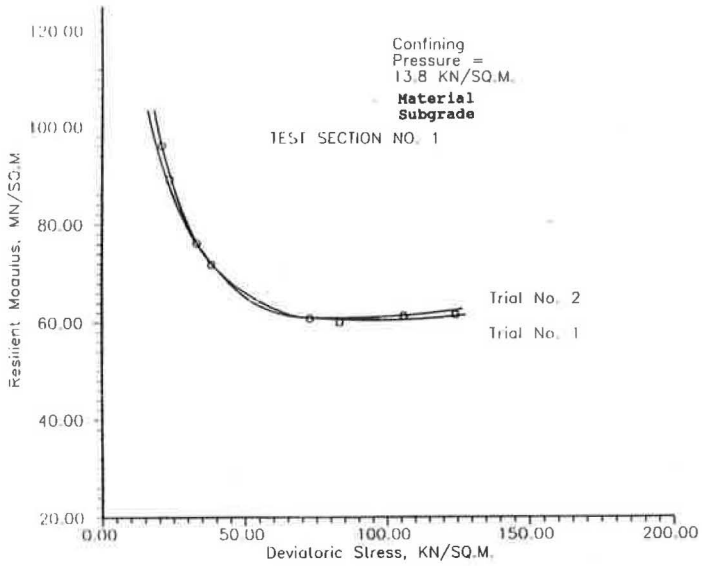


FIGURE 5 Repeatability of two experiments.

from 15 to 150 kN/m² were applied to samples of 15 test sections. Lateral pressures of 13.8 kN/m² (2 psi) and 20.7 kN/m² (3 psi) were applied, which are very close to the subgrade lateral pressures found by the computer program. Because there is no significant change in results under the cyclic lateral pressure or the constant lateral pressure (equivalent to the mean of the cyclic lateral pressure) (*9*), a constant lateral pressure is used in the laboratory study even though cyclic lateral pressure occurs under actual conditions. The duration of the loading pulse was 0.12 sec (*10*).

Tests for Other Soil Properties

The laboratory California bearing ratio (CBR) tests at field densities and in-situ moisture contents, liquid limit, plastic limit, and Proctor compaction tests were conducted on soil samples of the subgrades of all the test sections of national highways.

Repeated-Load Tests on Granular Materials

Two types of aggregate gradations were adopted for repeated-load triaxial tests. One gradation adopted is the same as that of Monismith et al. (*11,12*), and the other corresponds to that of the Indian Roads Congress (IRC-19-1977). The maximum size of the aggregate is 20 mm. Hicks and Monismith (*13*) found that the influence of grading on the resilient modulus for crushed rock is negligible. Hence, the results of repeated-load tests on IRC B-type screenings were used to analyze all layers of the WBM portion of the test sections. Dolerite chips were crushed to the required gradations, and 10 kg of material was prepared for each specimen. Specimens of 100-mm (4-in.) diameter and 200-mm (8-in.) height were cast using a split mold. With the help of a needle vibrator, dry densities of 2224 kg/m³ (139 lb/ft³) for the gradation given by Monismith et al. (*11,12*) and 2127 kg/m³ (133 lb/ft³) for the gradation given by IRC for B-type screenings were obtained. A 5-psi suction was applied during casting of the sample and was continued until the sample was fixed in the triaxial cell.

The procedures used to fix the sample and conduct the test are the same as those followed for soil samples, except for the following details.

Three sets of deviatoric stresses were applied for all samples. The values were 122.6 kN/m², 147.1 kN/m², and 196.1 kN/m². For each of the deviatoric stresses, seven sets of lateral pressures were applied (*14*): 69 kN/m² (10 psi), 138 kN/m² (20 psi), 207 kN/m² (30 psi), 276 kN/m² (40 psi), 345 kN/m² (50 psi), 414 kN/m² (60 psi), and 483 kN/m² (70 psi). All of these stresses are found in the field pavement structures (*6,10,11*). Using the results, relationships were found between (a) the resilient modulus and the lateral pressure, as shown in Figures 6 and 7, and (b) the resilient modulus and the sum of principal stresses, as shown in Figures 8 and 9. The results of this investigation are close to those of Monismith et al. (*11*).

EXPERIMENTS ON IN-SERVICE PAVEMENTS

Selection of Test Sections

Fifteen test sections were selected in the eastern parts of India, covering about 250 000 km² between the latitudes 19°N and 27°N and the longitudes 83°E and 88°E. For uniformity and quality control in the test sections, the following criteria were used:

1. The preferred length of the test section is 300 m.
2. The section should be a straight stretch with uniform soil characteristics and pavement structural composition. Steep longitudinal gradients and curves must be avoided. The stretch should be continuous with no major repairs and with no culverts in between.

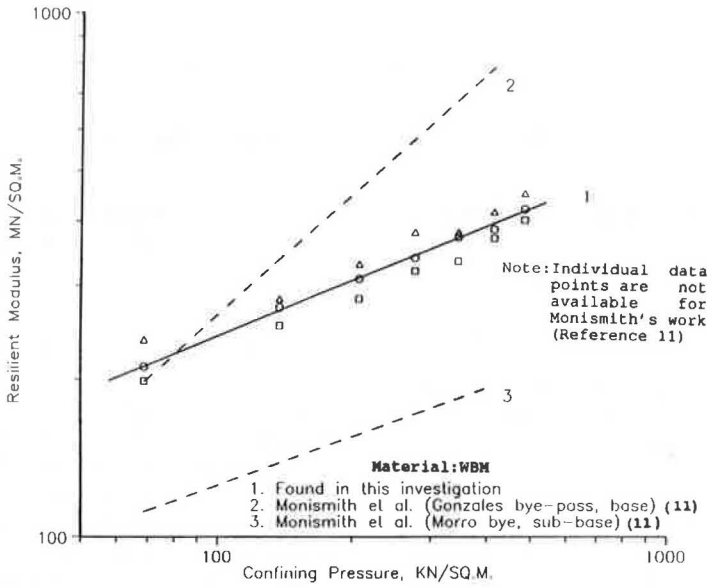


FIGURE 6 Confining pressure versus resilient modulus (*11*).

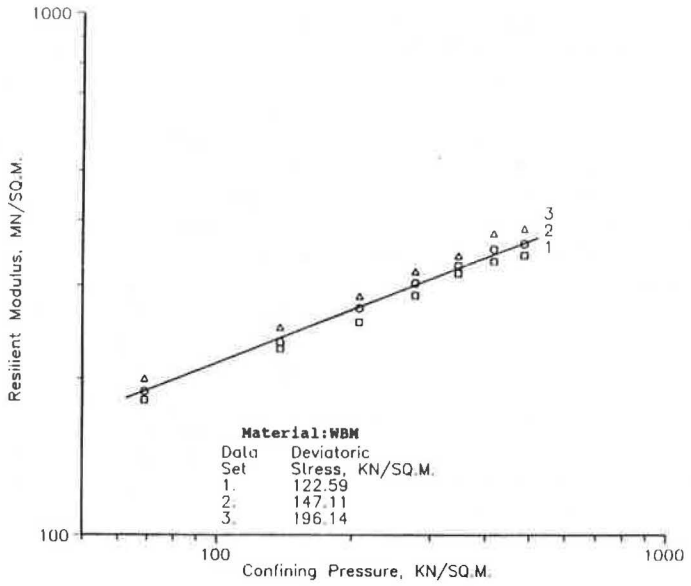


FIGURE 7 Confining pressure versus resilient modulus for granular materials (IRC-19-1977).

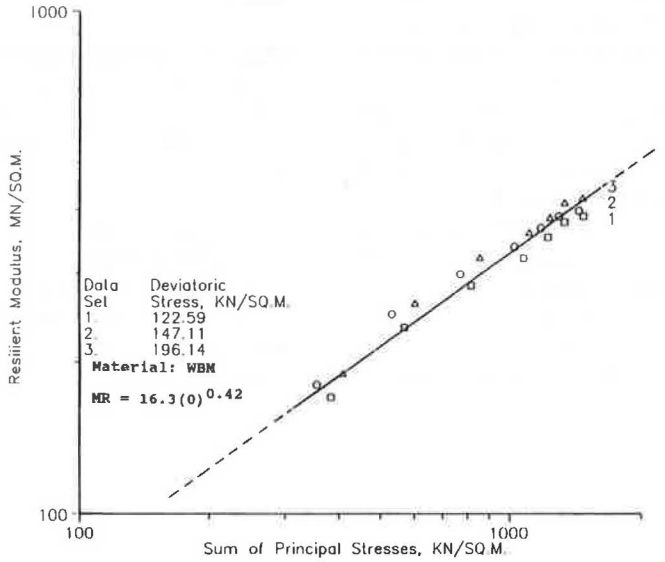


FIGURE 8 Sum of principal stresses versus resilient modulus (*11*).

3. The maximum height of the embankment should be less than 6 m.
4. The section should not be located in areas likely to be flooded.
5. The section should not be part of a newly constructed road.
6. The coefficient of variation of the Benkelman beam deflection data should be less than 33 percent to ensure the uniform strength of the test section.

Benkelman Beam Deflection Tests

The Benkelman beam test was conducted using the Canadian Good Roads Association's procedure (*15*) on the outer wheelpaths in both directions at 10-m intervals. For a 300-m test section, a total of 62 points were tested.

Measurement of Rutting, Cracking, and Patching

Rutting in wheelpaths was measured by a 3-m straightedge placed transversely on the carriageway surface. The observations were taken on both sides of the pavement. The maximum value of rutting in the wheel track was measured at 10-m intervals. The percentage of cracked and patched areas of the pavement was measured for each test section. The structural geometries, field densities, and moisture contents were recorded.

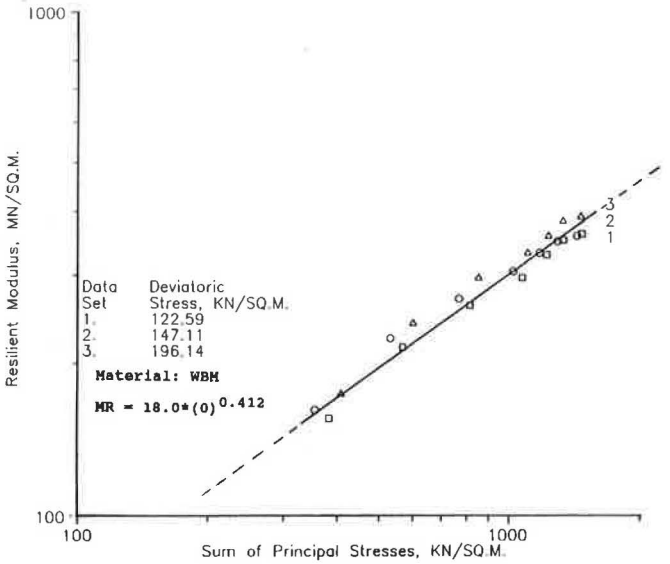


FIGURE 9 Sum of principal stresses versus resilient modulus.

Relationship Between CBR and Subgrade Modulus

The relationship between the laboratory CBR (at field density and in situ moisture content) and the resilient modulus was developed for various deviatoric stresses on the 15 test sections. The deviatoric stress was varied from 15 to 150 kN/m^2. Figure 10 shows that the resilient modulus (MR) values are between the lines E (MN/m^2) = 19.6 * CBR and E (MN/m^2) = 7.55 * CBR with a mean line as follows:

$$E = 12.48 * \text{CBR} \quad (3)$$

Similar work was carried out on the subgrade of the Alconbury Hill experimental road (*16*). The relationship between the in situ CBR value and the modulus of elasticity determined from the Rayleigh wave velocity, shown in Figure 11, was as follows:

$$E \text{ (MN/m}^2\text{)} = 13.3 * \text{CBR} \quad (4)$$

PREDICTION OF BENKELMAN BEAM DEFLECTION AND VERTICAL SUBGRADE STRAINS

Most roads in developing countries (including large portions of the national highways) have WBM bases with a thin bituminous surfacing in the form of premix carpet or surface dressing. Development of a suitable method for predicting surface deflections and stresses and strains for these pavement structures would be a valuable step in solving the problem of estimating the life period for a given thickness of WBM layer on a chosen subgrade soil. In this study the methodology adopted for stress analysis is similar to that used by Monismith et al. (*11*).

The resilient modulus of the subgrade soil was estimated from Equation 3. Subbase and base courses consist of untreated granular materials. Because these layers cannot withstand tensile stresses, twice the value of subgrade modulus was assigned (*17–19*). The vertical and radial stresses were obtained at different points using the finite element computer program. To these stresses the effect of self weight of the road structure was added. For each layer a point is selected at the center of the layer on the axis of the wheel load. For these points the sum of the principal stresses was calculated in the WBM layers, and deviatoric stresses were calculated in the subgrade soil. Using these values from the repeated-load experimental graphs (e.g., Figures 5 and 9), the moduli of the different layers were found. These modified stiffness values were then processed by the computer program. The iteration process was continued until the moduli obtained from the computer program coincided with those from the experimental data. Thus, the nonlinearity in the stiffness characteristics of the pavement materials is accounted for in the finite element computer program.

Table 1 presents a comparison of the predicted surface deflections obtained from the computer program and the measured deflections obtained by the Benkelman beam method for the test sections. The average difference in the results of the two methods is 5 percent, with a range of 1.5 to 13.1 percent. Most of the test sections had granular base topped with a thin bituminous surfacing in the form of premix carpet or surface dressing. The contribution of thin, open-graded, bituminous surfacings to the structural strength is negligible, and these highways were considered as full-depth granular highways. Although the bituminous surfacings of the five test sections (Sections 1, 9, 11, 12, and 14) had considerable thicknesses, severe grid pattern cracking leading to the breakout of the bituminous surfacings was found on the wheel tracks (because of the large volume of truck traffic). Because of this grid pattern cracking, the load-spreading capacity of the bituminous surfacing reduces considerably. Hence, for each of the five test sections the bituminous surfacing was considered part of the granular layer. The total thickness of WBM and surfacing (equivalent WBM) is presented in Table 1. The deflections can also be measured using a suitable measuring

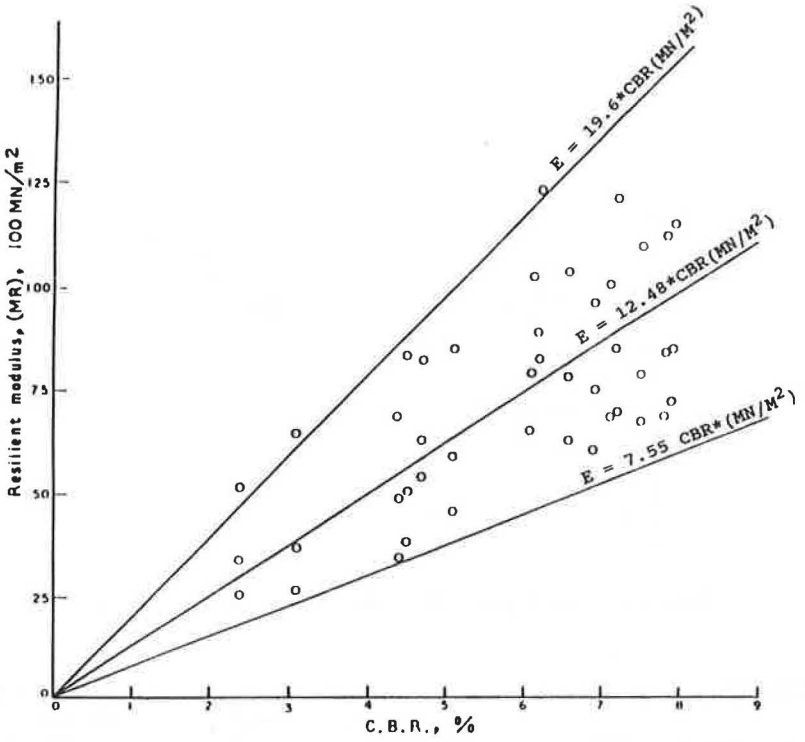


FIGURE 10 CBR versus resilient modulus.

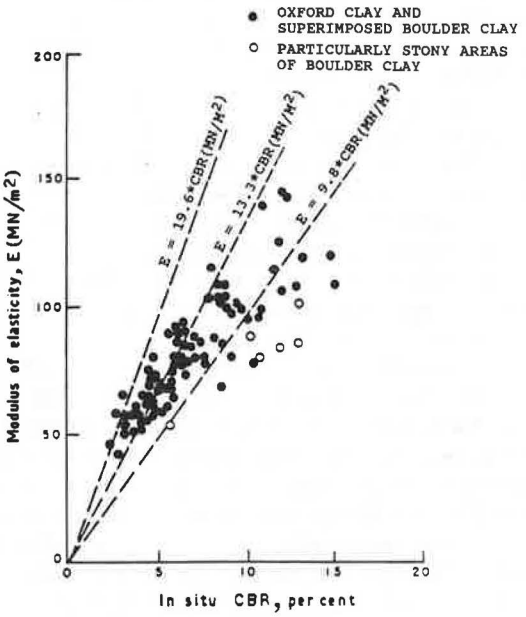


FIGURE 11 In situ CBR versus modulus of elasticity for subgrade of Alconbury Hill Experiment road (*16*).

device (e.g., the Benkelman beam). However, field measurements are costly and time-consuming, requiring interruption of the traffic (which may be inconvenient, especially on a busy freeway). Therefore, predicting the deflection would likely be useful to the field engineer in evaluating the structural condition of the pavement (*20*).

On average, the test truck stands on a test point for 20 sec during the Benkelman beam deflection test. From the test results given by Tangella (*6*), it can be observed that the effect of loading on resilient modulus is negligible (for a time range of 0.12 to 20 sec). Figure 12 shows the results of a typical subgrade soil of a test section. Hence, moduli values pertaining to 0.12-sec loading time were used to analyze the pavement structure. The loading time due to traffic is about 0.12 sec for a speed of 30 km/hr (*10*) for the test sections under consideration. The use of resilient moduli pertaining to 0.12-sec loading duration is suitable to predict the subgrade vertical strains for developing relationships among rut depth, subgrade vertical strain, and cumulative traffic in terms of equivalent single-axle loads (ESALs), as shown in the following section.

RESULTS AND CONCLUSIONS

Relationships were developed for 15 test sections on the national highways by carrying out regression analysis between (a) the laboratory CBR and the resilient modulus, (b) the average rut depth and the Benkelman beam deflection, (c) the average rut depth and the cracking and patching area, (d) the average rut depth and the vertical subgrade strain and cumulative ESALs, and (e) the average rut depth and WBM thickness and cumulative ESALs. Goodness of fit of the models, represented by the equations presented previously, to the observed data was evaluated by studying the correlation coefficients (R), the significance of each independent variable, the standard error of estimate, and the residuals. For this purpose, t-tests and f-tests were done. A summary of the characteristics of the test sections is presented in Table 2.

From the traffic data, including the axle equivalency factors and the traffic growth rate (*21*), the cumulative ESALs that

TABLE 1 COMPARISON OF PREDICTED AND MEASURED (BENKELMAN BEAM) DEFLECTIONS OF TEST SECTIONS

Test section no.	Location	Equivalent WBM thickness (mm)	Deflections Computed (mm)	Deflections Measured (mm)	Difference %
1.	Km 36.477 to 36.777, NH6	310	1.152	1.060	8.0
2.	Km 139.7 to 140.0, NH32	285	0.965	0.838	13.1
3.	Km 256.7 to 257.0, NH5	325	1.124	1.033	8.1
4.	Km 334.6 to 334.9, NH5	290	1.053	0.999	5.1
5.	Km 83.6 to 83.9, NH5	320	1.027	0.992	3.4
6.	Km 274.5 to 274.8, NH5	310	1.049	1.005	4.2
7.	Km 100.0 to 100.2, NH5	385	1.690	1.665	1.5
8.	Km 137.56 to 137.86, NH32	265	1.065	0.931	12.6
9.	Km 134.7 to 135.0, NH33	230	1.166	1.099	4.0
10.	Km 371.0 to 371.3, NH5	255	1.276	1.250	2.0
11.	Km 595.075 to 595.375, NH2	260	1.549	1.480	4.5
12.	Km 607.0 to 607.3, NH2	300	2.019	1.914	5.2
13.	Km 81.4 to 81.7, NH5	215	1.461	1.430	2.1
14.	Km 657.475 to 657.725, NH2	205	1.786	1.680	5.9
15.	Km 134.73 to 135.03, NH6	150	1.373	1.318	4.0

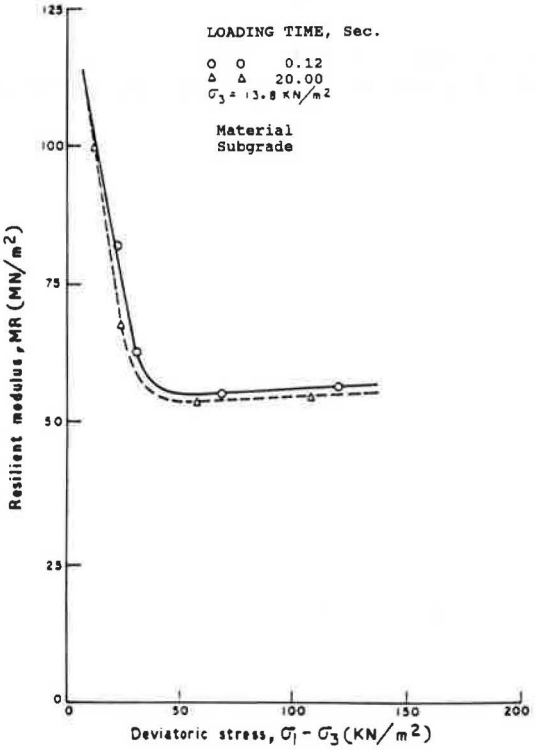


FIGURE 12 Resilient modulus versus deviatoric stress for subgrade soil of Test Section 10.

passed on each test section were found. The regression equation is expressed as follows:

$$RD = -0.265 + 6.79 * SVS + 3.08 * ESAL \quad (5)$$

where

RD = average rut depth (mm),
SVS = subgrade vertical strain ($\times 10^{-3}$) obtained from the computer output (RAOPAVE), and
ESAL = cumulative equivalent single-axle loads ($\times 10^7$).

Equation 5 has a squared multiple regression coefficient of 0.951, a calculated F value of 116.0, and a critical F value of 6.93 at 0.01 significance level. Because the calculated F value is greater than the critical F value, the null hypothesis is rejected, leaving the linear terms in the model. It would be useful, and seems a natural extension, to relate rut depth to gravel surfacing depth and cumulative axles. This relationship is shown by the following equation:

$$RD = 3.878 * ESAL - 0.0459 * TWBM \quad (6)$$

where TWBM equals the thickness of WBM, in millimeters.

Equation 6 has a squared multiple regression coefficient of 0.727, a calculated F value of 32.0, and a critical F value of 6.93 at 0.01 significance level.

Comparison of Rutting Model

For granular pavements, the loss of serviceability is caused mostly by excessive permanent deformation along the wheel-

TABLE 2 SUMMARY OF CHARACTERISTICS OF TEST SECTIONS

Test section no.	Rut depth (mm)	Total area of cracking and patching (%)	Cumulative no. of std. axles (x10 millions)	Subgrade vertical strain ($\times 10^{-3}$)	Lab. CBR (%)
1.	11.6	1.4	3.303	0.977	6.9
2.	9.4	0.2	0.485	1.059	6.2
3.	13.6	11.6	2.282	1.156	7.1
4.	16.5	13.8	1.446	1.111	7.9
5.	11.2	9.1	1.183	1.147	7.8
6.	13.8	2.3	2.327	1.191	7.5
7.	22.6	16.7	3.822	1.317	3.1
8.	11.9	0.4	2.154	1.350	7.2
9.	21.0	17.9	2.550	1.592	6.6
10.	13.7	1.1	1.446	1.595	4.7
11.	22.8	11.8	3.284	1.659	4.5
12.	25.3	10.1	3.714	2.004	2.4
13.	18.4	4.4	1.183	2.019	5.1
14.	29.8	25.8	4.922	2.458	4.4
15.	25.8	21.0	2.697	2.626	6.1

path. Hence, in this study rutting was adopted as the index for judging pavement performance, which is in agreement with British practice (*16,20,22*). An average rut depth of 15 mm is considered adequate for an overlay done at the optimal time (*20*). Putting this value of rut depth in Equation 5, the following rutting model was developed for the traffic range covered in this study:

$$SVS = 4.93 * 10^5 * ESAL^{-1.22} \quad (7)$$

where SVS equals the subgrade vertical strain in 0.001 mm/mm.

Equation 7 was compared with that of Shell (*23*), as shown in Figure 13:

$$SVS = 2.8 * 10^{-2} * ESAL^{-0.25} \quad (8)$$

The difference in the coefficients of these equations is caused by the difference in the material characteristics. Although the

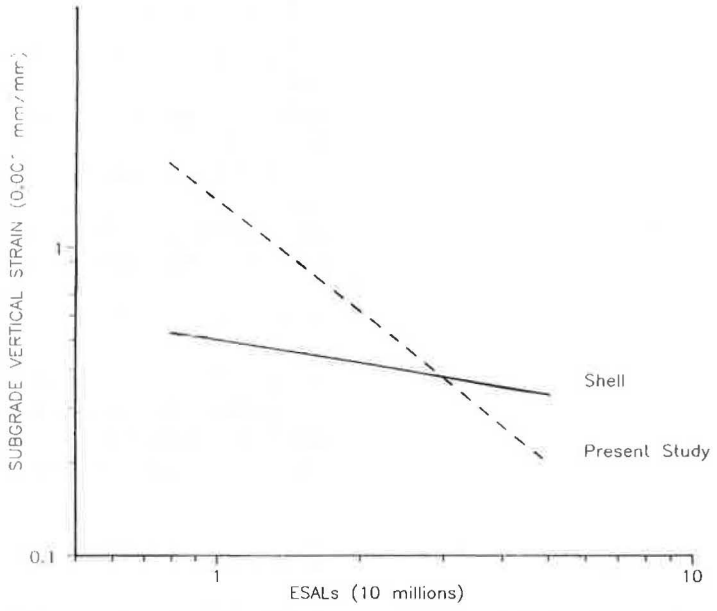


FIGURE 13 Comparison of rutting models.

difference of the corresponding coefficients in the two equations is considerable, the curves are close to one another when plotted. For an ESAL value of 30 million (a typical value—the ESAL range in this study is 8 to 45 million), both equations yielded a subgrade vertical strain of 0.00038 mm/mm, as shown in Figure 13. An average rut depth of 20 mm is considered adequate for the complete failure of a pavement structure (*6,19,20*). For this rut depth, both equations gave the same subgrade vertical strain (0.000348 mm/mm), for an ESAL value of 42 million.

Determination of Pavement Lives

The cumulative ESALs were found using the value of 20 mm for rut depth (considering a complete failure of pavement) and the subgrade vertical strain (obtained from the computer program) of each pavement section in Equation 5. The life period of the pavement structure was calculated from the current traffic data. The present age was subtracted from the life period of the pavement structure to obtain the remaining life (in years). The results are presented in Table 3. This table shows that, for five test sections (Sections 7, 11, 12, 14, and 15), the pavement life was exhausted because of the high magnitude of subgrade vertical strain and the large number of standard axles passed. For four test sections (Sections 1, 3, 6, and 9), the remaining life period is almost exhausted (less than 3.5 years). For the rest of the six test sections, the remaining life is longer (4.7 through 15 years) because of the low magnitude of subgrade vertical strain and the smaller number of standard axles passed.

Other Relationships

Regression analysis was also carried out between the average surface deflection (d) and the average rut depth (RD), both in millimeters. The equation developed is as follows:

$$d = 0.4838 + 0.0428 * \text{RD} \tag{9}$$

For Equation 9, the squared coefficient of correlation is 0.717, the calculated t value is 5.74, and the critical t value is 3.01 (for a significance level of 0.01). This equation was compared with that developed in the AASHO road test (*24*), which is given as follows:

$$d = 0.0096 + 0.0617 * \text{RD} \tag{10}$$

where d and RD are in inches.

For Equation 10, the squared coefficient of correlation is 0.6. The trend and the magnitude of variables are similar in Equations 9 and 10. From the equation developed in this investigation, the surface deflection found is 1.34 mm, whereas in the AASHO road test equation the surface deflection is 1.48 mm, for the rut depth of 20 mm.

The following equation was developed between the total cracking and patching area (CPA), in percent, and the average rut depth (RD), in millimeters:

$$\text{CPA} = -9.05 + 1.06 * \text{RD} \tag{11}$$

For Equation 11, the squared coefficient of correlation is 0.678, the calculated t value is 5.23, and the critical t value is

TABLE 3 CALCULATED LIVES OF PAVEMENT STRUCTURES

Test section no.	Av. no. of commercial vehicles per day	Present age (years)	Total no. of std. axles for full life period (x10 millions)	Remaining no. of std. axles (x10 millions)	Remaining life (years)
1.	3029	18	4.426	1.123	3.2
2.	1412	7	4.450	3.965	15.8
3.	3906	7	4.031	1.749	3.7
4.	2048	9	4.130	2.684	9.2
5.	1554	10	4.051	2.868	12.9
6.	3983	7	3.954	1.627	3.5
7.	3328	20	3.676	NIL	NIL
8.	1412	27	3.603	1.449	6.6
9.	2276	19	3.070	0.520	2.1
10.	2048	9	3.063	1.617	6.2
11.	3207	16	2.922	NIL	NIL
12.	3627	16	2.162	NIL	NIL
13.	1554	10	2.129	0.946	4.9
14.	4652	17	1.161	NIL	NIL
15.	2349	20	0.790	NIL	NIL

3.012 (for a significance level of 0.01). Equation 11 yields a CPA value of 12 percent when compared with the total pavement area, or 33 percent when compared with the wheelpath area, for a rut depth of 20 mm. For thin asphalt pavements, Craus et al. (*25*) suggest 30 percent cracking under the wheelpaths when limiting conditions are approached.

Limitations and Conclusion

The equations developed here are valid only for the range of conditions evaluated in the study (e.g., traffic is 8 to 45 million ESALs, CBR of soil is 3 to 8 percent, and surface deflection is 0.8 to 1.9 mm). The purpose of Equations 9 and 11 is to compare the results with those of the AASHO road test and of Crause et al. (*25*). For designing the overlays and to ensure longer serviceability, Equation 5 can be used to monitor the performance at any stage during the life period of a pavement.

REFERENCES

1. J. S. Przemieniecki. *Theory of Matrix Structural Analysis*. McGraw-Hill, New York, 1968.
2. O. C. Zienkiewicz and G. S. Hollister (eds.). *Stress Analysis*. Wiley, New York, 1965.
3. O. C. Zienkiewicz. *The Finite Element Method*. Tata McGraw-Hill, New Delhi, 1977.
4. J. M. Duncan, C. L. Monismith, and E. L. Wilson. Finite Element Analysis of Pavements. In *Highway Research Record 288*, HRB, National Research Council, Washington, D.C., 1968, pp. 18–33.
5. R. G. Ahlvin and H. H. Ulery. Tabulated Values for Determining the Complete Pattern of Stresses, Strains and Deflections Beneath Uniform Circular Load on a Homogeneous Half Space. *Bulletin 342*, HRB, National Research Council, Washington, D.C., 1962, pp. 1–13.
6. C. R. Tangella. *Performance Study of Flexible Pavements*. Ph.D. thesis. Indian Institute of Technology, Kharagpur, 1989.
7. S. R. Doddihal and B. B. Pandey. Stresses in Full Depth Granular Pavements. In *Transportation Research Record 954*, TRB, National Research Council, Washington, D.C., 1984, pp. 94–100.
8. C. R. Tangella and B. B. Pandey. Repeated Load Test Setup for Determining Plastic Deformation Characteristics of Subgrade Soils. *Indian Geotechnical Journal*, Vol. 13, No. 2, 1983, pp. 103–113.
9. S. F. Brown and A. F. L. Hyde. The Significance of Cyclic Confining Stress in Repeated Load Triaxial Testing of Granular Material. In *Transportation Research Record 537*, TRB, National Research Council, Washington, D.C., 1975, pp. 49–58.
10. R. D. Barksdale. Compressive Stress Pulse Times in Flexible Pavements for Use in Dynamic Testing. In *Highway Research Record 345*, HRB, National Research Council, Washington, D.C., 1971.
11. C. L. Monismith, H. B. Seed, F. G. Mitry, and C. K. Chan. Prediction of Pavement Deflections from Laboratory Tests. *Proc., 2nd International Conference on the Structural Design of Asphalt Pavements*, University of Michigan, Ann Arbor, 1967, pp. 109–140.
12. *Standard Specifications*. California Department of Transportation, Sacramento, 1984.
13. R. G. Hicks and C. L. Monismith. Factors Influencing the Resilient Response of Granular Materials. In *Highway Research Record 345*, HRB, National Research Council, Washington, D.C., 1971, pp. 15–31.
14. C. R. Tangella and B. B. Pandey. Resilient Modulus Characteristics of Granular Materials. In *Highway Research Bulletin 29*, Highway Research Board, Indian Roads Congress, New Delhi, 1988.
15. Canadian Good Roads Association. Pavement Evaluation Studies in Canada. *Proc., International Conference on the Structural Design of Asphalt Pavements*, Michigan, 1962, pp. 137–218.
16. A. R. Lee and D. Croney. British Full-Scale Pavement Experiments. *Proc., International Conference on the Structural Design of Asphalt Pavements*, Michigan, 1962, pp. 114–136.
17. C. L. Monismith. *Course Notes of CE 265: Pavement Design*. University of California, Berkeley, 1989.
18. E. J. Yoder and M. W. Witczak. *Principles of Pavement Design*. Wiley, New York, 1975, pp. 24–80.
19. C. R. Tangella. *Development of Asphalt Aggregate Mixture Analysis System*. Doctoral thesis. University of California, Berkeley, 1989.
20. D. Croney. *The Design and Performance of Road Pavements*. Her Majesty's Stationery Office, England, 1977.
21. P. G. Bhattacharya and B. B. Pandey. Flexural Fatigue Strength of Lime-Laterite Soil Mixtures. In *Transportation Research Record 1089*, TRB, National Research Council, Washington, D.C., 1986, pp. 86–92.
22. D. Croney and J. Allister. Full Scale Pavement Design Experiment on A.1 Alconbury Hill, Huntingdonshire. *Proc., Institute of Civil Engineers*, Vol. 30, Paper 6848, 1965, pp. 225–270.
23. *Shell Pavement Design Manual*. Shell International, London, England, 1978.
24. *Special Report 61A: The AASHO Road Test*. HRB, National Research Council, Washington, D.C., 1961.
25. J. Craus, R. Yuce, and C. L. Monismith. Fatigue Behavior of Thin Asphalt Concrete Layers in Flexible Pavement Structures. *Proc., Association of Asphalt Paving Technologists*, Vol. 53, 1984, pp. 559–582.

Publication of this paper sponsored by Committee on Flexible Pavement Design.

Evaluation of Louisiana Experimental Base Project with VESYS

WILLIAM O. HADLEY

Since the early 1900s, many empirical methods have been developed for the structural design of pavements. The empirical nature of these methods was necessary because of a limited knowledge of material behavior as well as limitations in the ability to solve boundary value problems. Empirical methods may be adequate for a range of established conditions; however, it is difficult to extrapolate such methods beyond the conditions for which they were developed. The desirability of extending the range of pavement design methods to include new materials, widely varying environmental conditions, and changing loading conditions requires a more fundamental and analytical approach to the design of pavement structural systems. The method should probably be based on a rational (theoretical) basis, with the capability to predict the performance of a pavement over its useful (i.e., design) life. One of the latest rational methods proposed is the VESYS IIIA computer-based approach developed through FHWA. The VESYS IIIA computer program was used to predict pavement performance in terms of rutting, fatigue cracking, and a present serviceability index (PSI) for the Louisiana Experimental Base Project. It was found that the VESYS IIIA mechanistic analysis package, in combination with material characterization information developed from resilient indirect tensile tests, can adequately predict rut depths over a short period of time but inadequately predicts fatigue cracking. Comparisons between measured and predicted PSI values indicated that the VESYS IIIA model may be adequate for short periods of evaluation.

Since the early 1900s, many empirical pavement design methods have been developed. The empirical nature of these methods was necessary because of a limited knowledge of material behavior as well as limitations in the ability to solve boundary value problems (*1*). In general, empirical methods yield satisfactory results when used within the limits for which they were derived, as evidenced by the good performance of many existing pavement structures. Empirical methods may be adequate for a range of established conditions; however, it is difficult to extrapolate such methods beyond the conditions for which they were developed.

The desirability of extending the range of pavement design methods to include new materials, widely varying environmental conditions, and changing loading conditions in an era of growing shortages of existing pavement materials requires that a new approach to the analysis and design of pavement structural systems be undertaken.

BACKGROUND

In recognition of this problem, the FHWA Office of Research initiated a project entitled New Methodology for Flexible Pavements. This project was aimed at developing a rationally based pavement design procedure with the capability to predict the performance of pavement over its useful life. As an initial step, a pavement design system was developed under an FHWA contract with the Massachusetts Institute of Technology (*2–4*). This work resulted in the creation of a computer program called VESYS IIM, which performed a structural analysis of a three-layer pavement system on a probabilistic basis. Subsequent improvements by FHWA resulted in an improved version of the computer program called VESYS III, which was developed to incorporate the best features of several existing versions of the VESYS IIM computer program and is capable of handling eight-layer pavements (*5*). One of the latest versions, VESYS IIIA, uses an elastic rather than a viscoelastic pavement evaluation approach.

The VESYS computer program predicts the performance of a pavement in terms of a present serviceability index (PSI), derived from the AASHTO road test procedures. The PSI is related to the fundamental structural conditions of integrity, continuity, and deformation of the pavement system. In the VESYS IIIA program, these fundamental entities are expressed as cracking, rutting, and pavement roughness. The magnitude and relative quantities of these responses are dependent upon input of materials properties of the pavement layers, the geometry of the pavement section, traffic data, and environmental conditions.

RESEARCH APPROACH

An essential element in a comprehensive evaluation of the effectiveness of mechanistic analysis and design packages in predicting pavement distress and performance is a comparison of the estimated results with actual results from in-service pavement sections. A group of 18 pavement sections constructed in conjunction with the Louisiana Experimental Base Project (*6*) was selected for this purpose. This selection was made because the following information was available for each of the pavement sections (*7,8*):

- The original construction parameters, including layer thicknesses, temperature conditions, asphalt content, and gradation;
- Sufficient field performance data, including PSI, rutting, and cracking; and
- General field conditions, including moisture contents, temperature conditions, and traffic loadings.

Texas Research and Development Foundation, 2602 Dellana Lane, Austin, Tex. 78746.

LITERATURE SURVEY

A number of research projects have been conducted to validate the practicability of the VESYS pavement design system. A design method for flexible pavements based on the VESYS IIM structural subsystem was evaluated by Kenis (*9*). All components of the design procedures were formulated to ensure inclusion of the inherent variabilities in traffic estimates, material properties, and environmental conditions. Estimates of the performance were produced and considered to be reasonable for the time measured.

An evaluation of flexible pavement design methodology based on field observations was conducted by Sharma et al. (*10*). In this study, field observations of distress and performance of flexible pavement test sections under accelerated traffic loading at the Pennsylvania State University Test Track facility were presented and correlated with corresponding values predicted by the VESYS IIM program. Results indicated that it was possible to predict the relative magnitudes of these distress and performance indicators.

LOUISIANA EXPERIMENTAL BASE PROJECT

The necessary requirements for this study were met by using the 18 different test sections constructed by the Louisiana Department of Transportation and Development (LADOTD) at LeCompte, Louisiana, for the Louisiana Experimental Base Project (*6*).

The test sections are located on US-167 and LA-71 between Meeker and Chambers in the central portion of the state of Louisiana. The location of the facility represents a compromise between the low wetlands of South Louisiana and the slight hills in the northern part of the state (*6*). The terrain at the test site is flat and affords poor drainage. Subgrade material is relatively uniform, basically fine-grained soil. In 1977 the mean variation in air temperature at the test site ranged from 39°F to 84°F, and the annual rainfall was typically 55.6 in. The roadway was opened to traffic in August 1976.

The main elements of the experimental design are presented in Table 1. The design includes asphaltic concrete surface thickness at two nominal levels (3.5 and 5.5 in.), base course materials at three levels (asphaltic concrete or black base, cement-stabilized soils, and cement-stabilized sand-clay-gravel), and design life at three levels (5, 10, and 15 years). The levels of thickness for each base course material were determined using AASHTO design procedures and the following Louisiana coefficients for material components:

- Surface course—0.44; and
- Base course—0.34 for asphaltic concrete, 0.15 for cement-stabilized soil, and 0.18 for cement-stabilized sand-clay gravel.

The 14 basic experimental test sections were supplemented with four control sections for reference, one at each end of the project and two within the experimental area. These control sections were composed nominally of 5.5 in. of asphaltic surface course over 7 in. of asphaltic concrete base course and 6 in. of soil cement. The design profiles of the various test sections are shown in Figure 1. Each test section is approximately 550 ft long, with a transition of 50 ft between each section. The 10- and 15-year design sections were placed in random order. However, the 5-year design sections (Sections 9–14) were grouped together to allow an overlay of this portion of the entire segment should early manifestation of distress become evident in any or all of the sections.

TABLE 1 EXPERIMENTAL DESIGN—LOUISIANA EXPERIMENTAL BASE PROJECT

Nominal Design Life (years)	Base Type (in.) by Surface Thickness					
	3.5 in.			5.5 in.		
	Black Base	Soil-Cement	Stab. SCG	Black Base	Soil-Cement	Stab. SCG
5	6	12	10	3	6	6
10	7.5	15		4.5	9	
15	11	20		8	16	

For this study, the 18 pavement sections were separated into five categories with a separate analysis completed for each category.

In some of the pavement test sections, soil cement layers were placed in two lifts. Core borings from these sections have indicated poor bonding between the lifts. As a consequence, those sections with the two-lift construction procedure were assumed to be a distinct type of pavement section containing two separate soil-cement base layers.

The following five types of pavement sections were considered:

1. Control sections,
2. Black-base sections,
3. Two-lift soil-cement sections,
4. Single-lift soil-cement sections, and
5. Cement-stabilized sand-clay-gravel sections.

For all five types of pavement sections, the wearing course and the binder course were treated as a single asphalt course. Each test section was constructed with a plant mix seal (PMS) covering the entire surface.

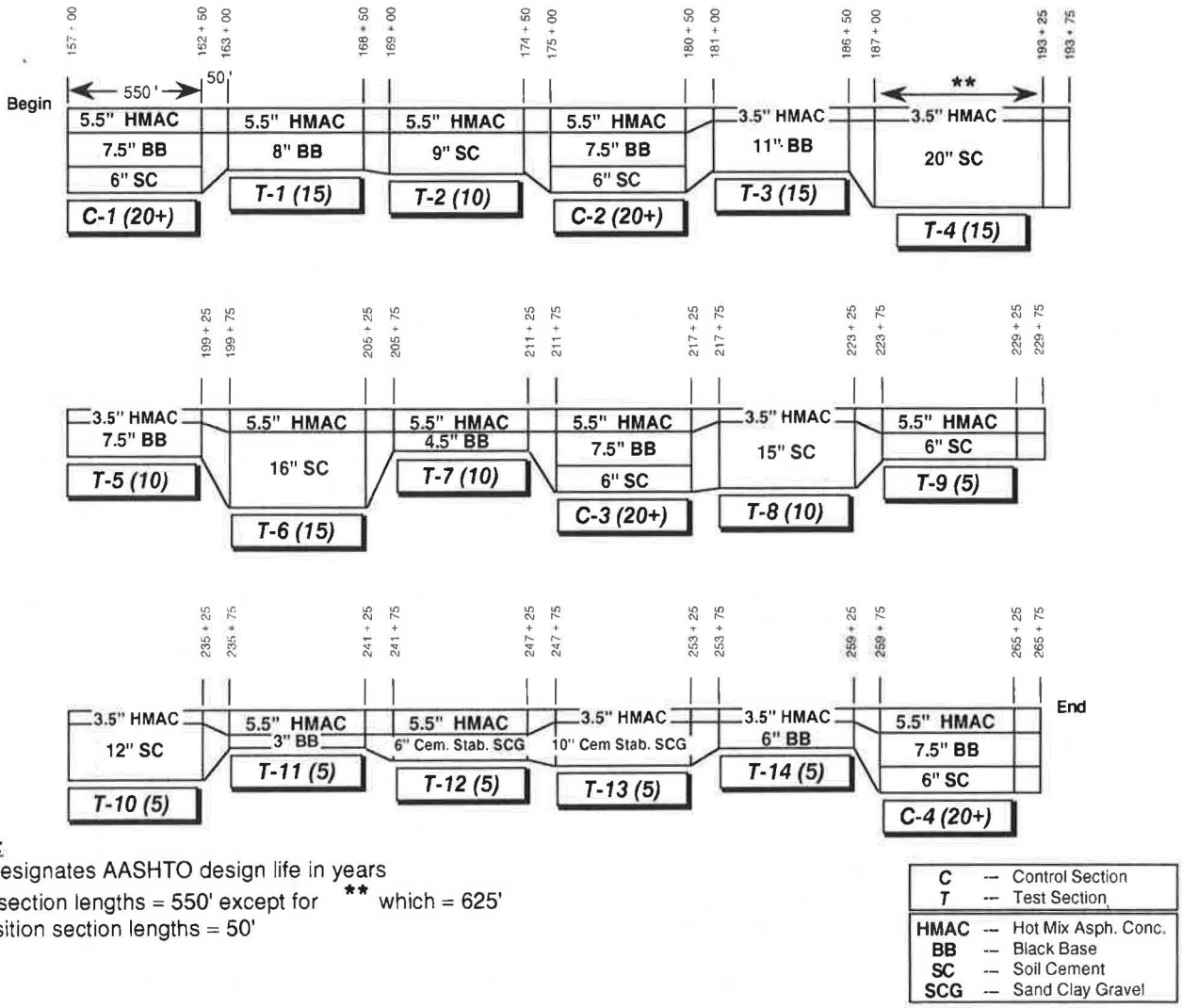
PROJECT INPUT VARIABLES

The development of performance results from the analysis packages required that certain input variables be specified. These variables were divided into the following four categories:

1. System geometry,
2. Environmental variables,
3. Traffic loadings, and
4. Mechanical properties of materials.

System Geometry

In VESYS IIIA models the system geometry is defined by the thickness of the various pavement structural layers and a subgrade considered to be semi-infinite in thickness. In this study the wearing and binder courses were combined to form a single layer. The average as-constructed layer thicknesses for each test section are presented in Table 2. These thickness



NOTES:

-- ( ) designates AASHTO design life in years
-- Test section lengths = 550' except for ** which = 625'
-- Transition section lengths = 50'

C	-- Control Section
T	-- Test Section
HMAC	-- Hot Mix Asph. Conc.
BB	-- Black Base
SC	-- Soil Cement
SCG	-- Sand Clay Gravel

FIGURE 1 Experimental base project layout.

values were used to define the pavement structural sections for the test sections. The PMS was not considered a structural layer and, hence, was not included in the models. Because the average as-constructed layer thicknesses (Table 2) exceed the design thicknesses (Table 1), the actual pavement design life would be expected to exceed the nominal design life.

Environmental Variable

Temperature and moisture contents are two major environmental conditions that can influence overall pavement response. The effect of moisture content on the engineering properties of subgrade, embankment, and select materials is usually reflected in the variability of material properties (*11*). Temperature effects on the properties of asphalt-bound layers can be inferred by using mean monthly ambient temperatures to establish representative moduli for each pavement section. Representative temperatures were obtained from the Weather Bureau, whereas in-situ moisture contents were obtained from LADOTD (*6*).

Traffic Loading

Previous attempts to validate the AASHTO design procedure in Louisiana were unsuccessful because of an inadequate traffic evaluation (*6*). To avoid a recurrence of this situation, periodic traffic counts and accurate truck weight measurements were taken at the project site. Traffic counts were taken yearly to establish growth patterns and to randomly measure large seasonal variation. A weigh-in-motion (WIM) device was used to make periodic truck weight studies in the outer lane of the roadway (*12*). Some difficulties were encountered in the calibration of the WIM system, and a complete record was not available for axle loads applied during each weighing period.

Serviceability Bounds

The system serviceability bounds are accounted for by such restraints as tolerance, terminal serviceability index, and the mean and standard deviation of the serviceability index at time zero. The tolerance is defined as the minimum accep-

TABLE 2 AS-CONSTRUCTED LAYER THICKNESSES, IN INCHES

Pavement Section	WC/BC	Layers BB	SC-1	SC-2	SCG	Sel.
C-1	6.97	6.31	6.63	—	—	9.00[1]
C-2	5.94	8.50	5.38	—	—	9.00[1]
C-3	5.88	7.01	6.75	—	—	9.00[1]
C-4	5.81	6.15	6.75	—	—	9.00[1]
T-1	7.03	7.75	—	—	—	15.00[2]
T-3	4.38	11.00	—	—	—	15.00[2]
T-5	3.51	9.25	—	—	—	15.00[2]
T-7	6.34	5.94	—	—	—	15.00[2]
T-11	5.94	4.70	—	—	—	15.00[2]
T-14	4.31	6.25	—	—	—	15.00[2]
T-4	3.72	—	11.78	7.85	—	6.00[3]
T-6	5.76	—	9.15	6.10	—	6.00[3]
T-8	3.88	—	8.10	7.78	—	6.00[3]
T-10	5.26	—	7.67	5.33	—	6.00[3]
T-2	6.16	—	8.13	—	—	9.25[4]
T-9	5.94	—	6.50	—	—	14.00[4]
T-12	5.82	—	—	—	8.375	12.00[4]
T-13	4.82	—	—	—	9.375	14.25[4]

NOTES: WC/BC = wearing and binder course layers combined; BB = black base layer; SC-1 = single-life soil cement layer; SC-2 = two-life soil cement layer; SCG = cement stabilized sand-clay-gravel layer; Sel = select layer; and — = no layer.
[1]Average thickness for C1–C4.
[2]Average for all black base sections.
[3]Thickness required because of thickness limitation of VESYS IIIA.
[4]Average thickness for section.

tance reliability of the pavement expressed as a percentile (*13*). A value of 50 percent (or mean value) was used. The terminal serviceability is that rating that can just be tolerated before overlay (*13*). A value of 2.5 was used because the sections under study are part of a primary highway. Initial serviceability indexes for each of the sections correspond to the Mays measurements obtained from the Louisiana Experimental Base Project before the sections were opened to traffic.

Mechanical Properties of Materials

The rutting and fatigue responses predicted by the VESYS IIIA program depend not only on the analytical technique but also on the material properties selected as input values for the computer program. Information developed from a resilient indirect tensile testing program (*7*) was used in calculating the modulus of elasticity, Poisson's ratio, permanent deformation, and fatigue input data for the asphalt, soil-cement, and cement-stabilized sand-clay-gravel layers. The ranges in the mechanical properties of the pavement materials modeled in this study are presented in Table 3.

The material properties of the select and embankment materials were obtained from the results of repeated-load triaxial compression tests conducted by the Asphalt Institute (*10*) on materials extracted from the pavement sections.

The permanent deformation variables, GNU and alpha, for the asphalt and soil-cement materials were obtained from the Materials Research Laboratory of Louisiana Tech University (*14*). The fatigue coefficients for VESYS IIIA were generated from previous test results (*1,7,14,15*).

The GNU and alpha values for the select and embankment materials were not determined directly but were correlated with values obtained by others (*16*) for similar materials.

FIELD VERIFICATION

Each of the 18 pavement sections was evaluated. The VESYS IIIA results were generated for each pavement section, including damage and performance parameters. From these results, it was possible to compare the predicted and measured responses for both the damage and performance model, thereby evaluating the accuracy of each model.

Rut Depths—Predicted Versus Measured

The ranges in rut depths are presented in Table 4 along with median estimates of rutting. The measured and predicted

TABLE 3 ESTIMATES OF MECHANICAL PROPERTIES OF MATERIALS

Layer	Modulus 10^5 psi	Poisson's Ratio	Permanent Deformation Parameters		Fatigue Parameter	
			Alpha	GNU	F_1	F_2
WC/BC	1.3 - 11.3[1]	.37-.39	.47	.025	$9x10^{-7}$ to $.1^3$	2.5-4.2[3]
BB	1.9 - 13.0[1]	.33-.36	.43	.021	$9x10^{-7}$ to $.1^3$	2.5-4.2[3]
SC	5.577	.25	1.0	0	---	---
SCG	3.979	.25	1.0	0	---	---
SEL	0.75-.200[2]	.35	.89	.068	---	---
EMBK	.067-.071[2]	.35	.735	.048	---	---

1 Corresponding to mean monthly ambient temperatures (MMAT)

2 Corresponding to location along test road

3 F_1 and F_2 values related to MMAT and particular test section

TABLE 4 MEASURED RUT DEPTHS WITH TIME IN YEARS

Design Life*	Test Sections		1.67	2.25	2.67	3.0	3.25	3.5	5.33	6.08	6.5	COMMENT
20y	C1-C4	low	0	0	0	0	0	0	0	.2	.2	black base
		high	.1	.1	.2	.3	.2	.3	.3	.4	.4	with
		median	.05	.05	.10	.15	.10	.15	.15	.30	.30	soil cement
15y	T1,3	low	0	0	0	0	.1	.1	0	.3	.2	
		high	.1	.1	.2	.3	.2	.3	.3	.5	.4	black base
		median	.05	.05	.10	.15	.15	.20	.15	.40	.30	sections
15y	T4,6	low	0	0	0	0	0	0	0	.1	.2	
		high	0	.1	.1	.2	.1	.2	.2	.3	.3	soil cement
		median	0	.05	.05	.10	.05	.10	.10	.15	.25	sections
10y	T5,T7	low	0	0	0	.1	.1	.2	.2	.2	.3	
		high	.1	0	.2	.4	.3	.4	.5	.6	.6	black base
		median	.05	0	.10	.25	.20	.30	.3	.40	.45	sections
10y	T2,8	low	0	0	0	.1	0	.1	-	.2	.2	
		high	.1	0	.2	.2	.2	.3	-	.5	.4	soil cement
		median	.05	0	.20	.15	.10	.20	-	.35	.30	sections
5y	T11,14	low	0	0	.1	.1	0	.1	.1	.2	.2	
		high	.1	0	.3	.3	.2	.3	.3	.4	.4	black base
		median	.05	0	.20	.20	.10	.20	.20	.30	.30	sections
5y	T9,10	low	0	0	0	.1	0	.1	.1	.2	.2	
		high	.1	.1	.1	.2	.1	.3	.5	.6	.4	black base
		median	.05	.05	.05	.15	.05	.20	.30	.40	.30	sections
5y	T12,13	low	0	0	0	.1	0	.1	.1	.1	.2	cement
		high	.1	0	.2	.2	.1	.2	.3	.3	.4	stabilized
		median	.05	0	.10	.15	.05	.15	.20	.20	.30	sand-clay-gravel

* Originally established nominal design life

(VESYS IIIA) median rut depths were plotted as a function of time for each pavement section in Figures 2–5.

In all the pavement sections, greater rut depths were predicted by VESYS IIIA during the first 2 years. As time progressed, rutting predictions comparable to the measured values were obtained.

Figure 2 shows that there was generally good agreement between the predicted and measured rutting depths for the control sections, particularly through the first 6 years. Although the measured rut depths are slightly greater after 6 years, the rate of rutting depicted by the VESYS IIIA predictions is considered reasonable.

Good agreement is also seen for the 15- and 10-year black-base sections between measured and predicted rut depths (see Figures 2 and 3, respectively). In Figure 3, the predicted rut depths are generally greater than the measured values for the 5-year design pavements. The agreement, however, is well within the expected measurement variation.

Similar good agreement between predicted (VESYS IIIA) rut depths and measured rut depths is shown in Figures 4 and 5 for the soil-cement and cement-stabilized sand-clay-gravel base sections.

In comparing the results for the control, black-base, and soil-cement and sand-clay-gravel sections, it is obvious that the amount of rutting is greater for the black-base sections than for the other sections. On the basis of measured data, the rate of rutting is greater than the predicted rate of rutting (VESYS IIIA) within the time frame of 3 to 7 years. However,

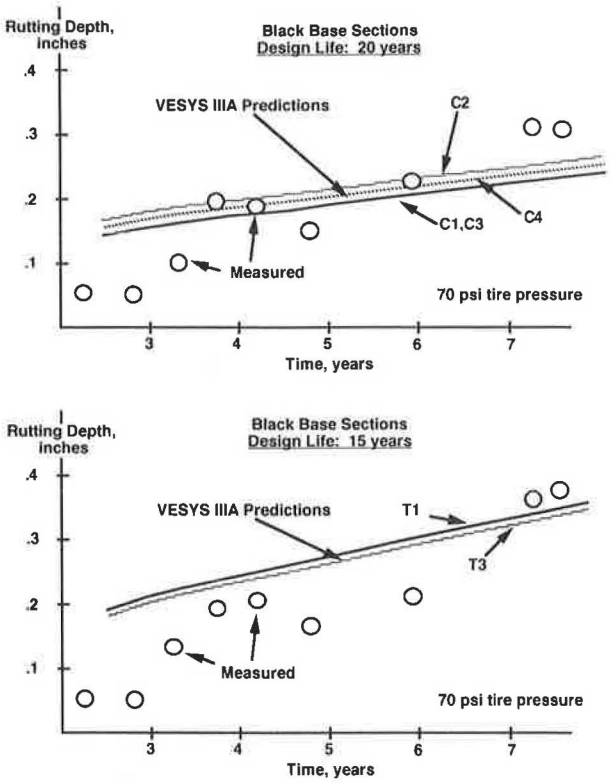


FIGURE 2 Predicted versus measured rutting depth: Control Sections 1–4 and Test Sections 1 and 3.

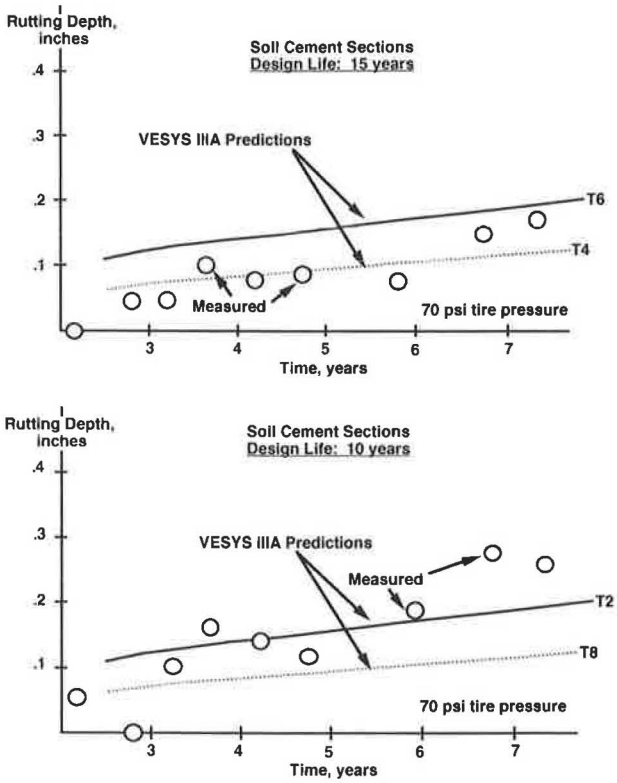


FIGURE 4 Predicted versus measured rutting depth: Test Sections 2, 4, 6, and 8.

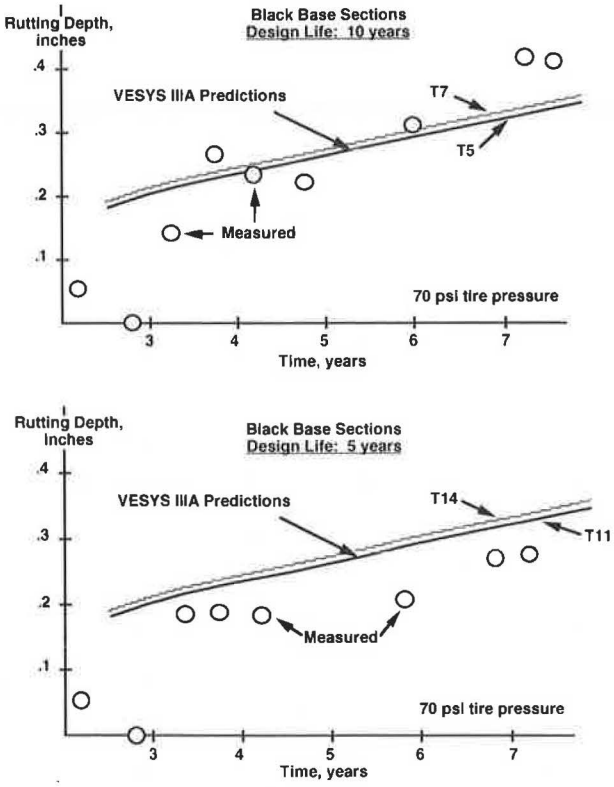


FIGURE 3 Predicted versus measured rutting depth: Test Sections 5, 7, 11, and 14.

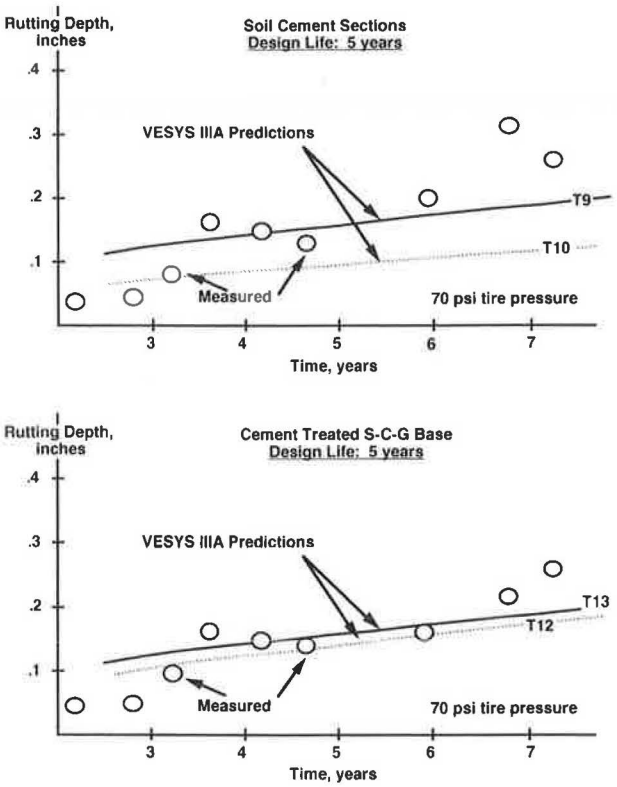


FIGURE 5 Predicted versus measured rutting depth: Test Sections 9, 10, 12, and 13.

the initial rate of predicted rutting was higher during the initial years of service and leveled off. It is expected that additional rut depth information will correspond reasonably well with predicted values. Because the correlation between measured and predicted rut depths is reasonable through 7 years, VESYS IIIA can be expected to effectively predict short-term rutting in flexible as well as composite pavement sections.

Cracking

Introduction

Pavement cracking can be separated into several categories. The category selected for this study was fatigue cracking. Fatigue cracking develops if excessive tensile strains (either in magnitude of load or number of applications) are produced in the bottom of a pavement layer. The rupture or cracking in the bottom of the layer eventually extends upward through the overlying layers to the pavement surface. Fatigue cracking is expected to occur both laterally and longitudinally along the inner edge of the individual tire of a dual set. The advanced stage of fatigue cracking is generally known as alligator cracking.

Measured and Projected Cracking

For the control and black-base sections (see Figure 6), fatigue cracking is projected to begin within the wearing course and binder layer in Year 9 and be 100 percent cracked by Year 19. On the other hand, VESYS IIIA analysis projected instantaneous fatigue cracking in the black-base layer for most of the black-base sections (see Figure 7). Because there is no evidence of this condition, the fatigue cracking models may be suspect. However, fatigue cracks may have developed in the black-base layer, but are not yet reflected through the wearing course and binder layer.

PSI

The PSI is a measure of the user's satisfaction with the level of service provided by the pavement system at a given time. The VESYS IIIA model predicts the PSI for each pavement section using the following relationship developed for the AASHTO road test (*11*):

$$PSI = PSI_i - 1.91 \log(1 + SV) - 0.01 (c + p) - 1.38R^2$$

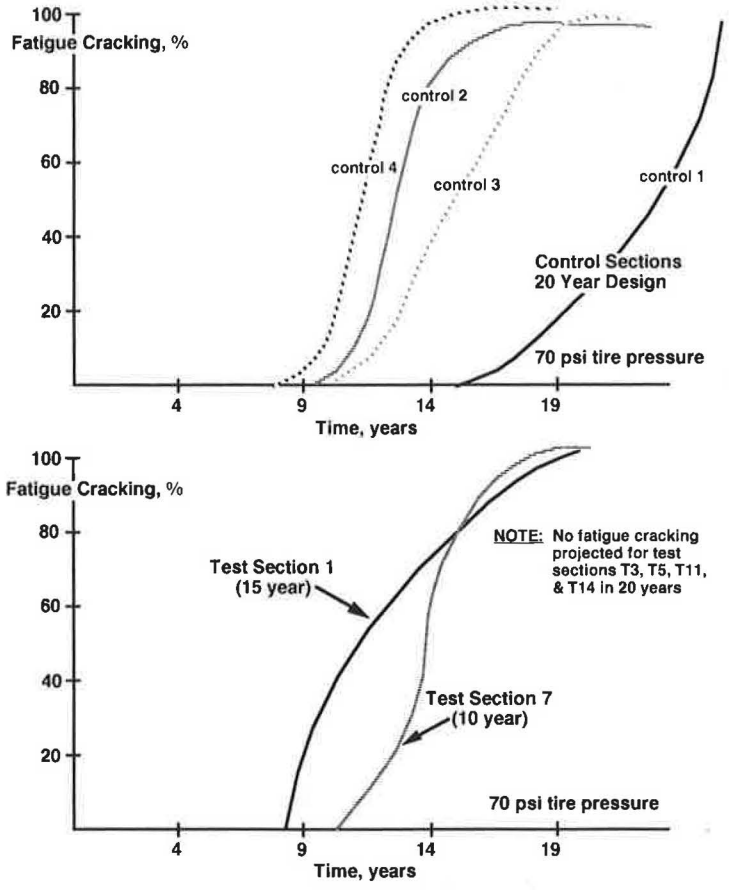


FIGURE 6 Projected fatigue cracking in wearing and binder layer with time: Control Sections 1–4 and Test Sections 1 and 7.

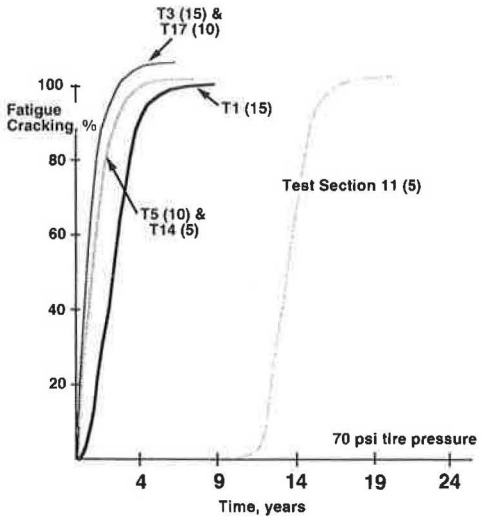


FIGURE 7 Projected fatigue cracking in black-base layer with time: black-base sections.

where

PSI_i = initial serviceability input,
SV = slope variance (roughness),
c = cracking (yd²/1,000 yd²),
p = patching (yd²/1,000 yd²), and
R = rut depth (in.).

LADOTD measured the initial PSIs in the field using the CHLOE Profilometer and the Mays Ride Meter (MRM). Subsequently, the MRM was used exclusively to measure the road roughness, or slope variance, of each of the 18 test sections.

The measured and predicted PSI values for the first 7 years are presented in Figures 8–12. From the results for the four control sections (see Figure 8), it is evident that there is good correlation between the measured and predicted PSI values. For these sections the VESYS IIIA program adequately predicted the PSI values. The initial PSI value can have a direct effect on the correlation between the measured and predicted

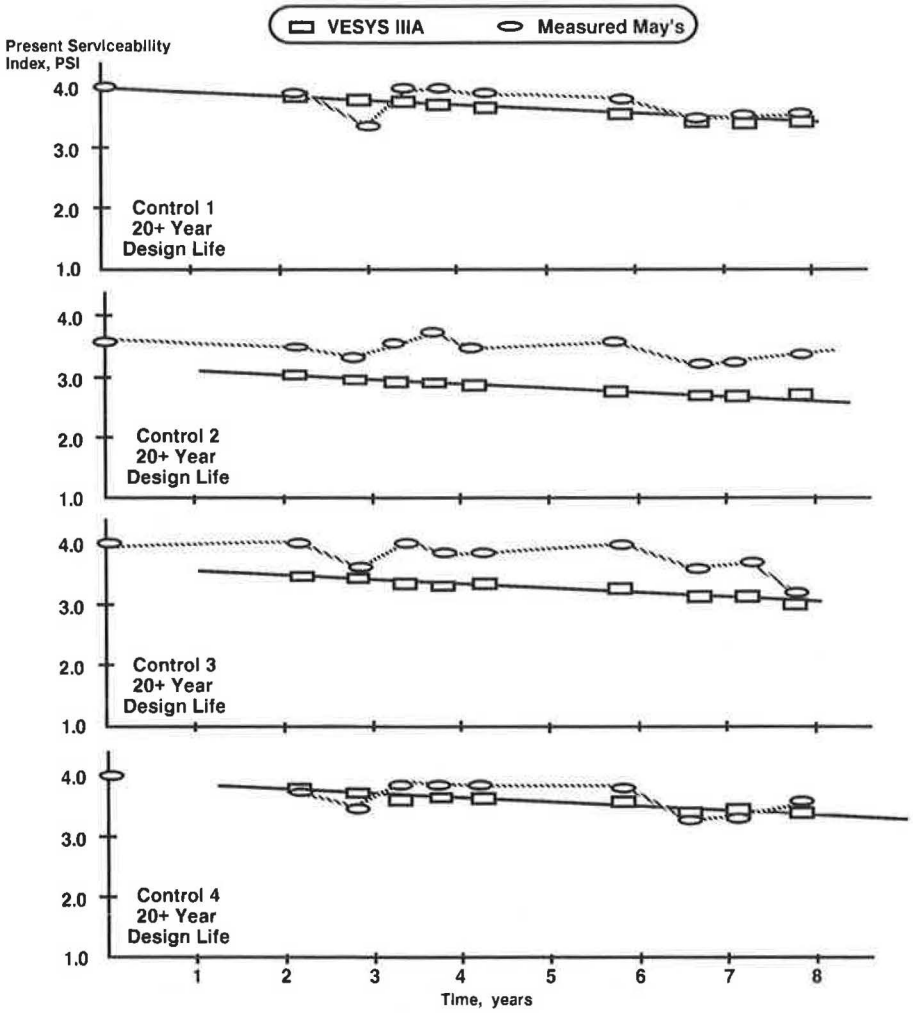


FIGURE 8 Comparisons of predicted (VESYS IIIA) and measured serviceability indexes: control sections.

values. For instance, PSI values in Year 3 for Control Sections 2 and 3 are greater than the initial PSI value. Obviously, a higher initial PSI value would have resulted in greater predicted values and an even better correlation between the measured and predicted ratings.

The PSI comparisons for the 15-year design section are presented in Figure 9. The plots show that there is better agreement between the measured and predicted PSI values for the soil-cement sections (i.e., T4 and T6) than for the black-base sections (i.e., T1 and T3). For these latter sections predicted (VESYS IIIA) values are quite a bit lower than the measured (MRM) values due primarily to the prediction of early fatigue cracking in the black-base layers (see Figure 7).

The PSI results for the 10-year design section are presented in Figure 10. In this case there is excellent agreement between the predicted (VESYS IIIA) and measured (MRM) values for Test Sections 2 and 5. For Test Sections 7 and 8, there was good agreement between predicted and measured values through Year 5. After that time the measured ratings were substantially decreased. These two test sections are, of course, adjacent to one another. It was expected that Test Section 8 would not perform as expected because of localized construction problems. The increase in measured rutting in Years 6 and 7 (see Figures 3 and 4) apparently contributed to the decrease in serviceability for Test Sections 7 and 8.

The serviceability results for the 5-year design sections are presented in Figures 11 and 12. There is good agreement between the measured and predicted PSI values for the two black-base sections (i.e., T11 and T14). In fact, in Year 7 both sections have very good serviceability ratings (3.0 or above) and exceeded their nominal design lives by 2 years (at least on the basis of a terminal PSI of 2.5).

For the soil-cement sections (i.e., T9 and T10) there was good agreement between the measured and predicted values for a period equal to their nominal design lives (i.e., 5-year design). After Year 6 there has been a noticeable drop in the measured PSI values below a terminal 2.5. However, it is believed that the measured PSI values have been biased by a disintegrating PMS, resulting in low slope variance values as measured by the MRM. On the basis of VESYS IIIA

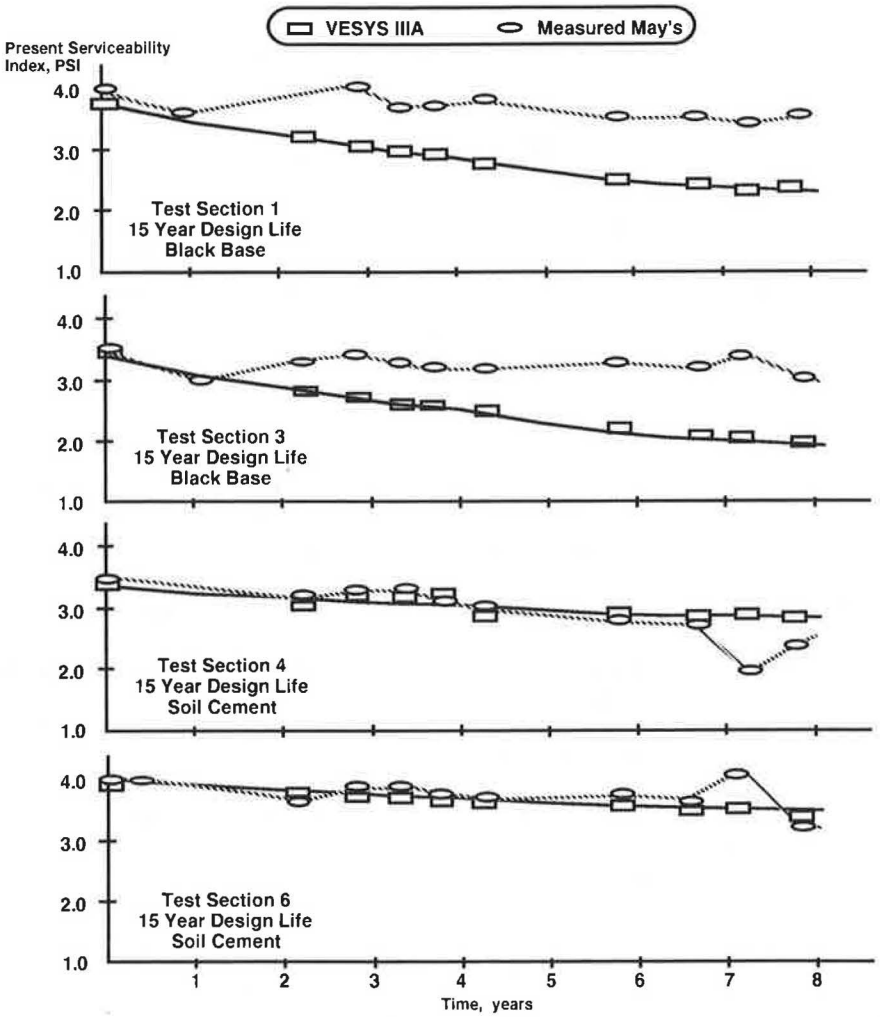


FIGURE 9 Comparisons of predicted (VESYS IIIA) and measured serviceability indexes: Test Sections 1, 3, 4, and 6.

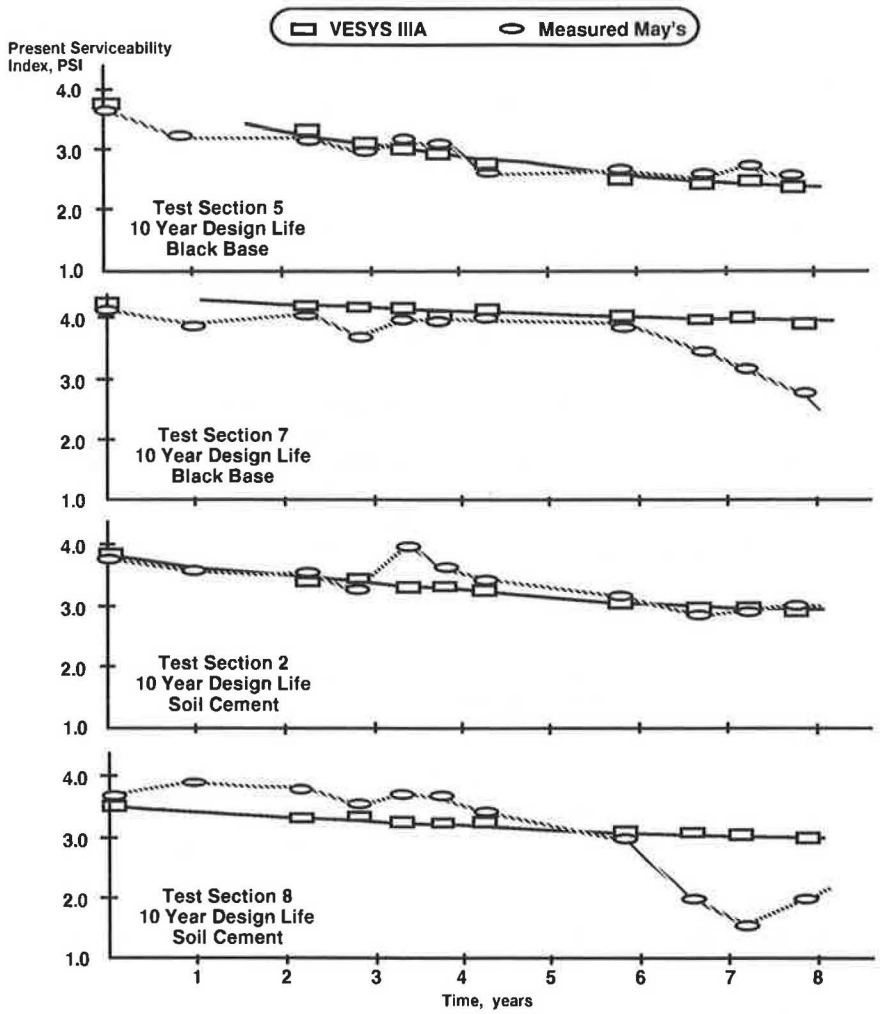


FIGURE 10 Comparisons of predicted (VESYS IIIA) and measured serviceability indexes: Test Sections 2, 5, 7, and 8.

predictions, these two sections should still be performing adequately.

Similar results are presented in Figure 12 for the cement-stabilized sand-clay-gravel sections (i.e., T12 and T13). There is excellent agreement between the predicted (VESYS IIIA) and measured (MRM) PSI values for a 6-year period. After the 6th year the measured PSI values dropped drastically, but they recovered slightly in Year 7. These two sections were also plagued by a disintegrating PMS, which could have resulted in lower MRM ratings as compared with VESYS IIIA predictions.

From the comparisons presented in Figures 8–12, it is apparent that VESYS IIIA can adequately predict pavement performance over a 5- to 7-year period of time.

CONCLUSIONS

The following conclusions were developed:

1. The VESYS IIIA mechanistic analysis package can adequately predict rut depths over a short period of time.

2. The indirect tensile test can produce material characterization information (both static and resilient models) that yields VESYS IIIA rutting predictions compatible with measured results.

3. VESYS IIIA cracking predictions using the indirect tensile characterization information predicted early fatigue cracking in most sections, but no actual significant amount of fatigue cracking developed. The combination of the VESYS fatigue algorithm and temperature-moduli-fatigue characterization information is suspect because reasonable predictions were not obtained. VESYS IIIA uses a single-wheel load of constant pressure rather than multiple-wheel loads, which probably produced a more critical condition in the upper layers of the pavement sections resulting in prediction of early and severe fatigue cracking.

4. Comparisons between measured and predicted PSI values showed the VESYS IIIA model to be adequate for short periods of evaluation even though the fatigue algorithm results are unrealistic. As a result the accuracy of the PSI predictions over long time periods may be questionable because the effects of other types of cracking (e.g., shrinkage and rut distortion cracking) are not considered.

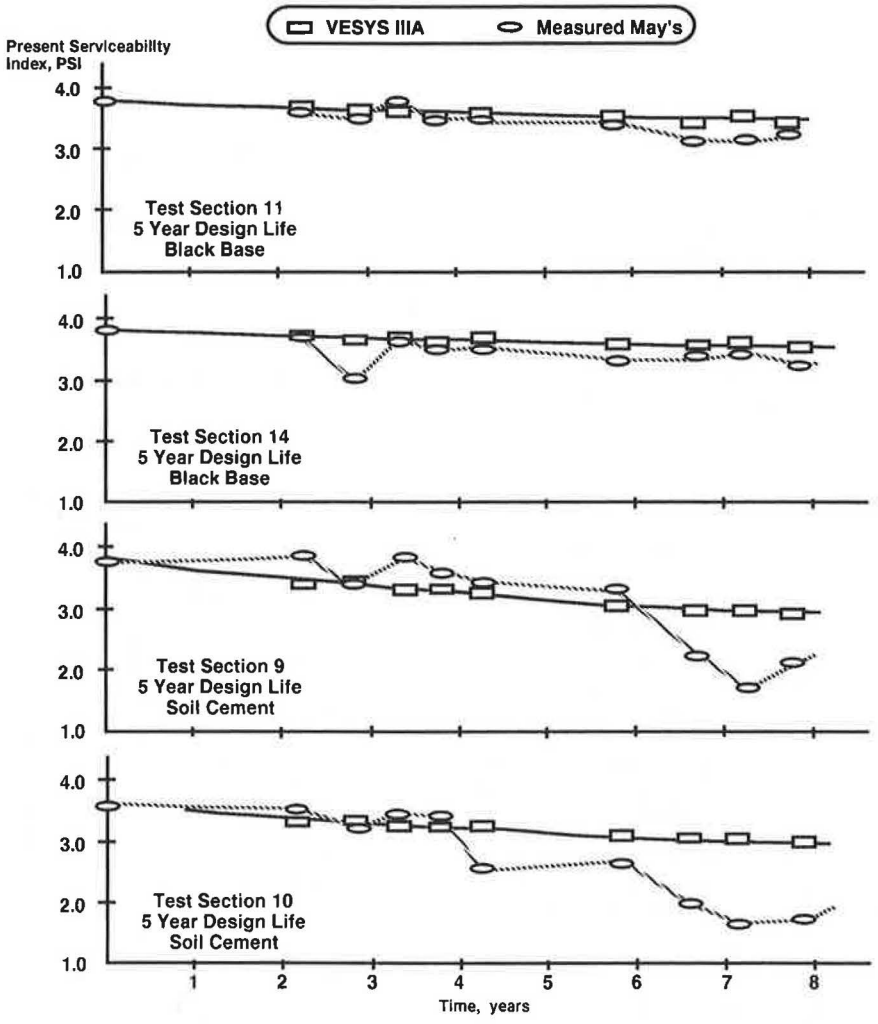


FIGURE 11 Comparisons of predicted (VESYS IIIA) and measured serviceability indexes: Test Sections 9, 10, 11, and 14.

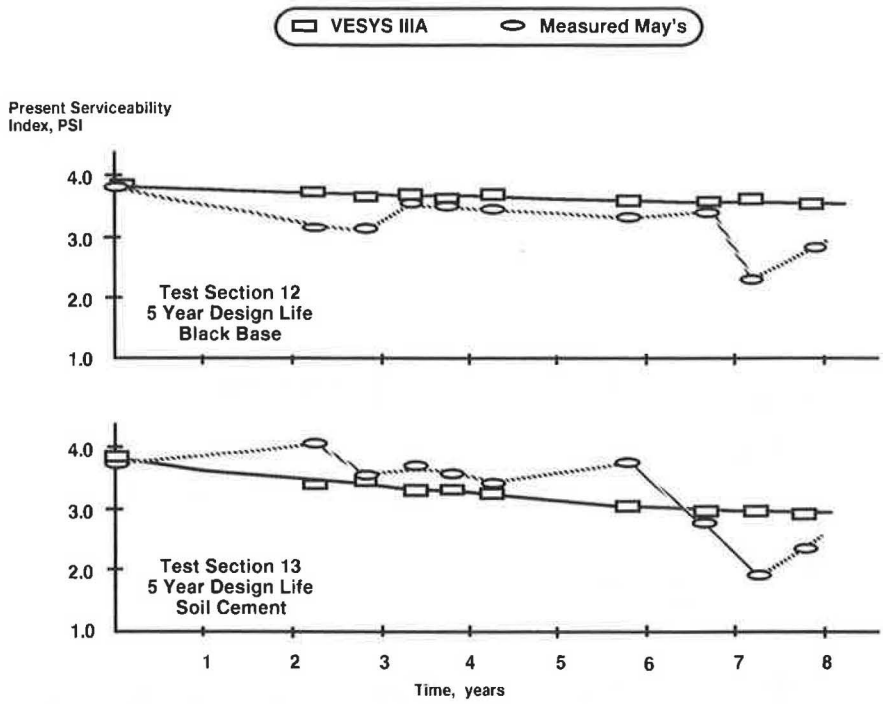


FIGURE 12 Comparisons of predicted (VESYS IIIA) and measured serviceability indexes: Test Sections 12 and 13.

REFERENCES

1. F. N. Finn, W. R. Hudson, B. F. McCullough, and K. Nair. An Evaluation of Basic Material Properties Affecting Behavior and Performance of Pavement Systems. Presented at 47th Annual Meeting of the Highway Research Board, Washington, D.C., Jan. 1968.
2. F. Moavenzadeh, J. E. Soussou, and H. K. Findakly. *Synthesis for Rational Design of Flexible Pavements, Part I*. School of Engineering, Massachusetts Institute of Technology, Cambridge, Jan. 1973.
3. J. E. Soussou, F. Moavenzadeh, and H. K. Findakly. *Synthesis for Rational Design of Flexible Pavements, Part II*. School of Engineering, Massachusetts Institute of Technology, Cambridge, Jan. 1973.
4. F. Moavenzadeh, J. E. Soussou, and H. K. Findakly. *Synthesis for Rational Design of Flexible Pavements, Part III*. School of Engineering, Massachusetts Institute of Technology, Cambridge, Feb. 1974.
5. *Interim VESYS III User's Guide*. FHWA, U.S. Department of Transportation, Jan. 1979.
6. J. W. Lyon. *Louisiana Experimental Base Project*. Interim Report 1. Office of Highways, Research and Development Section, Louisiana Department of Transportation and Development, Baton Rouge, Nov. 1979.
7. W. O. Hadley. *Fundamental Engineering Properties of Construction Materials*. Report 18-1. Materials Research Laboratory, Louisiana Tech University, Ruston, La., March 1983.
8. *Louisiana Experimental Base Project: Preliminary Summary of Asphalt Institute Test Results for Construction Sampling and Testing Program and for Field Sampling Program*. Asphalt Institute, College Park, Md., March 1983.
9. W. J. Kenis. *A Design for Flexible Pavements Using the VESYS Structural Subsystem*. FHWA, U.S. Department of Transportation, March 1976.
10. M. G. Sharma, W. J. Kenis, T. D. Larson, and W. L. Grambling. *Evaluation of Flexible Pavement Design Methodology Based Upon Field Observation at P.S.U. Test Track*. Pennsylvania Department of Transportation, Philadelphia.
11. W. J. Kenis. *Predictive Design Procedures—VESYS User's Manual*. FHWA, U.S. Department of Transportation, March 1976.
12. J. O. Burt and D. W. Dabin. *Weigh-in-Motion Systems Evaluation*. Research Report 104. Research and Development Section, Louisiana Department of Highways, Baton Rouge.
13. F. Moavenzadeh, J. E. Soussou, and H. K. Findakly. *Synthesis for Rational Design of Flexible Pavements*. Report FHWA-RD-75-29. FHWA, U.S. Department of Transportation, Oct. 1974.
14. W. O. Hadley. *Special Studies—Fundamental Engineering Properties of Construction Materials*. Report 78-3. Materials Research Laboratory, Louisiana Technical University, Ruston, La., March 1983.
15. W. O. Hadley. *Material Characterization and Inherent Variation Analysis*. Report 78-2. Materials Research Laboratory, Louisiana Technical University, Ruston, La., Jan. 1983.
16. D. I. Anderson, J. C. McBride, and D. E. Peterson. *Field Verification and Implementation of the VESYS IIM Structural Subsystem in Utah*, Report FHWA-RD-78-510. FHWA, U.S. Department of Transportation, Feb. 1978.

Publication of this paper sponsored by Committee on Flexible Pavement Design.

Relating Creep Testing to Rutting of Asphalt Concrete Mixes

VERNON J. MARKS, RODERICK W. MONROE, AND JOHN F. ADAM

The Iowa Department of Transportation began creep and resilient modulus testing of asphalt concrete mixtures in 1989. Part 1 of this research, reported in January 1990, was a laboratory study of hot-mix asphalt mixtures made with 0, 30, 60, 85, and 100 percent crushed gravel, crushed limestone, and crushed quartzite combined with uncrushed sand and gravel. Creep test results from Marshall specimens related well to the percent of crushed particles and the perceived resistance to rutting. The objective of this research, Part 2, was to determine if there was a meaningful correlation between pavement rut depth and the resilient modulus or the creep resistance factor. Cores with 4- and 6-in. diameters were drilled from rutted primary and Interstate pavements and from Interstate pavements with design changes intended to resist rutting. The top 2½ in. of each core, most of which was surface course, was used for creep and resilient modulus testing. There is a good correlation between the resilient modulus of 4- and 6-in.-diameter cores. Creep resistance factors of 4- and 6-in.-diameter cores also correlated well. There is a poor correlation between the resilient modulus and the creep resistance factor. The rut depth per million 18,000-lb equivalent single-axle loadings for these pavements did not correlate well with either the resilient modulus or the creep resistance factor.

Over the years, hot-mix asphalt (HMA) pavements have given outstanding performance. Experience has shown that HMA can be used on roadways carrying high volumes of heavy-truck traffic without a problem of rutting. Unfortunately, there are still instances in which objectionable rutting occurs. Improved test methods are needed to better evaluate the rutting potential of HMA mixes.

Researchers have identified numerous variables in asphalt concrete pavement design and construction having varying degrees of importance to pavement performance. These variables include the aggregate (type, porosity, gradation, and hardness), the crushing (jaw, cone, and hammer), and asphalt cement (content, grade, and quality), the mixing (drum or pugmill and temperature), and the laydown and compaction, to mention just a few. This large number of variations is one reason for the difficulty in developing a test that will relate HMA mix design to pavement performance. There are factors and conditions apart from the HMA mixture that affect the depth of rutting and the length of time before objectionable rutting occurs. Air temperature, heat of the sun, and truck loadings are the most important of the non-asphalt-related factors. Some pavements have provided a number of years of good performance without rutting until being subjected to a prolonged period of unusually high temperature (for Iowa, above 100°F). High temperature has contributed to substantial rutting in a short period of time. Hills and areas of starting and stopping are also factors that contribute to rutting problems.

Iowa Department of Transportation, 800 Lincoln Way, Ames, Iowa 50010.

A three-part study of creep and resilient modulus testing of HMA is being conducted. Part 1 (*1*), reported in January 1990, was a laboratory study of HMA mixtures made with 0, 30, 60, 85, and 100 percent crushed gravel, crushed limestone, and crushed quartzite combined with uncrushed sand and gravel. These aggregate combinations were used with 4, 5, and 6 percent asphalt cement (AC). Marshall specimens 2½ in. high by 4 in. in diameter were made using 75-blow compaction. Laboratory testing of these specimens included creep and resilient modulus testing. A creep resistance factor developed in Part 1 seemed to relate well to the percentage of crushed particles and the perceived resistance to rutting.

The objective of Part 2, reported here, was to determine if there was a meaningful correlation between pavement rut depth and the resilient modulus or the creep resistance factor.

SELECTION OF PAVEMENT SECTIONS

Cores with 4- and 6-in. diameters were drilled from two groups of pavement. One group was primary and Interstate pavements on which substantial rutting had been measured. The other group was Interstate pavements constructed since 1984 with mix designs based on 75-blow Marshall compaction and specifications requiring more than 70 percent crushed particles and compaction to an increased percent of laboratory density to reduce the potential for rutting. The descriptions of the sections are presented in Table 1.

TESTING EQUIPMENT

Road Rater

The Iowa Department of Transportation (DOT) measures pavement deflections with a Foundation Mechanics, Inc., Model 400 Road Rater. The standard test procedure for AC uses a peak-to-peak force of 1,185 lb from approximately 400 to 1,600 lb at a frequency of 25 Hz.

Resilient Modulus Apparatus

Resilient modulus testing was performed using a Retsina Mark VI resilient modulus nondestructive testing device, purchased in 1988 from the Retsina Co., Oakland, California. The Ret-

TABLE 1 DESCRIPTION OF CORING LOCATIONS

Site	County	Project #	Date of Construction	Highway	MP	Lane
1	Adair	IR-80-2(114)73--12-01	1987	I-80 EB	81.40	Dr
2	Adair	IR-80-2(107)86--12-01	1986	I-80 EB	95.45	Dr
3	Adair	IR-80-2(91)86--12-01	1982	I-80 EB	95.45	Pass
4	Cass	I-IR-80-1(131)42--14-78	1981	I-80 EB	52.2	Dr
5	Cass	I-IR-80-1(131)42--14-78	1981	I-80 WB	55.0	Pass
6	Cass	IR-80-1(161)56-12-15	1986	I-80 EB	59.7	Dr
7	Cass	I-EACIR-80-1(127)54--0E-15	1979-1980	I-80 EB	59.7	Pass
8	Cass	IR-80-1(161)56--12-15	1986	I-80 WB	59.9	Dr
9	Cherokee	EACF-3-2(5)--20-18	1979-1980	IA 3	44.25	WB
10	Cherokee	EACF-3-2(5)--20-18	1979-1980	IA 3	54	EB
11	Cherokee	FN-59-7(16)--21-18	1973	US 59	150.7	SB
12	Cherokee	FN-59-7(16)--21-18	1973	US 59	154	SB
13	Dallas	IR-80-3(52)99--12-25	1987	I-80 EB	109.65	Dr
14	Dickinson	F-71-9(9)--20-30	1978	US 71	231	SB
15	Harrison	FN-44-1(2)--21-43	1978-79	IA 44	1.5	WB
16	Harrison	IR-29-4(33)72--12-43	1987	I-29 SB	87.45	Dr
17	Harrison	EACIR-29-5(42)78--0C-43	1982	I-29 SB	87.45	Pass
18	Osceola	FR-60-4(20)--26-72	1986	IA 60	50.8	NB
19	Osceola	FR-60-4(20)--26-72	1986	IA 60	50.8	NB
20	Osceola	FR-60-4(20)--26-72	1986	IA 60	50.8	SB
21	Plymouth	EACF-75-1(36)--2K-97	1983	US 75 SB	5	Dr
22	Plymouth	FN-75-2(24)--21-75	1985	US 75 NB	5	Dr
23	Pocahontas	FN-4-4(1)--21-76	1970	IA 4	76+	NB
24	Pocahontas	FN-4-4(10)--21-76	1976	IA 4	93+	NB
25	Pottawattamie	EACIR-80-1(138)5--06-78	1983	I-80 WB	6	Dr
26	Pottawattamie	IR-80-1(146)0-12-78	1984	I-80 WB	11.00	Dr
27	Pottawattamie	EACIR-80-1(138)5--06-78	1983	I-80 EB	11.00	Dr
28	Pottawattamie	IR-80-1(146)0-12-78	1984	I-80 WB	18.00	Dr
29	Pottawattamie	EACIR-80-1(138)5--06-78	1983	I-80 EB	18.00	Dr
30	Sac	FN-175-4(4)--21-81	1986	IA 175	68.00	WB
31	Sac	FN-175-4(4)--21-81	1986	IA 175	68.1	EB
32	Sioux		1983	IA 10	28.25	EB
33	Warren	FI-35-2(93)43--29-91	1969	I-35 SB	52.0	Pass
34	Warren	IR-35-2(192)42--12-91	1986	I-35 SB	52.0	Dr
35	Warren	FI-35-2(95)57--29-91	1969	I-35 NB	61.9	Pass
36	Warren	IR-35-2(192)42--12-91	1986	I-35 NB	61.9	Dr
37	Woodbury	FR-12-1(8)--26-97 AC 13	1984	IA 12 WB	2	Dr
38	Woodbury	FR-12-1(8)--26-97 No AC 13	1984	IA 12 WB	2	Dr
39	Woodbury	IR-29-6(82)123--12-97	1986	I-29 SB	138.20	Dr
40	Woodbury	INP-29-8(12)151--15-97	1971	I-29 SB	146.2	Pass
41	Woodbury	IR-29-6(85)126--12-97	1988	I-29 SB	149.45	Dr

sina device was selected from among numerous resilient modulus testing systems because of its low cost, simplicity, and ease of operation. As described in ASTM D4123, for a cylindrical specimen, diametral loading results in a horizontal deformation that is related to resilient modulus by the following formula:

$$M = \frac{P(\nu + 0.2734)}{td}$$

where

M = resilient modulus (psi),
P = vertical load (lb),
ν = Poisson's ratio,
t = specimen thickness (in.), and
d = horizontal deformation (in.).

The device operates by applying a load pulse (0- to 1,000-lb range) diametrically through the specimen. Load duration (0.05 or 0.10 sec) and frequency (0.33, 0.5, or 1.0 Hz) are controlled by the operator. Horizontal deformations are sensed by transducers mounted on a yoke connected to the specimen. The number of cycles to be used in a test can be set by the operator. Results are calculated by a microprocessor and are presented by both a printer and a digital display.

Creep Test Device

The creep test device used was fabricated by Iowa DOT Materials Laboratory Machine Shop and Instrumentation personnel. The device consists of three pneumatically actuated load units mounted on a load frame and is capable of simultaneously testing three samples. An air regulator with digital display can deliver pressure of from 0 to 120 psi to the load units. The load units have a 12.4 to 1 force/pressure conversion ratio and a maximum output of 1,500 lb in the linear range. A compression load cell was used to calibrate the load units and develop the force/pressure conversion ratios. A brass load plate is centered on the frame directly under each load unit ram. A specimen is centered on the load plate, and another load plate is placed on top of the specimen. The specimen and top load plate are aligned directly beneath a load unit ram, through which a vertical force of from 0 to 1,500

lb can be applied. Dial gauges readable to 0.001 in. are mounted to the load unit rams, and vertical deformation of the specimen as a function of time is determined. The lower load frame and test specimens are placed in an insulated tank containing a temperature-controlled water bath. The operational range of the water bath is from 25°F to 140°F.

TEST PROCEDURES

Rut Depth and Road Rater Testing

The rut depths were measured beneath a 4-ft gauge at the location where the 4- and 6-in.-diameter cores were to be taken. The Road Rater deflection was determined just before coring. Only the accelerometer reading located on the pavement at the center of the loading plate is reported here. The 10- and 1-mil scales were used to determine the deflections in mils at the springtime ambient temperature. Pavement temperatures at the time of testing were recorded.

Drilling and Preparation of Test Specimens

Three 4-in.-diameter cores and three 6-in.-diameter cores were drilled using diamond core bits cooled with water. The cores were stored at 70°F in the laboratory until normal laboratory testing operations decreased enough that personnel were available. Often, the top surface of the core was not perpendicular to the axis of the core. Approximately ⅛ in. of the top of both the 4- and 6-in.-diameter cores was sawed off to obtain a surface perpendicular to the axis of the core. A 2½-in.-thick slice was then cut off of the top of both the 4- and 6-in.-diameter cores. The thickness of the test specimen has a definite effect on the change in height and failure in the creep test. The initial testing was conducted using 2½-in.-thick Marshall specimens. The 2½-in.-thick slice was selected to make the drilled cores relate to the laboratory-compacted Marshall specimens. An Iowa DOT standard thickness of 2½ in. has been established for resilient modulus and creep testing. Most of the tested material was surface course, but the surface course was often only 2 in. thick. Thus, ½ to ¾ in. of binder layer was included to yield a 2½-in.-thick specimen.

Resilient Modulus Testing

The testing temperature for resilient modulus was targeted at 77° ± 2°F. The only temperature control used was the ambient air temperature of the laboratory itself. At this time, Iowa DOT does not have the capability to test resilient modulus at elevated temperatures. The temperature of the specimen was determined by sandwiching a thermocouple wire between two specimens. If the indicated temperature was not 77° ± 2°F, the test was not performed.

After confirming that the temperature was within the desired range, a template was used to mark three 60° divisions on the diameter of the specimen. Specimen thickness was determined to 0.01 in. using a height comparator. Each specimen was placed in the frame and tested with the transducers directly opposite each other. After an individual test was completed, the specimen was reoriented by rotating it 60 degrees. The test was then repeated. Each specimen was again rotated 60 degrees, resulting in a total of three tests per specimen, each at an orientation of 60 degrees from the other two.

Each test consisted of 20 load cycles of 0.10 sec and a frequency of 0.33 Hz. It had been previously determined that preconditioning by subjecting the sample to a number of cyclic loads had no effect on the outcome; consequently, the practice of preconditioning as recommended in ASTM D4123 was not used. The three sets of 20 cycles were each repeated at loads of 50 and 75 lb.

This same testing pattern was performed on each of the three 4-in.-diameter and three 6-in.-diameter cores. All results for a set of three cores were then averaged to yield a single resilient modulus value. Final results were expressed in thousands of pounds per square inch (ksi).

Because the resilient modulus test is considered nondestructive at low loadings and moderate temperatures (the key factor being low horizontal deformation and accumulated deformation), the same cores were used for the creep test procedures.

Creep Test Procedure

After the cores were sawed to obtain the 2½-in. slice, the flat faces were polished by laying them on a belt sander using #50 grit paper. The sanding was done to remove surface irregularities that would result in uneven internal stress distribution and to allow the surface to be made as frictionless as possible. Surface friction reduction was further enhanced by applying a mixture of #2 graphite flakes and water- and temperature-resistant silicon gel lubricant to the polished core faces.

Sets of three cores of the same diameter from the same site were tested simultaneously. The testing temperature was 104°F, and the specimens were conditioned in 104°F water for ½ hr before testing.

The specimens were then subjected to a preload of 40 psi contact pressure for 2 min using a 4-in.-diameter load plate before testing. In order to achieve contact pressures of 200 psi during testing, a 3-in.-diameter top load plate was used instead of a 4-in.-diameter plate. After preloading, which was intended to properly seat the specimen, load plates, and ram and to compress any last-minute surface protrusions, the specimens were removed from the apparatus and their height measured to the nearest 0.0001 in. using a height comparator. The samples were then placed back in the apparatus, dial gauges were adjusted to read 0.500 in., and the creep loads were applied.

Contact pressure was increased from 0 to 40 psi in step loads of 8 psi applied for 1 min each. After 40 psi was reached, the dial gauges were read at 10-min intervals until 1 hr had passed. At this time, 8-psi step loads of 1-min duration were again applied until a contact pressure of 80 psi was attained. Dial gauge readings were again taken at 10-min intervals for 1 hour. This entire sequence was repeated until the final step of 200 psi for 1 hr was achieved or specimen failure occurred. Specimen failure is indicated by a rapid increase in height reduction or change in height of more than 0.05 in. The total elapsed time, the applied pressure at the time of failure, and the measured reduction in height just before failure were

recorded. If failure did not occur, total reduction in height at the end of the test (325 min) was used to calculate the creep resistance factor (CRF). The CRF was developed by Iowa DOT to provide a single quantitative number value for creep test results. The reasoning in developing the CRF was that a mixture that failed before the 200-psi loading at 325 min was less resistant to permanent deformation than one that would withstand the 200-psi loading with limited deformation. In addition, if two mixtures did not fail before the 200-psi loading, the amount of change in height was related to the resistance to deformation, and the mixture with the least change should result in the higher single quantitative CRF. The formula for the CRF is as follows:

$$CRF = \frac{t}{325}(100 - 1{,}000c)$$

where

CRF = creep resistance factor,
t = time in minutes at failure (0.05-in. height change), or 325 min if failure did not occur; and
c = change in height in inches, or 0.05 in. if failure occurred.

For example, if failure did not occur but the total change in height was 0.037 in., then

$$CRF = \frac{325}{325}[100 - (1{,}000)(0.037)]$$

$$= 63$$

In another example, if failure occurred at 265 min, then

$$CRF = \frac{265}{325}[100 - (1{,}000)(0.050)]$$

$$= 41$$

DISCUSSION OF RESULTS

The data are presented in Table 2. The percent AC was determined from tank stick measurements during construction. The percent of crushed particles was based on the intended percentages of the various aggregates. Construction report pavement histories provided average field voids and average percent of laboratory Marshall density.

TABLE 2 HMA MIX AND TESTING DATA

Site	AC %	% Cr. Part.	Marshall Comp. Blows	Lab Voids %	Field Voids %	Avg. Field Dens. %	Creep Resis. Factor 4"	Creep Resis. Factor 6"	Resilient Modulus Ksi 4"	Resilient Modulus Ksi 6"	ESAL	Rut Depth Inches	Rut Depth Per Million ESAL Inches	Road Rater Defl. Mils
1	5.8	85.0	75	4.5	7.9	96.0	32	30	1505	1375	1,542,389	0.05	0.05	1.3
2	5.2	70.0	75	4.8	8.2	96.5	30	36	1290	1030	2,172,285	0.25	0.10	0.8
3	5.0	45%RAP	50		6.6		21	20	980	537	3,400,000	0.60	0.20	0.9
4	5.2	70.0	50	3.6	7.7	96.8	12	12	1570	1255	3,687,311	0.55	0.15	0.9
5	5.2	70.0	50	3.6	7.7	96.8	20	19	1035	995	3,687,311	0.10	0.05	0.9
6	4.7	70.0	75	3.1	5.7	97.3	37	43	1385	1270	2,108,253	0.10	0.05	0.9
7	5.1	70.0	50	3.3	7.1	96.35	53	68	1425	1600	5,000,000	0.50	0.10	0.8
8	4.7	70.0	75	3.1	5.7	97.3	41	38	735	820	2,108,253	0.05	0.00	1.1
9	6.2	5.0	50	2.9	6.7	95.2	18	22	510	410	269,841	0.65	2.40	2.0
10	6.2	5.0	50	2.9	6.7	95.2	21	16	870	525	266,532	0.40	1.50	3.4
11	6.5	30.0	50	4.2	8.8	95.1	10	21	195	155	436,329	0.30	0.70	2.5
12	6.5	30.0	50	4.2	8.8	95.1	13	14	620	530	158,766	0.40	2.50	2.0
13	4.9	85.0	75	1.8	6.8	94.9	31	36	670	640	699,056	0.05	0.05	1.4
14	5.5	30.0	50	4.5	9.2	95.4	21	21	810	620	448,462	0.10	0.20	2.6
15	6.5	50.0	50	4.6	7.5	95.9	42	49	675	550	43,418	0.20	4.60	2.1
16	5.0	85.0	75	5.1	6.6	98.4	29	20	480	380	700,000	0.10	0.15	2.1
17	5.8	70.0	50	4.5	6.9	96.3	11	15	1250	1160	1,800,000	0.60	0.35	1.9
18	5.9	70.0	50	3.6	6.1	96.9	14	20	315	260	197,278	0.25	1.25	1.5
19	5.9	70.0	50	3.6	6.1	96.9	16	15	270	200	197,278	0.10	0.50	1.7
20	5.9	70.0	50	3.6	6.1	96.9	25	22	415	330	197,278	0.15	0.75	1.7
21			50				22	30	795	745	1,600,000	0.30	0.20	2.1
22	5.1	70.0	50	3.8	7.3	96.7	37	37	291	210	1,010,820	0.40	0.40	1.8
23	5.5	70.0	50	5.8			31	42	1125	1040	600,000	0.30	0.50	2.3
24	7.0	30.0	50	9.0	12.5	96.0	37	35	1285	1025	70,000	0.10	1.45	5.9
25	4.9	70.0	50	5.0	8.0	96.8	31	37	975	855	6,500,000	0.05	0.00	1.2
26	4.7	70.0	75	4.9	7.4	97.4	22	31	NA	1330	5,200,000	0.05	0.00	1.5
27	4.9	70.0	50	5.0	8.0	96.8	10	10	835	665	6,500,000	0.45	0.05	1.3
28	4.7	70.0	75	4.9	7.4	97.4	25	27	375	455	5,100,000	0.05	0.00	1.2
29	4.9	70.0	50	5.0	8.0	96.8	34	40	725	550	6,300,000	0.10	0.00	0.8
30			50				9	16	199	164	91,006	0.25	2.75	1.1
31			50				9	10	238	191	91,006	0.20	2.20	1.1
32							13	18	250	285	378,956	0.30	0.80	1.5
33	5.3	70.0	50		9.3	94.8	39	60	1450	1250	3,864,486	0.60	0.15	1.2
34	5.0	70.0	75	5.4	7.3	97.8	58	66	450	280	950,000	0.10	0.10	1.6
35	5.3	70.0	50		9.4	94.9	37	37	1910	1435	4,021,889	0.60	0.15	0.9
36	5.0	70.0	75	5.4	7.3	97.8	39	29	740	668	1,000,000	0.05	0.05	1.5
37	4.7	80.0	75	5.0	7.2	97.6	31	31	455	464	430,000	0.10	0.25	1.0
38	4.7	80.0	75	5.0	7.2	97.6	45	52	700	590	430,000	0.15	0.35	0.8
39	6.5	70.0	75	4.9	6.2	98.4	17	26	375	345	331,807	0.10	0.30	1.0
40	6.1		50	4.1	8.8	95.0	61	53	1110	520	6,800,000	0.30	0.05	0.8
41	5.6		75	3.7	6.4	97.4	31	23	690	565	414,407	0.35	0.85	1.0

Most of the 18,000-lb ESALs were obtained from pavement management computer records. When the ESALs were not available from those records, the current annual ESALs were used to estimate the accumulated ESALs.

On Interstate pavements, Iowa has used a program of removing the rutted driving lane and leaving the nonrutted passing lane. Five of the sites selected for drilling were the old and new HMA on which the driving lane had been replaced. In those cases, the rut depth and ESALs reported for the passing lane were those of the rutted driving lane just before its removal and replacement.

Interstate pavements constructed before 1984 were based on 50-blow Marshall compaction, and the 4-in.-diameter cores included in this research yielded an average CRF of 30 and an average resilient modulus of 1,170. With 75-blow compaction on Interstate projects constructed in 1984 and later, the average CRF was 33 and the average resilient modulus was 763.

For correlations with the CRF and resilient modulus, Site 15, with very low annual ESALs, resulted in data points that were substantially separated from all other data points. The Site 15 data were excluded from all correlations with rut depths per million ESALs.

A good correlation (r^2 = 0.89) between the resilient modulus of 4- and 6-in.-diameter cores (see Figure 1) was obtained. This finding demonstrates that the test is consistent and that it consistently evaluates the same properties. There was also relatively small variation between three cores of the same set.

Poor correlations were obtained between resilient modulus and rut depth per million ESALs. Resilient modulus of the 4-in.-diameter cores (see Figure 2) yielded a coefficient of determination (r^2) value of 0.15 with rut depth per million ESALs. There was some relationship, but apparently other factors had a significant effect. A correlation of the resilient modulus of 4-in.-diameter cores with rut depth per log of ESALs yielded an r^2 value of 0.06, which was even worse than using rut depth per million ESALs.

The correlation with the resilient modulus of 6-in.-diameter cores (see Figure 3) was similar, with an r^2 value of 0.17.

There was little correlation between the CRF and the resilient modulus of 4-in.-diameter cores (see Figure 4), with an r^2 of 0.11.

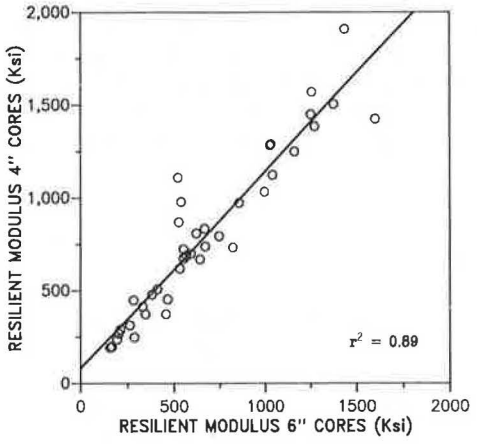


FIGURE 1 Resilient modulus of 4-in. versus 6-in. cores.

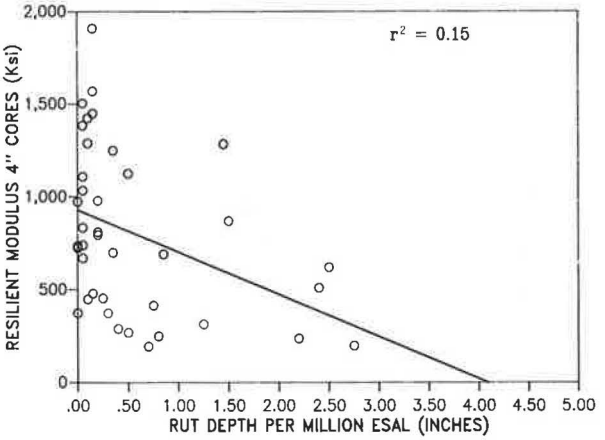


FIGURE 2 Resilient modulus of 4-in. cores versus rut depth per million ESALs (Site 15 excluded).

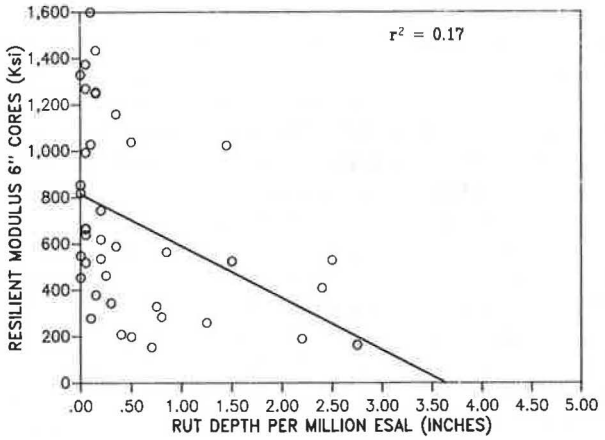


FIGURE 3 Resilient modulus of 6-in. cores versus rut depth per million ESALs (Site 15 excluded).

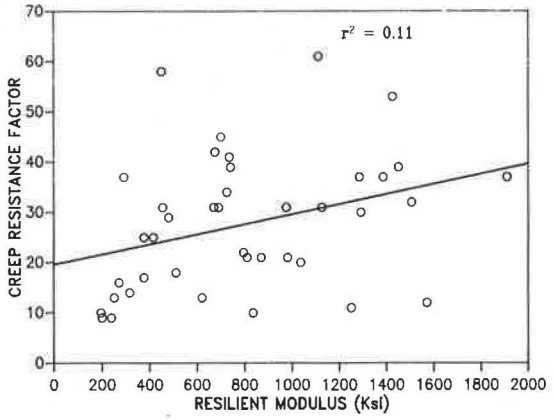


FIGURE 4 CRF versus resilient modulus for 4-in. cores.

The correlation of the CRF of 4- and 6-in.-diameter cores (see Figure 5) gave an r^2 of 0.81. The CRF of the 6-in.-diameter cores was about 10 percent greater than that for the 4-in.-diameter cores. On the basis of the good correlation and only 10 percent difference, it appears that 4-in.-diameter cores were adequate for creep testing. There was some concern that

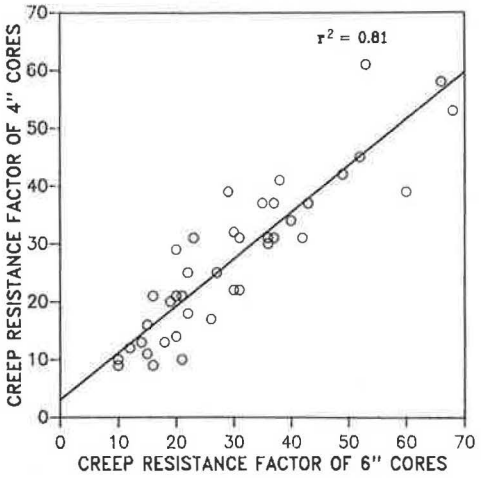


FIGURE 5 CRF of 4-in. versus 6.-in. cores.

there would be substantial difference of results between the 4- and 6-in.-diameter cores due to shearing in the 4-in.-diameter cores. The shear angle should vary with the amount of crushed particles in a mixture and be relatively vertical with a high percentage of crushed particles. With only 10 percent difference between the 4- and 6-in.-diameter cores, it would seem that shearing was of minimal contribution.

In Part 1 of this research, the CRF related very well to the percent of crushed particles in an HMA mixture. Unfortunately, it did not correlate well with the rut depth per million ESALs (see Figures 6 and 7), with an r^2 of 0.21 for the 4-in. diameter and an r^2 of 0.18 for the 6-in. diameter. A correlation of the CRF of 4-in.-diameter cores with rut depth per log of ESALs yielded an r^2 of 0.06. There were apparently a number of other factors, such as aging of the asphalt cement, that had a substantial effect on the results. The CRF may predominately evaluate the aggregate skeleton. In Part 2, the correlation with the resilient modulus and the CRF was similar, but neither exhibited a meaningful correlation with rut depth.

The Road Rater deflection data were obtained at pavement temperatures ranging from 40°F to 88°F. Through a nomogram the deflection readings given in Table 2 have been corrected to readings for 80°F. There was an interest in correlation of Road Rater deflections with rut depths and resilient modulus. The correlation of rut depth with Road Rater deflections yielded an r^2 of 0.00—absolutely no relationship. The correlation of Road Rater deflection with the resilient modulus of 4-in.-diameter cores also yielded an r^2 of 0.00. It would appear that the current rutting is not related to base failure and is, therefore, not related to the structural values from the Road Rater.

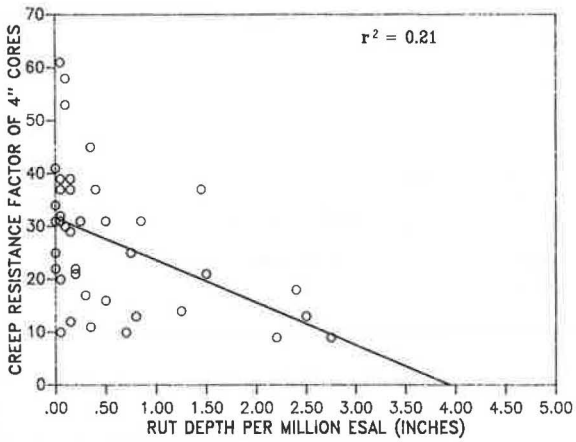


FIGURE 6 CRF of 4-in. cores versus rut depth per million ESALs (Site 15 excluded).

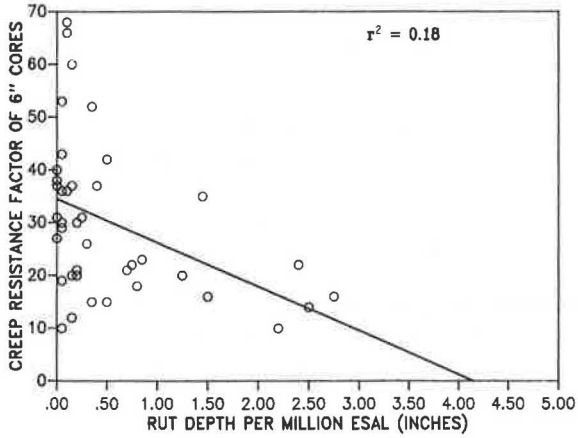


FIGURE 7 CRF of 6-in. cores versus rut depth per million ESALs (Site 15 excluded).

FUTURE RESEARCH

Part 3 of this research is currently in progress. The objective of Part 3 is to determine the relationship of creep and resilient modulus for (a) Marshall specimens from laboratory mixing for mix design, (b) Marshall specimens from construction plant mixing, and (c) cores drilled from the HMA pavement. Five 1990 projects were selected, ranging from an 85 percent crushed particle Interstate mix to a Type B mix (requiring at least 30 percent crushed particles) for a low-traffic-volume roadway. During construction of each project, a box sample of HMA mix was taken from a truck delivering mix to the paver. Three Marshall specimens were made in the laboratory for resilient modulus and creep testing.

For each project, three 4-in.-diameter cores were drilled from the compacted asphalt pavement at the location where the mix represented by the box sample was used. After trimming to obtain a plane perpendicular to the axis of the core, the top 2½ in. was cut off for resilient modulus and creep testing. Resilient modulus and creep resistance factor data are not yet available.

CONCLUSIONS

This research supports the following conclusions for creep and resilient modulus testing of HMA:

1. Results of both the resilient modulus and creep testing are relatively repeatable with small variation for cores from a particular HMA pavement.

2. There is a good correlation between the resilient modulus of 4- and 6-in.-diameter cores.
3. CRFs of 4- and 6-in.-diameter cores correlated very well.
4. For the HMA pavements selected, there is a poor correlation between rut depth per million ESALs and either resilient modulus or CRFs.

ACKNOWLEDGMENTS

The authors wish to express their appreciation to Willard Oppedal, Steve McCauley, Dan Seward, Todd Siefken, Larry Peterson, and Edna Madeiros for creep and resilient modulus testing. Kathy Davis, Todd Hansen, and Todde Folkerts were helpful in preparation of the report. FHWA funded the creep and resilient modulus testing.

REFERENCE

1. V. J. Marks, R. W. Monroe, and J. F. Adam. The Effects of Crushed Particles in Asphalt Mixtures. In *Transportation Research Record 1259*, TRB, National Research Council, Washington, D.C., 1990, pp. 91–106.

The contents of this paper reflect the views of the authors and do not necessarily reflect the official views of the Iowa Department of Transportation. This report does not constitute a standard, specification, or regulation.

Publication of this paper sponsored by Committee on Flexible Pavement Design.

Application of ASTM E1049-85 in Calculating Load Equivalence Factors from In Situ Strains

T. PAPAGIANNAKIS, A. OANCEA, N. ALI, J. CHAN, AND A. T. BERGAN

A comparative overview of the methods used to calculate mechanistic load equivalence factors (LEFs) is provided. In addition, an application of the rainflow/range-pair counting method (ASTM E1049-85) in calculating LEFs from in-situ pavement strains is demonstrated. The experimental program involved two test vehicles, with a BB truck providing the reference axle load. Asphalt concrete (AC) interfacial strains were measured at three vehicle speeds and three levels of axle load. Counting fatigue cycles according to the ASTM standard has shown that (a) the calculated LEFs decrease with vehicle speed, and (b) the LEFs for entire vehicles are substantially higher than the sum of the LEFs of their individual axle groups. This trend becomes more pronounced at higher vehicle speeds. The LEFs obtained by the rainflow/range-pair counting method were compared with those obtained by the Roads and Transportation Association of Canada method. The two sets of mechanistic LEFs were also compared with the empirical LEFs recommended by AASHTO. This comparison, however, was inconclusive and could not verify that one of the two mechanistic LEF methods best describes the fatigue cycles caused in AC by multiple axle loads.

Load equivalence factors (LEFs), defined as ratios of pavement life, have been the subject of study since the AASHO road test. They are calculated as follows:

$$\text{LEF}_x = \frac{N_{18}}{N_x} \tag{1}$$

where LEF_x is the equivalence factor of load x and N_{18} and N_x are the pavement lives (i.e., number of repetitions to terminal serviceability) for the BB axle and axle load x, respectively. LEFs obtained from empirical observations at the AASHO road test are still in use with few modifications (*1*).

A group of methods has been developed on the basis of mechanistic estimates of pavement life. Typically, a relationship is adopted relating pavement life to a pavement response parameter, as follows:

$$N = k_1\left(\frac{1}{\varepsilon}\right)^{k_2} \tag{2}$$

where ε is a selected pavement response parameter [usually interfacial asphalt concrete (AC) strain or surface deflection] and k_1 and k_2 are material constants determined through regression on fatigue test data. Substituting Equation 2 into Equation 1 gives the following:

$$\text{LEF}_x = \left(\frac{\varepsilon_x}{\varepsilon_{18}}\right)^{k_2} \tag{3}$$

Pavement response parameters are analytically calculated or measured using instrumented pavement sections. A variety of researchers (*2–10*) have proposed alternative methods for calculating mechanistic LEFs. Most of these studies (*2–4,6–8,10*) used only discrete (i.e., peak and valley) values of the pavement response curves. The main difference is in the way these peaks and valleys were processed to determine the damaging effect of multiple axles. There have been exceptions to the use of discrete pavement response values. Southgate and Deen (*5*) used strain energy to index pavement fatigue, whereas Govind and Walton (*9*) used the rate of change of strain for the same purpose. However, no evidence has been presented to date suggesting that such integral methods are more suited for describing pavement fatigue than are discrete methods.

In 1986 a standard for counting cycles in fatigue analysis was published (ASTM E1049-85). Four methods were documented:

- Level crossing method,
- Peak counting method,
- Simple-range counting method, and
- Rainflow counting and related methods.

The fourth method listed encompasses three procedures, namely, range-pair counting, rainflow counting, and simplified rainflow counting. Although the ASTM standard does not recommend one method over another, certain methods are clearly best suited for particular applications. The simplified rainflow method, for example, is best for prolonged and repeated load histories.

Two of the studies mentioned previously used methods documented by ASTM. Hutchinson et al. (*7*) applied the rainflow/range-pair counting method to calculate LEFs from surface deflections, whereas Hajek and Agarwal (*8*) applied the peak counting method to calculate LEFs from surface deflections and AC interfacial strains. As described in the following paragraphs, the difficulty in counting strain cycles results because AC interfacial strains go into compression under an approaching tire, peak in tension when the tire is directly over

T. Papagiannakis and A. Oancea, Memorial University of Newfoundland, St. John's, Newfoundland, Canada A1B 3X5. N. Ali, Technical University of Nova Scotia, P.O. Box 1000, Halifax, Nova Scotia, Canada B3J 1B5. J. Chan and A. T. Bergan, Transportation Center, University of Saskatchewan, Saskatoon, Saskatchewan, Canada S7N 0W0.

the sensor, and turn again into compression after the tire has passed over the sensor. This pattern repeats as subsequent tires go over the sensor (see Figure 1).

Oancea (*11*) presents a comparative assessment of all the methods used in the literature for calculating mechanistic LEFs (see Table 1). Among the methods described in the ASTM standard, the rainflow/range-pair counting method is best suited for counting pavement strain cycles under multiple axle loads. As shown in Figure 2, this method provides a direct relationship between strain history (shown as linear segments) and the stress-strain behavior of the AC. Indeed, Ranges 1–2 and 2–3 are directly related to stress-strain cycle 1–2–3, Ranges 3–4 and 4–5 are directly related to stress-strain cycle 3–4–5, and so on.

OBJECTIVES

To date, there have been no efforts to apply the rainflow/range-pair counting method for calculating LEFs from interfacial AC strains. Another issue that has not been addressed is the contribution to pavement fatigue from the strain history between the axles and axle groups of a vehicle. This role is fulfilled by addressing the following objectives:

- Demonstrate the application of the rainflow/range-pair counting method of ASTM E1049-85 in calculating LEFs of multiple axles from interfacial AC pavement strains.
- Use the rainflow/range-pair counting method to compare the LEFs of an entire vehicle with the sum of the LEFs of its individual axles and axle groups.

RAINFLOW/RANGE-PAIR COUNTING METHOD

The terminology used in explaining the range-pair counting procedure of the rainflow method is shown in Figure 3. The value of a range is equal to the sum of the absolute values of its peak and valley strains. As specified in ASTM E1049-85, the idea is to count a range as a cycle if it can be paired with a subsequent loading in the opposite direction. The steps involved in determining the cycles to be counted lead to a simple algorithm that takes into account all cycles, large and small. These steps are described as follows, naming the current range as n and the immediately preceding range as $n - 1$:

1. Read next peak or valley. If out of data, go to Step 5.
2. If there are less than three points, go to Step 1. Form ranges n and $n - 1$ using the three most recent points (i.e., peak and valley) that have not been discarded.
3. Compare the absolute magnitude of range n to that of range $n - 1$:

- *If* $|n| < |n - 1|$, go to Step 1.
- *If* $|n| \geq |n - 1|$, go to Step 4.

4. Count range $n - 1$ as one cycle and discard the points that define it.
5. If any cycles remain, start at the end of the sequence and count backwards. If a single peak remains, count it as one cycle.

This procedure does not differentiate between positive and negative ranges. It is clear, however, that the mode of fatigue failure should determine the type of cycle counted. That is, valley-peak-valley cycles should only be counted for tensile failure, whereas peak-valley-peak cycles should only be counted for compressive failure (e.g., rutting). ASTM E1049-85 presents an example of applying this method in counting fatigue cycles (see Figure 4).

Figures 5 and 6 show the application of this method for a single and a tandem axle, respectively. In accordance with the ASTM standard, full ranges are taken into account (i.e., from the compression trough to the tension peak), as opposed to previous methods in which the compressive strains were completely ignored (*4,6*). Whether this is appropriate for AC pavements may be disputed along with other fatigue concepts originally developed for metals. Only laboratory fatigue experimentation can verify that such fatigue concepts are indeed applicable for pavements as well as for metals.

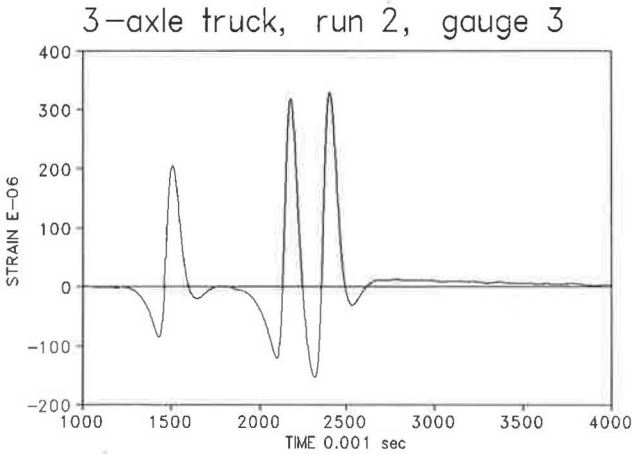
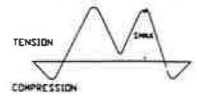
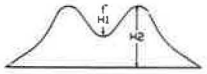
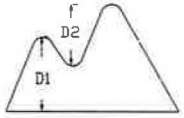
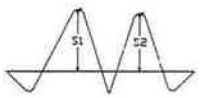
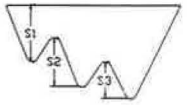
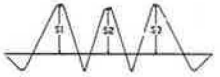
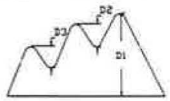
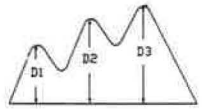
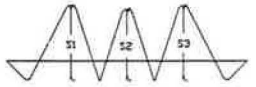


FIGURE 1 Strain pattern under a three-axle truck (*11*).

THE EXPERIMENT

The experiment was conducted in the summer of 1990 at the instrumented pavement site located on HW-16 north of Saskatoon, Canada. The site is equipped with a number of deflection, strain, and temperature transducers (*12*). The pavement structure at the site consists of 175 mm of AC, 100 mm of base, and 100 mm of subbase, laid on a glacial till subgrade. Two vehicles were tested: a three-axle single unit truck and a five-axle semitrailer truck (see Figure 7). Each test run was accompanied by a Benkelman beam truck, which provided the reference axle load. Vehicle runs were performed at three speeds (20, 40, and 50 km/hr) and for three levels of static axle load (see Table 2). A replicate run was performed for each test vehicle, speed, and axle load combination, bringing the total number of runs to 54 (two replicates × three speeds × three loads × three vehicles). Replicate runs were intended

TABLE 1 OVERVIEW OF MECHANISTIC LEF METHODS (*11*).

Deacon (1969)		
Calculated AC strain	$F = 2*\left(\frac{SMAX}{S18}\right)^c$	
Ramsamooj (1972)		
Stress intensity factors based on measurements	$F = \left(\frac{H1}{H18}\right)^4 + \left(\frac{H2}{H18}\right)^4$	
Christison (1978)		
Measured deflection	$F = \left(\frac{D1}{D18}\right)^c + \left(\frac{D2}{D18}\right)^c$	
Measured AC strain	$F = \left(\frac{S1}{S18}\right)^c + \left(K\frac{S1}{S18}\right)^c$ K= average ratio $\frac{S_2}{S_1}$	
Treybig (1983)		
Calculated subgrade strain	$F = \left(\frac{S1}{S18}\right)^c + \left(\frac{S2}{S18}\right)^c + \left(\frac{S3}{S18}\right)^c$	
Calculated AC strain	$F = \left(\frac{S1}{S18}\right)^c + \left(\frac{S2}{S18}\right)^c + \left(\frac{S3}{S18}\right)^c$	
Southgate (1985)		
Calculated strain energy density	$F = \frac{N18}{N}$	$\log(N) = \frac{\log(\epsilon_w) + 2.6777807}{-0.15471249}$
RTAC (1986)		
Measured deflection	as Christison (1978)	
Measured AC strain	as Treybig (1983)	
Hutchinson (1987)		
Measured deflection	$F = \left(\frac{D1}{D18}\right)^c + \left(\frac{D2}{D18}\right)^c + \left(\frac{D3}{D18}\right)^c$ ASTM/Range-Pair Counting	
Hajek (1989)		
Calculated & measured deflection	$F = \left(\frac{D1}{D18}\right)^c + \left(\frac{D2}{D18}\right)^c + \left(\frac{D3}{D18}\right)^c$ ASTM/Peak Counting	
Calculated & measured AC strain	$F = \left(\frac{S1}{S18}\right)^c + \left(\frac{S2}{S18}\right)^c + \left(\frac{S3}{S18}\right)^c$ ASTM/Peak Counting	
Govind (1989)		
Calculated AC stress	Damage Factors (LEF's) were calculated based on the rate of change of stress.	
Tseng (1990)		
Calculated AC strain	The AC strain pattern was used to modify the value of the exponent C.	

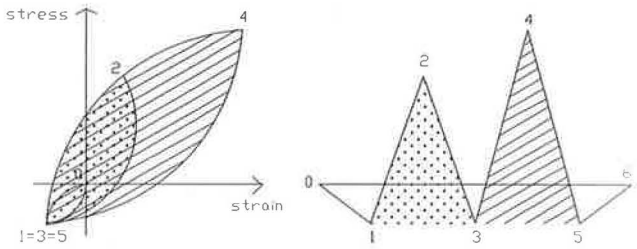


FIGURE 2 Fatigue cycles in a stress-strain diagram (*11*).

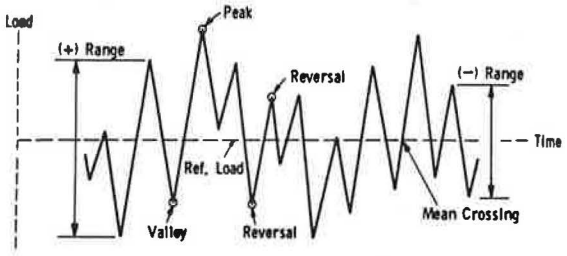
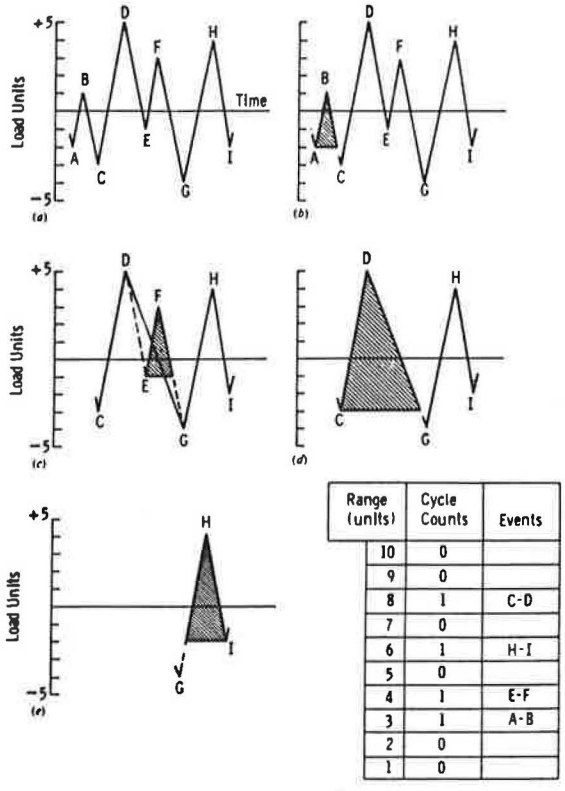


FIGURE 3 Rainflow counting terminology (ASTM E1049-85).



Range (units)	Cycle Counts	Events
10	0	
9	0	
8	1	C-D
7	0	
6	1	H-I
5	0	
4	1	E-F
3	1	A-B
2	0	
1	0	

FIGURE 4 Example of rainflow/range-pair counting method (ASTM E1049-85).

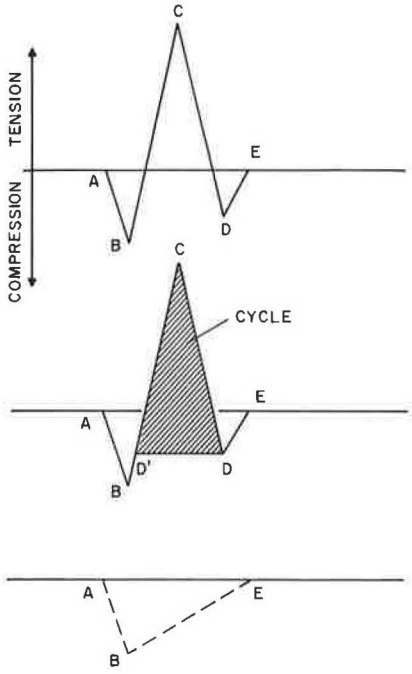


FIGURE 5 Strain cycle counting under a single axle.

to increase the chances of achieving equal lateral placement of the test vehicles and the BB truck with respect to the sensors. Lateral placement was determined by videotaping the passing vehicle axles and the pavement edgeline and scaling off the distance from the still image. The test lasted 2 days, during which the pavement temperature ranged between 26°C and 30°C. As a result, the pavement temperature was not considered a variable in the analysis.

DISCUSSION OF RESULTS

LEF values were calculated according to Equation 3 by following the strain counting method and selecting a k_2 value of 3.8. LEF calculations were limited to strains recorded by a particular sensor to avoid the measurement variability between sensors. Because of the small number of vehicle runs available, LEF calculations were made irrespectively of vehicle lateral placement, despite the observed sensitivity of the measured strains to lateral placement (see Figure 8). An effort was made to select the sensor that happened to be nearest to the outside tire of the pair of axles compared.

As expected, the measured strains exhibited large sensitivity to vehicle speed (see Figure 9). Therefore, only strains obtained at vehicle speeds within 10 percent were compared. Another source of variation in the calculated LEFs is vehicle dynamics. It is expected, however, that vehicle runs performed at roughly the same vehicle speeds will produce precise strain measurements, all other conditions (e.g., temperature and lateral placement) being equal. Replicate vehicle runs were shown to produce dynamic axle load waveforms repetitive in space (*13*). On the other hand, vehicle dynamics are expected to result in discrepancies when comparing mechanistic LEFs and empirical LEFs because the latter are

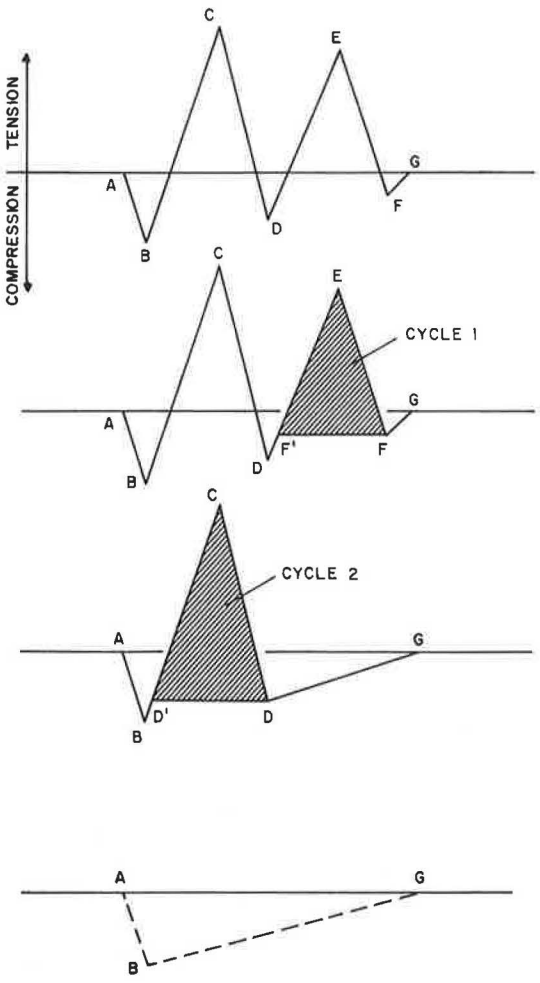


FIGURE 6 Strain cycle counting under tandem axles.

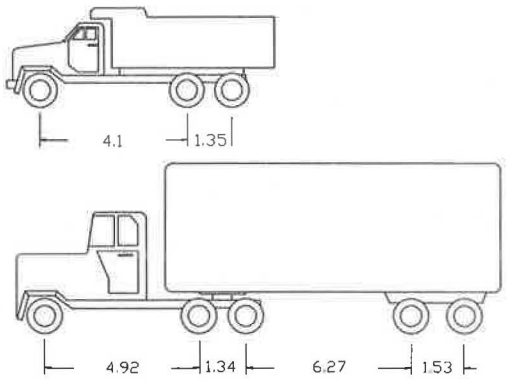


FIGURE 7 Axle spacing of test vehicles in meters.

based on static axle load values. No effort was made to account for this discrepancy. The results of the LEF calculations are presented in Tables 3 and 4 for the three-axle truck and the five-axle truck, respectively.

Two observations can be made:

- In general, the calculated LEFs decrease with vehicle speed.
- LEFs calculated for entire vehicles can be substantially higher than the sum of the LEFs of their individual axle groups (i.e., either single axles or tandem axles in this experiment). This trend becomes more pronounced as vehicle speeds increase.

The dependence of in-situ strains on vehicle speed is a direct result of the viscous properties of the AC. For a given pair of axle loads, strain ratios decrease with increasing vehicle speed and, as a result, LEFs decrease. Thus, mechanistic LEFs should be viewed as speed-specific. This conclusion agrees with the findings of Hutchinson et al. (*7*) but disagrees with the Roads and Transportation Association of Canada (RTAC) study (*6*), which states, "the magnitude of the response ratios did not exhibit a consistent trend with velocity" and, therefore, "the average of the three response ratios [obtained at 6, 13, and 50 km/hr] was used in the load equivalency predictions."

The second observation suggests that the damaging effect of a vehicle is not fully accounted for simply by adding the LEFs of its individual axle groups. This procedure ignores the strain cycles between axle groups, which are shown as cross-hatched areas in Figure 10. Obviously, the larger the number of axle groups in the vehicle, the larger this difference will be. The difference increases with increasing vehicle speed because the unloading time between axle groups decreases. It is therefore concluded that simply adding the damaging effect of axle groups underestimates the damaging effect of a vehicle.

The LEFs obtained at 50 km/hr using the rainflow/range-pair counting method were compared with two sets of values: (a) mechanistic LEFs obtained by the RTAC method (*6*) using the strain measurements at hand and (b) AASHTO LEFs based on the static axle loads measured, a terminal serviceability of 2.5, and a structural number (SN) of 3 in. (*1*). The comparisons are shown in Figures 11–14. In general, the differences between the two groups of mechanistic LEFs (i.e., ASTM and RTAC) are quite significant but exhibit no definite patterns. There is no doubt that the method used for counting fatigue cycles affects the magnitude of the strain cycles counted and the resulting LEFs. In general, there is a better agreement between the two sets of mechanistic LEFs than between any one of them and the empirical LEFs obtained from AASHTO. However, no quantitative assessment was attempted to determine which set is closer to the AASHTO LEFs because such a comparison would not be meaningful. As a result, no conclusive evidence could be produced to support one cycle counting method over another. Indeed, only laboratory fatigue testing can address this issue and specifically determine whether or not the compressive part of the strain history contributes to the fatigue of AC.

CONCLUSIONS

Counting fatigue cycles according to the rainflow/range-pair method of the ASTM E1049-85 standard has shown that

- The calculated LEFs decrease with vehicle speed.
- LEFs for entire vehicles are substantially higher than the sum of the LEFs of their individual axle groups. This trend becomes more pronounced at higher vehicle speeds.

TABLE 2 STATIC LOADS OF TEST VEHICLES IN KILOGRAMS

	3-AXLE TRUCK		5-AXLE TRUCK		
LOAD CODE	STEERING	TANDEM*	STEERING	TANDEM1	TANDEM2
1	4200	16300	4790	16890	17550
2	4160	13450	4500	10950	9250
3	4020	11240	4320	5020	2940

* Load values are suspect due to improper weighing procedure

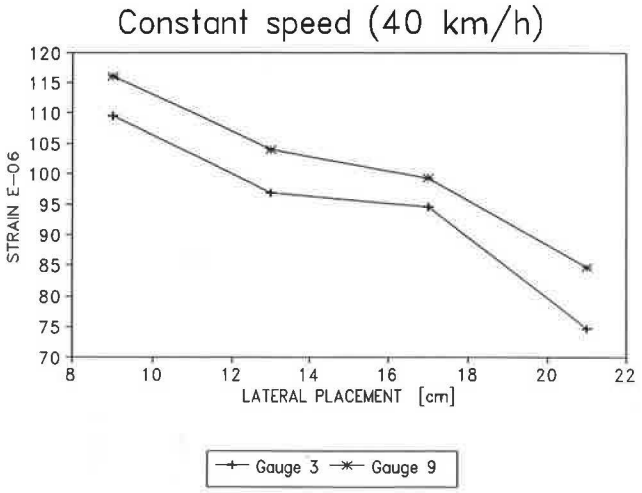


FIGURE 8 Strain versus lateral placement with respect to a sensor.

TABLE 3 LEFs FOR THREE-AXLE TRUCK

RUN	LOAD CODE	NOMINAL SPEED kmh	STEERING	TANDEM AXLE	SUM	WHOLE TRUCK
2		20	-	-	-	-
6	1	40	0.02	74.65	74.67	74.77
8		50	2E-06	3.39	3.39	3.39
11		20	-	-	-	-
14	2	40	7E-06	0.36	0.36	0.39
17		50	0.07	1.08	1.15	1.15
20		20	-	-	-	-
23	3	40	0.31	3.05	3.36	4.04
27		50	0.08	1.47	1.55	1.97

- Speed difference between test truck and BB truck > 10%

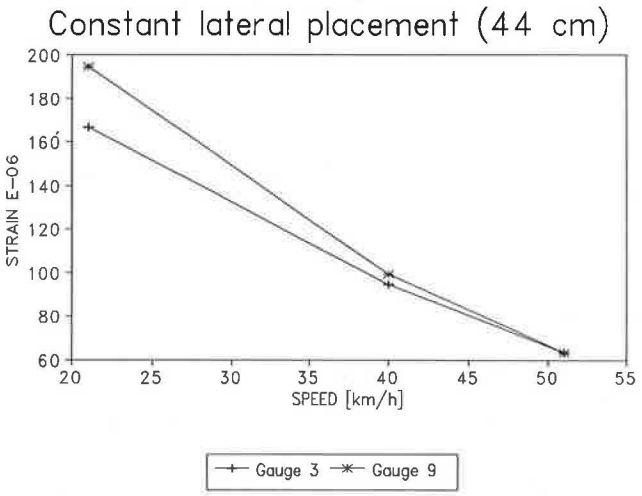


FIGURE 9 Strain versus vehicle speed.

TABLE 4 LEFs FOR FIVE-AXLE TRUCK

RUN	LOAD CODE	NOMINAL SPEED kmh	STEERING	TANDEM1	TANDEM2	AXLE SUM	WHOLE TRUCK
30		20	0.58	4.79	7.74	13.11	16.30
32	1	40	0.31	2.68	5.33	8.32	11.38
35		50	0.10	1.51	2.98	4.59	6.54
38		20	0.20	1.88	1.71	3.79	4.90
42	2	40	0.29	0.38	0.27	0.94	1.63
44		50	0.01	0.26	0.24	0.51	0.91
48		20	0.20	0.03	0.007	0.24	0.42
50	3	40	0.10	0.06	0.004	0.17	0.33
54		50	0.29	0.01	0.001	0.30	0.31

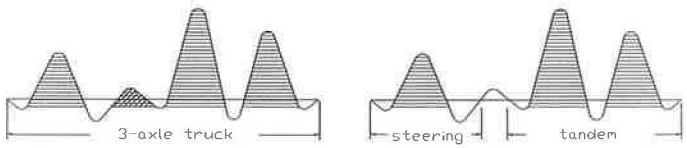


FIGURE 10 Strain cycles for the vehicle and individual axles and axle groups for three-axle truck.

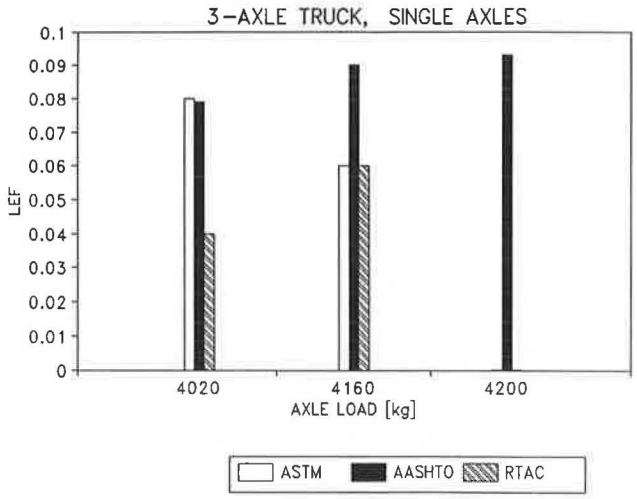


FIGURE 11 Comparison of LEFs for three-axle truck, single axle.

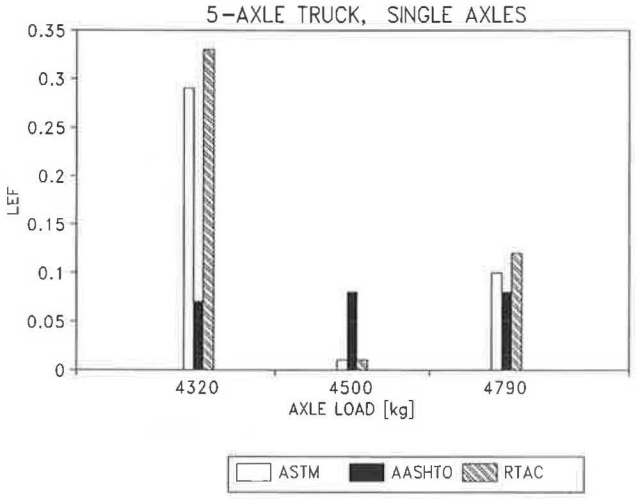


FIGURE 13 Comparison of LEFs for five-axle truck, single axle.

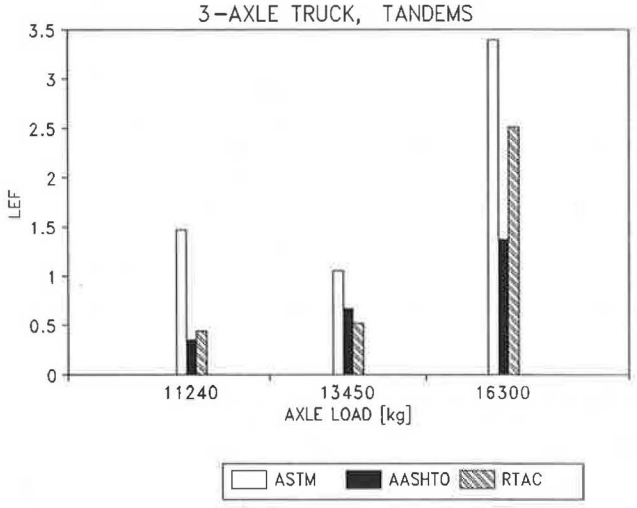


FIGURE 12 Comparison of LEFs for three-axle truck, tandem axle.

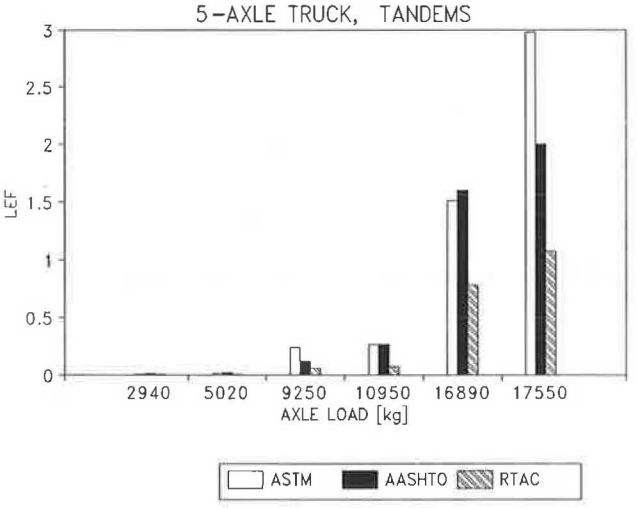


FIGURE 14 Comparison of LEFs for five-axle truck, tandem axle.

The LEFs obtained by the rainflow/range-pair counting method were compared with those obtained by the RTAC method. The two sets of mechanistic LEFs were also compared with the empirical LEFs recommended by AASHTO. This comparison, however, was inconclusive and could not verify that one of the two mechanistic LEF methods best describes the fatigue cycles caused in AC by multiple axle loads.

ACKNOWLEDGMENT

Field testing was accomplished with the cooperation of the Saskatchewan Department of Highways and Transportation.

REFERENCES

1. *AASHTO Guide for the Design of Pavement Structures*. AASHTO, Washington, D.C., 1986.
2. J. A. Deacon. Load Equivalency in Flexible Pavements. *Proc., Association of Asphalt Pavement Technologists*, Los Angeles, Calif., Vol. 38, 1969, pp. 465–494.
3. J. T. Christison, K. O. Anderson, and B. P. Shields. In-Situ Measurements of Strains and Deflections in a Full-Depth Asphaltic Concrete Pavement. *Proc., Association of Asphalt Pavement Technologists*, Minneapolis, Minn., Vol. 47, 1978, pp. 398–433.
4. H. J. Treybig. Equivalency Factor Development for Multiple Axle Configurations. In *Transportation Research Record 949*, TRB, National Research Council, Washington, D.C., 1983, pp. 32–44.
5. H. F. Southgate and R. C. Deen. *Effects of Load Distributions on Axle and Tire Configurations*. Research Report UKTRP-85-13. Kentucky Transportation Research Program, 1985.

6. Roads and Transportation Association of Canada. *Pavement Response to Heavy Vehicle Test Program. Part 2—Load Equivalence Factors*. Canroad Transportation Research Corporation, 1986.
7. B. G. Hutchinson, R. C. G. Haas, P. Meyer, K. Hadipour, and A. T. Papagiannakis. Equivalencies of Different Axle Load Groups. *Proc., 2nd North American Pavement Management Conference*, Toronto, Canada, Vol. 3, 1987, pp. 191–202.
8. J. J. Hajek and A. C. Agarwal. *Influence of Axle Group Spacing on Pavement Damage*. Research and Development Branch, Ontario Ministry of Transportation, 1989.
9. S. Govind and C. M. Walton. Fatigue Model to Assess Pavement Damage. In *Transportation Research Record 1227*, TRB, National Research Council, Washington, D.C., 1989, pp. 88–96.
10. K. H. Tseng and R. L. Lytton. Fatigue Damage Properties of Asphaltic Concrete Pavements. Presented at 69th Annual Meeting of the Transportation Research Board, Washington, D.C., 1990.
11. A. Oancea. *Load Equivalence Factors from In-Situ Strain: Applying ASTM E1049-85*. M.Eng. thesis. College of Engineering, Memorial University of Newfoundland, St. John's, Newfoundland, Canada, 1991.
12. B. Taylor. *The Development and Use of an Instrumented Pavement Section To Compare Heavy Vehicle Load Equivalencies*. Saskatchewan Department of Highways and Transportation, Regina, Saskatchewan, Canada, 1988.
13. A. T. Papagiannakis, R. C. G. Haas, J. H. F. Woodrooffe, and P. Leblanc. Effects of Dynamic Load on Flexible Pavements. In *Transportation Research Record 1207*, TRB, National Research Council, Washington, D.C., 1988, pp. 187–196.

Publication of this paper sponsored by Committee on Flexible Pavement Design.

A Reliable Resilient Modulus Testing System

RAFAEL F. PEZO, DONG-SOO KIM, KENNETH H. STOKOE II, AND WILLIAM R. HUDSON

In 1986 AASHTO adopted the resilient modulus test for use in the design of pavement structures to determine properties of roadbed soil and pavement components (AASHTO T274-82). The criticism that followed this adoption has resulted in the publication of several papers aimed at resolving the problems generated by the test method. The Strategic Highway Research Program's published modifications to the test procedure are examined, in particular. In addition, the experience gained in calibrating a resilient modulus testing system—as well as the results obtained from a pilot test program with cohesive soil—is presented. Finally, the comparison results obtained from testing companion cohesive specimens using the resilient modulus test and torsional testing techniques are reported. The results indicate that (a) strong uniform contact between the specimen and the top and bottom caps of the triaxial cell is required for accurate measurement of modulus; (b) synthetic samples of known properties can be useful for the detection of equipment compliances, as well as for assessing a reliable system; and (c) the resonant column and torsional shear apparatus provides a basic approach to characterizing pavement materials—an approach that was useful for comparison with the resilient modulus test.

In 1986 AASHTO (*1*) began using the resilient modulus (M_R) test in the design of flexible, rigid, and composite pavements. The M_R test is used to determine roadbed soil and pavement component properties, with the standard testing method determined by AASHTO T274-82.

Laboratory measurements of the deformational characteristics of subgrade materials can be complex because of the small strains that are typically involved in such pavement components. Moreover, experience in applying the cyclic triaxial test in geotechnical earthquake engineering has indicated that extreme care must be exercised when evaluating the deformational characteristics of soils, particularly at small to intermediate strain levels (10^{-3} to 10^{-1} percent). These strain levels are also the strain levels at which M_R testing is used. Other popular techniques used to characterize soil properties in this strain range include the torsional shear test and the resonant column test.

TESTING EQUIPMENT

M_R Testing Equipment

In general, the resilient moduli of cohesive and cohesionless materials are determined in a repeated-load triaxial compression test known as the M_R test. The equipment used in this test is similar to that used in common triaxial testing, although in this case some modification was required to facilitate the internally mounted load and deformation transducers. Because transducers are located inside the triaxial chamber, air is generally used as the cell fluid to provide confinement to the test samples. The external loading source, in most cases, is a closed-loop electrohydraulic system capable of providing a variable load of fixed cycle and load duration.

During the M_R test, specimens are subjected to testing sequences that consist of the application of different repeated axial deviator stresses (σ_d) under different confining pressures (σ_3). Also during the test, the recoverable axial strain (ε_a) is determined by measuring the resilient deformation of the sample across a known gauge length. M_R is thus defined as follows:

$$M_R = \sigma_d/\varepsilon_a \quad (1)$$

Applying the deviator stress results in an immediate axial deformation followed by a plastic deformation while the load is sustained, with a rebound occurring once the load is removed. The rebound, called the "resilient deformation," remains approximately constant throughout a large number of applications of a given load. Axial deviator stress is defined as the applied axial load (P) over the cross-sectional area of the sample (A):

$$\sigma_d = P/A \quad (2)$$

It is generally recommended that a load cell be used inside the test cell to offset the effect of friction on the loading piston. Deformation measurements may be taken with external or internal linear variable deformation transformers (LVDTs) fixed to the triaxial chamber. Axial strain is defined as the axial deformation (Δ) over the gauge length (Lg):

$$\varepsilon_a = \Delta/\mathrm{Lg} \quad (3)$$

Vinson (*2*) states that, during the load application, it is possible for deformations in the load train to be present; if an external LVDT is used, such deformations will be included and the results will have unacceptable errors. In order to avoid this problem, it is usually recommended that the displacement transducers be mounted inside the triaxial chamber.

The standard test for M_R of subgrade soils was specified in 1982 by AASHTO (AASHTO T274-82). The test method, which is generally accepted as fundamentally sound, requires

Center for Transportation Research, The University of Texas at Austin, Austin, Tex. 78712.

an evaluation of resilient moduli under a number of stress states for cohesive and cohesionless soils.

For cohesionless and cohesive soils, the M_R is expressed by Equations 4 and 5, respectively:

$$M_R = K_1\theta^{K_2} \quad (4)$$

$$M_R = K_1\sigma_d^{K_2} \quad (5)$$

where K_1 and K_2 are experimental constants determined from a set of test results with the use of statistical regression tools, and θ is the sum of principal stresses.

However, in recent years this test method has increasingly been criticized (*3–5*). Hence, in 1989 the Strategic Highway Research Program (SHRP) (*6*) published the laboratory testing procedure for determination of the M_R of unbound granular base and subbase materials and subgrade soils (SHRP Protocol P-46), which was essentially a modification of AASHTO T274-82.

At The University of Texas at Austin, M_R testing equipment has been implemented following the recommendations published by SHRP (*6*). This testing equipment included the following characteristics:

- A hydraulic loading system capable of applying repeated dynamic loads controlled under an MTS Systems Corp. closed-loop system. The shape and amplitude of the cyclic loading waveform are set by the use of a function generator, with the loading function continuously monitored by an oscilloscope and a plot strip chart. As specified by SHRP P-46 (*6*), the load pulse duration and cyclic loading are set at 0.10 and 1.00 sec, respectively, with a Haversine loading waveform.
- Two LVDTs, with a calibration range of 0.02 in. and mounted inside the triaxial chamber diametrically opposite each other, are used to monitor axial deformations for the whole length of the specimen (located at the top of the samples). All measurements from the LVDTs are referred to the base of the triaxial chamber, and the average of the two signals is used to estimate the strain value that is used for computing the M_R of the specimen.
- A 100-lb load cell mounted inside the triaxial chamber and centered on the top of the soil sample was used to monitor the actual deviator stress applied during the testing process.
- A data acquisition system was developed to record the signals emitted by the transducers. A data acquisition board was mounted inside an IBM XT personal computer; software was developed for acquiring, plotting, storing, and computing the M_R values of the test samples.

The M_R testing equipment used cannot accurately measure axial strains smaller than about 10^{-2} percent (because of the resolution of the transducers installed and the compliance of the system itself). Generally, this is a limitation common to all M_R testing equipment: when the sample undergoes smaller strains, erratic M_R values are calculated. Figure 1 shows the system assembled and used in the laboratories of the Department of Civil Engineering at The University of Texas at Austin.

Torsional Testing Equipment

Torsional RC

Torsional resonant column (RC) equipment of the fixed-free type was used in these tests. In the fixed-free configuration, the bottom of the test specimen is held fixed while the top (free end) is connected to a drive system used to excite and monitor torsional motion, as illustrated in Figure 2a.

The basic operational principle is to vibrate the cylindrical specimen in first-mode torsional motion. Once first mode is

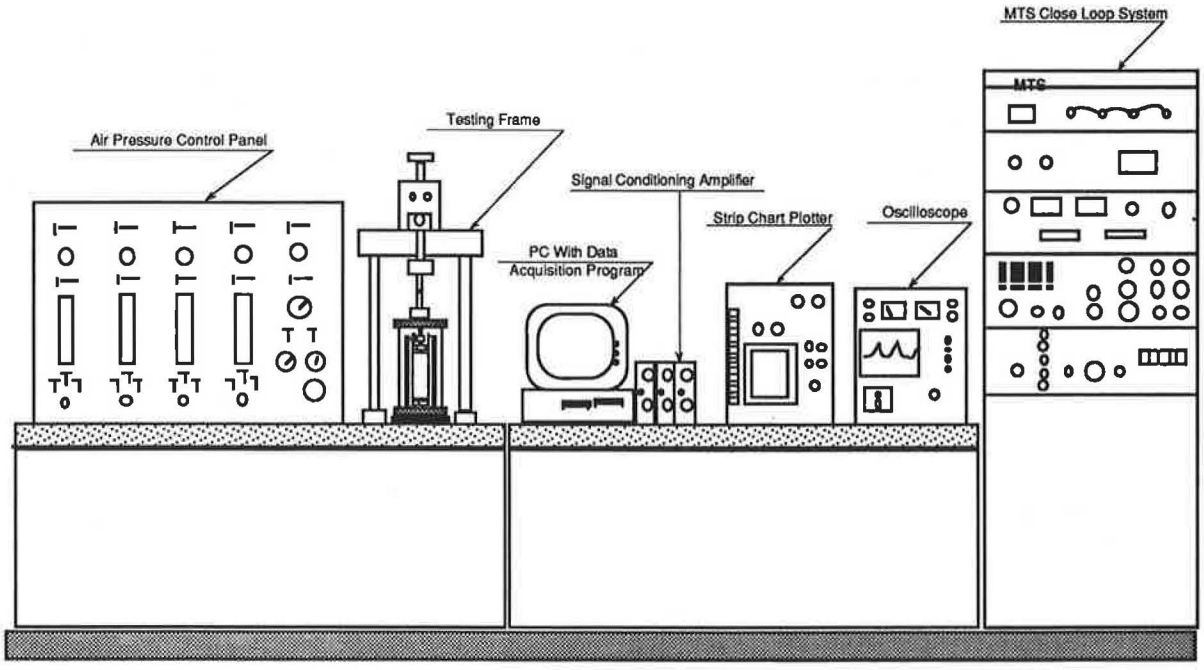
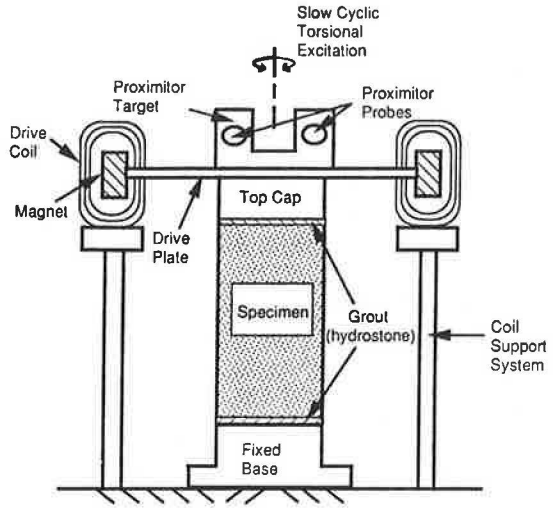
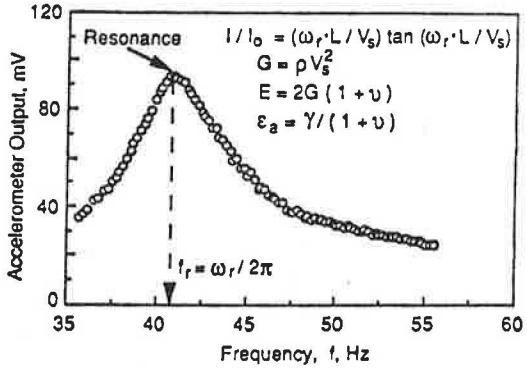


FIGURE 1 Sketch of M_R testing equipment developed at The University of Texas at Austin.



a. Specimen in Test Apparatus



b. Typical Measurement

FIGURE 2 Configuration of fixed-free RC test and typical test results.

established, measurements of the resonant frequency and amplitude of vibration are made, as shown in Figure 2b. These measurements are then combined with equipment characteristics and specimen size to calculate shear wave velocity (V_S), shear modulus (G), and shearing strain amplitude (γ) (ASTM D4015-87).

One-dimensional wave propagation in a circular rod is used to analyze the dynamic response of the specimen. The basic data reduction equation is expressed as follows:

$$I/I_0 = \omega_r L/V_S \tan(\omega_r L/V_S) \quad (6)$$

where

I = mass moment of inertia of the specimen,
I_0 = mass moment of inertia of drive system,
ω_r = resonant circular frequency,
L = length of the specimen, and
V_S = shear wave velocity.

Once the value of shear wave velocity is determined from Equation 6, shear modulus (G) and Young's modulus (E) of the specimen can be calculated from the following:

$$G = \rho V_S^2 \quad (7)$$

$$E = 2G(1 + \nu) \quad (8)$$

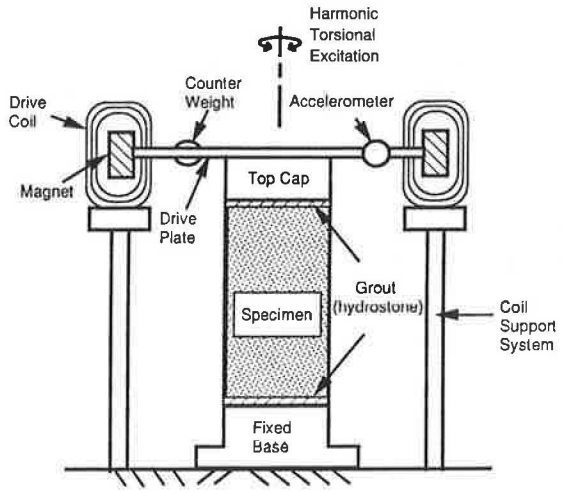
where ρ is the mass density and ν is Poisson's ratio of the specimen.

The shearing strain (γ) is calculated from the peak rotation of the top of the specimen at 0.67 times the radius of the solid sample (ASTM D4015-87). By following standard procedures in relating cyclic triaxial and RC results and by assuming that the material is homogeneous and isotropic, the axial strain is obtained compatible with this shearing strain:

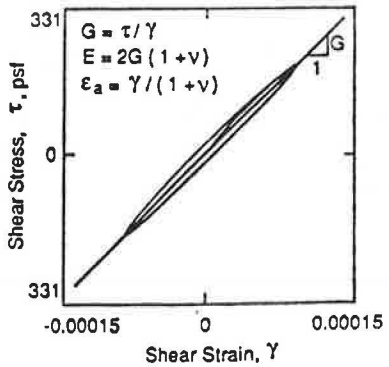
$$\varepsilon_a = \gamma/(1 + \nu) \quad (9)$$

TS Test

The torsional shear (TS) test is another method for determining shear and Young's moduli using the same RC equipment but operating it in a different fashion. In this test a cyclic torsional force with a given frequency, generally below 10 Hz, is applied at the top of the specimen while the bottom is held fixed, as shown in Figure 3a. Instead of determining a resonant frequency, the stress-strain hysteresis loop is determined from measuring the torque-twist response of the specimen.



a. Specimen in Test Apparatus



b. Typical Measurement

FIGURE 3 Configuration of TS test and typical test results.

Proximeters are used to measure twist while the current applied to the coils is calibrated to yield torque. Shear modulus (G) corresponds to the slope of a line through the end points of the hysteresis loop, as shown in Figure 3b. Using this technique, the shear modulus, defined as the ratio of shearing stress to shearing strain, is calculated from the following:

$$G = \tau/\gamma \tag{10}$$

Values of shearing strain are presented as single-amplitude values and are calculated at 0.67 times the radius of the specimen, just as in RC tests. Once G and γ are determined, Young's modulus and axial strain can be determined using Equations 8 and 9.

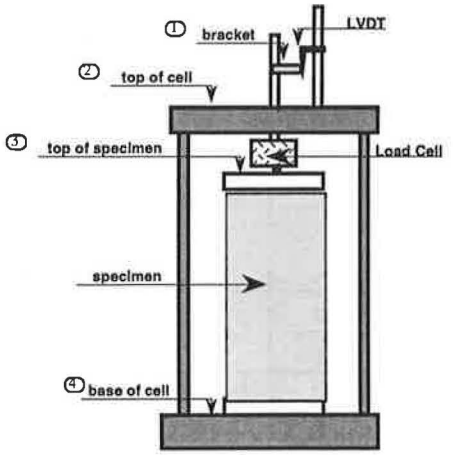
CALIBRATION OF M_R EQUIPMENT

As with all cyclic loading equipment, M_R equipment requires careful calibration of each of the deformational and loading transducers. In addition, calibration of the complete system is advisable if accurate results are to be determined for stiff specimens or for small-strain measurements. Calibrations of the individual transducers are standard procedures, but calibration of the whole system requires more than routine adjustments of its individual parts. To calibrate the entire M_R system, three synthetic samples of known stiffness properties (*7*) were used.

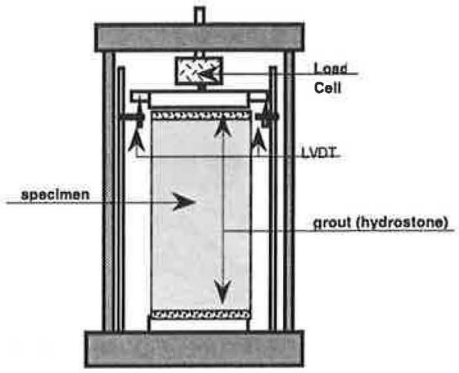
Calibration of the complete M_R system turned out to be an involved task, with several problems having to be overcome before a satisfactory state was achieved. Claros et al. (*8*) pointed out the necessity of changing the location of the LVDT used to record the axial deformation of the sample. At that time they were using an external LVDT that recorded the movement of a bracket attached to the loading piston, as shown in Figure 4a.

To find the best location for monitoring axial deformations, the relative movements of four points in the triaxial chamber were measured while performing the M_R test on synthetic samples. Figure 4a also shows the four points monitored in this inspection: the base and top of the triaxial chamber, the top of the specimen, and the external bracket. Microproximeters, placed on each of the chosen points, were hooked onto a computerized analyzer that recorded the voltage signal emitted by the transducers. In general, measuring the relative movements of those points at different levels of deviator stress revealed that (a) the base of the triaxial chamber is a good reference point for these measurements because it moves the least at any level of deviator stress and (b) a better position for monitoring axial deformations is the top of the specimen rather than the external bracket (used previously). In addition, the decision was made to use two LVDTs (instead of only one), located diametrically opposite at the top of the specimen. Each LVDT was supported by a steel bar attached to the base of the triaxial chamber. Modifications in the geometry of the top cap were also made to facilitate operation of the transducers. Figure 4b shows the final setup of the triaxial cell.

Once the final arrangement was selected, more testing with synthetic samples was performed. The new results, although closer to the moduli than those previously obtained by Claros et al. (*8*), were not close enough. In particular, values for the



a. Initial Set-Up as used by Claros et al. (8).



b. Final Set-Up.

FIGURE 4 Configuration of M_R test.

TU-960 specimen (the stiffest sample) were still lower by 50 percent. At this point, hydrostone paste was used to improve the connections between the specimen and the top and bottom platens. The connections were grouted in such a way that an even contact surface—and a good continuous connection—was achieved between the top and bottom steel platens and the synthetic samples. Then, the three synthetic samples were tested again. Testing consisted of applying various levels of deviator stresses at 10 Hz under no confining pressure and a temperature of 70°F. Several repetitions were performed to gain a better statistical representation of the values. Finally, new M_R values close to those published by Stokoe et al. (*7*) were obtained for the three synthetic samples. Table 1 presents the comparison of moduli of synthetic samples determined by M_R and torsional testing techniques. Figure 5 shows this comparison, as well as the deviation in the M_R obtained from not grouting the samples to the end platens. The deviations in the moduli caused by not grouting the samples to the end platens are significant for materials with an M_R value greater than 9,000 psi.

With this calibration, it was believed that there were no significant discrepancies in the comparisons of the M_R with the torsional testing techniques for the synthetic samples and that the final arrangement of the M_R testing equipment was capable of providing accurate measurements. It was obvious in this work that all measurements in the M_R testing equipment are sensitive both to specimen preparation and to the

TABLE 1 COMPARISON OF MODULI OF SYNTHETIC SAMPLES DETERMINED BY RESILIENT MODULUS AND TORSIONAL TESTING TECHNIQUES

SYNTHETIC SAMPLE	GROUTING	RESILIENT MODULUS M_R, psi	RESONANT COLUMN & TORSIONAL SHEAR E, psi	M_R/E	DEVIATION (%)
TU-700	NO	1888	2220 *	0.850	- 15.00
	YES	2252		1.014	+ 1.40
TU-900	NO	6550	8921 *	0.734	- 26.58
	YES	8880		0.995	- 0.45
TU-960	NO	22410	45735 *	0.490	- 51.00
	YES	44197		0.966	- 3.40

Note: (*) All moduli adjusted to a frequency of 10 Hz.

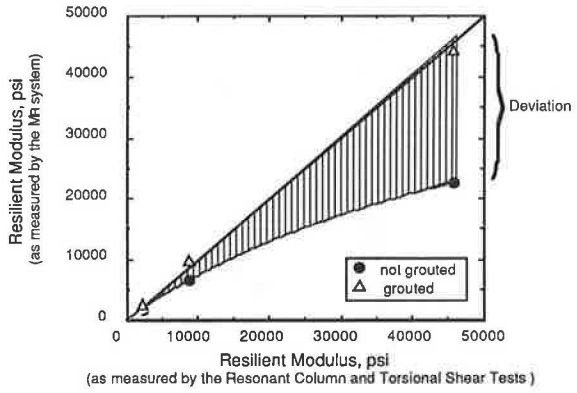


FIGURE 5 Variation of M_R for synthetic samples tested by the M_R system.

top and bottom cap connections. Extreme care must be taken to eliminate any compliance in the specimen-platen connections before testing.

TESTING MATERIAL AND TESTING PROGRAM

Once the M_R testing equipment was understood and calibrated, a pilot program of soil testing was initiated to determine, in depth, how the M_R is affected by the following parameters: soil type, water content, soil density, sample age, and the testing equipment itself.

Two different types of soils, one plastic (cohesive) and one nonplastic, were collected from the Austin, Texas, area. The analysis and evaluation of the results for the cohesive soil are nearly completed and are presented in the following paragraphs. Testing with the cohesionless soil is under way, and these results will be presented at a later date.

Material Properties of Cohesive Soil

Samples of cohesive soil were gathered from the intersection of MoPac and SH-183 in Austin. Preliminary tests were performed to establish the index properties of this disturbed soil following the guidelines presented by the state of Texas (*9*). The soil classifies as an A-7-6 soil, Type 2 (according to SHRP P-46), with 87.3 percent of finer, a liquid limit (LL) of 56 percent, and a plasticity index (PI) of 27 percent. To obtain a characteristic compaction curve, Test Method Tex-113E was followed. Figure 6 illustrates the compaction curve of this soil, in which the maximum dry density of 93.9 pcf was determined at 19.3 percent of moisture content.

Testing Program

To define the effect of water content and dry density of the soil on the M_R, samples were built with the same compacting effort of 6.64 ft-lb/in.^{3} with different water contents and dry densities. Four different levels of moisture content were selected for this experiment: one sample on the dry side of optimum, one at the optimum moisture content, and two samples on the wet side of optimum. Figure 6 shows these four points on the compaction curve. Each numbered point represents one specific condition of the soil in this testing program.

To determine the effect of sample age (age hardening or thixotropy), samples were tested at 2 days and 6 days after compaction. To compare M_R values from different testing equipment, companion specimens (two samples with identical characteristics) were prepared so that they could be tested at the same time: one with the M_R equipment and the other with the RC/TS testing apparatus.

The characteristics of the four pairs of soil samples included the following: (a) Companion Sample 1 had a moisture content of 17.3 percent (dry of optimum) and a dry density of 92.3 pcf; (b) Companion Sample 2 had a moisture content of 19.3 percent (optimum) and a dry density of 93.9 pcf (maximum); (c) Companion Sample 3 had a moisture content of 25.8 percent (wet of optimum) and a dry density of 89.2 pcf; and (d) Companion Sample 4 had a moisture content of 39.1 percent (wet of optimum) and a dry density of 77.9 pcf.

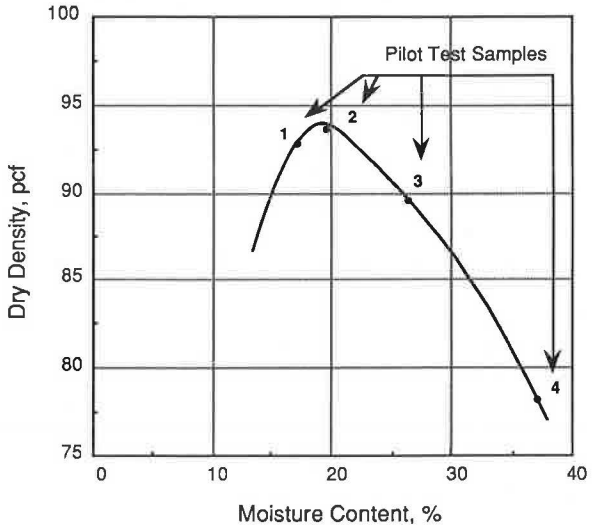


FIGURE 6 Compaction curve for cohesive soil compacted according to Test Method Tex-113E.

Sample Preparation

Specimens 2.8 in. in diameter and 5.60 in. in height were tested. The compacting effort for all specimens remained constant, with the compaction process based on Test Method Tex-113E, which is a modification of ASTM D1557 and AASHTO T180 methods. Once the samples were molded and well wrapped, they were stored in a constant temperature and humidity chamber for 1 day. After that, the companion samples were placed in each piece of testing equipment.

M_R Testing Procedure

In general, the cyclic triaxial tests (M_R) were run in accordance with SHRP Protocol P-46 (*6*). Details of this procedure follow.

Initially, each specimen was grouted to the top cap and base pedestal of the triaxial cell using a hydrostone paste. This procedure was used because, with the synthetic samples, it was found that those connections are important factors in evaluating M_R. Hydrostone paste has also proved useful in these tests because the levelness of the top cap can be easily adjusted to accommodate any unevenness in the ends. Two rubber membranes were placed around each specimen to prevent moisture loss or air migration during testing. After the sample was installed and its ends secured, it was allowed to cure overnight to ensure that the hydrostone reached its full strength and stiffness.

Testing of the sample began on the second day following compaction. First, the sample was subjected to a conditioning stage. For cohesive soil, SHRP Protocol P-46 (*6*) recommends the application of 200 loading repetitions of a 4-psi deviator stress under a 6-psi confining pressure. After this conditioning stage was completed, the testing sequence was followed. This testing sequence for cohesive soils consisted of applying 100 repetitions of each one of the following deviator stresses: 2, 4, 6, 8, and 10 psi (in ascending order) at each one of the confining pressures of 6, 4, and 2 psi (in descending order). To report the M_R values at different stress states, the strain values of the last five cycles of a particular testing sequence were recorded and averaged. In this way, M_R values were computed for a given level of deviator stress and axial strain. Then, by using all testing data recorded, simple linear regressions were developed and used to express M_R of the specimen in terms of the deviator stress, as expressed in Equation 5.

Over the following 4 days, the sample remained in the triaxial cell at atmospheric pressure. Six days after compaction the same sample was again tested using the same procedure. Following the testing, the specimen was taken out and destroyed to measure its final water content. This exercise confirmed that the samples, in general, did not experience any loss of moisture content.

Torsional Testing Procedures

Before testing in either the resonant or torsional shear mode, each specimen was fixed to the base pedestal and top cap (using hydrostone paste) and allowed to cure overnight, as in the M_R tests. This approach was meant to eliminate any slippage problem that might occur at low confining pressures. A rubber membrane was placed around each specimen to prevent moisture loss or air migration during testing.

Two days after compaction, a 2.8-in.-diameter specimen was tested under isotropic confining pressures of 2, 4, 6, 4, and 2 psi. At each pressure level, low-amplitude RC tests ($\gamma < 10^{-3}$ percent) were performed at 10-min intervals for 1 hour. Upon completing the low-amplitude RC tests, a series of TS tests was also performed at the unloading stages of 6, 4, and 2 psi. TS tests were performed mainly at a loading frequency of 0.5 Hz, with varying shearing strain amplitudes. To check the effect of frequency on stiffness, loading frequencies were changed at shearing strain amplitudes of about 10^{-3} and 10^{-2} percent. Loading frequencies of 0.05, 0.1, 0.5, 1, and 5 Hz were used. High-amplitude RC tests were then performed at each unloading pressure, changing the strain amplitude. Finally, low-amplitude RC tests were again performed to determine if any changes had occurred in the low-amplitude modulus from the TS and high-amplitude RC tests. Variation in the low-amplitude moduli measured before and after high-amplitude testing was less than 5 percent. Thus, it was determined that any changes in the soil skeleton caused by high-amplitude testing were negligible.

After completing the tests using the 2.8-in.-diameter sample, the same sample was trimmed to 1.5 in. in diameter and tested 6 days after compaction using the same procedures as used with the 2.8-in.-diameter sample. With the smaller-diameter sample, moduli at higher shearing strains, up to 10^{-1} percent, could be obtained, and moduli between torsional and M_R testing were more easily compared.

TEST RESULTS, DISCUSSION, AND COMPARISONS

Results from M_R Equipment

Results obtained from testing the four companion specimens using the M_R equipment were plotted and analyzed as suggested by SHRP Protocol P-46 (*6*). A typical result obtained in this pilot testing is shown in Figure 7, which shows plots of the results of Sample 2 tested at 2 and 6 days after compaction. Sample 2 exhibited the typical tendency of soils, which is that the modulus generally decreases with increasing deviator stresses and increasing axial strain amplitudes.

A summary of the M_R testing results obtained from the four companion specimens in terms of M_R coefficients, as expressed in Equation 5, is presented in Table 2 for the tests at 2 and 6 days.

The influence of age hardening on the two parameters, K_1 and K_2, is also presented in Table 2. As seen in the table, the age of the sample significantly affects these results. This phenomenon is not addressed in current M_R testing procedures—although it should be, at least for cohesive soils, if consistent and repeatable results are desired.

Comparison Between RC and TS Results

One advantage of the RC and TS device is that both tests can be performed on the same soil specimen over a large range

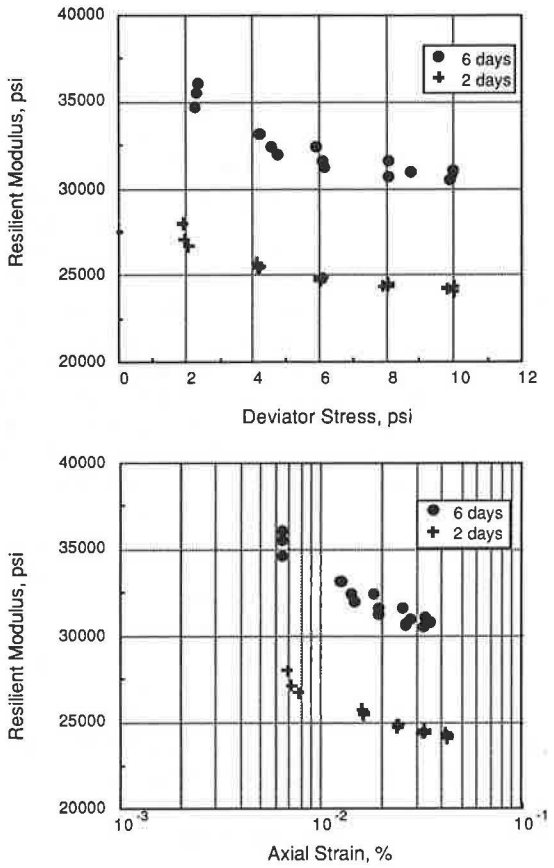


FIGURE 7 Influence on M_R of deviator stress and axial strain for Sample 2 tested 2 and 6 days after compaction.

of shearing strain amplitudes (10^{-4} to 10^{-1} percent). Values of shear moduli obtained from both tests were converted to the equivalent Young's modulus, E, using Equation 8. Typical results of a compacted clay specimen showing the variation of Young's modulus with equivalent axial strain are presented in Figure 8. At strain amplitudes below about 10^{-2} percent, moduli from RC and TS tests are independent of strain amplitude, and moduli from TS tests fall somewhat below the corresponding RC values at the same strain amplitude. This difference can be explained by the difference in loading frequencies between the two modes of testing, as discussed in the next subsection. At strains above 10^{-2} percent, it is shown that modulus decreases as strain amplitude increases in both tests.

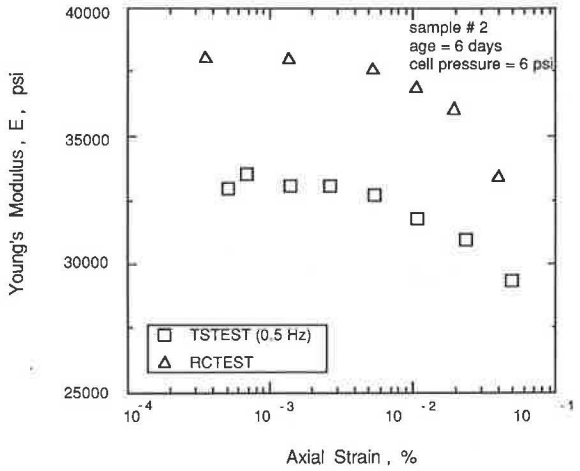


FIGURE 8 Variation in Young's modulus with axial strain for cohesive soil as determined by RC and TS tests.

Effect of Loading Frequencies

The effect of frequency can be determined by using a combination of RC and TS tests. Moduli determined by the RC test are based on first-mode resonant frequency, which depends on the stiffness of the specimen and on the mass moment of inertia of the drive plate. Loading frequency in the TS test can be varied by changing the input frequency.

Moduli determined by the RC and TS tests at various loading frequencies are plotted at axial strain amplitudes of 0.00067 and 0.02 percent in Figure 9. Modulus increases linearly as a function of the logarithm of loading frequency.

To quantify the influence of loading frequency on Young's modulus, E was normalized by the value of Young's modulus at a loading frequency of 0.5 Hz (at which high-amplitude TS tests were performed). Typical results are shown in Figure 10. Performing a least-square curve fitting on these data, the fitting curve yielded the effect of loading frequency on modulus, which was 5.78 percent per log cycle of loading frequency. Effects of loading frequencies on Samples 1, 2, 3, and 4 were 7.12, 5.78, 6.03, and 6.75 percent per log cycle of loading frequency, respectively.

Normalized Modulus

A more convenient way of presenting the change in modulus with strain amplitude is with a plot of normalized Young's

TABLE 2 RESILIENT MODULUS COEFFICIENTS FOR FOUR COMPANION SPECIMENS

SAMPLE	MOISTURE CONTENT (%)	RESULTS AT 2 DAYS AFTER COMPACTION		RESULTS AT 6 DAYS AFTER COMPACTION		AGING EFFECT ON MR COEFFICIENTS	
		K1	K2	K1	K2	K1 (6 days) / K1 (2 days)	K2 (6 days) / K2 (2 days)
1	17.30	46925	- 0.080	54677	- 0.038	1.165	0.467
2	19.20	28523	- 0.075	37949	- 0.095	1.333	1.267
3	25.80	29675	- 0.029	35768	- 0.045	1.205	1.551
4	39.10	6058	- 0.337	10273	- 0.261	1.696	0.774

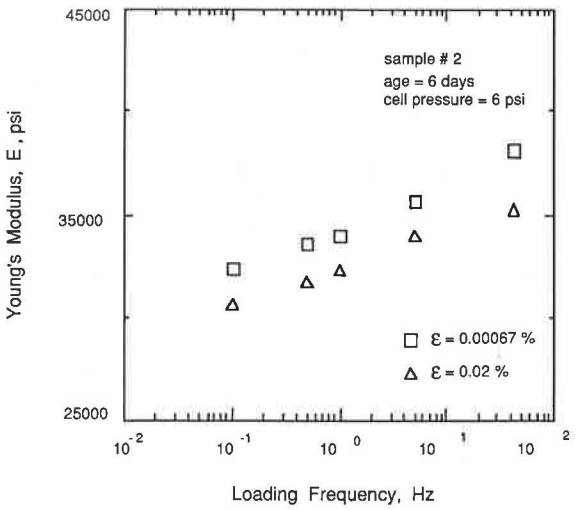


FIGURE 9 Variation in Young's modulus with frequency for cohesive soil as determined by RC and TS tests.

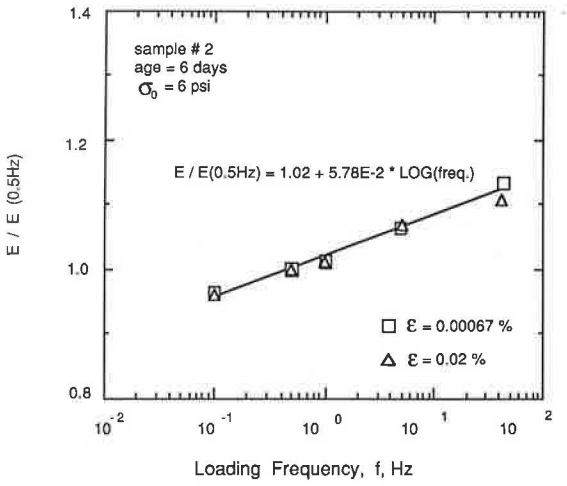


FIGURE 10 Normalization of Young's modulus with frequency for cohesive soil as determined by RC and TS tests.

modulus, E/E_{max}, versus the logarithm of axial strain. The high-amplitude data obtained by RC and TS tests at a confining pressure of 6 psi for four different samples are plotted with variations in the axial strain in Figure 11. Although the general tendency of samples with different moisture contents is almost the same (except Sample 1, which shows more brittle behavior), the samples have very different values of modulus. With this normalized curve and small-strain modulus values from field seismic tests, it is easy to predict the strain-dependent behavior of any subgrade material using the approach applied in geotechnical earthquake engineering.

Comparisons Between M_R and Torsional Testing Results

To determine the capability of the testing equipment, results obtained from the M_R and the RC and TS tests were compared. As previously mentioned in the section on M_R testing

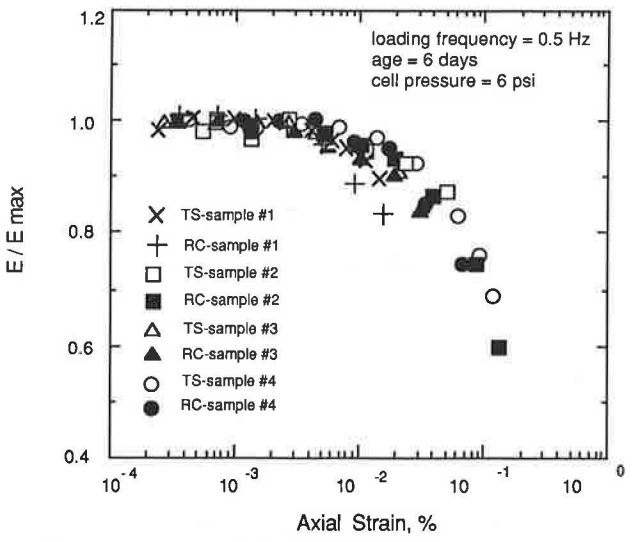


FIGURE 11 Variation in normalized Young's modulus with axial strain as determined by RC and TS tests.

with synthetic samples, good agreement was found between the moduli of the synthetic samples determined by both types of equipment. The synthetic specimens were easy to handle and test because their properties remained constant with time, were independent of strain amplitude and confining pressure, and could be repeatedly tested. In contrast, the comparison of the testing results for actual subgrade soils was more complicated.

In making that comparison, moduli obtained under RC and TS tests were converted to equivalent resilient moduli using Equations 8 and 9. In addition, the moduli were finally adjusted to an excitation frequency value of 10 Hz, which is the loading frequency of the M_R measurement.

Typical comparisons are shown in Figures 12 and 13. Figure 12 shows the variation in M_R with axial strain amplitude as determined by the three different testing methods for Sample 2. Overlapping the moduli obtained from M_R tests with the values from RC and TS tests provided sufficient evidence that a reliable system for measuring the elastic properties of subgrade materials had been developed. Figure 13, for Sample 4, shows an additionally encouraging overlap of moduli tested at 6 days and with a confining pressure of 6 psi.

CONCLUSIONS

M_R test equipment was evaluated using synthetic specimens and by performing pilot tests with cohesive soil. Torsional RC and TS tests were also used, with the moduli obtained from these tests comparing well with the values for the M_R test. The following conclusions can be drawn:

1. From the calibration of M_R equipment with synthetic specimens, it was found that strong contact between the specimen and top and bottom caps is important. For stiff materials, this factor is particularly crucial and can lead to erroneous estimates of modulus. The use of hydrostone paste provides a uniform contact between the specimen and end caps and eliminates additional movement at these points.

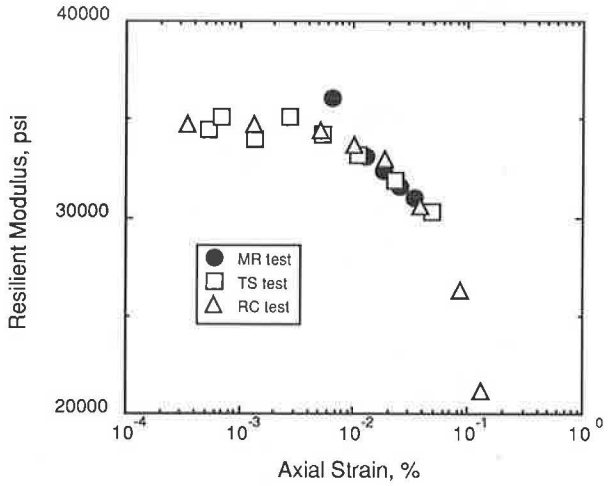


FIGURE 12 Comparison of M_R versus log (axial strain) and E versus log (axial strain) for cohesive Sample 2 tested at a confining pressure of 6 psi at 6 days after compaction.

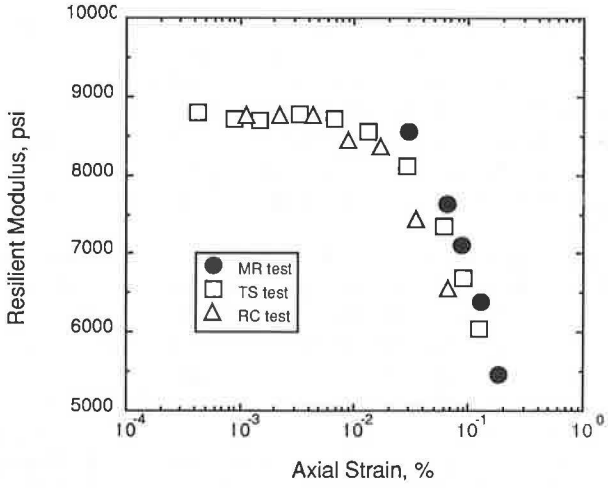


FIGURE 13 Comparison of M_R versus log (axial strain) and E versus log (axial strain) for cohesive Sample 4 tested at a confining pressure of 6 psi at 6 days after compaction.

2. Once the synthetic specimens were grouted in both the M_R and torsional devices, good agreement between moduli obtained from both tests was found.

3. In M_R testing the entire system requires calibration, not merely the individual transducers. To do this, testing synthetic samples of known properties can be used for the detection of equipment compliances, as well as for the assessment of a reliable system.

4. The pilot study with cohesive soil indicated that aging is an important factor in M_R measurements when no loss in water content is affected. Unfortunately, this factor is not taken into account in current M_R testing procedures.

5. Good comparisons were found between the moduli of cohesive soil measured with M_R and TS equipment. Two important points in the comparisons were that moduli had to be compared at both the same frequency and the same strain amplitude.

6. The RC and TS apparatus provides a powerful approach to the characterization of pavement materials over a wide range of strain amplitudes (10^{-4} to 10^{-1} percent) and can be considered an alternative technique to M_R testing.

ACKNOWLEDGMENTS

This work was supported by the Texas State Department of Highways and Public Transportation. The authors wish to express their appreciation for this support. In addition, the authors would like to thank Germán Claros for his assistance.

REFERENCES

1. *AASHTO Guide for Design of Pavement Structures, 1986*. Joint Task Force on Pavements, Highway Subcommittee on Design, AASHTO, Washington, D.C., 1986.
2. T. Vinson. Fundamentals of Resilient Modulus Testing. Presented at Workshop on Resilient Modulus Testing, Oregon State University, Corvallis, March 1989.
3. J. L. Brown. *Resilient Modulus and Pavement Design Practice*. Texas State Department of Highways and Public Transportation, Austin, 1989.
4. R. K. M. Ho. Repeated Load Tests on Untreated Soils, A Florida Experience. Presented at Workshop on Resilient Modulus Testing, Oregon State University, Corvallis, March 1989.
5. O.-K. Kim. Resilient Modulus Test in California DOT—Yesterday, Today and Tomorrow. Presented at Workshop on Resilient Modulus Testing, Oregon State University, Corvallis, March 1989.
6. *Resilient Modulus of Unbound Granular Base, Subbase Materials and Subgrade Soils*. SHRP Protocol P-46, UG07, SS07. Strategic Highway Research Program, 1989.
7. K. Stokoe, D. Kim, and R. Andrus. Development of Synthetic Specimens for Calibration and Evaluation of M_R Equipment. Presented at 69th Annual Meeting of the Transportation Research Board, Washington, D.C., Jan. 1990.
8. G. Claros, W. R. Hudson, and K. H. Stokoe. Modification to the Resilient Modulus Testing Procedure and the Use of Synthetic Samples for Equipment Calibration. Presented at the 69th Annual Meeting of the Transportation Research Board, Washington, D.C., Jan. 1990.
9. *Manual of Testing Procedures*, Vol. 1. Texas Highway Department, Jan. 1983.

Publication of this paper sponsored by Committee on Flexible Pavement Design.

Evaluation of Two-Layer Pavements Using Dimensional Analysis

LUTFI RAAD AND LYLA K. MARHAMO

Chart solutions for critical response parameters in two-layer pavements are developed using dimensional analysis. Multilayer elastic theory is applied, and simple dimensionless variables for critical response parameters are related to pavement geometry, material properties, and loading conditions. The solutions presented provide a comprehensive assessment of the physical behavior of two-layer systems under a wide variety of input variables. The proposed solutions are applied in the design and analysis of pavements using both functional and structural failure considerations.

Many transportation support systems could be modeled as two-layer structures. These structures could include, for example, a stabilized layer over subgrade or an existing pavement overlaid by a new surface layer. In general, pavements exhibit a wide range of material characteristics, such as complex particulate structure, stress-dependency, viscous and damping behavior, nonhomogeneity, and anisotropy. Although improved material models that simulate stress-dependent resilient behavior have been proposed and incorporate advanced numerical algorithms, such as the finite element method (*1,2*), the linear elastic theory is still considered by many to provide an acceptable approximation of real conditions. This theory, for example, is incorporated in a number of widely used design procedures, including those by Shell International Petroleum Company (*3*) and the Asphalt Institute (*4*). Moreover, a number of pavement evaluation methods that include nondestructive testing techniques use elastic theory to backcalculate average layer moduli that best fit surface deflection basins under applied loads (*5–7*). For pavement performance predictions, a number of limiting criteria have been expressed in terms of critical response parameters and number of load repetitions. These criteria are often determined from backcalculated stresses, strains, and deflections of existing field pavements using elastic theory (*8,9*). If such criteria are to be used in assessing pavement performance, the corresponding critical response parameters should be determined using similar analytical procedures, which will yield more meaningful and consistent predictions.

Dimensional analysis has been recognized by many investigators as a powerful tool for representing pavement analysis results (*10–13*). This method involves grouping analytical data into dimensionless parameters to provide an improved engineering approach for data presentation and interpretation. Chart solutions for critical response parameters in two-layer pavements are developed in the following paragraphs using dimensional analysis. Multilayer elastic theory is used, and simple dimensionless variables of critical pavement response parameters are related to pavement geometry, material properties, and loading conditions. The developed chart solutions, although complementary to other solutions and computer codes for predicting the response of pavement structures, have the added advantage of providing a simple and quick tool for the direct determination of critical response parameters in two-layer pavements. Moreover, they represent a comprehensive assessment of the physical behavior of two-layer pavements under a wide variety of input variables. The proposed solutions are applied here in the design and analysis of pavements using both functional and structural failure considerations.

L. Raad, Institute of Northern Engineering, University of Alaska, Fairbanks, Alaska 99775. L. K. Marhamo, Department of Civil Engineering, Massachusetts Institute of Technology, Cambridge, Mass. 02139.

ANALYSIS

Mechanistic methods of pavement design and evaluation require the determination of such critical response parameters as pavement stresses, strains, and deflections. In the two-layer systems analyzed, the response parameters include the following:

1. Tensile stresses and strains on the underside of the stabilized layer,
2. Vertical stresses and strains on top of the subgrade layer,
3. Surface deflections at the center of the applied load, and
4. Maximum shear stress in the subgrade.

These parameters are chosen on the basis of a number of pavement performance models (*3,8,9*). The two-layer system considered is shown in Figure 1.

Materials are assumed to be linear elastic, isotropic, and homogeneous. The surface layer is infinitely wide and has a uniform thickness H, a modulus of elasticity E_1, and Poisson's ratio ν_1. The subgrade layer is an elastic halfspace with elastic modulus E_2 and Poisson's ratio ν_2. The two-layer system is subjected to a uniform circular load having a radius R and intensity q. A summary of the cases analyzed is presented in Table 1. The following response parameters were determined using ELSYM5, a computer program for the analysis of elastic layers (*14*):

σ_x, ε_x = tensile stress and strain, respectively, on the underside of the stabilized layer;
σ_z, ε_z = vertical stress and strain, respectively, on top of the subgrade;

U = surface deflection at the center of the applied load; and

τ = maximum shear stress in the subgrade defined as $(\sigma_1 - \sigma_3)/2$, in which σ_1 and σ_3 are major and minor principal stresses, respectively.

These parameters were computed along the centerline of the applied surface load.

DIMENSIONLESS GROUPING OF RESPONSE PARAMETERS

Dimensional analysis was conducted to provide simple engineering solutions for pavement response parameters. These independent variables are grouped into (a) single-parameter correlations and (b) double-parameter correlations.

For single-parameter correlations, the required response parameters (i.e., stress, strain, and deflection) are expressed as follows:

$$X_i = f_i(E_1/E_2, H/R) \qquad i = 1 \text{ to } 6 \tag{1}$$

where X_i is a dimensionless parameter treated as an independent variable that could have the following forms:

$X_1 = \sigma_x/q$;

$X_2 = \sigma_z/q$;

$X_3 = \tau/q$;

$X_4 = E_2\varepsilon_x/q$;

$X_5 = E_2\varepsilon_z/q$; and

$X_6 = E_2U/Rq$.

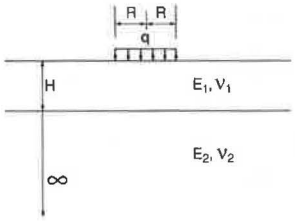


FIGURE 1 Representation of two-layer system.

Results of the analysis are shown in single-parameter charts (see Figures 2–7). These charts could be used to determine any of the response parameters defined in Equation 1. They also illustrate the trend of variation of these parameters in the practical ranges of E_1/E_2 and H/R.

Dimensional analysis was also conducted to develop double-parameter charts that would provide a more direct approach in the design and evaluation of two-layer pavements, particularly in relation to failure in the stabilized base or the subgrade. The dimensionless groupings are expressed as follows:

$$Y_i = g_i(Z_i, E_1/E_2, H/R) \qquad i = 1 \text{ to } 6$$

or

$$Z_i = W_i(Y_i, E_1/E_2, H/R) \qquad i = 1 \text{ to } 6 \tag{2}$$

where

$Y_1 = q/\sigma_z$;
$Y_2 = q/\sigma_z$;
$Y_3 = q/\tau$;
$Y_4 = q/\tau$;
$Y_5 = q/E_2\varepsilon_z$;
$Y_6 = q/E_2\varepsilon_z$;
$Z_1 = \sigma_x/\sigma_z$;
$Z_2 = E_2\varepsilon_x/\sigma_z$;
$Z_3 = \sigma_x/\tau$;
$Z_4 = E_2\varepsilon_x/\tau$;
$Z_5 = \sigma_x/E_2\varepsilon_z$; and
$Z_6 = \varepsilon_x/\varepsilon_z$.

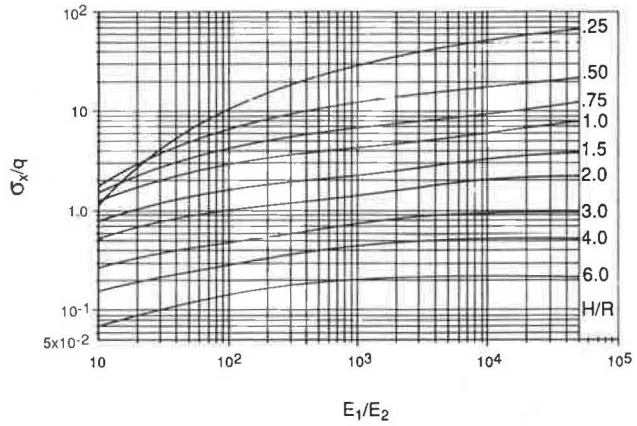


FIGURE 2 Solution chart for σ_x—two-layer theory.

TABLE 1 SUMMARY OF CASES ANALYZED

H/R	E_1/E_2	ν_1	ν_2
0.25, 0.50, 0.75, 1.0, 1.5, 2.0, 3.0, 4.0, 6.0	10,20,30,40,50,60,70,100,150, 200,300,400,500,600,700,1000, 1500, 2000,3000,4000,5000, 6000,7000,10000,15000 20000,30000,40000,5000	0.30	0.45

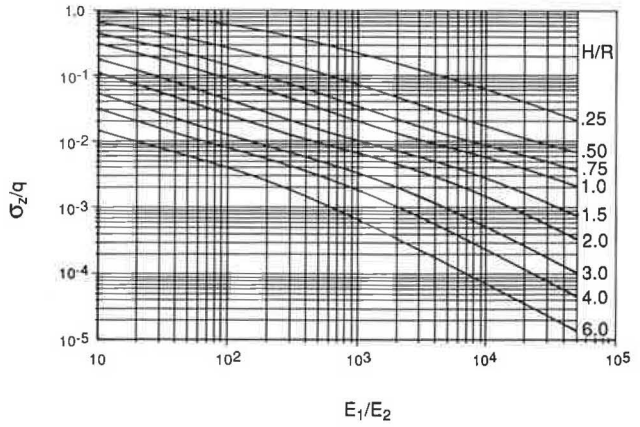


FIGURE 3 Solution chart for σ_z—two-layer theory.

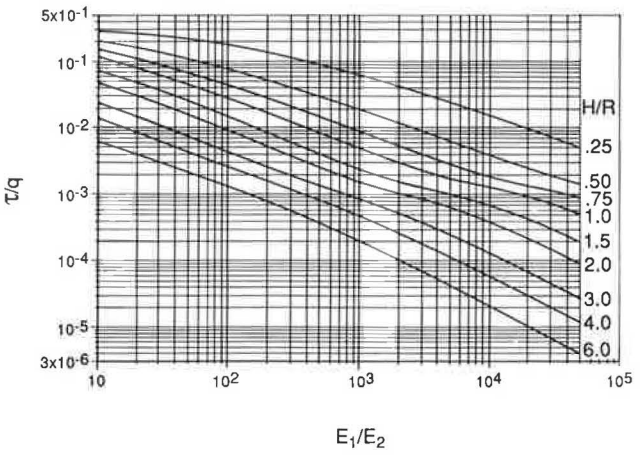


FIGURE 4 Solution chart for τ—two-layer theory.

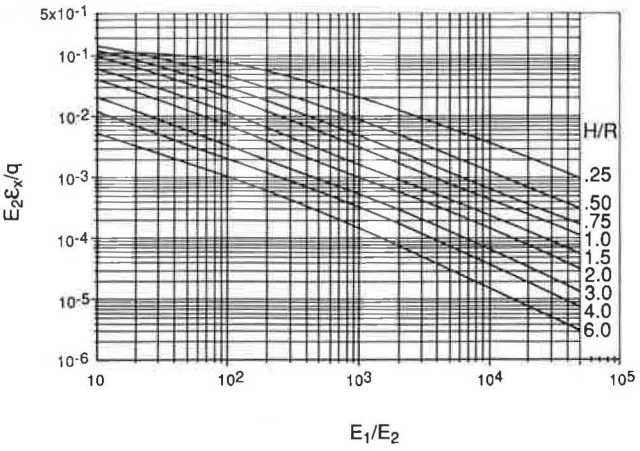


FIGURE 5 Solution chart for ε_x—two-layer theory.

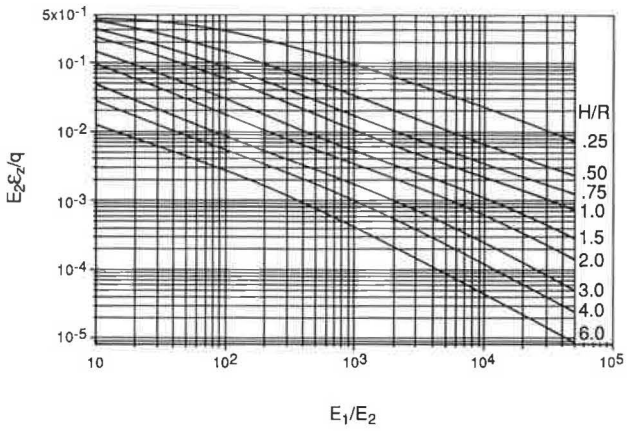


FIGURE 6 Solution chart for ε_z—two-layer theory.

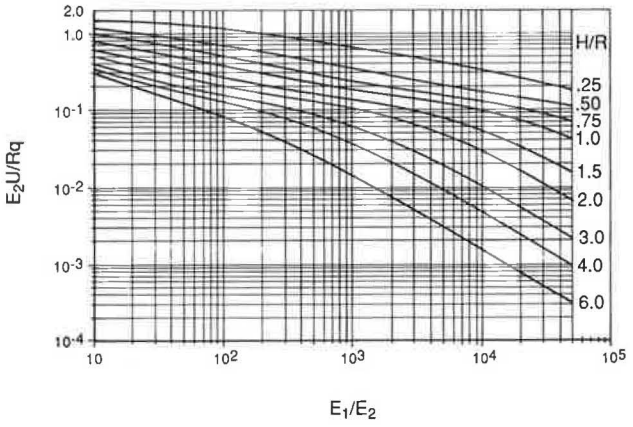


FIGURE 7 Solution chart for u—two-layer theory.

These correlations are presented in double-parameter charts, permitting the use of different combinations of pavement response variables in mechanistic design procedures (see Figures 8–13). In many cases, practical pavement design considerations require that fatigue failure of the stabilized base, rather than permanent deformation in the subgrade, be the governing performance criterion. This requirement necessitates the appropriate choice of pavement geometry (H/R) and material properties (E_1/E_2). In this regard, the ratio of response parameters defined by a given performance criteria (Z_i) should be less than the corresponding ratio resulting from the given loading condition.

APPLICATIONS

Results of dimensional analysis are used to assess the behavior of two-layer pavements under applied loads. Specifically, application of the proposed chart solutions in mechanistic pavement design and evaluation is illustrated using simple example problems. Furthermore, structural failure considerations are addressed, and improved solutions for predicting the structural capacity of two-layer systems are presented.

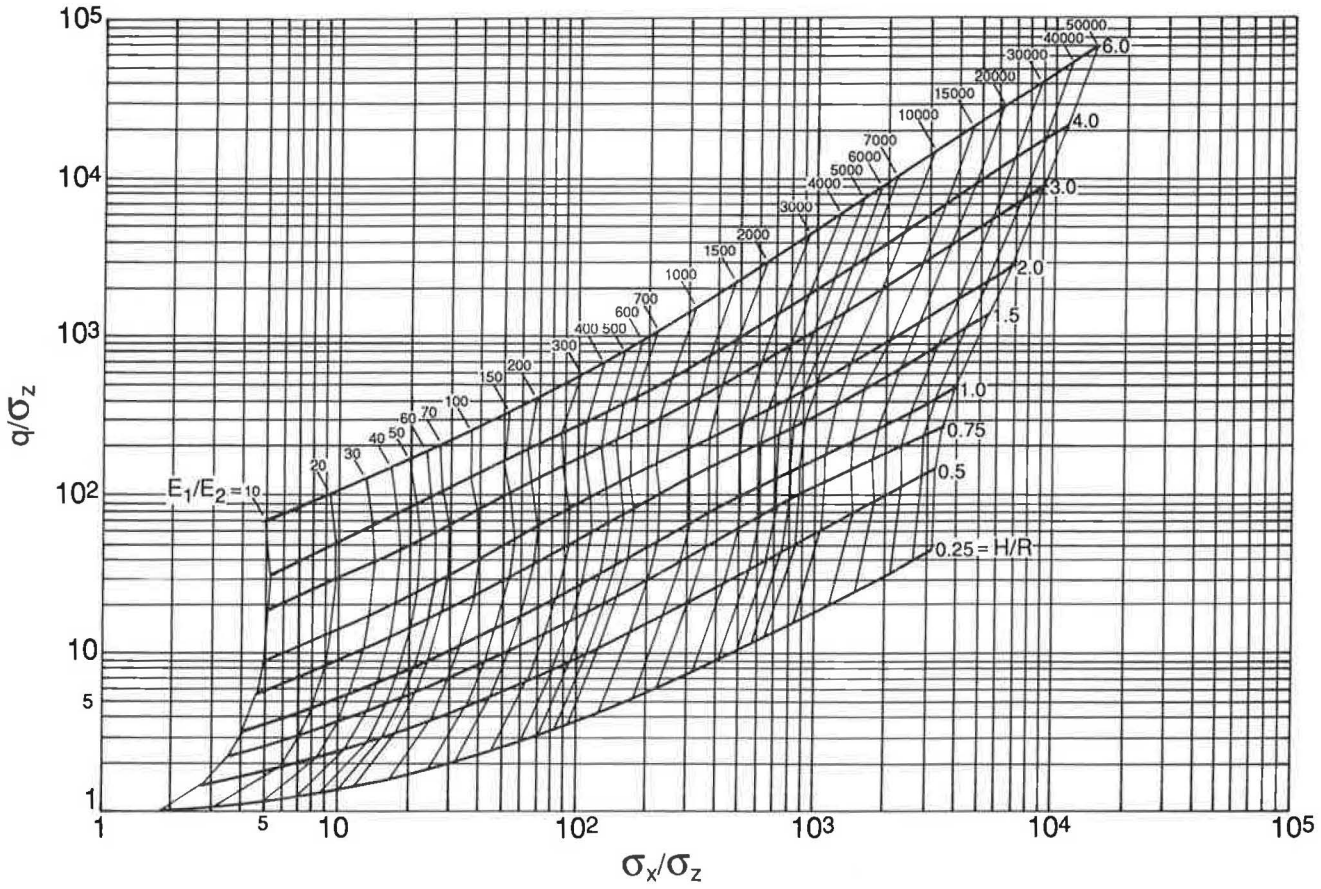


FIGURE 8 Solution chart for response parameters σ_x, σ_z—two-layer theory.

Mechanistic Pavement Design and Analysis

Example 1

Consider a pavement structure consisting of a stabilized base 15 in. thick having $E_1 = 200{,}000$ psi overlying a clay subgrade having $E_2 = 5{,}000$ psi. The pavement is subjected to a uniform tire pressure of 100 psi with a radius equal to 5 in. The tensile stress (σ_x) on the underside of the stabilized base and the vertical strain (ε_z) on top of the subgrade can be determined using Figure 12. In this case, $H/R = 3$ and $E_1/E_2 = 40$; therefore, $q/E_2\varepsilon_z = 58$ and $\sigma_x/E_2\varepsilon_z = 23$.

The corresponding values of ε_z and σ_x are

$$\varepsilon_z = \frac{100}{58 \times 5{,}000} = 3.45 \times 10^{-4}$$

$$\sigma_x = 23 \times 5{,}000 \times 3.45 \times 10^{-4} = 39.6 \text{ psi}$$

Example 2

If, in Example 1, it is required to determine the thickness of the stabilized base given the following limiting criteria: fatigue failure of stabilized base, $\sigma_x = 60$ psi, and permanent deformation failure of subgrade, $\varepsilon_z = 4 \times 10^{-4}$, then

$$q/E_2\varepsilon_z = \frac{100}{5{,}000 \times 4 \times 10^{-4}} = 50$$

From Figure 12, $E_1/E_2 = 40$, $H/R = 2.8$, and $\sigma_x/E_2\varepsilon_z = 22.4$; then $H = 2.8 \times 5 = 14$ in. and $\sigma_x = 5{,}000 \times 4 \times 10^{-4} \times 22.4 = 44.7$ psi.

The ratio $\sigma_x/E_2\varepsilon_z$ determined according to the given limiting criteria is

$$\sigma_x/E_2\varepsilon_z = \frac{60}{5{,}000 \times 4 \times 10^{-4}} = 30$$

For $E_1/E_2 = 40$ and H/R values ranging from 0.25 to 6, permanent deformation failure in the subgrade governs pavement performance provided $\sigma_x/E_2\varepsilon_z$, determined for a given set of limiting criteria, is greater than 23. In this example, $\sigma_x/E_2\varepsilon_z$ equals 30; hence, subgrade rutting precedes fatigue failure in the stabilized base. In order for fatigue to be the predominant mode of failure, pavement materials should conform to limiting criteria yielding values of $\sigma_x/E_2\varepsilon_z$ less than 14, as estimated from Figure 12 for $E_1/E_2 = 40$ and $H/R = 0.25$.

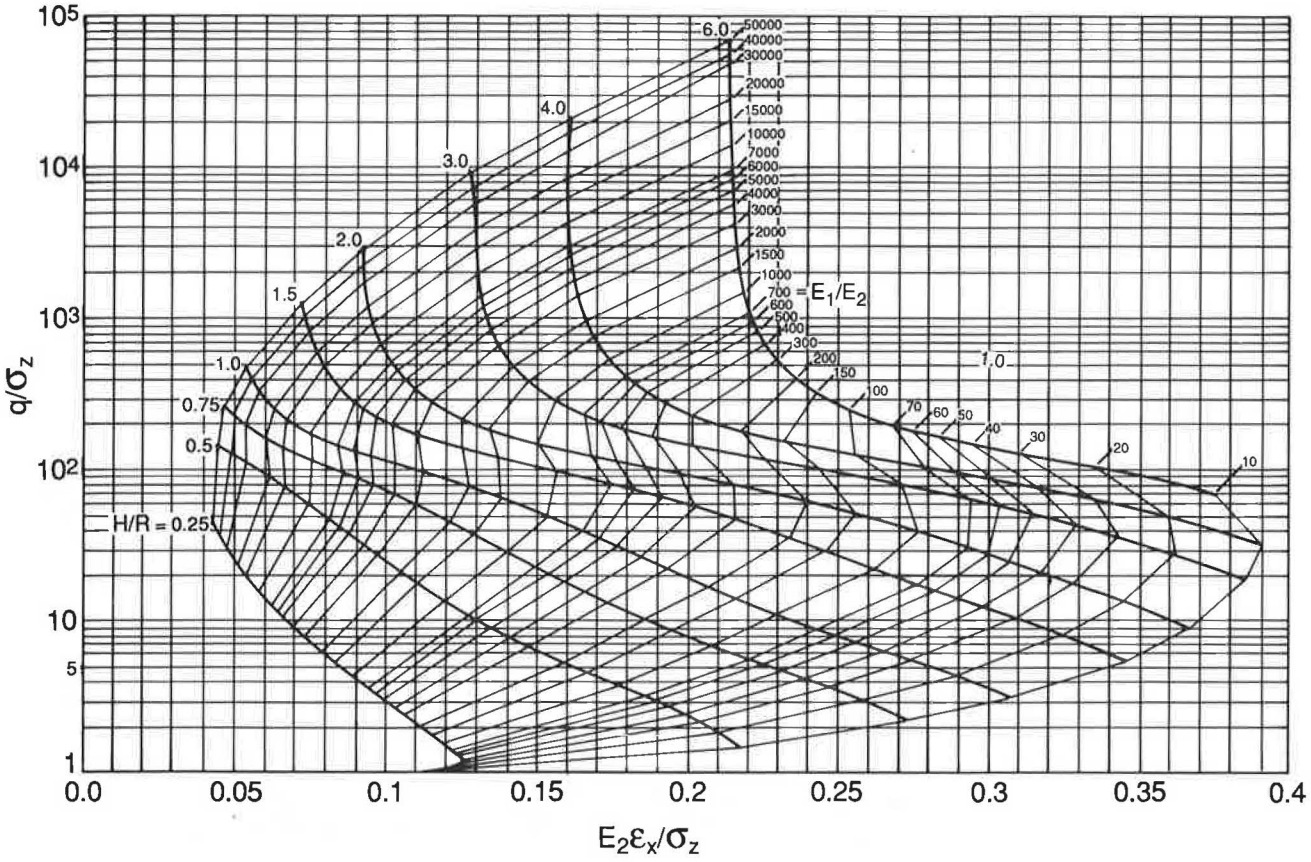


FIGURE 9 Solution chart for response parameters ε_x, σ_z—two-layer theory.

Structural Capacity Considerations

The overriding consideration in many pavement design problems is the serviceability and performance of the pavement structure under long-term repeated loading conditions. Mechanistic design procedures aim at minimizing fatigue and permanent deformation in the pavement system. In many cases, the structural adequacy of the pavement to support static loads or slowly moving loads needs to be addressed. Of particular significance in this case is the bearing capacity of the pavement structure. The bearing capacity of two-layer pavements consisting of a stabilized base over subgrade have been investigated by a number of researchers (*15–17*). The most comprehensive and complete work to date has been presented by Meyerhof (*15*), who used rigid-plastic analysis to determine the collapse load of concrete pavements. Meyerhof's work is applied here, together with results of dimensional analysis, to develop improved procedures of bearing capacity analysis.

The analysis assumes the following failure conditions:

1. Flexure failure initiation in the stabilized base,
2. Bearing capacity failure of the fine-grained subgrade, and
3. Ultimate collapse of the stabilized base.

Linear elastic analysis is used to address the first and second possible failure conditions. Flexure failure in the stabilized base occurs when the tensile stress (σ_x) on the underside of the base becomes equal to the flexure strength (T_f). Subgrade failure occurs when the vertical stress (σ_z) becomes equal to $6C$, where C is subgrade cohesion. This is consistent with bearing capacity estimates for saturated clays.

Flexure failure in the stabilized base and bearing capacity failure of the subgrade can be determined using the results of dimensional analysis presented previously. For example, chart solutions shown in Figure 8 can be used to determine the maximum and minimum ratios of σ_x/σ_z for a given E_1/E_2 and H/R ranging from 0.25 to 6. The maximum and minimum ratios of σ_x/σ_z are used to define the corresponding maximum and minimum values for the ratio of flexural strength of the stabilized base (T_f) to the cohesion of the subgrade (C) (i.e., $\sigma_x = T_f$, $\sigma_z = 6C$). This ratio is denoted as $(T_f/C)_l$, and its variation with E_1/E_2 is shown in Figure 14. For a given E_1/E_2, bearing capacity failure will initiate in the subgrade if the ratio T_f/C of the flexural strength of the stabilized layer to subgrade cohesion is greater than the maximum value of $(T_f/C)_l$. On the other hand, flexural failure initiation will occur if T_f/C is smaller than the minimum value of $(T_f/C)_l$. The ultimate surface pressure (q_u), associated either with bearing capacity failure of subgrade or with flexural failure of the base, is determined using the data in Figure 8. The variation of q_u with E_1/E_2 is shown in Figures 15 and 16. Estimates could be made for both interior and edge loading of base failure (Figure 15) and subgrade failure (Figure 16). Stresses

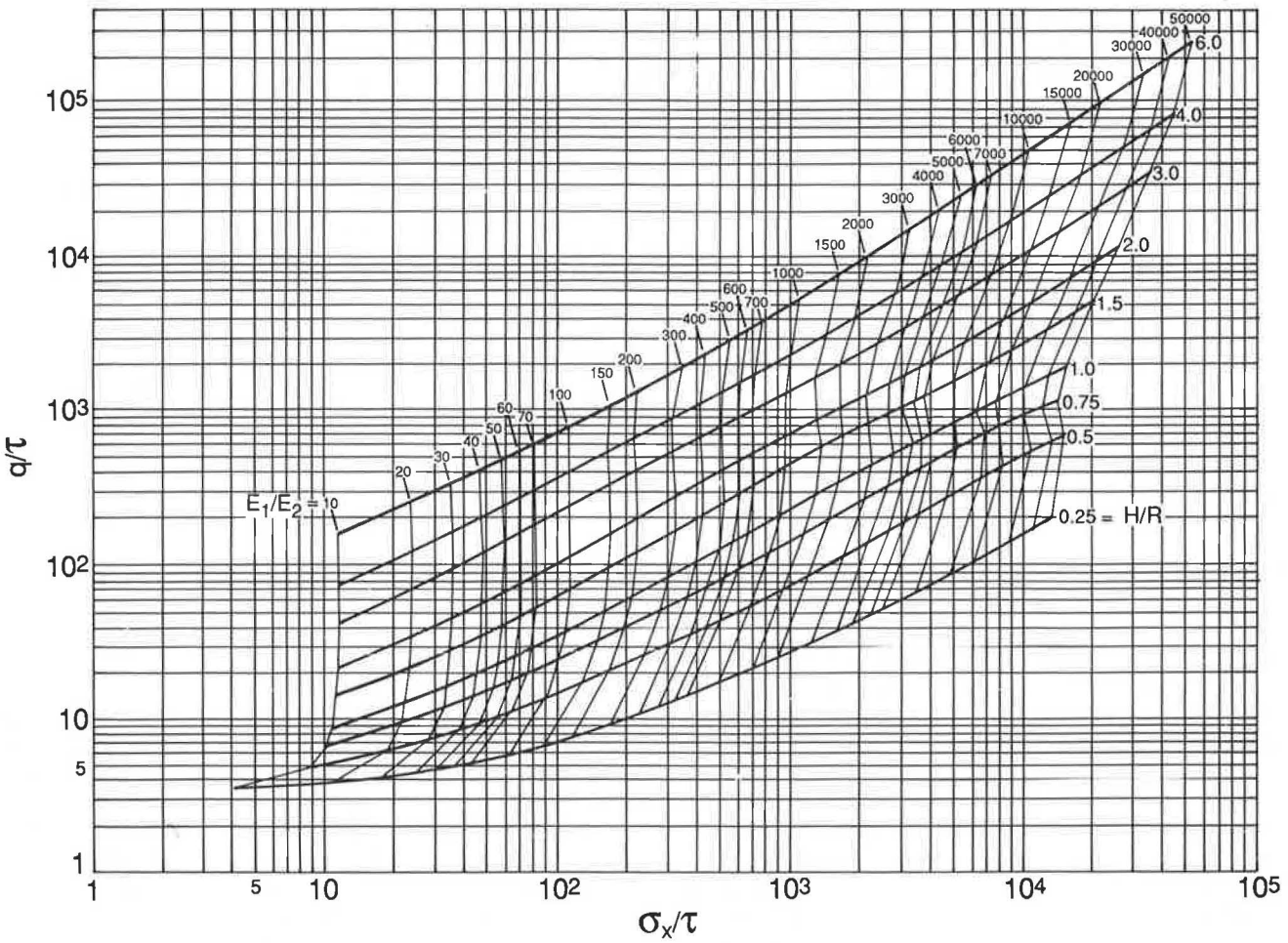


FIGURE 10 Solution chart for response parameters σ_x, τ—two-layer theory.

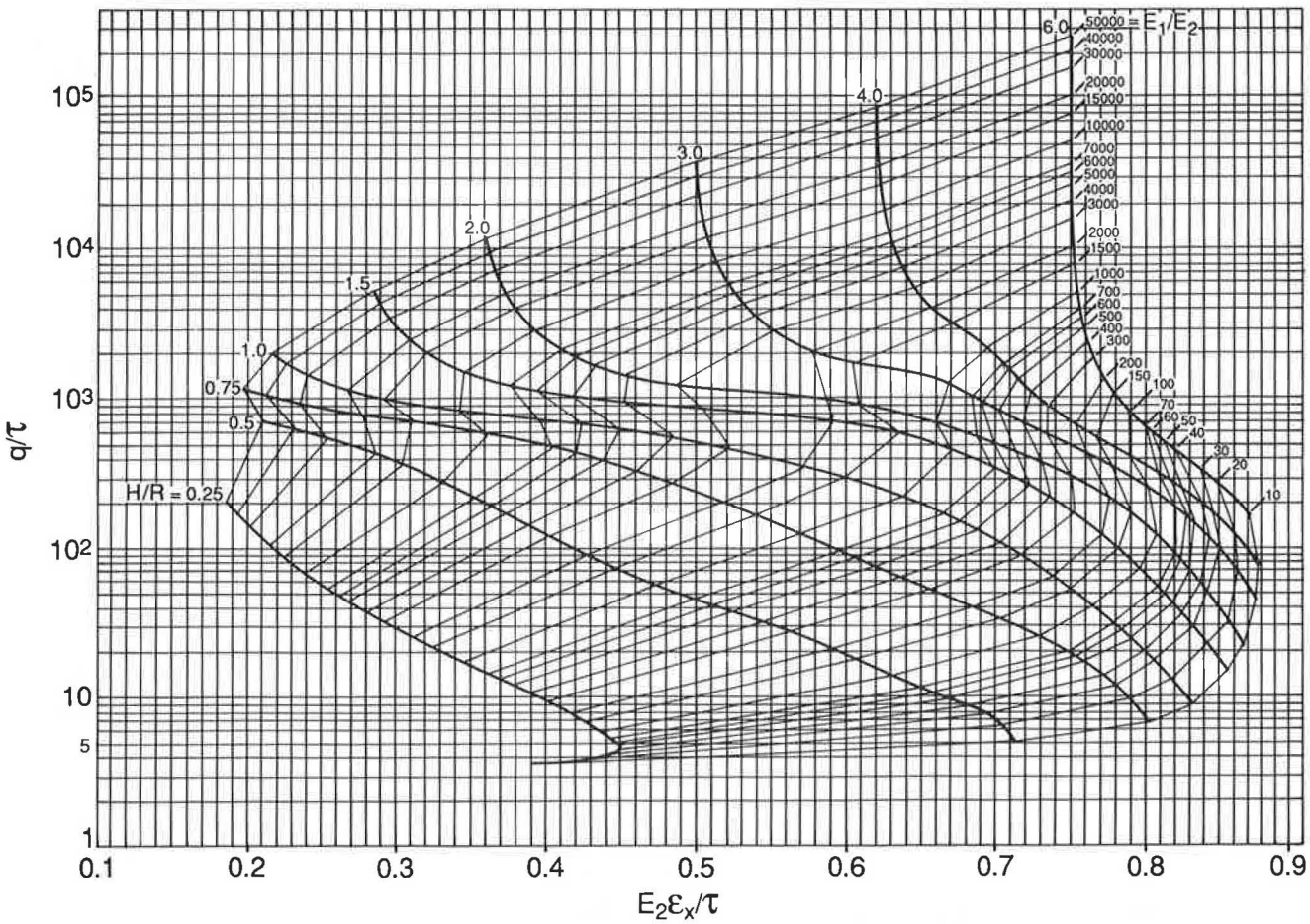


FIGURE 11 Solution chart for response parameters ε_x, τ—two-layer theory.

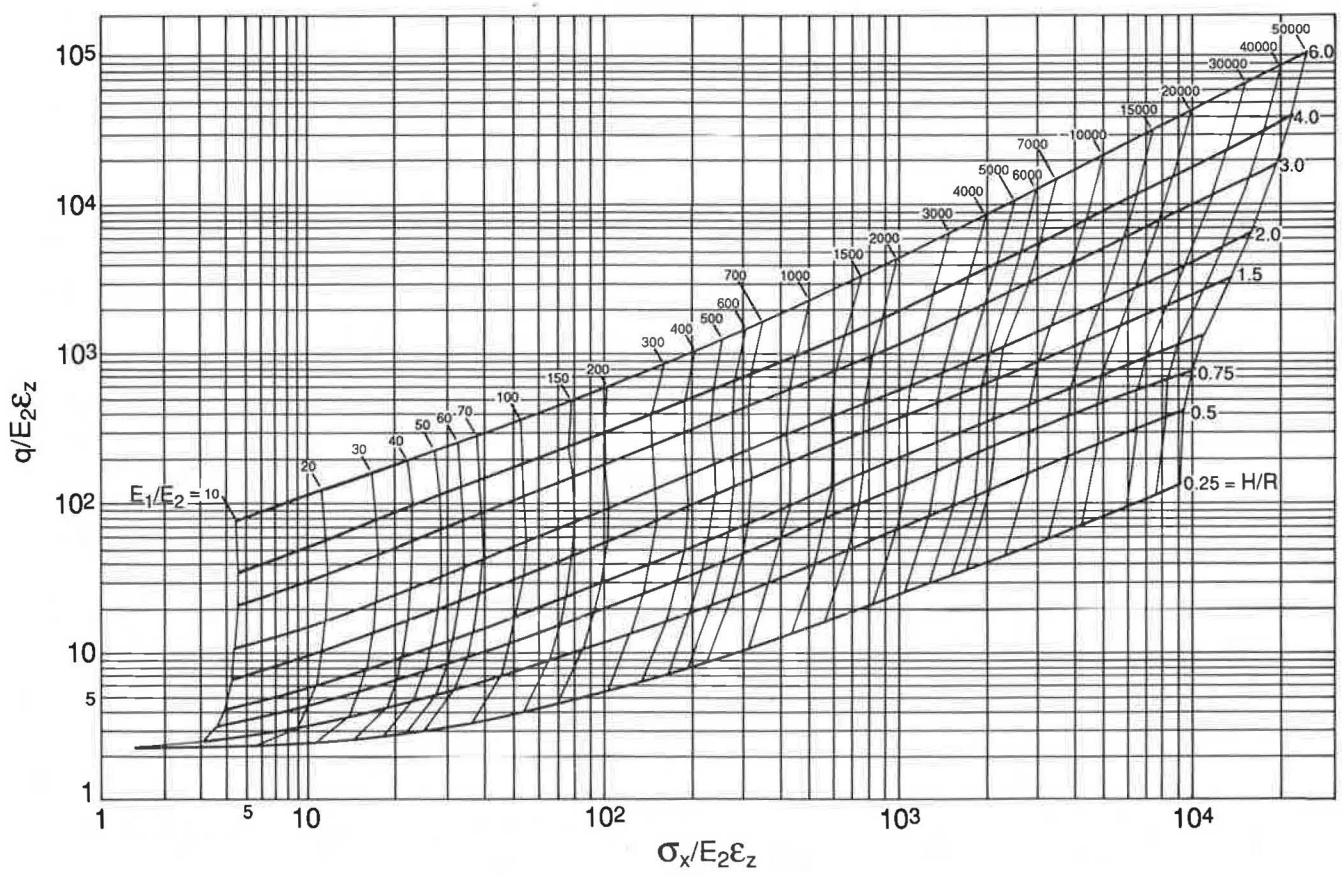


FIGURE 12 Solution chart for response parameters σ_x, ε_z—two-layer theory.

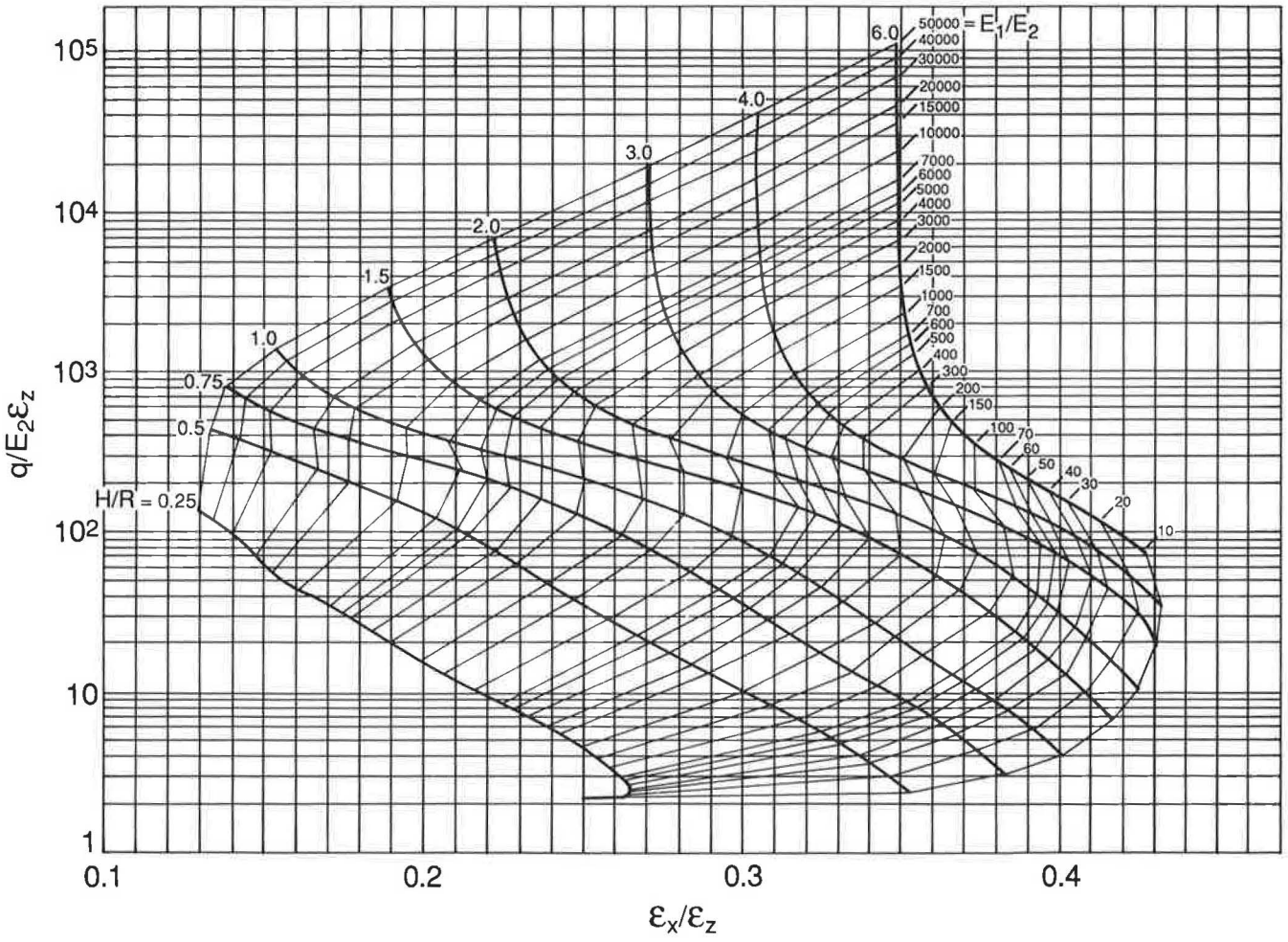


FIGURE 13 Solution chart for response parameters ε_x, ε_z—two-layer theory.

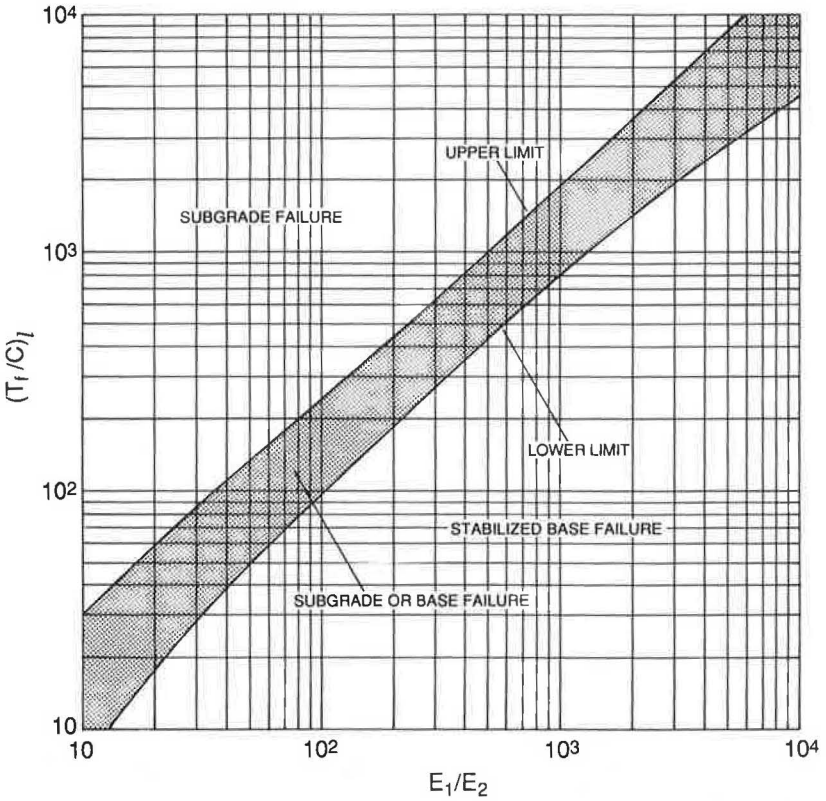


FIGURE 14 Limiting values for T_f/C associated with subgrade or base failure.

associated with edge loading are assumed to be 50 percent greater than those obtained for interior loading, as suggested by Mitchell et al. (*8*).

The ultimate collapse of the stabilized base follows flexural crack initiation on its underside or subgrade bearing capacity failure. The ultimate collapse load intensity (q_{uc}) is estimated using Meyerhof's approach (*15*). Meyerhof's equations could be rearranged and expressed as follows:

For interior loading,

$$\frac{q_{uc}}{T_f} = \frac{2/3}{(1 - R/3L)}\left(\frac{H}{R}\right)^2 \quad \left(\text{for } \frac{R}{L} > 0.2\right) \tag{3}$$

For edge loading,

$$\frac{q_{uc}}{T_f} = \left(\frac{\pi + 4}{6\pi}\right)\frac{1}{(1 - 2R/3L)}\left(\frac{H}{R}\right)^2 \left(\text{for } \frac{R}{L} > 0.2\right) \tag{4}$$

where L, the stiffness radius, is given by

$$L = \left[\frac{E_1(1 - \nu_2^2)H^3}{E_2(1 - \nu_1^2)^6}\right]^{1/3} \tag{5}$$

If failure initiation occurs in the stabilized base, the ultimate collapse load could be determined from Equation 3 or 4. In this case, it is assumed that, as cracking initiates on the underside of the base, both E_1 and E_2 will reduce and the ratio E_1/E_2 will remain essentially unchanged. Consequently, L will not change and q_{uc} will approach the same value predicted in Equations 3 and 4.

If, on the other hand, failure occurs first in the subgrade, then the subgrade modulus will decrease and approach zero and the corresponding value of R/L will also approach zero. For these conditions, a rigid-plastic behavior of the stabilized base will yield the following:

For interior loading,

$$\frac{q_{uc}}{T_f} = \frac{1}{3}\left(\frac{H}{R}\right)^2 \tag{6}$$

For edge loading,

$$\frac{q_{uc}}{T_f} = \left(\frac{\pi + 4}{12\pi}\right)\left(\frac{H}{R}\right)^2 \tag{7}$$

The collapse load, determined using rigid-plastic analysis, will correspond to the ultimate structural capacity of the system. A comparison between lower bound solutions for failure initiation q_u and ultimate collapse load intensity q_{uc} for the cases presented in Table 1 indicates that the ratio q_{uc}/q_u varies between 1 and 3.

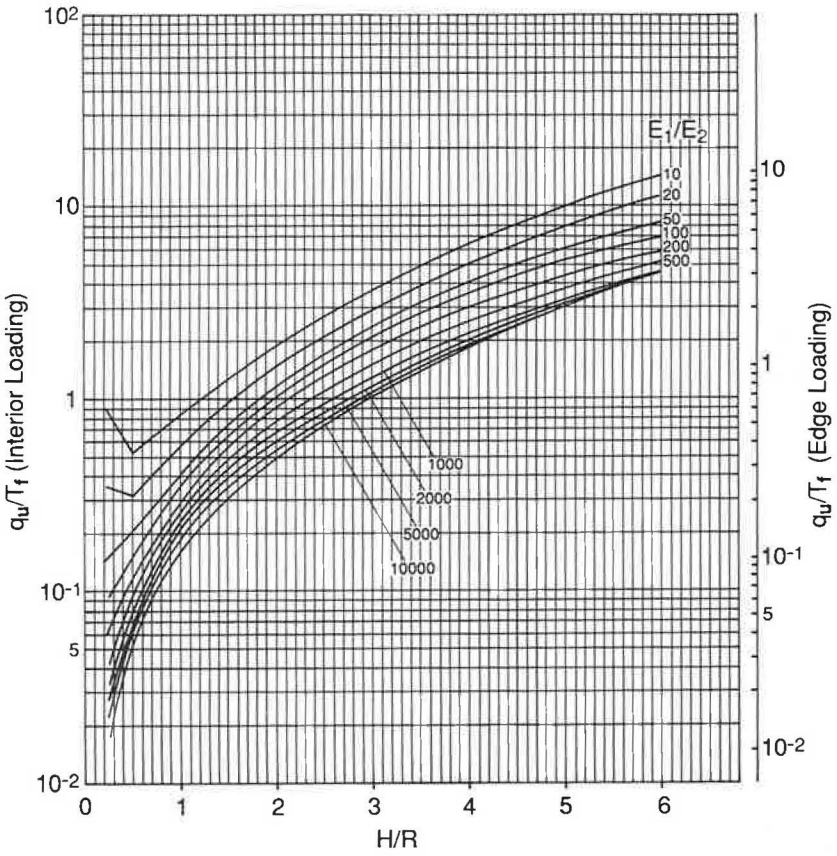


FIGURE 15 Surface load associated with flexure failure of base.

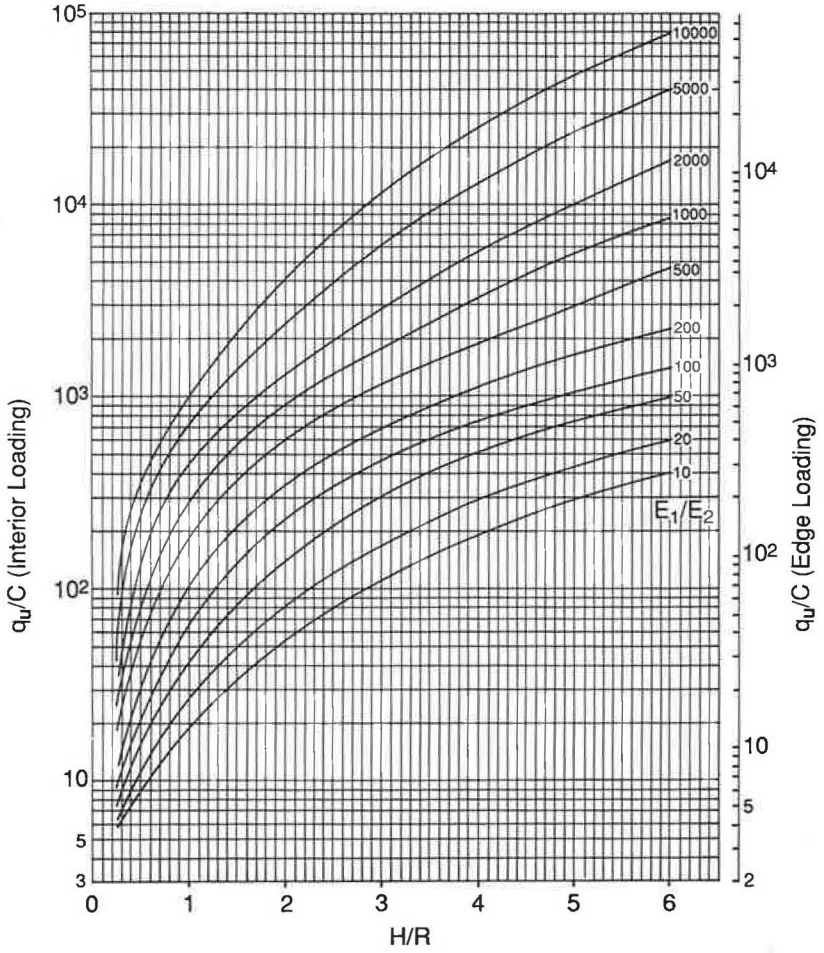


FIGURE 16 Surface load associated with bearing capacity failure of subgrade.

SUMMARY AND CONCLUSIONS

Dimensional analysis was applied to develop solutions for critical response parameters in two-layer pavements using linear elastic theory. Pavement response parameters, such as stresses, strains, and deflections, were grouped into dimensionless variables. Solutions were presented in charts that would allow simple determination of these parameters. These solutions could also be used to predict the performance of two-layer systems using available mechanistic models. Furthermore, these solutions could be implemented to assess whether fatigue failure in the surface layer or permanent deformation failure in the subgrade dominates the performance of the pavement under long-term repeated loads. Results of the analysis were also applied in developing an improved method to predict the structural capacity of stabilized layers over fine-grained subgrades under static or slowly moving loads.

The power of dimensional analysis in providing representative and simple engineering solutions for a wide range of pavement variables, including geometry, materials, and loading conditions, was illustrated. This capability is significant because of the need to develop meaningful interpretations of extensive experimental and analytical data as a result of ongoing pavement research programs.

REFERENCES

1. S. F. Brown and J. W. Pappin. Analysis of Pavements With Granular Basis. In *Transportation Research Record 810*, TRB, National Research Council, Washington, D.C., 1981, pp. 17–23.
2. L. Raad and J. L. Figueroa. Load Response of Transportation Support Systems. *Journal of the Transportation Engineering Division, ASCE*, Vol. 106, No. TE1, 1980, pp. 111–128.
3. *Shell Pavement Design Manual—Asphalt Pavements and Overlays for Road Traffic*. Shell International Petroleum Company Limited, London, England, 1978.
4. *Thickness Design—Asphalt Design for Air Carrier Airports*. Manual Series 11, 3rd ed., Asphalt Institute, College Park, Md., 1987.
5. R. L. Lytton. *Backcalculation of Pavement Layer Properties*. STP 1026. ASTM, Philadelphia, Pa., 1989, pp. 7–38.
6. L. H. Irwin. *User's Guide to MODCOMP2*. Cornell Local Roads Program Report 83-8. Cornell University, Ithaca, N.Y., 1983.
7. J. P. Mahoney, N. F. Coetzee, and R. N. Stubstad. *A Performance Comparison of Selected Backcalculation Computer Programs*. STP 1026. ASTM, Philadelphia, Pa., 1989, pp. 452–467.
8. M. I. Darter and A. J. Devos. *Structural Analysis of Asphaltic Cold Mixtures Used in Pavement Bases*. Research Report 505-4. Engineering Experiment Station, University of Illinois, Urbana, Aug. 1977.
9. M. W. Witczak. Design of Full Depth Asphalt Airfield Pavements. *Proc., 3rd International Conference on the Structural Design of Asphalt Pavements*, London, England, 1972, pp. 550–567.
10. D. M. Burmister. The Theory of Stresses and Displacements in Layered Systems and Application to the Design of Airport Runways. *HRB Proc.*, Vol. 23, 1943, pp. 126–144.
11. H. M. Westergaard. New Formulas for Stresses in Concrete Pavements of Airfields. *Transactions, ASCE*, Vol. 113, 1948, pp. 425–439.
12. K. R. Peattie. Stress and Strain Factors for Three Layer Elastic Systems. *Bulletin 342*, HRB, National Research Council, Washington, D.C., 1962.
13. A. M. Ioannides and R. A. Salsilli-Murua. Temperature Curling in Rigid Pavements: An Application of Dimensional Analysis. In *Transportation Research Record 1227*, TRB, National Research Council, Washington, D.C., 1989, pp. 1–11.
14. G. Ahlborn. *ELSYM5, A Computer Program for the Analysis of Elastic Layered Systems with Normal Loads*. ITTE, University of California, Berkeley, 1972.
15. G. G. Meyerhof. Load Carrying Capacity of Concrete Pavements. *Journal of the Soil Mechanics and Foundation Division, ASCE*, Vol. 88, No. SM3, June 1962, pp. 89–116.
16. L. Raad. Behavior of Stabilized Layers Under Repeated Loads. In *Transportation Research Record 1002*, TRB, National Research Council, Washington, D.C., 1985, pp. 72–79.
17. L. K. Marhamo. *Bearing Capacity of Cement-Treated Layers Over Soft Ground*. M.E. thesis. American University of Beirut.
18. J. K. Mitchell, P. Dzwilewski, and C. L. Monismith. *Behavior of Stabilized Soils Under Repeated Loading: A Summary Report with Suggested Structural Design Procedure*. Report 6. U.S. Army Engineer Waterways Experiment Station, Vicksburg, Miss., June 1974.

Publication of this paper sponsored by Committee on Flexible Pavement Design.

Permanent Deformation for Flexible Airfield Pavement Design

SAMUEL HANTHEQUESTE CARDOSO AND MATTHEW W. WITCZAK

The total permanent deformation of flexible airfield pavements is one of the best indicators of the overall performance of the pavement system. A methodology was developed to predict this distress mode under aircraft loadings on asphaltic concrete pavement systems. Particular emphasis is placed on the use of lateritic gravels intrinsic to many parts of Brazil. Using dynamic triaxial tests in the laboratory, models based on the California bearing ratio, state of stress, and number of load repetitions were developed for estimating the resilient modulus and the plastic deformation of lateritic base, subbase, and subgrade layers. The permanent deformation for flexible airfield pavement design (PDAPD) computer model was developed from modification of the existing Asphalt Institute DAMA program on the basis of multilayer elastic theory. The input variables necessary for this model come from three broad areas: the environment, the dynamic characteristics of the materials, and the traffic analysis. PDAPD, which can analyze up to 10-layer pavement structures, estimates the pavement damage on a monthly basis considering three criteria: fatigue of asphalt concrete layers, subgrade deformation, and total permanent deformation of the pavement. General verification of the PDAPD was accomplished by a computer analysis of numerous flexible-pavement airfield structures, designed in accordance with the FAA method. Although individual pavement section results varied, a good overall comparison in design life prediction occurs between the empirically based FAA approach and the mechanistic PDAPD model.

In the past 15 years, significant advancements have been made in knowledge of the permanent strain behavior of pavement layer materials, on the basis of dynamic laboratory tests as well as actual field behavior of the overall pavement system.

There is no doubt that permanent deformation is one of the major indicators of the overall performance of flexible pavements. In highways, where traffic is channelized, permanent deformation is generally characterized by rut depth magnitude. In airfield pavements, where aircraft traffic is distributed more laterally, the variability of permanent deformation of the pavement layers contributes to an increased roughness of the pavement surface.

Historically, initial mechanistic approaches for design of flexible pavement used two distress criteria: (a) limiting the tensile strain at the bottom of the asphalt concrete (AC) layer for repetitive load fatigue cracking and (b) limiting the compressive strain at the top of the subgrade layer to control permanent deformation. The latter criterion permits an estimation of the number of traffic load repetitions that would cause a certain amount of permanent deformation of the subgrade and, consequently, the pavement itself, assuming no deformability occurs within the pavement structure.

S. H. Cardoso, Division of Aeronautical Infrastructure Engineering, Technological Institute of Aeronautics, Sao Jose dos Campos, Brazil. M. W. Witczak, Department of Civil Engineering, University of Maryland, College Park, Md. 20742.

If a smooth runway roughness profile (relative to a standard for new construction or runway restoration) and a critical runway roughness profile (for the same pavement structure after a certain number of traffic load repetitions) are known, the difference between those two profiles is caused by the development of the total permanent deformation of the pavement system (*1*).

Several major pavement design organizations and methods recommend a minimum California bearing ratio (CBR) value of 80 or more for flexible airfield pavement base course materials. Although this specification is appropriate in geographic areas possessing adequate aggregate resources, it is a serious constraint and can greatly increase the costs of pavement construction when specification-quality materials are not available near the work site but adequate supplies of non-specification aggregates are locally present.

This situation is common in some areas of Brazil, where lateritic gravels are the main source of granular materials for base course. Frequently, these deposits do not meet minimum CBR specifications of base and subbase course use, but they have been used successfully in a wide variety of airfield pavements serving DC–9 and B–727 commercial traffic as well as a wide variety of military jet fighter aircraft (*2*).

The major objective of this study was to develop a methodology using the prediction of total permanent deformation as a major criterion for analyzing and designing airfield flexible pavements. In order to accomplish this goal, two major tasks were accomplished:

1. A comprehensive laboratory evaluation of the repeated load dynamic behavior of lateritic soils from Brazil relative to their resilient (elastic) and plastic behavior, and
2. The development of a computerized analytical pavement analysis program that would be able to consider (a) the nonlinear modulus response of these lateritic granular and subgrade pavement materials, (b) the climatic impact (because of high temperature and moisture) on pavement life as a consequence of changes of the in situ response of the pavement materials, and (c) the integration of the plastic deformation prediction of all pavement layers on the basis of a finite time interval (i.e., monthly).

THE MODEL

Model Background

The computerized permanent deformation for flexible airfield pavement design (PDAPD) model is represented by the flow chart shown in Figure 1 (*3*). The model was developed on the

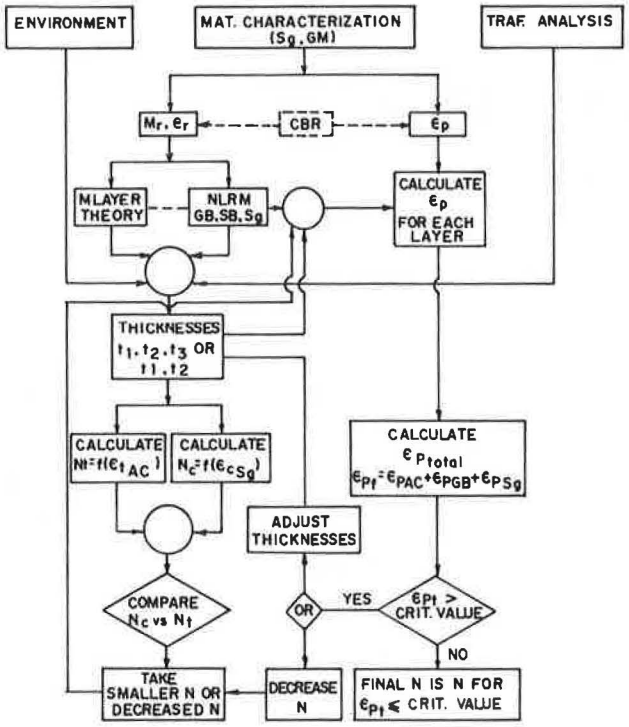


FIGURE 1 PDAPD model.

basis of a modified version of the DAMA computer program, developed by Witczak for the Asphalt Institute. The DAMA program was modified to incorporate nonlinearity of granular and subgrade materials, climatic condition in terms of temperature and moisture content of the pavement materials, and the prediction of permanent deformation for each pavement layer and sublayer, as well as the total pavement deformation.

Like the DAMA program, PDAPD analyzes a multilayered elastic pavement structure considering the cumulative damage for a dual wheel load system in three radial positions: (a) underneath the center of one tire, (b) at the edge of the tire, and (c) between tires.

The program calculates principal and bulk stresses, as well as strains at the surface and bottom of asphalt layers and at the mid depth of each granular and subgrade layer, except for the last subgrade layer, which is assumed to have an infinite thickness. The stresses and strains are calculated at the top of this layer.

The PDAPD program can accommodate one or more AC layers, four granular layers, and five subgrade layers. If the number of AC layers is larger than one, the summation of the number of these layers plus the granular layers must be less than or equal to five. In other words, the program is able to analyze up to 10 layers and sublayers.

Layer Moduli

Asphalt Layer Dynamic Modulus

The PDAPD computer program calculates the dynamic modulus for the asphalt layers considering the asphalt mixture characteristics, air temperature, and pavement temperature for each month, according to a predictive equation developed by Witczak (*4*).

Granular and Subgrade Layer Resilient Modulus

An extensive laboratory program to evaluate resilient and plastic responses of several lateritic gravels was conducted. In addition, a comprehensive set of compaction and CBR tests was done. Using these results, multiple stepwise regression analyses were conducted for six CBR levels (18.8, 28.8, 38.7, 43.5, 71.6, and 93.0 percent), five levels of confining pressure (3, 5, 10, 15, and 20 psi), and seven layers of deviator stress (3, 5, 10, 15, 20, 25, and 50 psi). Because it was not possible to mold or test specimens at all factorial levels, the final sample size was equivalent to 149 points of observation (*5*).

The best model, which has been incorporated in the PDAPD program, is as follows:

$$M_R = \frac{179.0412(\text{CBR})^{1.08774}(\theta)^{1.43833}}{(\sigma_1)^{1.18598}} \quad (1)$$

$(R^2 = 0.92; \text{SEE} = 0.082)$

where

M_R = resilient modulus (psi),
CBR = California bearing ratio,
θ = $\sigma_1 + \sigma_2 + \sigma_3$, the bulk stress or first invariant of stress (psi), and
σ_1 = major principal stress (psi).

The CBR variable explains 68.5 percent of the total variation in this model, whereas the inclusion of bulk stress (θ) and the major principal stress (σ_1) variables in the model increases the explained variation by 9.2 and 14.3 percent, respectively.

All of the nonlinear modulus calculations are done monthly using an iterative approach. The initial seed relationships used to start the stress-dependent moduli solutions are 1,300 × CBR and 400 × CBR, respectively, for base-subbase and subgrade layer-sublayer materials. With these initial seed values, the bulk stresses and major principal stresses are calculated for each unbound layer as shown in Figure 2.

On the basis of these stresses, new resilient moduli are calculated and compared with the previous values. If the absolute difference between the previous and current resilient modulus is larger than 5 percent, new values are assigned by taking the average between them. This procedure is repeated until the difference between the previous and the new resilient modulus is less than 5 percent for all layers. As previously noted, this process is repeated for each time increment (month) used in cumulative damage analysis. For each time interval, temperature and, hence, stiffness changes of the asphaltic layer occur. Thus, for each time period, the pavement stress states (i.e., moduli) vary.

Permanent Deformation

The bulk stress and the major principal stresses calculated from the final moduli iteration are then used to calculate the

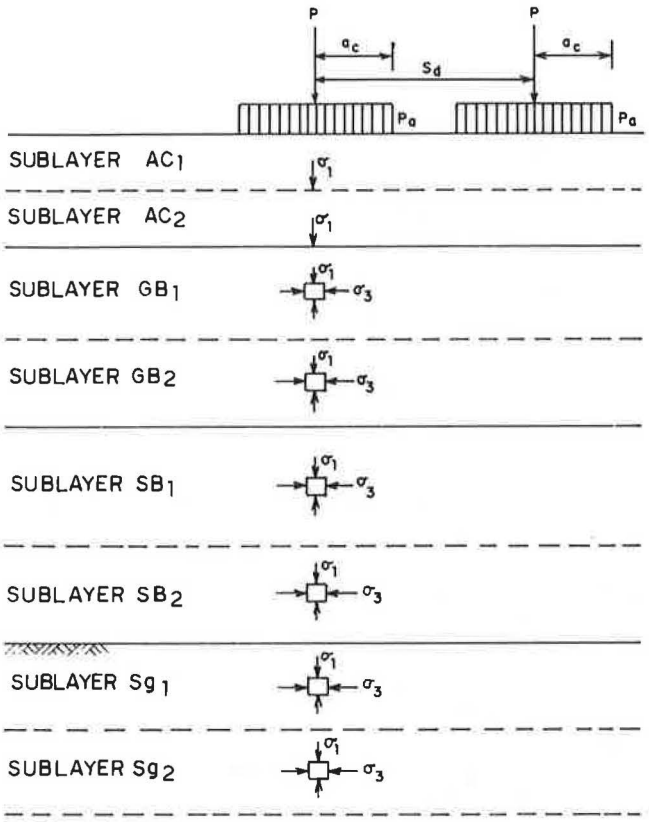


FIGURE 2 Pavement layers and sublayers for resilient and permanent deformation calculation.

permanent strain for each layer (using the monthly repetition level) according to the following equations. These equations were developed from a statistical multiple regression analysis of laboratory test results on the repeated load permanent deformation behavior of the lateritic materials. In this study, the most accurate approach was obtained by developing two separate plastic strain predictive models for CBR values greater than and less than 40 percent.

$$\varepsilon_p = \frac{128{,}748(N)^{0.1346}(\sigma_1)^{2.664}}{(\text{CBR})^{5.55}(\theta)^{1.1431}} \qquad \text{CBR} > 40 \qquad (2)$$

$$\varepsilon_p = \frac{(N)^{0.1878}(\sigma_1)^{6.0911}}{55.6313(\text{CBR})^{1.3605}(\theta)^{4.893}} \qquad \text{CBR} < 40 \qquad (3)$$

where ε_p is the plastic strain (in./in.) and N is the number of stress repetitions.

Equations 2 and 3 have regression statistics of $R^2 = 0.741$ and 0.882 and SEE = 0.245 and 0.171, respectively (*5*). In both equations, the most important varible is the CBR, followed by the major principal stress (σ_1), number of stress repetitions (N), and bulk stress (θ). The permanent deformation damage model used for the asphalt layer in PDAPD is

$$\Delta h_{ac} = 4.49\delta(N)^{0.25} \qquad (4)$$

where Δh_{ac} is the permanent deformation in the asphalt layer (in.) and δ is the elastic deformation (compression) within the asphalt layer itself (in.).

Distress and Life Predictions

The total predicted permanent deformation for the first month is obtained by accumulating the plastic deformation for each unbound layer (i.e., base, subbase, and subgrade) obtained as a function of CBR, bulk stress, and major principal stress for that particular month. This deformation is added to the predicted rutting within the asphalt layer. For the next month, the accumulation of plastic deformation for each unbound layer is the total permanent deformation estimated for the first 2 months (with CBR and state of stress for the second month) minus the amount of plastic deformation predicted, at the same conditions, for the first month. This process is continued until one of the following conditions occurs:

- For both fatigue fracture and deformation (subgrade strain criteria), the predicted pavement life is computed in months for a given airfield pavement system. The analysis is terminated at 240 months (20 years) if both criteria have predicted lives greater than this threshold value.
- For prediction of total permanent deformation, failure is assumed to occur when a permanent deformation of 1.22 in. (31.0 mm) is obtained. This failure level has been determined from several roughness studies conducted at Brazilian military airfields (*1,6,7*).

The computer output for total permanent deformation and the accumulated plastic deformation for each layer of material are presented in units of millimeters and inches.

PDAPD MODEL VERIFICATION

General Approach

Because verification through field tests was beyond the scope of this initial study, the general philosophy used was to analyze and compare performance for pavement structures designed in accordance with the FAA procedure (*8*). An investigation was conducted of the effect of several variables—thickness of AC (tac), granular base CBR (CBR_{gb}), subbase CBR (CBR_{sb}), and subgrade CBR (CBR_{sg})—on the resilient modulus (M_R) of the unbound layers, the predicted pavement life, and the plastic deformation of each pavement layer.

The pavement structures were designed by the FAA procedure for a B-727-100 aircraft having the following gear characteristics: 166-psi tire pressure, 34-in. dual spacing, and 38,500-lb wheel load. Pavement designs were considered for three levels of repetitions (20-year design): 60,000, 120,000, and 300,000. Table 1 presents the FAA pavement structures used to study the effect of thickness of AC on several variables. A total of 65 cases of pavement structures designed according to the FAA procedure were analyzed with the PDAPD model.

Resilient Modulus Studies

As previously noted, one study phase dealt with the influence of several layer properties on the predicted nonlinear M_R response of various layers generated by PDAPD within the FAA-designed structures. In all computer studies, the subgrade was subdivided into five sublayers with the last sublayer being of infinite thickness. The asphalt mixture characteristics, as

TABLE 1 FAA PAVEMENT STRUCTURES STUDIED

Subgrade CBR (%)	FAA Design Repetitions (N)	Thickness - inches					
		AC = 4"		AC = 5"*		AC = 8"**	
		GB	SB	GB	SB	GB	SB
5	60,000	11.0	22.0	11.0	22.0	5.4	22.0
	120,000	12.0	23.0	12.0	23.0	6.0	23.7
	300,000	13.0	25.0	13.0	25.0	6.0	27.4
10	60,000	11.5	8.5	11.5	8.5	5.9	8.5
	120,000	12.0	9.0	12.0	9.0	6.0	9.7
	300,000	13.0	9.5	13.0	9.5	6.0	11.9
15	60,000	11.0	3.5	11.0	3.5	5.4	3.5
	120,000	12.0	3.0	12.0	3.0	6.0	3.7
	300,000	13.0	3.0	13.0	3.0	6.0	5.4

Notes: (*) AC thickness increased by 1" without substitution of other layer materials.

(**) Granular base thickness set close to 6.0" and substitution ratios of 1.4 used between AC and Granular Base; 1.7 between Granular Base and Subbase.

well as the air and pavement temperatures, were kept constant to approximate the relatively uniform, warm climatic conditions in many areas of Brazil. The conditions selected resulted in a constant AC modulus of approximately 250,000 psi.

Influence of AC Thickness

In order to assess the influence of the asphalt thickness on layer M_R, thicknesses of 4 and 8 in. were investigated. These studies were made at three levels of subgrade CBR (5, 10, and 15 percent) using a subbase CBR of 20 percent and a base CBR of 100 percent. These results are shown in Figure 3.

The higher the subgrade CBR, the higher the resilient modulus for the granular base with a 4-in. AC surface. However, the resilient modulus of the granular base decreases with an increase of the subgrade CBR when the thickness of AC is increased to 8 in.

This finding can be explained relative to the nonlinear relationship noted in Equation 1. For lower subgrade CBR values and thicker AC layers, the major principal stress decreases significantly when the bulk stress (or confining pressure) is increased. This variation in the level of stress contributes to the increasing resilient modulus in that particular layer for low CBR values. However, when the subgrade CBR is increased, the level of vertical stress increases at the base course layer, which overcomes the influence of bulk stress (or confining pressure) resulting in a lower resilient modulus for the base layer.

Considering the resilient modulus for the subbase and subgrade layers, there are no significant changes caused by

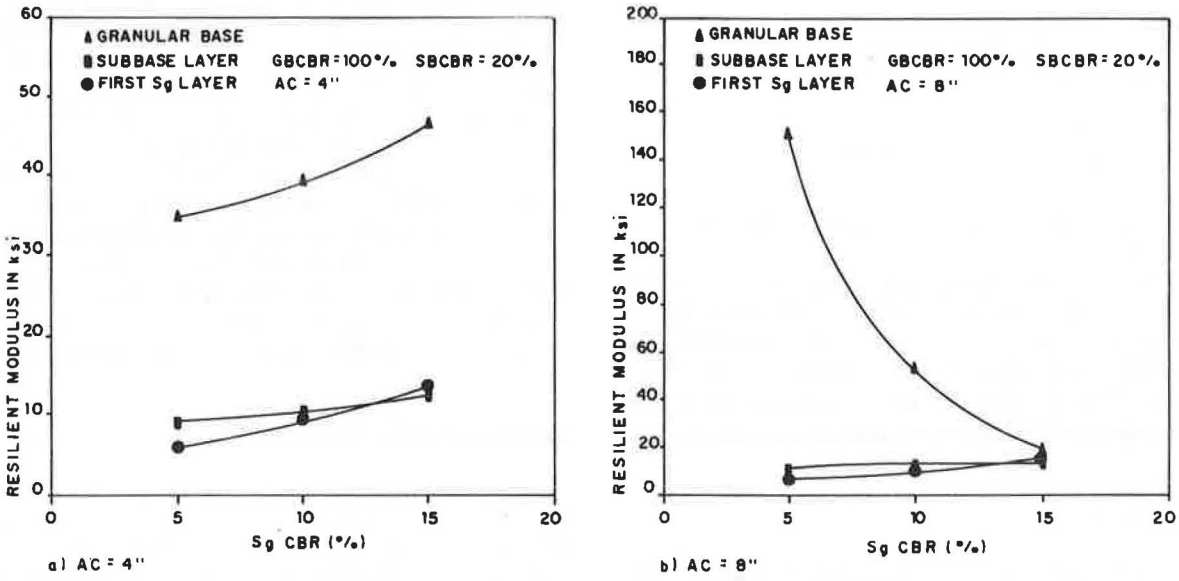


FIGURE 3 Effect of AC thickness on resilient modulus (design according to FAA procedure for 60,000 repetitions).

varying the asphalt thickness from 4 to 8 in. In other words, the resilient modulus of the granular base is more sensitive to the variation of AC thickness than that of other layers due to the relative stress state changes in the upper (base) pavement layers.

Influence of Base and Subbase CBR

The influence of base and subbase strength on modulus was investigated for pavements with a 4-in. asphalt surface layer. CBR values of 60, 80, and 100 percent for the granular base and 20 and 40 percent for the granular subbase layers were used in the analysis. The results are shown in Figure 4.

In addition to the increase of the resilient modulus of the base course with the increase in subgrade CBR (discussed previously), the resilient modulus increases with the increase of the granular base and subbase CBR value, as expected. On the other hand, the increase of the base strength from 60 to 80 percent did not significantly increase the resilient modulus for either the subbase layer or the subgrade layers.

The resilient modulus for the first subgrade sublayer was found to be approximately 1,000 × CBR. In fact, after analyzing more than 300 FAA pavement structures, it has been verified that the range for resilient modulus is within 800 to 1,200 × CBR value of the subgrade. This factor is obviously close to the well-known 1,500 × CBR relationship developed by Shell researchers and is also consistent with coefficient multipliers of CBR for unbound granular material, which consider stress sensitivity.

Pavement Life Studies

Influence of AC Thickness

Several studies were likewise undertaken to investigate the influence of pavement layer variables on the predicted life generated by PDAPD. As previously noted, the PDAPD program looks at fatigue fracture, subgrade deformation, and total pavement deformation of the system. Tables 2 and 3 present predicted life summaries indicating the relative influence of asphalt thickness and layer CBR values for subgrade, subbase, and base.

From the results presented in Table 2 it can be inferred that, for pavements designed according to FAA procedures, there is a relatively good agreement when predicting pavement life for pavements designed with 4-in. AC and 5 and 10 percent subgrade CBR. This finding is particularly true when the significant sensitivity of pavement variables to predicted repetitions to failure is considered.

If the CBR of the granular base is decreased to 60 percent instead of 100 percent and the AC thickness is increased by 1 in. (without any substitution of the other layer materials), the lives of the pavements still decrease by approximately 30 percent when designed for 5, 10, and 15 percent subgrade CBR. Comparisons made between pavements designed with 4 in. AC, 60 percent base CBR, and 20 percent subbase CBR (Table 2) and pavements designed with 5-in. AC (without any layer substitution), 60 percent base CBR, and 20 percent subbase CBR (Table 3) show that pavement life is always increased for the second case (5-in. AC). One example of these findings is shown in Figure 5.

These results definitely show that, for airfield pavements, it is possible to make design trade-offs among pavement layer thicknesses and qualities when base materials do not meet the standard specifications of minimum 80 percent CBR. These results also clearly explain the experience of Cardoso in the Brazilian Amazonian region, where lateritic base of 60 percent CBR has been used in some airfield pavements with good performance.

Another conclusion inferred from Table 2 is that the life (from a fatigue and total permanent deformation viewpoint) of pavements designed with an 8-in. AC surface layer decreases when the expected pavement life (according to the FAA procedure) increases. This result is accentuated for the

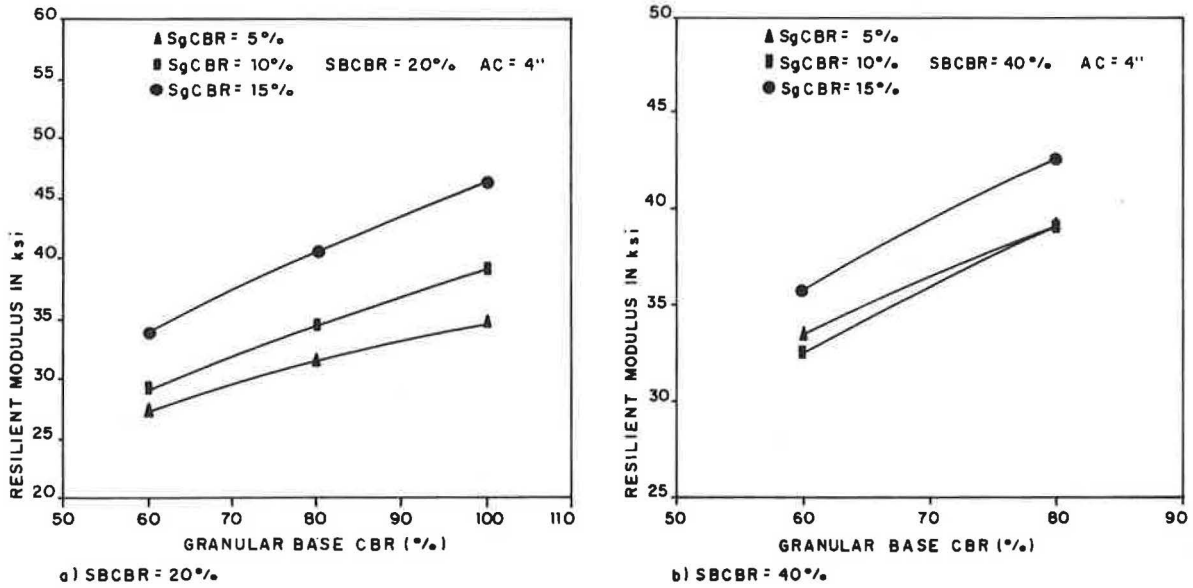


FIGURE 4 Effect of base and subbase CBR on base course resilient modulus.

TABLE 2 EFFECT OF AC THICKNESS ON PAVEMENT LIFE

Subgrade CBR (%)	Criterion	Traffic Repetitions (x 10,000) AC = 4"* P1	P2	P3	AC = 5"** P1	P2	P3	AC = 8"* P1	P2	P3
5	Fatigue	13.3	15.7	18.9	10.8	11.9	13.6	49.0	32.9	24.1
	Subgrade Def.	19.5	30.7	53.5	22.0	31.8	54.9	28.3	43.3	76.2
	Total Perm Def	5.6	(15.7)	(18.9)	2.8	6.3	(13.6)	(28.3)	21.3	7.7
10	Fatigue	19.6	21.0	24.5	14.3	15.4	16.4	26.2	26.9	27.3
	Subgrade Def.	21.0	25.9	36.7	26.2	32.5	45.5	36.7	49.3	70.6
	Total Perm Def	(19.6)	(21.0)	(24.5)	(14.3)	(15.4)	(16.4)	15.7	14.0	14.0
15	Fatigue	28.7	32.5	37.1	19.6	21.0	22.4	43.0	43.0	43.4
	Subgrade Def.	38.5	45.5	61.5	46.2	52.5	64.3	67.8	77.6	99.0
	Total Perm Def	(28.7)	(32.5)	(37.1)	(19.6)	(21.0)	(22.4)	(43.4)	29.7	25.5

Notes:

1. **Structures P1, P2, P3 are FAA designs for 60,000, 120,000, and 300,000 repetitions respectively.**
2. **(*) Granular Base CBR = 100%**
   Granular Subbase CBR = 20%
3. **(**) Granular Base CBR = 60%**
   Granular Subbase CBR = 20%
4. **Numbers in parentheses () are Traffic Repetitions greater than Value shown.**

subgrade of 5 percent CBR and for the total permanent deformation criterion, as shown in Figure 6.

This finding can be explained by the increase of the subbase thickness done to compensate for the change in thickness of the AC layer. Besides the effect of the thicker subbase layer, the subbase material of 20 percent CBR also contributed to increasing the permanent deformation in that particular layer. In addition, for the 8-in. AC pavement the base course resilient moduli were affected by the variation in stress, as pointed out earlier. These results suggest that layer substitution ratios (and their subsequent use to determine equivalent structures) have to be analyzed carefully, considering all possible failure models. This finding is consistent with state-of-the-art knowledge of substitution ratios in highway and airfield design.

Influence of Base and Subbase CBR Values

The effect of the base and subbase CBR values on pavement life can be analyzed through the data presented in Table 3 and shown in Figures 7, 8, and 9, for the fatigue criterion, subgrade deformation criterion, and total plastic deformation criterion, respectively. The results indicate that the higher the base course or subbase CBR, the higher the pavement life in terms of any of the three criteria when the pavements are designed according to FAA procedure and the materials meet the required specifications.

Considering the fatigue and subgrade deformation criteria (Figures 7 and 8, respectively), the lower the subgrade CBR, the greater the benefit of a higher subbase CBR on the pavement life. On the other hand, the effect of higher subbase CBR on the pavement life in terms of the total plastic deformation criterion is not positive for pavements with 60 percent granular base CBR designed with 4-in. AC. As previously stated, the use of lower-quality materials for the base course must be viewed as a trade-off or balance among the pavement layer thicknesses, particularly with increases of the asphalt surface thickness.

Layer Permanent Deformation

Influence of AC Thickness

The contribution of each pavement material to permanent deformation is presented in Table 4. These values represent the average of the values obtained for pavements designed according to the FAA procedure for 60,000, 120,000, and 300,000 repetitions in a 20-year period. The mean value was used because there were no major differences among the three values for the various FAA pavement structures investigated.

From this table, it is clear that the higher the subgrade CBR, the greater the percentage contribution of the AC and subgrade layers to the total permanent deformation and the lower the contribution of the granular layers. Figure 9 shows that the plastic deformation is more distributed among the pavement materials when the subgrade CBR is increased from 5 to 15 percent.

Research studies conducted by Chou (*9*) on the effect of a stress factor on plastic deformation of subgrades are in agreement with these findings. Chou found that rutting of the subgrade was a function of the stress factor, defined as follows:

$$\text{Stress factor} = 28.5W^{0.5} \cdot \text{CBR}^{0.635} \quad (5)$$

TABLE 3 EFFECT OF BASE AND SUBBASE CBR ON PAVEMENT LIFE

Gran. Base CBR (%)	Subgrade CBR (%)	Criterion	Traffic Repetitions (x 10,000) Subbase CBR = 20% P1	P2	P3	Subbase CBR = 40% P1	P2	P3
60	5	Fatigue	8.9	10.0	11.2	14.9	17.3	19.8
		Sq DF.	15.6	22.8	39.3	25.1	37.3	74.6
		T.P.D.	0.5	1.2	4.0	0.4	0.5	1.3
	10	Fatigue	12.0	12.7	13.9	15.8	16.9	18.5
		Sq DF.	17.5	21.7	30.4	21.0	26.2	36.7
		T.P.D.	3.4	4.2	7.0	1.3	1.4	1.3
	15	Fatigue	16.5	18.0	19.1	19.4	20.3	21.5
		Sq DF.	31.2	35.8	44.4	33.5	37.9	47.0
		T.P.D.	(16.5)	(18.0)	(19.1)	7.3	13.3	18.4
80	5	Fatigue	11.2	12.8	14.8	20.1	22.7	27.8
		Sq DF.	16.2	25.7	45.5	27.6	42.6	83.4
		T.P.D.	3.3	10.3	(14.8)	4.5	9.6	22.3
	10	Fatigue	15.8	19.1	17.0	21.3	23.1	26.0
		Sq DF.	19.6	34.6	23.9	23.9	29.8	42.2
		T.P.D.	15.7	(19.1)	(17.0)	15.0	18.9	(26.0)
	15	Fatigue	22.5	27.7	25.1	26.9	28.7	31.3
		Sq DF.	35.0	51.6	40.8	37.8	43.4	54.8
		T.P.D.	(22.5)	(27.7)	(25.1)	(26.9)	(28.7)	(31.3)
100	5	Fatigue	13.3	15.7	18.9	-	-	-
		Sq DF.	19.4	30.8	53.4	-	-	-
		T.P.D.	5.4	(15.7)	(18.9)	-	-	-
	10	Fatigue	19.3	21.0	24.3	-	-	-
		Sq DF.	21.0	25.9	36.4	-	-	-
		T.P.D.	(19.3)	(21.0)	(24.3)	-	-	-
	15	Fatigue	28.6	32.4	37.1	-	-	-
		Sq DF.	38.4	45.2	57.8	-	-	-
		T.P.D.	(28.6)	(32.4)	(37.1)	-	-	-

Notes: 1. Structures P1, P2, P3 are FAA designs for 60,000, 120,000, and 300,000 repetitions respectively.

2. Numbers in parentheses () are Traffic Repetitions greater than Value shown.

where W is the equivalent single-wheel load and CBR is the subgrade strength.

On the basis of this equation, the higher the strength of the subgrade, the higher the stress factor and, consequently, the greater the percentage contribution of the subgrade to the total plastic deformation of the pavements.

The thicker the AC layer, the higher the permanent deformation for this layer and the lower the contribution of the granular layers. Table 4 shows that pavements designed for a subgrade of 5 percent CBR result in an increase of the plastic deformation contribution from 4 to 31 percent within the AC layer and a decrease from 92 to 65 percent for the granular layers when the AC thickness is increased from 4 to 8 in.

Influence of Base and Subbase CBR Values

Table 5 presents the contribution of each pavement layer material to total permanent deformation as a function of differing subgrade, subbase, and base strengths. The data indicate that increasing the subbase CBR (at the same base CBR) slightly increases the contribution of the granular layers to plastic deformation.

Once these pavement structures are designed according to the FAA procedure, the same discussion conducted for subgrades is applicable for subbase materials. In other words, the higher the subbase CBR, the higher the stress factor for that particular layer and the higher the percentage contribution of this layer to the total plastic deformation (*9*). The contribution of the granular layers to the plastic deformation decreases with an increase of the granular base CBR, whereas the AC and subgrade layer contributions simultaneously increase.

The results of the contribution of each pavement material to total permanent deformation agree with the literature (*10–13*).

After these preliminary results and verification of the PDAPD model, 3 years of analytical studies (more than 300 pavement

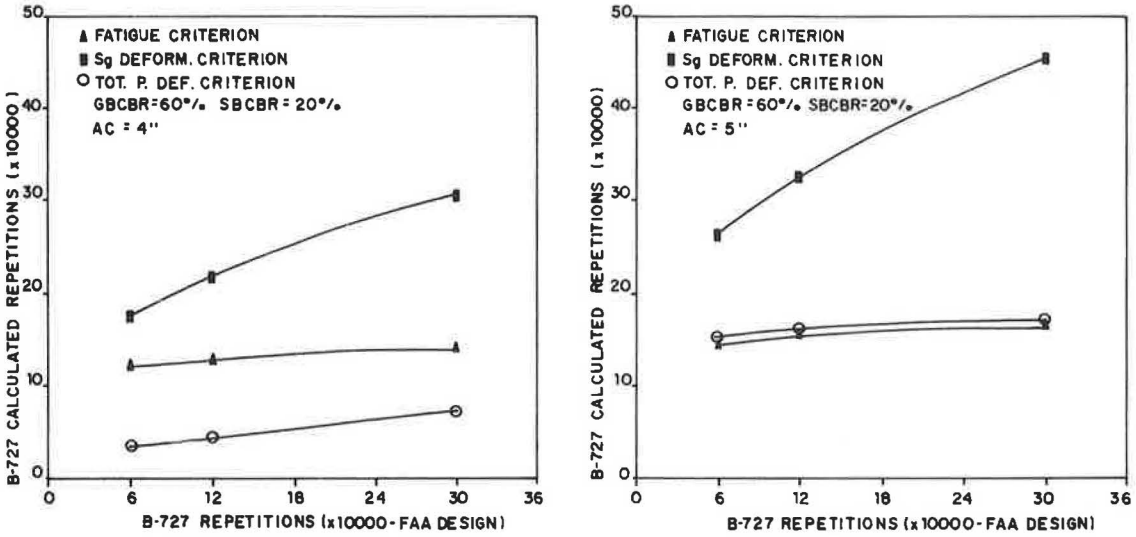


FIGURE 5 Effect of AC thickness on pavement life (subgrade CBR = 10 percent).

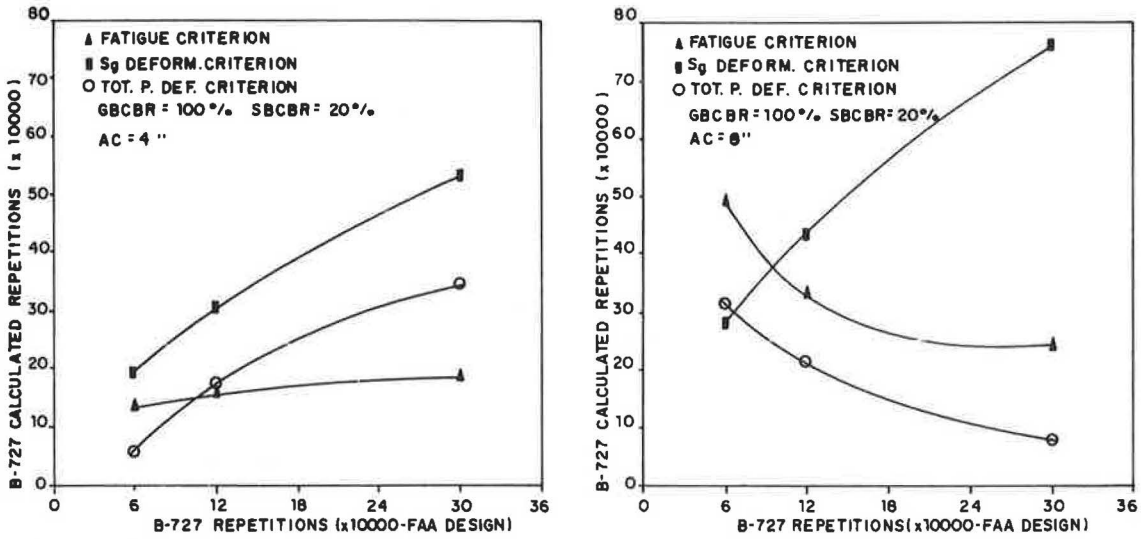


FIGURE 6 Effect of AC thickness on pavement life (design according to FAA procedure for 60,000 repetitions).

structures analyzed) and field studies (pavement evaluation and analysis of overlay design) were conducted. In general, these Brazilian studies reinforced the general findings, usefulness, and overall utility of the PDAPD model.

CONCLUSIONS

The PDAPD model was developed to focus on the design and analysis of flexible airfield pavements using lateritic base and subbase gravels for Brazilian conditions. Following are some of the major capabilities of the model:

- The model calculates the dynamic modulus of AC layers on a monthly basis by considering environmental and asphalt mixture properties.
- The model calculates the resilient modulus for any layer of pavement having up to 10 layers, taking into consideration the nonlinearity of lateritic base, subbase, and subgrade materials, as well as the expected variation of their strength on a monthly basis.
- The model calculates the plastic information of each layer from the subgrade to the asphalt surface and accumulates the total permanent deformation for the pavement structure on a monthly basis. The permanent deformation of the asphalt layers is modeled with the use of the elastic deformation within the layers caused by a particular aircraft type. The plastic deformations of the lateritic base, subbase, and subgrade layers are calculated through statistical models developed in this study on the basis of dynamic (repeated) load permanent deformation laboratory results. These models incorporate the

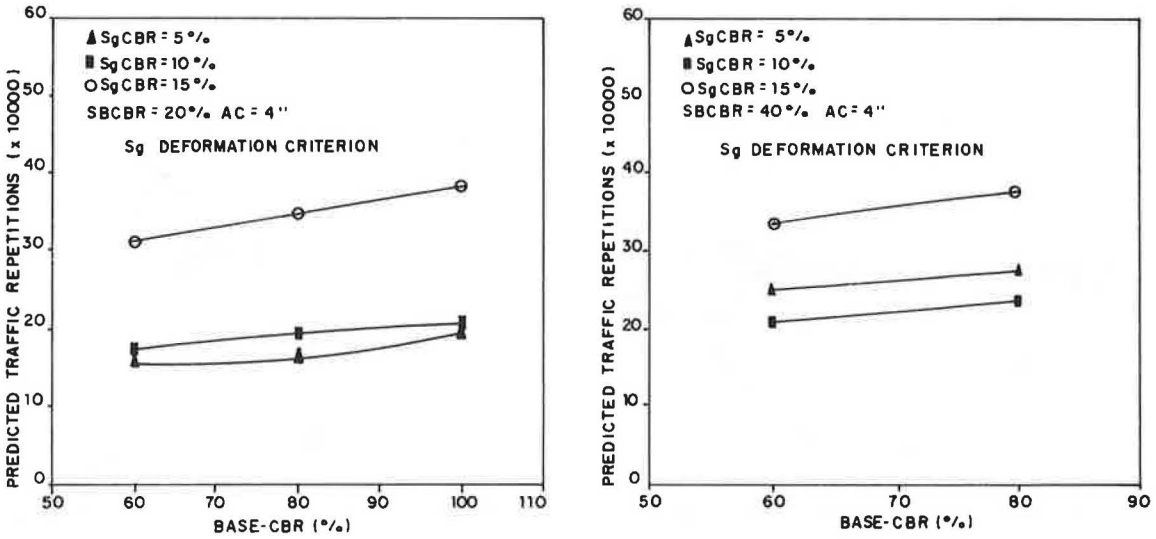


FIGURE 7 Effect of subbase and base CBR on pavement life (subgrade deformation criterion).

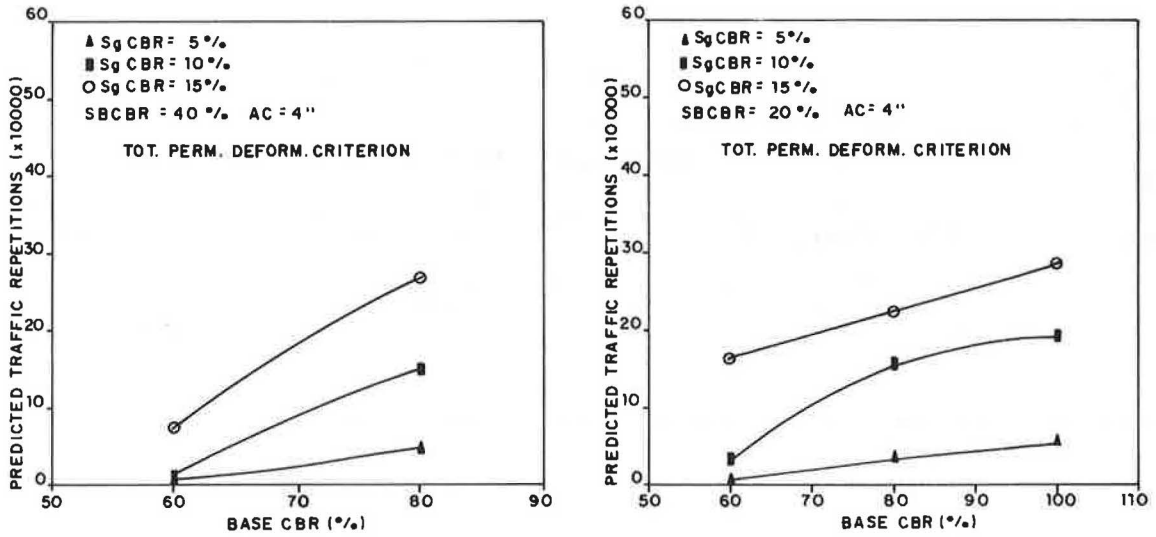


FIGURE 8 Effect of subbase and base CBR on pavement life (total permanent deformation criterion).

material strength by CBR and the state of stress at the middle of the depth of each layer.

- The computer program can be used to analyze airfield flexible pavements, taking into consideration all aspects presented in the PDAPD model. Three basic criteria are used: (a) tensile strain at the bottom of the AC layers (fatigue), (b) compressive strain at the top of the subgrade (subgrade deformation), and (c) total permanent deformation.

A preliminary verification study of the PDAPD model was done by analyzing 65 cases of pavement structures designed according to the FAA procedure for three levels of load applications. Following are the main conclusions of that study:

- The resilient modulus of the lateritic granular base increases with an increase of the CBR strengths of the subgrade, subbase, and base course. The granular base modulus is more sensitive to thicker AC layers than to changes in either the subbase or subgrade CBR.
- For over 300 pavement structures studied to date, the resilient modulus of the first subgrade layer was found to be around 1,000 × CBR (range of 800 to 1,200 × CBR).
- For pavement life, the fatigue criterion was more critical than the subgrade deformation criterion on all pavement structures studied for the B-727-100 aircraft. For pavements designed with a 4-in. asphalt layer, the total plastic deformation criterion was less critical than the subgrade deformation criterion. This same trend was not found for pavements designed with an 8-in.-thick asphalt layer, which suggests that the substitution of layer materials must be cautiously conducted.

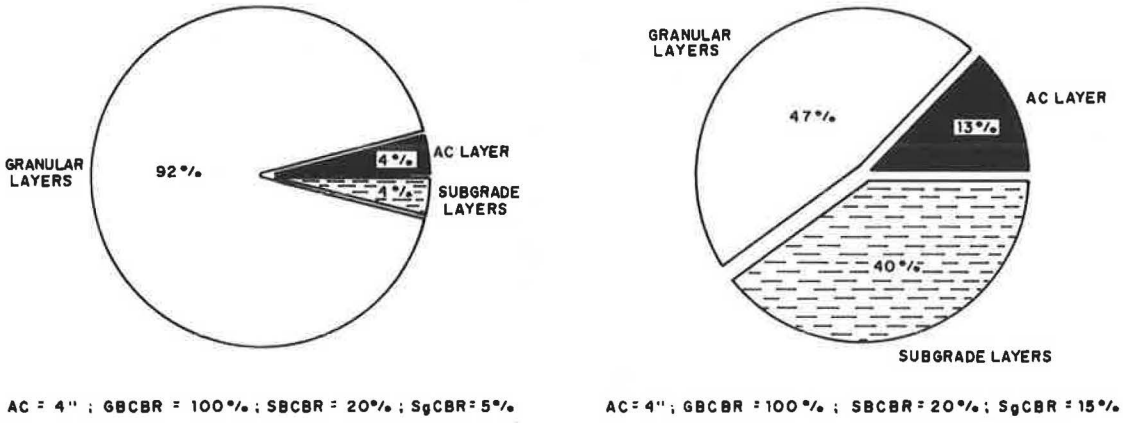


FIGURE 9 Contribution of plastic deformation from each type of material.

TABLE 4 EFFECT OF AC THICKNESS ON LAYER CONTRIBUTION PERCENTAGE OF TOTAL PERMANENT DEFORMATION

Subgrade CBR (%)	Percent of Total Permanent Deformation (%)								
	AC = 4"			AC = 5"			AC = 8"		
	AC	Gran	Sg	AC	Gran	Sg	AC	Gran	Sg
5	4.0	92.0	4.0	4.0	93.0	3.0	31.0	65.0	4.0
10	6.0	76.0	18.0	7.0	81.0	12.0	55.0	34.0	11.0
15	13.0	47.0	40.0	11.0	66.0	23.0	67.0	17.0	16.0

TABLE 5 EFFECT OF BASE AND SUBBASE CBR ON LAYER CONTRIBUTION PERCENTAGE OF TOTAL PERMANENT DEFORMATION

Granular Base CBR (%)	Subgrade CBR (%)	Percent of Total Permanent Deformation (%)					
		Subbase CBR = 20%			Subbase CBR = 40%		
		AC	Gran	Sg	AC	Gran	Sg
60	5	2.0	96.0	2.0	1.0	97.0	2.0
	10	4.0	85.0	11.0	3.0	89.0	8.0
	15	7.0	71.0	22.0	6.0	76.0	18.0
80	5	3.0	94.0	3.0	3.0	95.0	2.0
	10	6.0	78.0	16.0	5.0	83.0	12.0
	15	11.0	54.0	35.0	9.0	65.0	26.0
100	5	4.0	92.0	4.0	-	-	-
	10	6.0	76.0	18.0	-	-	-
	15	13.0	47.0	40.0	-	-	-

- If the same conditions (required by the FAA procedure) are kept constant but a 60 percent material is used for the base instead of 100 percent and the asphalt layer thickness is increased by only 1 in., similar performance (life) is obtained for pavements designed for the three levels of load applications studied. The findings strongly suggest that in designing airfield pavements it is possible to make a trade-off among the pavement layer thicknesses and material quality when the materials do not meet the CBR standard specifications.
- For pavements designed with 4 in. of asphalt surfacing, the higher the base or subbase CBR, the longer the pavement life for all three failure criteria.
- The higher the subgrade CBR, the more distributed the plastic deformation percentage among the pavement materials (AC, base and subbase, and subgrade layers). The thicker the AC layer, the larger the plastic deformation for this layer. In addition, the contribution of the granular layers for the total permanent deformation becomes smaller.

These results provide an example of the flexibility and ability of the PDAPD model for designing and analyzing flexible airfield pavements. In particular, PDAPD has significant potential when materials do not meet the standard requirements and specifications currently in use.

REFERENCES

1. S. H. Cardoso, A. G. Neto, and E. Colen. *Evaluation of PCN and Surface Condition of Uberlandia Airport Pavements* (in Portuguese). Final report. INFRAERO; Technological Institute of Aeronautics, Sao Jose dos Campos, Brazil, May 1990.
2. S. H. Cardoso. *Development of Methods for Designing Flexible and Semi-Rigid Airfield Pavements*. (in Portuguese). Partial reports. INFRAERO; Technological Institute of Aeronautics, Sao Jose dos Campos, Brazil, Nov. 1988, July 1989, Oct. 1989, Feb. 1990.
3. S. H. Cardoso. *Procedure for Flexible Airfield Pavement Design Based on Permanent Deformation*. Ph.D. dissertation. University of Maryland, College Park, 1987.
4. *Research and Development of the Asphalt Institute's Thickness Design Manual (MS-1)*, 9th ed. Research Report 82-2-RR-82-2. Asphalt Institute, College Park, Md., 1982.
5. S. H. Cardoso. Development of Models for Estimating Resilient Modulus and Permanent Deformation Based on CBR and Triaxial Dynamic Test Results. *Proc., International Conference on Roads and Road Transport Problems*, New Delhi, India, Dec. 1988, pp. 336–344.
6. S. H. Cardoso. *Studies of Surface Unevenness of Runways of Two Military Airfields* (in Portuguese, abstract in English). M.Sc. thesis. Federal University of Rio de Janeiro, 1982.
7. S. H. Cardoso, J. de Medina, and E. L. Neto. Procedure for Runway Roughness Evaluation with Rod and Level. *Proc., 2nd International Symposium on Pavement Evaluation and Overlay Design*, Rio de Janeiro, Vol. II, 1989.
8. *Airport Pavement Design and Evaluation*. Advisory Circular AC 150/5320-6C. FAA, U.S. Department of Transportation, July 1978.
9. Y. T. Chou. Analysis of Pavement Designed by CBR Equation. *Transportation Engineering Journal, ASCE*, Vol. 104, No. TE4, July 1978, pp. 457–474.
10. J. Morris. *The Prediction of Permanent Deformation in Asphalt Concrete Pavements*. Department of Civil Engineering, University of Waterloo, Canada, Sept. 1973.
11. R. D. Barksdale. Performance of Asphalt Concrete Pavements. *Transportation Engineering Journal, ASCE*, Vol. 103, No. TE1, Jan. 1977, pp. 55–73.
12. R. D. Barksdale. Performance of Crushed-Stone Base Courses. In *Transportation Research Record 954*, TRB, National Research Council, Washington, D.C., 1984, pp. 78–87.
13. W. R. Barker. *Prediction of Pavement Roughness*. Miscellaneous Paper GL-82-11. U.S. Army Engineer Waterways Experiment Station, Vicksburg, Miss., 1982.

Publication of this paper sponsored by Committee on Flexible Pavement Design.

Comparison and Reanalysis of AASHO Road Test Rigid Pavement Data

W. RONALD HUDSON, MICHAEL T. MCNERNEY, AND TERRY DOSSEY

Three different computer analyses of the AASHO Road Test for rigid pavements are reviewed, along with their resultant pavement performance equations. A fourth analysis, which is a revision of one of the three, is then briefly presented. A review is provided of the original AASHO least-squares regression analysis of the serviceability data collected during the 2 years of the Road Test. In their book, *Road Work*, Small and Winston propose that the original AASHO analysis overestimates the life of thick rigid pavements and that a right-censored survival regression analysis would be more correct. Most of the thicker rigid test sections of the AASHO road test were incorporated into Interstate 80 and received 12 additional years of heavy-truck traffic. A review is provided of a report by the Illinois Department of Transportation (DOT) in which Little and McKenzie reanalyze the AASHO data, including the additional traffic, using the least-squares method of regression analysis. For comparison, the survival regression analysis proposed by Small and Winston is reanalyzed using the additional data collected by Illinois DOT on the rehabilitated AASHO roadway. It was concluded that the Small/Winston analysis significantly underestimated the life of thick rigid pavements. The original AASHO method overestimated the life of thick rigid pavements, but not as significantly as the Small/Winston analysis underestimated it. A proposed revision to the Small/Winston model results in a performance prediction for thick rigid pavements slightly greater than the Little and McKenzie revision to the original AASHO analysis. Because of the lack of distress for the thicker rigid pavements in the Road Test, the Small/Winston survival analysis for the AASHO Road Test rigid test sections is not valid.

The AASHO Road Test was conducted between November 1958 and November 1960 and applied 1.114 million axle passes of each loaded vehicle type on five of six test loops for a total of 10 lanes (*1*). Most of the thicker rigid sections were not significantly distressed and were later incorporated into the construction of Interstate 80. Additional trafficking of these sections was carefully measured and reported by the Illinois Department of Transportation (DOT), and an analysis of the data was given by Little and McKenzie (*2*).

In their book, *Road Work*, Small and Winston (*3*) state that the original analysis done for the AASHO Road Test was in error. They purport that current techniques of survival analysis show that the fourth power law of equivalent loading should be a third power. Small and Winston believe that this error in the design equation is responsible for rigid Interstate highway pavements lasting, in their estimation, only 13.5 years rather than a typical design life of 20 or 25 years (*4*). On the basis of this assumption, they claim that an $8 billion saving in maintenance costs would be achieved if designers would build the nations' pavements 1 or 2 in. thicker.

The methods and performance equations from the three separate analyses of the data obtained from the AASHO Road Test rigid pavements are compared. The three analyses include (a) the original AASHO analysis, (b) the *Road Work* analysis by Small and Winston (*3*), and (c) the Illinois analysis of additional traffic on AASHO test sections reported by Little and McKenzie (*2*). A fourth analysis is presented using the *Road Work* survival analysis procedure supplemented with the additional traffic data on the rehabilitated AASHO roadway.

W. R. Hudson and T. Dossey, University of Texas at Austin, Suite 6.10, ECJ Hall, Austin, Tex. 78712. M. T. McNerney, Texas Research and Development Foundation, 2602 Dellana Lane, Austin, Tex. 78746.

AASHO ROAD TEST ANALYSIS

The original analysis of the AASHO Road Test, which led to the *AASHTO Interim Design Guide*, is briefly reviewed in this section. Significant aspects and differences relating to the number of test sections used, type of numerical analysis, and number of traffic and serviceability data sets of each test section are highlighted.

The AASHO Road Test consisted of six test loops of rigid and flexible pavements. Rigid pavement thicknesses of 12.5, 11, 9.5, 8, 6.5, 5, 3.5, and 2.5 in. were tested. Axle loads consisted of 2-, 6-, 12-, 18-, 22.4-, and 30-kip single axles and 24-, 32-, 40-, and 48-kip tandem axles. Figure 1 shows a tabular listing of the rigid test sections. The maximum number of axle repetitions applied was 1,113,800 over a 2-year period. A total of 264 Design 1 rigid pavement test sections were loaded during the test. Variations were made in subbase thickness and type reinforcement. The thinnest rigid pavement test sections that were loaded by 18-kip single axles were 5 in. thick.

The original analysis of the Road Test data was comprehensive and incorporated several different mathematical models. The analysis considered all test sections, including the cases where thinner sections outlasted thicker sections in the same loop and lane. The traffic loading was continued to a terminal serviceability index of 1.5 to ensure that the data would represent the complete serviceability curve. Many of the test sections never reached a present serviceability index (PSI) of 1.5, and several had not reached a PSI of 2.5 at the conclusion of the Road Test. At least five different PSI readings for each test section were included in the numerical analysis, even if that section had not yet reached 2.5 or 1.5 PSI.

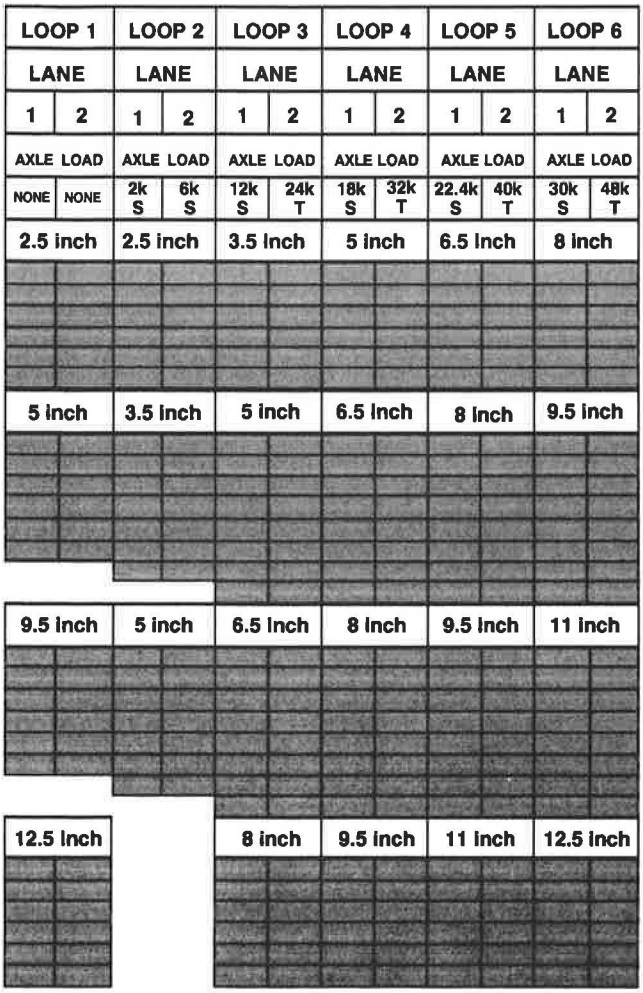


FIGURE 1 AASHO Road Test: Design 1, rigid test sections.

Of the methods tested, the one that yielded the best fit at the Road Test was a regression analysis using least squares.

The general form of the original Road Test performance equation is as follows:

$$\log W = \log \rho + \frac{G}{\beta}$$

where

W = number of load applications,
ρ and β = complex functions of design and load, and
G = serviceability loss term.

For rigid pavements, the expressions for ρ, β, and G are

$$\rho = \frac{10^{5.85}(D_2 + 1)^{7.35} L_2^{3.28}}{(L_1 + L_2)^{4.62}}$$

$$\beta = 1 + \frac{3.63(L_1 + L_2)^{5.20}}{(D_2 + 1)^{8.46} L_2^{3.52}}$$

$$G = \log \frac{4.5 - P_t}{3}$$

where

L_1 = axle load (kips),
L_2 = 1 for single axles and 2 for tandem axles,
D_2 = slab thickness (in.), and
P_t = terminal serviceability index.

For the 18-kip single axle load, when $L_1 = 18$ and $L_2 = 1$, the log ρ and β terms reduce to

$$\log \rho = -0.058 + 7.35 \log(D_2 + 1)$$

$$\beta = 1 + [10^{7.209} \times (D + 1)^{-8.46}]$$

ROAD WORK ANALYSIS OF AASHO ROAD TEST

In *Road Work*, Small and Winston (*3*) reanalyzed the original AASHO Road Test data using modern analytical techniques. The model they used to analyze the data was described as the Tobit model—an econometric model developed in the early 1950s by James Tobin (*5*) as a tool for the economic analysis of household expenditures. The Tobit model assumes that some type of left-censoring mechanism is present when estimating an equation from data. The term "left-censored data" refers to a situation in which data may be lost before the event or time occurs. In Tobin's example, the amount of money people spend on luxury items is expected to be zero until some lower limit of income is reached. At this lower limit, which could be different for each household, the amount spent is some function of total income.

The model is functionally the same as a lifetime, or right-censored, survival analysis. The lifetime model is frequently used when the data—for example, laboratory mice—have only two possible options: (a) the mice die at some time during the experiment or (b) they survive the entire length of the experiment. Right-censored data mean that some of the possible events may not have occurred when data collection is terminated.

The major distinction between the lifetime and Tobit analyses is that incomplete observations in pavement studies are considered to be right- rather than left-censored. At the AASHO Road Test, it was not possible to allow every section to receive sufficient loadings to reach a 1.5 PSI. For 196 of the 264 rigid pavement sections, only partial information concerning the actual number of applied loads to failure was available after 2 years. However, that those sections survived a number of given loadings and reached a certain PSI level is useful information that should be efficiently used. In the *Road Work* analysis, any pavement section that had not yet reached a 2.5 serviceability index was considered a survivor and was therefore not included in the analysis in the same manner as other sections. Thus, the serviceability index of that test section was censored.

The Tobit, or survival, regression analysis is currently available in the commercial software Statistical Analysis System (SAS) as the LIFEREG procedure (*6*). The *Road Work* analysis was also completed using the commercial software SHAZAM (*4*).

The *Road Work* rigid pavement data were obtained from Small in order to rerun his analysis. The data consisted of

only 73 uncensored observations out of the 264 test sections of the AASHO road test. Figure 2 is a graphical representation of these 73 observations. Each data point is a recording of the number of axle repetitions when each section reached a 2.5 serviceability index. A close inspection of the 73 observations reveals that only 3 of the 44 test sections of 9.5-in. thickness were included and that none of the 11- or 12.5-in. thick test sections were included because they did not fail. If the PSI is greater than 2.5, whether it be 2.6 or 4.5 PSI (nearly new condition), no PSI value is given to any of these test sections in the *Road Work* analysis. The mean thickness of the observed test sections in the *Road Work* analysis was only 5.8 in. A tabular listing of the subtotal of test sections with respect to thickness is presented in Table 1.

The data provided by Small were checked, and his analysis was duplicated using the LIFEREG procedure. This procedure achieved exactly the same results reported in *Road Work*. The resulting equation is logarithmic, and rough comparisons can be made if the AASHO equation is converted from base 10 logarithms to natural logarithms. In Table 2, a comparison is presented showing the Small/Winston results and this duplication. The most significant difference is the coefficient of the load term (A_1), which is only 3.24 in the Small/Winston term and 4.62 in the AASHO term. The significance of these equations for a typical 10-in. rigid pavement is a prediction of 9.3 million equivalent single axle loads (ESALs) for the Small/Winston equation and 28.6 million for the AASHO equation.

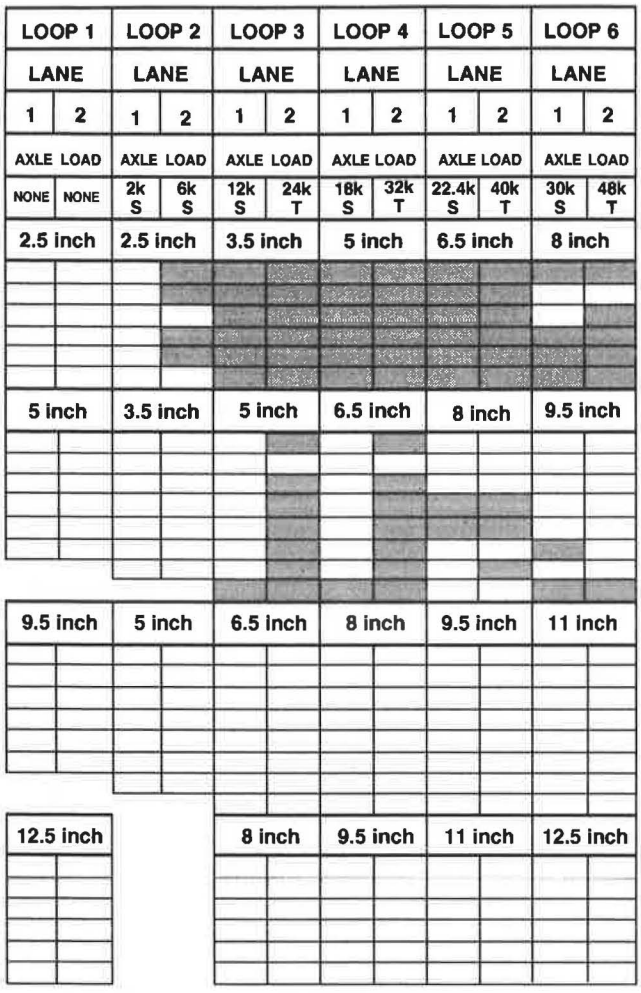


FIGURE 2 AASHO Road Test: rigid test sections with less than 2.5 PSI.

TABLE 1 TEST SECTION DATA USED FOR SMALL/WINSTON MODEL

Pavement Thickness (in.)	Number		
	AASHO Test Sections	Censored	Observed
2.5	12	8	4
3.5	26	14	12
5	42	22	20
6.5	44	24	20
8	56	42	14
9.5	44	41	3
11	28	28	0
12.5	12	12	0
Total	264	191	73

Load coefficient (A_2) = 3.24; standard error = 0.2595; thickness coefficient (A_1) = 5.04; and standard error = 0.3285.

Because the Small/Winston analysis only used PSI data from the three poorest-performing 9.5-in.-thick test sections and censored all 81 other 9.5-, 11-, and 12.5-in.-thick sections, it would seem that extrapolation into these thicker sections would be less accurate than the least-squares method. From a plot of the comparisons in Figure 3 of predicted ESALs for various thicknesses at 2.5 PSI, it is obvious that the two predictions are far apart for thick sections.

ILLINOIS DOT ANALYSIS OF REHABILITATED TEST SECTIONS

After the AASHO Road Test, many thicker rigid test sections remained in excellent condition. The other sections were rehabilitated as new 10-in.-thick rigid test sections constructed to duplicate the original AASHO construction practices. This rehabilitated roadway was incorporated into I-80 to continue the research on this historic road test. For inclusion into the new study of the rehabilitated roadway, the rigid test sections had to be at least 8 in. thick and structurally sound, with no visible signs of deterioration. A few 8-in. sections, most of the 9.5-in. sections, and all of the 11- and 12.5-in. sections were retained as original test sections. The rehabilitated test facility included 84 original Design 1 rigid test sections, 10 original Design 3 rigid test sections, and 74 new 10-in.-thick rigid test sections. All of these were in the eastbound roadway, but only half of each were in the outside lane.

The facility was opened to traffic in November 1962 and initially received an average daily traffic (ADT) of 3,500 veh/day. The traffic consisted of 71 percent passenger cars, 6 percent single-unit trucks, and 23 percent multiple-unit trucks. More than 96 percent of the heavy trucks used the outer lane; therefore, only the outer lane was evaluated. In 1973 the ADT was 15,700. In 1974 the ADT dropped to 14,000 due to the fuel shortage but began to rise when the fuel shortage eased. The annual growth rate of ADT during the first 10 years was a very high 22 percent.

TABLE 2 COMPARISON OF PERFORMANCE EQUATIONS

	A_0	(Std Error)	A_1	(Std Error)	A_2	(Std Error)	A_3	(Std Error)	ESALs Predicted
AASHO	13.53		7.08		4.53		3.17		28.6
Small/Winston	13.505	(0.307)	5.041	(0.329)	3.241	(0.260)	2.270	(0.242)	9.3

$\ln N = A_0 + A_1 \ln (D + 1) - A_2 \ln (L_1 + L_2) + A_3 \ln (L_2)$
where
D = thickness;
L_1 = load in Kips;
L_2 = number of axles.

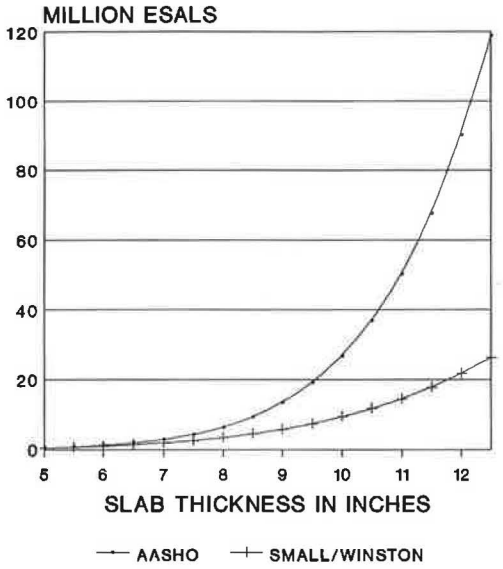


FIGURE 3 Comparison of predicted ESALs.

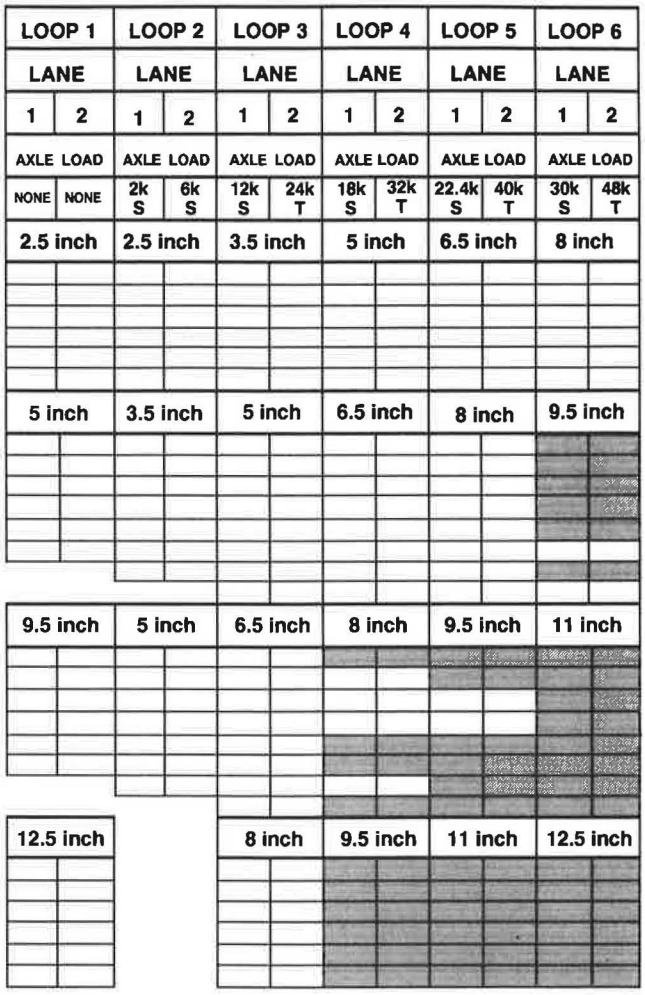


FIGURE 4 AASHO Road Test: rigid test sections included in I-80.

All of the 9.5-, 11-, and 12.5-in. test sections of AASHO Loop 6, Lane 2 (48-kip tandem loading), were retained as original test sections and received 10 million ESALs of additional mixed loading, except for two 9.5-in. test sections (372 and 340). All of the 9.5- and 11-in. test sections of AASHO Loop 5, Lane 2 (40-kip tandem loading), were retained and received 10 million ESALs of additional mixed loading, except two 9.5-in. test sections (526 and 536). All of the 9.5-in. sections of AASHO Loop 4, Lane 2 (32-kip tandem loading), were continued for additional traffic in the outer lane for 12 years. All of the sections retained as original in Loops 4, 5, and 6 that were in Lane 1 (18-, 22.4-, and 30-kip single-axle loading) received additional traffic in the experiment but were incorporated into I-80 as the inside lane, and therefore received much less heavy traffic. Figure 4 shows a listing of the AASHO test sections that received traffic in the Illinois study.

The results of the additional trafficking of these original test sections were published by Illinois DOT (*2*). Analysis of the data by Little and McKenzie concluded that the Road Test performance equation failed to predict the serviceability trend for the 11- and 12.5-in. rigid pavement sections with the same precision that was achieved for the 8- and 9.5-in. pavements. They concluded that the Road Test performance equation fit the 9.5-in. rigid pavement data well. Because the 11- and 12.5-in. rigid pavements showed so little change in serviceability index during the AASHO Road Test, Little and McKenzie theorized that the road test equation extrapolation in this area might be improved by further analysis.

Little and McKenzie (*2*) performed an analysis of the improved data on the additional trafficking of the test sections using the same least-squares analysis as was originally performed. Being careful to take data from five different traffic levels (usually 1968, 1969, 1971, 1972, and 1974), the analysis was performed and the following revised performance equation was reported (assuming beta equal to 1):

$$\log W_{18} = 2.724 + 4.50 \log(D_2 + 1) + G$$

This equation can be compared with the original AASHO equation in the same format:

$$\log W_{18} = -0.058 + 7.35 \log(D_2 + 1) + G$$

PROJECTION OF SMALL/WINSTON ANALYSIS WITH ILLINOIS DOT DATA

Because Small and Winston (*3*) reference the Illinois DOT data to support their findings, it was assumed that their analysis would concur with the findings of Little and McKenzie (*2*). The data from the Illinois study were applied to the Small/Winston method of survival analysis, and the results were surprising.

The Small/Winston analysis used only three 9.5-in. test sections (339, 340, and 371). All 41 remaining 9.5-in. test sections were censored at 1.114 million axle passes. However, 18 of the original 9.5-in. test sections and several 11- and 12.5-in. test sections could now be included into the analysis with additional traffic. By rerunning the Small/Winston analysis with this additional traffic data from the Illinois study, new coefficients of the Small/Winston performance equation could be computed.

Illinois DOT was contacted, but the exact data used in the study were not available other than those tabulated in the report. The Illinois report (*2*) states that only two 9.5-in. sections reached a 2.5 PSI after 12 years of traffic. The Small/Winston data were run with one of the Loop 4 sections and one of the Loop 6 sections as observations assuming to reach 2.5 PSI at 9.6 and 18.6 million ESALs; the 16 remaining 9.5-in. pavements in the high traffic lane were censored at their respective ESALs.

To further define the equation, the 11- and 12.5-in. pavements were added into the analysis using the same procedure. The six 12.5-in. pavements in Loop 6, Lane 2, were censored at 18.6 million ESALs. The 11-in. pavements in Loop 5, Lane 2, were censored at 14 million ESALs, and the 11-in. pavements in Loop 6, Lane 2, were censored at 18.6 million ESALs. The analysis was run with the sections shown in Figure 5, and the results are presented in Table 3. Table 4 presents a comparison of the AASHO, Small/Winston, and revised Small/Winston performance equations.

To prevent possible criticism of the use of mixed ESAL traffic as calculated by AASHTO, and to test the sensitivity of the findings, the analysis was run with different assumptions of traffic. All mixed traffic was assumed to be 32-kip tandem axle loads from typical five-axle tractor-trailer combinations, and the number of passes that would have been the AASHTO equivalent of 10 million ESALs was backcalculated. It was then possible to substitute the additional traffic into the LIFEREG procedure as 32-kip tandem axle loads rather than 18-kip single axle equivalents to see if this change would make a significant difference. The LIFEREG procedure was then rerun, with very little change in results:

- Load coefficient (A_2) = 4.35, standard error = 0.212; and
- Thickness coefficient (A_1) = 6.52, standard error = 0.242.

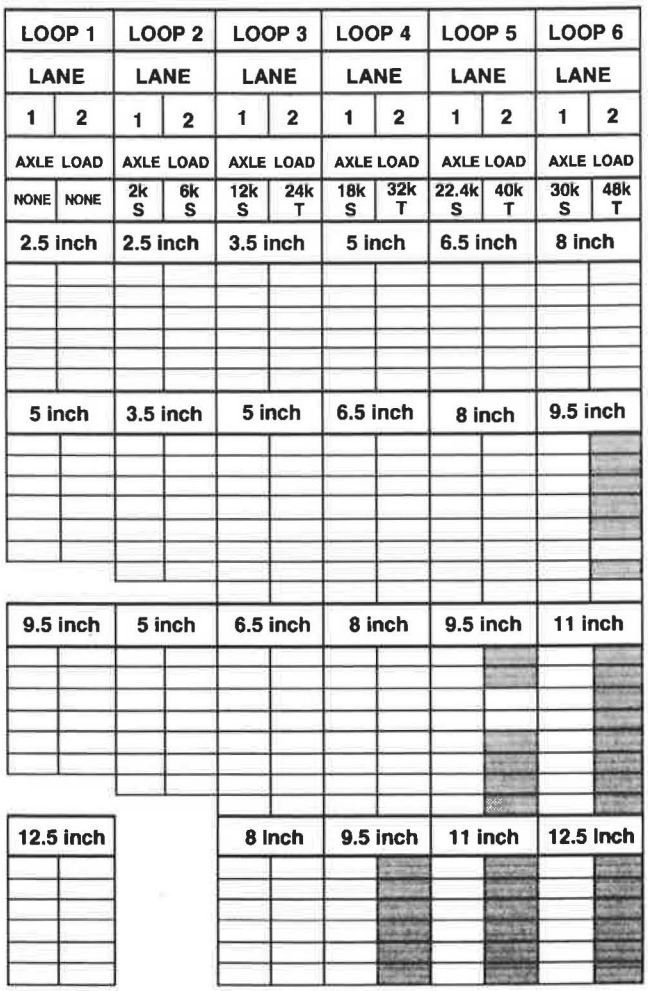


FIGURE 5 AASHO Road Test: rigid test sections added in revised analysis.

The survival analysis method uses only one PSI point in time for each observed test section versus the five minimum PSI points of the AASHO least-squares analysis. The large error in the *Road Work* model exists because so few thick rigid sections were uncensored (only 3 at 9.5 in. or thicker); the least-squares analysis at least attempts to extrapolate when the other 81 (9.5 in. or thicker) test sections will reach terminal serviceability. The censored test sections in the survival analysis have no PSI value; therefore, the analysis cannot estimate whether the censored test section is at 2.6 PSI or still nearly smooth at 4.5 or greater PSI. As more traffic was recorded, fewer test sections were censored and many others were censored at higher traffic levels, thus increasing the accuracy.

COMPARISON OF AASHTO, ILLINOIS DOT, AND SMALL/WINSTON ANALYSES

Figure 6 shows a graphical depiction of the AASHO, Illinois DOT, Small/Winston, and revised Small/Winston performance equations. Because the Small/Winston performance equations only predict loading at 2.5 PSI and no beta term

TABLE 3 DISTRIBUTION OF TEST SECTIONS BY THICKNESS

PAVEMENT THICKNESS	CENSORED @ 1.114 MILLION AXLE PASSES	CENSORED @ 11.6 MILLION ESALS	CENSORED @ 14 MILLION ESALS	CENSORED @ 18.6 MILLION ESALS	OBSERVED
2.5	8				4
3.5	14				12
5.0	22				20
6.5	24				20
8.0	42				14
9.5	23	5	6	5	5
11.0	14		6	8	0
12.5	6			6	0
TOTALS:	153	5	12	19	75

RESULTS:

LOAD COEFFICIENT A_2 = 4.46 STANDARD ERROR = 0.247

THICKNESS COEFFICIENT A_1 = 6.72 STANDARD ERROR = 0.277

TABLE 4 COMPARISON OF PERFORMANCE EQUATIONS

	A_0	(Std Error)	A_1	(Std Error)	A_2	(Std Error)	A_3	(Std Error)	Predicted (Millions)
AASHO	13.53		7.08		4.53		3.17		28.6
Small/Winston	13.51	(0.307)	5.04	(0.329)	3.24	(0.260)	2.27	(0.242)	9.3
Revised Small/Winston	14.02	(0.379)	6.72	(0.277)	4.46	(0.247)	3.09	(0.257)	24.1

$$\ln N = A_0 + A_1 \ln (D + 1) - A_2 \ln (L_1 + L_2) + A_3 \ln (L_2)$$

where

D = thickness;

L_1 = load in Kips;

L_2 = number of axles.

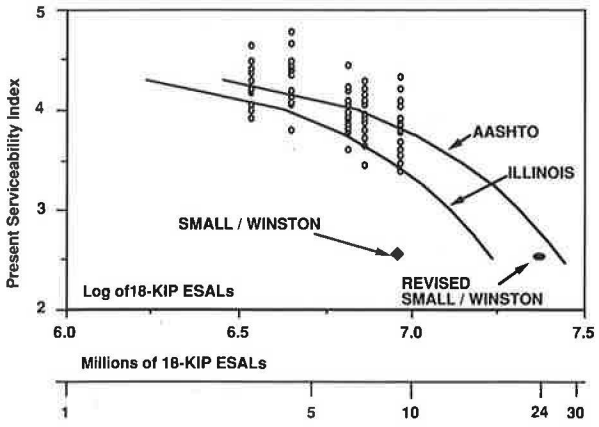


FIGURE 6 Performance of 10-in. rigid sections of rehabilitated AASHO roadway.

exists to convert to a terminal serviceability index other than 2.5, they are graphically represented only as a point.

When compared with the new 10-in. rigid test sections of the rehabilitated Illinois roadway, it is clear that the original Small/Winston analysis significantly underestimates the life of 10-in. rigid pavements (see Figure 6). The revised Small/Winston analysis is very close to the AASHO and Illinois performance equations for 2.5 PSI. The Illinois performance equation is a little more conservative in its prediction of pavement life than the AASHO equation because it underestimates most of the observed test sections. The AASHO equation seems to predict the average of the performance of the test sections with nearly half underestimated and half overestimated.

Figure 7 shows a graphical depiction of the ESAL prediction of the four different performance equations for a terminal serviceability index of 2.5 over a range of thickness. This

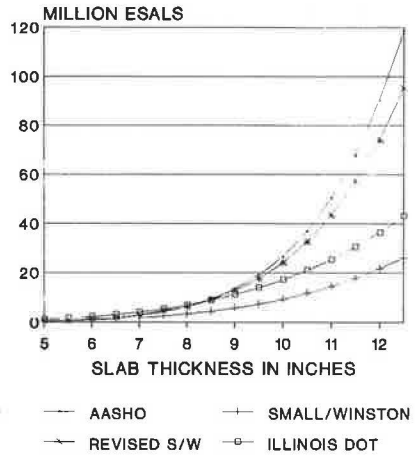


FIGURE 7 Comparison of predicted ESALs.

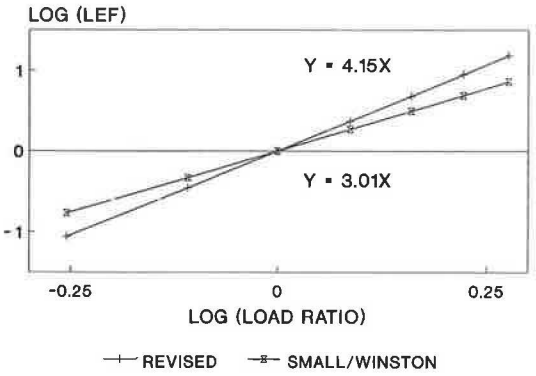


FIGURE 8 Determination of load factor.

figure shows that the revised Small/Winston model predicts an even greater number of ESALs than the Illinois study for pavement thickness greater than 9 in.

LOAD POWER FACTOR

The fourth power law commonly referred to by engineers is more properly called a load power factor. The load power factor gives a measure of the sensitivity of load equivalence factor (LEF) to load. It is defined as the log of LEF divided by the log of the load ratio (R), where R is the ratio of the load divided by the reference load—usually 18 kips.

LEFs estimate the amount of damage done by a given load compared with the damage from a standard 18-kip axle. The *AASHTO Interim Design Guide* gives a table of LEFs for a wide range of loads, axles, and pavement thicknesses. Similar LEFs can be calculated using the Small/Winston model by dividing the number of predicted 18-kip axle passes to failure by the predicted axle passes for the nonstandard load; the results are different from those of AASHTO.

The load power factor given by AASHTO is approximately 4.3. Using the above method, Figure 8 shows the load power factor to be 3.01 for the Small/Winston model and 4.05 for the revised Small/Winston model.

CONCLUSIONS

1. The AASHTO performance equation overestimates the prediction of traffic for thicknesses greater than 9.5 in.
2. The Small/Winston analysis of the AASHO Road Test data provides a poor prediction of the serviceability of thick rigid pavements and severely underestimates the lifetimes of rigid pavements greater than 8.0 in. in thickness.
3. The Small/Winston method of analysis is excellent if sufficient data for thick rigid pavements are used. The revision to the Small/Winston performance equation that was based on additional traffic data for the original AASHO thick rigid test sections is an excellent analytical procedure.
4. The revised Small/Winston performance equation gives even higher predictions of 18-kip ESAL loads than does the original AASHO performance equation revised by Little and McKenzie when both used the data of additional trafficking of the thick rigid test sections.
5. The load power factor for equivalent loading is not a third power as claimed in the *Road Work* analysis but is at least a fourth power, as confirmed by the revised Small/Winston model.

REFERENCES

1. *Special Report 61E: The AASHO Road Test, Report 5, Pavement Research*. HRB, National Research Council, Washington, D.C., 1962.
2. R. J. Little and L. J. McKenzie. *Performance of Pavement Test Sections in the AASHO Test Road*. Physical Research Report 76. FHWA-IL-PR-76. Illinois Department of Transportation; FHWA, U.S. Department of Transportation, 1977.
3. K. Small, C. Winston, and C. Evans. *Road Work: A New Pricing and Investment Policy*. The Brookings Institution, Washington, D.C., 1989.
4. K. Small and C. Winston. Optimal Highway Durability. *American Economic Review*, Vol. 78, June 1988, pp. 560–569.
5. J. Tobin. *Estimation of Relationships for Limited Dependent Variables*.
6. *SAS User's Guide: Statistics, Version 5 Edition*. SAS Institute, Cary, N.C., 1985.

Publication of this paper sponsored by Committee on Rigid Pavement Design.

Behavior of a Rigid Pavement Under Moving Dynamic Loads

MUHAMMAD A. NASIM, STEVEN M. KARAMIHAS, THOMAS D. GILLESPIE, WILL HANSEN, AND DAVID CEBON

Computer programs for calculating strain histories in rigid pavements under heavy-truck traffic have been developed. A finite-element structural model, ILLI-SLAB, was modified to generate influence functions, which are combined with the dynamic loads under the wheels of a truck to predict the strain time histories at points of interest in the pavement. Using experimental measurements of pavement response, it is demonstrated that these programs are capable of predicting strains in a rigid pavement when the truck dynamic loads and pavement properties are known. Variations in truck speed cause some variations in strain not replicated by the pavement model, which has no speed-dependent effects. Behavior in the vicinity of a pavement crack is difficult to predict because of the unknown load transfer properties of the crack, the inconsistent load transfer performance from test to test, and an apparent but unexplained sensitivity of load transfer performance to truck travel speed.

Pavements deteriorate because of many factors, one of these being the moving dynamic loads of heavy vehicles. Rigid pavement structures are traditionally analyzed by examining the stress and strain responses in the vicinity of a static load imposed on the surface of a plate supported by an elastic foundation (*1–3*). The analyses have been extended by consideration of nonlinear foundation models (*4*) and, to a limited extent, inclusion of dynamic axle loads (*5*). Few rigid pavement models have been validated by comparison with field experiments. Although static analysis provides a systematic method to quantify the load-bearing properties of a pavement structure, it does not lend itself to analysis of the cyclic stresses and strains caused by the moving dynamic loads of a passing truck. At best the static analysis methods only allow static responses from the analytical computations to be compared with experimental measurements. In the absence of a developed methodology for computing localized response to a passing truck, the analyst is hindered in studying the mechanics of the truck loading and pavement response process.

In NCHRP Project 1-25(1) (*6*), the interaction of trucks and pavements is being investigated by an analytical approach. The analytical tools that have been developed in the conduct of this work provide an opportunity for the first time to compare theoretical predictions of strain time histories by rigid pavement models with experimental measurements. The methodology used and the agreement that can be obtained with experimental measurements are described in the following paragraphs.

M. A. Nasim and W. Hansen, Department of Civil Engineering, The University of Michigan, GG Brown Building, Ann Arbor, Mich. 48109. S. M. Karamihas and T. D. Gillespie, The University of Michigan Transportation Research Institute, 2901 Baxter Road, Ann Arbor, Mich. 48109. D. Cebon, Department of Mechanical Engineering, Cambridge University Engineering Department, Cambridge, CB2 1PZ, England.

RIGID PAVEMENT MODEL

The most commonly accepted method of modeling rigid pavement structures is with a finite element representation of the slab supported by an elastic base. Numerous models have been developed for this purpose (*3,7–10*), most being functionally similar to the ILLI-SLAB program developed by the University of Illinois (*7*), which was made available for use in this work.

ILLI-SLAB is a static model capable of calculating pavement response at any location as a consequence of a single-point load defined by a pressure applied to a contact area. The input to ILLI-SLAB is a parameter list describing the pavement design, the finite element mesh to be used, and the load and its application point. The pavement design parameters are thickness of slab and subbase (if any), elastic modulus of the slab and subbase, modulus of subgrade reaction, and joint information (such as load transfer devices and width of joints). Dowels are described in terms of material properties and dimensional information. Special attention is given to joints allowing treatment in four ways: doweled joints, joints with aggregate interlock, joints with dowels and aggregate interlock, and free joints. For doweled joints, torsion, moment, and shear effects of the dowel bars can be selectively considered.

The finite element mesh is described by the coordinates of a rectangular grid of nodes. Up to 10 slabs can be modeled in the longitudinal direction, but this procedure requires considerable computer memory. It is usually necessary to model at least three slabs with two joints to properly represent end effects. The load is defined by a pressure acting over a rectangular area on the pavement slab. The program calculates the stresses and deflections at each node of the finite element mesh. It generates a printed output of the response at all points selected by the user.

In order to calculate the pavement response to a load moving along the surface, an approach that incorporates influence functions can be used. Because the load from a truck wheel moves along a wheelpath, it is sufficient to know how the stress or strain response at a point of interest is influenced by a load applied anywhere on the wheelpath. This relationship between applied load and the response at a point of interest

is called an influence function. The influence function is defined as follows:

$$I_{ij} = \frac{R_j}{L_i} \quad (1)$$

where

I_{ij} = influence function for Point j caused by a load at Point i;
R_j = response (stress, strain, or deflection) at Point j; and
L_i = load at Point i.

Because the pavement models are linear, the influence function is not load dependent, and the response to loading from the multiple wheels of a truck can be determined by superposition of the responses to individual wheels.

The ILLI-SLAB model was modified to calculate influence functions by adding a subroutine that runs the model sequentially with a unit load applied at each point along a defined wheelpath. In the modified form the program saves the response at every node in a file, with separate files for each load position. Names are automatically assigned to each file using a common prefix and sequential numbering. At the completion of the run, the files are reprocessed to obtain the influence function for all selected node positions. This procedure is accomplished by extracting the response for the point of interest from the file for each load position and saving it in an influence function file for that point. In addition, the program performs certain housekeeping functions, such as maintaining a record of file identifications and the load and response positions.

The modified version of ILLI-SLAB can be run in desktop computer environments but requires at least 8 megabytes of random access memory (RAM). The computation time, of course, depends directly on the finite element mesh size and the number of load positions along the road. (For example, a 40-ft slab with a 3-in. node interval takes about 1 min 20 sec of computation time per load position on a Macintosh IIci computer.) Although computation time may be lengthy, once the calculations have been completed for a given pavement design, the output can be stored on disk and the calculations need not be repeated. The influence functions can then be used to determine the response to any arbitrary set of dynamic wheel loads.

A typical influence function for stress in the longitudinal direction at a point on the bottom of a 40-ft × 12-ft × 9.5-in. slab near its midpoint is shown in Figure 1. The pavement response to a moving load is readily seen in the influence function. As a tire approaches, compressive stress begins to build but changes sharply to a much larger tensile stress when the tire is directly above the point. The reverse pattern is observed as the tire departs from the point of interest. The overall area in which the function is nonzero is the deflection basin. The influence functions for all regions in the interior of the slab are similar to that shown in the figure.

The influence functions of points near joints, cracks, or free ends may have much different characteristics. A typical influence function for a point near a crack or joint is shown in Figure 2. Influence functions of these forms can be used in analyzing pavement response due to moving dynamic vehicle loads.

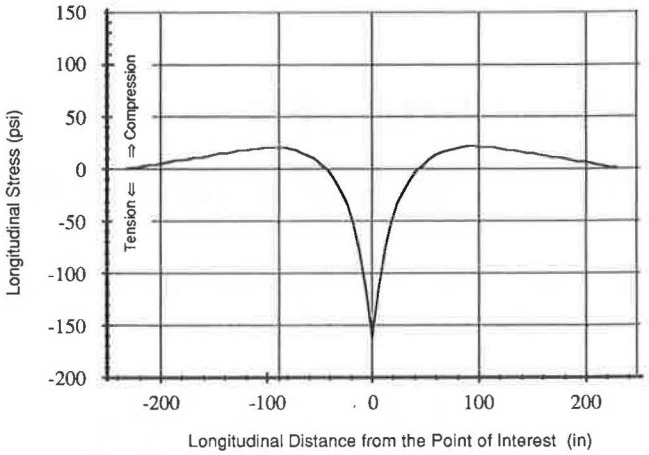


FIGURE 1 Typical theoretical influence function for longitudinal stress at bottom surface in mid-region of a slab.

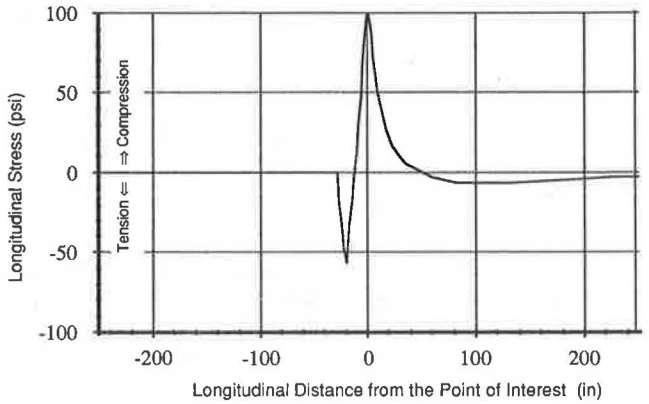


FIGURE 2 Theoretical influence function for response at top of the slab near a crack.

COMBINATION OF LOADS WITH INFLUENCE FUNCTIONS

Once the influence functions are obtained, they are combined with records of truck dynamic wheel forces to produce a time history of the pavement response at the point of interest. The process is one in which the influence function is combined with dynamic load histories for all wheels of the truck. For every time step, the position of each wheel on the road surface is determined along with its instantaneous load. The response in the pavement is then compared for the loads from all the wheels at their respective positions according to the following equation:

$$R_j(t) = \sum_{i=1}^{n} I_{ij} L_i(t) \quad (2)$$

where

$R_j(t)$ = response at Point j at time t,
$L_i(t)$ = load at Point i at time t, and
n = number of wheels on the truck.

Repeating this process for every time step as the truck passes in the vicinity of the point of interest produces the stress or strain time history for that point. Calculating the response in this manner is only valid when the pavement response is proportional to the applied load, and it neglects any dependency on inertia or damping of the pavement.

The program RIGID COMBINE was written to perform the combination process for rigid pavements. The program is configured to accept dynamic wheel loads from any source, providing they are in a standard format. Thus, it can be used to predict pavement response either from records of wheel loads measured on a truck or from an analytical model of vehicle dynamics.

The combination is performed by selecting a starting point for the truck at which the leading tire is sufficiently distant from the point of interest that the influence function is zero. The truck is moved along in a series of discrete time steps, and for each step the aggregate response is computed at the point of interest from the combined influence of all the truck tires. The procedure is as follows:

1. Find the position of each tire relative to the point of interest,
2. Look up the value of the influence function for a unit load at the position of each tire,
3. Look up the dynamic load that each tire is exerting on the road at this instant,
4. Scale the influence of each tire by the dynamic load to get the component of response caused by that tire at the point of interest, and
5. Sum up the response due to all the tires.

This sum is the response at the point of interest to all wheels of the truck for the particular time step. To get a complete time history of the response, the computation is repeated for a series of time steps selected to be small enough to reflect the rapid variations in dynamic wheel loads and the rapidly changing position of the wheels on the slab. Generally, time steps corresponding to about 3 in. of truck movement along the slab are necessary. Once the influence functions and truck dynamic loads are determined, calculation of road response using the method previously described can be carried out for the whole slab on a desktop computer in under a minute.

The output of the combination is a time record of pavement response due to vehicle dynamic wheel loadings. An example of a calculated response derived from measured truck dynamic wheel loads is shown in Figure 3. The figure shows the stress response in the longitudinal direction at a point on the bottom surface of a 40-ft × 12-ft × 9.5-in. slab, at a location 29 ft from the upstream end, on the nearside edge, when traversed by a three-axle straight truck. The first tensile peak is the response when the steering axle goes over the point of interest; the other two peaks correspond to the two rear axles.

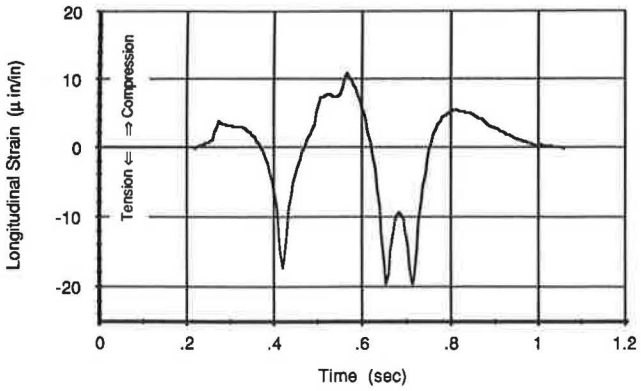


FIGURE 3 Calculated response on bottom surface of a 40 ft × 12 ft × 9.5 in. slab at a location 29 ft from upstream end, on nearside edge.

FIELD EXPERIMENTS

Experiments were conducted on instrumental rigid pavement sections of US-50 near Carlyle, Illinois, using an instrumented truck to acquire data for validating vehicle and pavement models (*6*). The pavement construction was reinforced portland cement concrete slabs, 40 ft in length, laid on a stabilized subbase. The test section was a 9.5-in.-thick slab with a 4-in. subbase of econocrete. The joints were doweled. The pavement was instrumented by the University of Illinois and the Illinois Department of Transportation at the time of construction (*11*). Strain gauges were installed ½ in. from the top and bottom surfaces of the slab according to the layout shown in Figure 4. Odd numbers correspond to gauges on the top surface of the slab and even numbers to gauges on the bottom.

A three-axle straight truck was provided by the PACCAR Technical Center on which the axles were instrumented with strain gauges and accelerometers appropriate for measuring the dynamic forces imposed on the road (*6*). Static tests, as well as dynamic tests over the speed range of 0 to 60 mph, were conducted on various test sections. A typical example of measured dynamic wheel forces is shown in Figure 5.

The University of Illinois provided instrumentation for measuring and recording pavement strains. The combined instrumentation systems were configured to record dynamic loads under each of the truck wheels simultaneously with the pavement strains, using a common marker signal to synchronize the records and to provide precise measurements of the longitudinal position of the vehicle as it passed over the test site. The lateral location of the moving wheels relative to the gauges is important, affecting both the magnitude and shape of the strain histories. Therefore, means were provided in the testing to record the lateral position of the truck wheels.

An example of the measured strain response of Gauge 4 is shown in Figure 6 for a test speed of 50 mph. As the truck front wheel approaches the gauge, a low-level compressive stress builds and then rapidly changes to a much larger tensile spike as the wheel moves over the top of the gauge. When the front wheel leaves the gauge, the stress returns to compression. The approach of the leading tandem axle adds to the compression until the axle arrives at the gauge and again creates a tensile peak. The gap between the leading and trailing tandem axles is large enough that the stress can diminish between the axles but not revert to compression. The third tensile spike occurs as the trailing axle passes over the gauge. As the trailing tandem axle leaves the gauge, the stress reverts to low-level compression, diminishing to zero as the truck departs.

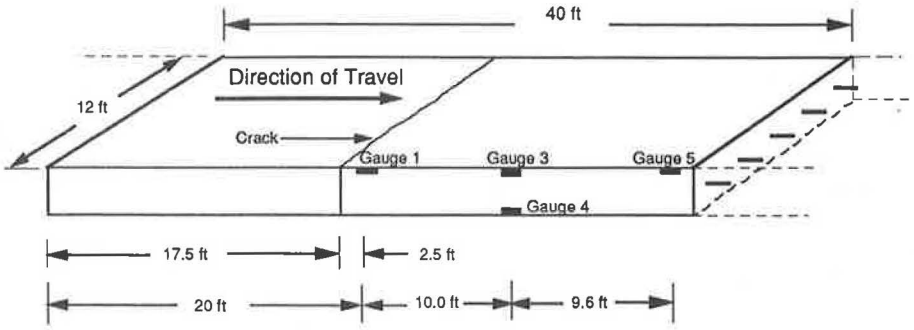


FIGURE 4 Layout of strain gauges on PCC test section near Carlyle, Illinois.

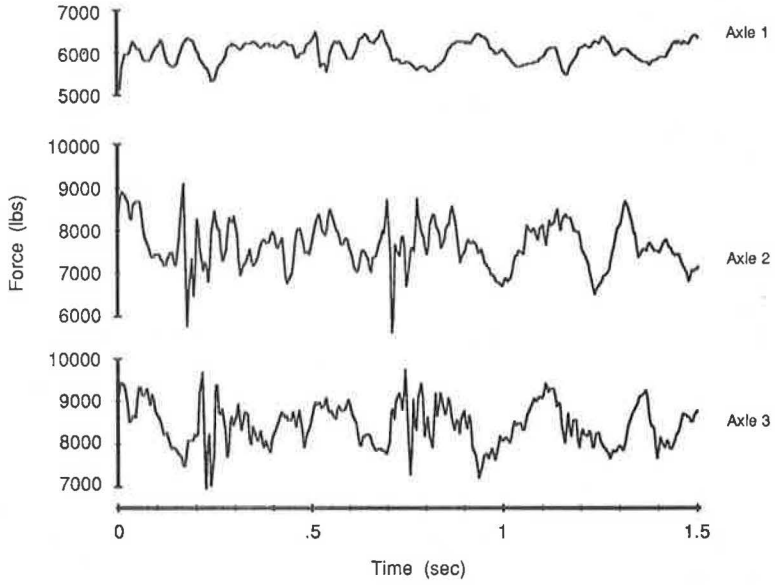


FIGURE 5 Measured dynamic wheel forces on nearside wheels of three-axle test vehicle, 50 mph.

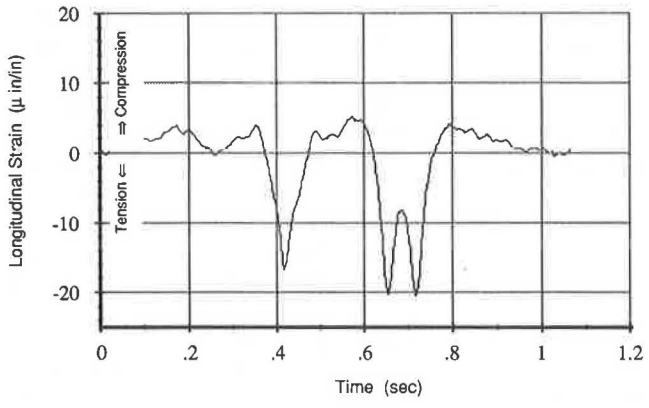


FIGURE 6 Measured response of Gauge 4, 50 mph.

VALIDATION RESULTS

As a step in validation of the rigid pavement model used in NCHRP Project 1–25(1) (*6*), the strains calculated by the pavement model were compared with those experimentally measured by a number of gauges in the test pavement. The dynamic loads generated by the truck were measured concurrently with the pavement responses. These loads were used as input to the pavement model to eliminate errors arising from uncertainties in the truck loading in the comparison. RIGID COMBINE was used to calculate the time histories of the strains in the pavement under the actual truck dynamic load conditions.

Figure 7 compares simulated and measured strains for Gauge 4 for one of the tests. As evidenced by this graph, very good agreement is possible, particularly in prediction of the shape and magnitudes of the tensile strains. In early simulations, the agreement was not as good as that shown in the figure because all the pavement parameters (particularly the subbase modulus) were not known precisely. Recognizing this fact, the pavement parameters were varied within the range of possible uncertainty to pick values that showed the best agreement. The main disparities in Figure 7 occur in prediction of the compressive strains, but because they are generally of low level and are not damaging to the slab, the agreement here is less critical.

Gauge 4 is located in an area of the slab that is distant from any joints or cracks. Near a joint or crack, the behavior of pavement may be markedly different, depending on the load transfer across the discontinuity. If the load transfer characteristics are very good, the response in that region will be

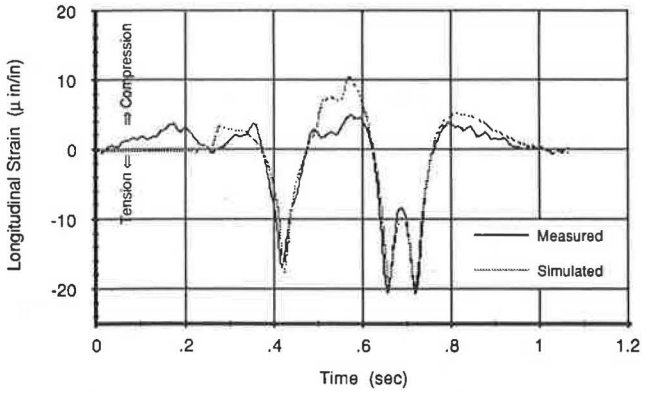


FIGURE 7 Comparison between measured and calculated responses of Gauge 4, 50 mph.

similar to that of a continuous pavement. However, if the load transfer is poor, stress reversals can occur.

The test slab had a full-depth transverse crack 2.5 ft ahead of Gauge 1 resulting from shrinkage early in the life of the pavement. To model the crack, an additional weak joint was introduced in the finite element model at that location in the slab. (The geometry of the slab, crack, and gauges is shown in Figure 4.) The measured and calculated response of Gauge 1 is shown in Figure 8.

Before the front wheel of the truck crosses the crack, Gauge 1 experiences only a low level of tensile strain due to the poor load transfer across the crack (presumably caused by aggregate interlock or some continuity in the reinforcing mat). As the axle advances across the crack, the gauge immediately experiences a large tensile strain, which changes to compression as the wheel reaches the gauge. On its departure, the strain relaxes again to approximately zero.

This pattern is repeated approximately 3 sec later when the leading tandem axle crosses the crack. Initially, the gauge goes into tension, which changes quickly to compression as the axle passes across the gauge. The reduction of the compressive stress as the axle leaves the gauge is accelerated by the approaching load of the trailing tandem axle, 50 in. behind the leading axle. When the trailing axle crosses the crack, its response is superimposed on that of the previous axles. The prediction of the compressive strain as the leading tandem axle crosses the gauge is not very accurate—the error probably being due to the uncertainty about load transfer properties of the crack. The prediction of strain under the influence of the trailing axle is more accurate for this portion of the cycle because there is no longer any load on the upstream side of the crack; therefore, there is no significant load transfer effect to be taken into account. After all axles have passed the gauge, the strain returns to compression and then relaxes to zero in a fairly predictable fashion.

The effectiveness of the load transfer across a crack has a strong influence on the strain cycles produced in the slab in the vicinity of the crack. Figure 9 shows how the predicted strain history at the Gauge 1 position varies with the load transfer effectiveness. With full load transfer (no crack), the top surface experiences a low-level tension broken by compressive strain peaks as the wheels pass over the point of interest. In the case of no load transfer, large tensile strains are experienced as each wheel traverses the crack. For intermediate levels of load transfer, an intermediate response is obtained.

The measured response shown in Figure 8 presents one example of how the test pavement behaved at Gauge 1 under loading from the truck, but, by and large, the load transfer obtained at the crack was inconsistent from test to test. Figure 10 shows the results from Gauge 1 for three repeat tests at a nominal speed of 5 mph on the site. The major features in the strain cycles are repeatable. However, the strains in Region A of Figure 10 (when the leading tandem axle approached the crack) are quite erratic. Comparing the measured response with the predictions in Figure 9, it would appear that the load transfer effectiveness varied significantly between tests—in one case behaving similar to the full load transfer case and in another approaching the no-load transfer case. Examination of the truck dynamic load records indicated that this marked variation from test to test was not due to variations in the dynamic loads on the axles of the truck, which were quite repeatable. That the strain varied erratically in this region in the course of individual tests leads to the conclusion that the load transfer mechanism is inconsistent. Such behavior might be expected from a nonlinearity that is heavily dependent on friction.

Testing at different speeds revealed an additional phenomenon in the pavement that is not fully explained. As the test speed increased, greater levels of tensile strain were observed with the approach of the leading tandem axle. Figure 11 shows

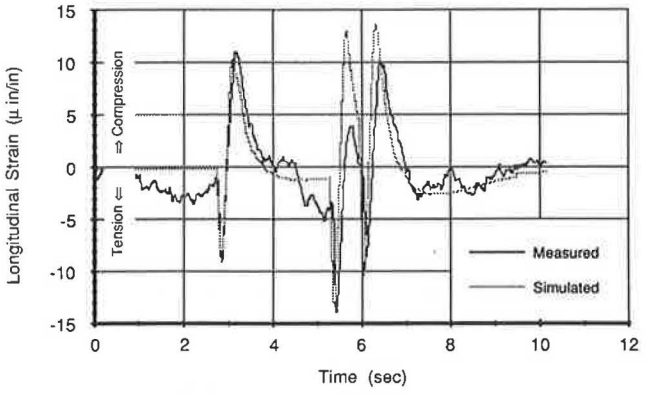


FIGURE 8 Comparison between measured and calculated responses of Gauge 1 (near crack), 5 mph.

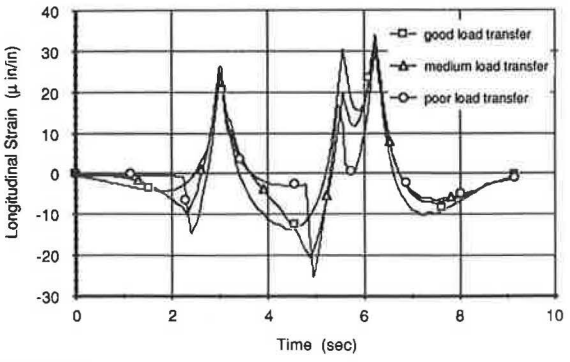


FIGURE 9 Effect of load transfer at a crack on theoretical strain cycles at top surface.

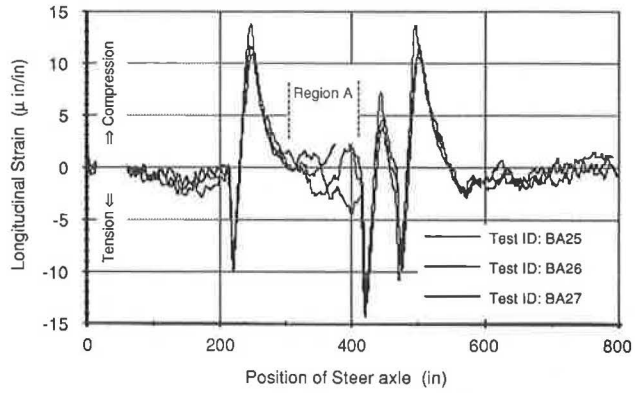


FIGURE 10 Variations in strain histories in repeat tests, Gauge 1, 5 mph.

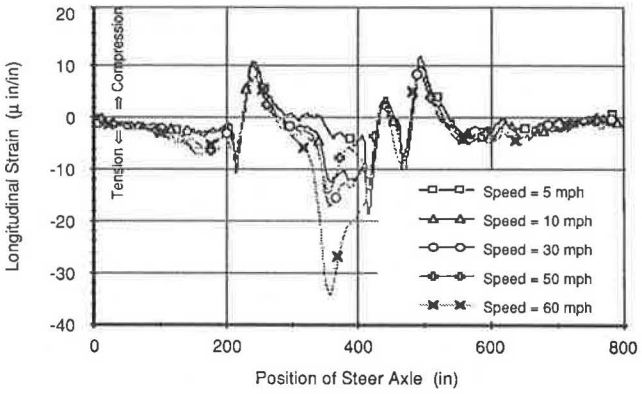


FIGURE 11 Variation in strain histories as a function of vehicle speed in repeat tests at Gauge 1.

example strain records from Gauge 1 at five speeds for this test section. The most remarkable observation is the very high level of tensile strain experienced as the leading tandem approached the crack at high speed. The tensile strain of 15 (μin./in.) seen at 5 mph is indicative of the strain from the weight of the leading tandem axle as it mounts the cantilevered end of the slab. At 60 mph, the tensile cycle reaches more than twice that amplitude. Examination of the axle load records for the truck showed only moderate dynamic variations, not nearly large enough to account for doubling of the strain. Therefore, this effect must be attributed to a phenomenon in the pavement.

Comparison of the maximum tensile strains at the bottom of the slab (as shown in Figure 6) and the tensile strain at the top of the slab near the crack (as shown in Figure 11) reveals that the top surface strains can be 70 percent higher. Simulations with the pavement model indicate that even larger tensile strains can occur on the top of the slab at a distance of 5 ft from the crack. Although traditional analyses assume that the primary failure mode for rigid pavements arises from cracks starting at the bottom of the slab due to the tension of flexural loading, these observations indicate that larger tensile strains can occur on the top surface if a shrinkage crack forms. These same mechanisms would be at work when a joint loses its strength. In either case, a secondary crack is likely to initiate on the top surface several feet from the discontinuity.

In general the experimental data do not show the pavement response increasing with travel speed of the truck in regions distant from the crack. Figure 12 compares the strain measured on Gauge 4 at 5 and 60 mph. The reduction in the magnitude of the strain peaks at 60 mph under the first and last axles is not explained by changes in dynamic axle loads or by lateral tracking errors. This finding was established by computing the pavement response for the measured truck loads and comparing them with the measured response at each speed, using only tests in which the wheeltracks passed within 2 in. of the strain gauge location. Figure 13 shows the ratio of measured to predicted strain at Gauge 4 as a function of speed. Although there is scatter in the data, a significant trend with speed is apparent. The response appears to increase slightly at low speeds and to decrease at higher speeds. Speed dependence has been observed in other experimental studies, particularly for flexible pavements (*12*), although the initial increase with speed observed here is unusual. In Figure 13, the speed dependence is thought to be caused by dynamic motion of the slab due to its significant mass (which is the same order of magnitude as the truck) and damping in the foundation. (These characteristics were not included in the finite element model.) In general, it is difficult to measure

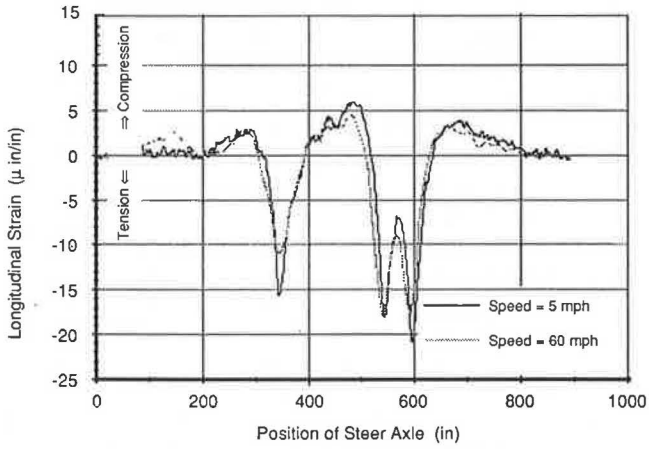


FIGURE 12 Comparison of measured response at 5 and 60 mph, Gauge 4.

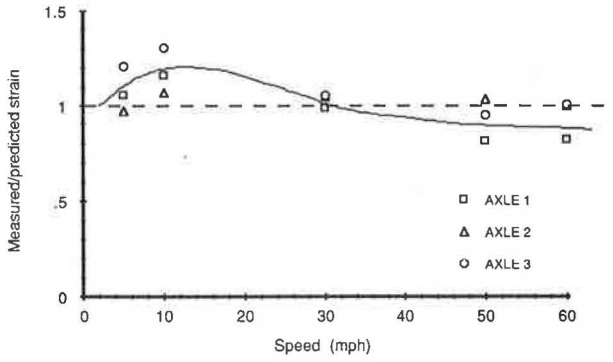


FIGURE 13 Effect of speed on normalized pavement response.

the speed effect accurately because of the influence of dynamic axle loads. This problem has been overcome by including the dynamic loads in the theoretical response calculation, which is a significant benefit of the calculation procedure developed in this study.

Although these data are inconclusive, they are included to show the contrast with pavement behavior near a crack and to illustrate that, under some conditions, rigid pavement response in interior regions of the slab can diminish with increased truck travel speed.

CONCLUSIONS

A method has been developed for calculating the time history of the response of a rigid pavement to moving dynamic loads of trucks. The method, validated with a program of experimental measurements, has provided the following insights into rigid pavement behavior:

- Typical finite element models of rigid pavements, such as ILLI-SLAB, are capable of predicting responses to static loads when pavement properties are known. Coupling these models with programs that allow computation of strain time histories at a point in the pavement (MODIFIED ILLI-SLAB and COMBINE) provides a new and powerful tool for investigating truck-pavement interaction.
- Experimental measurements of strain induced by truck wheel loading show large tensile strains on the top surface of the slab associated with the wheels traversing a crack. This mechanism would encourage development of secondary cracks in the top surface several feet from the location of a shrinkage crack. The theoretical pavement models can predict the qualitative behavior of response in the vicinity of a crack but are limited by the uncertainty and variability of the load transfer properties of the crack.
- The experimental data give some evidence that strains in the interior region of a slab diminish with increasing speed of travel but may increase with speed in the vicinity of the crack. The existing pavement structural models are not able to predict this speed-dependent behavior.

ACKNOWLEDGMENTS

This work was carried out under the sponsorship of NCHRP. The authors wish to thank the University of Illinois, the Illinois Department of Transportation, and the PACCAR Technical Center for their support and cooperation in conduct of the experimental tests.

REFERENCES

1. H. M. Westergaard. Computation of Stresses in Concrete Roads. *HRB Proc.*, Vol. 5, Pt. I, 1926, pp. 90–112.
2. W. R. Hudson and H. Matlock. Analysis of Discontinuous Orthotropic Pavement Slabs Subjected to Combined Loads. In *Highway Research Record 131*, HRB, National Research Council, Washington, D.C., 1966, pp. 1–39.
3. A. M. Ioannides, M. R. Thompson, and E. J. Barenberg. Finite Element Analysis of Slab-on-Grade Using a Variety of Support Models. *Proc., 3rd International Conference on Concrete Pavements Design and Rehabilitation*, Purdue University, West Lafayette, Ind., April 1985, pp. 309–324.
4. A. M. Ioannides and J. P. Donnelly. Three-Dimensional Analysis of Slab on Stress-Dependent Foundation. In *Transportation Research Record 1196*, TRB, National Research Council, Washington, D.C., 1988, pp.72–84.
5. M. J. Markow, J. K. Hedrick, B. D. Brademeyer, and E. Abbo. Analyzing the Interaction Between Dynamic Vehicle Loads and Highway Pavements. In *Transportation Research Record 1196*, TRB, National Research Council, Washington, D.C., 1988, pp. 161–169.
6. D. Cebon and T. D. Gillespie. *Effect of Heavy Vehicle Characteristics on Pavement Response and Performance. Phase II, Model Validation Studies*. NCHRP 1-25(1). UMTRI, June 1989.
7. A. Tabatabaie and E. J. Barenberg. Finite Element Analysis of Jointed or Cracked Concrete Pavements. In *Transportation Research Record 671*, TRB, National Research Council, Washington, D.C., 1978, pp. 11–19.
8. Y. H. Huang and S. T. Wang. Finite Element Analysis of Concrete Slabs and Its Implications for Rigid Pavements. In *Highway Research Record 466*, HRB, National Research Council, Washington, D.C., 1973, pp. 55–69.
9. Y. T. Chou. *Structural Analysis Computer Programs for Rigid Multi-Component Structures with Discontinuities—WESLIQUID and WESLAYER*. Technical Report GL-80. U.S. Army Engineer Waterways Experiment Station, Vicksburg, Miss., Sept. 1980.
10. M. Tia, J. M. Armaghani, C. L. Wu, S. Lei, and K. L. Toye. FEACONS III Computer Program for Analysis of Jointed Concrete Pavements. In *Transportation Research Record 1136*, TRB, National Research Council, Washington, D.C., 1987, pp. 12–22.
11. E. J. Barenberg and D. G. Zollinger. Validation of Pavement Designs Using Instrumented Pavements. Presented at 69th Annual Meeting of the Transportation Research Board, Washington, D.C., 1990.
12. D. Cebon. Vehicle-Generated Road Damage: A Review. *Vehicle System Dynamics*, Vol. 18, 1989, pp. 107–150.

Publication of this paper sponsored by Committee on Rigid Pavement Design.

Development and Application of Randomness Index for Continuously Reinforced Concrete Pavement

YOUNG-CHAN SUH, B. FRANK MCCULLOUGH, AND KENNETH D. HANKINS

Transverse cracks in continuously reinforced concrete (CRC) pavements have various shapes in the field. The randomness of a crack increases the probability of the formation of secondary cracks and consequently increases the possibility of punchouts and Y-cracks, which are the major form of distress in CRC pavements. If the factors affecting the randomness of cracks can be identified and controlled, the pavement life will be increased. So far insufficient attention has been given to the shapes of cracks in concrete pavement design and construction. As a first step toward the study of randomness, a methodology for objectively quantifying the degree of randomness of the crack was developed. The concept for a randomness index, to be used as a tool to represent the degree of randomness, is introduced. The technique used in the derivation of present serviceability index (PSI) was used in developing the randomness index. An example of the application of the randomness index to an experimental study is also presented. It was found from the experimental study that the construction season, coarse aggregate type, and time of crack occurrence significantly affect the randomness of cracks.

Cracks in continuously reinforced concrete (CRC) pavements have various shapes; some of them are fairly straight, and some are winding. Cracks that meander increase the possibility of secondary cracks, which result in punchouts—the major form of distress of CRC pavements. Pavements will perform differently in the long term if there is a big difference in the shapes of their cracks, even though other conditions are the same (see Figure 1). Therefore, the engineer should try to avoid excessively random cracks at the design stage.

The first step in the randomness study was development of a methodology to objectively quantify the degree of randomness of cracks. Using this methodology, the factors influencing the randomness of cracks can be identified. If these factors can be controlled, the randomness of cracks and the resulting distress can be minimized, which should lead to longer pavement life.

The concept of a randomness index (RI) is introduced in the following paragraphs. The technique used in developing the RI is exactly the same as that used in the derivation of the present serviceability index (PSI) (*1*), which has been widely used since the AASHO Road Test. In this technique, subjective ratings of each crack were made by a group of panel members, and a mathematical model was developed by correlating the average rating with several measurable characteristics of the crack so that the rating of any crack can be predicted in the future without any further rating. This prediction is accomplished by inserting the physically measured values into the model. The variables in the model include the length of the crack and the number of concrete blocks formed by cracks, joints, or a pavement edge.

Center for Transportation Research, College of Engineering, The University of Texas at Austin, 3208 Red River, Austin, Tex. 78705-2650.

DEVELOPMENT OF RI

Definitions

A randomness rating (RR) is the mean of the individual randomness ratings made by the panel members. An individual randomness rating is a subjective rating of the randomness of a specific crack by an individual rater.

The RI is a mathematical model for predicting the RR using certain physical measurements of the crack.

Randomness Rating

The randomness of 51 cracks was rated subjectively by a panel of 12 persons (8 from the Center for Transportation Research at The University of Texas at Austin and 4 from the Texas State Department of Highways and Public Transportation) working in the pavement area.

A wide range of cracks, in terms of randomness, was selected for rating from CRC pavements in Houston; some selected cracks were meandering, some fairly straight, and some in between. Some cracks were connected with one or more secondary cracks (i.e., Y-cracks).

Slides of the selected cracks were shown to the raters. The rating scale they used was exactly the same as that used by the panel members of the present serviceability rating (*1*). The scale was as follows:

- 5.0: very good (almost straight cracks),
- 4.0: good,
- 3.0: fair,
- 2.0: poor, and
- 1.0: very poor (very meandering).

The rater was instructed to exclude from consideration all features not related to the shape of the crack itself, such as width of the crack and spalling. Ratings were recorded to the nearest tenth. The acceptability of each crack in terms of the

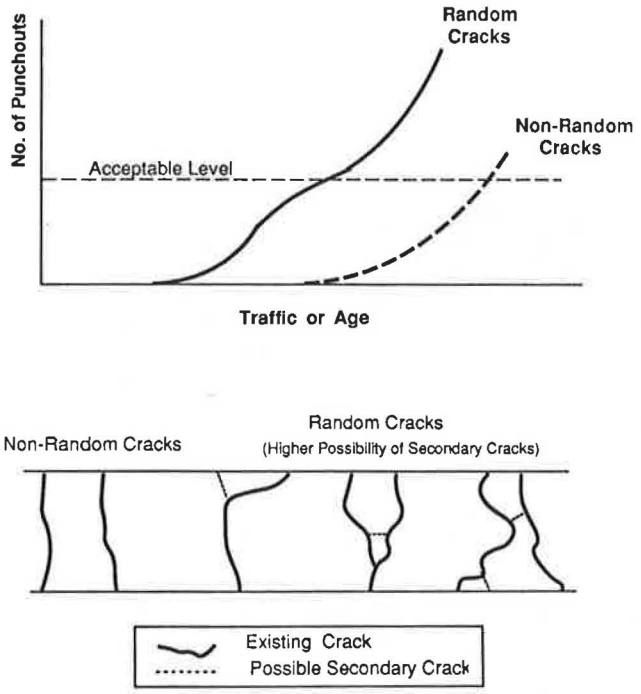


FIGURE 1 Effect of shape of cracks on pavement performance.

shape of the crack was also judged. Raters were told to decide the acceptability by asking themselves, "If I were a pavement designer, would I want to design to avoid this kind of crack in the future?" The form used in the panel rating is shown in Figure 2.

Results of Randomness Rating

The RR value of each crack (the average of the 12 individual ratings) is given in the second column of Table 1. The mean of RRs of the 51 cracks rated was 3.6. The standard deviation of ratings among raters for each crack is given in the third column of the table. The average of the standard deviation was 0.5.

The fourth column of Table 1 represents the panel responses to the acceptability question. For a particular crack, the table shows what percent of the panel judged the shape of the crack to be acceptable. The remaining percent of the panel considered it unacceptable. Figure 3 shows the relationship between acceptability and the corresponding RR values. The curve in Figure 3 indicates that the 50th percentile for acceptability occurs when the RR is about 2.5.

Derivation of Randomness Index

A mathematical model of RI is derived by correlating the RR with objectively measured values taken from the correspond-

CRACK ID	RATING	ACCEPTABLE?
B113		YES NO
B199		YES NO
C5		YES NO
A43		YES NO
A16		YES NO
B75		YES NO
B165		YES NO
C151		YES NO
A13		YES NO
D170		YES NO
D167		YES NO
D17		YES NO
D139		YES NO
B128		YES NO
A7		YES NO
D16		YES NO
A24		YES NO
A9		YES NO
B14		YES NO
D20		YES NO
D13		YES NO
B18		YES NO
C14		YES NO
F16		YES NO
D5		YES NO
G4		YES NO
F5		YES NO
E15		YES NO

RATER

CRACK ID	RATING	ACCEPTABLE?
B10		YES NO
C61		YES NO
H5		YES NO
H17		YES NO
E13		YES NO
B6		YES NO
E5		YES NO
G9		YES NO
E7		YES NO
H4		YES NO
E17		YES NO
G21		YES NO
E10		YES NO
C8		YES NO
D19		YES NO
B15		YES NO
D10		YES NO
A22		YES NO
B4		YES NO
A70		YES NO
A128		YES NO
A143		YES NO
B35		YES NO
		YES NO
		YES NO
		YES NO
		YES NO
		YES NO

FIGURE 2 Individual randomness rating form.

TABLE 1 SUMMARY OF THE DEVELOPMENT OF THE RI

Crack ID	RR	Std. dev of RR among raters	Percent acceptability	R (percent)	N	RI	Residual
B113	2.0	0.6	0	9.4	2	1.7	0.3
B199	2.4	0.6	42	8.7	1	2.1	0.3
C5	3.3	0.9	83	6.9	0	3.2	0.1
A43	3.6	0.7	100	6.5	0	3.2	0.3
A16	3.3	0.8	100	5.8	0	3.3	0.0
B75	2.3	0.4	17	5.8	2	1.9	0.4
B165	3.5	0.8	92	5.8	0	3.3	0.2
C151	2.4	0.7	25	5.1	1	2.4	0.0
A13	3.2	0.8	100	5.0	0	3.4	-0.2
D170	4.2	0.4	100	4.7	0	3.5	0.7
D167	1.8	0.6	0	4.7	2	2.0	-0.2
D17	3.3	0.7	100	4.7	0	3.5	-0.1
D139	3.5	0.6	100	4.7	0	3.5	0.1
B128	3.6	0.5	100	4.3	0	3.5	0.0
A7	3.4	0.7	92	4.3	0	3.5	-0.1
D16	3.5	0.7	100	4.0	0	3.6	-0.1
A24	3.8	0.5	100	3.6	0	3.7	0.1
A9	4.0	0.5	100	3.6	0	3.7	0.3
B14	4.0	0.5	100	3.6	0	3.7	0.4
D20	3.8	0.5	100	3.2	0	3.8	0.1
D13	3.9	0.5	100	3.2	0	3.8	0.2
B18	3.7	0.5	100	2.9	0	3.8	-0.1
C14	3.5	0.5	92	2.9	0	3.8	-0.3
F16	3.9	0.4	100	2.9	0	3.8	0.1
D5	3.7	0.6	100	2.5	0	3.9	-0.2
G4	4.2	0.4	100	2.5	0	3.9	0.2
F5	4.3	0.3	100	2.5	0	3.9	0.4
E15	4.4	0.3	100	2.2	0	4.0	0.3
B10	4.0	0.5	100	2.2	0	4.0	0.0
C61	4.3	0.2	100	2.2	0	4.0	0.2
H5	3.8	0.3	100	1.8	0	4.2	-0.4
H17	4.1	0.4	100	1.8	0	4.2	-0.1
E13	4.2	0.3	100	1.8	0	4.2	0.0
B6	4.1	0.3	100	1.4	0	4.4	-0.2
E5	4.1	0.4	100	1.4	0	4.4	-0.2
G9	4.6	0.4	100	1.1	0	4.5	0.1
E7	4.7	0.2	100	0.4	0	5.0	-0.3
H4	4.4	0.4	100	1.1	0	4.5	-0.1
E17	4.6	0.2	100	1.4	0	4.4	0.3
G21	4.0	0.3	100	2.2	0	4.0	-0.1
E10	3.9	0.3	100	2.2	0	4.0	-0.1
C8	3.8	0.3	100	3.6	0	3.7	0.1
D19	3.8	0.3	100	3.6	0	3.7	0.1
B15	3.5	0.6	100	4.3	0	3.5	-0.1
D10	3.3	0.6	100	4.7	0	3.5	-0.2
A22	3.3	0.5	100	5.8	0	3.3	-0.1
B4	3.2	0.6	90	5.8	0	3.3	-0.2
A70	2.8	0.7	100	6.5	0	3.2	-0.4
A128	2.0	0.6	0	6.9	1	2.2	-0.2
A143	2.9	0.7	100	8.3	0	3.1	-0.2
B35	1.2	0.6	0	13.8	2	1.6	-0.3
Mean	3.6	0.5				3.5	0.0

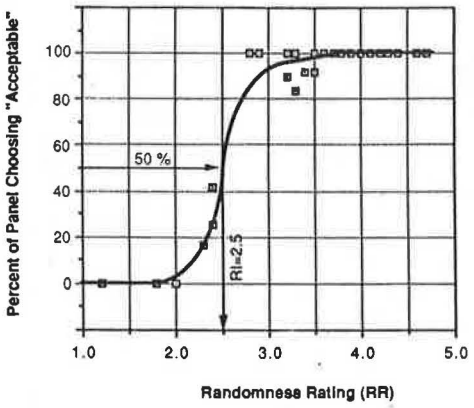


FIGURE 3 Relationship between acceptability and corresponding RR.

ing cracks. The RI model can be used to obtain an estimate of the RR for any crack without the need for any further rating. The RR of a crack is represented by the following:

$$\mathrm{RR} = \mathrm{RI} + E \tag{1}$$

where E is the residual not explained by the mathematical model.

Measured variables include the length of the crack in a lane (L), the lane width (W), and the number of concrete blocks (N) that are associated with the crack and enclosed by secondary cracks, the pavement edge, or joints (see Figure 4). These characteristics are selected because they are simple to measure and because the effects of secondary cracks, such as Y-cracks or punchouts, are reflected by the number of separated concrete blocks (N). The length of the crack was measured using the edge of a roller-tape (see Figure 5). The measurements were performed along the path of the crack, through the longest path when a secondary crack existed (see Figure 4). The number and shape of secondary cracks determine the number of concrete blocks enclosed by cracks. Randomness (R) is represented by the difference between the

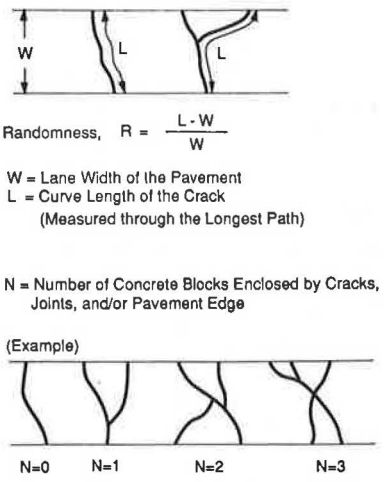


FIGURE 4 R and N in the RI model.



FIGURE 5 Measurement of crack length using edge of roller-tape.

length of the crack and the lane width, divided by the lane width, as follows:

$$R = \frac{L - W}{W} \times 100 \quad \text{in percent} \tag{2}$$

where

R = randomness,
L = curve length of the crack, and
W = lane width.

The R and N values for the rated cracks are given in the fifth and sixth columns of Table 1.

Using the general linear model procedure in the Statistical Analysis System (SAS), a mathematical model for the RI, which is a function of R and N, was developed:

$$\mathrm{RI} = \frac{5.463}{(R + 1)^{0.259}(N + 1)^{0.510}} \tag{3}$$

The R^2 value of this model is 0.9, indicating that 90 percent of variability of RR is explained by the model. Both variables, R and N, are significant, even at the 0.0001 level. The correlation between RI and RR is shown in Figure 6. Figure 7

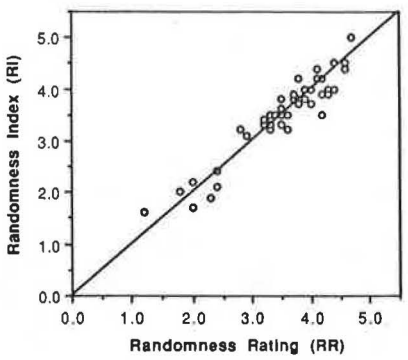


FIGURE 6 Correlation between RI and RR.

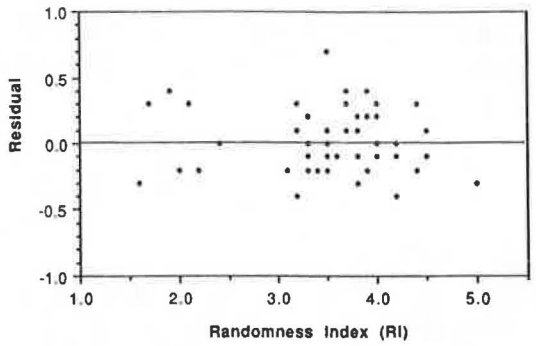


FIGURE 7 Plot of randomly scattered residuals of the RI model.

shows the random scattering of the residuals of the model, indicating that the model fits the data well. The range of the resulting RI values is from 0 to 5.46. The maximum RI value occurs when the crack is a straight line ($R = 0$) without any secondary crack ($N = 0$). In practice, there is no perfectly straight crack in concrete. Therefore, most of the cracks have an RI of less than 5.0. Figures 8–11 show cracks with RI values of 4.8, 3.2, 2.3, and 1.8, respectively.



FIGURE 8 Crack with RI value of 4.8 ($R = 0.7$ percent and $N = 0$).

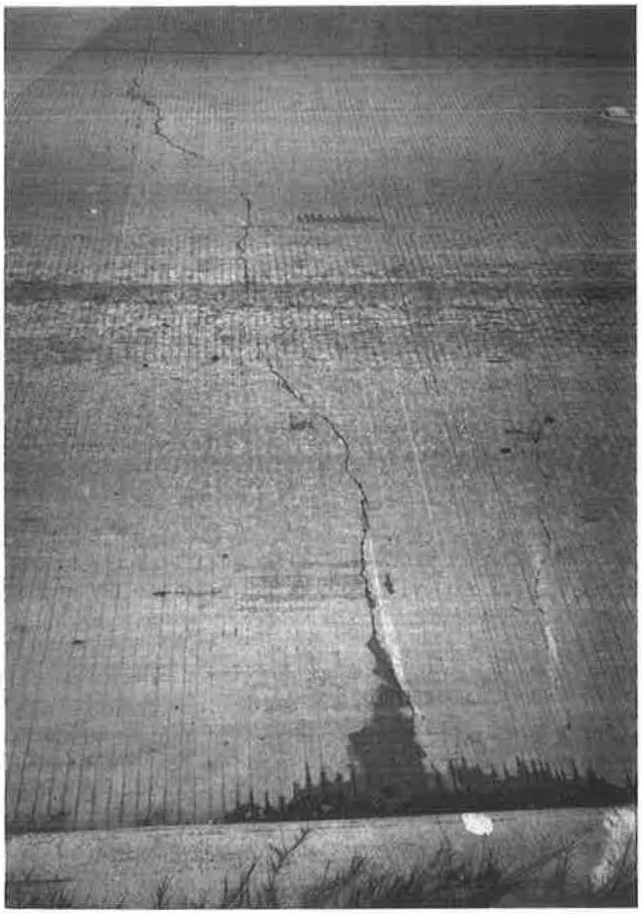


FIGURE 9 Crack with RI value of 3.2 ($R = 6.6$ percent and $N = 0$).

EXAMPLE APPLICATION

The RI developed in the previous sections is applied to the transverse cracks of several experimental test sections. The objective of this experiment is to find the significant factors affecting the randomness of cracks in CRC pavements.

The experiment test sections consisted of four CRC pavement projects constructed in Houston, Texas, in 1989 and 1990. One project was constructed in the summer (with a maximum air temperature of approximately 95°F) and the other three projects were constructed in the winter (with a maximum air temperature of approximately 60°F to 75°F). Each project included two types of coarse aggregate (siliceous river gravel and limestone) and four different amounts of longitudinal steel. The length of each project was 1,840 ft. More details on the test sections are provided by Suh (*2*).

The lengths of transverse cracks in a traffic lane (L) and the corresponding lane widths (W) were measured and the separated concrete blocks (N) were counted for the 220 randomly selected cracks from the experimental CRC pavements. The RI value for each crack was calculated using Equations 2 and 3.

Calculated RI values are plotted by projects and coarse aggregate types in Figure 12. The marks on the tops of the

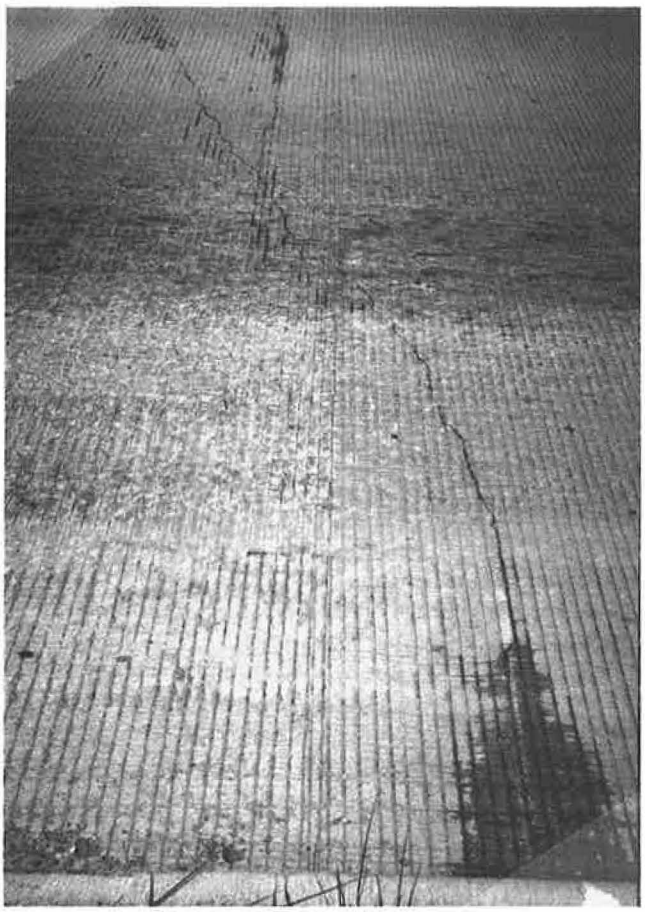


FIGURE 10 Crack with RI value of 2.3 (R = 5.8 percent and N = 1).

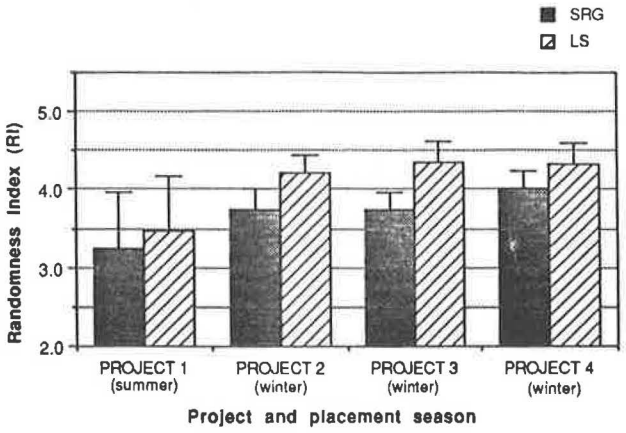


FIGURE 11 Crack with RI value of 1.8 (R = 7.3 percent and N = 2).

columns represent the standard deviations of each category. Because variations in RIs among different steel designs were small, this variable is not included in the plot for simplification. Figure 12 shows that summer construction (Project 1) resulted in lower RI values (cracks are more random) with greater standard deviations than winter construction (Projects 2–4). Figure 12 also shows that concrete with limestone aggregates has higher values of RI than does concrete with siliceous river gravel.

The general linear model procedure in SAS was used to see if these differences are statistically significant. Variables considered were project, coarse aggregate type, amount of longitudinal steel, time of crack occurrence, and two factor interactions of these factors. Three or more factor interactions were ignored. Time of crack occurrence was included in the analysis because the early-age cracks have a higher tendency to meander.

It was found from the statistical analysis that the significant factors at the 0.05 significance level are project, coarse aggregate type, and time of crack occurrence. As expected, the effect of the amount of longitudinal steel was not a significant factor in the randomness of cracks. The interaction between project and coarse aggregate type was also significant at the 0.05 level. The other two factor interactions were not significant.



Note: 'T' marks on each column represent standard deviation of RI's.

FIGURE 12 Average RI values for each project and coarse aggregate type.

The effect of time of crack occurrence obtained from the statistical analysis is shown Figure 13. The cracks occurring during the first night of construction exhibited much more randomness (had a much lower RI value) than cracks that occurred later. This finding might be because of the soft and heterogeneous state of concrete at the early ages. To keep

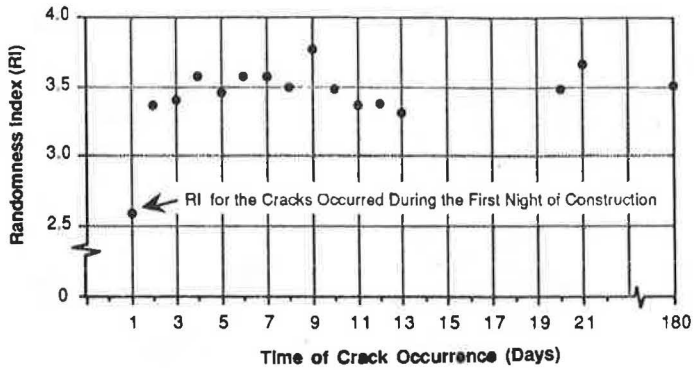


FIGURE 13 Effect of time of crack occurrence on randomness of crack.

the cracks from meandering excessively, the cracks occurring during the first night of construction should be avoided by proper construction and curing.

The experiments show that early-age cracks are more prevalent in summer construction than in winter construction. The higher tendency for early-age cracks, and consequently more meandering cracks, for summer construction might be due to the large temperature differential resulting from the rapid temperature increase (from fast hydration of the cement caused by the high ambient and fresh concrete temperatures) and consequent cooling during the first night after construction (*2*). Because the temperature differential for winter construction was small during the first 24 hr because of the slow hydration of cement, few cracks were observed during that time.

The reason for a tendency toward higher meandering of cracks in concrete with siliceous river gravel than in that with limestone is not clear. However, possible reasons could be less bond with cement mortar, less strain capacity, higher thermal coefficient, and so on.

CONCLUSIONS

An RI for objectively quantifying the randomness of cracks in terms of their shapes has been developed. The technique used was the same as that used in the derivation of PSI in the AASHO Road Test. Subjective ratings of each crack were made by a group of panel members, and a mathematical model was developed by correlating the average rating with several measurable characteristics of the crack. The measured variables needed for the model include the length of the crack, the lane width, and the number of concrete blocks enclosed by cracks, joints, or a pavement edge.

The concept of RI can be used in identifying the factors affecting the randomness of cracks and in quantifying the effects. The reliability of concrete pavements can be increased by controlling these factors.

It was found in an example application using the RI that construction season, coarse aggregate type, and time of crack occurrence are significant factors influencing the randomness of cracks. To minimize random cracking, cool weather construction with the use of limestone aggregate, rather than siliceous river gravel aggregate, is recommended.

REFERENCES

1. W. N. Carey, Jr., and P. E. Irick. The Pavement Serviceability-Performance Concept. *Bulletin 250*, HRB, National Research Council, Washington, D.C., 1960.
2. Y. C. Suh. *Early-Age Behavior of CRC Pavement and Calibration of the Failure Prediction Model in CRCP-7*. Ph.D. dissertation. The University of Texas, Austin, May 1991.

Publication of this paper sponsored by Committee on Rigid Pavement Design.

Field-Calibrated Mechanistic-Empirical Models for Jointed Concrete Pavements

MICHAEL I. DARTER, KURT D. SMITH, AND DAVID G. PESHKIN

Field-calibrated mechanistic-empirical models have been developed for key performance indicators of jointed concrete pavements. Performance data from nearly 500 in-service pavements were used along with mechanistic and empirical variables to develop improved prediction models for joint faulting, slab cracking, joint spalling, and present serviceability rating. The models should prove extremely valuable in checking the performance capabilities of various pavement designs determined by other means and in determining the relative impact of different design variables on concrete pavement performance. However, the models must be used with care and applied judiciously because it is imperative that they not be extended beyond the conditions for which they were developed.

Over the past several years, various models have been developed to predict the performance of in-service concrete pavements. These models can be useful tools in predicting the performance capabilities of a concrete pavement design or in evaluating the impact of different design features on pavement performance. However, there has been some concern about the accuracy of these models and their applicability. A recent FHWA study used performance data from 95 in-service concrete pavements from around the country and evaluated such prediction models as the AASHTO design equation (*1*), the PEARDARP models (*2–4*), the NCHRP 277 (COPES) models (*5*), and the PFAULT faulting models (*6*). The FHWA study found that all of the models were deficient and unable to accurately predict the performance of the in-service concrete pavements (*7*).

Because of the deficiencies of the existing models, improved models were developed using both mechanistic and empirical concepts, which more accurately predict the performance of in-service concrete pavements. To accomplish this, the data from the 95 concrete pavement sections collected under the FHWA study (*7*) were combined with the over 400 concrete pavement sections from the NCHRP 277 (COPES) study (*5*) to allow for a large number of sections and a variety of different pavement designs and design features. Wherever possible, mechanistic variables and functional forms were included. New models were developed for transverse joint faulting (doweled and nondoweled), transverse slab cracking [jointed plain concrete pavement (JPCP) only], transverse joint spalling, and present serviceability rating (PSR). Although there are some limitations with the new models, they are nevertheless believed to be more accurate and more comprehensive than any other prediction models currently available.

ERES Consultants, Inc., 8 Dunlap Court, Savoy, Ill. 61874.

NEW PREDICTION MODELS

Transverse Joint Faulting

Transverse joint faulting is a major distress type that causes loss of serviceability in a jointed concrete pavement. Many jointed concrete pavements have shown serious faulting, which has contributed to the need for expending funds for their rehabilitation.

Design engineers have attempted to reduce faulting through many different ways, including the use of dowel bars, thicker slabs, nonerodible bases, permeable bases, and shorter joint spacing. Many of these attempts have been unsuccessful or only partially successful. Procedures are urgently needed to assist designers in developing joint designs that will experience limited faulting over their service life, yet not result in large initial construction costs due to overdesign.

The data base assembled for this work was greatly expanded and included pavement sections with new design features, such as permeable bases, thick slabs, and the use of dowels in dry climates. There were some areas in which few sections were available, such as doweled slabs in dry-nonfreeze areas (e.g., southwestern United States).

Two prediction models were developed using the combined data bases: one for nondoweled pavements and one for doweled pavements. Because of the mechanisms involved in faulting, it was not useful to combine these two design types into one model. The models were developed using a combination of mechanistic and empirical approaches. The form of the model was based on observations of the development of faulting from field pavements. Key variables that affect faulting were identified from theory and from the data base analysis. Both linear and nonlinear regression techniques were used. Linear regression was used to help identify significant factors in the data base, and nonlinear regression was used to establish the final coefficients on the factors in the form of the model established.

Doweled Concrete Pavements

The mechanistic-empirical faulting model for doweled concrete pavement is as follows:

$$FAULT = ESAL^{0.5280} * [0.1204 + 0.04048 * (BSTRESS1/1000)^{0.3388} + 0.007353 * (AVJSPACE/10)^{0.6725} - 0.1492$$

$$* (\text{KSTAT}/100)^{0.05911} - 0.01868 * \text{DRAIN}$$

$$- 0.00879 * \text{EDGESUP} - 0.00959 * \text{STYPE}] \quad (1)$$

where

FAULT = mean transverse joint faulting (in.);
ESAL = cumulative 18-kip equivalent single axle loads (ESALs) (millions);
BSTRESS = maximum concrete bearing stress using closed-form equation (psi) = $f_d * P * T * [K_d * (2 + \text{BETA} * \text{OPENING})/(4 * E_s * I * \text{BETA}^3)]$;
BETA = $[K_d * \text{DOWEL}/(4 * E_s * I)]^{0.25}$;
f_d = distribution factor = $2 * 12/(l + 12)$;
l = radius of relative stiffness (in.) = $\{E_c * \text{THICK}^3/[12 * (1 - u^2) * \text{KSTAT}]\}^{0.25}$;
E_c = concrete modulus of elasticity (psi) = $14.4 * 150^{1.5} * \text{MR}_{28}^{0.77}$;
I = moment of inertia of dowel bar cross section (in.^{4}) = $0.25 * 3.1416 * (\text{DOWEL}/2)^4$;
THICK = slab thickness (in.);
MR_{28} = concrete modulus of rupture at 28 days (psi);
u = Poisson's ratio, set to 0.15;
P = applied wheel load, set to 9,000 lb;
T = percent transferred load, set to 0.45;
K_d = modulus of dowel support, set to 1,500,000 pci;
BETA = relative stiffness of the dowel-concrete system;
DOWEL = dowel diameter (in.);
E_s = modulus of elasticity of the dowel bar (psi);
KSTAT = effective modulus of subgrade reaction on the top of base (psi/in.);
OPENING = average transverse joint opening (in.) = CON * AVJSPACE * 12 * (ALPHA * TRANGE/2 + e);
AVJSPACE = average transverse joint spacing (ft);
CON = adjustment factor due to base/slab frictional restraint (0.65 if stabilized base, 0.80 if aggregate base or lean concrete base with bond breaker);
ALPHA = thermal coefficient of contraction of portland cement concrete (PCC), set to 0.000006/°F;
TRANGE = annual temperature range (°F);
e = drying shrinkage coefficient of PCC, set to 0.00015 strain;
DRAIN = index for drainage condition (0 if no edge support exists, 1 if edge subdrain exists);
EDGESUP = index for edge support (0 if no edge support exists, 1 if edge support exists); and
STYPE = index for AASHTO subgrade soil classification (0 if A–4 to A–7, 1 if A–1 to A–3).

Statistics:

R^2 = 0.67,
SEE = 0.057 in., and
n = 559 data points.

The bearing stress between the concrete and the dowel was computed using an equation developed by Ioannides et al. (*8*).

The prediction model presented includes many variables that have been shown by theory and field investigations to affect faulting. These variables include repeated heavy traffic loadings, dowel bearing stress (which is greatly affected by dowel diameter), joint spacing, effective k-value, longitudinal drains, edge support from tied PCC shoulders or widened traffic lanes, and type of subgrade.

A sensitivity of the doweled faulting model is shown in Figures 1 and 2. Dowel diameter (for a constant dowel spacing of 12 in.) and provision for subdrainage are observed to be the most critical design factors affecting transverse joint faulting.

Nondoweled Concrete Pavements

The faulting model for nondoweled concrete pavement slabs is as follows:

$$\text{FAULT} = \text{ESAL}^{0.2500} * [0.000038$$

$$+ 0.01830 * (100 * \text{OPENING})^{0.5585}$$

$$+ 0.000619 * (100 * \text{DEFLAMI})^{1.7229}$$

$$+ 0.0400 * (\text{FI}/1000)^{1.9840} + 0.00565 * \text{BTERM}$$

$$- 0.00770 * \text{EDGESUP} - 0.00263 * \text{STYPE}$$

$$- 0.00891 * \text{DRAIN}] \quad (2)$$

where

TRANGE = annual temperature range (minimum average January temperature − maximum average July temperature) (°F);
DEFLAMI = Ioannides' corner deflection (in.) (*8*) $P * (1.2 - 0.88 * 1.4142 * a/l)/(\text{KSTAT} * l^2)$;
a = radius of the applied load, set to 5.64 in. and assuming tire pressure = 90 psi;
BTERM = base type factor = $10 * [\text{ESAL}^{0.2076} * (0.04546 + 0.05115 * \text{GB} + 0.007279 * \text{CTB} + 0.003183 * \text{ATB} - 0.003714 * \text{OGB} - 0.006441 * \text{LCB})]$;
GB = dummy variable for dense-graded aggregate base (1 if aggregate base, 0 otherwise);
CTB = dummy variable for dense-graded, cement-treated base (1 if cement-treated base, 0 otherwise);
ATB = dummy variable for dense-graded, asphalt-treated base (1 if asphalt-treated base, 0 otherwise);
OGB = dummy variable for open-graded aggregate base or open-graded, asphalt-treated base (1 if open-graded base, 0 otherwise);
LCB = dummy variable for lean concrete base (1 if lean concrete base, 0 otherwise); and
FI = freezing index (degree-days).

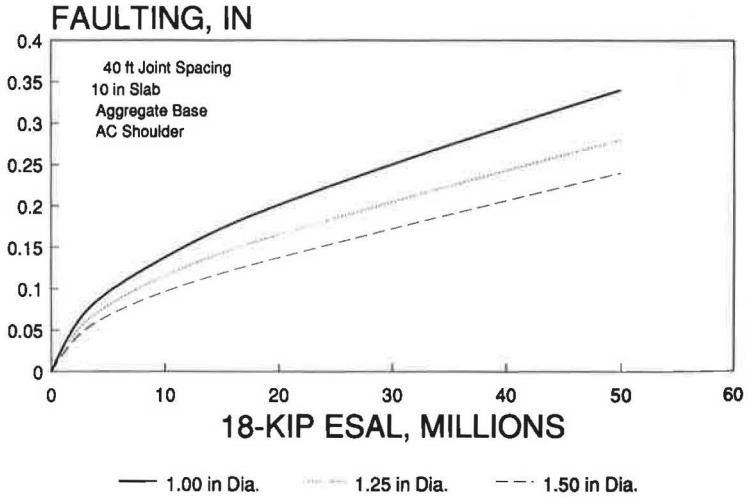


FIGURE 1 Sensitivity of doweled faulting model to dowel diamater.

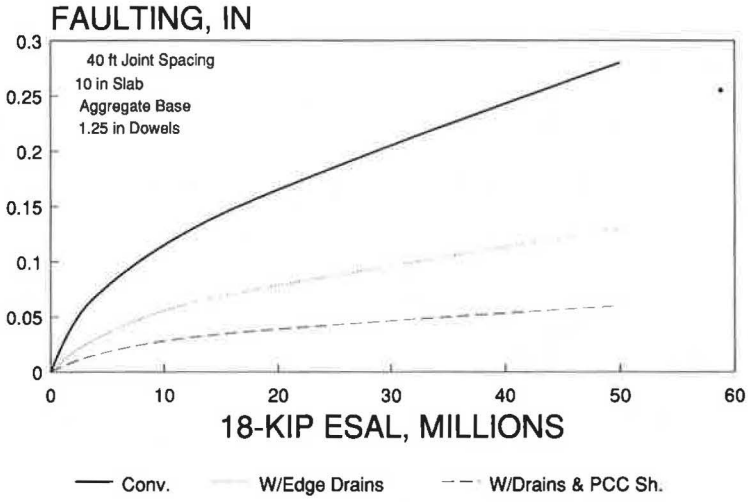


FIGURE 2 Sensitivity of doweled faulting model to drainage and shoulder type.

Statistics:

$R^2 = 0.81$,
SEE = 0.028 in., and
$n = 398$.

The corner deflection used in the nondoweled faulting model was computed using a relationship developed by Ioannides et al. (*8*).

The prediction model presented includes many variables that have been shown by theory and field investigations to affect faulting of nondoweled joints. These variables include repeated heavy traffic loadings, base type, free corner deflection (which is a function of slab thickness and effective *k*-values), joint opening (which is a function of temperature, joint spacing, and slab-base friction), climate, longitudinal drains, edge support from tied PCC shoulders or widened traffic lanes, and type of subgrade.

A sensitivity of the doweled and nondoweled faulting model is shown in Figure 3. Base type, drainage, joint spacing, and ESALs are observed to be the most critical design factors affecting transverse joint faulting.

These mechanistic-empirical models for joint faulting can be used for checking joint designs to determine if the design will prevent significant faulting for the given design traffic, climate, and subgrade soils. Examples of applying this type of model for checking joint designs are given by Heinrichs et al. (*6*).

Transverse Cracking

Transverse cracking in concrete slabs may occur for a number of reasons. Large temperature gradients through the slab, heavy-truck loadings, and shrinkage of the concrete immediately after placement can all produce stresses in the slab that can result in transverse cracking. Once initiated, transverse cracks are entry points for water and incompressibles and can deteriorate further under traffic loadings. The pres-

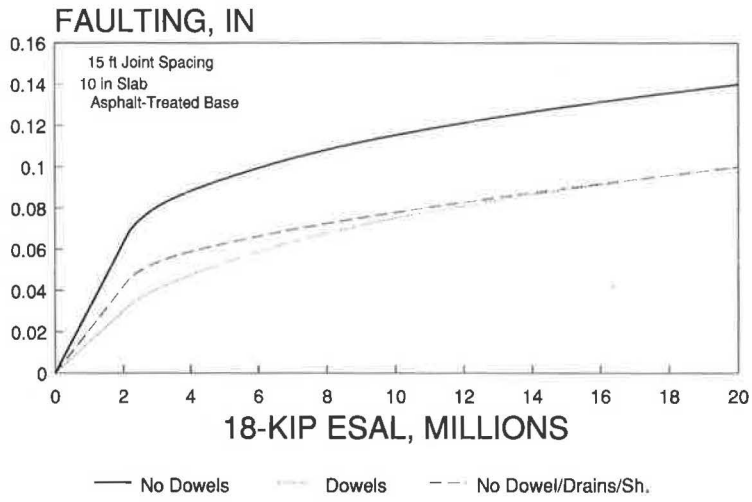


FIGURE 3 Sensitivity of faulting models to dowels, drainage, and shoulder type.

ence of excessive transverse cracking can significantly detract from the overall serviceability of a concrete pavement.

Transverse cracks can occur both in JPCP and in jointed reinforced concrete pavements (JRCP). However, the mechanism influencing their occurrence in each pavement type is different. For example, transverse cracks occurring in JPCP are usually caused by either thermal curling or truck loading (fatigue), whereas transverse cracks occurring in JRCP are generally caused by thermal curling and shrinkage. In fact, JRCP is actually designed to crack. That is, the long joint spacing for JRCP (generally 40 ft or longer) produces excessive thermal stresses that result in transverse cracking. However, the slabs contain reinforcing steel, which is expected to hold the cracks tight. Efforts were concentrated on developing a model for transverse cracking in JPCP.

The model developed was based on a fatigue-consumption approach similar to that used by Darter (*9*). This concept theorizes that a concrete pavement has a finite life and can withstand a maximum allowable number of repetitions, N, of a given traffic loading until a critical proportion of slabs are cracked. Every individual traffic loading applied, n, decreases the life of the pavement by an infinitesimal amount. Theoretically, when $\Sigma n/N = 1$, fracture of 50 percent of the concrete slabs occurs. However, because of the range in variability of materials, traffic loading, and other properties, there is a large variation in fatigue life that results in a distribution around the $\Sigma n/N = 1$ point.

The following paragraphs outline the procedure followed in the development of the JPCP cracking model, using only the 52 JPCP sections from the FHWA study.

Applied n

On the basis of historical traffic data, W–4 tables, and on-site weigh-in-motion (WIM) data, the number of 18-kip ESAL applications was estimated for each JPCP section. However, not all of these loadings were located at the slab edge. Studies have shown that trucks encroach into an edge loading condition (say, within 12 in. of the slab edge) only between 3 and 7 percent of the time (*10*). Thus, it was assumed that an average of 5 percent of the trucks loaded the slab at the critical edge location. However, if a pavement section had a widened outside traffic lane, it was assumed that only 0.1 percent of the truck lane loadings produced an edge loading condition (*10*). The edge loading condition is considered critical for JPCP because this location has the maximum stress in the slab under temperature and traffic loading and will be the point of crack initiation.

For example, if a pavement has endured an estimated 10 million 18-kip ESAL applications, it is assumed that only 5 percent, or 0.5 million, ESAL applications occur at the critical edge location; therefore, $n = 0.5$ million. Similarly, if the pavement has a widened outside traffic lane, only 0.1 percent, or 0.01 million, 18-kip ESAL applications ($n = 0.01$ million) are assumed to occur at the critical edge location.

As the indicator for applied loadings, 18-kip ESAL applications were selected because this quantity is easier to compute than detailed axle load data. Detailed axle load information would provide more accurate results but can often be a tedious and difficult computation; furthermore, reliable axle load data are not always readily available. Additionally, as illustrated in the following paragraphs, a fairly good relation was obtained using the 18-kip ESAL applications.

The load equivalency factors used in estimating ESAL applications are from the AASHO Road Test and are based on serviceability rather than cracking. Therefore, there is some error associated with using ESAL applications as the loading factor in the fatigue analysis. Cracking-based load equivalency factors would undoubtedly provide a better estimate of 18-kip ESAL applications, although nearly all of the loss of serviceability at the AASHO Road Test was due to slab cracking caused by erosion and loss of support.

Allowable N

The maximum allowable number of repetitions, N, is computed using concrete fatigue damage considerations. First, stresses at the concrete slab edge were computed for a com-

bination of traffic loading and thermal curling. These stresses were calculated using equations developed by Darter (*9*). A 9,000-lb wheel load was assumed for the load calculation, and the yearly average thermal gradients presented in Table 1 were assumed for the thermal curling calculation. These thermal gradients are daytime gradients, which represent the critical thermal curling condition when thermal stresses and load stresses are additive. By considering the gradients, the total stress at the slab edge due to loading and thermal curling was determined.

The stress at the slab edge was reduced, however, if tied concrete shoulders were present. Tied concrete shoulders are expected to provide support to the mainline pavement and thereby reduce the magnitude of the critical edge stress. Because the deflection load transfer between the mainline pavement and tied concrete shoulder had been obtained during field testing, the amount of support, or edge stress reduction, could be estimated from Figure 4. This figure provides the equivalent stress load transfer for a given deflection load transfer, and this stress load transfer was used to determine the amount of support (and hence the reduction in the number of 18-kip ESAL applications) provided by the concrete shoulders. For example, if the deflection load transfer efficiency (LTE) for a concrete shoulder is 43 percent, the equivalent stress LTE is approximately 14 percent (only 14 percent of the stress is being transferred). Therefore, because

$$\text{Total stress} = \text{stress}_{\text{loaded}} + \text{stress}_{\text{unloaded}}$$

and

$$\text{Stress LTE} = \text{stress}_{\text{unloaded}}/\text{stress}_{\text{loaded}}$$

then

$$\text{Total stress} = \text{stress}_{\text{loaded}} + \text{stress}_{\text{loaded}} * \text{stress LTE}$$

or

$$\text{Stress}_{\text{loaded}} = \text{total stress}/(1 + \text{stress LTE}) \quad (3)$$

Thus, for this example, the computed (total) edge stress would be multiplied by a factor of [1/(1 + 0.14)], or 0.88.

The stress equations provided by Darter (*9*) require several section-specific design inputs, including slab thickness, composite *k*-value, and slab length. For sections with random slab lengths (e.g., 12, 13, 19, and 18 ft), each slab length was considered individually because the stresses produced on each slab would be different. The percentage of slabs cracked was broken down according to slab length. In this way, there were actually 184 cases representing the 52 JPCP sections.

TABLE 1 YEARLY AVERAGE DAYTIME THERMAL GRADIENTS USED IN CURLING COMPUTATIONS, °F/IN. (*9*)

Slab Thickness, in	Wet-Nonfreeze Climatic Zone	Dry/Wet-Freeze Climatic Zones	Dry-Nonfreeze Climatic Zone
8	1.40	1.13	1.41
9	1.30	1.05	1.31
10	1.21	0.96	1.21
11	1.11	0.87	1.10
12	1.01	0.79	1.00

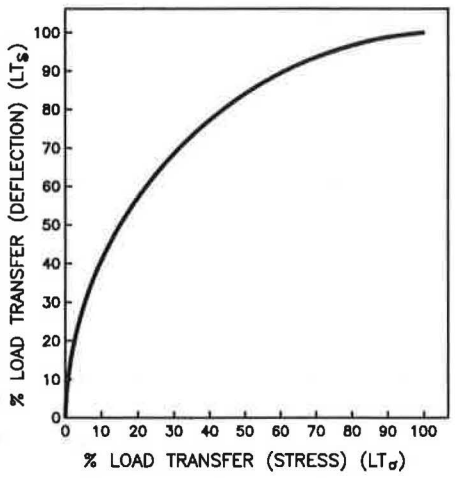


FIGURE 4 Relationship between deflection and stress load transfer.

With the critical stress value calculated for the slab edge, the stress ratio was computed. The stress ratio is defined as the ratio of the edge stress to the 28-day modulus of rupture (third point). This value was then directly entered into the following field-derived fatigue equation:

$$\log_{10} N = 2.13 * (1/\text{SR})^{1.2} \quad (4)$$

where N is the allowable 18-kip applications and SR is the stress ratio (ratio of computed edge stress to 28-day modulus of rupture).

Equation 4 was originally developed for airfield slabs that had been loaded with aircraft gears, but it has shown good results in highway applications (*11*). The curve is very different from those typically derived in laboratory beam testing.

JPCP Cracking Model

With the determination of n and N, cumulative fatigue damage (n/N) was calculated for each JPCP section (or for each individual slab length for JPCP sections with random joint spacing). The base 10 logarithm was taken of each fatigue damage value and plotted against the corresponding percent slabs cracked, as shown by the individual data points in Figure 5. This figure indicates that most transverse slab cracking occurs in a vertical band between -2 and $+2$. Thus, as fatigue damage approaches 1 [i.e., as $\log_{10}(n/N)$ approaches 0], the likelihood of transverse slab cracking increases greatly. The range of values results because of variations in material properties, erosion, traffic estimations, and other factors.

Linear and nonlinear regression procedures were used to try to fit a model through the data. Although there was a large scatter of data, a reasonable model was fit through the

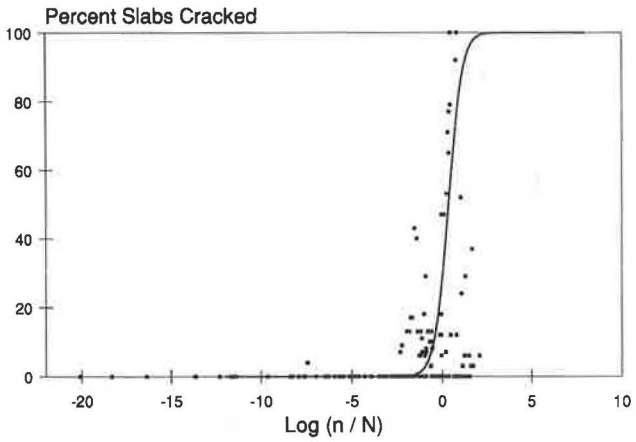


FIGURE 5 Percent slab cracking as a function of accumulated fatigue damage.

data. The model, which is plotted in Figure 5, is given as follows:

$$P = \frac{1}{0.01 + 0.03 * [20^{-\log(n/N)}]} \quad (5)$$

where P is the percent of slabs cracked and n is the actual number of 18-kip ESAL applications at the slab edge.

Equation 5 fits the data fairly well and is in the classical S-shaped curve, which is thought of as representing actual distress development. As such, the curve meets the required boundary conditions (i.e., zero slab cracking for zero fatigue damage and 100 percent slab cracking for infinite fatigue damage). The curve comes close to meeting the theoretical 50 percent slab cracking for $\Sigma\ n/N = 1$.

A sensitivity analysis was performed using the equation for several key pavement design inputs. Figure 6 shows slab cracking as a function of 18-kip lane (not edge) ESAL applications for different shoulder types. The section with a tied PCC shoulder (20 percent stress load transfer efficiency assumed) and the section with a widened outside traffic lane and AC shoulder exhibit little, if any, transverse cracking. However, the section with the AC shoulder displays a significant amount of transverse cracking.

Figure 7 shows a similar sensitivity analysis for joint spacing. The positive influence of shorter slabs on reducing transverse cracking is clearly evident. The reduction in slab cracking between 20- and 15-ft slabs is significant, but additional benefit is also seen in reducing the joint spacing to 10 ft.

Figure 8 shows a sensitivity analysis of the transverse cracking model with respect to slab thickness. The 8-in. slab exhibits extensive slab cracking early in its life. Increasing the slab thickness from 8 to 10 in. has an enormous effect on reducing the development of fatigue cracking. Likewise, an increase in slab thickness from 10 to 12 in. reduces the amount of transverse slab cracking to essentially zero.

Although the cracking model employs a mechanistic approach to the development of transverse cracking, there are other factors currently not incorporated (e.g., thermal coefficient of expansion and friction from the base) that also are believed to contribute to cracking.

Transverse Joint Spalling

Joint and corner spalling is defined as any type of fracture or deterioration of the transverse joints, excluding corner breaks. Only medium- and high-severity joint spalling is included in the prediction models.

A wide range of designs are included in this evaluation. The combined data base used in the evaluation provided 262 data points for JPCP and 280 data points for JRCP. The data were cleaned to remove any sections that had unusual load transfer mechanisms (e.g., ACME devices) or that were constructed using ineffective joint forming methods (e.g., Unitube joint inserts). This procedure was followed because these devices may actually contribute to joint spalling, and new construction does not use the devices.

The data represent a wide range of climates from the major climatic zones across the United States: wet-freeze, wet-nonfreeze, dry-freeze, and dry-nonfreeze. The only exception

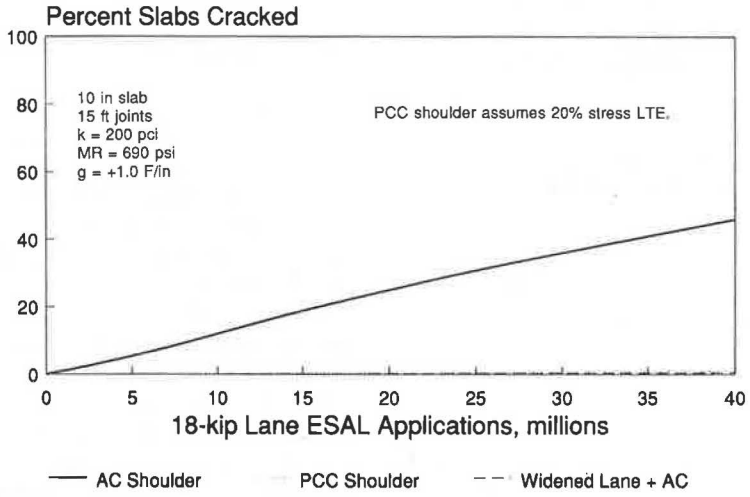


FIGURE 6 Sensitivity of JPCP cracking model to shoulder type.

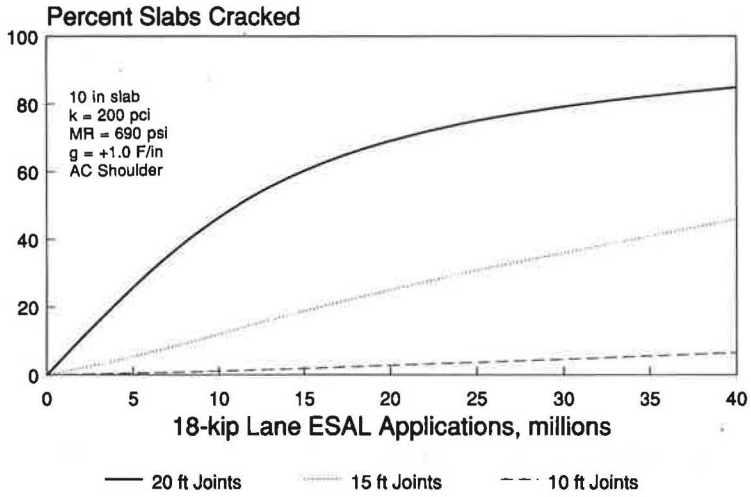


FIGURE 7 Sensitivity of JPCP cracking model to joint spacing.

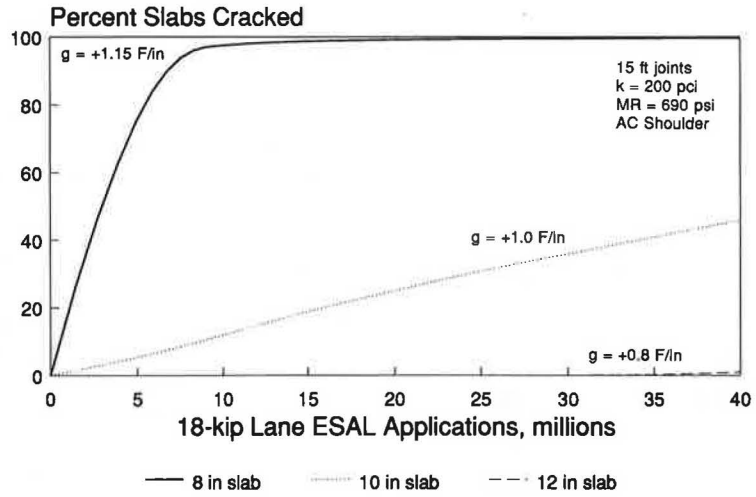


FIGURE 8 Sensitivity of JPCP cracking model to slab thickness.

was that there were no JRCP sections located in dry-nonfreeze areas.

Prediction models were developed separately for JPCP and JRCP. Extensive efforts to develop a single model for joint spalling were unsuccessful. One reason may be that most of the joint spalling for JPCP was of medium severity; few joints had high-severity spalling. JRCP sections, however, had a much greater proportion of joints exhibiting high-severity joint spalling.

JPCP Joint Spalling Model

The final joint spalling model for JPCP is given as follows:

$$\text{JTSPALL} = \text{AGE}^{2.178} * (0.0221 + 0.5494\,\text{DCRACK} - 0.0135\,\text{LIQSEAL} - 0.0419\,\text{PREFSEAL} + 0.0000362\,\text{FI}) \quad (6)$$

where

JTSPALL = number of medium-high joint spalls per mile;
AGE = age since original construction (years);
DCRACK = 0 if no D-cracking exists, 1 if D-cracking exists;
LIQSEAL = 0 if no liquid sealant exists in joint, 1 if liquid sealant exists in joint;
PREFSEAL = 0 if no preformed compression seal exists, 1 if preformed compression seal exists; and
FI = freezing index (degree-days below freezing).

Statistics:

R^2 = 0.59,
SEE = 15 joints/mi, and
n = 262.

The sensitivity of the model is shown in Figures 9 and 10. Figure 9 shows the average effect that joint sealants have on

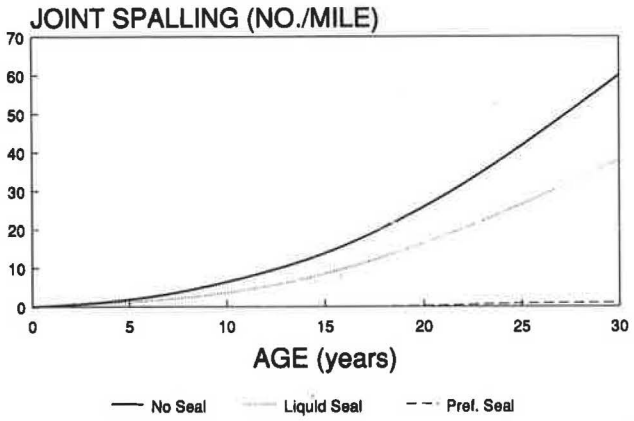


FIGURE 9 Sensitivity of JPCP spalling model to joint sealant type.

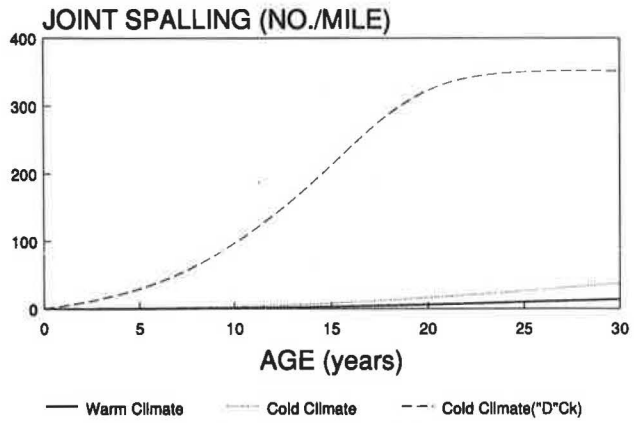


FIGURE 10 Sensitivity of JPCP spalling model to climate.

a JPCP in a cold climate (FI = 400, no D-cracking). Having a liquid joint sealant reduces the amount of spalling by nearly 50 percent over a 30-year period. A preformed sealant reduces the amount of joint spalling to essentially zero over a 30-year period. Because incompressibles are believed to be the major cause of joint spalling, it appears that preformed sealants are capable of keeping incompressibles from infiltrating the joints for a significant period of time.

Figure 10 shows the dramatic effect of D-cracking on joint spalling. It also shows the effect of a warm climate (FI = 0) and a freezing climate (FI = 400) on the development of joint spalling.

JRCP Joint Spalling Model

The final joint spalling model for JRCP is given as follows:

$$\text{JTSPALL} = \text{AGE}^{4.1232} * (0.00024 + 0.0000269\ \text{DCRACK} + 0.000307\ \text{REACTAGG} - 0.000033\ \text{LIQSEAL} - 0.0003\ \text{PREFSEAL} + 0.00000014\ \text{FI}) \quad (7)$$

where REACTAGG is 0 if no reactive aggregate exists and 1 if reactive aggregate exists.

Statistics:

$R^2 = 0.47$,
SEE = 13 joints/mi, and
$n = 280$.

A sensitivity of the model is shown in Figure 11. This figure shows the average effect that joint sealants have on a JRCP in a cold climate (FI = 400, no D-cracking). Having a liquid joint sealant reduces the amount of spalling by about 11 percent over a 30-year period. However, a preformed sealant reduces the amount of joint spalling to essentially zero over the same 30-year period.

Present Serviceability Rating

The performance data were also used to develop predictive models for the mean panel PSR. The models were of the form where PSR is the dependent (y) variable and pavement distress types are the independent (x) variables.

The prediction of panel PSR ratings has been modeled several ways in the past. The original PSR equation from the AASHO Road Test was based on both roughness and distress (*12*). Many other models have been developed solely on the basis of roughness (*13*) or visual distress (*14*).

The best way to predict PSR is using roughness. However, a PSR model based only on key distress types is useful in mechanistic-empirical design of pavements to approximately relate physical deterioration (that can be estimated using other models) to serviceability, or user response.

PSR prediction models were developed both for JPCP and for JRCP. Although all measured types of distress were initially considered, only three key distress types proved significant: joint faulting, joint deterioration (spalling), and trans-

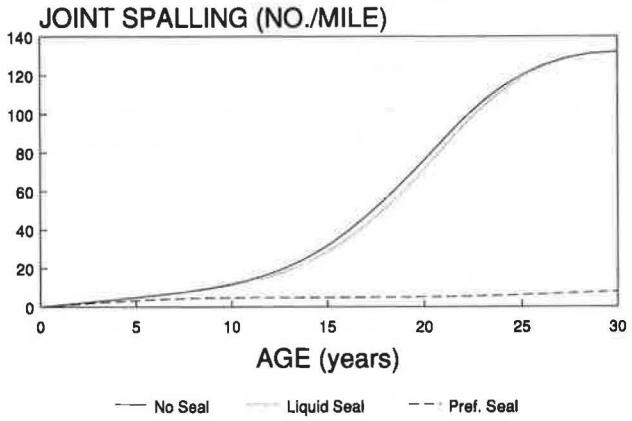


FIGURE 11 Sensitivity of JRCP spalling model to joint sealant type.

verse cracking. The presence of full-depth patching was also of significance and was included in the equations.

The models for each pavement type are as follows:

Jointed Plain Concrete Pavements

$$PSR = 4.356 - 0.0182\,TFAULT - 0.00313\,SPALL - 0.00162\,TCRKS - 0.00317\,FDR \quad (8)$$

where

PSR = mean panel rating of pavement (0 to 5 AASHTO scale),
TFAULT = cumulative transverse joint faulting (in./mi),
SPALL = number of deteriorated (medium- and high-severity) transverse joints per mile,
TCRKS = number of transverse cracks (all severities) per mile, and
FDR = number of full-depth repairs per mile.

Statistics:

$R^2 = 0.58$,
SEE = 0.31 (units of PSR), and
$n = 282$.

Jointed Reinforced Concrete Pavements

$$PSR = 4.333 - 0.0539\,TFAULT - 0.00372\,SPALL - 0.00425\,MHTCRKS - 0.000531\,FDR \quad (9)$$

where MHTCRKS is the number of medium- and high-severity cracks per mile.

Statistics:

$R^2 = 0.64$,
SEE = 0.37 (units of PSR), and
$n = 434$.

The values of R^2 and SEE are similar to those of the original PSR models developed at the AASHO Road Test (*12*).

Examination of the PSR models indicates that transverse joint faulting has the greatest effect on reducing the PSR. Spalling, transverse cracking, and full-depth repairs have a much smaller effect on reducing PSR.

The primary limitation of these models is that they do not include either all distress types or long-wavelength roughness, such as would be caused by settlements or heaves. In fact, the relatively low R^2 values and high standard errors clearly indicate that other sources of variation in PSR exist.

These models are not intended to be used to predict PSR (or PSI) in place of roughness, because it can be demonstrated that measured roughness is the best way to predict serviceability. These models are intended for use in predicting serviceability when only key distress types are available. Even then, the models should be used with caution, recognizing their limitations.

EXAMPLE USE OF MODELS

An example application of the models for checking concrete pavement designs is presented in Table 2. It is assumed that the thickness of the slab has been determined using an agency-approved method and that the various design features (such as load transfer, base type, and AC shoulder) have been selected in accordance with agency policy or procedures. The inputs needed for each model are listed in Table 2 under the appropriate heading.

The original design was tested using the models. In the first iteration, the level of faulting (0.14 in.) and the amount of slab cracking (88 percent) resulting from the analysis are both unacceptable. The amount of joint spalling is acceptable, however, and the estimate of the overall serviceability is marginal for this pavement type and traffic loading.

A target design value for the faulting of nondoweled pavements is 0.07 in., whereas a target design value for slab cracking is 10 to 15 percent of the slabs cracked. To accomplish this, several design changes were made to the original design: tied PCC shoulders were added, the joint spacing was shortened to 15 ft, and an open-graded permeable base with edge drains was included. This revised design was again tested using the models in the second iteration. The result of this change is that joint faulting is marginally acceptable, although slab cracking is still somewhat high. Joint spalling is still acceptable and the PSR is quite adequate. However, because of the faulting and cracking, the design requires specific features to restrict the development of these distresses: 1.25-in. dowel bars to control the faulting and a 10-in. slab to reduce the cracking. This design change was tested using the models in the third iteration, and the results indicate that the design is more than adequate.

SUMMARY

Several performance prediction models for concrete pavements have been presented. A combination of theory, mechanistic variables, and field performance data was used in the development of the models. Because of the large data base of in-service pavements from which they were developed, these models are believed to possess the most comprehensive and accurate prediction capability to date.

The models can be useful in checking pavement designs for the development of faulting, cracking, joint spalling, and serviceability loss. They can also be used to develop design guidelines for joint load transfer, widened traffic lanes, tied shoulders, permeable bases, and many other design variables. However, the models must be used with care and not extended beyond the inference space from which they were developed.

ACKNOWLEDGMENTS

This paper is based on the results of a research project conducted by ERES Consultants, Inc., for FHWA. The authors are grateful for the assistance provided by Ying-Haur Lee and Ricardo Salsilli of the University of Illinois in the development of the models. In addition, the direction and guidance pro-

TABLE 2 EXAMPLE APPLICATION OF MODELS TO CHECK CONCRETE PAVEMENT DESIGN

Initial Design

9 in JPCP — No Dowels
Asphalt-Treated Base (k = 200) — Cold Climate
20-ft joint spacing — Fine-grained subgrade

Faulting Inputs			Cracking Inputs			Spalling Inputs		
ESAL	=	10 million	ESAL	=	10 million	AGE	=	20 years
CON	=	0.65	n	=	0.5 million (5% * 10 million)	DCRACK	=	None
AVJSPACE	=	20 ft				FI	=	600
ALPHA	=	0.000006 strain/°F	MR_m	=	700 psi (28-day modulus of rupture)	Sealant Type	=	Hot-poured rubberized (liquid)
TRANGE	=	75 °F						
e	=	0.00015 strain shrinkage	g	=	1.05 °F / in (thermal gradient)			
E_c	=	4,200,000 psi						
P	=	9000 lb	P	=	9000 lb (wheel load)			
a	=	5.64 in						
KSTAT	=	200 psi/in	JTSPACE	=	20 ft			
THICK	=	9 in	Shlder Type	=	AC			
μ	=	0.15	KSTAT	=	200 psi/in			
Base Type	=	4 in asphalt treated	ES	=	341 psi (edge stress, from reference 9)			
FI	=	600						
DRAIN	=	None						
EDGESUP	=	AC Shoulder	N	=	46,610 applications (from Eq. 4)			
STYPE	=	Fine-grained soil						

Iteration No. 1 - original design

Predicted Faulting = 0.14 in (from Eq. 2)
Predicted Cracking = 88 percent of the slabs (from Eq. 4)
Predicted Spalling = 20 joints/mile (from Eq. 6)
Predicted PSR = 3.2 (from Eq. 8 after converted to consistent units)

Design not adequate; faulting and slab cracking unacceptable.

Iteration No. 2 - PCC shoulders, 15 ft joint spacing, permeable base with edge drains

Predicted Faulting = 0.09 in
Predicted Cracking = 25 percent of the slabs (assuming 45 percent stress load transfer across the shoulder)
Predicted Spalling = 20 joints/mile
Predicted PSR = 3.7

Design marginally adequate for faulting, inadequate for slab cracking.

Iteration No. 3 - 1.25 in dowel bars, 10 in slab

Predicted Faulting = 0.03 in
Predicted Cracking = 0.1 percent of the slabs
Predicted Spalling = 20 joints/mile
Predicted PSR = 4.1

Based upon the results of this iteration, the design, as revised, is acceptable.

vided by Roger M. Larson, FHWA contract manager, is gratefully acknowledged.

REFERENCES

1. *AASHTO Guide for Design of Pavement Structures, 1986.* AASHTO, Washington, D.C., 1986.
2. A. J. van Wijk. *Rigid Pavement Pumping: Volume 1—Subbase Erosion; Volume 2—Economic Modeling.* Final Report. FHWA, U.S. Department of Transportation, Sept. 1985.
3. A. J. van Wijk, J. Larralde, C. W. Lovell, and W. F. Chen. Pumping Prediction Model for Highway Concrete Pavements. *Journal of Transportation Engineering, ASCE*, Vol. 115, No. 2, March 1989.
4. A. J. van Wijk. *Purdue Economic Analysis of Rehabilitation and Design Alternatives for Rigid Pavements: A User's Manual for PEARDARP.* Final Report. FHWA, U.S. Department of Transportation, Sept. 1985.
5. M. I. Darter, J. M. Becker, M. B. Snyder, and R. E. Smith. *NCHRP Report 277: Portland Cement Concrete Pavement Evaluation System—COPES.* TRB, National Research Council, Washington, D.C., Sept. 1985.
6. K. W. Heinrichs, M. J. Liu, M. I. Darter, S. H. Carpenter, and A. M. Ioannides. *Rigid Pavement Analysis and Design.* Report FHWA-RD-88-068. FHWA, U.S. Department of Transportation, July 1989.
7. K. D. Smith, A. L. Mueller, M. I. Darter, and D. G. Peshkin. *Performance of Jointed Concrete Pavements, Volume II—Evaluation and Modification of Concrete Pavement Design and Analysis Models.* Report FHWA-RD-89-137. FHWA, U.S. Department of Transportation, Aug. 1990.
8. A. M. Ioannides, M. R. Thompson, and E. J. Barenberg. Westergaard Solutions Reconsidered. In *Transportation Research Record 1043*, TRB, National Research Council, Washington, D.C., 1985.
9. M. I. Darter. *Design of Zero-Maintenance Plain Jointed Pavement, Volume 1—Development of Design Procedures.* Report FHWA-RD-77-111. FHWA, U.S. Department of Transportation, April 1977.
10. R. F. Benekohal, K. T. Hall, and H. W. Miller. Effect of Lane Widening on Lateral Distribution of Truck Wheels. In *Transportation Research Record 1286*, TRB, National Research Council, Washington, D.C., 1990.
11. M. I. Darter. *A Comparison Between Corps of Engineers and ERES Consultants, Inc. Rigid Pavement Design Procedures.* U.S. Air Force SAC Command, Aug. 1988.
12. *Special Report 61E: The AASHO Road Test, Report 5—Pavement Research.* HRB, National Research Council, Washington, D.C., 1962.
13. M. I. Darter and E. J. Barenberg. *Zero-Maintenance Pavements: Results of Field Studies on the Performance Requirements and Capabilities of Conventional Pavement Systems.* Report FHWA-RD-76-105. FHWA, U.S. Department of Transportation, 1976.
14. K. T. Hall, J. M. Connor, M. I. Darter, and S. H. Carpenter. *Rehabilitation of Concrete Pavements, Volume III—Concrete Pavement Evaluation and Rehabilitation System.* Report FHWA-RD-88-073. FHWA, U.S. Department of Transportation, July 1989.

This document is disseminated under the sponsorship of the U.S. Department of Transportation in the interest of information exchange. The U.S. government assumes no liability for its contents or use thereof. The contents reflect the views of the authors, who are solely responsible for the facts and accuracy of the data presented. The contents do not necessarily reflect the official views or policy of the U.S. Department of Transportation.

Publication of this paper sponsored by Committee on Rigid Pavement Design.

Model of Slab Cracking for Portland Cement Concrete Pavements

M. Poblete, P. Ceza, J. David, R. Espinosa, A. García, and J. Gónzalez

A predictive model of slab cracking has been developed by considering the actual behavior of Chile's portland cement concrete (PCC) pavements. The approach used is mechanistic-empirical and is based on a structural modeling of the jointed pavement using a finite elements program. The model incorporates realistic boundary conditions of upward concave slabs under yearly cyclic moisture warping and daily cyclic temperature curling, obtained from measurements in the climatic zone of central Chile. Fatigue consumption in the slabs was evaluated for the actual traffic loads passing during each group of hours in each season to determine the different levels of upward concavities. The accumulated fatigue consumption of all pavements was calculated and plotted against the percentage of cracked slabs observed in the field. The resulting model is a unique S-shaped curve that is useful for indicating the effect of many design variables on cracking.

The National Highway Administration of Chile has been engaged in implementing a pavement management system to efficiently administer the financial resources annually allocated to rehabilitation. In order to prepare and evaluate its maintenance and rehabilitation programs, Chile is attempting to use the Highway Design and Maintenance Standards Model (HDM) (*1*) developed by the World Bank, which includes distress models obtained from research in several countries and covers diverse environments, traffic conditions, and types of asphalt roads. Until recently, no specific applications of distress modeling were developed for rigid pavements.

A previous effort in the development of distress equations for rigid pavements is the COPES empirical approach, developed in the United States at the University of Illinois (*2*). The results of that approach evidently represent the characteristic environmental and design conditions of U.S. contributing data. In the Chilean case the results of extensive research (*3–6*) are showing that the actual behavior of in-service pavements seems to differ in some important ways; therefore, the development of appropriate distress models for the Chilean climate has been undertaken. The approach is mechanistic-empirical and is based on a structural modeling of the pavement using a finite element program especially developed to incorporate realistic boundary conditions as observed in the field (*7*).

This research was conducted by the University of Chile. Precise measurements were carried out periodically on 21 test sections established along the primary highway network (*8*). These pavements have joints spaced between 3.5 and 5.0 m apart, with no dowels. The 0.20- to 0.26-m-thick slabs are supported on granular and cement-treated bases that were mostly reconstructed on old portland cement concrete (PCC) and asphalt concrete (AC) pavements. Shoulders consist of compacted granular material topped with an asphalt surface treatment. Considered as a whole, over 75 percent of the 21 test section pavements are performing satisfactorily after 6 to 12 years of heavy in-service traffic. However, some sections are developing premature cracking, as shown in Figure 1. No significant roughness has yet been measured.

Facultad de Ciencias Fisicas y Matematicas, Insituto de Investigaciones y Ensayes de Materiales, Universidad de Chile, Plaza Ercilla 883, Casillia 1420, Santiago, Chile.

OBSERVED BEHAVIOR OF CHILEAN PCC PAVEMENTS

Several years of precise measurements of slab internal temperatures and vertical displacements, as well as joint openings, at the 21 test sections have clearly shown the existence of an upward concavity in all slabs, with the edges and corners tending to remain unsupported most of the time (*5*). The causes for this condition are related to the combined action of climatic features affecting the pavement since construction.

Daily temperature variations induce upward curling typically during the cooling period between 6:00 p.m. and 10:00 a.m., depending on the season, cloudiness, and site latitude. As a result of semiempirical modeling of internal temperatures, calibrated with actual field measurements, the accumulated hours at various intervals of thermal gradient lead to the conclusion that the pavement remains cooler at the top surface than at the bottom roughly two-thirds of the time (*9*).

On the other hand, rainfall is highly concentrated in the winter season, followed by long periods of little or no rain, producing yearly variations of moisture differentials through the slab thickness. In fact, the internal moisture has wider variations near the surface, which is exposed to evaporation, than at the protected bottom; therefore, the pavement slabs tend to be permanently upward warped, reaching a maximum at the end of autumn and a minimum during the rainy season (*10*). This effect has been consistently verified with field measurements, particularly through the corner displacements measured at the moment of zero thermal gradient, as shown in Figure 2 for different days in a 3-year period.

Another possible factor contributing to the upward concavity of the pavement slabs is related to the irreversible drying shrinkage of the concrete slab surface that occurs during the first hours of concrete hardening (*11*).

Considering the additive effects of the irreversible drying shrinkage, the moisture differential, and the thermal gradients

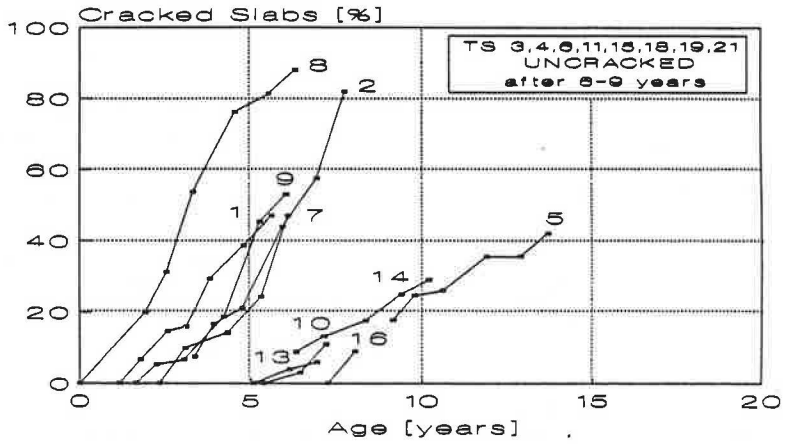


FIGURE 1 Evolution of slab cracking in test section pavements (transverse and corner cracks).

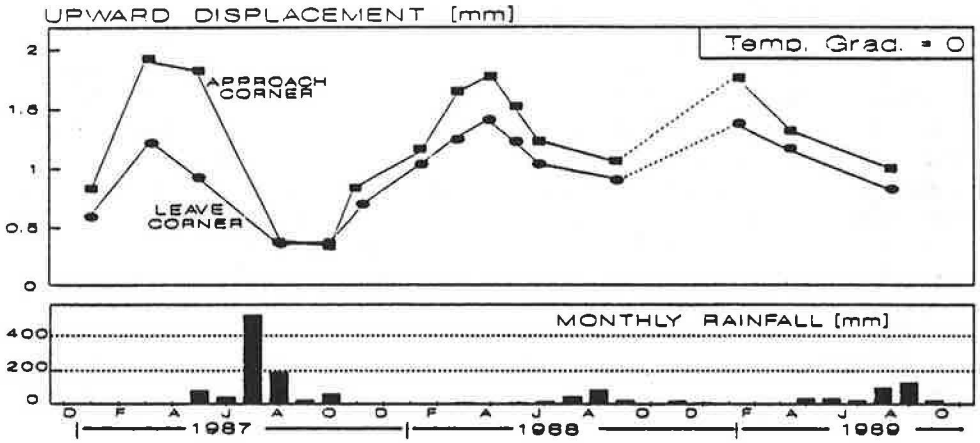


FIGURE 2 Annual cyclic variations of slab nonload deformations and rainfall for typical test section pavement.

in the concrete, a predominant upward concavity in all pavement slabs is therefore controlling the structural condition to be considered in the stress analysis (see Figure 3a). The downward concavity (see Figure 3b), traditionally considered critical (*12*), could only be produced during the first hours of high solar radiation on a sunny summer day while the edges are still free to rotate. However, compressions develop at the transverse edges as soon as the mean temperature increases and, therefore, some degree of longitudinal continuity is attained, leading the whole pavement to behave as a rather continuous strip supported along the longitudinal edges (see Figure 3c). As a consequence, the condition of downward concavity is not considered critical as far as the accumulation of fatigue damage is concerned, although the concrete may develop high stresses during short periods of time.

Under the traffic loadings acting on the upward concave slabs, the fatigue of the concrete is manifested by transversal cracking, usually beginning from the middle of the edges. Sometimes, curved corner cracks also develop, as shown in Figure 4. As verified through boreholes at the test section slab, cracking always starts from the upper surface and progresses downward.

Slab-to-slab cracking was measured at each test section by means of a visual survey conducted annually during the 5 years of research. From the analysis of all data, three indexes that were found to be useful for modeling purposes include (a) the percentage of slabs with any type of crack, (b) the accumulated length of cracks (m/km) and (c) the average number of pieces per slab. These indexes were related to the results of the structural analysis of the pavement slabs to generate a model of slab cracking.

DEVELOPMENT OF SLAB CRACKING MODEL

For structural modeling, the pavement is considered to be a system composed of a series of slabs of similar geometry and material characteristics. Boundary conditions of each slab are controlled by the reduced support on the base and by the interaction with adjacent slabs through the joint efficiency, or load transfer, in transversal and longitudinal edges (*3*). Such a system is simultaneously stressed by the body forces acting on the slabs with varying degrees of upward concavity and by the repeated loads of traffic.

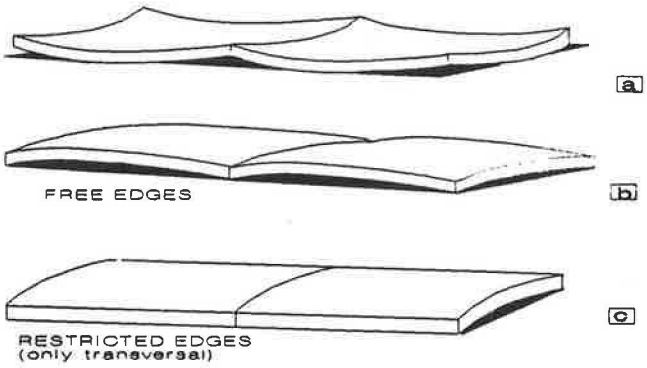


FIGURE 3 Typical shapes of slabs deformed by temperature: (a) upward concave slabs, (b) and (c) downward concave slabs.

An approach for solving this complex, nonlinear, multivariable problem is the concept of fatigue consumption accumulated in the slab concrete from the first traffic passing over the pavement until the moment of evaluation (*12*). At that time, the accumulated fatigue consumption is compared with some index of slab cracking actually observed in the field.

In order to calculate stresses under different levels of upward concavity, traffic must not only be known in volume and in axle load distribution but also discriminated by hour and season. A statistical processing of the traffic data (*6*) showed that average daily traffic (ADT) in the 21 sections ranged between 4,000 and 12,000 veh/day, of which 26 percent are heavy trucks and 9 percent buses, mainly passing between 6:00 a.m. and 8:00 p.m. The heavy vehicles were divided into single, tandem, and tridem axles, with the load distribution shown in Figure 5 based on weigh-in-motion data.

To calculate tensile stresses, the finite element method was used with the slabs being modeled as a system of thick, interacting plates capable of admitting nonlinear distribution of internal temperature through the slab thickness. The slab support was modeled by a set of continuous springs of subgrade reaction modulus Kw, which are not capable of taking tension. Therefore, iterations are needed until the partial support condition is satisfied. To consider the interaction between slabs, special joint elements were developed to restrict edge displacements and rotations. At longitudinal edges the condition of free border is realistic, both at the exterior edge with the granular shoulder and at the interior edge, where a significant level of deflection is needed to mobilize the effect of adjacent slabs through the keyed longitudinal joint. The program PAVIDIEM, developed for a personal computer, was checked with cases of known direct stress solutions, such as those provided by the Westergaard and Spangler equations (*13*), and indirectly against such widely used programs as SAP–4 and others using solid elements (*14*). Most important, the calculated displacements were compared with actual field measurements.

In a previous analysis the most critical position of the three types of loaded axles was investigated on a typical pavement with upward concave slabs. In all cases the maximum tensile stress is at the upper slab surface and toward the central portion of the slab when the loaded axle is crossing the transverse joints, particularly when the outer wheels are at the corner. Tensile stresses are also high at the middle zone of the edges, as shown by the isograms in Figure 6. For evaluation purposes, the wheels are positioned at some distance from the edge, where most traffic actually passes.

These results are in good agreement with the actual pattern of slab cracking (see Figure 4), which typically starts at the edges and progresses down and inward until the complete breakage of the slab. This empirical observation demonstrates that those high stress points are indeed critical in accumulating fatigue consumption.

The full range of conditions encountered in the actual pavements includes different slab geometry and material properties; varying degrees of partial support, joint efficiency, and internal temperature and moisture differentials; and the three types of axles and load magnitudes. Considering the great number of cases needed to cover all these conditions, which are excessively time-consuming in a conventional finite element analysis, about 1,800 specific cases were selected to develop a mathematical model of practical use. The resulting dimensionless equation, shown in Figure 7, has an estimated error of less than 10 percent for the finite element solution. In the equation, joint efficiency (J) is the simple ratio of the leave and approach corner deflections when the load is in the approach side (*2*), and ΔTeq is a negative equivalent temperature differential that includes all components of upward concavity, as discussed previously.

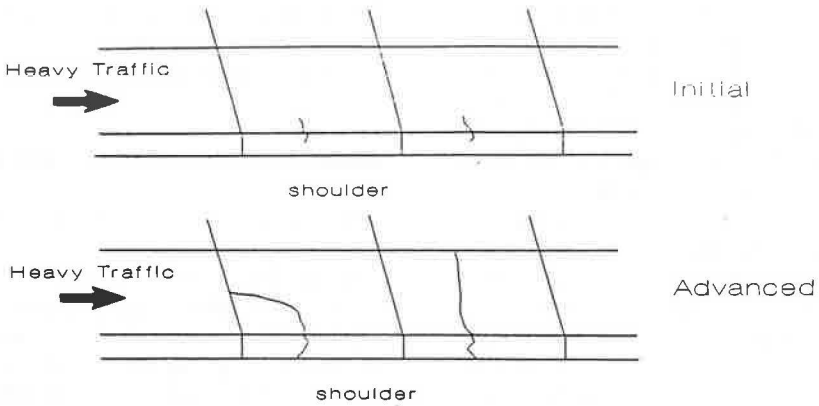


FIGURE 4 Typical pattern of slab cracking developed in in-service PCC pavements.

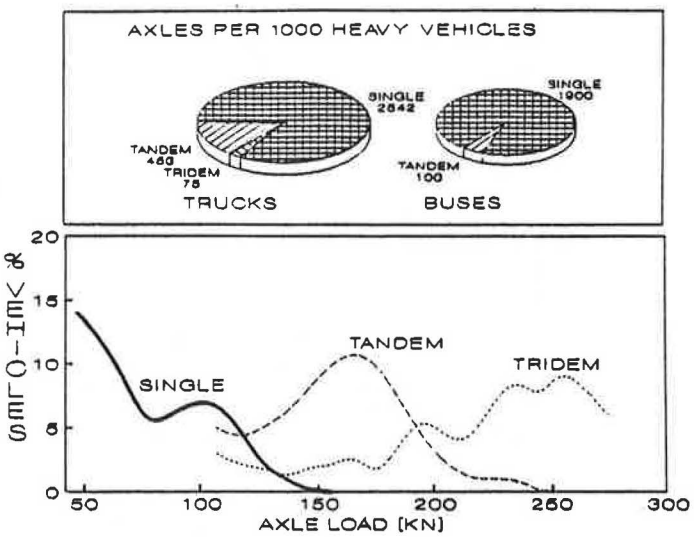


FIGURE 5 Traffic composition and axle load composition.

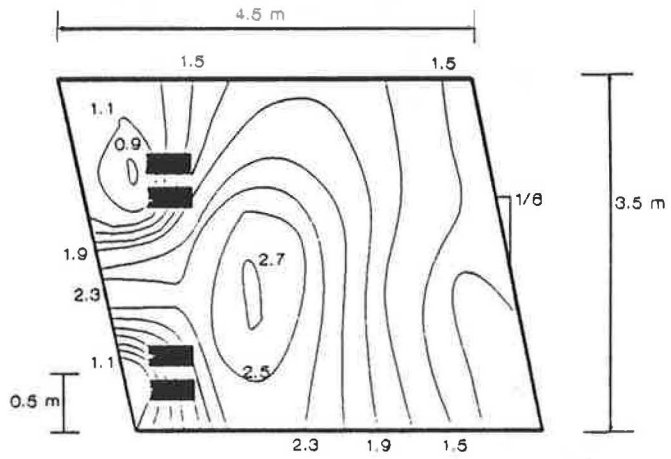


FIGURE 6 Tensile stresses (MPa) at upper surface of upward concave slab produced by a 110-kN single-axle load.

Kw was derived from the center point deflections under truck wheel loads actually measured in each test section pavement. All deflections measured at the central point of slabs keep practically constant, with reduced magnitude at every season, indicating that the base support remains essentially stable throughout the year. The numerical Kw values are about 10 times greater than were expected from repetitive plate load tests.

The fatigue consumption was calculated on the basis of an applicable concrete fatigue curve. To that purpose cyclic flexural tests were performed on a prismatic specimen molded with concrete of the same characteristics as those used in the Chilean pavements (*15*), which verified the general trend of results gathered by Darter (*16*) and shown in Figure 8. The University of Chile research also emphasized the importance of selecting realistic values of the modulus of rupture (MR) of concrete when calculating $S_{max} = \sigma_{max}/MR$, especially regarding the possible existence of initial cracks in the tensile stressed surface.

The influence of repetitive alternating stresses producing tension on top and bottom surfaces needs to be further researched. For modeling purposes the average trend representing 50 percent probability of failure was selected to correspond with similar probability of slab cracking in the field.

Determining the accumulated fatigue consumption of each climatic parameter that modifies the slab boundary conditions is an extremely complex task. To approach a reasonable solution, a full-year period was discriminated into three seasons; each with separated cloudy, sunny, and partial cloudy weather conditions. At the same time, the daily cyclic temperature variations were divided into three hour groups to account for the conditions of negative, nearly zero, and positive gradients (°C/mm), as presented in Table 1.

By applying the stress equation to each level of axle loading in each of the previously defined conditions, the number of allowable repetitions (N) can be found using the selected fatigue curve. Letting n represent the number of actual load repetitions, known from traffic data in each environmental

$$\frac{\sigma}{E} = K_1\left[K_2\frac{Q}{e^2E} - \left(\frac{20\,J\,Q}{e^2E}\right)^{K_3} + \left(K_4\frac{W}{e^2E} + K_5\frac{Q}{e^2E}\right)\alpha\,\Delta Teq\right]^{K_6}\left(\frac{L}{l}\right)^{K_7}\left(\frac{A}{l}\right)^{K_8}$$

$$\left[\text{AXLE LOAD} - \left(\text{JOINT EFFICIENCY}\right) + \left(\text{SLAB WEIGHT} + \text{AXLE LOAD}\right) * \text{UPWARD CONCAVITY}\right] * \text{SLAB GEOMETRY}$$

VARIABLES

σ :Maximum tensile stress at the upper face of slab
Q :Axle Load
e,L,A:Slab thickness, length, width
W :Slab weight
J :Joint efficiency (0 - 100 %)
E, ν :Concrete moduli
α :Coefficient of thermal expansion
Δ Teq :Equivalent temperature differential <= 0
(temperature + moisture + permanent)

$l = \sqrt[4]{\frac{e^3E}{12(1-\nu^2)Kw}}$: Relative stiffness

Kw :Subgrade reaction

	SINGLE	TANDEM	TRIDEM
K_1	$5.80*10^{-6}$	$8.08*10^{-6}$	$6.43*10^{-6}$
K_2	$1.7*10^{3}$	$8.5*10^{3}$	$8*10^{3}$
K_3	0.3	0.2	0.1
K_4	$4.3*10^{8}$	$3*10^{8}$	$4*10^{8}$
K_5	$1.5*10^{8}$	$9*10^{7}$	$8.*10^{7}$
K_6	0.85	0.83	0.81
K_7	0.25	0.30	0.35
K_8	0.48	0.40	0.38
r^2	0.94	0.92	0.92

FIGURE 7 Proposed stress equation.

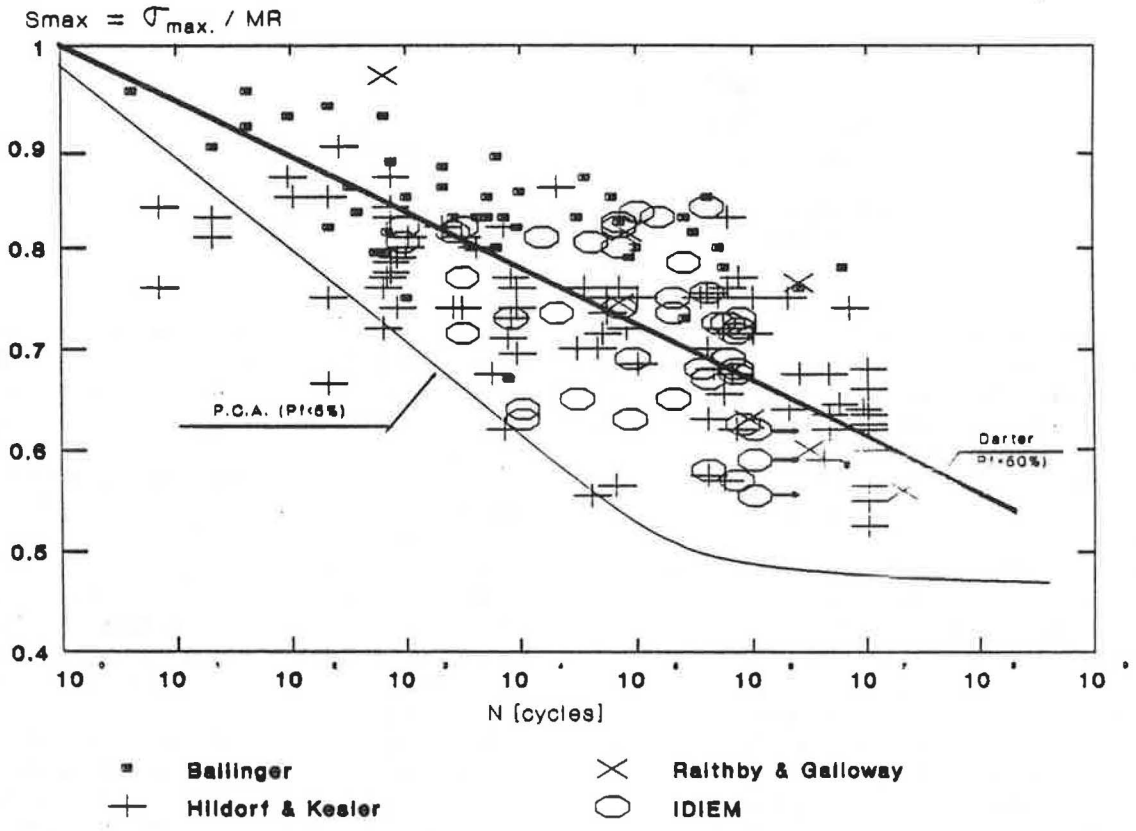


FIGURE 8 Set of flexural test results compiled from different authors.

TABLE 1 DAILY CYCLIC TEMPERATURE VARIATIONS

WEATHER	SEASON	HOUR GROUP		
		9 PM - 9 AM	9-11 AM/ 5-9 PM	11 AM - 5 PM
Sunny	S	- 0.055	0	+ 0.075
	W	- 0.030	0	+ 0.050
Cloudy	S	- 0.042	0	+ 0.055
	W	- 0.015	0	+ 0.025
Partial	S	- 0.030	0	+ 0.040
	W	- 0.005	0	+ 0.010

S: Summer (Jan - Apr) W: Winter (May - Aug) S: Spring (Sept - Dec)

condition, the fatigue consumption was evaluated as n/N. According to Miner, the accumulated fatigue consumption (D) is the aggregation of all individual n/N values, as shown in Figure 9.

Using the accumulated fatigue consumption as a variable that integrates all controlling factors described here, the various curves of slab cracking as a function of age (see Figure 1) have been unified into a single trend, as shown in Figure 10. The proposed curve is the result of a pavement evaluation for a 50 percent probability of slab cracking within a homogeneous section, where the modulus of rupture and other factors are assumed constant. Therefore, it is not surprising to have fatigue consumption values greater than 1 when the slab cracking has affected more than half of the slabs in a pavement section.

COMPARISON OF SLAB CRACKING INDEXES

From an analysis of the visual surveying data, the alternative indexes of total crack length per kilometer and average number of fragments per slab are found to be related to the percentage of cracked slab, as shown in Figure 11. These indexes are complementary to the model and serve to better define the extent of a maintenance or rehabilitation plan.

COMMENTS

The model of cracking explains well the type of cracking occurring in Chile, as shown in Figure 4. The present model of slab cracking has been developed for the structural condition of a predominant upward concavity producing partial support localized under the central part of the slab. This condition, being characteristic of Chile's PCC pavements, is believed to be much more widespread than currently acknowledged, as in Florida (*17*), California (*18*), Spain, and other locations. This approach is substantially different than the traditional theory used by the Portland Cement Association, Darter, and others. The proposed methodology, which is based on the analytical modeling of an empirical behavior, permits the explicit consideration of an ample variety of climatic parameters, conditions of slab support, and joint load transfer. It is well suited for successive future adjustments from additional field data gathered at more advanced states of distress.

The model is also thought to be good for the design of a pavement structure, varying the different parameters of slab geometry, load transfer, and slab support, at any climatic location. The method is capable of introducing a desired final state of cracking, depending on the level of functional distress that can be considered allowable.

The results presented deal with the fatigue consumption associated with structural distress or cracking in rather new pavements, which does not necessarily result in a serviceability loss because there is a time lapse between the appearance of a crack and the subsequent deterioration being noticeable by road users. For instance, if the pavement is reaching a state of 90 percent cracked slabs, four or five fragments can be expected as average in a section, meaning that some specific slabs may be presenting a much higher

$$D = \sum_{1}^{P} \underbrace{\sum_{1}^{S} \sum_{1}^{W} \sum_{1}^{H}}_{\text{ENVIRONMENT}} \underbrace{\sum_{1}^{A} \sum_{1}^{L}}_{\text{TRAFFIC}} \left[\frac{n}{N}\right]$$

P : Period of evaluation, in years
S : Seasons (Summer, Winter, Spring)
W : Weather conditions (Sunny, Cloudy, Partial)
H : Hour groups in a day
A : Types of axle (single, tandem, tridem)
L : Load intervals

FIGURE 9 Criteria of fatigue consumption aggregation.

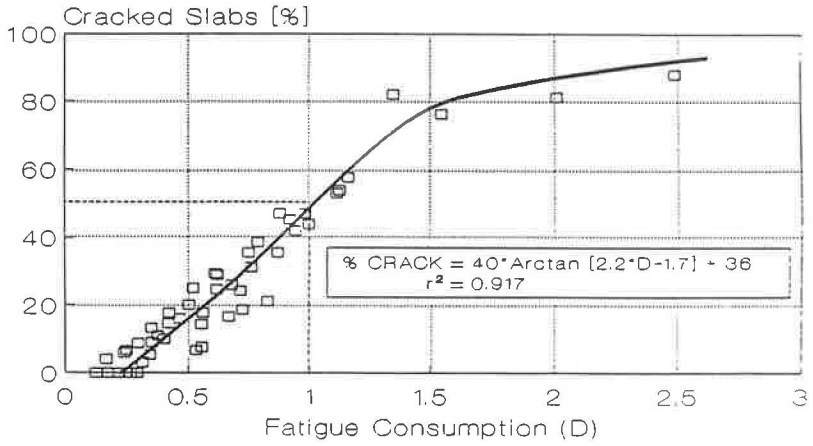


FIGURE 10 Model of slab cracking.

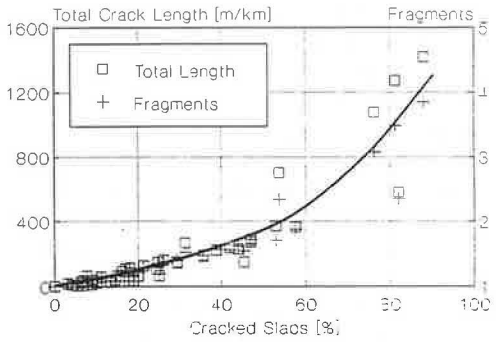


FIGURE 11 Empirical relationships between slab cracking indexes.

degree of fragmentation, which would be clearly noticeable by the road user. Beyond the limit of 90 to 95 percent cracked slabs, the distress process is represented by the indexes of fragmentation or crack length, or both. Such evolution needs further observation, which is not yet available.

CONCLUSIONS

Upward warping and curling evidenced by precise field measurements in the climatic conditions of central Chile are found to be the controlling boundary conditions to introduce into mechanistic analysis. On the basis of fatigue consumption, a pavement evaluation method considering the actual behavior of Chile's PCC pavements has been developed. The resulting model is a unique S-shaped curve, integrating the evolution of all pavements under consideration. The cracking model is useful for the design level in showing the effects of many important variables on slab cracking.

ACKNOWLEDGMENTS

Grateful acknowledgment is due to the National Highway Administration of Chile for the permission to publish the study results and to all colleges associated with the project at the University of Chile. Special appreciation is extended to M. Darter for reviewing the manuscript.

REFERENCES

1. T. Watanatada, C. Harral, W. Paterson, A. Dhareshwar, A. Bhandari, and K. Tsunokawa. *The Highway Design and Maintenance Standard Model*. Transportation Department, World Bank, Washington, D.C., 1987.
2. M. Darter, J. Becker, M. Snider, and R. Smith. *NCHRP Report 277: Portland Cement Concrete Pavement Evaluation System COPES*. TRB, National Research Council, Washington, D.C., 1985.
3. M. Poblete, R. Valenzuela, and R. Salsilli. Load Transfer in Undoweled Transverse Joints of PCC Pavements. In *Transportation Research Record 1207*, TRB, National Research Council, Washington, D.C., 1988.
4. M. Poblete, R. Valenzuela, E. Clasing, J. Salgado, and P. Gutierrez. Faulting Evaluation in Undoweled PCC Pavements with Slabs Curled Upward. Presented at 4th International Conference on Concrete Pavement Design and Rehabilitation, Purdue University, West Lafayette, Ind., April 1989.
5. M. Poblete, R. Salsilli, R. Valenzuela, A. Bull, and P. Sprätz. Field Evaluation of Thermal Deformations in Undoweled PCC Pavement Slabs. In *Transportation Research Record 1207*, TRB, National Research Council, Washington, D.C., 1988.
6. IDIEM, University of Chile. *Final Report to the Concrete Pavements Research Project, Volume I* (in Spanish). National Highway Administration, Chile, 1989.
7. IDIEM, University of Chile. *Final Report to the Concrete Pavements Research Project, Volume III* (in Spanish). National Highway Administration, Chile, 1989.
8. IDIEM, University of Chile. *Field Instrumentation, Equipments and Measurements Methodology* (in Spanish). National Highway Administration, Chile, 1986.
9. P. Ceza. *Study of Temperature Distribution in a Concrete Pavement Structure* (in Spanish). Civil Engineering thesis. University of Chile, Santiago, 1986.
10. M. Poblete, A. García, J. David, P. Ceza, and R. Espinosa. Moisture Effects on the Behavior of PCC Pavements. Presented at 2nd International Workshop on the Design and Evaluation of Concrete Pavements, Siguenza, Spain, Oct. 1990.
11. A. Zachlehner. *Concrete Pavement Stress by Hydration and Atmospheric Effects*. Publication 57. Testing Office for Highway Construction, Technical University of Munich, Germany, 1989.
12. *Thickness Design for Concrete Highway and Street Pavements*. Report EB 109 P. Portland Cement Association, 1984.
13. A. Ioannides, R. Thompson, and J. Barenberg. *Westergaard Solution Reconsidered*. Transportation Research Laboratory, De-

partment of Civil Engineering, University of Illinois, Urbana, Champaign, 1986.
14. J. Bathe. *SAP 4, A Structural Analysis Program for Static and Dynamic Response of Linear Systems*. University of California, Berkeley, 1973.
15. G. Moreno. *Concrete Fatigue Characteristics of Chilean PCC Pavements* (in Spanish). Civil Engineering thesis. University of Chile, Santiago, 1988.
16. M. Darter. Design of Zero-Maintenance Plain Jointed Pavement. Report FHWA-RD-77-11. FHWA, U.S. Department of Transportation, June 1977.
17. J. M. Richardson and J. M. Armaghani. Stress Caused by Temperature Gradient in Portland Cement Concrete Pavements. In *Transportation Research Record 1121*, TRB, National Research Council, Washington, D.C., 1987, pp. 7–13.
18. W. Ames. Concrete Pavement Design and Rehabilitation in California. Presented at 3rd International Conference on Concrete Pavement Design and Rehabilitation, Purdue University, West Lafayette, Ind., April 1985.

Publication of this paper sponsored by Committee on Rigid Pavement Design.

Factors Affecting Deterioration of Transverse Cracks in Jointed Reinforced Concrete Pavements

ZAFAR I. RAJA AND MARK B. SNYDER

Jointed reinforced concrete pavement (JRCP) develops transverse cracks as the drying and thermal shrinkage of the concrete is resisted by friction with the supporting layers. These cracks deteriorate with time and traffic because of loss of load transfer capacity. However, rapid deterioration of these cracks has been observed on some recently constructed projects. This rapid crack deterioration leads to accelerated maintenance requirements and shortened service lives. A synthesis of factors that may reduce aggregate interlock load transfer is presented, and research efforts currently under way at Michigan State University aimed at evaluating the relative effects of several of these factors on transverse crack deterioration in JRCP are described. The ongoing work involves the collection and analysis of load transfer data from the testing of a series of large-scale pavement test specimens that are subjected to repeated applications of loads simulating the passage of heavy-truck traffic. The test variables selected for the study include type of coarse aggregate, gradation of coarse aggregate, treatment of coarse aggregate (virgin, recycled, and blend), source of coarse aggregate, foundation support, reinforcing steel quantity and type, and amount of slab tension.

Jointed reinforced concrete pavement (JRCP) typically develops transverse cracks over the first several years of its service life as contractions of the slab (caused by combinations of drying and thermal shrinkage) are restrained by friction between the slab and supporting layers. Transverse cracks may also be initiated by combinations of curling, warping, and load-related stresses. Most JRCP designs rely on aggregate or grain interlock to transfer shear loads across these cracks. The loss of aggregate interlock due to opening of these cracks permits increased slab deflections, as well as the infiltration of water and intrusion of incompressibles into the cracks. These factors, in turn, lead to pumping and crack deterioration through faulting and spalling. Continued pumping eventually leads to a loss of support beneath the slabs, which greatly increases load-related stresses in the slab and can result in fatigue cracking. Thus, the transverse cracks must exhibit good long-term load transfer characteristics to minimize the development and severity of distresses. The concept of aggregate interlock is described in the following paragraphs, and factors that may accelerate the loss of aggregate interlock load transfer are discussed. Research being conducted at Michigan State University to evaluate the relative impacts of selected factors on JRCP transverse crack performance is also described.

Department of Civil and Environmental Engineering, Michigan State University, E. Lansing, Mich. 48824.

LOAD TRANSFER ACROSS TRANSVERSE CRACKS

The ability of transverse cracks and joints to transfer load is a major factor in the structural performance of the crack or joint and the surrounding slabs. This ability, typically referred to as load transfer efficiency, can be described in different ways, including deflection load transfer efficiency and stress load transfer efficiency. Several formulas for computing load transfer efficiency have been adopted by various researchers; the definitions used here are as follows:

$$\%LT = d_{UL}/(d_{UL} + d_L) \times 100 \quad (1)$$

where

$\%LT$ = percent load transfer,
d_{UL} = deflection of the unloaded side of the crack or joint, and
d_L = deflection of the loaded side of the crack or joint (*1*).

In Equation 1, the maximum load transfer that can be achieved is 50 percent. This value is obtained when the two slabs deflect an equal amount. Other deflection-based formulas include the one first proposed by Teller and Cashell (*2*):

$$\%LT = 2 \times d_{UL}/(d_{UL} + d_L) \times 100 \quad (2)$$

where d_{UL} is the deflection of the unloaded slab and d_L is the deflection of the loaded slab (*2–4*).

Load transfer efficiency can be computed on the basis of stress using formulas similar to those just described for load transfer based on deflection. Sutherland and Cashell (*5*) used the following definition to compute load transfer efficiency on the basis of stress:

$$E = (f_f - f_j)/(f_f - f_i) \quad (3)$$

where

E = joint efficiency,
f_f = stress for a given load applied at a free edge,
f_j = stress for a given load applied at the crack or joint edge, and
f_i = stress for a given load applied at the slab interior.

Most JRCP designs rely on aggregate or grain interlock to achieve the necessary load transfer capacity across transverse cracks. Deterioration of these cracks has been found to be strongly related to loss of load transfer efficiency. Therefore, a discussion on the mechanisms, models, performance, and endurance of aggregate interlock is presented in the succeeding paragraphs.

Aggregate Interlock Mechanism

Aggregate interlock is the simplest means of load transfer; the protrusions in one fractured face mesh with the recesses in the other to provide shear resistance along the fractured face. At the time of crack development, the vertical surfaces of the crack are usually rough and irregular. The majority of the coarse aggregate particles typically remain embedded in either of the crack faces. As a wheel approaches a crack, differential vertical displacement of the two slab fragments takes place, causing the particles of one face of the crack to come into contact with the matrix of the other face. Further differential vertical movement is then restricted by the bearing and friction of the aggregate particles along the crack surface. A portion of the wheel load is transferred from one side of the crack to the other through the shear developed by the interlocking action of the aggregate particles at the fractured faces of the crack. This action is commonly referred to as aggregate, or grain, interlock.

Substantial shear forces can be transmitted through this mechanism if the cracks remain tight. JRCP typically contains a small amount of longitudinal reinforcement, often referred to as temperature and shrinkage reinforcement, to help ensure that these cracks do not open appreciably.

Aggregate Interlock Models

Several models have been proposed to explain the aggregate interlock mechanism. One model (*6*) distinguishes between interlock due to local roughness and that due to global roughness of the crack face (see Figure 1). It is postulated that local roughness (or micro texture) causes interlocking of the fine aggregate particles, which is principally a bearing or crushing action, and that global roughness (or macro texture) causes interlocking of coarse aggregate particles, principally a sliding and overriding action. Local roughness is believed to be responsible for most aggregate interlock effects when crack widths are less than 0.01 in. It is further postulated that the effects of local roughness predominate in the early loading cycles and that global roughness predominates in later cycles as crack widths increase and local roughness is reduced.

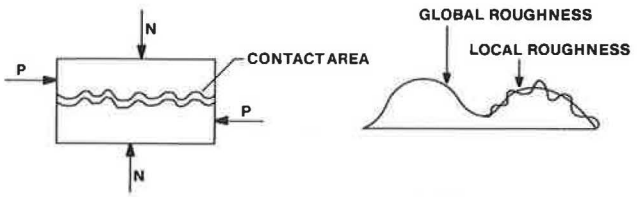


FIGURE 1 Local and global roughness model of aggregate interlock mechanism (*6*).

An alternative model proposes that aggregate interlock is caused by the sliding resistance of two rigid surfaces. These surfaces have been represented by a sawtooth shape (see Figure 2) (*7*,p.357) and by a series of parabolic segments (*8*).

A more recent model (*9*) suggests that concrete is a two-phase material of aggregate and cement matrix that can be modeled as a distribution of rigid spheres of a range of sizes embedded to various depths within a deformable rigid-plastic matrix (see Figure 3). In this model, shear forces are resisted by a combination of crushing and sliding of the rigid spheres into and over a softer cement matrix; contact and interaction between spheres projecting from opposite crack faces are not considered.

Millard and Johnson (*10*) devised a laboratory test to examine aggregate interlock and to determine whether any of the theoretical models could be verified. Their test results do not support the local and global roughness and frictional sliding models. However, they found a fairly consistent agreement between the test results and the two-phase model. These researchers concluded that "the aggregate interlock test results show that the two-phase model, involving a combination of crushing and sliding of the crack faces, is the most realistic one" (*10*).

Aggregate Interlock Performance

An extensive review of the literature reveals that the development of load transfer through aggregate interlock has been studied by several researchers since the early 1900s. However, with the exception of a field study conducted by the Michigan State Highway Department (*1*) to evaluate the aggregate interlock load transfer across reinforced transverse cracks, most of these previous studies were concerned with weakened-plane transverse joints. The studies have shown that a few variables

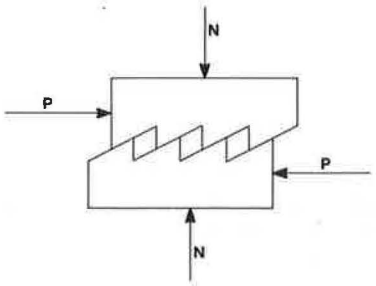


FIGURE 2 Frictional sliding model of aggregate interlock mechanism (*7*,*8*).

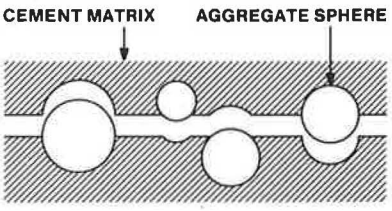


FIGURE 3 Two-phase model of aggregate interlock mechanism (*9*).

predominantly affect development and endurance of load transfer through aggregate interlock. These variables include width of crack opening and texture of the crack face.

Effect of Width of Crack Opening

The results of previous investigations have clearly established that the width of the crack opening has the most pronounced effect on the load transfer capacity of transverse cracks and joints through aggregate interlock. Benkelman (*1*) showed that opening these cracks by as little as 0.03 in. produces a loss of load transfer of 50 percent (see Figure 4). Colley and Humphrey (*3*) observed a similar trend in their studies of aggregate interlock behavior (see Figure 5). These researchers found that "when test load, slab thickness, and subbase were held constant, joint effectiveness decreased as the joint opening was increased" (*3*). Nowlen (*4*) reported a loss of 45 to 55 percent for the same amount of opening, depending on maximum size of aggregate. Similarly, studies by Darter (*11*) have shown that the drop in load transfer is from 20 to 60 percent for 0.03-in. openings, depending on the level of support provided by the foundation. A numerical study by Soroushian et al. (*12*) also indicated that the stiffness and ultimate strength of aggregate interlock decreases significantly with increases in crack width. This loss of load transfer capacity results from a loss of contact between the two slab fragments, requiring some differential vertical movement of the slab fragments before contact and bearing can take place.

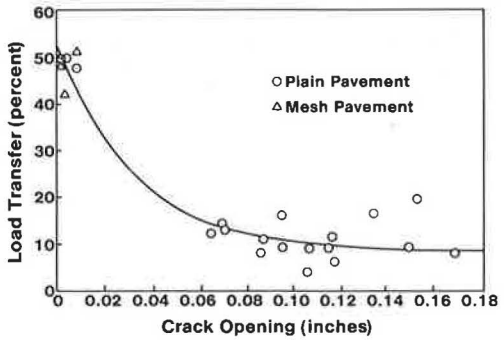


FIGURE 4 Relationship between crack opening and percentage of load transferred (from Equation 1) (*1*).

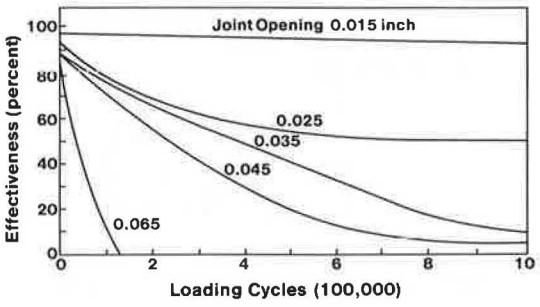


FIGURE 5 Influence of joint opening on effectiveness percentage (from Equation 2) (*3*).

Thus, for these cracks to exhibit good load transfer characteristics, it is imperative that reinforcement serve its intended purpose, that is, to hold the fractured concrete in close interlock.

The results of Benkelman's study (*1*) effectively illustrated the impact of reinforcement on load transfer capacity of transverse cracks (see Figure 6). This figure shows that a smaller percentage of load is transferred across cracks in plain concrete than across those in pavement containing reinforcement, even during the summer months. Moreover, plain concrete cracks undergo a significant drop in load transfer from summer to fall because of the seasonal opening of these cracks, whereas properly reinforced sections experience practically no loss of load transfer during the cold months. Benkelman attributed the small increase in load transfer between fall and winter to higher temperatures at the time of winter loadings compared with the tests made in autumn. Thus, Benkelman concluded that "when roughened edges of two slabs are held firmly together the aggregate interlock may be expected to function perfectly and permanently as a load-transfer medium" (*1*).

Effect of Texture of Crack Face

The aggregate interlock load transfer capacity of transverse cracks and joints has been found to be related to the texture of the crack face. The crack face texture is primarily a function of the type and size of the coarse aggregate, the maturity of the concrete at the time of fracture, and the strength of the concrete. Angular, rough-surfaced aggregates (such as crushed stone) generally provide better interlock and load transfer over narrow crack openings than do rounded, smooth-surface aggregates (such as natural gravels). This contention is supported by Colley and Humphrey (*3*), who contend that con-

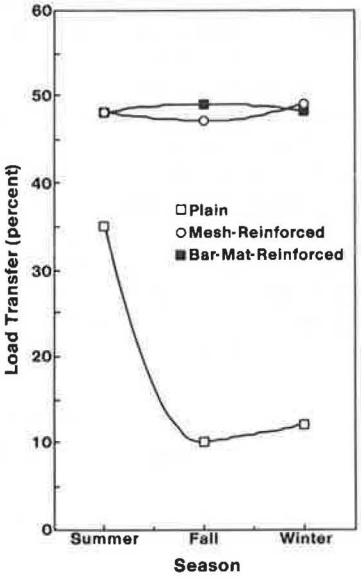


FIGURE 6 Restraining effect of reinforcement on load transfer capacity of transverse cracks (*1*).

cretes made using crushed limestone and crushed gravel coarse aggregates had higher load transfer effectiveness values than those made with natural rounded gravels.

The key factor that determines the texture of the crack face is the mode of concrete fracture. Depending on the bond strength, concrete may fracture in two different ways: (a) around the aggregate or (b) through the aggregate. When concrete fractures around the aggregate, many pullouts of aggregate particles exist, resulting in a rough interface. The results of the Nowlen study (*4*) show that early fracture (i.e., when the aggregate-paste bond is relatively weak) results in many pullouts. However, at later times of cracking, concrete strength has increased and pullouts are diminished because of higher aggregate-paste bond strengths, resulting in more numerous aggregate fractures. The study concluded that "for equal joint openings early fracture of the joint faces with resulting aggregate pullouts contributed to high effectiveness initially, and also to endurance of good effectiveness under repeated loads" (*4*).

When coarse aggregate fractures occur during crack formation, the advantages of angular, rough-surfaced aggregate are largely lost because fracture of aggregate results in a smoother crack face. Sutherland and Cashell (*5*) found that concretes made using natural round gravel had better aggregate interlock load transfer characteristics than concretes made using similarly graded crushed limestone. They attributed the greater load transfer efficiency of the joints in concrete made using rounded gravel to the development of aggregate projections along the crack face. These projections resulted from the poorer aggregate-paste bond, which allowed aggregates to pull out of the matrix rather than fracture. Concretes made using crushed stone tended to crack through the aggregate, producing a smoother crack face and lower levels of interlock load transfer efficiency.

Sutherland and Cashell (*5*) and Nowlen (*4*) also studied the effect of coarse aggregate size on the performance of load transfer through aggregate interlock. The results of these studies agree that large coarse aggregates provide more interlock and higher load transfer efficiencies than small coarse aggregates, particularly for large joint openings (see Figures 7 and 8). However, these figures also show that, although load transfer efficiency generally increases with increasing aggregate size, load transfer efficiency decreases rapidly with increasing joint width, regardless of aggregate size. Sutherland and Cashell concluded that "aggregate interlock was effective in stress

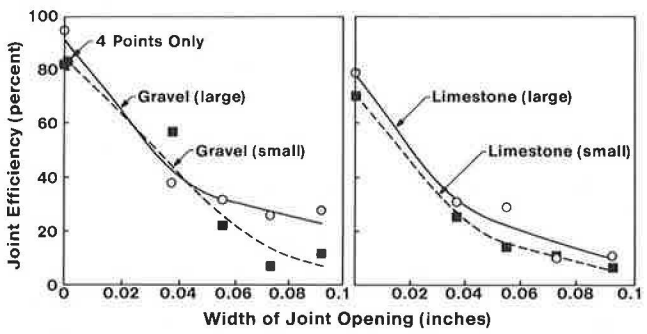


FIGURE 7 Effect of size of coarse aggregate on relationship between joint opening and joint efficiency (*5*).

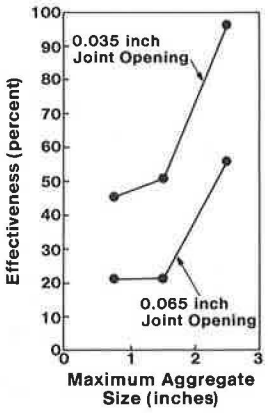


FIGURE 8 Influence of aggregate size on joint effectiveness (*4*).

control when the joints were closed or under compression, but that it was not dependable when the joints opened 0.037 in. or more irrespective of the type or maximum size of aggregate in concrete" (*5*).

The resistance of the crack faces against shear displacements is also affected by the compressive strength of concrete. Studies have shown that increasing the concrete compressive strength considerably increased the aggregate interlock stiffness and ultimate strength (*10,12*). It was suggested that, when increases in concrete compressive strength are due at least in part to increases in the matrix strength, resistance against contact area deformations is also larger so that higher shear stiffnesses are obtained.

Aggregate Interlock Endurance

Maintenance of adequate load transfer through aggregate interlock over a large number of heavy-truck load applications is critical to the satisfactory long-term performance of JRCP. The interlocking features of cracks and joints can be worn through repeated slippage and abrasion of the two vertical faces under accumulated load applications. It follows that hard materials, which are resistant to abrasion, should provide good load transfer effectiveness longer than soft materials, which abrade easily. Nowlen (*4*) confirmed this contention. He found that slabs built with aggregates with good abrasion resistance [Los Angeles abrasion loss values (LA) = 17 and 28] were superior in effective endurance to those built with aggregates having poor abrasion resistance (LA = 46).

Colley and Humphrey (*3*) found that load transfer effectiveness decreases as the number of load applications increases. They noted, however, that 90 percent of the decrease occurs during the first 500,000 load repetitions. These researchers introduced the concept of an endurance index (EI), which represents the ability of a joint or crack to retain load transfer effectiveness under load repetitions. The following model was developed to predict the EI as a function of the most significant variables in their test program:

$$EI = 230hk^{1/2}/Pw \quad (4)$$

where

EI = endurance index,
h = depth of roughened interface (in.),
k = foundation modulus (psi/in.),
P = wheel load (lb), and
w = joint opening (in.).

The EI is particularly sensitive to variations in foundation strength and joint openings, as shown in Figures 9 and 10. For example, increasing the k value of the foundation from 90 to 450 psi/in. increases the EI by a factor of about 2.6 times for a 7-in. slab and about 2 times for a 9-in. slab. This increase in EI results because strong foundation support reduces the magnitude of the differential vertical deflections, thereby allowing the application of more load cycles to produce a given loss of interlock and load transfer. This finding was verified numerically by Ioannides and Korovesis (*13*). Figure 10 shows that EI decreases as the joint opening increases. For example, increasing the joint opening from 0.025 to 0.065 in. decreases the EI by a factor of about 6 for a 7-in. slab and about 3 for a 9-in. slab.

CURRENT RESEARCH NEEDS

As described previously, studies conducted to date have revealed a large number of variables that may have some impact on the rate of deterioration of load transfer capacity through aggregate interlock of transverse cracks and joints in JRCP. Variables that significantly affect load transfer through aggregate interlock include (but may not be limited to) the following:

- Width of crack opening,
- Restraining impact of reinforcement (percent steel),
- Type of coarse aggregate,
- Size of coarse aggregate,
- Paste-aggregate bond strength,
- Compressive strength of concrete,
- Hardness of coarse aggregate (abrasion resistance),
- Applied load magnitude,
- Applied load repetitions,
- Foundation support, and
- Depth of roughened interface (interlocking area).

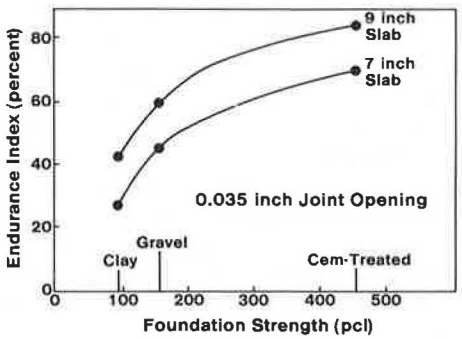


FIGURE 9 Effect of foundation strength on endurance index (*3*).

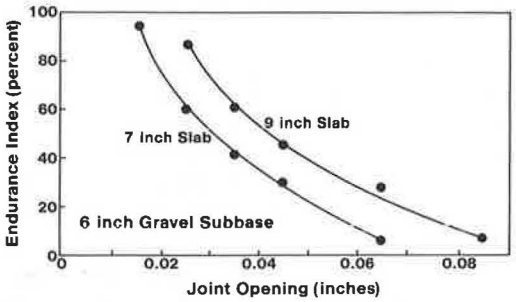


FIGURE 10 Effect of joint opening on endurance index (*3*).

Past research efforts, with the exception of the Benkelman study (*1*), have been directed only at the evaluation of weakened-plane transverse joints. Transverse joints are designed to allow horizontal slab movements and are thus different in design and function than transverse cracks in JRCP, which contain steel reinforcement that is intended to hold these cracks tight and resist any horizontal movement. Because of these design and functional differences, different variables affect the performance of joints and cracks. For example, the opening and failure of reinforced cracks are influenced by the design and performance of the reinforcing steel. Abrasion and attrition of the aggregates, daily and seasonal temperature variations, the presence of nonfunctional transverse joints (because of misaligned or corroded dowels or malfunctioning dowel assemblies), and the presence of expansion joints can also produce excessive crack movements. Many of these factors have not been evaluated in the context of transverse crack performance.

The performance of steel reinforcement in keeping JRCP transverse cracks from opening has historically been quite variable. Although many JRCP cracks remain tight throughout the pavement design life, there have been many documented cases of steel rupture, suggesting that the coefficient of friction or interlock between the slab and subbase may be much higher than traditionally assumed values. For example, temperature reinforcement is typically designed to withstand the stresses that would be produced in the presence of a subbase friction coefficient of 1.5 to 2 without allowing excessive crack opening. However, some types of granular and stabilized bases have been found to produce much higher levels of friction or interlock with the paving slab. This higher friction increases the slab and steel tension, which may cause permanent elongation or rupture of the steel and opening of the transverse cracks. These facts suggest that research efforts should be directed toward better characterization of the effects of slab tension and reinforcement on the performance of reinforced transverse cracks that are subjected to repeated heavy loads.

Another variable that merits further research is the effect of foundation support on crack load transfer capacity and endurance. A cracked slab supported on a fairly stiff foundation will experience little differential vertical movement across the cracks, even if they open substantially. However, pavements built on softer or unstable foundations can be expected to exhibit poor crack load transfer efficiency endurance. This factor is suspected of playing a major role in the rapid deterioration of cracks on at least one construction proj-

ect (*14*). Further research will help to quantify the role that foundation support plays in JRCP crack deterioration.

Previous research has not addressed some key issues currently facing pavement engineers. For example, current pavement design often calls for the use of smaller top-size aggregates (e.g., $\frac{3}{4}$ in. or less) as part of an effort to improve pavement durability. However, rapid deterioration of transverse cracks has been observed in recently constructed JRCP containing small-sized coarse aggregate. Cores taken at some of these projects have exhibited straight vertical crack faces with little roughness or meander. In many cases, the crack face has been ground almost to a sandpaper finish, indicating that little, if any, mechanical interlock will exist across even a tight crack (*14*). Such conditions reduce the vertical shear capacity of these cracks to near zero and can result in accelerated crack deterioration (i.e., spalling, faulting, and pumping) under repeated heavy-traffic load applications. Additional research must be devoted to determining the role of aggregate top size and gradation in the deterioration of reinforced transverse cracks.

High-quality aggregates suitable for use in highway construction are in short supply at many locations. One source of potentially high-quality aggregates is the recycling of concrete pavements that are in need of reconstruction. Coarse aggregates produced by recycling old pavements are often crushed to smaller sizes to improve the durability of the new pavement (especially if the old pavement exhibited durability-related distresses). These aggregates may also exhibit very different bonding characteristics with the cement paste due to local variations in the water-cement ratio caused by their nonuniform (and sometimes high) moisture absorption characteristics. Furthermore, these aggregates may fracture differently (and more readily) than natural aggregates, producing unusual crack face textures. A number of projects constructed using small-sized, recycled coarse aggregate have developed transverse cracks that deteriorated rapidly. Further study is needed to determine the effects of using various quantities of recycled concrete containing different types and gradations of virgin aggregate.

CURRENT RESEARCH

In light of the previously described research needs, a laboratory experimental research effort is under way at Michigan State University to evaluate the relative impacts of the following selected factors on JRCP transverse crack performance:

1. Coarse aggregate top size (1.0 versus 1.5 versus 2.5 in.),
2. Coarse aggregate treatment (virgin versus recycled versus recycled-virgin blend),
3. Coarse aggregate type (gravel versus limestone versus slag),
4. Coarse aggregate source (Gravel 1 versus Gravel 2, Limestone 1 versus Limestone 2),
5. Pavement support conditions (low versus medium versus high),
6. Reinforcing steel quantity (typical versus high),
7. Reinforcing steel type (smooth versus deformed), and
8. Slab tension (typical versus high).

The focus of this research is the development, execution, and analysis of a laboratory experiment involving the collection and analysis of load transfer data from the testing of a series of large-scale test specimens that are subjected to repeated applications of loads simulating the passage of heavy-truck traffic (see Figure 11). The test specimens are PCC-reinforced slabs, approximately 4.5 ft wide by 10 ft long and 9 in. thick at the transverse crack. The crack is forced near midslab after approximately 18 hr of curing. The test apparatus provides approximately uniform support for the specimen through the use of an artificial foundation (vibration isolation padding rated at specific k-values). Desired levels of foundation support are achieved by providing various thickness and type combinations of artificial foundation materials. The test equipment allows placement of slabs in tension before and during testing to simulate thermal and drying shrinkage in the field, which may exacerbate the effects of heavy-vehicle loads.

The application of traffic loads is accomplished using a pair of hydraulic actuators, of 11-kip capacity, which are mounted on the test frame. These actuators apply a sequence of load pulses to contact pads (simulating tire imprint areas) on the approach and leave sides of the crack to simulate field loading conditions for the outer wheel path of Interstate highway pavements. The maximum applied load is 9,000 lb (one-half of a standard 18,000-lb single-axle load). Most specimens are subjected to 600,000 load applications in a sequence simulating a wheel crossing the crack at 55 mph.

All testing and data collection are controlled by a 286-based personal computer that has been equipped with a high-speed, high-resolution data acquisition system. This system allows the coordinated control of both actuators as well as the collection of load and deflection data. All test data are collected following the completion of 1, 2,000, 5,000, 10,000, 20,000, 50,000, 100,000, 300,000, and 600,000 load applications.

The study is designed to estimate the main effects of each of the test variables being considered and to identify general single- and multivariable influences on crack deterioration. This information will be used to develop preliminary design guidelines and guide specifications for future JRCP design

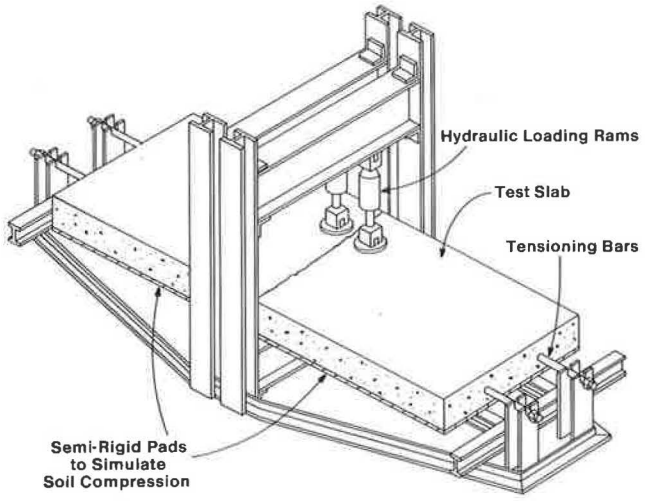


FIGURE 11 Isometric view of test frame.

and construction. It will also be used to suggest avenues of study for future research. The study is scheduled for completion in 1991.

SUMMARY

JRCP develops transverse cracks as the drying and thermal shrinkage of the concrete is resisted by friction with the supporting layers. Most JRCP designs rely on aggregate, or grain, interlock to achieve necessary load transfer capacity across these cracks. The cracks must exhibit good long-term load transfer characteristics to minimize the development and severity of various distresses (such as spalling, faulting, and pumping). However, the cracks deteriorate with time and traffic due to loss of aggregate interlock load transfer capacity.

Some of the significant factors that affect aggregate interlock load transfer capacity include width of the crack opening and texture of the crack face. Several other factors that may affect the performance of JRCP transverse crack and, hence, merit evaluation include coarse aggregate type and gradation, coarse aggregate treatment (virgin, recycled, and blend), coarse aggregate source, foundation support, reinforcing steel type and quantity, and amount of slab tension.

A research effort is under way at Michigan State University to evaluate the relative impacts of these factors on transverse crack deterioration in JRCP.

REFERENCES

1. A. C. Benkelman. Tests of Aggregate Interlock at Joints and Cracks. *Engineering News Record*, Vol. III, No. 8, Aug. 1933, pp. 227–232.
2. L. W. Teller and H. D. Cashell. Performance of Dowelled Joints Under Repetitive Loading. *Bulletin 217*, HRB, National Research Council, Washington, D.C., 1959.
3. B. E. Colley and H. A. Humphrey. Aggregate Interlock at Joints in Concrete Pavements. In *Highway Research Record 189*, HRB, National Research Council, Washington, D.C., 1967, pp. 1–18.
4. W. J. Nowlen. Influence of Aggregate Properties on Effectiveness of Interlock Joints in Concrete Pavements. *Journal of the PCA, Research and Development Laboratories*, Vol. 10, No. 2, May 1968, pp. 2–8.
5. E. C. Sutherland and H. D. Cashell. Structural Efficiency of Transverse Weakened-Plane Joints. *Public Roads*, Vol. 24, No. 4, April-June 1945.
6. J. P. Laible, R. N. White, and P. Gergely. Experimental Investigation of Seismic Shear Transfer Across Cracks in Concrete Nuclear Containment Vessels. In *Reinforced Concrete Structures in Seismic Zones*. ACI Special Publication SP-53. American Concrete Institute, Detroit, Mich., 1977, pp. 203–226.
7. R. Jimenez, P. Gergely, and R. N. White. *Shear Transfer Across Cracks in Reinforced Concrete*. Report 78-4. Cornell University, Ithaca, N.Y., Aug. 1978.
8. M. N. Fardis and O. Buyukozturk. Shear Transfer Model for Reinforced Concrete. *Proc., American Society of Civil Engineers*, Vol. 105, No. EM2, April 1979, pp. 225–275.
9. J. C. Walraven. Fundamental Analysis of Aggregate Interlock. *Journal of the Structural Division, ASCE*, Vol. 107, No. 11, Nov. 1981, pp. 2245–2270.
10. S. G. Millard and R. P. Johnson. Shear Transfer Across Cracks in Reinforced Concrete Due to Aggregate Interlock and to Dowel Action. *Magazine of Concrete Research*, Vol. 36, No. 126, March 1984.
11. M. I. Darter. *Design of Zero-Maintenance Plain Jointed Pavements: Volume 1.1—Development of Design Procedures*. FHWA, U.S. Department of Transportation, June 1977.
12. P. Soroushian, K. Obaseki, and K. Choi. Analysis of Aggregate Interlock Behavior at Cracks in Reinforced Concrete. *Magazine of Concrete Research*, Vol. 40, No. 142, March 1988, pp. 43–49.
13. A. M. Ioannides and G. T. Korovesis. Aggregate Interlock: Pure-Shear Load Transfer Mechanism. Presented at 69th Annual Meeting of the Transportation Research Board, Washington, D.C., 1990.
14. M. I. Darter. *Initial Evaluation of Michigan JRCP Crack Deterioration*. Michigan Concrete Paving Association, Mahomet, Ill., Dec. 1988, rev. Feb. 1989.

Publication of this paper sponsored by Committee on Rigid Pavement Design.

California Experience with Cracking and Seating of Concrete Pavements

GORDON K. WELLS, JOSEPH B. HANNON, AND NELSON H. PREDOEHL

The California Department of Transportation (Caltrans) is currently using the portland cement concrete pavement (PCCP) rehabilitation technique of cracking and seating (C&S) before placement of an asphalt concrete (AC) pavement overlay to prevent or retard reflection cracking from the underlying PCCP. Field measurements of differential vertical slab deflections and AC overlay performance are compared for various C&S projects. Construction techniques, specifications, pavement breaking equipment, and cracking patterns are discussed, along with problem areas and solutions. An experimental procedure for seating broken slabs is also described. AC overlay performance data are presented for various projects constructed with and without C&S of PCCP, with variable overlay thicknesses and with and without pavement reinforcing fabric (PRF). It is concluded that the C&S strategy is beneficial in preventing and retarding reflection cracking in AC overlays on PCCP by reducing thermal movements of existing PCCP, restoring slab support, and reducing differential vertical deflections of PCCP slabs. These AC overlays, with a few exceptions, are providing excellent performance after 5 to 7 years of service.

The rehabilitation of severely distressed portland cement concrete pavement (PCCP) in California has historically been accomplished by overlaying with asphalt concrete (AC). Before about 1982, these overlays were generally selected using a standard thickness varying from 0.30 to 0.50 ft, depending on the condition of the existing PCCP. Although the initial ride quality was restored by these overlays, their performance varied and reflection cracking was inevitable, as shown in Figure 1.

Sherman (*1*) suggests that the thickness required to retard reflection cracking of AC overlays "appears to be a variable that depends on several factors: (a) type of pavement being overlaid (AC or PCC); (b) type of distress (alligator cracking, block cracking, transverse thermal cracks, longitudinal cracks, or PCC joint cracks); (c) climate; and (d) number and weight of axle loads."

Most reflection cracking in AC overlays over PCCP is the result of differential vertical movement or displacement (Δ-verts) at joints and cracks under loadings by heavy vehicles, especially where the existing PCCP slabs are curled or faulted. McGhee (*2*) has suggested that the rate of crack development is a function of the frequency of wheel loadings and the magnitude of vertical movement (Δ-vert) caused by these loadings. On the basis of his findings, McGhee has also suggested that, wherever Δ-verts are 0.002 in. or greater, early reflection cracking is a possibility but that, where Δ-verts are 0.008 in. or greater, reflection cracking is almost a certainty. Caltrans (*3*), in an investigation of AC overlays with paving fabric, has generally confirmed McGhee's findings. Also, Caltrans has found that, for the transitional area of Δ-verts (measurements between 0.003 and 0.008 in.), paving fabric interlayers in AC overlays were somewhat effective in delaying reflection cracking of joints or cracks for about 1 year, compared with overlays without a paving fabric interlayer.

Generally, Δ-vert is measured by applying a moving 18-kip single-axle load across each side of a joint or crack and measuring the maximum deflection relative to the adjoining slab. Caltrans uses a modified Benkelman beam apparatus, as shown in Figure 2.

For existing AC pavements, Caltrans assumes that an AC overlay of one-half the existing AC pavement thickness is required to sufficiently retard reflection cracking. Pavement-reinforcing fabric (PRF) is assumed to provide an AC thickness equivalency of 0.10 ft in retarding reflection cracking. No structural value is given to the PRF. Caltrans considers 0.35 ft of AC as the maximum overlay thickness required for reflection crack control over AC pavement.

The prevention of reflection cracking in AC overlays on AC pavement is generally solvable. However, reflection cracking of AC overlays on PCC pavement has been a continuing problem, and considerable effort has been made throughout the nation to address this issue (*1,2,4*).

The most promising strategy in recent years that has received national attention has been the cracking and seating (C&S), or breaking and seating, of PCC pavement as a pretreatment to AC overlaying.

An early, undocumented attempt to crack and seat a PCCP was tried by Caltrans near Tracy, California, in late 1960 using procedures that had previously been used in Minnesota with a heavy roller (*5*). For this operation Caltrans attempted to use a 50-t pneumatic roller before placing an AC overlay. However, the operation was considered unsuccessful because no cracking appeared in the PCCP surface after several passes of the roller. The main reason for the poor success of this operation was that it occurred in late summer when the subgrade was dry and provided good support.

The first genuine approach by Caltrans to the C&S strategy with actual pavement breakers in conjunction with heavy rollers was conducted in 1982. Since that date, Caltrans has rehabilitated approximately 100 projects, representing over 1,000 lane-mi of PCCP truck lanes, with generally good success. Before adopting its current strategy, Caltrans evaluated several C&S patterns and AC overlay thicknesses with and without PRF interlayers. Some of these projects, as well as projects by other states, are listed as state-of-the-art by Crawford

Office of Pavement, Division of New Technology, Materials and Research, State of California Department of Transportation, 5900 Folsom Boulevard, Sacramento, Calif. 95819-0128.

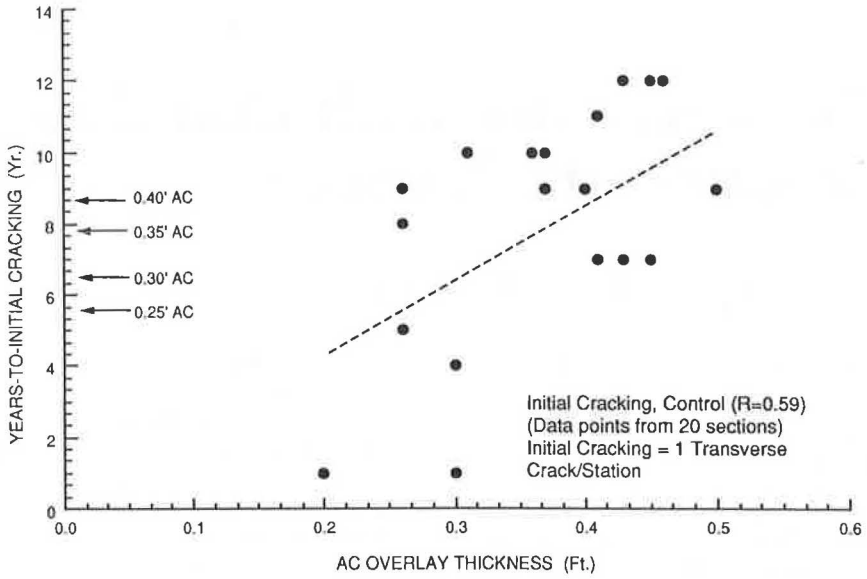


FIGURE 1 Effect of AC overlay thickness on overlay performance over distressed PCC pavement without C&S and PRF.

(*4*). In 1985 Smith (*6*) also discussed the overall strategy and evaluation procedures used by Caltrans.

The current strategy used by Caltrans calls for the nominal 6-ft (transverse) by 4-ft (longitudinal) C&S pattern described here, followed by placement of a 0.10-ft AC leveling course, a PRF, and 0.25 ft of additional AC (placed in lifts of 0.10 and 0.15 ft). The installation of edge drains, when combined with the PRF, minimizes the potential for entry and entrapment of storm water and the pumping action of the PCCP segments under the AC overlay.

Caltrans research (*6–8*) has shown that reflection cracking through AC overlays can be reduced by cracking PCCP into subpanels followed by rolling to seat and establish full slab support on the base before placing the AC overlay. The benefits of cracking and seating are as follows:

- Reduced slab size so that thermal movements of subpanels are negligible,
- Restored full slab support by the base,
- Reduced magnitude and effect of slab curl, and
- Minimized reflection cracking in the new AC overlay.

Caltrans has experimented with cracked subpanel dimensions of 6- by 4-ft, 4- by 4-ft, and 3- by 4-ft (transverse by longitudinal) and with rubblizing (*9*).

The main objective of C&S for Caltrans is to reduce slab size, which offsets thermal movements by only sacrificing a minimal loss in structural support and still allows a minimum amount of reflection cracking to be tolerated during the 10-year design life of the overlay. The most effective crack pattern to meet this objective for California PCC pavement is the 6-ft (transverse) by 4-ft (longitudinal) subpanel. A problem with the 4- by 4-ft subpanel occurs when traffic is allowed to use the cracked PCCP before overlay; the wheelpath areas then coincide with the 4-ft longitudinal crack, causing severe PCCP spalling. Rubblizing the PCCP is considered by Caltrans to be too severe because it reduces the pavement's structural value to an equivalent unbound base material requiring more AC cover. Also, traffic cannot use the rubblized lane the following day, which is critical in urban areas with high traffic volumes.

California PCCP that has been subjected to the C&S and AC overlay strategy has been plain jointed, undoweled PCCP with thicknesses ranging from 0.67 to 0.75 ft over cement-treated bases. Transverse joint spacings on these projects have averaged about 15 ft with a 2 ft in 12 ft counterclockwise skew. Before rehabilitation, these pavements experienced poor ride with joint faulting and third-stage cracking (slabs broken into three or more pieces with interconnected cracks) in excess of 10 percent for all truck lanes.

Cracking and seating of PCCP is considered by Caltrans to be one of the highest forms of recycling because it allows for the rehabilitation of an existing PCCP by an AC overlay and the PCCP retains most of its residual strength. The AC overlay can also be easily recycled when it reaches its design life.

CONSTRUCTION TECHNIQUES

Caltrans has investigated four types of cracking equipment currently in general use in California that incorporate unique modes to crack the PCCP (*8,9*). The following equipment was investigated:

- CMI Corporation; Model H16;
- Resonant Technology Company, Model B4;
- Wolverine Technology, Inc., whiphammer; and
- Wirtgen AG, guillotine drop hammer.

All of these devices proved capable of cracking California PCCPs to significantly reduce Δ-vert measurements at joints and transverse cracks. The CMI Model H16 and Wolverine whiphammer machines were found to cause shattering of the

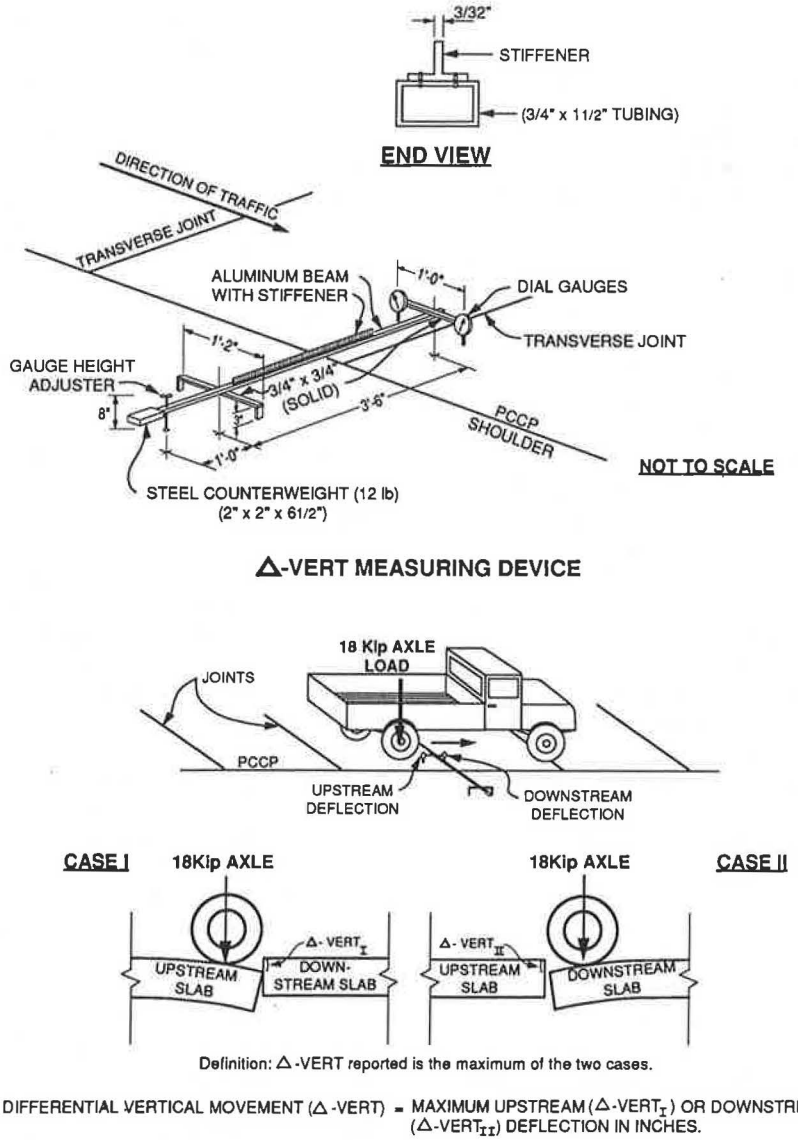


FIGURE 2 Δ-vert measuring device and procedure.

PCCP below the point of impact regardless of the shape of the impact bit used. Sharp impact heads caused the most severe surface shattering. Also, impacts within 1 ft of any existing joints or cracks or previously induced cracks caused severe spalling of the pavement, particularly at the intersections of cracked lines.

Resonant Technology's Model B4 resonant beam was found capable of producing a continuous, single longitudinal crack; however, it could not crack transversely on a 12-ft-wide lane because of its size and restricted maneuverability.

To determine if the PCCP had achieved continuous induced cracks, water was used to wash the surface and make the cracks more visible. This procedure was supplemented by cores taken at intervals throughout the project to determine if the cracks extended through the PCCP.

Caltrans currently specifies a nominal 6-ft transverse by 4-ft longitudinal subpanel after cracking. If existing panels are already cracked into segments, the segments are further cracked into nominally equal-sized square or rectangular pieces having a transverse dimension of not more than 6 ft and a longitudinal dimension of 3 to 5 ft, when feasible.

The current Caltrans Standard Special Provision (SSP 41.25) states that,

> equipment for cracking concrete pavement shall be capable of impacting the pavement with a variable force which can be controlled in force and point of impact in order to produce continuous cracking without extensive surface spalling over 0.10 foot in depth along the crack and without excessive shattering of the pavement or base. Unguided free-falling weights such as "headache balls" shall not be used. The Contractor shall demonstrate, to the satisfaction of the Engineer, the ability of the selected equipment and procedure to produce cracking of acceptable quality.

Seating cracked PCCPs may be performed either by an oscillating pneumatic-tired roller weighing not less than 15 t

or by a vibratory sheepsfoot roller exerting a dynamic centrifugal force of at least 20,000 lb. A minimum of five passes of the seating equipment in either direction is made over the cracked lane at a speed not to exceed 5 mph. Construction experience shows that vibratory sheepsfoot rollers are effective in seating subpanels, but the operation has been destructive to these machines on hard pavements; therefore, this equipment is rarely used.

A promising technique that is currently under evaluation by Caltrans would eliminate the separate rolling operation to seat the cracked PCCP before overlay. This technique would take advantage of a vibratory steel-tired roller to provide slab seating when compacting the initial ½-in. maximum, dense-graded AC leveling course (G. K. Wells, unpublished memorandum, Caltrans). The first evaluation of this technique was conducted on a project north of Yreka, California, on I-5. A test section 500 ft long was not seated in the conventional manner using a pneumatic-tired roller. Instead, a Tempo RS188A steel-tired, vibratory breakdown roller, vibrating at 2,200 cycles/min, provided compaction to the 0.10-ft-thick leveling course on both a conventionally seated control test section and the unseated test section. After paving was completed, Dynaflect deflection measurements were taken on both test sections. A statistical analysis of the deflection data showed virtually no difference between seating the cracked PCCP with a rubber-tired roller before placing the leveling course and seating the cracked PCCP during the placement of the leveling course using vibratory rollers currently allowed for AC breakdown compaction. If further tests prove successful, this method will eliminate one operation and one lane closure.

After completion of the normal C&S operation, a 0.10-ft-thick, dense-graded AC leveling course is placed. This procedure is followed by a hot AR4000 asphalt tack coat applied to the traveled way width, plus an additional 2 ft into each shoulder. A nonwoven PRF is placed on the tack coat immediately after the tack coat application.

Caltrans experience indicates that the tack coat application rate is dependent on the surface texture of the underlying pavement and the absorptiveness of the PRF. The tack coat film has to be sufficient to saturate the fabric when drawn up through the fabric by the heat of the overlying AC layer during its placement and still provide adequate bond to that layer. If the tack coat is too thin, proper bonding of the upper and lower AC courses with the PRF will not occur, resulting in failure of the surfacing caused by slippage along the PRF interface. A tack coat applied at too heavy a rate will not only saturate the PRF but may result in surface bleeding. For the current Caltrans strategy, the overlying AC courses would normally consist of a 0.10-ft-thick, ½-in. maximum, dense-graded layer followed by placement of a 0.15-ft-thick, ½- or ¾-in. maximum, dense-graded AC (DGAC) surface course.

On the basis of finite element analyses performed during a cooperative research study with the University of California (*10*), it is considered optimum to place the fabric on the AC leveling course 0.10 ft above the PCC pavement surface. An alternative to the total DGAC strategy for areas of high traffic volume in combination with high rainfall might also consist of placing the 0.15-ft DGAC layer directly on the PRF followed by a 0.10-ft open-graded AC (OGAC) surface course.

Another modification of the current overlay strategy following C&S of the PCCP consists of placing an Arizona three-layer system of either 0.10 ft of DGAC or 0.10 ft of OGAC directly on the C&S PCCP before placing a rubberized stress-absorbing membrane interlayer (SAMI) (i.e., preheated, precoated screenings with rubber asphalt binder). This procedure is followed by either a 0.08-ft or a 0.10-ft OGAC surface course. In 1985 a project was constructed by Caltrans with test sections of this type on Route 4 near Pittsburg, California. The pavement on this project is uncracked after 4 years of service. The success of this project has encouraged Caltrans engineers to propose construction of similar test sections on two other projects to be constructed in the near future. This strategy allows the overlay thickness to be reduced from the current strategy (0.23 versus 0.35 ft).

AC OVERLAY PERFORMANCE

Effect of C&S on Δ-vert

Because the reduction in Δ-vert of PCCP slabs is essential in preventing reflection cracking in AC overlays, Δ-vert measurements, as previously described, were obtained on test sections of several initial C&S projects to evaluate this construction procedure. However, only two of these projects were monitored for measurements during various phases of the construction operation (i.e., before cracking, after cracking, after seating, and after traffic had driven on the C&S PCCP for periods up to almost a month). A summary of Δ-vert measurements for these two projects is presented in Table 1. The results show that the magnitude of Δ-vert measurements is reduced by the cracking (breaking) operation to an average of 0.002 in. or less in all sections. This finding is also graphically portrayed in Figure 3 for the Bakersfield site. Generally, the results show that Δ-vert measurements may be further reduced by the seating operation. For sections on which traffic was allowed to use the C&S roadway before overlaying, it appeared that unseating may have resulted with a slight increase in Δ-vert measurements. The magnitude of these measurements tended to increase with longer periods of traffic exposure. Although the magnitude of Δ-vert measurements on these two projects was not extreme, other projects with higher magnitudes before C&S are presented in Table 2 for projects at Albany and Los Banos. Included in this table are performance data and other pertinent design and construction information for test sections at seven different locations constructed between 1982 and 1984. These projects were constructed to analyze the effects of C&S of PCC pavement and the inclusion of PRF in AC overlays. In addition, Δ-verts measured just before the C&S operation are shown in Figure 4 for the Albany project.

The AC overlay performance data for the previously described experimental sections are presented in Table 3 using the current Caltrans C&S and AC overlay strategy (0.35-ft DGAC overlay with a fabric interlayer) as an index for comparison. Most of these experimental sections were modifications of the current strategy with variable AC overlay thicknesses. Thus, the table compares overlays less than 0.35 ft and those greater than 0.35 ft with the current strategy. The data show that C&S has been effective in retarding and reducing transverse reflective cracking during the 5- to 7-year service life of these overlays. Figure 5 shows that the C&S

TABLE 1 SUMMARY OF Δ-VERT MEASUREMENTS (18-kip LOAD)

Section Const. (Date)	Number of Test Locations	Δ-Vert (10^{-3} inches) Before C&S Range	Before C&S Average	After Cracking Range	After Cracking Average	After Seating Range	After Seating Average	After Seating & Traffic Range	After Seating & Traffic Average
								(After 3 Weeks)	
Davis (6/82) (03-Yol-8.0-0.0/2.2) (WB #3 lane)	37 to 40 (Sta 180 to 195)	0 to 10	4	0 to 5	1	0 to 4	2	0 to 9	3
								(After 1 Day)	
Bakersfield (5/83) (06-Ker-99-9.0/10.5 SB#3 lane)	13 (Sta 881 to 887)	5 to 16	9	—	—	—	—	—	—
	10 to 13 (Sta 875 to 881)	3 to 15	9	0 to 4	2	0 to 3	1	0 to 2	1
	14 (Sta 869 to 875)	3 to 19	10	—	—	—	—	—	—
	13 (Sta 863 to 869)	1 to 19	8	0 to 3	1	—	—	0 to 4	2
	12 to 13 (Sta 857 to 863)	2 to 13	5	0 to 2	1	0 to 3	1	0 to 3	1
	4 to 13 (Sta 851 to 857)	3 to 15	6	0 to 2	2	—	—	—	—
	7 (Sta 845 to 851)	2 to 9	5	—	—	—	—	—	—
Average of all Sections	13 to 86 (Sta 845-887)	1 to 19	8	0 to 4	1	0 to 3	1	0 to 4	1

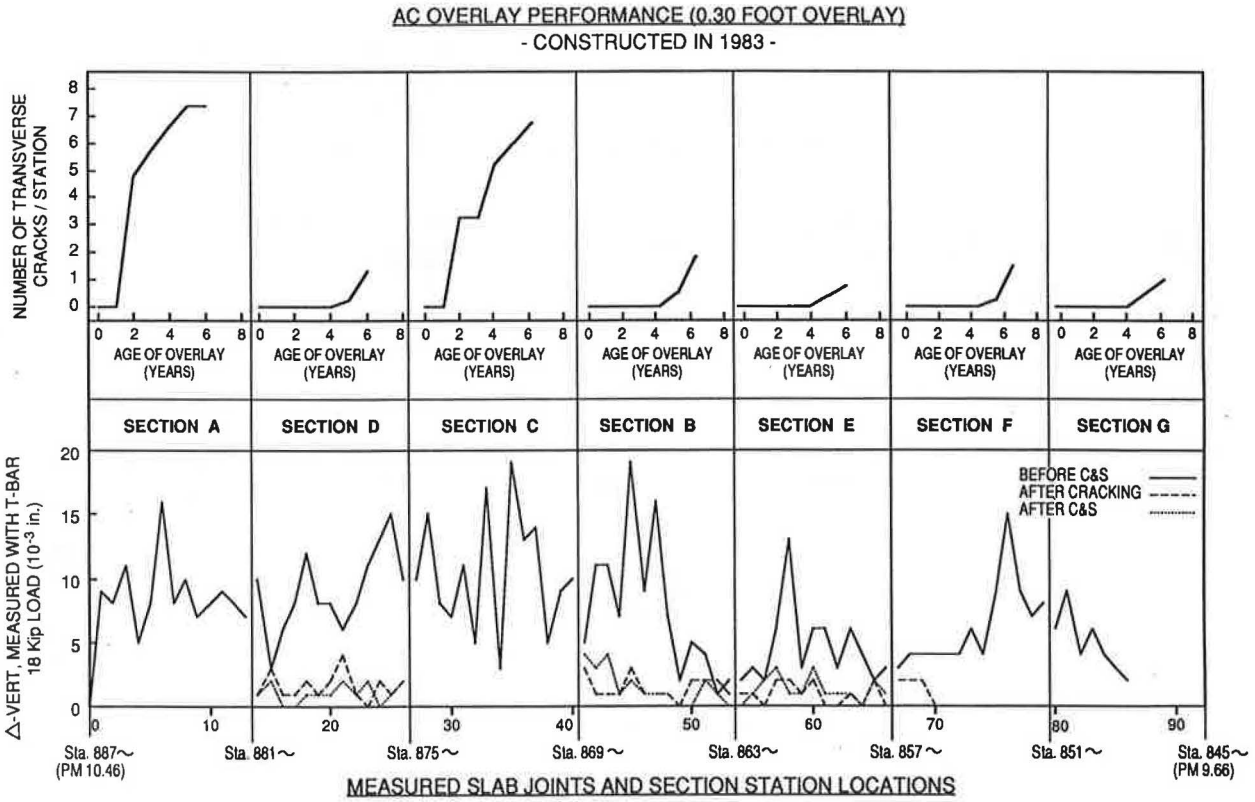


FIGURE 3 Record of Δ-vert measurements and reflective transverse cracks by year at Bakersfield.

TABLE 2 AC OVERLAY PERFORMANCE OF PRF TEST SECTIONS OVER C&S PCC PAVEMENT

Location (Outside or Truck Lane Unless Indicated)	Overlay Construction Date (Climate Data)	C&S Equipment Name of Breaker Type - Load - Type Bit	Section (length-feet)	Overlay[2] Thickness (feet)	Differential Vertical Movement (Δ-Vert) (10^{-3} inches)	Initial[3] Cracking (years)	Latest Cracking Summary			
							Alligator % w.t. length	Trans-verse No/100'	Longi-[4] tudinal Ft/100'	Last Survey Year
ALBANY (04-Ala-80-7.68/7.52) Contract 04-382434 Project CA-81-10 ADT = 160,000 (1985) % Trucks = 8 (1984)	6/1982 Northern coastal climate. Mild summers, cool wet winters. Rainfall = 16 in/yr	Breaker: ENSCO Breaker Hydraulic Vertical Acting Ram-impact 43,000 lb., 3"x5" Head, 3'x4' slabs.	PRF (Petromat) C&S (648)	0.26 (Surface 0.10' OGAC)	Prior to C&S, 33 to 41	Uncracked after 7 yrs	0	0	0	1989
# Trucks/day = 12,800 T.I. 14.0 (10 year)		Seating: 5 passesVib. 15 ton Sheepsfoot roller-Dynapac CA25PD 5 passes Bros Rubber-Tired Roller SP4000) 31,000 lb.	Control PRF, (Petromat). Not cracked, but was seated (252)	0.26 (Surface 0.10' OGAC)	Prior to seating, 48	2	0	4	26	↓
BAKERSFIELD (06-Ker-99-9.0/10.5) Contract 6-213504 Project CA-82-11	5/1983 Valley climate. Hot summers, Cool wet winters.	Breaker: BMC Broderson MH42B Drop Hammer, 10'-13' drop,	Control, No PRF, No C&S (600)	0.30	5 to16, Avg. 9	2	0	7	27	1989
ADT = 23,000 (1985) % Trucks = 32 (1984) # Trucks/day = 7360 T.I. 13.0 (10 year) Typical C&S:	Rainfall = 6 in/yr	1300 lb Head, Chisel End & Blunt End Bits used. Seating: Pneumatic Roller 13T	PRF, C&S, (Pneumatic Roller) (600)	0.30	Before C&S, 9 Avg. After C&S, 1 Avg.	6	0	1	30*	↓
Blunt end bit, Vibratory Roller Seating.		10 passes, Michigan R805 (one section),	Control, PRF No C&S (600)	0.30	3 to 19, Avg.10	2	0	7	21	↓
PRF = Petromat		Vibratory Sheepfoot 13T, Bomag BW210 PDB 10 coverages. (Remaining	No PRF C&S (600) (Typical)	0.30	Before C&S, 8 Avg. After C&S, 2 Avg.	5	0	2	26	↓
		Sections)	PRF, C&S (600) (chisel end bit)	0.30	Before C&S, 5 Avg. After C&S, 1 Avg.	6	0	1	12	↓
			PRF, Crack No Seat (600)	0.30	Before C&S, 6 Avg. After C&S, 2 Avg.	6	0	1	29*	↓
			PRF, C&S (600) (Typical)	0.30	Before C&S, 5 Avg. After C&S, Not Determined	5	0	1	27	↓
DAVIS (03-Yol-80-0.0/5.8) Contract 03-229804 Project CA-81-04 ADT = 65,000 (1985)	6/1982 Valley climate Hot dry summer. Cool wet winter. Rainfall = 16 in/yr	Breaker: Hydraulic Ram CMI-H16 impact force 12000 lb 1st day,	C&S, PRF (500')	0.54	Before C&S, 4 Avg. After C&S, 2 Avg.	Uncracked after 7 yrs.	0	0	1	1989
% Trucks = 9 (1984) # Trucks/day = 5850 T.I. 12.0 (10 yr)	C&S (500)	6000 lb 2nd day. 3'x4' slabs, 5'x6' slabs	C&S, No PRF, (500)	0.51	" "	" "	0	0	3	↓
PRF = Petromat		Seating: Vibratory sheeps-foot Roller,	C&S, PRF (500)	0.52	" "	" "	0	0	0	↓
		Dynapac CA 25P 10 passes, 44000 lb load	No C&S, Double PRF, (600)	0.48	Not Determined	" "	0	0	0	↓
			Control No C&S No PRF (400 ft.)	0.45	Not Determined	7	0	1	24	↓
			No C&S No PRF (400 ft.)	0.41	" "	7	0	1	7	↓

Remarks: (*) Some of the longitudinal cracking at this location occurred in the wheelpaths in these sections.

TABLE 2 (*continued on next page*)

TABLE 2 (*continued*)

Location (Outside or Truck Lane Unless Indicated)	Overlay Construction Date (Climate Data)	C&S Equipment Name of Breaker Type - Load - Type Bit	Section (length-feet)	Overlay[2] Thickness (feet)	Differential Vertical Movement (Δ-Vert) (10^{-3} inches)	Initial[3] Cracking (years)	Latest Cracking Summary: Alligator % w.t. length	Trans-verse No/100'	Longi-[4] tudinal Ft/100'	Last Survey Year
			No C&S No PRF (400 ft.)	0.30	" "	4	0	3	79	↓
LOS BANOS (10-Mer-152-11.32/12.43) Contract 10-260904 Project CA-83-10 ADT= 8100 (1985) % Trucks = 44 (1984) # Trucks/day = 3564 T.I. 12.0 (10 yr)	6/1984 Valley Climate. Hot dry summers. Cool wet winters. Rainfall = 8 in/yr	Breaker: Falling wt. Breaker, Rounded Impact Bit or Tool Hammer wt 1300 lbs Dropped 7ft (9100 ft-lb) Seating: 30 Ton Pneumatic Roller	Control, C&S No PRF, (900)	0.30	Not Determined	Uncracked after 5 yrs.	0	0	0	1989
			C&S PRF, (Petromat) (900)	0.30	Not Determined	" "	0	0	0	↓
			C&S, PRF, (Reepav) (900)	0.30	Before C&S, 12 to 38, Avg. 23	" "	0	0	0	↓
			C&S, PRF (Reepav) (900)	0.20	Not Determined	" "	0	0	0	↓
			C&S, PRF (Petromat) (900)	0.20	Not Determined	" "	0	0	0	↓
			Control, C&S No PRF (900)	0.20	Not Determined	" "	0	0	0	↓
SANTA BARBARA (05-SB-101-1.28/2.42) Contract 05-293604 Project CA-83-09 ADT = 48,500 (1985) % Trucks = 7.5 (1985) # Trucks/day = 3637 T.I. 11.0 (10 yr)	9/1984 Coastal climate. Mild summer. Wet winter. Rainfall = 20 in/yr	Breaker: Arrow-Hydro Hammer, Drop Hammer, Std. Spec, 4'x6' slabs Seating: Spec provisions Min. 25 ton roller with min 25000 pound effective load, 10 coverages.	C&S, PRF (Trevira) (500)	0.30	Not Determined	" "	0	0	0	1989
			Control (500), C&S. No PRF	0.19	Not Determined	" "	0	0	8	↓
			C&S, PRF, (Reepav) (500)	0.20	Not Determined	" "	0	0	7	↓
			C&S, PRF (Petromat) (500)	0.19	Not Determined	4	0	1	88	↓
			C&S, PRF (Reepav) (500)	0.30	Not Determined	Uncracked after 5 yrs.	0	0	1	↓
			C&S, PRF (Reepav) (500)	0.26	Not Determined	" "	0	0	68	↓
			Control, C&S, No PRF (500)	0.28	Not Determined	" "	0	0	42	↓
			C&S, Inverted OGAC-Control, No PRF, (500)	0.29	Not Determined	" "	0	0	0	1989

Overall Summary: Edge raveling in almost all sections in the above project and some severe raveling in wheel track of thicker control section. Appears to be the result of possible insufficient binder or segregation. Break-outs in some raveled areas but no cracking. Generally, longitudinal cracking is at outer pavement edge.

YREKA (02-SIS-5-43.0/51.2) Contract 02-195904 Project CA-83-07 ADT = 9400 (1985) % Trucks = 30 (1985) # Trucks/day = 2820 T.I. = 11.5 (10 yr)	7/1984 Northern interior. Mild to hot summers. Cold snowy winters. Rainfall = 19 in/yr	Breaker: Falling wt. Hydro-Hammer Per Spec Provision Seating: Per Special Provisions	No C&S PRF (600)	0.30	Not Determined	Uncracked after 5 yrs.	0	0	0	1989
			C&S, No PRF (600)	0.30	Not Determined	" "	0	0	0	↓
			No C&S, No PRF (600)	0.30	Not Determined	5	0	2	0	↓
			C&S, PRF (600)	0.30	Not Determined.	Uncracked after 5 yrs.	0	0	0	↓
			No PRF No C&S (600)	0.20	Not Determined	4	0	5	0	↓

TABLE 2 (*continued on next page*)

TABLE 2 (*continued*)

Location (Outside or Truck Lane Unless Indicated)	Overlay Construction Date (Climate Data)	C&S Equipment Name of Breaker Type - Load - Type Bit	Section (length-feet)	Overlay[2] Thickness (feet)	Differential Vertical Movement (Δ-Vert) (10^{-3} inches)	Initial[3] Cracking (years)	Latest Cracking Summary: Alligator % w.t. length	Trans-verse No/100'	Longi-[4] tudinal Ft/100'	Last Survey Year
			No PRF C&S (600)	0.20	Not Determined	3 trans-verse cracks in 600' in 5 yrs.	0	0.5	0	↓
			C&S, No PRF (600)	0.20	Not Determined	4	0	3	0	↓
			No C&S PRF (600)	0.20	Not Determined	1 trans-verse crack in 600' in 5 yrs.	0	0.2	0	↓

Remark: Yreka sections were inadvertently chip sealed in summer of 1988 (4 years old). May have concealed some cracks for approximately 1 year.

1. PRF = Pavement Reinforcing Fabric.
2. All fabric interlayers were placed over a 0.08 foot to 0.10 foot leveling course which is included in the overlay thickness.
3. Initial cracking = 5% to 10% alligator cracking (Caltrans Type B) or 1 transverse crack/100 feet.
4. All longitudinal cracking over construction joints (edge of lane at shoulder or adjoining lane) unless indicated. Longitudinal cracking not counted in determining initial cracking.

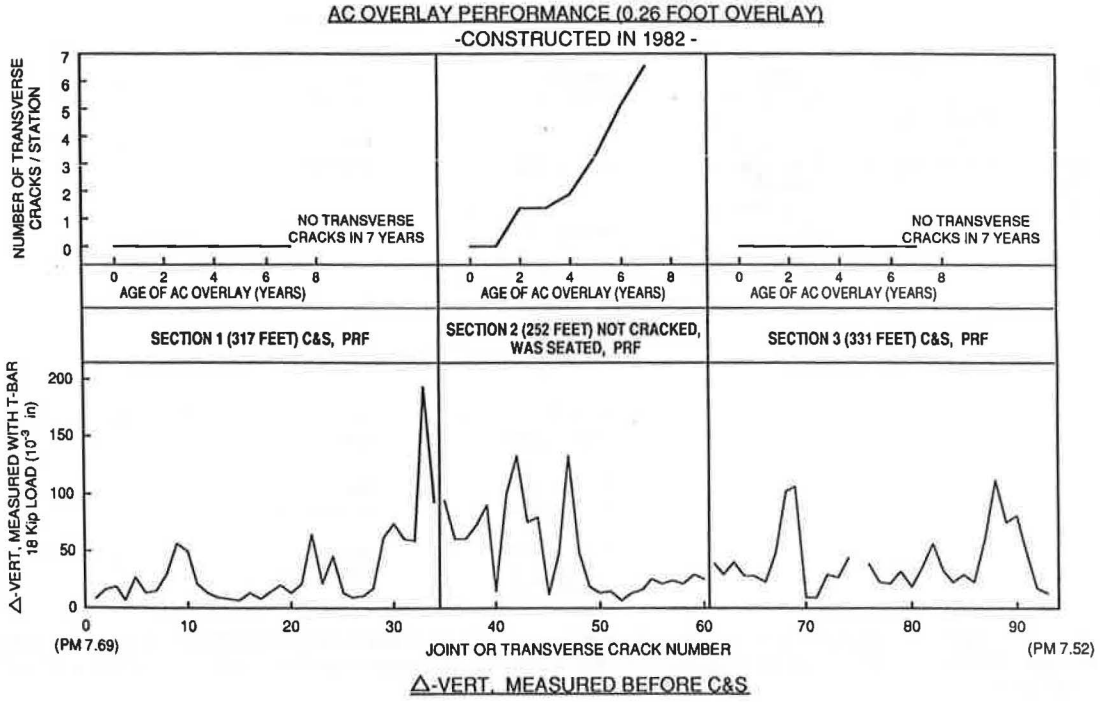


FIGURE 4 Record of Δ-vert measurements and reflective transverse cracks by year at Albany.

operation was the most significant factor in the performance of these overlays through 5.5 years of service.

A further comparison of the effects of C&S can be made by referring to Figures 3 and 4, which compare AC overlay performance with the Δ-vert measurements taken on the existing PCC pavements before overlay. These figures show that a reduction in Δ-vert to approximately 0.003 in. or less was very effective in retarding and reducing reflective transverse cracking in AC overlays, regardless of pre-C&S Δ-vert measurements. The plots in Figure 3 confirm McGhee's assertion (*2*) that AC overlays placed over pavements with a Δ-vert of approximately 0.008 to 0.010 in. and larger will have reflective transverse cracking.

Performance Review of C&S Projects

Since the first rehabilitation project (1982) that used C&S of a PCC pavement to reduce horizontal and vertical stresses, approximately 100 projects have been constructed using the C&S strategy. Seven of the earliest of these projects were studied as test sections. The performance of these test projects

TABLE 3 SUMMARY OF AC OVERLAY PERFORMANCE OVER C&S PCC PAVEMENT

Type Section	AC Overlay Thickness (Foot)	Average Δ-Vert* (10^{-3} In)	Number of Sections Locations	Average Age of AC Overlays	Latest Cracking by Type (1989)			
					Alligator Type B** % W.P.	Transverse No/STA	Longitudinal L. Ft/100 L. Ft.	Years*** to Initial Cracking
C&S w/PRF	(0.19 to 0.34) Avg. .26	<3	16 (5)	5.4	0	<1	16	Does not yet qualify as having initial cracking.
	(0.35 to 0.53) Avg. .52	<3	2(1)	7.0	0	0	0	
	Overall Avg. 0.29	<3	18(5)	5.5	0	<1	14	
C&S No PRF	0.19 to 0.34 Avg. .25	<3	7(4)	5.3	0	<1	11	Does not yet qualify as having initial cracking.
	0.35 to 0.51 Avg. 0.51	<3	1(1)	7.0	0	0	3	
	Overall Avg. 0.29	<3	8(5)	5.5	0	<1	10	
No C&S w/PRF	0.19 to 0.34 Avg. 0.27	2 of 4 Sect. Range 3 to 133 Avg. 29	4(3)	5.8	0	4	12	3.3+
	0.35 to 0.49 Avg. 0.49	Range 0 to 10 Avg. 4	2(1)	7.0	0	0	0	7+
	Overall Avg. 0.31		6(4)	6.2	0	2	8	4.5+
No C&S No PRF	0.19 to 0.34 Avg. 0.27	One location Range 5 to 16 Avg. 9	4(3)	5.8	0	4	27	4.5
	0.35 to 0.45 Avg. 0.43	Not determined	2(1)	7	0	1	16	7
	Overall Avg. 0.33		6(4)	6.2	0	3	23	5.3

Note: Data from Table 2.

* After C&S, all sections that were measured had Δ-Verts of less than 3 x 10^{-3} inches. Refer to Table 2 for measurements.

** No connected wheel path cracking (Caltrans Type B alligator cracking) in any of the sections, but in some sections (indicated for Bakersfield and Santa Barbara sites) there are minor amounts of longitudinal cracking in the wheelpath (Caltrans Type A alligator cracking).

*** Initial Cracking = one transverse crack/Station (100 lineal feet) or 5 to 10% alligator cracking (Caltrans Type B).

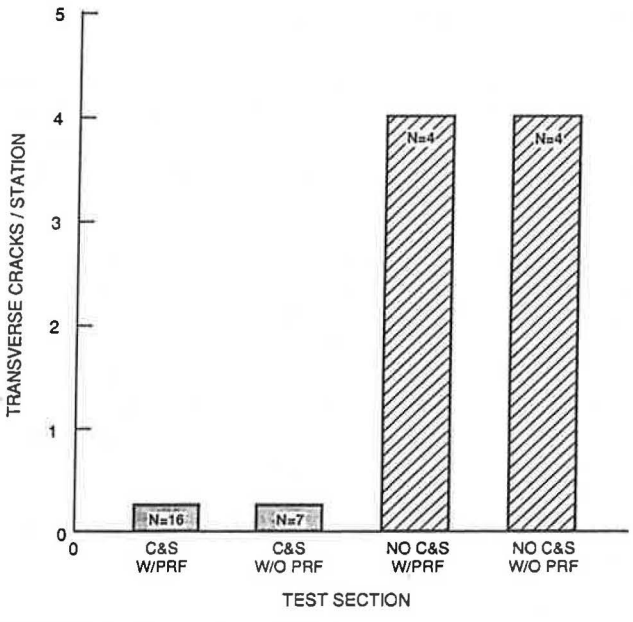


FIGURE 5 Comparison of C&S and non-C&S sections with AC overlays <0.35 ft (data from Table 3, average age 5.5 years).

is reported in Table 3 and Figure 5. Their performance after an average of 5.5 years of service shows that C&S is an effective strategy in retarding and reducing reflective transverse cracking in the AC overlays of underlying PCCP joints and cracks.

A performance analysis of 36 other projects that were rehabilitated with variable AC overlays using the C&S strategy is shown in Figures 6 and 7. Figure 6 shows that only a small portion (about 10 percent) of the 36 projects selected from the 1989 Pavement Management System (PMS) survey have initial cracking (no more than one transverse crack per station) after approximately 5 years of service. These data compare favorably with the data from the C&S test sections presented in Table 3. Figure 7 shows that some of the projects with AC overlay thicknesses ≤0.30 ft also have minor amounts of small block and alligator cracking (≤3 percent type "B"), probably due to localized partial slab movements.

The benefits of the C&S strategy are shown in Figure 8, which compares the performance of AC overlays over C&S and non-C&S, with and without PRF. Also compared is a plot of the performance of the 36 projects (PMS surveys), which confirms the findings from the initial test sections.

In general, the C&S and AC overlay strategy has worked successfully in minimizing reflection cracking on most Caltrans projects. However, seven projects have been constructed on I-5 in Caltrans District 2 (northern California) with mixed results. Several of these projects have experienced

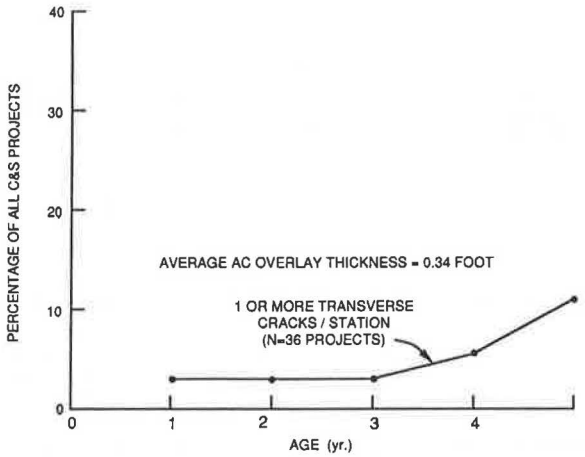


FIGURE 6 Transverse cracking on C&S projects (on the basis of 1989 PMS).

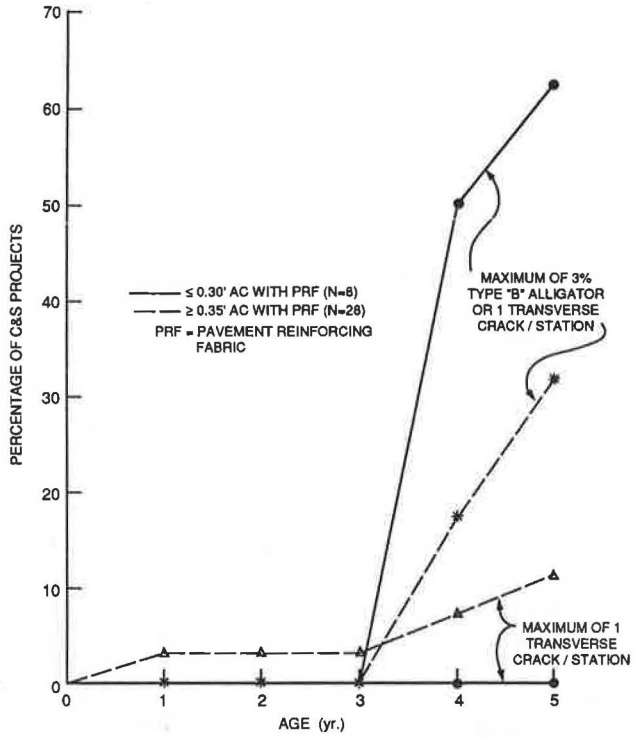


FIGURE 7 Distress history of C&S projects with different AC overlay thickness (on the basis of 1989 PMS).

premature distress (longitudinal and alligator cracking) of the AC surface. The reasons for this early distress are the subject of an ongoing study. The majority of the projects may have been constructed with aggregates in the AC overlay, which tend to strip in the presence of moisture. The early failures appear to be the result of stripping above and below the PRF layer and are the only Caltrans C&S projects that have experienced any significant levels of distress. This occurrence is believed to be a materials problem and is not a fault of the C&S strategy. Thus, these projects are not included in this overall evaluation of C&S.

The current strategy of C&S with 0.35-ft AC and a PRF interlayer has, with the exceptions described, provided ex-

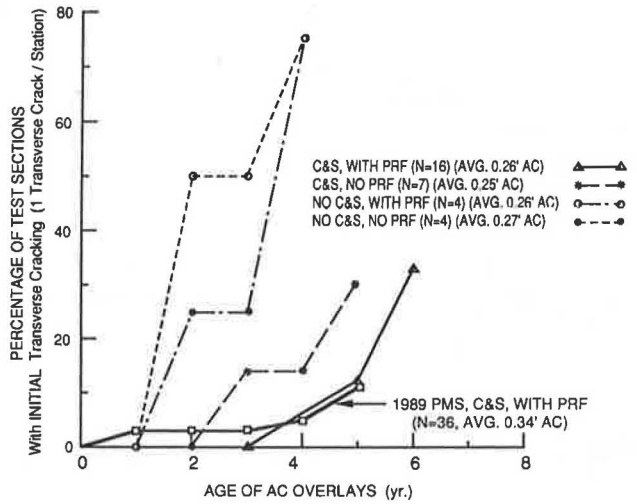


FIGURE 8 Transverse cracking in C&S test sections, ≤0.40-ft AC (data from Table 2 and Figure 6).

cellent performance for most situations in California. However, it is proposed that this strategy be modified somewhat for future projects in which a structural need exists (i.e., projects in areas with a high water table in combination with soft, unstabilized subgrades). The current strategy is questionable for these potential problem areas, where the need for structural adequacy governs over reflection cracking. One strategy that is proposed is to increase the AC overlay thickness above the fabric by an additional 0.25 ft. The final overlay strategy would consist of a 0.10-ft DGAC leveling course, PRF, and a 0.50-ft DGAC placed in three lifts. This modified strategy complements the current strategy by providing a recyclable AC surface or a base for new PCCP to be placed at some future date.

COST-EFFECTIVENESS OF C&S

The current strategy of C&S with a 0.35-ft AC overlay and a PRF interlayer has proven to be a cost-effective solution for rehabilitation of PCCP in California. This strategy has provided significant savings when compared with other alternatives. For example, the AC thickness required to provide equivalent crack retardation performance over non-C&S PCCP would probably be an additional 0.15 ft or more. Currently, the estimated cost of C&S is \$0.50 to \$0.75/yd², which is less than the cost of the additional AC thickness.

Other alternatives to the current strategy could include an unbounded PCCP overlay and removal and replacement or recycling of the existing PCCP and base. However, preliminary cost comparisons using initial and life cycle costs have shown the current strategy to be more cost-effective in addressing reflection cracking. The recycle alternative could become more cost-competitive as good aggregate sources become scarce.

CONCLUSIONS

1. Cracking and seating of unreinforced, undoweled PCCP is effective in retarding and reducing reflection cracking in AC overlays.

2. C&S is effective in reestablishing base support for existing PCCP and in reducing Δ-verts to acceptable levels.

3. The current Caltrans C&S and AC overlay strategy is cost-effective and, with minor exceptions, will provide the desired service life of 10 years.

4. Preliminary findings suggest that it may be possible to eliminate the PCCP seating operation, and additional research is under way.

5. Only about 10 percent of the AC overlays constructed with the C&S strategy exhibited initial cracking after 5 years of service, compared with 75 percent of AC overlays on non-C&S PCCP after 4 years.

6. PRF in an AC overlay over C&S PCCP is primarily a moisture barrier but can retard initial cracking an average of 1 year longer than overlays without PRF.

7. Modifications to the AC overlay and C&S strategy using OGAC layers have been effective in retarding reflection cracking.

8. The use of PRF in AC overlays of C&S PCCP requires further study for situations in which stripping can occur.

9. The 6-ft (transverse) by 4-ft (longitudinal) PCCP subpanel cracking pattern has generally been effective in controlling reflection cracking in AC overlays on PCCP.

REFERENCES

1. G. Sherman. *NCHRP Synthesis 92: Minimizing Reflection Cracking of Pavement Overlays*. TRB, National Research Council, Washington, D.C., Sept. 1982.
2. K. H. McGhee. *Efforts To Reduce Reflective Cracking of Bituminous Concrete Overlays of Portland Cement Concrete Pavements*. Virginia Highway and Transportation Research Council, Charlottesville, Va., Nov. 1975.
3. N. H. Predoehl. *Evaluation of Paving Fabric Test Installations in California*. Report FHWA/CA/TL-90/02. California Department of Transportation; FHWA, U.S. Department of Transportation, Feb. 1990.
4. C. Crawford. Cracking and Seating of PCC Pavements Prior to Overlaying with Hot Mix Asphalt-State-of-The-Art. In *National Asphalt Pavement Association Information Series 98/87*, National Asphalt Pavement Association, Riverdale, Md., June 1987.
5. P. G. Velz. Effects of Pavement Breaker Rolling on Crack Reflectance in Bituminous Overlays. *Bulletin 290*, HRB, National Research Council, Washington, D.C., 1961, pp. 39–52.
6. R. D. Smith. California Implements Crack and Seat Strategy. *Roads and Bridges*, May 1985, pp. 30–33.
7. G. K. Wells and S. Wiley. *Evaluate Effectiveness of PCCP Rehabilitation Techniques*. Report FHWA/CA/TL-87/10. California Department of Transportation; FHWA, U.S. Department of Transportation, Aug. 1987.
8. R. D. Smith. *Construction Evaluated. Report CA-82-05*. California Department of Transportation, Sacramento, July 1983.
9. L. deLaubenfels. *Construction Evaluated. Report CA-82-05*. California Department of Transportation, Sacramento, Sept. 1985.
10. R. Yuce, P. A. Seddon, C. L. Monismith, and N. Markevitch. *Analytical Study of Fabric Interlayer Effects*. Report FHWA/CA/TL-84/05. California Department of Transportation; FHWA, U.S. Department of Transportation, June 1984.

Publication of this paper sponsored by Committee on Pavement Rehabilitation.

Performance of Asphalt Concrete Resurfacing of Jointed Reinforced Concrete Pavement on the Illinois Interstate Highway System

KATHLEEN T. HALL, MICHAEL I. DARTER, AND JAMES P. HALL

A study was conducted on the survival of asphalt concrete (AC) overlays on the Illinois Interstate highway system. Data were obtained from the Illinois Pavement Feedback System (IPFS) data base for 410 AC overlay construction sections placed on jointed reinforced and continuously reinforced concrete pavement (JRCP and CRCP) between 1964 and 1989. The overlays ranged in thickness from 1.5 to 6.0 in. Both in-service life and 18-kip equivalent single-axle loads (ESALs) carried to rehabilitation of the overlay were analyzed through the use of survival curves. The survival of the 213 AC overlays of JRCP sections is reported. The mean age and accumulated ESALs at the time of overlay rehabilitation were estimated for categories of overlay thickness (thin and thick) and portland cement concrete durability (with and without D cracking). The analysis indicated that each of the factors considered, along with traffic level, had a significant effect on the life of the overlays. Thick overlays lasted substantially longer and carried substantially more traffic than thin overlays on both D-cracked and non-D-cracked pavement. Both thin and thick overlays performed much better on pavements without D cracking than on pavements with D cracking.

Resurfacing has been used extensively to extend the life of deteriorating portland cement concrete (PCC) pavements. Resurfacing is by far the most common method of rehabilitation used today throughout the United States. Other major rehabilitation techniques include restoration without overlay and reconstruction, which is often used in conjunction with recycling.

The Illinois Interstate highway system consists of approximately 800 pavement sections (1,700 centerline miles total) of heavily trafficked multiple-lane pavements that were constructed largely between 1957 and 1980. These pavement sections range in length from one-quarter to 10 mi, with an average length of about 3 mi. About one-third of these pavements were originally constructed as jointed reinforced concrete pavement (JRCP); the remaining two-thirds were originally constructed as continuously reinforced concrete pavement (CRCP). The performance of these sections was analyzed by Dwiggins et al. (*1*).

Traffic on these pavements, expressed in terms of 18-kip equivalent single-axle loads (ESALs) has been far greater than anticipated. A recent traffic loading evaluation (*2*) indicated that in 1986, ESALs on Illinois Interstates averaged 1.2 million per year in one direction in the outer traffic lane, ranging from 300,000 to 7 million per year. The same study indicated that annual ESALs on these pavements grew at a compounded rate of 8 percent between 1956 and 1986. An Illinois Interstate pavement section subjected to an average traffic level and overlaid in 1986 could therefore be expected to accumulate more than 17 million additional ESALs in the next 10 years.

As of 1990, the Illinois Department of Transportation (IDOT) had resurfaced nearly one-half of the 1,700-mi Interstate highway system. Nearly all of the resurfacing has been with asphalt concrete (AC) overlays of various thicknesses. A few CRCP overlays have been placed (*3*). Before resurfacing, some repairs are typically done on the JRCP or CRCP, including full-depth repair with AC or PCC, partial-depth repairs with AC, edge drain installation, and shoulder repair.

Information on the performance of AC overlays placed JRCP is presented. (An insufficient number of AC overlays of CRCP sections has failed to provide reliable estimates of their mean performance life.) Data for this evaluation were obtained from the Illinois Pavement Feedback System (IPFS) data base (*4*). Comparisons are made between the performance of different AC thicknesses (thin and thick) on JRCP and the effect of durability D cracking of the original JRCP. These results can be used to feed back information to improve the overlay design and construction procedures to enhance service life.

CAUSES OF AC OVERLAY FAILURE

The predominant distresses in AC overlays of PCC pavements that most often determine when a second rehabilitation is required are deteriorated reflection cracks, localized distress caused by D cracking in the PCC layer, rutting, and deterioration of AC patches and expansion joints.

Reflection Cracking

The basic mechanism of reflection cracking in AC overlays of PCC pavements is strain concentration in the overlay caused

K. T. Hall and M. I. Darter, Department of Civil Engineering, University of Illinois at Urbana-Champaign, Newmark Civil Engineering Laboratory, 205 N. Mathews Avenue, Urbana, Ill. 61801. J. P. Hall, Illinois Department of Transportation, DOT Administration Building, 2300 S. Dirksen Parkway, Springfield, Ill. 62764.

by movement in the vicinity of joints or cracks in the existing PCC slab. This movement may be either bending or shear induced by loads, or may be horizontal contraction induced by temperature changes. Load-induced movements are influenced by the thickness of the overlay and the thickness and stiffness of the existing pavement. Temperature-induced movements are influenced by daily and seasonal temperature variations, the coefficient of thermal expansion of the existing pavement, and the spacing of cracks (*5*).

In an AC overlay of jointed PCC pavement (JPCP or JRCP), reflection cracks typically develop relatively soon after the overlay is placed (often in less than 1 year). The rate at which they deteriorate depends on the factors listed earlier as well as the traffic level. Thorough repair of deteriorated joints and working cracks using full-depth dowelled PCC repairs reduces the rate of reflection crack occurrence and deterioration, so long as good load transfer is obtained at the full-depth repair joints. Other preoverlay repairs that will discourage reflection crack occurrence and subsequent deterioration include subdrainage improvement, subsealing of slabs that have lost support, and restoring load transfer at joints and cracks with dowels grouted in slots (*5*).

A variety of reflection crack control measures have been used in attempts to control the rates of reflection crack occurrence and deterioration. Any one of the following treatments may be used in an effort to control reflection cracking in an AC overlay of jointed PCC pavement (*5*).

1. Placing a synthetic fabric or a stress-absorbing interlayer before or within the AC overlay. The effectiveness of this technique is questionable.
2. Placing a bituminous-stabilized granular interlayer (large-sized stone) before or in combination with placement of the AC overlay.
3. Sawing and sealing joints in the AC overlay at locations coinciding with joints in the underlying PCC slab.
4. Breaking or cracking and seating the PCC slab before placement of the AC overlay. This technique is intended to reduce the size of PCC pieces and seats them in the underlying base material, which reduces horizontal (and possibly vertical) movements across the cracks.
5. Rubblizing the PCC slab before placement of the AC overlay. This technique reduces the size of PCC pieces to a maximum of about 12 in. and essentially reduces the slab to a high-strength granular base course.
6. Increasing AC overlay thickness. Reflection cracks will take more time to propagate through a thicker overlay and will deteriorate more slowly.

Reflection cracking can have a considerable (often controlling) influence on the life of an AC overlay of jointed PCC pavement. Deteriorated reflection cracks reduce a pavement's serviceability and also require frequent maintenance, such as sealing and patching. Reflection cracks also permit water to enter the pavement structure, which may result in loss of bond between the AC overlay and existing PCC surface and result in stripping in the AC. For this reason, reflection cracks should be sealed as soon as they appear and be resealed periodically throughout the life of the overlay. Sealing low-severity reflection cracks may also be effective in retarding their progression to medium and high severity levels (*5*).

With an AC overlay on CRCP, permanent patching of punchouts and working cracks with tied or welded reinforced PCC full-depth repairs will delay for many years the occurrence and deterioration of reflection cracks. Improving subdrainage conditions and subsealing in areas where the slab has lost support will also discourage reflection crack occurrence and deterioration. Reflection crack control treatments are not necessary for AC overlays on CRCP as long as permanent PCC-tied repairs are used for deteriorated areas and cracks (*5*).

The importance of preoverlay repair to the prevention of reflection cracking in an AC overlay of CRCP was demonstrated in a 10-year overlay performance study conducted from 1978 to 1988 (*6*). Every patch, crack, and joint in a 6.6-mi section of Interstate 57 near Manteno, Illinois, was mapped before the AC overlay was placed. Distress surveys and nondestructive deflection tests were performed on the overlaid pavement immediately after overlay placement, and after 1, 5, and 10 years. The only cracks that reflected through the overlay were those that were deteriorated (medium or high severity) and were not repaired with a permanent reinforced concrete patch before overlay. More than 90 percent of the tied PCC patches that were placed before the overlay could not be detected in the AC overlay by reflection cracks even after 10 years of service. However, the patch locations are known by station, and also by patch numbers stamped in the overlay. A more detailed description of the performance of this project was provided by Hall and Darter (*6*).

D Cracking

D cracking is progressive deterioration of PCC that occurs as a result of freeze-thaw damage. D cracking occurs frequently in PCC pavements in the northeastern, north central, and south-central regions of the United States (*7*). The major factors which influence the likelihood that a pavement will develop D cracking are availability of moisture (including quality of base drainage) (*8*), occurrence of freeze-thaw cycles (*9*), coarse aggregate composition (sedimentary rocks such as limestone and dolomite are generally most susceptible) (*10*), pore size distribution of the coarse aggregate (*11–14*), and maximum aggregate size (*15,16*). The fine aggregate does not influence the likelihod of D cracking (*9,17*). The level of air entrainment, likewise, does not affect D cracking (*18*) (although air entrainment does improve resistance to scaling caused by freeze-thaw damage in the cement mortar). The composition or brand of cement has little or no influence on D cracking (*9–11,17,19*). Although D cracking is not caused by traffic loads, it eventually results in severe deterioration of the PCC, particularly near joints and cracks, and reduces the structural capacity of the pavement.

D cracking occurs in Illinois primarily in PCC pavements constructed with gravel, rather than crushed stone. The Illinois DOT found in a 1979 survey that only 42 percent of the Interstate system was free of D cracking. Low-severity D cracking was present on 40 percent of the system, medium-severity D cracking on 12 percent, and high-severity D cracking on 6 percent (*20*). It has also been Illinois' experience that D cracking results in more severe deterioration in CRCP than in JRCP. One explanation proposed for this is that the many

fine cracks that naturally occur in CRCP offer more locations for infiltration of water into the PCC (*7*). Another possible explanation is that CRCP sections in Illinois are constructed on cement- or asphalt-stabilized base courses, which have worse drainage characteristics than the granular base courses on which JRCP sections are constructed.

In a thorough investigation of D cracking in AC-PCC pavements in Illinois, it was found that AC overlays do not halt the progression of D cracking, and in some cases accelerate it (*21*). Although the AC layer insulates the PCC to some extent, thereby increasing the minimum pavement temperature and decreasing the number of freeze-thaw cycles in the PCC, it also decreases the rate of freezing, which is detrimental. In the laboratory, PCC samples subjected to 400 freeze-thaw cycles (equivalent to, for example, about 4 years of exposure near St. Louis), experienced reductions in split tensile strength of 20 percent. Samples with 2- and 4-in. AC overlays experienced greater strength losses than samples with no overlays (*21*).

It has also been observed in the laboratory that autogenous healing occurs in D-cracked PCC samples when freeze-thaw testing is stopped and the samples are exposed to warmer temperatures. In the field, this autogenous healing may recover some of the strength lost because of D cracking. It is conceivable that in some areas in Illinois, for example, warming during the summer could achieve strength gains that would offset strength losses caused by freeze-thaw damage in the winter. This recovery process could only continue until the unhydrated cement in the PCC was consumed, after which the strength would be expected to steadily decline with successive winters. Although only a hypothesis, this process may explain why some pavements do not manifest significant D cracking until they are 10 years old or more.

D cracking may also reduce the bond between the PCC and an AC overlay (*21*). Loss of bond can result in increased rutting in the AC and reduced structural response of the AC-PCC pavement.

The strength loss caused by D cracking is evident on a 9-mi AC overlay section on Interstate 70 near Marshall, Illinois. Severe D cracking of the 8-in. CRCP existed before the AC overlay was placed in 1980. The D cracking has continued, and in combination with a high volume of repeated heavy loads (10 million ESALs since 1980), has caused the concrete to completely disintegrate in some locations. Pumping of concrete fines is evident at several locations in the wheelpaths and at the edge joint. Nondestructive deflection testing was performed along the project using a falling weight deflectometer (FWD). Sixteen cores were also taken at various cracks, localized failures, and apparently sound sections. Nearly all of the cores indicated severe disintegration of the CRCP slab. Higher FWD deflections and lower backcalculated moduli of the CRCP slab corresponded to higher-severity cracks or failures and to more deteriorated area in the underlying CRCP. Large areas along this project are exhibiting major localized slab disintegration.

Rutting

Rutting is another major distress in AC overlays of PCC pavements. Wheelpath ruts of ⅓ to ½ in. are considered by many highway agencies to pose a safety hazard, because of the potential for hydroplaning, wheel spray, and vehicle handling difficulties (*22*).

The four mechanisms that cause rutting in AC are deformation of supporting layers, consolidation caused by insufficient compaction during construction, surface wear caused by studded tires and tire chains, and plastic deformation of the AC mix. Rutting caused by permanent deformation of supporting layers occurs only in flexible pavements (e.g., AC over granular base). Rutting caused by insufficient compaction generally does not contribute significantly to rutting in AC overlays of PCC. Rutting caused by surface wear occurs on both AC and PCC pavements in some western states where studded tires are still used, but it is not seen in Illinois.

The primary mechanism of rutting in AC-PCC pavements is plastic flow of the mix laterally away from the wheelpaths, because of shear stress produced by applied loads. This plastic deformation normally occurs relatively slowly and develops into ruts of significant depth after several years. Mix deficiencies that increase an AC overlay's tendency to rut are rounded aggregates, excessive fines, improper aggregate gradation, stripping-susceptible aggregates, low air void content, low asphalt cement viscosity, and high asphalt content (*22*).

The magnitude of shear stress experienced by the overlay under loading also depends on the AC-PCC interface bonding condition and the AC thickness, as shown in Figure 1. Shear stress in the AC is lowest when the AC and PCC are fully bonded, and increases when bond is lost. When the AC and PCC are fully bonded, AC shear stress increases with overlay thickness. This process has been cited as a possible reason that thin overlays do not fail primarily because of rutting. When the AC and PCC are not bonded, AC shear stress is highest for overlays between 4 and 6 in. thick (*23*). Premature rutting, which develops unusually rapidly and reaches a critical level within 1 or 2 years, occurs sometimes in a poorly designed AC mix as a result of shear failure. Premature rutting has occurred in some AC overlays on Illinois Interstates, particularly in overlays placed before about 1984, as a result of poor AC mix design or poor field control. For example, several miles of AC overlays placed on I-55 and I-70 before 1984 rutted prematurely. These overlays were either removed by cold milling and replaced with new overlays or were cold milled and not replaced. An IDOT task force investigated the occurrences of premature rutting and concluded that the AC

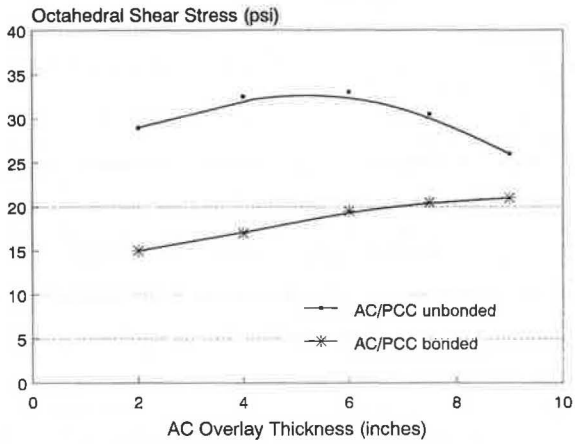


FIGURE 1 Variation of maximum octahedral shear stress in AC overlay of PCC pavement (*23*).

mix used for overlays at that time had gradation problems and low air voids. Changes in the mix design were made to correct these and other minor problems and were implemented during the 1984 construction season (*24*). This change in Illinois' AC mix design must be taken into consideration when comparing the rutting behavior of overlays placed before 1984 with the rutting behavior of overlays placed after that time.

Preoverlay AC Patches and Expansion Joints

Placement of full-depth AC patches and expansion joints in many CRCP and JRCP pavements before overlay often results in significant distress in the AC overlay. Besides creating a hump in the overlay surface, transverse cracks reflect through the overlay and typically deteriorate quickly. This increases roughness and maintenance requirements.

Major Deterioration Modes by Pavement Type

The relative performance of different types of AC-PCC pavement in Illinois might be generalized in the following descending order:

1. AC with Sound CRCP. When adequate preoverlay repair is done, good to excellent performance has been observed for pavements in this category. The experimental project on I-57 at Manteno is a good example (*6*). The performance life of AC over non-D-cracked CRCP is most likely to be controlled by rutting rather than reflection cracking or structural distress.
2. AC with Sound JRCP. Fair to good performance has been observed for pavements in this category. Reflection cracking at joints, including full-depth repair joints, is often the predominant mode of failure, unless premature rutting occurs.
3. AC with D-Cracked JRCP. Fair to poor performance has been observed for pavements in this category. Extensive preoverlay repair (i.e., full-depth repair at nearly every joint and midslab cracks in many slabs) is typically required, and even so, the D cracking may continue to progress in the PCC slab after being overlaid. Reflection cracking competes with D cracking as the predominant mode of failure.
4. AC with D-Cracked CRCP. Fair to very poor performance has been observed for pavements in this category. D cracking has been found to shorten the life of bare CRCP in Illinois much more than it does the life of bare JRCP (*1*). Although not yet quantified, the same trend may exist after overlay. Field investigations of AC with D-cracked CRCP sections (e.g., I-70 at Marshall) suggest that the deterioration of the PCC slab may be much more extensive than distress observations indicate.

SURVIVAL ANALYSIS OF AC-PCC

Previous AC Overlay Survival Studies

Perhaps the only systematic study of the performance lives of AC-PCC pavements was conducted by Elliott for the IDOT in 1971 (*25*). In the course of developing a design procedure for AC overlays of PCC pavements, Elliott studied the time to second overlay for AC overlays placed in the 1950s and 1960s on PCC pavements in Illinois and produced the survival curve shown in Figure 2. The average performance life of first AC overlays greater than 2 in. thick on PCC pavements was found to be 14 years. Elliott also attempted to determine the average performance life of second AC overlays, but found the number of these in service at the time too few and their performance too inconsistent to draw any clear conclusions.

Since 1971, truck traffic volumes and load magnitudes on Illinois highways have increased substantially. The mix design used for AC overlays in Illinois has also changed since 1971, and the PCC pavements have gotten older, have sustained more structural damage, and in many cases, have deteriorated dramatically as a result of D cracking. The average life of the AC overlays Elliott studied is not likely to be the same as the average life of AC overlays placed in the 1970s and 1980s. Thus, for this study, Elliott's analysis of the life of AC overlays in Illinois was repeated using the most recent performance data available.

Description of Overlay Database

The data used for this analysis were obtained from the IPFS data base (*4*). Only pavement sections that received an AC overlay were selected for the overlay analysis. Data retrieved from the IPFS data base included the route number, beginning milepost, length, direction, pavement type, D cracking variable, first overlay thickness and year, second overlay thickness and year, age of first overlay, and cumulative ESALs on the first overlay. A few sections were discarded because first overlay thickness or ESAL data were missing.

The method used to calculate ESALs was described by Darter et al. (*2*). The ESALs used in the overlay survival analysis were derived from load equivalency factors for PCC pavements. Because there were no AC-PCC pavement sections studied at the AASHO Road Test, strictly speaking there are no load equivalency factors available for calculating ESALs for this type of pavement. Rigid pavement load equivalency factors were considered more appropriate for use in this analysis than flexible pavement load equivalency factors,

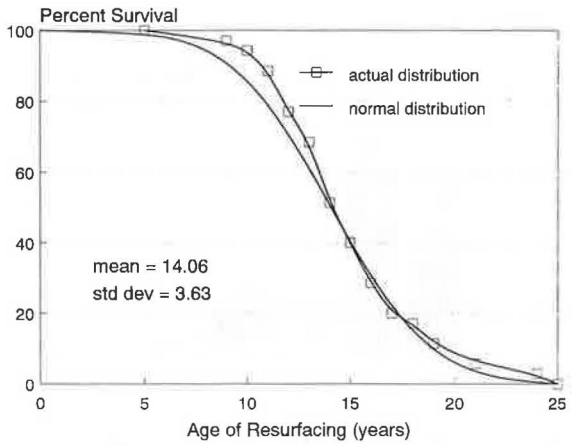


FIGURE 2 Survival of AC overlays of PCC placed in Illinois in the 1950s and 1960s (*25*).

because the structural response of AC-PCC pavement to traffic loading is more like that of PCC pavement than AC pavement. In addition, rigid load equivalency factors can be shown to more closely indicate the development of AC rutting under different axle weights and configurations than flexible load equivalency factors (S. H. Carpenter, unpublished data).

The overlaid pavements were placed in eight different categories, defined by the original pavement type (JRCP or CRCP), D cracking, and AC overlay thickness. The number of overlaid pavement sections in each of the categories is presented in Table 1.

The distribution of AC overlay thicknesses in the data base is shown in Figure 3. Of the 410 total sections, 323 received thin overlays (less than 4 in.) and 87 received thick overlays (4 in. or more). Most of the overlays were 3 or 3.25 in. thick (119 and 201 sections, respectively). The means and ranges of thin and thick overlays of JRCP and CRCP are presented in Table 2.

The distribution of AC overlay ages is shown in Figure 4. Eighty-seven percent of the overlaid sections are 10 years old or fewer. The distribution of AC overlay ESALs is shown in Figure 5. Eighty-three percent of the sections have carried fewer than 10 million ESALs.

Description of Survival Analysis Method

Survival analysis is a statistical method for determining the distribution of lives, as well as the life expectancy, or mean life, of subjects in an experiment. This analysis method, which is widely used in scientific and actuarial research, is more appropriate than simple computation of the average life of subjects whose life has ended when not all subjects in the experiment have yet reached the end of their life. (In statistical terms, such subjects are termed "right-censored observations.") Survival analysis is described in greater detail in the literature (e.g., *26–28*).

The survival analysis of AC overlays was conducted by the same procedure used in a previous study for bare JRCP and CRCP (*1*). The points for the survival curves were obtained using the LIFETEST procedure available in the PC SAS software (*26*). Survival curves were generated for each category on the basis of both overlay age and cumulative 18-kip ESALs in the outer traffic lane on the overlay.

An overlay was considered to have failed when a second overlay was placed, or in a few cases, if the first overlay was

TABLE 1 NUMBER OF AC OVERLAY SECTIONS IN EACH CATEGORY

OVERLAY CATEGORY	JRCP		CRCP	
	non D cracked	D cracked	non D cracked	D cracked
THIN	81	72	65	105
THICK	35	25	2	25

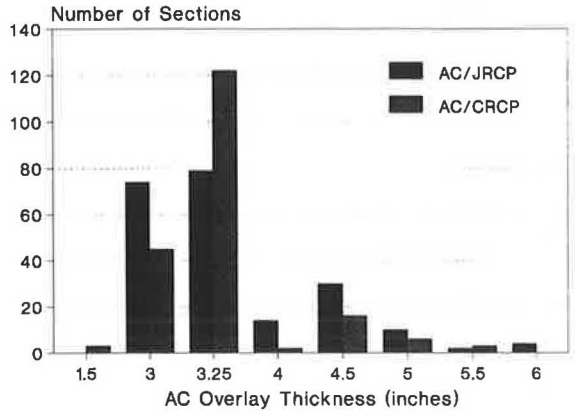


FIGURE 3 Distribution of AC overlay thicknesses on Illinois Interstates.

TABLE 2 MEAN AND RANGE OF AC OVERLAY THICKNESSES

OVERLAY CATEGORY	JRCP			CRCP		
	Mean (in)	Min (in)	Max (in)	Mean (in)	Min (in)	Max (in)
THIN	3.13	3.0	3.25	3.15	1.5	3.25
THICK	4.60	4.0	6.0	4.69	4.0	5.5

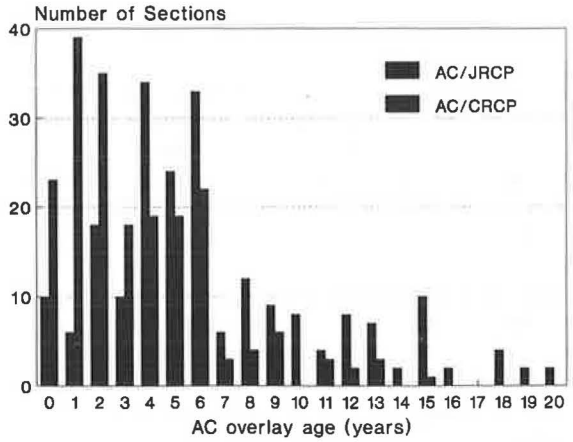


FIGURE 4 Distribution of AC overlay ages on Illinois Interstates.

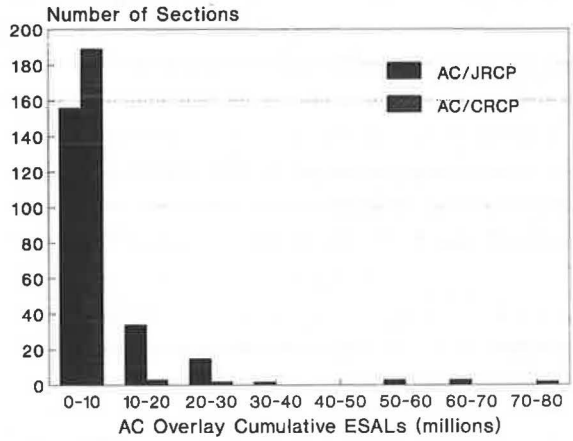


FIGURE 5 Distribution of cumulative ESALs on AC overlays on Illinois Interstates.

cold milled because of severe rutting. A point is generated on a survival curve for each age or ESAL corresponding to at least one failed section. Ages or ESALs that do not correspond to at least one failed section are not used in the analysis. The percent failure for a given age or number of ESALs is equal to the probability that a given section will fail when it reaches that age or number of ESALs. The greater the number of surviving sections at a given age, the lower the percent failures is for that age, hence, the lower the probability of failure at that age.

In addition to the survival distribution, a mean life is computed by the LIFETEST procedure. The computed mean life sometimes differs from the median (50th percentile) life, which is an indication that the survival distribution is not symmetric. Furthermore, if the last observation in the data set is censored (e.g., if the oldest overlay in the data set has not yet failed), the estimated mean life is biased and may be lower than the true mean.

SURVIVAL OF AC OVERLAYS OF JRCP

The mean lives of AC overlays (in terms of age and number of ESALs) in each of the four JRCP categories are presented in Table 3. Clear differences in AC overlay survival exist between D-cracked and non-D-cracked JRCP, and between thin and thick overlays.

AC-JRCP Survival in Years

The age survival curves for thin AC overlays of D-cracked and non-D-cracked JRCP are shown in Figure 6. The age survival curves for thick AC overlays of D-cracked and non-D-cracked JRCP are shown in Figure 7. In terms of age, the survival analysis indicates that D cracking of the existing JRCP slab affects the lives of thin AC overlays more than the lives of thick AC overlays. Thin AC overlays lasted 60 percent longer on non-D-cracked JRCP than on D-cracked JRCP (11.9 versus 7.3 years), whereas thick AC overlays lasted 13 percent longer on non-D-cracked JRCP than on D-cracked JRCP (16.4 versus 14.5 years).

The survival analysis also indicates that in terms of age, overlay thickness affects the lives of AC overlays on D-cracked JRCP more than the lives of AC overlays on non-D-cracked JRCP. Thick AC overlays of D-cracked JRCP sections lasted twice as long as thin AC overlays of D-cracked JRCP sections (14.5 versus 7.3 years). Thick AC overlays of non-D-cracked JRCP sections lasted about 40 percent longer than thin AC overlays of non-D-cracked JRCP sections (16.4 versus 11.9 years).

TABLE 3 MEAN LIVES OF AC OVERLAYS OF JRCP

OVERLAY CATEGORY	AGE (years)		ESAL (million)	
	non D cracked	D cracked	non D cracked	D cracked
THIN	11.9	7.3	18.4	6.3
THICK	16.4	14.5	45.4	14.7

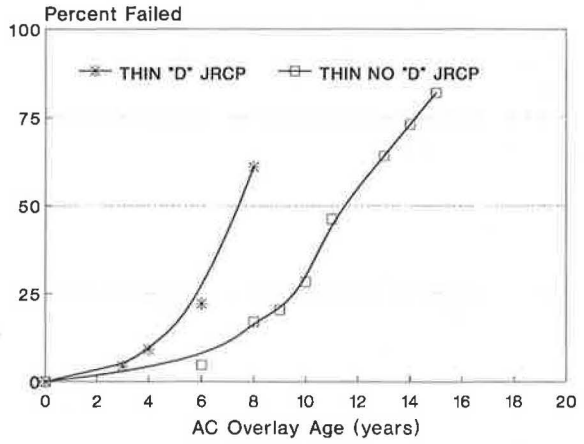


FIGURE 6 Age survival curves for thin AC overlays of JRCP.

AC-JRCP Survival Under Traffic

The ESAL survival curves for thin AC overlays of D-cracked and non-D-cracked JRCP are shown in Figure 8. The ESAL

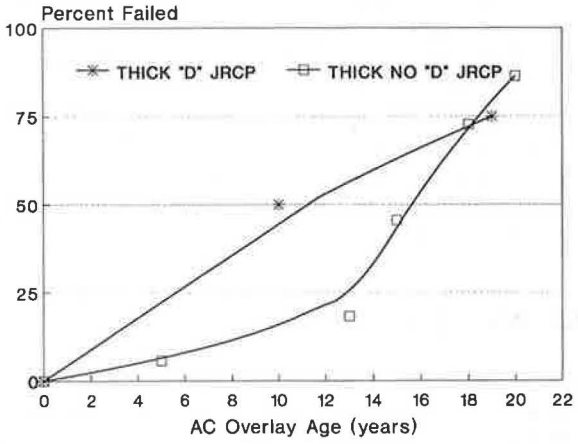


FIGURE 7 Age survival curves for thick AC overlays of JRCP.

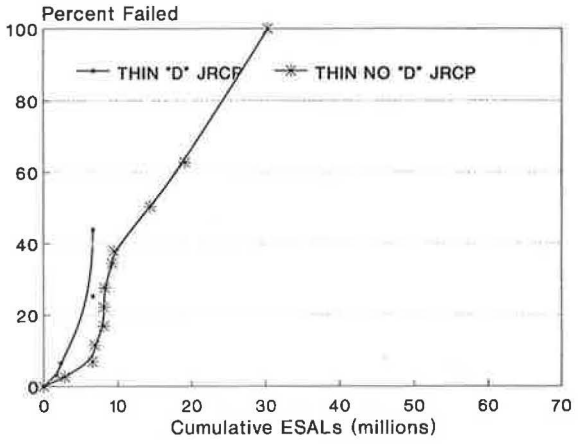


FIGURE 8 ESAL survival curves for thin AC overlays of JRCP.

survival curves for thin AC overlays of D-cracked and non-D-cracked JRCP are shown in Figure 9. In terms of traffic, the effect of D cracking on overlay survival is similar for thin and thick overlays. Thin AC overlays of non-D-cracked JRCP carried 2.9 times more traffic than thin AC overlays of D-cracked JRCP (18.4 versus 6.3 million ESALs). Thick AC overlays of non-D-cracked JRCP carried 3.1 times more traffic than thick AC overlays of D-cracked JRCP (45.4 versus 14.7 million ESALs).

The effect of overlay thickness on survival is also similar for D-cracked and non-D-cracked JRCP when considered in terms of traffic. Thick AC overlays of D-cracked JRCP sections lasted 2.3 times longer than thin AC overlays of D-cracked JRCP sections (14.7 versus 6.3 million ESALs). Thick AC overlays of non-D-cracked JRCP sections lasted 2.5 times longer than thin AC overlays of non-D-cracked JRCP sections (45.4 versus 18.4 million ESALs).

Percent AC-JRCP Sections Failed

At the time of this analysis, 25 percent of the thin AC overlays on non-D-cracked JRCP sections had failed, and 11 percent of the thin AC overlays on D-cracked JRCP had failed. Roughly the same proportions of thick AC overlays had failed as well: 31 percent on non-D-cracked sections and 12 percent on D-cracked sections. These failure percentages are considered sufficiently large for preliminary estimation of the AC overlay survival distributions. However, the shapes of the survival distributions and the mean lives in each of the categories examined are expected to change in the future as more sections reach failure and the ability to estimate the means and distributions improves.

SURVIVAL OF AC OVERLAYS OF CRCP

At the time of this analysis, most of the AC overlays of CRCP were less than 7 years old, and only 6 percent had failed. It is therefore too early to draw any reliable conclusions about the probable shapes of the survival curves or the mean lives of thin or thick AC overlays on D-cracked or non-D-cracked CRCP. However, subjective assessments of the performance of several AC-overlaid CRCP sections suggest that the trends will be similar to those of AC-overlaid JRCP; that is, better performance on non-D-cracked pavement and better performance with thicker overlays.

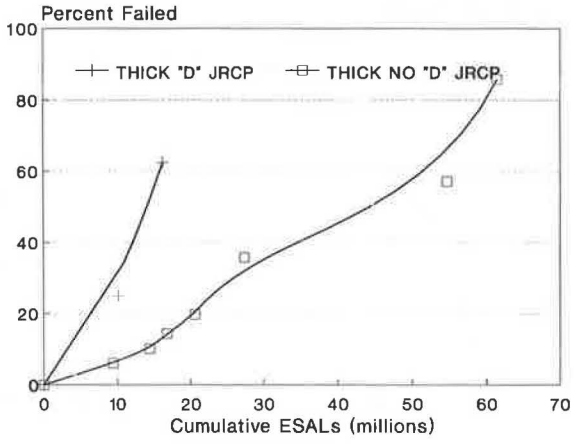


FIGURE 9 ESAL survival curves for thick AC overlays of JRCP.

SUMMARY

The predominant distresses that most often control the life of AC-PCC pavement are reflection cracking, D cracking, rutting, and AC patch deterioration. The degree to which these distresses affect AC overlay life depends primarily on the thickness of the AC overlay, the type of original slab (JRCP or CRCP), and whether or not the PCC has D cracking.

In terms of age, the beneficial effect of increased overlay thickness is significant for both non-D-cracked JRCP and D-cracked JRCP, and is more pronounced for the latter (40 and 100 percent longer life, respectively). The detrimental effect of D cracking is significant for both thick and thin AC overlays, and is more pronounced for the latter (12 and 38 percent shorter life, respectively). In terms of traffic, the effects of overlay thickness and D cracking are similar—thick AC overlays carry about 2.5 times more traffic than thin AC overlays, and AC overlays of non-D-cracked JRCP carry about 3 times more traffic than AC overlays of D-cracked JRCP. The analysis highlights the notably poor performance of thin AC overlays of D-cracked JRCP (mean life 7.3 years, 6.3 million ESALs), as well as the notably good performance of thick AC overlays of non-D-cracked JRCP (mean life 16.4 years, 45.4 million ESALs). Too few AC overlays of CRCP sections have yet failed to reliably estimate the mean lives or survival distributions of AC-CRCP on Illinois Interstates.

For the purposes of this analysis, an overlay was considered to have failed either when a second overlay was placed or when cold milling was done. This measure of overlay performance is rough, but it is the only measure available for use in the analysis. Historical distress data that might be used to determine the condition of an overlay before placement of a second overlay are not available.

The performance of AC overlays of PCC pavements is strongly influenced by the condition of the overlaid PCC, i.e., the extent of deterioration present in the original pavement and the type and amount of preoverlay repair performed. Funding limitations frequently necessitate delaying resurfacing projects, and performing less than complete repair of deteriorated areas on projects that are resurfaced. Thus, the availability of funds has a definite impact on the performance of resurfacing projects.

REFERENCES

1. M. E. Dwiggins, M. I. Darter, J. P. Hall, C. F. Flowers, and J. B. DuBose. *Pavement Performance Analysis of the Illinois Interstate Highway System*. Report FHWA-IL-UI-220. University of Illinois at Champagne-Urbana and Illinois Department of Transportation, Springfield, 1989.
2. M. I. Darter, R. A. Salsilli, M. E. Dwiggins, T. Fitch, and A. Lundberg. *Analysis of Traffic Loadings on Interstate Highways in Illinois*. Report FHWA-IL-UI-222, University of Illinois at Urbana-Champaign and Illinois Department of Transportation, Springfield, 1989.

3. D. L. Lippert and J. B. DuBose. Performance Evaluation of Concrete Overlays. Report FHWA/IL/PR-101, Illinois Department of Transportation, Springfield, 1988.
4. M. E. Dwiggins, J. P. Hall, M. I. Darter, C. F. Flowers, and J. B. DuBose. Logical and Physical Design of the Illinois Pavement Feedback System. Report FHWA-IL-UI-219. University of Illinois at Urbana-Champaign and Illinois Department of Transportation, Springfield, 1988.
5. M. I. Darter, R. P. Elliott, and K. T. Hall. *Revision of AASHTO Overlay Design Procedures*. Draft Final Report, NCHRP Project 20-7/Task 39, TRB, National Research Council, Washington, D.C., 1990.
6. K. T. Hall and M. I. Darter. Rehabilitation Performance and Cost-Effectiveness: A Ten-Year Case Study. In *Transportation Research Record 1215*, TRB, National Research Council, Washington, D.C., 1990.
7. D. R. Schwartz. *NCHRP Synthesis of Highway Practice 134: D-Cracking of Concrete Pavements*. TRB, National Research Council, Washington, D.C., 1987.
8. D. Stark. Field and Laboratory Studies of the Effects of Subbase Type on the Development of D-Cracking, In *Highway Research Record 342*, HRB, National Research Council, Washington, D.C., 1970.
9. R. J. Girard, E. W. Meyers, G. D. Manchester, and W. L. Trimm. D-Cracking: Pavement Design and Construction Variables. In *Transportation Research Record 853*, TRB, National Research Council, Washington, D.C., 1982.
10. D. Stark. *Characteristics and Utilization of Coarse Aggregates Associated with D-Cracking*. Research and Development Bulletin RD047.01p. Portland Cement Association, Skokie, Ill., 1976.
11. P. Klieger, G. Monfore, D. Stark, and W. Teske. D-Cracking of Concrete Pavements in Ohio. Report Ohio-DOT-11-74, Portland Cement Association, Skokie, Ill., 1974.
12. M. R. Thompson, M. P. Olsen, and B. J. Dempsey. *Synthesis Report: D-Cracking in Portland Cement Concrete Pavements*. Report FHWA/IL/UI-187, University of Illinois at Urbana-Champaign, 1980.
13. M. Kaneuji. *Correlation Between Pore Size Distribution and Freeze-Thaw Durability of Coarse Aggregate in Concrete*. Report JHRP-78-15, Purdue University, West Lafayette, Ind., 1978.
14. V. J. Marks and W. Dubberke. Durability of Concrete and the Iowa Pore Index Test. In *Transportation Research Record 853*, TRB, National Research Council, Washington, D.C., 1982.
15. G. Verbeck, P. Klieger, D. Stark, and W. Teske. *D-Cracking of Concrete Pavements in Ohio*. First Interim Report, No. 72-04, Ohio Department of Highways, Columbus, 1972.
16. D. Stark and P. Klieger. Effect of Maximum Size of Coarse Aggregate on D-Cracking in Concrete Pavements. In *Highway Research Record 441*, HRB, National Research Council, Washington, D.C., 1973.
17. P. Klieger, D. Stark, and W. Teske. *The Influence of Environment and Materials on D-Cracking*. Report FHWA-OH-78-06, Ohio Department of Transportation, Columbus, 1978.
18. *Twenty-Year Report on the Long-Time Study of Cement Performance in Concrete*. Research Department Bulletin 175, Research and Development Laboratories, Portland Cement Association, Skokie, Ill., 1965.
19. *Investigations of "D" Cracking in PCC Pavements: Phase 2*. Report 72-4. Division of Materials and Research, Missouri State Highway Department. Jefferson City, Mo., 1972.
20. *A Preliminary Investigation of the D-Cracking Problem in Illinois*. Bureau of Materials and Physical Research, Illinois Department of Transportation, Springfield, 1979.
21. D. J. Janssen, B. J. Dempsey, J. B. DuBose, and A. J. Patel. Predicting the Progression of D Cracking. IHR Project 417, University of Illinois at Urbana-Champaign and Illinois Department of Transportation, Springfield, 1986.
22. *Report of the AASHTO Joint Task Force on Rutting*. AASHTO, Washington, D.C., 1989.
23. S. H. Carpenter and T. J. Freeman. Characterizing Premature Deformation in Asphalt Concrete Placed over Portland Cement Concrete Pavements. In *Transportation Research Record 1070*, TRB, National Research Council, Washington, D.C., 1986.
24. E. E. Harm. *Illinois Rutting Report*. 13th Annual Asphalt Paving Seminar, Fort Collins, Colo., Bituminous Task Force on Stability and Durability, Illinois Department of Transportation, Springfield, 1985.
25. R. P. Elliott. *Thickness Design Procedure for Bituminous Resurfacings of Portland Cement Concrete Pavements*. Research and Development Report 30, Illinois Department of Transportation, Springfield, 1971.
26. SAS Institute, Inc. *SAS User's Guide: Statistics*, Version 5. Cary, N.C., 1985.
27. E. T. Lee, *Statistical Methods for Survival Data Analysis*. Wadsworth, 1980.
28. D. R. Cox and D. Oakes. *Analysis of Survival Data*, Chapman and Hall, 1984.

Publication of this paper sponsored by Committee on Pavement Rehabilitation.

Crack and Seat Performance

KEUN-WOOK YI

The effectiveness of the crack and seat process in preventing reflection cracking on asphaltic overlays of portland cement concrete pavement (PCCP) is evaluated. New Mexico has approximately 145 mi of PCCP existing on the Interstate system. In a 4-year period from 1984 to 1988, 110 mi was rehabilitated using the crack and seat process. The existing portland cement concrete was cracked and seated and overlaid with asphalt concrete. To further reduce reflection cracking, a paving fabric was used. The areas that were cracked and seated were inspected for distresses, mainly reflection cracking. Roughly 3 percent of the cracked and seated sections exhibited low-severity transverse reflection cracking, whereas the experimental sections not cracked and seated exhibited a high rate of transverse cracking. The crack and seat process with paving fabrics is greatly reducing the reflection cracking that has been a major problem in asphalt overlays of PCCP. This method seems to be a sound alternative for rehabilitating the existing PCCP.

The portland cement concrete pavement (PCCP) in New Mexico is approaching the end of its design life, with deterioration of the PCCP becoming apparent. The deterioration, such as spalling, cracking, joint deterioration, and faulted joints, affects riding comfort and road safety, and increases maintenance costs and vehicle operating costs. The deteriorated PCCP must be replaced or rehabilitated. Slab replacement is costly and causes lengthy traffic delays. To avoid the high costs and delays associated with concrete slab replacement, the PCCP can be rehabilitated by the following methods (*1*):

1. Portland cement concrete (PCC) overlay,
2. Recycled PCCP, and
3. Asphaltic concrete (AC) overlay.

A PCC overlay was used on I-25 in Albuquerque. This method has since been rejected because it is not economical although it is performing well. The recycled PCCP has not been used in New Mexico because the cost is high compared with that of AC overlays.

Reflection cracking is a major problem associated with AC overlays of PCCP. This cracking, which is defined as the surface duplication of cracks and joint patterns of the underlying PCCP, is caused by horizontal and vertical movements of the PCCP (*2*). The horizontal movements are caused by the expansion and contraction of the PCCP slab, whereas the vertical movements are caused by a load moving from one PCCP slab to another.

The purpose of the crack and seat process of PCCP is to reduce the stresses on the AC material that are caused by the horizontal and vertical movements of the underlying PCCP (*2*). In this process, the PCCP is cracked to create smaller pieces that move less than large slabs. When the slab movements are reduced, the stresses that cause reflection cracking are also reduced. The PCCP is first cracked and then seated using a roller to remove any voids under the cracked PCCP, which further reduces the vertical movements of the PCCP slabs.

Materials Laboratory Bureau, New Mexico State Highway and Transportation Department, P.O. Box 1149, Santa Fe, N. Mex. 87504–1149.

DESIGN PROCEDURE

Information about the existing roadway is compiled as part of the design and construction process. The information includes the following:

1. Existing typical sections,
2. Strength of the subgrade,
3. Maintenance history,
4. Traffic summary statistics, and
5. Traffic projections.

After gathering the required information, the pavement designer makes a visual inspection of the existing pavement. The pavement distresses are defined using the *Highway Pavement Distress Identification Manual* (*3*).

The New Mexico State Highway and Transportation Department (NMSH&TD) uses the structural deficiency analysis to determine the thickness of plant mix bituminous pavement (PMBP) overlays. The required structural number is calculated using the following:

1. R-value,
2. Regional factor,
3. Traffic projections,
4. Serviceability index, and
5. Design life.

According to Lukanen (*4*), the recommended structural layer coefficients are as follows:

Crack Spacing (ft)	*Structural Layer Coefficient*
1	0.25
2	0.35
3	0.45

The crack spacing required by the NMSH&TD's *Special Provisions for Cracking and Seating Concrete Pavement* (Item No. 451101), is 18 to 24 in. with a maximum spacing of 30 in. By interpolating the data, the crack spacing of 18 in. yields a structural layer coefficient of 0.3 whereas the crack spacing of 24 in. yields a coefficient of 0.35. Because the 18-in. spacing

has the lower coefficient, it yields a thicker overlay. Thus, it provides the roadway with a more conservative design.

The NMSH&TD recommends that a minimum of 4½ in. of overlay be placed to prevent reflection cracking. The minimum 4½-in. overlay is based on a review of crack and seat work done in other states and in NMSH&TD's Research Bureau. The Research Bureau used a Model 2000 Road-Rater to measure the dynamic deflection response under the following conditions:

1. After the PCCP had been cracked and seated, and
2. After a 5-in. PMBP overlay had been constructed.

These deflections yielded the material characteristics presented in Table 1.

Using the results from this testing and the NMSH&TD elastic-layer program for flexible pavements, a 2½-in. PMBP overlay would be required for this particular project. But experience has shown that the additional thickness is needed to prevent reflection cracking.

TABLE 1 MATERIAL CHARACTERISTICS AS DEFINED BY ROAD-RATER

MATERIAL DESCRIPTION	THICKNESS (IN)	POISSON'S RATIO	MODULUS (PSI)
PMBP	5.0	0.35	900,000
CRACKED AND SEATED PCCP	8.0	0.20	500,000
CTB	5.0	0.25	175,000
SUBGRADE	-	0.45	8,000

from Project IR-040-5(39)276
- indefinite thickness

CONSTRUCTION PROCEDURE

The construction procedure consists of the following:

1. Removing and replacing the unsuitable slab,
2. Cracking the existing PCCP,
3. Seating the cracked PCCP, and
4. Overlaying with asphalt (PMBP).

Smaller pieces are created by cracking the existing PCCP, minimizing excessive temperature strains of the larger slabs. This process also curtails the horizontal movement in the slabs and reduces the reflection cracking. The existing PCCP is not cracked enough to reduce pavement to rubble but it should contain hairline cracks that extend through the entire depth of the existing PCCP. These hairline cracks allow the load to transfer from one small piece of the cracked PCCP to the next through aggregate interlock, which also allows the PCCP to retain more of its original structural integrity, thus minimizing the overlay thickness required.

The cracking of the pavement can be accomplished by several methods. The types of devices that can be used for cracking the pavement are

1. Modified pile driver,
2. Pecking hammer, and
3. Transverse bar drop (guillotine) hammer.

The guillotine hammer is the only device that has been used in New Mexico. The guillotine hammer is a device that consists of a transverse weight that is dropped from a predetermined height. The height of the hammer is determined by a trial method in which a small section of the project is chosen. The hammer is dropped from different heights onto this section to determine the drop height that is required to create a vertical hairline crack throughout the entire depth of the PCCP.

Once the pavement has been cracked, the surface is cleaned using a power broom, compressed air, or other approved methods. The pavement is proof-rolled with a pneumatic roller weighing at least 50 tons. The rolling continues until the cracked pavement is well seated.

Once the PCCP is seated, a leveling course of 1.5 in. is placed. The leveling course is followed by an interlayer, usually of some type of paving fabric (e.g., Petromat). The interlayer is then covered with a minimum of 3 in. of PMBP. Finally, open-graded friction course is placed on top of the final lift of the PMBP.

FIELD EVALUATION

Background Information

Over the years, the NMSH&TD has primarily built PCCP consisting of 8 or 9 in. of PCCP over 4 in. of cement-treated base (CTB). Most of the jobs that are included in this study have 8 in. of PCCP over 4 in. of CTB; two jobs have 9 in. of PCCP over 4 in. of CTB. None of the crack and seat projects had control sections except for Project IR-040-5(40)282, which contains nine different test sections. The project number can be interpreted in the following manner. The first two letters stand for the type of funding. In this case, IR stands for Interstate system rehabilitation. The next three digits are used to identify the route. For example, 040 represents I-40. The next important set of numbers are the last three digits in the project number. These numbers represent the milepost (MP) at which the project begins. Table 2 presents original pavement data (*1*).

Cost

The cost per square yard of cracking and seating varied from $0.25 to $0.80 with an average cost of $0.40. The costs per square yard and the total costs of each of the crack and seat projects are presented in Table 3.

Project Summary

- IR-010-1(49)21. This project was completed in 1987. There are no signs of reflection cracking throughout the project.
- IR-010-1(55)28. This project was completed in 1987. There are no signs of reflection cracking on the pavement.
- IR-010-1(68)55. This project was completed in 1987. There are no signs of reflection cracking in the pavement. However, there is low-severity rutting.

TABLE 2 CRACK AND SEAT PROJECT DATA WITH ORIGINAL PAVEMENT DATA

Project Location	Const. Date	Orig. Const. Date	Original Surfacing Data(inches) PCCP	CTB	UTB	ATB	SB	Design AASHTO Soil Class.	Design R Value	Condition of the PCCP at the time of Crack and Seat Fault.	Crack.	Pump.	JS	RA
Interstate 10														
MP 21	1987	1972/75	9	4				A-4/A-6	20	L-M	M	M-H	Yes	No*
MP 28	1987	1962	EBL 8	4	4			A-4/A-6	22	L-M	M-H	M-H	Yes	No*
			WBL 8	3		4	8	A-6/A-7	10					
MP 55	1987	1963/65	EBL 8		4		4	A-6	25	M	M	M-H	Yes	No*
			WBL 8	3		2.5	13	A-4/A-6	15					
MP 63	1987	1965	EBL 8	4	4			A-4/A-6	20	L-M	M	M-H	Yes	Yes*
			WBL 8	3		4	6	A-2-4/A-6	33					
MP 70	1986	1964	EBL 8	4					25/33	L-M	M-H	H	Yes	Yes*
			WBL 8	4				A-4/A-6	17					
Interstate 40														
MP 26	1987	1965	8	4	6			A-2-4/A-6	33	M-H	H	M-H	Yes	No*
MP 31	1987	58/63/64	8	4	4			A-2-4/A-6	33	M-H	H	M-H	Yes	No*
MP 184	1989		8	4	4			A-4/A-6	**	M	H		No	No
MP 200	1989	1968/69	8	4				A-4/A-6	**		H		No	No
MP 271	1986	1970	8	5				A-4	32	M-H	M-H	H	Yes	Yes*
MP 276	1984	1962/63	8	4				A-4/A-6	5-12	M-H	M-H	M-H	Yes	No*
MP 282	1989	1964	EBL 8	4			4	A-4/A-6	**	M-H		M-H	Yes	No
			WBL 8		3	Built over Old US66 2.5" PMBP, 3" UTB, 3" Minimum SB								
MP 291	1986	1963	8	4	4			A-4/A-6	20	M-H	M-H	M-H	Yes	No*
MP 300	1985	1962	8	4				A-2-4/A-6	33	M-H	M-H	H	Yes	No*
MP 308	1986	1961	8	4			4	A-4/A-6	21	M-H	M-H	H	Yes	No*
MP 313	1986	1961	8	4			4	A-4/A-6	21	M-H	M-H	H	Yes	No*
MP 326	1987	1969	9	4				A-4/A-6	20	L-M	M-H	M	Yes	No*

* data from "Crack and Seat Performance", John Higgins
** no data found

SYMBOLS
PCCP-Portland Cement Concrete Pavement ATB-Asphalt Treated Base CTB-Cement Treated Base
UTB-Untreated Base SB-Subbase RA-Reactive Aggregate Degradation JS-Joint Seal Missing
L-Low M-Medium H-High

• IR-010-2(69)63. This project was completed in 1987. There are no signs of reflection cracking in the pavement. However, there is low- to medium-severity rutting.

• IR-010-2(62)70. This project was completed in 1986. There are no signs of reflection cracking in the pavement. However, there is low- to medium-severity rutting.

• IR-040-1(82)26. This project was completed in 1987. This project does not exhibit any pavement distress.

• IR-040-1(83)31. This project was completed in 1987. This project does not exhibit any pavement distress.

• IR-040-4(40)184. This project was completed in 1989; more time will be needed before an evaluation can be completed.

• IR-040-4(42)200. This project was completed in 1989; more time will be needed before an evaluation can be completed.

• IR-040-5(41)271. This project was completed in 1986. There are no signs of reflection cracking in the pavement. However, there is low- to medium-severity rutting.

• IR-040-5(39)276. This project was completed in 1984; it is the oldest crack and seat project in the state. There is a longitudinal crack near mile marker 279 that is caused by the construction joint of the asphaltic overlay. It is not a reflection crack from the crack and seat process. This project has low- to medium-severity rutting.

• IR-040-5(40)282. This project was completed in 1988. The project contains nine test sections on the eastbound driving lane, each 950 ft in length (see Figure 1). There were two different types of interlayers used in these test sections. One interlayer was the standard paving fabric called AmoPave. The other was Glasgrid, the experimental interlayer used in this project. Glasgrid is a fiber reinforcement mesh for asphaltic concrete purported to prevent reflection cracking. Sections 1 through 6 were cracked and seated. These sections are exhibiting no signs of cracking in the driving lane. Sections 7 through 9 were not cracked and seated. These sections are exhibiting some cracking. Section 7, which contains no interlayer, is exhibiting twice as many cracks (see Figure 2) as Sections 8 and 9, which had the interlayers. The test sections were inspected by James A Scherocman, P.E., consulting engineer, on February 18, 1990. The resulting numbers of cracks are presented in Table 4. The rest of the project was constructed using one of the standard paving fabrics. The project exhibits some transverse cracking in the shoulders and low-severity rutting at the beginning of the project, but no reflection cracking.

• IR-040-5(43)291. This project was completed in 1986. The roadway displays low-severity transverse cracks. These cracks are located throughout the project but they are randomly located and there is no set pattern to them. The number and total length of the cracks are minimal. The roadway also exhibits low- to medium-severity rutting.

• IR-040-5(42)300. This project was completed in 1985. At approximately MP 300.5, they are low-severity transverse cracks. These cracks are in the westbound lane approximately 40 ft apart (see Figure 3). When a core was taken at one of

TABLE 3 COST OF CRACKING AND SEATING

Project Number	Letting Date	Amount of Crack & Seat (SY)	Cost per SY	Total Cost
IR-010-1(49)21	October 1986	200,200	$0.25	$50,050**
IR-010-1(55)28	September 1986	167,050	$0.25	$41,763**
IR-010-2(68)55	May 1987	226,010*	$0.30	$67,803**
IR-010-2(69)63	May 1987	206,620*	$0.30	$61,986**
IR-010-2(62)70	January 1986	304,150	$0.50	$152,075**
IR-040-1(82)26	July 1987	52,900*	$0.35	$18,515**
IR-040-1(83)31	June 1987	92,750*	$0.30	$27,825**
IR-040-4(40)184	March 1988	229,375*	$0.30	$68,813
IR-040-4(42)200	March 1988	180,230*	$0.25	$45,058
IR-040-5(41)271	June 1985	170,830	$0.30	$51,249**
IR-040-5(39)276	June 1984	84,500	$0.77	$65,065**
IR-040-5(40)282	July 1987	245,000*	$0.30	$73,500
IR-040-5(43)291	April 1986	244,050	$0.35	$85,418**
IR-040-5(42)300	March 1985	242,980	$0.35	$85,043**
IR-040-6(41)308	May 1985	130,100	$0.55	$71,555**
IR-040-6(42)313	November 1985	147,000	$0.65	$95,550**
IR-040-6(43)326	August 1986	104,700	$0.80	$83,760**

* - Plan Quantity

** - from "Crack and Seat Performance", John Higgins,FHWA,1987

SY - Square Yards

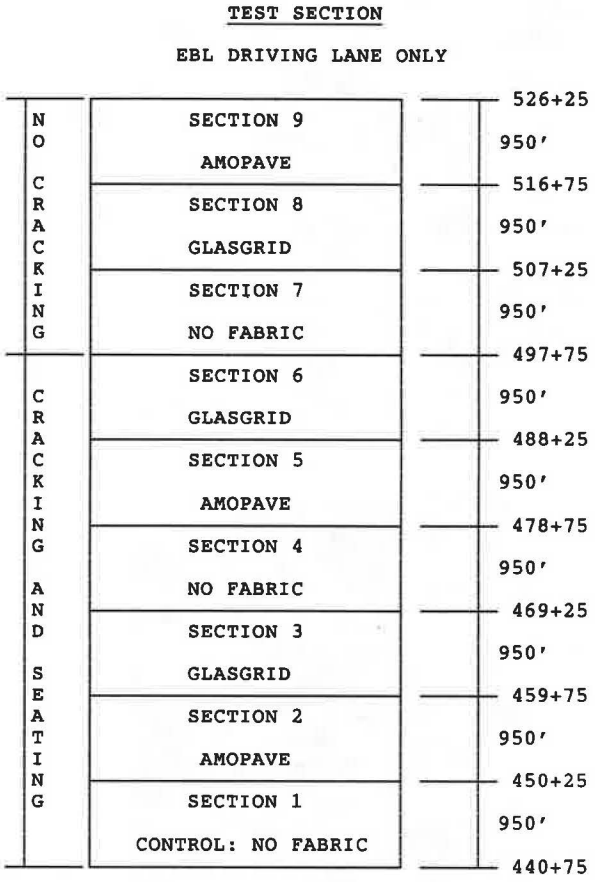


FIGURE 1 Test section.



FIGURE 2 Condition of the roadway on Project IR-040-5(40)282 in the control section without cracking and seating or paving fabric. Note the two transverse cracks spaced approximately 40 ft apart.



FIGURE 3 Reflection cracking evident in a section near MP 300.5 on Project IR-040-5(42)300.

TABLE 4 NUMBER OF CRACKS IN THE EXPERIMENTAL SECTION

	Crack & Seat						No Crack & Seat		
	No Fabric		Glasgrid AmoPave		AmoPave No Fabric	Glasgrid	No Fabric		AmoPave Glasgrid
Location of cracks	Section 1	Section 2	Section 3	Section 4	Section 5	Section 6	Section 7	Section 8	Section 9
Driving Lane									
Inside WP Only	0	0	0	0	0	0	0	0	0
Outside WP Only	0	0	0	0	0	0	3	0	6
Full Width	0	0	0	0	0	0	23	10	8
Full width plus partial passing lane	0	0	0	0	0	0	4	3	1
Passing Lane									
Full width	0	3	5	0	0	0	0	0	0
Full width plus partial driving lane	0	5	3	0	0	0	0	0	0
Full Width-both lanes	0	1	0	0	0	0	2	0	0

NOTE: WP = Wheel Path

the cracks, it revealed that the PCCP was cracked and faulted underneath the transverse crack. In the same lane, there are low-severity transverse cracks near MP 304.5. These are approximately 60 ft apart. There are longitudinal cracks along the center of the eastbound lanes. In one particular area near MP 306.5, there is a cracking pattern that can best be described as a reflective corner break (see Figure 4).

- IR-040-6(41)308. This project was constructed in 1986. The overlay is exhibiting no pavement distress.
- IR-040-6(42)313. This project was constructed in 1986. The overlay is exhibiting no pavement distress.
- IR-040-6(43)326. This project was constructed in 1987. The overlay is exhibiting no pavement distress.

SUMMARY AND CONCLUSIONS

Summary

The crack and seat rehabilitation for PCCP pavement has been used in the State of New Mexico since 1984.

Such projects make up approximately 110 mi or 440 lane-mi of New Mexico's Interstate system. Of the 440 lane-mi, less than 15 lane-mi exhibit reflective cracking. Most of the cracks are low-severity transverse cracks. Throughout several of the crack and seat projects, there appears to be the beginning of reflection cracking. These had not propagated into reflection cracks as of the data of inspection. When cores were taken in these areas, they revealed that there was no reflection cracking present. There are a few areas exhibiting low-severity longitudinal cracks. These longitudinal cracks are located on the edges and in the middle of the lanes. These cracks are caused by construction joints and flexible shoulders adjacent to the PCCP rather than reflection cracks. Many areas were also exhibiting rutting. However, rutting was not a problem associated with the crack and seat process.



FIGURE 4 Reflection cracking, better described as reflective corner break, on Project IR-040-5(42)300.

Conclusions

The test sections in Project IR-040-5(40)282 indicate that the crack and seat process is an effective method of controlling reflection cracking.

The results of the crack and seat process have been excellent, with approximately 3 percent of the current jobs demonstrating low-severity reflection cracking. Currently, this process seems to be a viable method of rehabilitating PCCP. The cost of the process is low compared with other methods of PCCP rehabilitation. The average cost of cracking and seating PCCP is $0.40 per square yard. The low cost makes cracking and seating an excellent alternative.

Recommendations

1. Crack and seat projects need to be monitored and evaluated on a yearly basis.
2. Areas with reflection cracks should be observed for further deterioration. These cracks need to be sealed to minimize any future subgrade damage.
3. The crack and seat process should continue to be used.
4. The test sections on Project IR-040-5(40)282 should continue to be monitored for the crack retarding effect of the interlayer.

ACKNOWLEDGMENTS

The author would like to take this opportunity to thank the New Mexico State Highway and Transportation Department and FHWA for support in the preparation of this report. The author would also like to thank Douglas I. Hanson, Susan Gallaher, and Peter McDonald for their assistance and support.

REFERENCES

1. J. Higgins. *Crack and Seat Performance The New Mexico Experience*, New Mexico Division, FHWA, Dec. 1987.
2. M. R. Thompson. *NCHRP Synthesis of Highway Practice 144: Breaking/Cracking and Seating Concrete Pavements*. TRB, National Research Council, Washington D.C., 1989.
3. R. E. Smith, M. I. Darter, and S. M. Martin. *Highway Pavement Distress Identification Manual*. Report DOT-FH-11-9175/NCHRP 1-19. FHWA, U.S. Department of Transportation, 1986.
4. E. O. Lukanen. *Structural Evaluation of Crack and Seat Overlay Pavements*. Midwest Pavement Management, Inc., Sept. 1986.
5. J. H. Tenison. *Deflection Analysis of IR-040-5(39)276*. New Mexico State Highway and Transportation Department, Santa Fe, 1984.

Publication of this paper sponsored by Committee on Pavement Rehabilitation.

Crack Monitoring System for Cracked and Seated PCC Pavements

NADER TABATABAEE AND PETER SEBAALY

A mechanical gauge was developed to monitor the movement of crack or joint openings in portland cement concrete structures (in general) and in overlaid and portland cement concrete pavements (in particular). Designed to be inexpensive and simple to operate, this gauge can record maximum, minimum, and instantaneous crack or joint openings. The design and manufacturing of such a gauge along with the field data collected from the prototype gauges installed at the Pavement Durability Research Facility of the Pennsylvania Transportation Institute are presented. The gauges were monitored from January 1990 to the end of February 1990 and from May 1990 to the middle of July 1990. These monitoring periods gave a wide range of expected temperatures and joint openings. Specific recommendations are made for recording minimum and maximum pavement temperature over the monitoring period.

Many miles of the aging portland cement concrete (PCC) pavements of the Interstates will require resurfacing to restore rideability, structural strength, and skid resistance. One way of restoring a good level of performance for these pavements is to apply asphalt overlay. However, this type of rehabilitation has suffered from extensive reflection cracking. Reflection cracks are believed to be caused mainly by horizontal and differential vertical movement at joints and cracks in the existing PCC (with the horizontal movements being considered more critical) (*1*). The horizontal movements are caused by contraction and expansion of the concrete slab because of seasonal and daily temperature cycles as well as traffic loading. The vertical movements are mainly caused by traffic loading. These movements induce excessive tensile and shearing stresses in the asphalt concrete overlay, leading to initiation and propagation of cracks.

Researchers have investigated several procedures intended to reduce or eliminate reflection cracking: fabrics, open-graded crack absorbent layers, sawing and sealing of overlay, bond breakers, and cracking or breaking and seating of the slab before overlay. Cracking and seating is one of the procedures widely used to reduce reflection cracking.

The FHWA *Pavement Rehabilitation Manual* defines the cracking and seating as follows (*2*):

> The intent of pavement cracking and seating is to create concrete pieces that are small enough to reduce horizontal slab movement to a point where thermal stresses which contribute to reflective cracking will be greatly reduced, yet still be large enough and still have some aggregate interlock between pieces so the majority of the original structural strength of PCC pavement is retained. Seating of the broken slabs after cracking is intended to reestablish support between the subbase and the slab where voids may have existed.

On the basis of the previous discussion and the *Pavement Rehabilitation Manual*'s (*2*) definition of the crack and seat activity, the movement of the slab under the asphalt concrete overlay represents the most critical factor. Whether that movement is caused by thermal expansion or contraction, by traffic loading, or by a combination of the two is not important. What is important is that the crack and seat operation should reduce or eliminate those critical movements. The FHWA has initiated a field project to evaluate the effect of the size of the broken slab on the horizontal movement at the joint or crack (*3*). This special project will evaluate the effectiveness of the break and seat technique on jointed reinforced concrete pavements. Break and seat is basically a crack and seat operation with a typical broken slab size of 6 to 18 in (15 to 45 cm), whereas the typical range for crack and seat is in the range of 18 to 48 in (45 to 120 cm) (*3,4*). It will also attempt to identify the minimum amount of breaking needed to destroy slab action while minimizing the loss of structural value in the old slabs. The instrumentation required for this project was identified as a simple, low-cost gauge to monitor the minimum and maximum movements of the slabs and a device to monitor minimum and maximum pavement temperature.

Instrumenting rigid pavement slabs to monitor their joint openings and their warping and curling has been accomplished mainly through the use of linear variable differential transformers (LVDTs). Poblete et al. (*5*) have used thermocouple and LVDTs to monitor the temperature gradients and movement of the slab corners and joints in 21 test sections on the Chilcan highway system. Armaghani et al. (*6*) also used thermocouple and LVDTs to monitor the response of a specially designed test road at the Florida Department of Transportation. Both of these projects used LVDTs to monitor the joint opening and the movement of slabs under traffic and environmental actions.

To measure the total joint or crack movement using LVDT sensors, continuous monitoring of the system is required. In other words, each monitoring sensor must be connected to a specific conditioning and data acquisition unit. The cost of such a system is prohibitively high and would be overkill for the purpose of simply monitoring the total joint or crack movement. In the FHWA project, several test sections will be cracked and seated with different size break patterns before

N. Tabatabaee, Pennsylvania Transportation Institute, Research Building B, University Park, Pa. 16802. P. Sebaaly, Department of Civil Engineering, University of Nevada at Reno, Reno, Nev. 89557.

overlay, and the horizontal movement at the cracks and joints will be monitored. Because a large number of sites will be monitored, an inexpensive gauge was developed to monitor the maximum and minimum crack or joint opening. The design, construction, installation, and other characteristics of the gauge and the data from a field installation study conducted at the Pavement Durability Research Facility of the Pennsylvania Transportation Institute (PTI) are discussed.

CRACK MONITOR GAUGE

A number of criteria were considered critical for the design of the crack monitor gauge. Specifically, the gauge must be accurate, inexpensive, easy to install, simple to operate, and durable. In addition, because the gauge will be used in remote areas over long periods of time, it must operate without electrical power. These requirements rule out the use of any electronic instruments and make mechanical gauges virtually the only option.

One type of mechanical crack monitor gauge is available through Avongard and Soiltest. However, that gauge only measures the instantaneous crack or joint opening, with a resolution of 0.020 in. (0.5 mm). Currently, a mechanical gauge that can register maximum, minimum, and instantaneous crack or joint openings is not commercially available. The total cost of the gauge designed and built in this research is approximately $15.

Design

Figure 1 shows the schematics of the mechanical gauge designed for this project. The gauge consists of two separate parts: a base plate and an overlapping plate. The base plate is firmly attached to the left side of the crack or joint (approach side). It contains a 2.5-in. (64-mm) slot along which two pins can slide with some degree of friction. Each end of the slot has a keyhole to facilitate replacement of the pins, if necessary. There is also a fixed reference pin that is used to measure the relative position of the sliding pins.

The overlapping plate consists of a remote arm that is placed between the pins on the base plate and a flat portion that is firmly attached to the right side of the crack or joint (leave side). As the crack or joint widens, the remote arm pulls the right pin toward the right until the crack or joint reaches its maximum opening. When the crack or joint opening starts to close, the remote arm moves toward the left pin. As the crack or joint resumes its initial opening and continues to narrow, the remote arm pushes the left pin toward the pin position corresponding to the minimum crack or joint opening. It is assumed that the crack monitor gauge is installed such that the base plate will be located at the left side of the joint or crack and the overlapping plate is at the right side. However, in some cases the gauge assembly may be rotated 180 degrees to facilitate its installation.

Fabrication

Figures 2 and 3 are engineering drawings of the designed gauge. The overall dimensions given in Figures 2 and 3 are not critical. However, they have been selected to facilitate precise manufacturing and appropriate installation and operation of the gauge. The gauge is fabricated from 1/16- or 1/32-in.-thick (1.6- or 0.8-mm-thick) stainless steel plate.

Aluminum or hard plastic plates 1/16 in. (1.6 mm) thick can also be used in certain applications. For most applications, stainless steel or aluminum is preferred over plastic because the overlapping plate remote arm can be easily adapted to accommodate any possible lateral misalignment of the sides of the crack or joint. Stainless steel is stronger and more resistant to environmental effects than aluminum. However, it is heavier and more expensive.

The sliding pins are made of 5/16-in.-diameter (7.9-mm-diameter) Teflon rods. The sliding motion of the pins in the slot is frictional to prevent any accidental movement of the pins caused by vibration. However, the friction between the pins and slot should not be so high as to prevent the sliding of the pins.

Accuracy

Satisfactory performance of the crack monitor gauge depends on several factors, including proper manufacturing, installation, and measurement. The key point to be considered when installing the gauge is that each plate must be firmly connected to its appropriate side of the crack or joint such that the connections do not yield under the force caused by contraction or expansion of the slab. This can be minimized by using a stiff epoxy compound for the attachment of the gauge. Further, the gauge components must be properly aligned to each other and parallel to the top of the slab.

Accurate measurement of the positions of the sliding pins relative to the reference pin can be ensured by using a digital

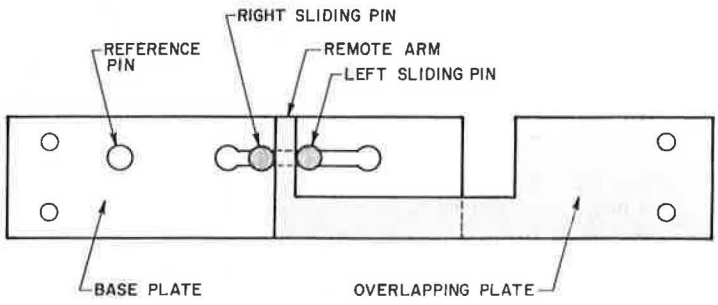


FIGURE 1 Schematics of the crack monitor gauge.

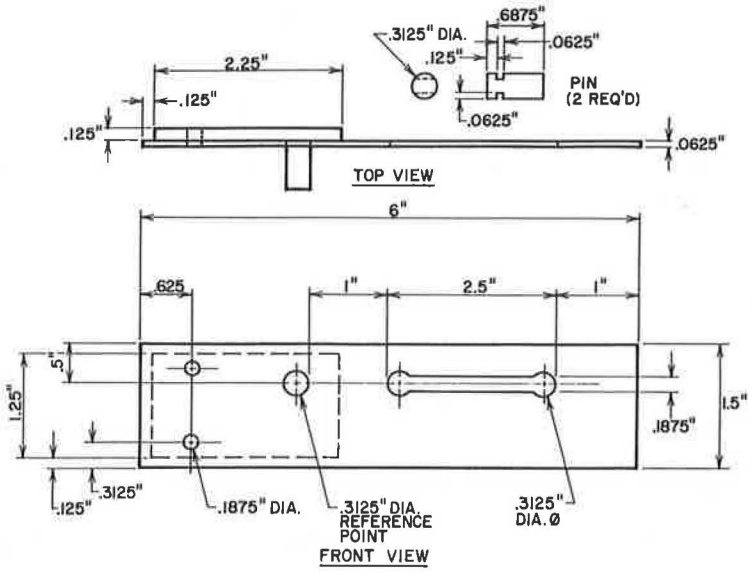


FIGURE 2 Engineering drawing of the base plate of the crack monitor gauge.

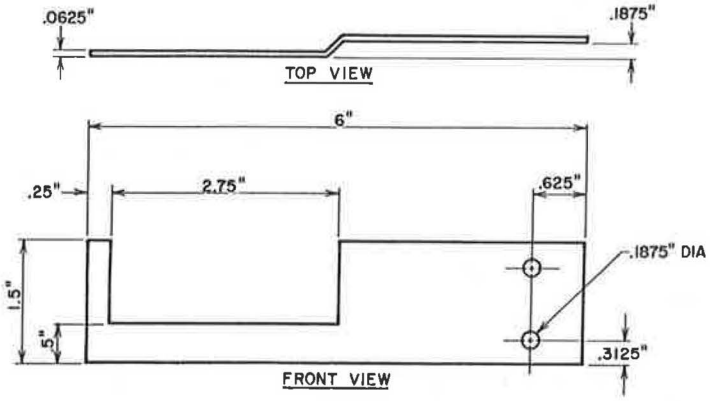


FIGURE 3 Engineering drawing of the overlapping plate of the crack monitor gauge.

caliper with adjustable friction at its thumbwheel. The friction of the thumbwheel should be set to its minimum value such that the measuring jaws of the caliper do not move the pins during the measurement.

Digital calipers can usually resolve measurements to 0.0005 in. (0.01 mm) and have an accuracy of ±0.001 in. (0.025 mm). Considering the possible error of the operator, the expected accuracy of the readings from the crack monitor gauge is about ±0.01 in. (0.25 mm).

Field Installation

The crack monitor gauge has been specifically designed to monitor crack or joint movement of PCC pavement slabs. However, the gauge can be used to monitor cracks in many other types of structures as well. The installation procedure described in this section pertains to its use on cracked and seated jointed concrete pavement slabs that are overlaid with asphalt concrete and have a paved shoulder. The gauge is designed to be installed on the edge of the slab at the outside lane-shoulder longitudinal joint.

After cracking and seating of the old concrete pavement slab, the station numbers of the cracks or joints selected for monitoring should be recorded and referenced. The candidate crack or joint should not exhibit a large lateral misalignment between both sides of the crack or joint nor have badly broken edges. Given the overall dimension of the crack monitor gauge, the minimum dimension of broken slab pieces required for installation is 1 ft (30 cm). When the break pattern specified is less than this dimension, breaking operations must be prohibited within 2 ft (60 cm) of the joint or crack to be instrumented. The crack monitor gauges will be retrofitted after the rehabilitation process is concluded including bringing the shoulder to grade. The gauge can be installed by applying epoxy to the mounting surfaces of the gauge as well to the lower and the side edges of the base plate, as shown in Figure 4. Detailed installation of the gauge was described by Tabatabaee and Sebaaly (*7*).

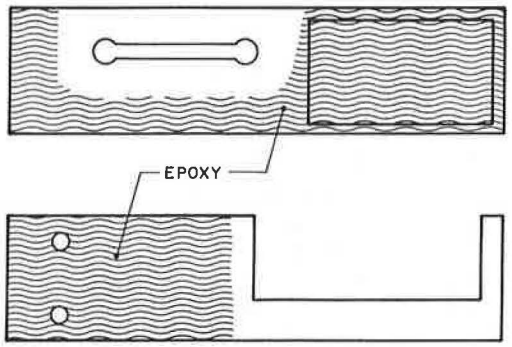


FIGURE 4 Application of epoxy to the mounting surfaces of the crack monitor gauge.

OPERATION AND MEASUREMENT

At the beginning of the gauge monitoring period, the crack or joint opening (W_i) should be accurately measured and recorded on the data sheet (Figure 5). Then the sliding pins should be pushed against both sides of the remote arm, and the distance between the fixed reference pin and the left sliding pin (R_i) should be measured and recorded with an inside caliper (see Figure 6). This reading will also be used as the reference distance for calculation of the maximum and minimum crack or joint openings of the first period. At the end of each monitoring period, the distances between the reference pin and the new positions of the sliding pins are measured

Location: Top Gauge
Date of installation: 01/24

Initial Joint Opening, mm (Wi): 6.13
Initial Reference Distance, mm (Ri): 41.96

Date	Time	Measured Parameter, mm			Calculated Parameter, mm		
		Referenc Distance Rn	Close Marker SD	Far Marker LD	Joint Opening Instant Wn	Minimum Wmin	Maximum Wmax
01/25	14:05	41.96	41.96	55.50	6.13	6.13	6.63
01/26	14:25	42.02	41.85	55.57	6.19	6.02	6.70
01/30	16:45	42.35	42.29	55.94	6.52	6.46	7.07
01/31	14:00	42.72	42.35	55.96	6.89	6.52	7.09
02/01	15:00	42.67	42.59	56.12	6.84	6.76	7.25
02/16	14:00	42.62	41.48	56.02	6.79	5.65	7.15
02/23	11:30	41.50	41.33	56.17	5.67	5.50	7.30
05/02	18:15	41.38	39.34	57.23	5.55	3.51	8.36
05/11	15:30	39.90	39.47	54.66	4.07	3.64	5.79
05/17	15:30	40.06	39.39	54.49	4.23	3.56	5.62
05/22	12:45	39.63	39.63	54.22	3.80	3.80	5.35
05/30	15:45	39.93	39.33	54.20	4.10	3.50	5.33
06/06	12:15	39.40	39.12	54.06	3.57	3.29	5.19
06/15	15:49	39.31	39.05	53.62	3.48	3.22	4.75
06/20	12:30	39.08	38.94	53.15	3.25	3.11	4.28
07/09	09:30	39.15	39.04	53.43	3.32	3.21	4.56
		39.32	NA	NA	3.49	NA	NA

Footnote:

Wn = Rn + Wi - Ri
Wmin = Wn - (Rn - SD)
Wmax = Wn + LD - (Rn + b + d)
b = Width of the remote arm = 6.62 mm
d = diameter of the left sliding pin = 6.42 mm

FIGURE 5 Data sheet for a rigid pavement joint at the PTI Pavement Durability Research Facility.

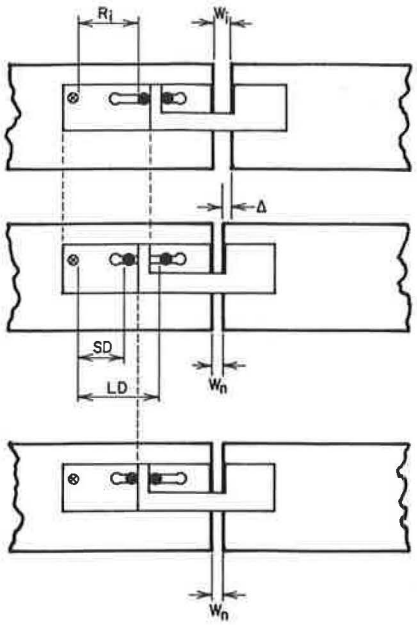


FIGURE 6 Schematics of operation of crack monitor gauge.

using an inside caliper and recorded on the data sheet (SD and LD). The sliding pins are then manually pushed against both sides of the remote arm, and the distance between the reference pin and the left sliding pin (R_n) is measured and recorded on the next line of the data sheet (to be used as the reference distance for the next monitoring period). Once these parameters have been measured for a given period, the maximum, minimum, and instantaneous crack or joint openings over that period may be calculated.

If the crack or joint opening changes by an amount equal to Δ in one direction, the remote arm moves by the same amount in the same direction (see Figure 6). Therefore,

$$W_n = W_i + \Delta \tag{1}$$

and

$$R_n = R_i + \Delta \tag{2}$$

where

W_i = initial joint opening,
W_n = instantaneous joint opening,
R_i = initial reference distance, and
R_n = instantaneous reference distance.

The elimination of Δ between Equations 1 and 2 by subtracting both sides and rearranging yields.

$$W_n = W_i + R_n - R_i \tag{3}$$

When the concrete slabs expand, the crack or joint opening becomes smaller. From the discussion with reference to Figure 6, this reduction in the joint opening is equivalent to the

distance that the left pin is pushed to the left by the remote arm.

Crack or joint opening reduction during the period

= (Initial short distance) − (Current short distance)

$$= R_n - \text{SD} \quad (4)$$

where SD is the short distance (the distance between the reference pin and the left sliding pin).

Subtracting the joint opening reduction (Equation 4) from the instantaneous joint opening results in the minimum joint opening during the period:

$$W_{\min} = W_n - (R_n - \text{SD}) \quad (5)$$

As the concrete slabs contract, the joint opening increases and the remote arm pulls the right pin to the right. This increase in crack or joint opening is equivalent to the distance that the right pin has moved:

$$\text{Original position of right pin} = R_n + b + d \quad (6)$$

Crack or joint opening increase during the period

$$= \text{LD} - (R_n + b + d) \quad (7)$$

where

b = width of the remote arm,
d = diameter of the left pin, and
LD = long distance (the distance between the reference pin and right sliding pin).

Adding the joint opening increase (Equation 7) to the instantaneous joint opening yields the maximum crack or joint opening:

$$W_{\max} = W_n + \text{LD} - (R_n + b + d) \quad (8)$$

The equations are valid for any consistent units of measurement.

TEMPERATURE SENSOR

In order to monitor maximum and minimum crack or joint movement in PCC pavements, a continuous record of pavement temperature is essential. The most practical device that can provide a continuous temperature history for the pavement and that does not need electricity for monitoring and recording is a chart-recording stem thermometer. By installing two of these units, one at the top and one at the bottom of the pavement slab, a complete temperature history as well as gradient temperatures can be obtained for the pavement. These units come with a 24-hr or 7-day recording chart and cost approximately $280 per unit.

Another alternative is to use a temperature-measuring device that can record maximum and minimum temperatures in the pavement over a period of time. Two devices of this type are commercially available: gas-actuated and bimetallic thermometers. The former type is more accurate and costs approximately $180 per unit. The latter type is more rugged and costs only approximately $65 per unit.

The sensing element in this device is the bimetallic element, a single, low-mass helix that fits inside the thermometer stem. The bimetallic element is responsive to temperature changes. In order to improve its accuracy, the element is usually heat treated, aged (to relieve inherent stresses), and coated with a viscous silicon to reduce pointer oscillation and enhance temperature transmission.

These thermometers are constructed from stainless steel. They are available in 3- and 5-in.-diameter (76- and 127-mm-diameter) display faces (dials) and come in various stem lengths and temperature ranges and models. The location of the stem relative to the display dial varies among available models.

For measuring extreme temperatures experienced by pavement, the model with a 4-in. (100-mm) stem, 3-in. (76-mm) display dial, and working range of −40°F to 160°F (−40°C to 71°C) is recommended. A special order is required to customize these thermometers with minimum and maximum pointers.

The bimetallic thermometers should be installed close to the crack monitor gauges. The detailed installation procedure for this device was described by Tabatabaee and Sebaaly (*7*).

FIELD STUDY

In order to study the performance of the crack monitor gauges, two gauges were installed at a transverse joint of two PCC slabs at the PTI's Pavement Durability Research Facility. To investigate the appropriate depth for installation of the gauges, two gauges were installed at different depths. These gauges were installed 1 and 5 in. (2.5 and 12.5 cm) below the top of a 10-in.-thick (25-cm-thick) slab. The gauges were monitored from January 1990 to the end of February 1990 and from May 1990 to the middle of July 1990.

Figures 7 and 8 show minimum and maximum air temperatures during the monitoring periods. Figures 9–12 show the minimum and maximum joint openings as measured by the crack monitor gauges at the top and middepth of the instrumented joint.

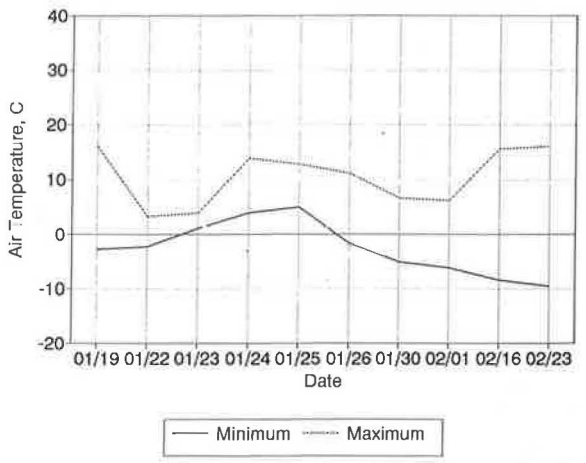


FIGURE 7 Minimum and maximum air temperature for January and February 1990.

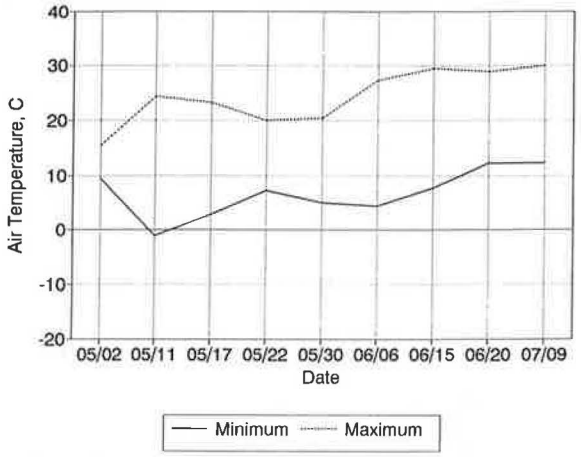


FIGURE 8 Minimum and maximum air temperature for May, June, and July 1990.

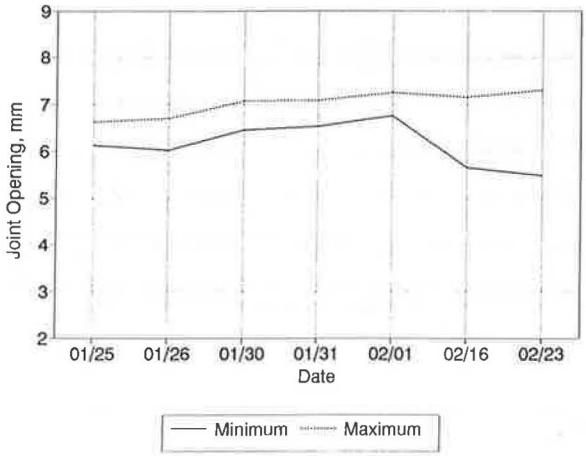


FIGURE 9 Joint opening measured by the top gauge during January and February 1990.

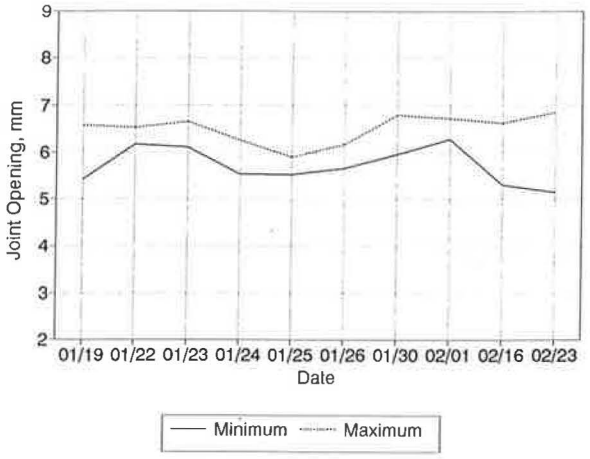


FIGURE 10 Joint opening measured by the middepth gauge during January and February 1990.

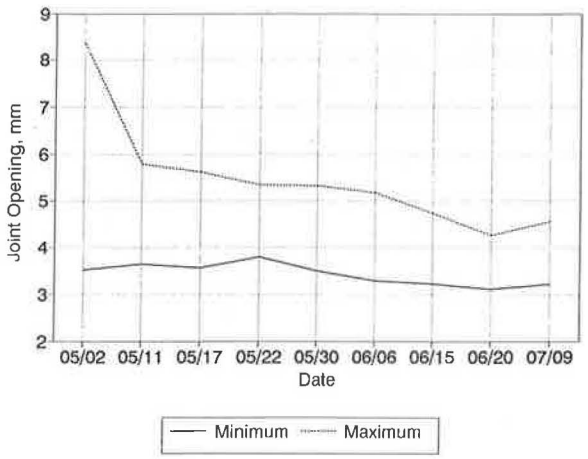


FIGURE 11 Joint opening measured by the top gauge during May, June, and July 1990.

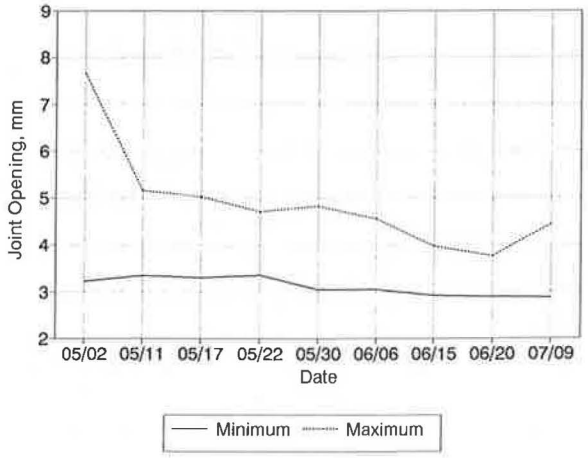


FIGURE 12 Joint opening measured by the middepth gauge during May, June, and July 1990.

Figure 7 indicates that the average air temperature (i.e., the average of minimum and maximum values) is about 37°F (2.8°C) throughout January and February. Figure 8 indicates that the average air temperature is about 60°F (15.5°C) throughout May, June, and July. Comparison of Figures 9 and 10 with Figures 11 and 12 indicates that the joint openings are larger for the period of January and February than for May, June, and July. This effect can be explained by the lower temperatures during January and February than during May, June, and July. Another interesting aspect of these measurements is that the range of maximum and minimum joint openings of the top gauge on January 26 is about 0.027 in. (0.68 mm) (Figure 9); the corresponding difference between the maximum and minimum temperatures is around 55°F (13°C). On the other hand, the difference between the maximum and minimum joint openings of the top gauge on May 17 is about 0.081 in. (2.06 mm) (Figure 11); the corresponding difference between the maximum and minimum temperatures is about 69°F (21°C).

According to these values, there is a direct relationship between the maximum and minimum air temperatures and joint openings. However, this relationship is not linear. For crack and seat applications, the range of joint openings is critical because it represents the amount of crack movement and the potential of cracking at the bottom of the asphalt concrete overlay. In other words, the range of movement of the PCC slab over a wide range of crack openings is more critical than the higher absolute maximum or lower minimum of crack openings. Therefore, any gauge used to monitor the movements of PCC broken slabs must have at least the capability of measuring both the maximum and minimum crack openings.

SUMMARY

A mechanical gauge was developed to monitor the movement of crack or joint openings in PCC pavements. Although it was designed specifically for monitoring crack or joint movement in rigid pavements, the gauge can be used for other types of concrete structures as well. Measurements of maximum, minimum, and instantaneous crack or joint openings can be obtained from this gauge. Low cost, high accuracy, and ease of installation and operation are some of the characteristics of this mechanical gauge.

The field data obtained from the installation of two prototype gauges at the PTI Pavement Durability Research Facility indicated that there is a direct relationship between the range of maximum and minimum air temperature and the range of joint openings. However, this relationship is not linear. It is expected that the wider ranges of temperature will occur during the summer months. However, under high temperatures, the asphalt concrete overlay can withstand larger amounts of movements. Therefore, the combination of a wider range of PCC slab movements and the degree of brittleness of the asphalt concrete overlay (as a function air and pavement temperatures) will dictate the critical situation under which the cracks from the broken PCC slab will propagate through the asphalt concrete overlay.

ACKNOWLEDGMENT

The authors would like to acknowledge that the FHWA provided the funds for this project.

REFERENCES

1. G. Sherman. *NCHRP Synthesis of Highway Practice 92: Minimizing Reflection Cracking of Pavement Overlays*, TRB, National Research Council, Washington, D.C., Sept. 1982.
2. *Pavement Rehabilitation Manual*. Pavement Division Office of Highway Operations. FHWA U.S. Department of Transportation, Sept. 1975.
3. *Break and Seat of Jointed Reinforced Concrete Pavements*. Special Project 202, Technical Resource Forum, FHWA, U.S. Department of Transportation, June 1989.
4. W. P. Kilareski and S. M. Stoffels. *Structural Overlay Strategies for Jointed Concrete Pavements: Volume II: Cracking and Seating of Concrete Slabs Prior to AC Overlay*, Report FHWA-RD-89-143. FHWA, U.S. Department of Transportation, Sept. 1990.
5. M. Poblete, R. Salsilli, R. Valenzuela, A. Bull, and P. Spratz. Field Evaluation of Thermal Deformations in Undoweled PCC Pavement Slabs. In *Transportation Research Record 1207*, TRB, National Research Council, Washington, D.C., 1988.
6. J. M. Armaghani, T. J. Larsen, and L. L. Smith. Temperature Response of Concrete Pavements. *Transportation Research Record 1121*, TRB, National Research Council, Washington, D.C., 1987.
7. N. Tabatabaee and P. Sebaaly. *Design, Fabrication, and Operation of the Pavement Crack Monitor Gauge*. Report FHWA-PA-033 + 86-11, Pennsylvania Department of Transportation, Harrisburg, May 1990.

Publication of this paper sponsored by Committee on Pavement Rehabilitation.

Concrete Pavement Rehabilitation and Overlay: Ontario's Experience

THOMAS J. KAZMIEROWSKI AND HARRY J. STURM

Currently, highway authorities are faced with the challenge of rehabilitating portland cement concrete (PCC) pavements on high-volume freeways. In 1989, the Ministry of Transportation of Ontario (MTO) initiated a demonstration contract to rehabilitate one such freeway using various PCC pavement repair techniques in one direction and an unbounded PCC overlay in the opposing direction. The site used to demonstrate these procedures is classed as a four-lane divided arterial with 30,000 average annual daily traffic, 10 percent classified as commercial. The existing pavement consisted of 230-mm mesh-reinforced dowelled PCC with a 21.3-m joint spacing constructed in 1963. The rehabilitation techniques used included full-depth repair, partial-depth repair, diamond grinding, and joint sealant replacement on the northbound lanes that had experienced moderate deterioration. The southbound lanes received a 180-mm-thick plain jointed unbonded PCC overlay to address the severe D cracking and spalling of all joints and cracks. Design and construction details and the performance of the pavement, before and after rehabilitation, are discussed in terms of load transfer efficiencies and pavement edge deflections based on falling weight deflectometer testing; roughness using the profilograph, the portable universal roughness device, and the automatic road analyzer; skid resistance using the ASTM brake force trailer; pavement condition ratings; and a crack survey. Observations of noise levels, traffic volumes, and surface texture are also presented.

Repair of portland cement concrete (PCC) pavement in Ontario has always posed a challenge. Traditionally, rigid pavements have been rehabilitated by removing severely distressed concrete full depth and spalls partial depth and then filling with asphaltic concrete. The patched PCC pavement was then generally overlain with varying thicknesses of hot mix depending on the serviceability level of the pavement and the road classification. This repair technique was used extensively and performed adequately in the short term; however, over time the hot-mix patches began to distort, which significantly reduced the pavement ride.

In order to improve on the Ministry's traditional PCC pavement repair methods, a number of alternative rehabilitation techniques have been tried over the last few years. Some of the techniques tried and proven successful included full-depth removal of distressed concrete and replacement with either normal or fast-track PCC (*1*). Subsealing of concrete pavement has also been used to stabilize slabs that were severely stepped or faulted (*2*). A demonstration contract using PCC pavement rehabilitation techniques, unique in Canada, was a project on Highway 126 in London, Ontario, undertaken during the summer of 1989.

This project used the most diverse PCC pavement rehabilitation techniques ever attempted by Ontario. The repair techniques ranged from partial- and full-depth repairs to diamond grinding on the northbound lanes (NBLs) and an unbonded concrete overlay on the southbound lanes (SBLs).

T. J. Kazmierowski, Pavement Design, Evaluation, and Management Section, Ministry of Transportation of Ontario, 2nd Floor, West Building, 1201 Wilson Avenue, Downsview, Ontario, Canada M3M 1J8. H. J. Sturm, Canadian Portland Cement Association, 1500 Don Mills Road, Suite 501, Toronto, Ontario, Canada M3B 3K4.

BACKGROUND

Highway 126 is located on the eastern limit of the City of London, Ontario. Classified as a four-lane divided arterial, this facility experiences traffic volumes ranging from 19,000 to 30,000 average annual daily traffic, and of that, approximately 3,000 are commercial vehicles. There is a high percentage of commuter traffic.

The existing pavement was constructed in 1963 with 225 mm of mesh-reinforced PCC on 300 mm of granular base and subbase materials. The pavement was constructed with a 21.3-m joint spacing and load transfer dowel bars. The joints were sealed with preformed neoprene seals.

The pavement serviceability varied dramatically between the NBLs and the SBLs. The pavement condition on the NBLs was relatively good considering the 26-year service life. The main distresses were three transverse cracks per slab with one of these being very severe, some spalling at joints and cracks, and a moderately polished surface. The joints exhibited minimal stepping and good load transfer. The joint seals were 80 to 90 percent intact, although significant bond failure was apparent throughout.

The pavement condition on the SBLs was considerably worse with numerous full- and partial-width transverse cracks in each slab, severe D cracking and spalling of all joints throughout, and moderate pavement edge distress. Deterioration had advanced to the stage where routine maintenance activities could no longer preserve a safe riding surface.

The variance in pavement performance was attributed to the two types of aggregate used on the opposing lanes. The NBLs were constructed using a pit run gravel source for the coarse aggregate, and the coarse aggregate for the SBLs came from a quarried limestone source. The quarried aggregate exhibited absorptive characteristics and was highly susceptible to D cracking under freeze-thaw conditions.

DESIGN

The design for this project included PCC rehabilitation methods on the NBLs and an unbonded concrete overlay on the

SBLs. This option of concrete repairs with PCC, diamond grinding, and an unbonded concrete overlay was selected because it best addressed the actual performance deficiencies exhibited by the pavement and provided the longest anticipated service life.

NORTHBOUND LANE REHABILITATION

The work on the NBLs involved full-depth (1940 m²) and partial-depth PCC repairs, diamond grinding of the surface (29 900 m²) and sealing of all joints and cracks (5,450 m). One fairly significant revision was made to the earlier specification for full-depth repairs. These required that the contractor use mechanically mounted hydraulic drills (a gang drill) to cut holes for installation of dowel bars. This new requirement was made to ensure that the holes were drilled in line with the pavement axis and also that they were not elongated or out of round. Adequate load transfer at the patch interface is one of the most critical aspects of the design of full-depth repairs.

A plan view of the full-depth repair is shown in Figure 1. The standard repair size is 2 m long by either one or two lanes wide. General dowel bar layout and references to jointing are also provided on this drawing. Longitudinal tie bars were only used in repair sections greater than 2 m in length, and consisted of 15-mm deformed bars placed on 600-mm centers.

To provide load transfer between the existing and repaired slabs, 32-mm-diameter by 450-mm-long epoxy-coated smooth dowels were resin grouted into the existing pavement at 300-mm intervals, midheight in the slab. The exposed length of the dowel and the concrete face were coated with a bond breaker to ensure that a working contraction joint was provided. A 25-MPa portland cement was used in the repairs. Figure 2 shows the details of the full-depth repair and placement of the dowel bars.

Partial depth repairs with PCC had not previously been undertaken in Ontario, so new drawings and specifications for this work were developed. Typical drawings used for this work are shown in Figure 3. The specification required all unsound spalled concrete to be removed; an average removal depth of 75 mm was used for estimating. Where spalls extended deeper than half the slab thickness, a full-depth repair was specified. Following removal and immediately before placement of 25-MPa concrete, the exposed surfaces had to be abrasive blast–cleaned, and then coated with a PCC paste. Where the repair was adjacent to a crack or joint, a gap had to be formed in this area to allow for expansion at the joint or crack and to prevent spalling of the patch. Proper patch isolation is critical to minimize compression failure of the patch.

Following curing of full- and partial-depth repairs, the complete northbound pavement surface was retextured by diamond grinding. Diamond grinding was specified to improve skid resistance, restore a smooth surface profile and reinstate an acceptable ride to the pavement surface. The grinding specification required specialized equipment with a minimum 900-mm-wide grinding head, having at least 60 diamond blades per 300 mm of width. The final surface texture to be achieved was also specified.

Following texturing of the concrete surface, all existing joints and cracks were cleaned of old joint sealant and incompressibles. Before sealant application, all joints were sandblasted, cleaned, and dried with a hot-air lance. A bond breaker was placed at the bottom of the joint and then sealed with a hot-poured rubberized sealant. The joints between the full-depth repair areas and the existing concrete were treated similarly except a saw cut for the sealant was required.

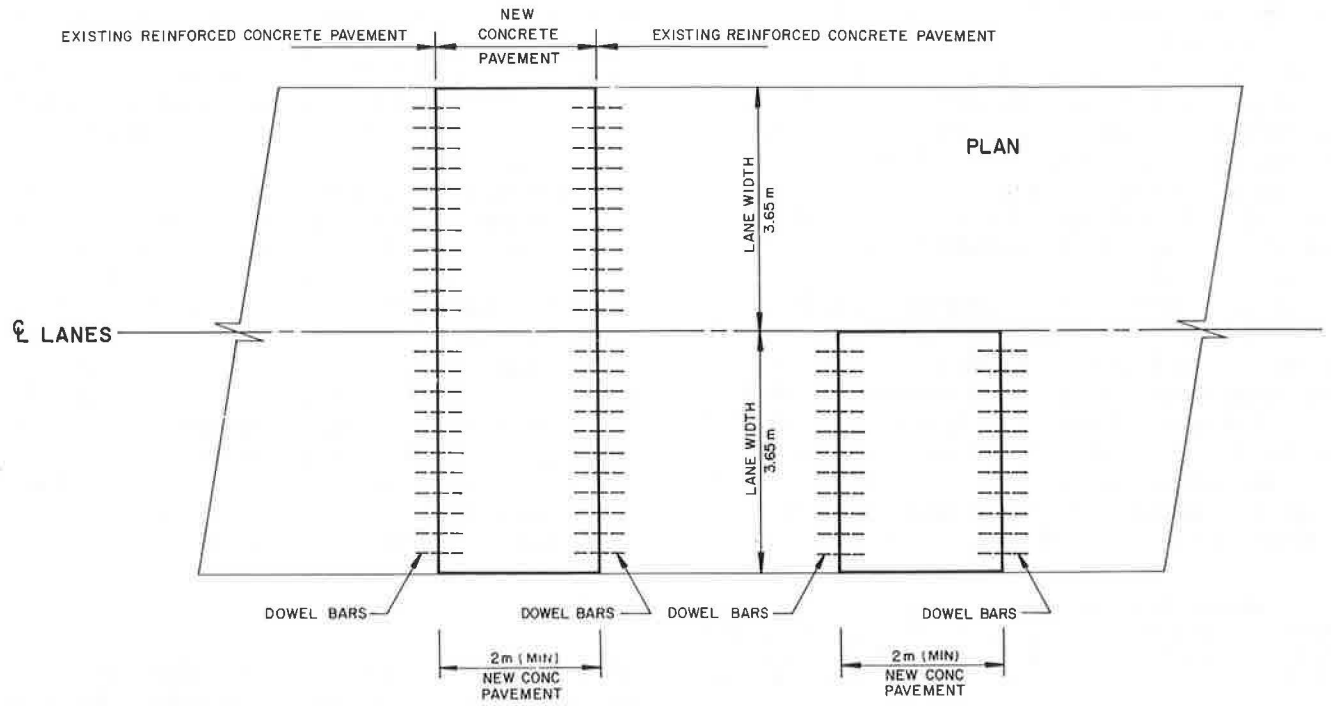


FIGURE 1 Full-depth concrete repairs plan view.

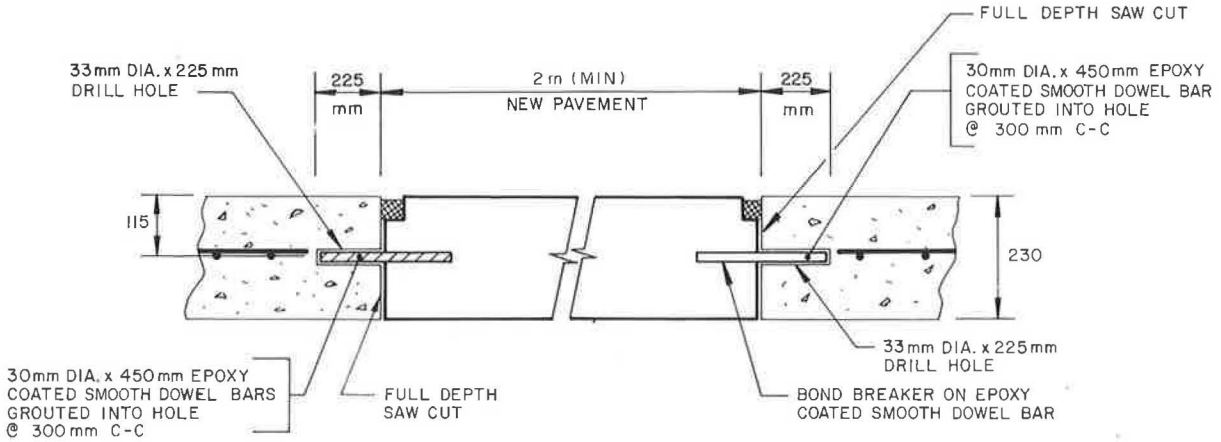


FIGURE 2 Full-depth concrete repair cross-section.

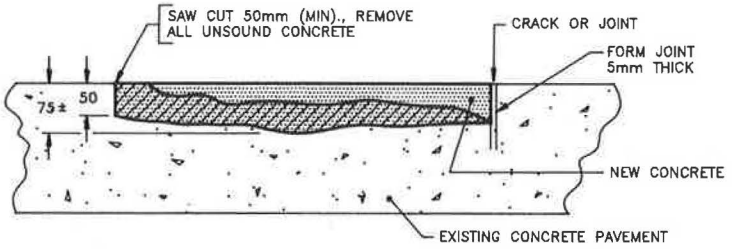


FIGURE 3 Concrete spall repairs.

SOUTHBOUND LANE REHABILITATION

The design of the unbonded concrete overlay on the SBLs included the removal of any loose spalled material from the existing badly cracked pavement. The spalled areas (427 m^2) were then patched with hot mix and a 20-mm asphaltic sand mix bond breaker (884 tonnes) was specified over the existing pavement surface. The sand mix was placed to prevent bonding between the new and old PCC pavements and minimize reflection cracking in the overlay. Following placement of the bond breaker, a 180-mm-thick unreinforced plain-jointed concrete pavement (38 200 m^2) was placed. A typical cross section showing these details is provided in Figure 4.

Slipforming of the unbonded overlay was carried out using Ontario's revised specifications and drawings for concrete pavement. The revisions were based on experience gained on the experimental concrete pavement sections on Highway 3N (*3*,*4*).

CONSTRUCTION

Generally, construction of the concrete repairs, diamond grinding, and the unbonded overlay went smoothly following the initial start-up difficulties.

During construction, the highway was closed to traffic, which simplified construction staging. Sawcutting for full-depth repairs was carried out in advance of slab removal and replacement.

Initially, during removal of the full-depth concrete some spalling of the existing concrete at the sawcut edge occurred where only two sawcuts were made. The contractor then elected to make a third sawcut on one side of the repair to remove a small 150-mm-wide slab before removal of the larger 2-m slab. This operation eliminated all spalling at the edge of the repair area. The contractor used a backhoe to remove the concrete slabs and disturbance of the underlying granular was negligible. Concrete removal was only undertaken where the placement of concrete could be completed on the same day. This minimized disturbance of the exposed granulars caused by construction activity and infiltrated water.

Following removal of concrete, drilling for dowel bars was completed using a Tamrock gang drill. This system worked well and increased production significantly over the single drills used on previous contracts.

After air cleaning of the holes, the dowel bars were epoxied into place using a two-part epoxy cartridge system. This method ensured that epoxy was uniformly distributed throughout the hole. The dowel bars were then inserted and rotated, and the grout was forced forward, enveloping the bar. The exposed ends of the dowel bars were then coated with grease (a bond-breaking agent) to allow for longitudinal movement of the pavement slabs.

Normal PCC, 25-MPa mix, was placed and finished flush with the existing slabs using a razor back screed. Matching of surface tolerances was not critical because the entire surface was to be diamond ground.

Spall repairs were undertaken following full-depth repairs. They involved sawcutting around the spalled area to a depth of 50 mm and removing all unsound concrete. Spall repairs located adjacent to existing cracks or joints were removed, leaving small sections of sound concrete between repairs. These small sound areas fractured and spalled off in a day or two

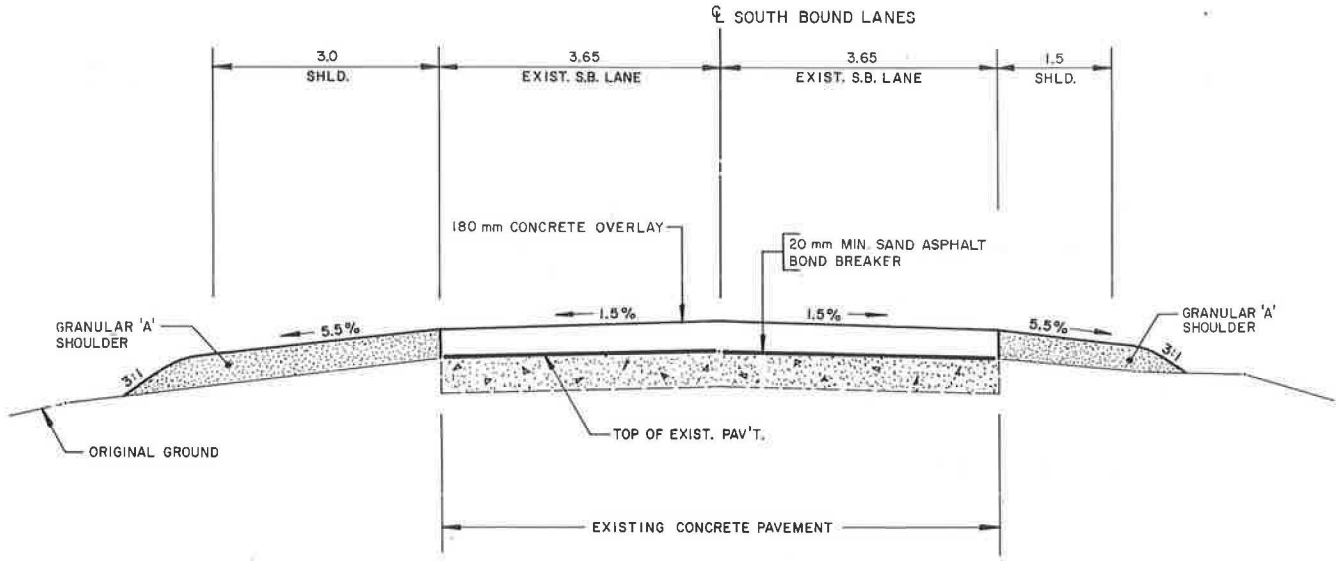


FIGURE 4 Unbonded concrete overlay.

as the pavement expanded. In order to avoid this problem, the entire joint width was repaired.

Following placement and curing of these repairs, the NBLs were diamond ground. The grinding equipment comprised a grinding head mounted between the forward and rear wheels of a weighted frame. This arrangement planed the surface for a minimum depth of 1.5 mm, both retexturizing and reprofiling the concrete surface. An integral vacuum system was used to pick up the cuttings. This slurry was stored in a mobile tank and disposed of at the local sewage treatment plant.

Once diamond grinding was completed, the cracks were routed, cleaned, and sealed with hot-poured rubberized asphalt. A short test section of silicone sealant was placed on the NBL cracks.

Construction of the unbonded concrete overlay on the SBLs went smoothly following a few initial breakdowns on the slipform paver. The two lanes were slipformed simultaneously with longitudinal tie bars being inserted every 600 mm on the centerline. The plastic concrete surface was dragged longitudinally with a burlap mat and tined transversely to achieve the specified surface texture. Speed change lanes were then slipformed and tied onto the outside of the core lanes where required.

Skewed joints were sawcut into the overlay at random intervals varying from 3.7 to 5.8 m. No uncontrolled cracking of the pavement occurred as sawcutting was not required within 12 hr after placement.

The pavement ride was somewhat better than the previous slipforming project, which was in part because of a requirement for stringline control on both sides of the slipform paver. Pavement ride is discussed in further detail in the following section.

PAVEMENT PERFORMANCE

Roughness Measurements

The ride of a pavement is the most visible sign of pavement condition to the traveling public, therefore the collection and analysis of the ride condition or roughness data were undertaken.

Just after construction and before opening to traffic, roughness was measured using the California profilograph. (SBLs only) and the portable universal roughness device (PURD).

The profilograph measurements were taken on the new concrete overlay with readings taken in both wheelpaths of the driving and passing lanes. The average profilograph reading, profile index, for the length of the project in the driving lane was 11.09 in. mi (10.66 in. mi in the passing lane). These readings were taken before grinding 21 locations at which the roadway did not meet the surface tolerance specifications of 3 mm in 3 m. These numbers compare reasonably well with those obtained by other authorities constructing considerably larger quantities of concrete pavement. Many of these agencies have performance specifications requiring a ride ranging from a high of 12 in./mi to as low as 7 in./mi with incentive bonuses for smoother pavements.

Roughness measurements using the PURD were also taken. The PURD is a trailer-mounted accelerometer-based mechanical measuring device operated at constant highway speed, which measures and calculates the root-mean-square vertical acceleration, in thousandths of g, of the trailer axle as an indicator of pavement roughness. PURD measurements are converted into a ride rating, RCR, using a transfer function for use in pavement management applications.

Both pavements were tested for roughness using the PURD before rehabilitation, after rehabilitation just before opening to traffic, and in the spring of 1990. All four traffic lanes were tested.

The ride was improved significantly following rehabilitation with a reduction in roughness from an average of 800 mg for all lanes (RCR of 5.8) to 230 mg (RCR of 9.2) for the NBLs and 360 mg (RCR of 7.8) for the SBLs. See Figure 5 for the details. The 8-month postconstruction PURD testing does not indicate any significant change in ride except on the SBLs where the ride has improved slightly. This effect is probably because of wearing of coarse projections on the tined surface. The detailed PURD measurements are shown in Figure 5 and summarized in Figure 6.

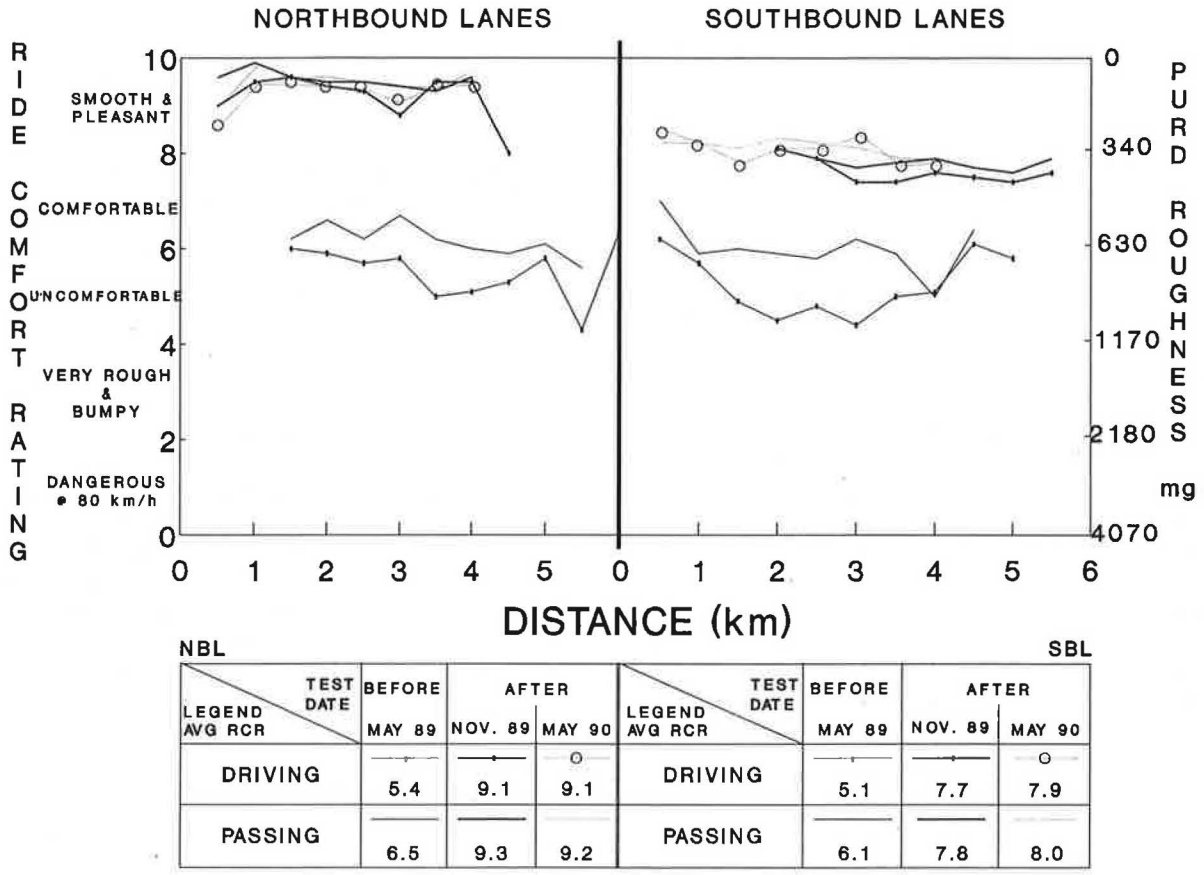


FIGURE 5 PURD roughness survey.

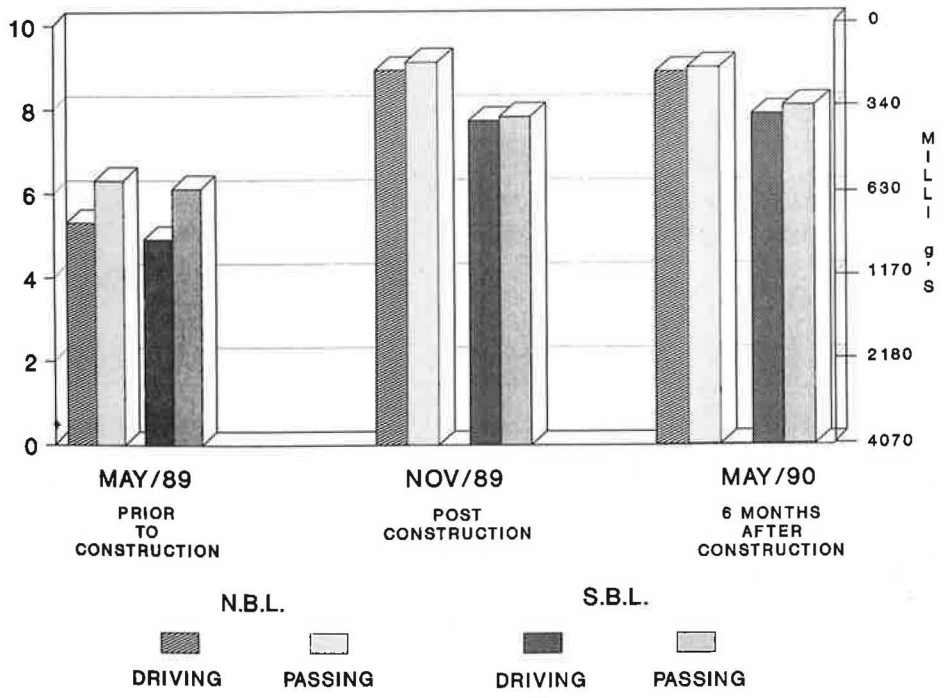


FIGURE 6 Summary of PURD survey.

The roughness numbers for the diamond-ground surface indicate a very smooth surface was obtained. The slipformed concrete, which averages 360 mg, is somewhat rougher than the diamond-ground surface; however, it is only slightly rougher than the ride achieved on a new asphalt surface.

Skid Testing

In North America, the most commonly accepted method for measuring skid resistance is the skid trailer conforming to ASTM Standard E274. The test unit consists of a towing vehicle and a brake force trailer on which a wheel locks. The horizontal and vertical forces that are required to pull the locked wheel over wet pavement are measured. Water is applied to the pavement directly in front of the locked wheel. The measured friction force is described as a skid number (SN) at a specific speed, for example SN80 at 80 km/hr.

Skid resistance testing was completed before construction and twice after construction and the data are detailed in Figure 7 and summarized in Figure 8. The test results immediately after construction indicate there was a substantial increase in skid resistance on both the NBLs and SBLs, as expected. The skid numbers in the SBLs increased to an average of 55 for both lanes from 18.3 and 28.9 in the driving and passing lanes, respectively. On the diamond-ground surface, the skid numbers improved from an average of 24.8 and 35.1 to 48.0 and 50.4 for the driving and passing lanes, respectively.

Skid numbers of this magnitude indicate a good friction factor and are similar to numbers obtained on premium hot-mix surface courses (5). The corduroy type of texture developed by grinding visually indicates high frictional resistance. The ridges improve the surface macrotexture and provide an escape route for moisture under a tire. The broken peaks, concrete fractured between the blades, improve microtexture.

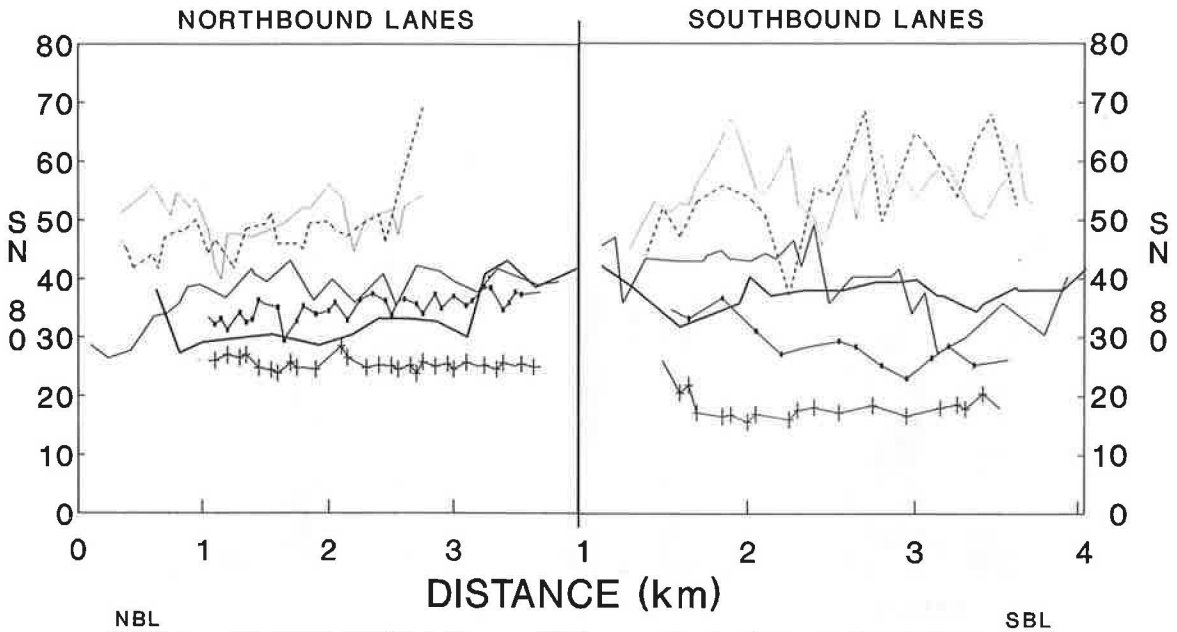
Testing in the spring of 1990 has shown a fairly significant reduction in skid number from the initial postconstruction number and confirmed expectations. The 1990 skid tests provided average numbers of 37 and 40 in the passing lanes and 35 and 36 in the driving lanes for NBLs and SBLs, respectively. These numbers are somewhat lower than those ranging from 48 to 55 obtained in the immediate postconstruction tests.

Visual observations indicate that the microtexture in the wheelpaths on both the NBLs and SBLs has undergone some polishing.

On the basis of previous experience, this decrease was anticipated as the initial sharp projections of both the ground and drag-tined surfaces were worn or sheared by traffic and snow removal operations. This elimination of sharp projections reduces skid resistance, particularly in the short term. The rate of friction loss in the long term is heavily dependent on traffic volume, abrasion of maintenance activities, and the aggregate mineralogy.

Sound Level Measurements

Sound level measurements were undertaken on Highway 126 before and following rehabilitation. Because highway noise



NBL

LEGEND / AVG SKID \ TEST DATE	BEFORE MAY 89	AFTER NOV. 89	AFTER MAY 90
DRIVING	25	48	35
PASSING	35	50	37

SBL

LEGEND / AVG SKID \ TEST DATE	BEFORE MAY 89	AFTER NOV. 89	AFTER MAY 90
DRIVING	18	55	36
PASSING	29	55	40

FIGURE 7 Skid resistance survey.

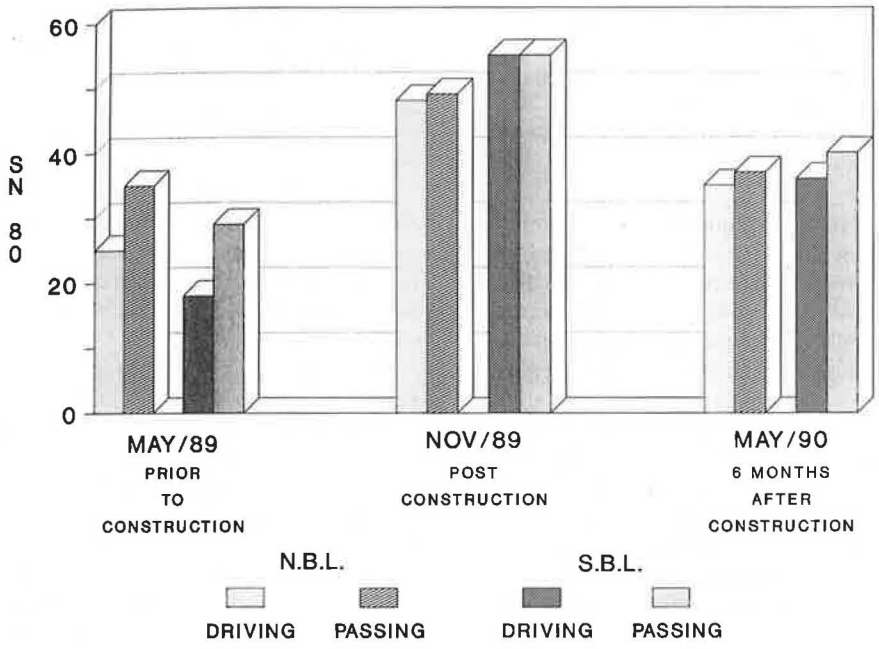


FIGURE 8 Summary of skid survey.

is becoming an ever-increasing environmental concern to the public, it is important to collect and maintain this information.

The procedure used to evaluate pavement noise on this project was to measure sound emissions from individual vehicle passbys at a 15-m distance from the traveled lane. The results are plotted on Figure 9 and indicate that the diamond-ground surface was approximately 1 dBA quieter than the old worn concrete and the MTO sample. The ground surface is only 1 dBA louder than the open-graded friction course used for its low noise and good skid resistance characteristics. The MTO sample was provided by Jung et al. (*6*) and was derived by testing several hundred vehicles on a variety of pavement surfaces across the province.

The burlap-dragged and transversely tined concrete surface was approximately 1 dBA noisier than the worn concrete and MTO sample. The new concrete on the SBLs should become quieter as some of the very coarse tining wears off.

Load Response Characteristics

In order to compare the load-deflection characteristics and the joint load transfer efficiencies of the rehabilitated pavement, a nondestructive load testing program was conducted. Deflection testing was completed using the Dynatest 8000 falling-weight deflectometer (FWD). The FWD simulates various axle loadings by dropping a mass onto the pavement from various heights. A load cell is used to measure the transmitted load to the pavement and seven seismic sensors are used to measure displacement of the pavement.

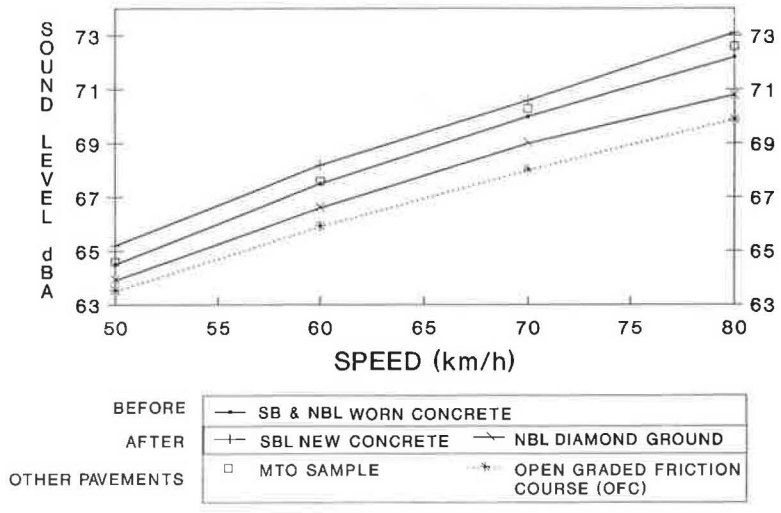


FIGURE 9 Pavement noise emission of automobiles.

The deflection measurements required to calculate load transfer for the approach and leave sides of the joint were obtained simultaneously with the corner slab measurements by straddling the joint using a trailing sensor.

The majority of the testing was performed early in the day to minimize the influence of slab curl resulting from differential slab temperatures.

Before rehabilitation, slabs were randomly selected for testing of corner to center deflection ratios and load transfer efficiency across joints. This information was used for design to determine whether voids existed below the slabs and to establish the need for stabilization of the joints by subsealing.

Overall deflection testing indicated that the existing pavements, both NBLs and SBLs were in a stable condition before rehabilitation. Load transfer across joints or cracks tested varied from a mean value of 78 to 89 percent on the NBLs and from 67 to 83 percent on the SBLs. Load transfer efficiency of 70 to 100 percent is generally observed in relatively new pavements and is considered acceptable (*7*). These test values also indicated that voids beneath the slabs were very small or nonexistent. The corner to center deflection ratio testing on the old pavement verified acceptable slab support on the basis of mean values ranging from 3.3 to 5.9 in the NBLs and from 4.4 to 4.8 in the SBLs. Following rehabilitation, and before opening to traffic, deflection testing was undertaken at the same locations or at the nearest point to the preconstruction testing. This work was undertaken to evaluate the performance of the repairs and to provide a general comparison on the overall performance of the rehabilitation work.

Testing on the unbonded concrete overlay indicated a substantial improvement in both load transfer and corner to center deflection ratios, as expected. The postconstruction load transfer testing indicated mean values ranging from 88 to 91 percent, an increase of 5 to 24 percent over mean preconstruction levels. The load transfer was also more uniform among the joints tested as evidenced by the reduction in the range and standard deviation of test values. The corner to center deflection ratios were also substantially improved after rehabilitation with similar trends to those observed for load transfer. This information is shown graphically in Figure 10.

On the NBLs, postconstruction tests for load transfer and corner to center deflection ratios were carried out on unrepaired joints and slabs as well as repaired sections. The results for the unrepaired sections were very similar to preconstruction results with some minor changes within normal test variations.

The results of FWD testing across the full-depth repair joints indicated load transfer had been reduced in areas where improvements were anticipated. A general pattern of lower load transfer values, in the order of 20 percent, was observed when loads were applied on the repair itself versus loading on the old concrete. These data are shown graphically in Figure 11a.

This pattern may be explained by surficial loosening and softening of the granular base in the repair area during full-depth repair activities. These activities may create a thin loosened zone susceptible to deformation. The mechanism for the reduction of load transfer is inconclusive and will require further investigation.

The use of grease as a bond-breaking agent on the dowel bars in the repair has also been suggested as a possible contributor to reduced load transfer. The grease may create a small void around the dowel bar. Further investigation will also be required in this area.

Previous studies (*8*) have found that reduced load transfer is usually observed when the load is applied on the unrepaired concrete. This pattern was found to be a result of voids above the grouted bar in the existing concrete pavement. Results on this project are opposite to these previous studies.

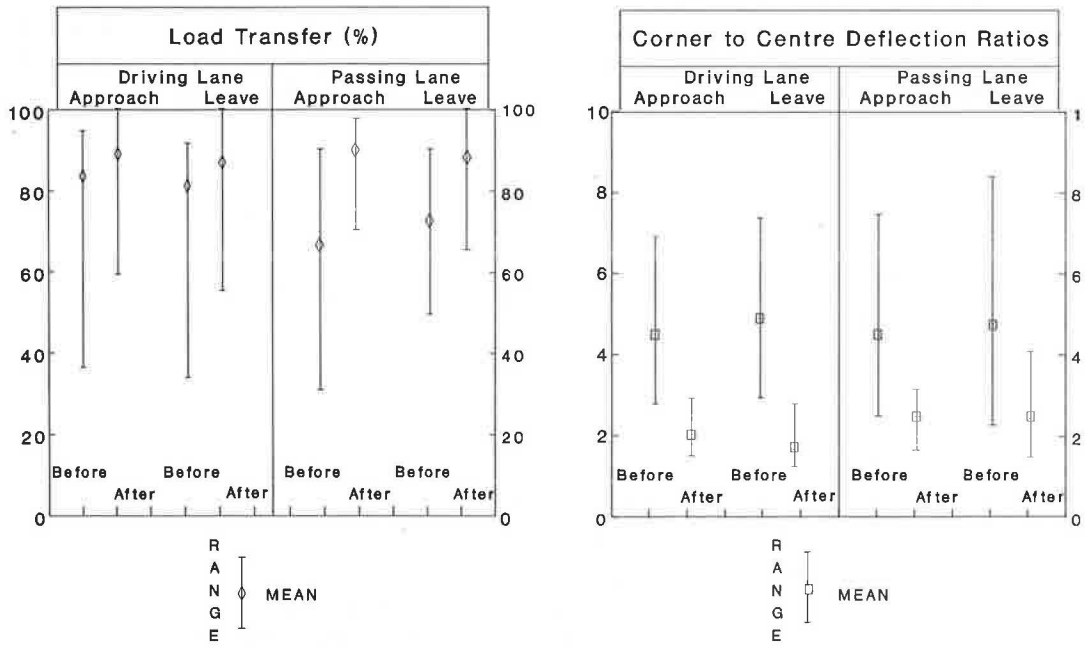


FIGURE 10 Load deflection results, SBLs.

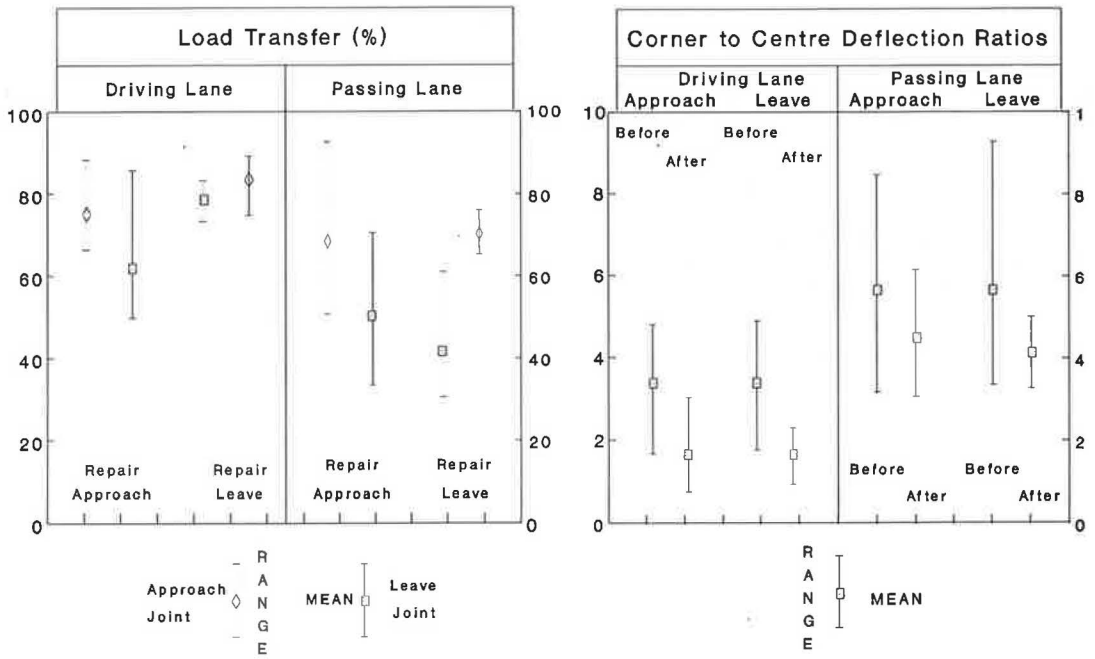


FIGURE 11 Load deflection results, NBLs.

Generally corner to center slab deflection ratios were improved following rehabilitation, as anticipated. The most significant improvement was in the reduction of the range of values obtained for corner to center deflection ratios. This result indicates that the weakest locations were improved and the entire length of the pavement has experienced an increase in stiffness and slab support, as shown in Figure 11b.

CONCLUSIONS

This report summarizes the successful design and construction of one of the most innovative PCC pavement rehabilitation projects undertaken in Ontario. It also provides an overview of the initial performance of these rehabilitated PCC pavements. Monitoring and data collection is continuing and future performance results will be documented.

The following general conclusions are based on short-term postconstruction results:

1. A significant improvement in ride and skid resistance is attainable using diamond grinding techniques. Postconstruction ride and skid resistance measurements were as good as, if not better than, those values obtained with premium hot-mix surface course.
2. The integrity and continuity of the overall pavement structure was improved by undertaking full-depth repairs and the unbonded concrete overlay.
3. Noise level testing indicates that immediate postconstruction pavement noise levels are slightly lower for the diamond-ground surface when compared to preconstruction levels and marginally higher for the unbonded overlay.
4. The actual construction costs for this project were virtually identical to those obtained in estimates.
5. As an overall conclusion, the Highway 126 project has proven that full PCC pavement rehabilitation can be successfully and economically carried out in Ontario. These techniques provide an alternative methodology for addressing the rehabilitation of Ontario's aging highway infrastructure.

Several aspects of PCC pavement rehabilitation requiring further developmental work include the following:

1. Improvements in retrofitting load transfer devices to minimize subbase disturbance for full-depth repairs;
2. Improved methods of detecting and removing deteriorated concrete and replacement with economical high early strength patch materials;
3. Investigate and monitor the long-term skid resistance of diamond-ground pavements; and
4. Develop an end result surface tolerance specification for burlap dragged-tined and diamond-ground pavement surfaces in Ontario.

ACKNOWLEDGMENT

Grateful acknowledgment is extended to R. Mepham, K. Helwig, G. Musgrove, J. Smith, K. Merkus, F. Marciello, and C. Blaney for their valuable contributions to data acquisition and summation for this project.

The authors appreciate the permission given by the Ministry of Transportation of Ontario to publish and present this paper.

REFERENCES

1. H. J. Sturm, T. J. Kazmierowski, R. Rollings, and K. Carter. Fast Trace Concrete Pavement Repairs, Ontario's Experience. Presented at RTAC Annual Conference, Ministry of Transportation, Downsview, Ontario, 1989.
2. T. J. Kazmierowski and G. A. Wrong. Experimental Cement Grout Subsealing of a Concrete Pavement in Ontario. Presented at RTAC

Annual Conference, Ministry of Transportation, Downsview, Ontario, 1986.
3. T. J. Kazmierowski, G. A. Wrong, and W. A. Phang. Design Construction, Performance of Four Experimental Concrete Pavement Sections in Ontario. Ministry of Transportation, Downsview, Ontario, Dec. 1985.
4. T. J. Kazmierowski and G. A. Wrong. Six Years Experience with Experimental Concrete Pavement Sections in Ontario. *Proc., 4th International Conference on Concrete Pavement Design and Rehabilitation*, Purdue University, West Lafayette, Ind., 1989.
5. J. Ryell, J. T. Corkill, and G. R. Musgrove. Skid Resistance of Bituminous Pavement Test Sections—Highway 401, Toronto By-Pass. Report IR67 MTC, Ontario, April 1978.
6. F. W. Jung, C. T. Blaney, and A. L. Kazakov. Noise Emission Levels for Vehicles in Ontario. HOS-85-02.
7. K. T. Hall, M. I. Darter, M. B. Snyder, and S. H. Carpenter. Nation Wide Performance of Concrete Pavement Rehabilitation. *Proc., International Conference on Concrete Pavement Design and Rehabilitation*, Purdue University, West Lafayette, Ind., 1989.
8. M. B. Snyder and D. L. Lippert. Field Performance of Experimental Full-Depth Repair Joint Load-Transfer Systems in Illinois. In *Transportation Research Record 1272*, TRB National Research Council, Washington, D.C., 1990.

Publication of this paper sponsored by Committee on Pavement Rehabilitation.

Theoretical Implications of the AASHTO 1986 Nondestructive Testing Method 2 for Pavement Evaluation

ANASTASIOS M. IOANNIDES

The conventional classification of pavement design procedures into "empirical" and "mechanistic" is reexamined. It is submitted that the term "mechanistic" originally denoted a data interpretation methodology based on the laws of engineering mechanics, proposed as an alternative to the statistical interpretation techniques used extensively in the interpretation of AASHO Road Test data. Current mechanistic design procedures retain statistical/empirical correlations, but this is a matter of practical expediency, pending improvements in analytical capabilities. On the other hand, incorporating mechanistic results into a statistical/empirical framework rarely leads to reliable conclusions. A case in point is provided by AASHTO 1986 Nondestructive Testing Method 2 (NDTM2), which combines the mechanistic layered elastic theory with the purely statistical/empirical structural number concept. The derivation of the NDTM2 equations is traced and simplified, and a number of theoretical shortcomings are highlighted. It is recommended that use of NDTM2 be discouraged and that efforts for the gradual elimination of statistical/empirical constructs [e.g., structural number, equivalent single-axle load (ESAL), and Miner's fatigue concepts] be intensified. Attempts to define statistical/empirical parameters [e.g., layer coefficients, present serviceability index (PSI), and load equivalency factors] using mechanistic theoretical tools should be abandoned.

Following the AASHO Road Test (1958–1960), a conventional nomenclature evolved according to which pavement design procedures are generally classified as either "empirical" or "mechanistic." Despite widespread use of these two terms, a surprising lack of agreement exists today among practicing pavement engineers as to the terms' precise meaning. Even a brief review of the pertinent literature reveals that relatively little effort has been expended in clarifying the distinguishing features of each approach. Investigators adopt instead the term that lends most credibility to a proposed new design procedure, with "mechanistic" being considered somehow superior. Since both "empirical" and "mechanistic" design procedures were in existence long before the adoption of the current terminology, it must be recognized that the meaning ascribed today to these terms has been greatly influenced by the concepts stemming from the AASHO Road Test experience.

Consider first the dictionary definitions of the two terms. "Empirical" means "relying upon or derived from observation or experiment," or "guided by experience and not theory" (*1*). Since observation and experience are indispensible ingredients of any credible and reliable scientific endeavor, it is not immediately evident why "empirical" pavement design procedures are often nowadays considered largely out of date and are described as based on rules of thumb dictating the development of "a more rational approach" (*2*).

On the other hand, a "mechanistic" procedure is one "of or pertaining to mechanics as a branch of physics," or "of or tending to explain phenomena only by reference to physical or biological causes" (*1*). The term "rational" is no longer used very often in current pavement literature, perhaps in view of its judgmental undertones. In its technical meaning, however, "rational" appears to have been an early synonym for "mechanistic," "in the sense of having reason and understanding, of properly relating causes and effects" (*3*), and implying the use "of accurate predictions of stresses and strains in various parts of the layered system through the use of structural analysis techniques" (*4*). "Theoretical" is another term that has been used quite often as a synonym to "mechanistic," although its diminishing popularity probably reflects "a certain disenchantment in the attitude of investigators toward the application of pure elastic theory" (*5*). The pioneers of the theoretical approach, however, never advocated the use of "pure" theory stripped of observation, experience, or common sense. Westergaard (*6*) dismissed as "irrelevant" the comments of a certain Turner, who compared the use of the theory of elasticity with the use of the discredited phlogiston theory in the middle ages, but would probably have endorsed the following statement of Burmister (*7*):

> Every important advance in science and engineering has stemmed from theoretical working hypotheses, which have brought phenomena into the realm of greater certainty and have served as a guide to experimentation and investigation. It should be realized, however, that no theory or statement of physical laws in any science or engineering is complete in its present form. It cannot fully and adequately include, explain, and take into account present apparent "exceptions to the rule," outside its realm of validity of limiting boundary conditions. Yet such theories and statements of physical laws have provided the essential stimulus and guide to major scientific advances, and have established the nature and basic form of the physical laws governing phenomena.

Why then did the term "theoretical"—used extensively in other civil engineering design disciplines—need to be replaced by the term "mechanistic," one used almost exclusively by pavement engineers?

Department of Civil Engineering, University of Illinois at Urbana-Champaign, 205 N. Mathews Ave. #2230C, Urbana, Ill. 61801.

SCOPE OF PAPER

It is submitted that the term "mechanistic" was coined in the late 1960s to denote an alternative methodology to the statistical approach used in interpreting the data collected during the AASHO Road Test. Thus, it was not originally intended to be in opposition to the empirical process of collecting data to validate an engineering theory. Consider, for example, the comments of Vesic and Saxena (*8*), who were among the first to use the term "mechanistic" in the sense usually ascribed to it today:

> The aim of this study is to provide a rational, mechanistic interpretation of measurements and observations made on rigid pavements during the AASHO Road Test. . . . Unfortunately in most [previous] analyses of AASHO Road Test data, [the present serviceability index] has been related to wheel loads on a purely empirical basis, though with elaborate statistical analyses . . . [The finding of this study] confirms the soundness of a rational, mechanistic approach to design of rigid pavements. It demonstrates beyond doubt that failure in pavement performance is not a phenomenon of chance, as some statistical approaches tend to suggest, but a phenomenon that has a definite mechanical cause.

Such comments reveal that the term "mechanistic" originally referred to the approach used in data interpretation rather than to the nature or source of the information to be interpreted. Vesic and Saxena used the same "empirical" data collected during the AASHO Road Test that previous statistical analyses had also employed. Furthermore, they applied computational tools available at the time (namely, the discrete element method) to generate additional "numerical" or "theoretical" data. The main departure of their "mechanistic" interpretation method lay precisely in the fact that instead of statistical correlations, they sought to develop cause-and-effect relationships based on reasoned understanding of the physical laws governing the mechanisms of the distresses observed in the field. Such relationships may be arrived at by adhering to the principles of structural or continuum mechanics, which provide the working hypotheses to be verified by observation and experience. In contrast, current experimental factorial designs and empirical interpretation techniques focus almost exclusively on testing statistical hypotheses, which in many instances are not substantiated—or are sometimes contradicted—by engineering analysis and design concepts.

With respect to the source of data, "empirical" may be juxtaposed to "analytical" or "numerical," but not in the sense of mutually exclusive opposites, because comparisons between measurements in the field or in the laboratory and computational results have been a powerful method of unraveling the phenomena observed and validating engineering working hypotheses. In regard to approaches to data interpretation, "mechanistic" denotes a procedure that relies on the use of engineering theory and mechanics, and should be contrasted to "statistical/empirical." This composite term defines more succintly the cardinal difference between the two approaches.

The main issue upon which this paper focusses is whether and under what conditions "mechanistic" and "statistical/empirical" data interpretation techniques can be synergistic and when they are mutually exclusive and immiscible. The discussion centers around Nondestructive Testing (NDT) Method 2 (NDTM2) of the 1986 AASHTO Design Guide (*9*), not so much because of the practical significance of this particular aspect of the Guide, but because NDTM2 provides a good case in point for the development of broad conclusions that could have enormous repercussions on prevailing experimental design philosophies and data interpretation approaches. In addition, the paper addresses some of the concerns raised by practicing professionals with respect to the application of NDTM2. The development of the pertinent formidable equations is traced and documented, and a corrected and considerably simpler form of the equations is presented.

To facilitate the flow of the arguments presented, the following convention is adopted. The 1986 *AASHTO Guide for Design of Pavement Structures* (*9*) is referred to herein simply as "the Guide." References to page, equation, figure, and section numbers, as well as appendixes to the Guide are preceded by the letter *G*. For example, "p. GIII-31" refers to page III-31 in the Guide; "Equation (GPP.4)" refers to Equation (PP.4), found in Appendix PP of the Guide; and so forth. The Guide itself provides no numbers for the equations in Chapter 5 of Part III. To clarify references to these equations, they will be numbered consecutively, starting with Equation G1 on p. GIII-77. Symbols used in the Guide are often complicated by superfluous subscripts. A simplified, uniform system of symbols has been adopted in this paper. For easy reference, Table 1 presents a comparison of the symbols used in this paper and those in Part III (Chapter 5) of the Guide, as well as in Appendixes GN, GNN, and GPP.

NDT METHODS IN AASHTO OVERLAY DESIGN

The AASHTO overlay design methodology is presented in Chapter 5 of Part III of the Guide. Procedures are described for "all types of overlay placed on any type of pavement

TABLE 1 COMPARISON OF SYMBOLS USED

	PAPER	PT.III	APP.GN	APP.GNN	APP.GPP
In situ layer modulus	E_i	E_i	–	E_{im}	E_l
In situ layer thickness	h_i	h_i	–	h_{im}	h_i
In situ layer Poisson ratio	μ_i	u_i	–	μ_{im}	u_i
Transformed top layer modulus	E_1	–	–	E_{sgb}	E_e
Transformed top layer thickness	h	h_t	h_t	T_{cgb}	h_t
Transformed top layer Poisson ratio	μ_1	–	–	μ_{sgb}	u_e
Equivalent thickness	h_e, g_e	H_e	h_e	h_{1e}	h_e
Subgrade modulus	E_s	E_{sg}	E_{Rs}	E_{sg}	E_{Rs}
Subgrade Poisson ratio	$\mu_s(=0.5)$	u_{sg}	u_{Rs}	μ_{sg}	u_{Rs}

structure," and nondestructive testing is endorsed for use in material characterization for determining the in situ structural capacity of the existing pavement. Two different NDT methods are described for this purpose. In contrast to earlier methodologies that relied exclusively on maximum deflection measurements, both these methods employ measurements at additional locations.

NDT Method 1 is termed "Pavement Layer Moduli Prediction Technique" (p. GIII-32) and corresponds to the conventional NDT backcalculation schemes that have recently become very popular. Several sensor measurements are made, and an iterative computer code is used to match the measured deflection basin with a theoretically predicted one, thereby leading to estimates of the in situ layer moduli.

On the other hand, NDT Method 2 is offered as an alternative when a "manual" (noncomputerized) method is desired (p. GIII-86), or "in the event that the concept/philosophy/analysis using deflection basins to interpret the E_i values is not considered feasible" (p. GNN-16). The method employs only two deflection measurements, one under the center of the load and one at a sufficiently large radial distance ("outer geophone"). This "Direct Structural Capacity Prediction Technique" bypasses the backcalculation of each layer modulus, E_i, relying instead on an approximate approach first proposed by Ullidtz (*10*) for determining the soil modulus, E_s, on the basis of one distant deflection measurement.

DEVELOPMENT OF NDTM2 EQUATIONS

Reduction of Multilayered Pavement to Two-Layered System

The basic equations governing the application of NDTM2 are summarized on p. GN-8. Their derivation is presented in Appendix GPP, in which additional references are made to Appendix GNN, where a somewhat different derivation is presented. The review of NDTM2 presented below considers both these appendixes simultaneously, highlighting their essential similarity and areas of disagreement.

The theoretical basis for NDTM2 consists of a generalization of the classical method of equivalent thicknesses (MET), most definitively described by Odemark in 1949 (*11*). It appears, however, that because this important study was published in Swedish, only a few investigators have had access to more than scant (and not always accurate) references to Odemark's work, in a small number of publications in English. As a result, the derivation presented in the Guide is not based directly on Odemark's work. There is a single reference to Thenn de Barros (p. GPP-3), but it appears that the method employed is more akin to that suggested by Barber.

The derivation of the pertinent equations begins with the assertion that "a layered pavement system can be viewed as an equivalent thickness of any arbitrary selected material type" (p. GNN-11). Thus, the in situ multilayered pavement may be reduced to a two-layered system, the top layer of which is characterized by "transformed" modulus, thickness, and Poisson ratio values whereas the subgrade characteristics remain unchanged. The following expression (slightly modified for clarity) is given in Appendix GNN for the transformed top-layer thickness:

$$T_{egb} = \sum_{i=1}^{n} h_{im}\left[\frac{E_{im}}{E_{sgb}}\frac{(1-\mu_{sgb}^2)}{(1-\mu_{im}^2)}\right]^{1/3} \quad (1)$$

(See Equation GNN.23.) That this is not entirely in accordance with the MET concept as proposed by Odemark (*11*) becomes evident when one compares this equation with Equation G5, given on p. GIII-86:

$$H_e = 0.9\sum_{i=1}^{n} h_i\left\{\frac{[E_i(1-u_{sg}^2)]}{[E_{sg}(1-u_i^2)]}\right\}^{1/3} \quad (2)$$

(See Equation G5.)

In Equation G5, modular ratios are determined with respect to the actual in situ modulus of elasticity of the subgrade, E_{sg}, rather than that of an "arbitrary material," E_{sgb}, and the multilayered pavement system is transformed into a homogeneous foundation. Equation G5 is readily recognized as a generalization of the formula proposed by Odemark (*11*), intended to transform the overlying layer in a two-layer system into an equivalent thickness of the same material as the subgrade, rendering the pavement a single-layer system. A correction factor, f, of 0.9 was introduced by Odemark (*11*) to ensure better agreement between the MET and the more accurate layered elastic theory (*12*).

It should be noted, however, that Odemark's suggestion was specifically intended only for the reduction of an in situ two-layered system, presumably because of the approximation involved in a transformation of this type. Furthermore, $f = 0.9$ pertains only to a two-layered system in which $\mu_1 = \mu_s = 0.5$. Odemark indicated that $f = 0.83$ for $\mu_1 = 1/6$ and $\mu_s = 0.5$. Use of $f = 0.9$ for a general multilayer system is not justified, especially if Poisson ratios are retained. The mere omission of f in Equation GNN.23 may alone account for a discrepancy of up to 20 percent. This would certainly justify neglecting the contribution of the Poisson ratio terms in MET applications. For these reasons, the following form of Equation 2 is recommended:

$$h_e = 0.9\sum_{i=1}^{n} h_i\left(\frac{E_i}{E_s}\right)^{1/3} \quad (3)$$

Use of Equation 3 when $n > 3$ should be discouraged, except to provide a rough indication of the "equivalent thickness."

In contrast, Appendix GPP suggests a transformation resulting in an equivalent modulus rather than an equivalent thickness. Thus, the $(n-1)$ pavement layers are reduced to a single one, whose thickness is the same total thickness, h_t, as in the real system, whereas its modulus is the "equivalent transformed material modulus," E_e (p. GPP-3). The following formula is proposed for the calculation of E_e (appropriately corrected):

$$E_e = \left\{\sum_{i=1}^{n-1}\frac{h_i}{h_t}\left[\frac{E_i(1-u_e^2)}{(1-u_i^2)}\right]^{1/3}\right\}^3 \quad (4)$$

(See Equation GPP.1.) This expression is a generalization of the concept proposed by Thenn de Barros (*14*), who described his original formula as "approximate," and only intended to reduce a three-layered system to a two-layered system (i.e.,

$n \leq 3$). The Thenn de Barros formula can be written as follows:

$$E_e = \left(\sum_{i=1}^{2} \frac{h_i}{h_t} E_i^{1/3} \right)^3 \quad (5)$$

Omission of the μ-terms in Equation 5 is consistent with the approximate nature of such a transformation and the uncertainties involved in estimating Poisson ratios for pavement materials. Thus, Equation 5 is recommended as a simpler form of Equation 4 (GPP.1).

The formulation finally adopted in NDTM2 (as revealed by the equations presented in Appendix GN, p. GN-8) follows the "equivalent modulus" transformation of Appendix GPP. This choice is justified, because Appendix GPP follows the original Thenn de Barros proposal quite closely, whereas a considerable extrapolation of the Odemark formulation is represented by the Appendix GNN approach. Yet, except for the difference in the manner in which the actual n-layered system is reduced to a two-layered one, the derivations presented in both Appendixes GNN and GPP are identical. For the sake of clarity and generality, therefore, the evaluation of the derivations presented below will consider a two-layered system consisting of a top layer (h, E_1, μ_1) resting on a semiinfinite foundation (E_s, μ_s).

Reduction of Two-Layered System to Homogeneous Half-Space

The derivation begins by considering plate load tests performed on the real (multilayered) as well as on the equivalent (two-layered) pavement systems. For the latter, Burmister (*13*) gives the maximum (central) deflection as

$$\Delta_0 = 2pa \frac{(1 - \mu_s^2)}{E_s} F_w \quad (6)$$

(see Equations GPP.19 and GNN.26), in which a is the radius of the plate and p is the applied (uniform) pressure. For $\mu_s = 0.5$, this expression is simplified to

$$\Delta_0 = 1.5 \frac{pa}{E_s} F_w \quad (7)$$

The parameter F_w is the so-called "Burmister two-layer deflection term." It is a nondimensional correction factor that, applied to the corresponding one-layer expression by Boussinesq (*15*), permits the determination of Δ_0 in a two-layered system. Burmister (*13*) presented values of F_w in a chart, assuming $\mu_1 = \mu_s = 0.5$, and showed that F_w is a function only of the ratios h/a and E_1/E_s. A similar chart for $\mu_1 = 0.2$ and $\mu_s = 0.4$ was presented by Burmister (*16*), whereas Thenn de Barros (*14*) derived the corresponding chart for $\mu_1 = \mu_s = 0.35$. The latter also notes the following concerning the Poisson ratio values:

> The numerical value of the factor [F_w] is different [depending on the assumed values for μ_1 and μ_s] for the same values of the parameters [(h/a) and (E_1/E_s)], but the deflections computed by [Equation 6 (GNN.26 and GPP.19) in each case] are very close. The reduction of Poisson's ratio from 0.5 to 0.35 increases the deflection of layered systems by less than 10 percent, for the practical range of the parameters. The average increase is about 7 percent. The actual value of Poisson's ratio of pavement structures is not known, but it is likely to be between 0.35 and 0.5. This difference can be ignored in practical applications.

These comments justify adopting Equation 7 instead of Equation 6 (GNN.26 and GPP.19). An additional consideration favoring such a simplification relates to the nature of the conventional plate load test. This is conducted using a rigid plate for which slightly different expressions are more appropriate (*17*). Adopting the "flexible load" expressions given by Equations 6 (GNN.26 and GPP.19) and 7 introduces a discrepancy of about 20 percent. Once again, the comments of Thenn de Barros (*14*) are enlightening:

> [Deflections] computed for the case of a flexible bearing area . . . should be multiplied by a "bearing factor" [in] the case of a rigid plate. The exact value of this factor cannot be determined at this time. It can be safely stated that for the layered systems of interest in pavement design the bearing factor must be between $\pi/4$ and 1, probably closer to 1. From analogy with the uniform medium, it is evident that the surface layers have a greater influence on the difference between deflections of rigid and flexible bearing areas. If the surface layers are relatively stiff, this difference should be small. Taking into account the overall inaccuracies of modeling the pavement by an elastic layered system, it is suggested that the same deflection factors [i.e., flexible load] should be tentatively used in deflection analysis of pavement systems loaded with rigid plates."

Returning now to the Burmister deflection term, F_w, the Guide quotes the following equation for its explicit calculation:

$$F_w = \frac{E_s}{E_1} \frac{(1 - \mu_1^2)}{(1 - \mu_s^2)} + F_b \left(1 - \frac{E_s}{E_1} \right) \quad (8)$$

(See Equations GPP.20 and GNN.27.)

The Guide suggests the following equation for the term F_b:

$$F_b = \{[1 + (h_e/a)^2]^{1/2} - (h_e/a)\} \times \left\{ 1 + \frac{(h_e/a)}{2(1 - \mu_s)[1 + (h_e/a)^2]^{1/2}} \right\} \quad (9)$$

(see Equations GPP.21 and GNN.27) with

$$h_e = 0.9h \left(\frac{E_1}{E_s} \frac{(1 - \mu_s^2)}{(1 - \mu_1^2)} \right)^{1/3} \quad (10)$$

(see Equations GPP.22 and GNN.29).

Equation 10 (GPP.22 and GNN.29) can be readily recognized as an "extension" (by the inclusion of the μ-terms) of Equation 3 for $n = 2$. Through the use of this equation, the original in situ multilayered pavement, which had been reduced according to Thenn de Barros into a two-layered system, is now transformed according to Odemark into a homogeneous half-space. This double transformation alone

is justification for dropping the μ-terms. Thus, Equation 10 (GPP.22 and GNN.29) may be simplified to

$$h_e = 0.9h\left(\frac{E_1}{E_s}\right)^{1/3} \tag{11}$$

which is the exact form proposed by Odemark (*11*).

Now, the term F_b defined by Equation 9 (GPP.21) is similarly recognized as the so-called "Boussinesq deflection factor" describing the attenuation of the center-line deflection with depth in a homogeneous half-space (*18*). Equation 9 (GPP.21) gives the value of this factor at $r = 0$, $z = h_e$, and by setting $\mu_s = 0.5$, the equation reduces to

$$F_b = \frac{1}{[1 + (h_e/a)^2]^{1/2}} \tag{12}$$

It is evident that the complexity of Equation 9 (GPP.21) is all but eliminated by assuming $\mu_s = 0.5$.

The derivation of Equation 8 (GPP.20 and GNN.27) is more perplexing. Poulos and Davis (*18*) present a similar formula, which they attribute to Palmer and Barber (*12*). Their equation assumes $\mu_1 = \mu_s = 0.5$ and results in the following expression for F_w:

$$F_w = (E_s/E_1) + \frac{a}{[a^2 + h^2(E_1/E_s)^{2/3}]^{1/2}}[1 - (E_s/E_1)] \tag{13}$$

Implicit in Equation 13 is a transformation of the two-layered system into a homogeneous half-space by deriving an equivalent thickness as follows [after Poulos and Davis (*18*), corrected for an evident typographical error]:

$$h_e = h\left[(E_1/E_s)\frac{(1 - \mu_s^2)}{(1 - \mu_1^2)}\right]^{1/3} \tag{14}$$

Equation 14 assumes that $f = 1.0$, as was common before the publication of Odemark's work in 1949. If $\mu_1 = \mu_s = 0.5$, Equation 14 can be introduced into Equation 13 to yield

$$F_w = (E_s/E_1) + F_b(h_e/a)[1 - (E_s/E_1)] \tag{15}$$

in which F_b is a function of (h_e/a) as defined by Equation 12. Thus, it is concluded that Equation 8 (GPP.20) constitutes once again an extension through the introduction of the μ-terms of Equation 13, whereas Equation 15 is its simpler, preferable form.

A thorough review of the pertinent literature reveals that Equation 14 was first presented by Barber (*12*, Closure), whereas the derivation of Equation 13 was outlined very briefly by Barber in a subsequent discussion (*19*). Examination of this derivation reveals a discrepancy between Equation 15 and the corresponding formula proposed by Odemark (*11*). Both Barber and Odemark begin by asserting that the maximum deflection in a two-layered system, Δ_0, consists of two parts:

1. The deflection due to the subgrade, Δ_s; and
2. The compression of the upper layer, Δ_1, that is, the difference in the deflection observed at its surface and the corresponding one experienced at its underside.

Both these investigators are in essential agreement concerning the calculation of Δ_s, as the deflection at depth $z = h_e$ in the homogeneous half-space with modulus, E_s. It is in the calculation of Δ_1 that the aforementioned discrepancy arises. Odemark (*11*) provides more details as to how Δ_1 is determined. This is accomplished by transforming the two-layered system into a homogeneous half-space of modulus E_1, which reduces the thickness of the top layer from h to

$$g_e = n_1 h \tag{16}$$

where n_1 is equal to about 0.9 for $\mu_1 = \mu_s = 0.5$. According to Odemark,

$$\Delta_1 = 1.5\frac{pa}{E_1}[1 - E_b(g_e/a)] \tag{17}$$

Note that F_b in Equation 17 is a function of the equivalent thickness, g_e, rather than of h_e, which was used in the calculation of Δ_s. Barber, on the other hand, uses h_e for Δ_1 as well. It is evident, therefore, that Equation 15 expresses the sum of Δ_s and Δ_1, both determined as functions of h_e, as suggested by Barber. The consequence of this discrepancy, however, on the calculation of Δ_0 is quite benign. Δ_s is significantly larger than Δ_1 in most cases, which perhaps explains in part why the discrepancy has gone unnoticed until now. Comparisons with Burmister (*13*) indicate that the error introduced by Equation 15 increases as E_1/E_s increases, that is, as h_e diverges from h. This is the case of a stronger top layer on a weaker subgrade. The discrepancy also increases as h/a decreases, that is, when a larger loaded area is applied on a thinner top layer. Note, however, that in both these cases, the contribution of Δ_1 to the total deflection, Δ_0, is relatively minor. For example, for $E_1/E_s = 10{,}000$ and $h/a = 0.1$, the error in Δ_1 itself is about 17 percent, but the resulting error in Δ_0 is less than 0.01 percent. It is not surprising, therefore, that Barber reported that his method is "practically the same numerically" as that of Burmister (*13*).

Use of h_e in the calculation of both Δ_s and Δ_1 fortuitously permits writing the relatively simpler expression for F_w, given by Equations 8 or 15. The more rigorous form (assuming $\mu_s = 0.5$) should have been

$$F_w = (E_s/E_1)[1 - F_b(g_e/a)] + F_b(h_e/a) \tag{18}$$

which is identical to the corresponding formula presented by Odemark (*11*).

In light of the above discussion, it is recommended that the equations presented in Table 2 be adopted instead of the corresponding ones in the Guide.

Derivation of Structural Number Equations

The structural number (SN) equations presented in Appendixes GPP and GNN (and summarized on p. GN-8) can be simplified considerably by the adoption of the proposed equations and by neglecting the Poisson ratio terms. The derivation presented below follows Appendixes GPP and GNN closely in all other respects and yields equations in which the inch is the unit of length and the pound is the unit of force.

TABLE 2 RECOMMENDED EQUATIONS

Argument	Equation Recommended	Instead of Equation
Δ_0	7	GPP.19 or GNN.26
F_w	18	GPP.20 or GNN.27
F_b	12	GPP.21 or GNN.28
h_e	11	GPP.22 or GNN.29
g_e	16	–

By definition,

$$SN = \sum_{i=1}^{n-1} h_i a_i \tag{19}$$

(see Equations GPP.2 and GNN.8). For two "structurally equivalent" layers, that is, layers making the same contribution to SN,

$$h_g = \frac{a_i}{a_g} h_i \qquad i, g = 1, \ldots n-1; g \neq i \tag{20}$$

(see Equations GPP.3 and GNN.9) or

$$a_i = \frac{h_g}{h_i} a_g \tag{21}$$

(see Equations GPP.4 and GNN.10).

According to the Guide (pp. GPP-3 and GNN-8), the structural number of any layer, SN_i, is directly proportional to the layer flexural stiffness. Thus, ignoring Poisson effects,

$$SN_i = h_i a_i \propto E_i h_i^3 \tag{22}$$

whence

$$\frac{h_g}{h_i} = \frac{a_i}{a_g} = \left(\frac{E_i}{E_g}\right)^{1/3} \tag{23}$$

(Cf. Equations GPP.7 and GNN.12.)

Substituting into Equation 19 (Equations GPP.2 or GNN.8),

$$SN = \sum_{i=1}^{n-1} h_i a_i = \sum_{i=1}^{n-1} h_i a_g \left(\frac{E_i}{E_g}\right)^{1/3} \tag{24}$$

in which E_g and a_g are constants describing an arbitrary "standard" material. Thus, each in situ layer can be transformed into an equivalent thickness of the standard material using Equation 20 (GPP.3). Ignoring the loss in accuracy involved in each such transformation, Equation 24 (GPP.9) can be written as

$$SN = \frac{a_g}{E_g^{1/3}} \sum_{i=1}^{n-1} h_i E_i^{1/3} \tag{25}$$

(Cf. Equations GPP.16 and GNN.21.)

The values of $E_g = 30{,}000$ psi and $a_g = 0.14$ are adopted in the Guide, which correspond to the AASHO Road Test results for the crushed stone granular base:

$$SN = \frac{0.14}{30{,}000^{1/3}} \sum_{i=1}^{n-1} h_i E_i^{1/3} \tag{26}$$

(cf. Equation GPP.16; see Equation GNN.25) or

$$SN = 0.0045 \sum_{i=1}^{n-1} h_i E_i^{1/3} \tag{27}$$

(cf. Equation GPP.17; see Equation GNN.25).

For the two-layer system considered above (h, E_1, E_s), the last equation results in

$$E_1 = \left(\frac{SN}{0.0045h}\right)^3 \tag{28}$$

(cf. Equation GPP.18) or

$$h = \frac{SN}{0.0045 E_1^{1/3}} \tag{29}$$

Combining Equation 29 with Equation 11 yields, upon division of both sides by the radius of the applied (plate) load, a,

$$(h_e/a) = 200 \frac{SN}{a} \frac{1}{E_s^{1/3}} \tag{30}$$

(cf. Equations GPP.23 and GNN.32), whence

$$(h_e/a)^2 = 40{,}000 \frac{SN^2}{a^2} \frac{1}{E_s^{2/3}} \tag{31}$$

(cf. Equations GPP.24 and GNN.33). Substituting this expression into Equation 12 results in

$$F_b = \frac{1}{\left(1 + 40{,}000 \frac{SN^2}{a^2} \frac{1}{E_s^{2/3}}\right)^{1/2}} \tag{32}$$

(cf. Equation GPP.27). Equation 18 therefore gives (assuming $g_e \approx h$)

$$F_w = (E_s/E_1)\left\{1 - \frac{1}{[1 + (h/a)^2]^{1/2}}\right\} + \frac{1}{\left(1 + 40{,}000 \frac{SN^2}{a^2} \frac{1}{E_s^{2/3}}\right)} \tag{33}$$

Now Equation 7 may be introduced into Equation 33 to yield

$$\Delta_0 = 1.5\frac{P}{\pi a}\left(\frac{1}{E_1}\left\{1 - \frac{1}{[1 + (h/a)^2]^{1/2}}\right\} + \frac{1}{E_s\left(1 + 40{,}000\dfrac{SN^2}{a^2}\dfrac{1}{E_s^{2/3}}\right)^{1/2}}\right) \quad (34)$$

Substituting for E_1 according to the modified Equation 28 (GPP.18),

$$\Delta_0 = 1.5\frac{P}{\pi a}\left\{\frac{(0.0045h)^3}{SN^3}\left[1 - \frac{1}{[1 + (h/a)^2]^{1/2}}\right] + \frac{1}{E_s\left(1 + 40{,}000\dfrac{SN^2}{a^2}\dfrac{1}{E_s^{2/3}}\right)^{1/2}}\right\} \quad (35)$$

(cf. Equation GPP.26).

STRUCTURAL NUMBER CONCEPT: ASSUMPTIONS AND DEFINITIONS

NDT-Method 2 provides an illustration of the problems that may arise when statistical/empirical and mechanistic data interpretation procedures are combined. NDT methods and backcalculation schemes are sophisticated mechanistic tools, developed recently and employed successfully in pavement studies. Notwithstanding any approximations they introduce, the equations derived on the basis of layered elastic theory (including MET) are also mechanistic in nature. The fundamental weakness of the mathematical derivations presented in Appendixes GNN and GPP lies in the fact that such mechanistic, rigorous, and analytical methods are combined—by necessity—with the entirely statistical/empirical structural number concept, developed on the basis of AASHO Road Test data. It is ironic that this very fact is heralded in the Guide as one of the strengths of the design procedure presented (p. GNN-11). The fundamental presuppositions underlying the structural number concept are discussed below, and their incompatibility with a mechanistic understanding of the pavement system is highlighted.

The assumptions and definitions constituting the concept of the structural number may be stated explicitly as follows. The pavement consists of series of interchangeable individual layers, whose contribution to the structural behavior of the pavement system is uniquely defined by each layer's intrinsic, individual, and unchanging characteristics, namely, thickness and layer coefficient. Deriving from its statistical/empirical nature is the fact that the structural number concept ignores the effect of the interactions between the various layers of the pavement system. Instead, it considers that a given layer behaves (or contributes to the structural capacity of the system) in exactly the same manner, independent of the pavement layer sequence it finds itself in. The adequacy of the structural number concept has been the subject of considerable debate (*20–24*). On the other hand, the simplification it affords in pavement design is unquestionable.

The major weakness of the structural number concept is that emphasis is placed exclusively on pavement materials, rather than on the behavior of the pavement as a system of interacting components. This limitation is also inherent in the conventional classification of all pavements as "flexible" or "rigid," primarily on account of the material of the surface layer. Furthermore, the structural number concept ignores the influence on pavement system behavior of two very important factors, namely, subgrade support and geometry of the applied load. In real in situ pavement systems exhibiting nonlinear or stress-dependent behavior, the concept also ignores the effect of load level. Thus, this statistical/empirical concept may be expected to serve its intended purpose as a design tool adequately only as long as these factors are similar to those prevailing at the AASHO Road Test, which provided the original data from which the structural number concept was developed.

Consider now the understanding of the pavement as a structural system, inherent in layered elastic theory. This is illustrated by the solution to the two-layered system problem, first presented by Burmister (*13*), who showed on the basis of mathematical formulations that the behavior of such a pavement system is uniquely defined by two dimensionless ratios, namely, h/a and E_1/E_s. Note that the effect of load level is essentially eliminated by the use of linear elasticity, whereas the applied pressure, p, is introduced simply as a multiplication term in the complete Burmister equations (see, for example, Equation 7). The major load attribute identified by theory is load geometry, which is reflected in the presence of load radius, a, in one of the two dimensionless ratios.

It is worth reflecting on the implications of the Burmister solution. Layered elastic theory states that the behavior of the pavement system is the result of the relative magnitude of the structural parameters of the component layers. The contribution of the thickness of the top layer can only be assessed after it has been compared with the size of the applied load, in the form of the h/a ratio. Similarly, the contribution of the elastic modulus of a given layer is of limited consequence when considered by itself. The dimensionless ratio E_1/E_s clearly illustrates that the governing system characteristic is the relative stiffness of the various layers, including the supporting foundation.

The same understanding and definition of a pavement system (as consisting of the interaction of the placed layers, of the natural supporting subgrade, and of the geometry of the applied load) is also evident in Westergaard's treatment of the slab-on-grade problem (*25*). Traditionally, comparisons of the layered elastic and plate theories have tended to highlight only the points on which Westergaard's analysis differs from that of Burmister. Yet, the congruence of these two pioneers on what constitutes a pavement is of much more fundamental significance.

According to plate theory, the governing dimensionless ratio is a/l, where l is the radius of relative stiffness of the slab-subgrade system (*26*). Thus, in a single ratio, a/l, all three fundamental components of a pavement system (overlying manmade layers, supporting natural medium, and geometry of applied load) are lumped in a manner that reflects their

interaction and the significance of their relative (rather than absolute) magnitudes.

The understanding of the pavement system underlying the works of such respectable investigators as Westergaard and Burmister is based on a mechanistic evaluation of engineering behavior, not merely of materials. Consequently, structural response is a function of the relative (not absolute) magnitudes of the layer elastic characteristics and incorporates the effect of subgrade support and of the geometry of the applied load. This philosophy is therefore incompatible with the structural number concept.

CAN LAYER COEFFICIENTS BE DERIVED USING LAYERED ELASTIC THEORY?

A similar problem arises when layered elastic theory is used in determining layer coefficients for each of the in situ materials, as required by NDTM2. With the proliferation of a wide variety of construction materials and loading and support conditions in recent years, the adequacy of the original AASHO Road Test layer coefficients has been considerably decreased. This has created the need for the development of additional layer coefficients. The most common approach for this purpose has been the utilization of layered elastic theory (*27–31*). Thus, it is implicitly assumed that a layer coefficient can be uniquely defined if one knows the elastic characteristics (E_i, μ_i) of the material in that layer.

For the purposes of NDTM2, in particular, the following assertion is made at the start of the derivation presented in Appendix GPP: "If one views [two] pavement layers as having equal SN values, it can be concluded that the '[flexural] stiffness' $[E_i h_i^3/12(1 - \mu_i^2)]$ of both layers is also identical" (p. GPP-3). The weakness of this assertion lies in the following: The structural contribution of a layer is in a qualitative sense proportional to its flexural stiffness only if the material is linear, elastic, homogeneous, and isotropic. In practice, this translates to a bound material whose load-distributing capacity derives primarily from its ability to bend rather than to compress. Portland cement concrete slabs are comfortably within this category, but cement-treated or asphalt-treated materials may also be reasonable candidates.

Unbound granular materials, possessing no tensile strength, cannot be described adequately in terms of a "flexural stiffness." A case can be made that the concept is not even applicable to asphalt concrete. Although this material may possess significant tensile strength, it also exhibits a strongly viscoelastic, temperature- and loading-rate-dependent behavior, incompatible with the requirements of beam or slab bending theory. Furthermore, even for a system consisting of a series of layers each of which exhibits primarily flexural characteristics, total structural capacity is not merely proportional to the additive sum of the individual "flexural stiffness" of the layers. This is because the layers interact, each being influenced by and influencing every other layer. Thus, sequencing of layers, subgrade support provided, and geometry (if not the magnitude as well) of applied loadings need to be taken into account when structural system response is assessed.

A simple example suffices as illustration of the weakness of the basic assertion in Appendix GPP, quoted above, as well as the pitfalls of deriving layer coefficients using layered elastic theory. Consider a 4-in.-thick asphalt concrete (AC) layer whose modulus is 200 ksi. From Figure G2.5 (p. GII-19), $a_1 = 0.3$. The SN value for this layer is

$$SN_1 = h_1 a_1 = 4 \times 0.3 = 1.2$$

A granular layer with a modulus of 25 ksi and a layer coefficient, a_2, of 0.12 (from Figure G2.6, p. GII-20) will have the same structural number if its thickness, h_2, is 10 in. Then

$$SN_2 = h_2 a_2 = 10 \times 0.12 = 1.2 = SN_1$$

According to Appendix GPP, the following should be true:

$$\frac{E_1 h_1^3}{12(1 - \mu_1^2)} = \frac{E_2 h_2^3}{12(1 - \mu_2^2)} \tag{36}$$

(cf. Equation GPP.5).

Yet, for the AC layer (ignoring the contribution of the μ-terms)

$$E_1 h_1^3 = 200{,}000 \times (4)^3 = 12{,}800{,}000 \text{ lb-in.}$$

whereas for the granular layer

$$E_2 h_2^3 = 25{,}000 \times (10)^3 = 25{,}000{,}000 \text{ lb-in.}$$

Thus, the two quantities assumed to be equal by Equation 36 (GPP.5) are really in the ratio of 1:2. If asphalt concrete is considered to be the reference material, a prediction with respect to the granular layer would be off by 100 percent, simply on account of Equation 36 (GPP.5). In a multiple-layer structure involving several transformations of the type described by Equations GPP.10 through GPP.13, discrepancies of a similar magnitude may be expected to be compounded, and not necessarily in an additive fashion.

Furthermore, the log-log relationship between maximum deflection, Δ_0, and the effective in situ structural number, SN_{xeff}, as a function of E_s derived in Appendix GPP for the Falling Weight Deflectometer (Figure GPP.2) conceals the extreme sensitivity of SN_{xeff} to Δ_0. When this figure is redrawn on an arithmetic plot, it becomes apparent that a very small error in Δ_0 can lead to a considerable error in SN_{xeff}, particularly for stiffer subgrades.

CONCLUSIONS AND RECOMMENDATIONS

A major problem facing researchers attempting to expand or improve the AASHTO design procedures is the incorporation of mechanistic concepts into a statistical/empirical framework. Recent investigations at the University of Illinois have provided a considerable amount of evidence that such a process rarely leads to reliable conclusions. The reverse approach, that is, the incorporation of statistical/empirical concepts in a mechanistic methodology, has been routinely adopted by practically all current design procedures. The most common statistical/empirical ingredients of current "mechanistic-based" procedures are the equivalent single axle load (ESAL) con-

cept and the so-called "Miner's linear cumulative fatigue hypothesis." It is perhaps the proliferation of mechanistic-plus-statistical/empirical amalgams that has resulted in the assumption that statistical/empirical-plus-mechanistic mixtures are permissible, too. It must be recognized, however, that in the pursuit of developing a mechanistic procedure, use of statistical/empirical concepts is merely a matter of practical expediency. Concepts based exclusively on a statistical interpretation of accumulated information without any consideration of system behavior and factor interactions may provide the necessary bridges over gaps remaining in our ability to analyze mechanistically the complex problems associated with pavement design. As the state of the art in pavement modeling and analysis methods is improved, however, one by one these gaps are closed. Consequently, the statistical/empirical bridges are gradually being substituted by more reliable mechanistic planks, based on sound theoretical precepts, verified and calibrated—where necessary—by experimental field or laboratory observations. The verification and calibration process is by definition empirical, and is most effective when it employs statistics merely as a curve-fitting tool. Whenever possible, the fundamental cause-and-effect relations involved in the phenomena observed empirically should be interpreted in the light of mathematical formulations of basic laws of engineering mechanics, rather than heuristic rules of thumb that are valid only in a statistical sense. Efforts aimed at replacing statistical/empirical constructs (e.g. SN, ESAL, and Miner's fatigue concepts) by more mechanistic procedures should therefore be intensified, and attempts to define statistical/empirical parameters (e.g., layer coefficients, PSI, and load equivalency factors) using mechanistic theoretical tools should be abandoned.

Such considerations coupled with the theoretical weaknesses identified above suggest that use of NDTM2 should be discouraged. The justification for the original development of NDTM2, namely, the difficulty of conducting conventional deflection basin (backcalculation) analyses as required by NDT Method 1, can no longer be considered valid. Equipment for deflection basin testing is nowadays readily available, and comprehensive backcalculation programs have been developed for all types of pavements and are routinely used. Worth mentioning in particular is a backcalculation program developed recently (*32*, *33*) that evaluates directly the in situ subgrade modulus, k, thus eliminating the need for questionable correlations between E_s and k. If NDTM2 were to be used at all, it would be advisable to use the simpler, corrected equations derived in this paper, instead of those in the Guide.

REFERENCES

1. W. Morris, ed. *The American Heritage Dictionary of the English Language*. Houghton Mifflin, Boston, Mass., 1973.
2. E. J. Yoder and M. W. Witczak. Principles of Pavement Design, 2nd ed. John Wiley, New York, 1975.
3. S. Thenn de Barros. A Critical Review of Present Knowledge of the Problem of Rational Thickness Design of Flexible Pavements. In *Highway Research Record 71*, HRB, National Research Council, Washington, D.C., 1965, pp. 105–128.
4. B. G. Hutchinson and R. C. G. Haas. A Systems Analysis of the Highway Pavement Design Process. In *Highway Research Record 239*, HRB, National Research Council, Washington, D.C., 1968, pp. 1–24.
5. A. Rico Rodriguez, H. del Castillo, and G. F. Sowers. *Soil Mechanics in Highway Engineering*. Trans Tech Publications, Clausthal-Zellerfeld, Federal Republic of Germany, 1988, 843 pp.
6. H. M. Westergaard. Stress Concentrations in Plates Loaded Over Small Areas. *Transactions, ASCE*, Vol. 108, 1943, pp. 831–886.
7. D. M. Burmister. Evaluation of Pavement Systems of the WASHO Road Test by Layered System Methods. *Bulletin 177*, HRB, National Research Council, Washington, D.C., 1958, pp. 26–54.
8. A. S. Vesic and S. K. Saxena. *NCHRP Report 97; Analysis of Structural Behavior of AASHO Road Test Rigid Pavements*. HRB National Research Council, Washington, D.C., 1970, 35 pp.
9. AASHTO Guide for Design of Pavement Structures. AASHTO, Washington, D.C., 1986.
10. P. Ullidtz. Overlay and Stage by Stage Design. *Proc., 4th International Conference on the Structural Design of Asphalt Pavements*, Vol. 1, University of Michigan, Ann Arbor, Aug. 22–26, 1977, pp. 722–735.
11. N. Odemark. Investigations as to the Elastic Properties of Soils and Design of Pavements According to the Theory of Elasticity. (In Swedish), Statens Väginstitut, Stockholm, Sweden, 1949. (English Translation by M. A. Hibbs and J. Silfwerbrand, A. M. Ioannides, ed., 1990.)
12. L. A. Palmer and E. S. Barber. Soil Displacement Under a Circular Loaded Area. *HRB Proc.* Vol. 20, pp. 279–286, Discussion and Closure by E. S. Barber, pp. 319–332.
13. D. M. Burmister. Theory of Stresses and Displacements in Layered Systems and Applications to the Design of Airport Runways. *HRB Proc.*, Vol 23, 1943, pp. 126–144.
14. S. Thenn de Barros. Deflection Factor Charts for Two- and Three-Layer Elastic Systems. In *Highway Research Record 145*, HRB, National Research Council, Washington, D.C., 1966, pp. 83–108.
15. M. J. Boussinesq. Application des Potentiels. Gauthier-Villars, Paris, France, 1885.
16. D. M. Burmister. Applications of Layered System Concepts and Principles to Interpretations and Evaluations of Asphalt Pavement Performances and to Design and Construction. *Proc., 1st International Conference on the Structural Design of Asphalt Pavements*. University of Michigan, Ann Arbor, Aug. 20–24, 1962, pp. 441–453.
17. A. P. S. Selvadurai. Elastic Analysis of Soil-Foundation Interaction. *Developments in Geotechnical Engineering*, Vol. 17, Elsevier, Amsterdam, The Netherlands, 1979.
18. H. G. Poulos and E. H. Davis, Elastic Solutions for Soil and Rock Mechanics. John Wiley, New York, 1974.
19. E. S. Barber. Discussion of "Theory of Stresses and Displacements in Layered Systems and Applications to the Design of Airport Runways," by D. M. Burmister, *HRB Proc.*, Vol. 23, p. 146.
20. M. I. Darter and A. J. Devos. *Structural Analysis of Asphaltic Cold Mixtures Used in Pavement Bases*. Civil Engineering Studies, Transportation Engineering Series 19, Illinois Cooperative Highway Research Program Series 171, University of Illinois, Urbana, Aug. 1977.
21. M. Gomez and M. R. Thompson. *Structural Coefficients and Thickness Equivalency Ratios*. Civil Engineering Studies, Transportation Engineering Series 38, Illinois Cooperative Highway Research Program Series 202, University of Illinois, Urbana, June, 1983.
22. R. L. Terrel and C. L. Monismith. Evaluation of Asphalt-Treated Base Course Materials. *Proc., Association of Asphalt Paving Technologists Technical Sessions*, Atlanta, Ga. Feb. 26–28, Vol. 37, 1968, pp. 159–199.
23. B. S. Coffman, G. Ilves, and W. Edwards. Theoretical Asphaltic Concrete Equivalences, In *Highway Research Record 239*, HRB, National Research Council, Washington, D.C., 1968, pp. 95–119.
24. F. P. Nichols. Discussion of "Design of Flexible Pavements in Virginia Using AASHO Road Test Results," by N. K. Vaswani, In *Highway Research Record 291*, HRB, National Research Council, Washington, D.C., 1969, pp. 101–103.
25. H. M. Westergaard. Stresses in Concrete Pavements Computed by Theoretical Analysis. *Public Roads*, Vol. 7, No. 2, pp. 25–35, April, 1926. Also in *Proc., 5th Annual Meeting of the Highway*

Research Board, Part I, under title Computation of Stresses in Concrete Roads, 1926, pp. 90–112.
26. A. M. Ioannides. Discussion of "Response and Performance of Alternate Launch and Recovery Surfaces that Contain Layers of Stabilized Material," by R. R. Costigan and M. R. Thompson. In *Transportation Research Record 1095*, TRB, National Research Council, Washington, D.C., 1986, pp. 70–71.
27. C. J. Van Til, B. F. McCullough, B. A. Vallerga, and R. G. Hicks. *NCHRP Report 128: Evaluation of AASHO Interim Guides for Design of Pavement Structures*. HRB, National Research Council, Washington, D.C., 1972.
28. G. Rada and M. W. Witczak. Material Layer Coefficients of Unbound Granular Materials from Resilient Modulus. In *Transportation Research Record 852*, TRB, National Research Council, Washington, D.C., 1982, pp. 15–21.
29. N. K. Vaswani. Design of Pavements Using Deflection Equations from AASHO Road Test Results. In *Highway Research Record 239*, HRB, National Research Council, Washington, D.C., 1968, pp. 76–94.
30. N. K. Vaswani. Design of Flexible Pavements in Virginia Using AASHO Road Test Results. In *Highway Research Record 291*, HRB, National Research Council, Washington, D.C., 1969, pp. 89–103.
31. N. K. Vaswani. Optimum Structural Strength of Materials in Flexible Pavements. In *Highway Research Record 329*, HRB, National Research Council, Washington, D.C., 1970, pp. 77–97.
32. A. M. Ioannides. Dimensional Analysis in NDT Rigid Pavement Evaluation. *Journal of Transportation Engineering, ASCE*, Vol. 166, No. 1, Jan./Feb., 1990, pp. 23–36.
33. A. M. Ioannides, E. J. Barenberg, and J. A. Lary. Interpretation of Falling Weight Deflectometer Results Using Principles of Dimensional Analysis. *Proc., 4th International Conference on Concrete Pavement Design and Rehabilitation*, Purdue University, West Lafayette, Ind., 1989, pp. 231–247.

Publication of this paper sponsored by Committee on Pavement Rehabilitation.

Case Studies in Rehabilitation Strategy Development

MICHAEL I. DARTER AND KATHLEEN T. HALL

The performance and rehabilitation of jointed concrete pavements was recently investigated in a major national field study. Among the products of the research were detailed guidelines prepared to assist practicing engineers in determining when restoration was likely to be cost-effective, and when a structural overlay was required. The data base for this project included 95 sections of joint reinforced concrete pavement and joint plain concrete pavement in their first performance period. Thirteen of these sections were selected for use as case studies in rehabilitation strategy development. The sections were selected to cover the range of four major climatic zones of the United States, as well as a range of pavement conditions from good to poor (assessed on the basis of cracking, joint deterioration, joint faulting, pumping, and serviceability). The EXPEAR computer program was used to evaluate the current condition of each pavement section, predict its future condition without rehabilitation, and compare the predicted performance and cost-effectiveness of various rehabilitation strategies. The case studies demonstrated that restoration is the most cost-effective alternative for pavements that are structurally adequate and do not have concrete durability problems.

Restoration is a rehabilitation strategy that involves a combination of methods for repairing distress, improving ride quality, and extending pavement life without a structural overlay. Restoration techniques for jointed concrete pavements include the following:

1. Full-depth repair of joints, cracks, and corner breaks;
2. Partial-depth repair of spalls;
3. Grinding to remove faults and studded tire ruts and to improve surface friction;
4. Grooving to improve surface friction;
5. Subsealing to fill voids under slab corners;
6. Slabjacking to improve the pavement's longitudinal profile;
7. Load transfer restoration at joints and cracks;
8. Joint resealing;
9. Crack sealing;
10. Subdrainage improvement; and
11. Shoulder improvement.

Concrete pavement restoration typically involves a combination of several of these techniques. Over the past 25 years, many states have gained experience with restoration, and detailed information on design, construction, and performance of various restoration techniques is available from a variety of sources. (*1–4*)

M. I. Darter, ERES Consultants, Inc., 8 Dunlap Court, Savoy, Ill. 61874. K. T. Hall, University of Illinois at Urbana–Champaign, 1206 Newmark Lab, 205 N. Mathews, Urbana, Ill. 61801.

Little guidance is available, however, to assist the practicing engineer in determining whether a particular pavement is a good candidate for restoration, or whether another rehabilitation strategy would be more appropriate. Restoration has been applied to many pavements which were really in need of structural improvement. The result, even if the restoration is well designed and well constructed, is short rehabilitation life, high life cycle costs, and diminished confidence in the effectiveness of restoration among engineers and highway users. It is possible for practicing engineers to assess the appropriateness of restoration, using information available about the design and condition of a particular pavement section, rehabilitation performance prediction models, and rehabilitation cost data. The EXPEAR computer program can be used for the purpose of comparing rehabilitation strategies for 13 pavement projects across the United States and representing a wide range of pavement conditions.

PAVEMENT PERFORMANCE AND REHABILITATION NEEDS

Maintenance Versus Restoration

The success of restoration depends on good design and construction, but it also depends on application of restoration at the appropriate time in the performance life of a pavement. The earliest time that restoration should be done is relatively easy to identify. Early in a pavement's life, its condition is excellent and its rate of deterioration is slow. For several years, routine or preventative maintenance is more cost-effective than any rehabilitation strategy. Restoration is generally not warranted until distresses such as cracking, faulting, and joint spalling have developed to the point that they detract from the pavement's serviceability. When annual maintenance costs equal or exceed the equivalent annual cost of restoration, the restoration work is justified.

Restoration Versus Resurfacing

It is more difficult to identify the latest point in the pavement's life at which restoration is likely to be cost-effective, i.e., the point at which the pavement has carried so much traffic and sustained so much structural damage that an overlay is needed. It is conceivable that resurfacing may be done before this point and be more cost-effective than restoration, primarily because of the ability of overlays to reduce deflections and slow deterioration in the slab. Early resurfacing seldom oc-

curs, however, because of funding limitations. More frequently, restoration is performed some years after the time when it has the greatest potential to cost-effectively extend the pavement's life, and in some cases, after the time when a structural improvement is warranted. The longer the delay, the less likely it is that restoration will be able to compete with resurfacing in performance and cost-effectiveness.

Indicators of Structural Deficiency

The following is a list of key distresses and levels that should be considered in assessing structural damage in jointed concrete pavement. The critical values suggested are based on observations of joint plain concrete pavement (JPCP) and joint reinforced concrete pavement (JRCP) performance in previous studies (*4–6*) as well as from the data base, and from use of EXPEAR (*7*) to predict the performance of restoration on pavements with varying levels of deterioration.

1. Transverse cracking provides direct evidence of fatigue damage. In JRCP, low-severity cracks are considered a normal consequence of drying shrinkage after construction, and are not considered structural distresses. In JPCP, unless the joint spacing is too long, transverse cracking of any severity is evidence of structural damage. Suggested critical levels for transverse cracking are 10 percent slabs cracked or 70 cracks per mile (all severities) for JPCP, and 70 cracks per mile (medium or high severity) for JRCP.
2. Longitudinal cracking in highway pavements is almost always caused initially by factors other than traffic (e.g., poor joint construction or foundation movement), but under traffic it can deteriorate to such an extent that it constitutes structural damage. More than 500 ft of longitudinal cracking per mile is suggested as a critical level for both JPCP and JRCP.
3. Joint faulting and pumping are not generally considered structural distresses, but they are caused by traffic loads and are visible indications of progressive loss of joint load transfer and erosion of slab support. Suggested critical levels of joint faulting are 0.10 in. for JPCP and 0.25 in. for JRCP.
4. Corner breaks, which occur as a result of substantial erosion of slab support and high corner deflections, are definite indications of structural damage. The suggested critical level for corner breaks is 25 per mile for both JPCP and JRCP.
5. Transverse joint spalling that reduces the thickness of the slab at the joints should be considered structural damage because it diminishes the structural integrity of the slab and is progressive in nature. It is often caused by poor joint construction, dowel bar corrosion, D cracking, or reactive aggregates. Suggested critical levels for joint spalling are 50 spalled joints per mile (medium or high severity) for JPCP and 25 spalled joints per mile (medium or high severity) for JRCP.

If JRCP or JPCP exhibits levels of structural damage beyond those listed, the pavement has probably reached or passed the point at which the rate of deterioration begins to accelerate rapidly. At this stage, a structural improvement is most appropriate. Restoration work performed on a pavement that has deteriorated past this point is likely to provide a relatively short performance life under medium to heavy traffic conditions. Attempting to delay a structural improvement by continued patching may result in annual maintenance costs so high that they completely offset any savings achieved by the delay.

Although visible distress is a good indicator of structural damage, it cannot give a complete picture of the extent of underlying deterioration. Coring and deflection testing are strongly recommended on any project being seriously considered for rehabilitation.

PAVEMENT EVALUATION AND REHABILITATION USING EXPEAR

EXPEAR is a computerized system to assist highway engineers in project-level evaluation of concrete highway pavements, development of feasible rehabilitation strategies, and prediction of rehabilitation performance and cost-effectiveness. EXPEAR is intended for use in rehabilitation planning and design for high-volume (e.g., Interstate) conventional concrete pavements [JRCP, JPCP, and continuously reinforced concrete pavement (CRCP)]. EXPEAR was originally developed for the FHWA (*7*) and has been further developed with the support of the Illinois Department of Transportation (IDOT). Additional work on EXPEAR has been supported by the FHWA under this research study (*8*). Additional information on the development of EXPEAR is available (*9–11*). The current version is EXPEAR 1.4, which possesses the capabilities to do life cycle cost analysis and delay rehabilitation up to 5 years.

EXPEAR has been developed in the form of a knowledge-based expert system, which simulates a consultation between an engineer and an expert in concrete pavements. EXPEAR uses information about the pavement to guide the engineer through evaluation of a pavement's present condition and development of one or more feasible rehabilitation strategies. The procedure was developed through extensive interviewing of authorities on concrete pavement performance. In addition, predictive models are used to estimate future pavement performance with and without rehabilitation.

CASE STUDIES

Sections Evaluated

The data base developed under this contract includes 95 sections of JPCP and JRCP in their first performance period (*6*). Thirteen of these sections were selected for evaluation with the EXPEAR program. The sections, both JRCP and JPCP and located in all four major climatic zones, are presented in Table 1. The condition of each section was subjectively assessed as good, fair, or poor on the basis of observed distress and serviceability. Pavements rated as good had little or no cracking or joint deterioration, minimal joint faulting, no pumping, and a present serviceability rating (PSR) of 3.5 or more. Fair pavements had at least one of the following: moderate cracking or joint deterioration because of D cracking or reactive aggregate distress), moderate to high faulting (exceeding the critical level), visible pumping, or PSR less then 3.5. Pavements rated as poor had at least two and in most

TABLE 1 CASE STUDIES SELECTED FROM THE FHWA-ERES DATA BASE

Section	Climate	Type	Condition	Cracking (no/mile)	Joint Deterioration (no/mile)	Joint Faulting (inch)	Pumping	PSR (0-5)
AZ 1-6	DNF	JPCP	Good	0	5	0.01	None	3.5
FL 2	WNF	JPCP	Good	0	0	0.01	None	3.7
MI 3	WF	JRCP	Good	0	0	0.02	None	4.8
MN 3	DF	JRCP	Good	0	0	0.00	None	3.8
MN 2-3	DF	JRCP	Good	0	5	0.05	None	4.0
CA 6	DNF	JPCP	Fair	0	2	0.15	None	3.4
NC 1-8	WNF	JPCP	Fair	20	5	0.22	None	3.3
NC 2	WNF	JPCP	Fair	0	0	0.02	High	4.2
NJ 2	WF	JRCP	Fair	24	14	0.06	None	3.8
CA 1-3	DNF	JPCP	Poor	30	10	0.10	Medium	3.0
MI 4-1	WF	JRCP	Poor	222	0	0.12	None	2.4
MI 1-10b	WF	JPCP	Poor	0	219	0.19	Low	2.8
MN 1-8	DF	JRCP	Poor	102	141	0.09	None	3.4

Notes: Condition rating (good, fair, or poor) is subjective assessment of overall pavement condition, based on visible distress and PSR in outer traffic lane.

Sections CA 6 and CA 1-3 have low-severity reactive aggregate distress.

cases three or four of the following: substantial cracking or joint deterioration (exceeding critical levels), high faulting (exceeding the critical level), visible pumping, and PSR less than 3.0.

Evaluation Procedure

All EXPEAR input data required for each section were obtained from the data base. The following steps were carried out for each of the 13 projects.

1. Input data were verified by state employees and project team members familiar with the sections.
2. A pavement evaluation was concluded and future performance was predicted without any rehabilitation.
3. The following rehabilitation alternatives were considered:

- Restoration;
- Resurfacing options [conventional asphalt concrete (AC) overlay, crack and seat AC overlay, saw and seal AC overlay, bonded PCC overlay, and unbonded PCC overlay]; and
- Reconstruction with JPCP or JRCP.

4. Rehabilitation performance was predicted using models contained in EXPEAR for distress after restoration (faulting, cracking, joint spalling, and PSR), resurfacing (rutting and reflective cracking for AC overlays; faulting, cracking, and joint spalling for PCC overlays) and reconstruction (faulting, cracking, joint spalling, and PSR).
5. Life cycle costs were estimated using Illinois statewide average costs. The costs include traffic control and other miscellaneous costs normally associated with the alternatives (guardrails, signs, etc.).

Because of the highly variable nature of pavement rehabilitation costs throughout the United States, the cost analyses should be considered only as examples for comparison of the relative cost-effectiveness of various strategies.

All of the projects were surveyed in 1987 and analyzed using EXPEAR in 1989. This 2-year delay is taken into account in the analyses: EXPEAR calibrates the performance prediction models to the 1987 distress and levels, predicts the distress levels in 1989, and uses these levels to compute rehabilitation quantities and costs. For some projects in very good condition, the rehabilitation was delayed an additional few years in the analysis.

AZ 1–6, Good Condition

Table 2 presents the results of the analysis of AZ 1–6, a section of 9-in. JPCP located on Route 360 near Phoenix, Arizona, in a dry, nonfreezing climatic zone. The pavement has carried about 2 million 18-kip equivalent single-axle loads (ESALs) in the outer traffic lane since its construction in 1981. When surveyed in 1987, its PSR value was 3.5, and the only notable distress was some joint spalling. Joint resealing had been attempted, without much success, a year earlier.

Given the low truck level on this pavement section, joint spalling on this pavement section is not predicted to increase significantly over the 20-year analysis period considered, and no other distresses are predicted to reach critical levels. As Table 2 indicates, the strategy with the lowest annual cost is restoration. Restoration could probably also safely be delayed for several years.

FL 2, Good Condition

Table 3 presents the results of the analysis of FL 2, a section of 13-in. JPCP located on I-75 near Tampa, Florida, in a wet, nonfreezing climatic zone. The pavement has carried about 2 million ESALs in the outer traffic lane since its construction

TABLE 2 RESULTS OF EXPEAR ANALYSIS OF AZ 1–6

PAVEMENT DESIGN

Highway:	Route 360 near Phoenix
Pavement type:	9-inch JPCP
Year constructed:	1981
Joint spacing:	15-13-15-17 feet
Dowels:	Undoweled
Base:	4-inch lean concrete
Subgrade:	A-6
Shoulders:	Tied PCC outer, AC inner
Drains:	No drains

TRAFFIC

Current 2-way ADT:	97,770
Percent trucks:	3.8
Lanes each direction:	3
Accumulated ESAL:	2.01 million (outer lane)

EXISTING PAVEMENT CONDITION

Year surveyed:	1987
PSR:	3.5
Deteriorated cracks:	0/mile
Deteriorated joints:	5/mile (outer lane) 20/mile (middle lane)
Joint faulting:	0.01 inch
Longitudinal cracks:	0 feet/mile
Pumping:	None
PCC surface:	Tined, not polished
Joint sealant damage:	Medium severity (resealed 1986)
"D" cracking:	None
Reactive aggregate:	None
Settlements/heaves:	None
Shoulder condition:	Excellent
Lane/shoulder joint:	Fair

PHYSICAL TESTING RECOMMENDATIONS

No physical testing warranted.

FUTURE CONDITION WITHOUT REHABILITATION

Some joint deterioration is present, but no significant increase of any type of deterioration is predicted over the next 20-year period.

CONSEQUENCE OF DELAYING REHABILITATION

Rehabilitation may safely be delayed. Some joint resealing and joint spall repair is recommended.

PREDICTED LIFE OF REHABILITATION

Alternative	Years	Unacceptable
Restoration	20+	
3-inch ACOL	7	Ref. cracking
5-inch crack/seat AC OL	6	Rutting
3-inch saw/seal AC OL	8	Rutting
3-inch bonded PCC OL	20+	
8-inch unbonded PCC OL	20+	
9-inch reconstruction	20+	

RESULTS OF LIFE-CYCLE COST ANALYSIS

Alternative	Initial Cost	Annual Cost
Restoration	59,200	3,800
3-inch AC OL	274,600	41,500
5-inch crack/seat AC OL	273,200	47,500
3-inch saw/seal AC OL	284,300	38,200
3-inch bonded PCC OL	368,800	23,400
8-inch unbonded PCC OL	514,200	32,600
9-inch reconstruction	506,000	32,000

Cost per 2-lane mile, based on predicted lives shown above (20 years for bonded overlay, unbonded overlay, and reconstruction) and discount rate of 3 percent.

RECOMMENDED REHABILITATION (1989)

Minor restoration work (spall repair and joint resealing) could be done to improve rideability and prevent water and incompressible infiltration.

Rehabilitation Techniques	Quantity
Full-depth repair of joints	200 sy
Reseal transverse joints	9450 ft
Reseal lane/shoulder joints	10560 ft

Quantity per 2-lane mile and shoulders.

in 1986. When surveyed in 1987, its PSR was 3.7, it had no cracking or joint spalling, and faulting at transverse joints averaged only 0.01 in. The only distress noted was low-severity joint sealant damage.

As Table 3 indicates, the only rehabilitation work needed is joint resealing, which could be done now or delayed a few years with no adverse affects. No other rehabilitation is predicted to be required for this pavement for the next 20 years. It is obvious that none of the available overlay strategies could compete in cost-effectiveness with restoration over the 20-year analysis period.

MI 3, Good Condition

Table 4 presents the results of the analysis of MI 3, a section of 10-in. JRCP located on I-94 near Marshall, Michigan, in a wet, freezing climatic zone. The pavement has carried about 2.8 million ESALs in the outer traffic lane since its construction in 1986. When surveyed in 1987, its PSR was 4.8, it had no crack or joint deterioration, and minimal faulting. No significant distresses were noted. EXPEAR predicted that the condition of the pavement would be acceptable for at least another 9 years. No restoration or other rehabilitation is warranted now. However, the pavement was underdesigned for the traffic levels anticipated on I-94, and full-depth repair of deteriorated joints and cracks will probably be needed in the future.

MN 3, Good Condition

Table 5 presents the results of the analysis of MN 3, a section of 9-in. JRCP located on I-90 near Austin, Minnesota, in a dry, freezing climatic zone. The pavement has carried about 1.5 million ESALs in the outer traffic lane since its construction in 1984. When surveyed in 1987, its PSR was 3.8, it had no cracking or joint deterioration, and minimal faulting. The only problem identified in EXPEAR's evaluation of the pavement was a possible subdrainage deficiency. As Table 5 indicates, subdrainage improvements could be done at low cost to ensure good long-term performance. There is no predicted need for other restoration work or other rehabilitation over the 20-year analysis period.

MN 2–3, Good Condition

Table 6 presents the results of the analysis of MN 2–3, a section of 9-in. JRCP located on I-90 near Albert Lea, Minnesota, in a dry, freezing climatic zone. The pavement has carried about 2.8 million ESALs in the outer traffic lane since its construction in 1976. When surveyed in 1987, its PSR was 4.0, it had no cracking, some joint spalling (5 per mile), and some joint faulting (0.05 in.). The transverse joints and lane-shoulder joints are poorly sealed.

As Table 6 indicates, restoration could be performed now at low cost, or could safely be delayed a few years. The costs

TABLE 3 RESULTS OF EXPEAR ANALYSIS OF FL 2

PAVEMENT DESIGN

Highway:	I-75 near Tampa
Pavement type:	13-inch JPCP, 14-foot lanes
Year constructed:	1986
Joint spacing:	13-12-18-19 feet
Dowels:	Doweled, 1.25-inch diameter
Base:	6-inch untreated aggregate
Subgrade:	A-3
Shoulders:	Tied PCC
Drains:	No drains present

TRAFFIC

Current 2-way ADT:	28,700
Percent trucks:	20.0
Lanes each direction:	2
Accumulated ESAL:	2.00 million (outer lane)

EXISTING PAVEMENT CONDITION

Year surveyed:	1987
PSR:	3.7
Deteriorated cracks:	0/mile
Deteriorated joints:	0/mile
Joint faulting:	0.01 inch
Longitudinal cracks:	0 feet/mile
Pumping:	None
PCC surface:	Tined, not polished
Joint sealant damage:	Low severity
"D" cracking:	None
Reactive aggregate:	None
Settlements/heaves:	None
Shoulder condition:	Excellent
Lane/shoulder joint:	Good

Overall: The only deficiency is an inadequate joint sealant reservoir width for the existing sealant type.

PHYSICAL TESTING RECOMMENDATIONS
No physical testing warranted.

FUTURE CONDITION WITHOUT REHABILITATION

Serviceability:	> 3.5 for 20 years
Faulting:	< 0.10 inch for 20 years
Joint deterioration:	0/mile for 20 years
Cracking:	1/mile in 20 years

CONSEQUENCE OF DELAYING REHABILITATION
Other than resealing transverse joints, no major rehabilitation is required now or over the next 20 years. Resealing may be delayed a few years with no adverse effects.

PREDICTED LIFE OF REHABILITATION

Alternative	Years	Unacceptable
Restoration	20+	

RESULTS OF LIFE-CYCLE COST ANALYSIS

Alternative	Initial Cost	Annual Cost
Restoration	19,900	1,100

Cost per 2-lane mile, based on predicted life shown above (20 years) and discount rate of 3 percent.

RECOMMENDED REHABILITATION (1989)
Reseal transverse joints to correct sealant reservoir shape factor.

Rehabilitation Technique	Quantity
Reseal transverse joints	11372 ft

Quantity per 2-lane mile and shoulders.

TABLE 4 RESULTS OF EXPEAR ANALYSIS OF MI 3

PAVEMENT DESIGN

Highway:	I-94 near Marshall
Pavement type:	10-inch JRCP
Year constructed:	1986
Joint spacing:	41 feet
Joint sealant:	Preformed
Dowels:	1.25-inch diameter
Reinforcement:	0.168 in^2/ft
Base:	4-inch permeable untreated aggregate
Subgrade:	A-4
Shoulders:	Tied PCC
Drains:	Yes

TRAFFIC

Current 2-way ADT:	31,300
Percent trucks:	22
Lanes each direction:	2
Accumulated ESAL:	2.77 million (outer lane)

EXISTING PAVEMENT CONDITION (outer lane)

Year surveyed:	1987
PSR:	4.8
Deteriorated cracks:	0/mile
Crack faulting:	0.0 inch
Deteriorated joints:	0/mile
Joint faulting:	0.02 inch
Longitudinal cracks:	0 feet/mile
Long. joint spall:	0 feet
Pumping:	None
PCC surface:	Tined
Joint sealant damage:	Low
"D" cracking:	None
Settlements/heaves:	None
Shoulder condition:	Good
Lane/shoulder joint:	Good

Overall: Traffic lanes and shoulders show no deterioration.

PHYSICAL TESTING RECOMMENDATIONS
No physical testing warranted.

FUTURE CONDITION WITHOUT REHABILITATION

Serviceability:	PSR > 3.0 over 20 years
Deteriorated joints:	> 27/mile in 2003
Deteriorated cracks:	> 75/mile in 1996
Faulting:	< 0.25 inch over 20 years

CONSEQUENCE OF DELAYING REHABILITATION
None.

PREDICTED LIFE OF REHABILITATION
No rehabilitation needed for at least 9 years.

RESULTS OF LIFE-CYCLE COST ANALYSIS
None.

RECOMMENDED REHABILITATION
No rehabilitation is needed for at least 9 years. At that time, full-depth repair of joints and cracks will be needed. The pavement was underdesigned for the very heavy traffic on I-94.

TABLE 5 RESULTS OF EXPEAR ANALYSIS OF MN 3

PAVEMENT DESIGN

Highway:	I-90 near Austin
Pavement type:	9-inch JRCP
Year constructed:	1984
Joint spacing:	27 feet
Dowels:	1-inch diameter
Reinforcement:	0.054 in^2/ft
Base:	4-inch untreated
Subgrade:	A-4
Shoulders:	AC
Drains:	None

TRAFFIC

Current 2-way ADT:	10,600
Percent trucks:	15
Lanes each direction:	2
Accumulated ESAL:	1.5 million (outer lane)

EXISTING PAVEMENT CONDITION (outer lane)

Year surveyed:	1987
PSR:	3.8
Deteriorated cracks:	0/mile
Crack faulting:	0.00 inch
Deteriorated joints:	0/mile
Joint faulting:	0.02 inch
Longitudinal cracks:	0 feet/mile
Pumping:	None
PCC surface:	Tined
Joint sealant damage:	Low severity
"D" cracking:	None
Settlements/heaves:	None
Shoulder condition:	Good
Lane/shoulder joint:	Poor

Overall: Only minor deterioration. A subdrainage deficiency is indicated by dense base, impermeable subgrade, inadequate ditches and heavy traffic.

PHYSICAL TESTING RECOMMENDATIONS

No deflection testing needed. Coring at center slab. Core examination and materials testing, including permeability of base. No roughness or skid testing needed.

FUTURE CONDITION WITHOUT REHABILITATION

Serviceability:	PSR < 3.0 in 2005
Deteriorated joints:	> 0.27/mile in 2006
Deteriorated cracks:	> 75/mile in 2006
Pumping:	Medium in 2001

CONSEQUENCE OF DELAYING REHABILITATION

Subdrainage improvement would delay future pumping and related distresses.

PREDICTED LIFE OF REHABILITATION (1992)

Alternative	Years	Unacceptable
Restoration	20+	

RESULTS OF LIFE-CYCLE COST ANALYSIS

Alternative	Initial Cost	Annual Cost
Restoration	37,800	2,200

Cost per 2-lane mile, based on predicted life (20 years) and discount rate of 3 percent.

RECOMMENDED REHABILITATION

Subdrainage improvement would extend life of pavement.

Rehabilitation Techniques	Quantity
Install subdrains	5280 ft

Quantity per 2-lane mile and shoulders.

TABLE 6 RESULTS OF EXPEAR ANALYSIS OF MN 2–3

PAVEMENT DESIGN

Highway:	I-90 near Albert Lea
Pavement type:	9-inch JRCP
Year constructed:	1976
Joint spacing:	27 feet
Dowels:	1-inch diameter
Reinforcement:	0.097 in^2/ft
Base:	5-inch untreated
Subgrade:	A-2
Shoulders:	AC
Drains:	None

TRAFFIC

Current 2-way ADT:	3,900
Percent trucks:	20
Lanes each direction:	2
Accumulated ESAL:	2.78 million (outer lane)

EXISTING PAVEMENT CONDITION (outer lane)

Year surveyed:	1987
PSR:	4.0
Deteriorated cracks:	0/mile
Crack faulting:	0.00 inch
Deteriorated joints:	5/mile
Joint faulting:	0.05 inch
Longitudinal cracks:	0 feet/mile
Pumping:	None
PCC surface:	Tined
Joint sealant damage:	Medium severity
"D" cracking:	None
Settlements/heaves:	None
Shoulder condition:	Good
Lane/shoulder joint:	Poor

Overall: Traffic lanes show some joint deterioration and faulting. Shoulders are in good condition, except the lane/shoulder joint.

PHYSICAL TESTING RECOMMENDATIONS

Deflection testing not needed. No coring or materials testing needed. No roughness or skid testing needed.

FUTURE CONDITION WITHOUT REHABILITATION

Deteriorated joints:	> 27/mile in 2004

CONSEQUENCE OF DELAYING REHABILITATION

Joint deterioration may increase if joint sealant is not replaced. Excessive water may enter section if longitudinal lane/shoulder joint not resealed.

PREDICTED LIFE OF REHABILITATION (1992)

Alternative	Years	Unacceptable
Restoration	20+	Joint deterioration

RESULTS OF LIFE-CYCLE COST ANALYSIS

Alternative	Initial Cost	Annual Cost
Restoration	44,500	3,100

Cost per 2-lane mile, based on predicted life (20 years) and discount rate of 3 percent.

RECOMMENDED REHABILITATION (1992)

Minor restoration work in 5 years may extend life of pavement.

Restoration Technique	Quantity
Full-depth repair joints	133 sy
Full-depth repair cracks	25 sy
Reseal transverse joints	4493 ft
Reseal lane/shoulder joint	10560 ft

Quantity per 2-lane mile and shoulders.

and quantities presented in Table 6 are for restoration work in 1992.

CA 6, Fair Condition

Table 7 presents the results of the analysis of CA 6, a section of 9-in. JPCP located on Route 14 near Solemint, California, in a dry, nonfreezing climatic zone. The pavement has carried about 4.4 million ESALs in the outer traffic lane since its construction in 1980. When surveyed in 1987, its PSR was 3.4, it had no transverse cracking, and some joint spalling and longitudinal cracking. Faulting at transverse joints averaged 0.15 in. and the joints were not sealed. The PCC slab exhibited low-severity reactive aggregate distress.

As Table 7 indicates, EXPEAR predicted a relatively short life for restoration (6 years), primarily because more joint deterioration is predicted in the future as a result of the reactive aggregate. As a result, three overlay options have lower equivalent annual costs than restoration. The alternative with the lowest annual cost is a 3-in. AC overlay with sawed and sealed joints.

NC 1–8, Fair Condition

Table 8 presents the results of the analysis of NC 1–8, a section of 9-in. JPCP located on I-95 near Rocky Mount, North Carolina, in a wet, nonfreezing climatic zone. The pavement has carried about 9.1 million ESALs in the outer traffic lane since its construction in 1967. When surveyed in 1987, its PSR was 3.3, it had some transverse cracking (20 per mile), some joint spalling (5 per mile), and faulting of 0.22 in. at transverse joints.

Although faulting is already high, the PSR is currently acceptable, and was predicted by EXPEAR to remain above the critical level of 3.0 for another 5 years. Rehabilitation could be performed now, or could be delayed a few years. As Table 8 indicates, restoration and overlay alternatives have comparable predicted lives, but restoration has the lowest annual cost.

NC 2, Fair Condition

Table 9 presents the results of the analysis of NC 2, a section of 11-in. JPCP located on I-85 near Greensboro, North Carolina, in a wet, nonfreezing climatic zone. The pavement has carried about 5.8 million ESALs in the outer traffic lane since its construction in 1982. When surveyed in 1987, its PSR was 4.2, it had no transverse cracking or joint spalling, and minimal faulting. The only noted distresses were high-severity pumping and low-severity joint sealant damage, including a drainage deficiency. As Table 9 indicates, EXPEAR recommended that subdrainage improvements not be delayed. Excellent performance is predicted for restoration over the 20-year analysis period, and the annual cost is very low.

NJ 2, Fair Condition

Table 10 presents the results of the analysis of NJ 2, a section of 10-in. JRCP located on Route 130 near Yardsville, New Jersey, in a wet, freezing climatic zone. The pavement has

TABLE 7 RESULTS OF EXPEAR ANALYSIS OF CA 6

PAVEMENT DESIGN

Highway:	Route 14 near Solemint
Pavement type:	9-inch JPCP
Year constructed:	1980
Joint spacing:	12-13-15-14 feet
Dowels:	Undoweled
Base:	4.2-inch lean concrete
Subgrade:	A-2
Shoulders:	AC
Drains:	Drains present

TRAFFIC

Current 2-way ADT:	46,000
Percent trucks:	9.0
Lanes each direction:	3
Accumulated ESAL:	4.43 million (outer lane)

EXISTING PAVEMENT CONDITION

Year surveyed:	1987
PSR:	3.4
Deteriorated cracks:	0/mile
Deteriorated joints:	2/mile
Joint faulting:	0.15 inch
Longitudinal cracks:	51 feet/mile
Pumping:	None
PCC surface:	Tined, not polished
Joint sealant damage:	High severity (not sealed)
"D" cracking:	None
Reactive aggregate:	Low severity
Settlements/heaves:	None
Shoulder condition:	Excellent
Lane/shoulder joint:	Poor

PHYSICAL TESTING RECOMMENDATIONS

Coring at representative deteriorated transverse joints. Coring at longitudinal joint and crack. Test strength of PCC surface and lean concrete base. Observe erosion at top of lean concrete base. Petrographic exam of PCC for aggregate reactivity.

FUTURE CONDITION WITHOUT REHABILITATION

Faulting: > 0.10 inch in 1987

CONSEQUENCE OF DELAYING REHABILITATION

Faulting is currently unacceptable.

PREDICTED LIFE OF REHABILITATION

Alternative	Years	Unacceptable
Restoration	6	Jt. deterioration
3-inch AC OL	8	Rutting, rf crck
5-inch crack/seat AC OL	9	Rutting
3-inch saw/seal AC OL	12	Rutting, rf crck
7-inch unbonded PCC OL	20+	

RESULTS OF LIFE-CYCLE COST ANALYSIS

Alternative	Initial Cost	Annual Cost
Restoration	248,800	43,300
3-inch AC OL	312,900	42,000
5-inch crack/seat AC OL	406,800	49,200
3-inch saw/seal AC OL	335,800	31,800
7-inch unbonded PCC OL	619,400	39,200

Cost per 2-lane mile, based on predicted lives shown above (20 years for unbonded overlay) and discount rate of 3 percent.

RECOMMENDED REHABILITATION (1989)

3-inch AC overlay with sawed and sealed joints is the most cost-effective alternative, with a life of about 12 years.

Rehabilitation Technique	Quantity
Full-depth repair of joints	434 sy
Full-depth repair of cracks	10 sy
Reseal transverse joints	9910 ft
Reseal lane/shoulder joint	10560 ft
3-inch saw/seal AC OL	22293 sy

Quantity per 2-lane mile and shoulders.

TABLE 8 RESULTS OF EXPEAR ANALYSIS OF NC 1–8

PAVEMENT DESIGN

Highway:	I-95 near Rocky Mount
Pavement type:	9-inch JPCP
Year constructed:	1967
Joint spacing:	30 feet
Dowels:	Undoweled
Base:	4-inch untreated aggregate
Subgrade:	A-2
Shoulders:	AC
Drains:	No drains present

TRAFFIC

Current 2-way ADT:	19,100
Percent trucks:	9.0
Lanes each direction:	2
Accumulated ESAL:	9.14 million (outer lane)

EXISTING PAVEMENT CONDITION

Year surveyed:	1987
PSR:	3.3
Deteriorated cracks:	20/mile
Deteriorated joints:	5/mile
Joint faulting:	0.22 inch
Longitudinal cracks:	0 feet/mile
Pumping:	None
PCC surface:	Tined, not polished
Joint sealant damage:	Low severity
"D" cracking:	None
Reactive aggregate:	None
Settlements/heaves:	None
Shoulder condition:	Good
Lane/shoulder joint:	Poor

Overall: Excessive faulting indicates a load transfer deficiency. Some joint and crack deterioration present, reducing serviceability.

PHYSICAL TESTING RECOMMENDATIONS

Deflection test for structure analysis and void detection. Core at center of slab to obtain material samples. Core representative deteriorated joints. Test strength of PCC cores.

FUTURE CONDITION WITHOUT REHABILITATION

Serviceability:	PSR < 3.0 in 1994
Faulting:	> 0.10 inch in 1987
Joint deterioration:	5/mile for 20 years
Cracking:	24/mile in 20 years

CONSEQUENCE OF DELAYING REHABILITATION

Faulting is already high, but PSR is rated above 3.0. A few years of delay can be tolerated.

PREDICTED LIFE OF REHABILITATION

Alternative	Years	Unacceptable
Restoration	14	Faulting
3-inch AC OL	10	Ref. cracking
5-inch crack/seat AC OL	14	Ref. cracking
3-inch saw/seal AC OL	15	Ref. cracking
7-inch unbonded PCC OL	20+	
11-inch reconstruction	20+	

RESULTS OF LIFE-CYCLE COST ANALYSIS

Alternative	Initial Cost	Annual Cost
Restoration	105,000	6,000
3-inch AC OL	303,000	28,900
5-inch crack/seat AC OL	428,000	23,100
3-inch saw/seal AC OL	313,000	21,400
7-inch unbonded PCC OL	635,000	30,200
11-inch reconstruction	506,000	29,300

Cost per 2-lane mile, based on predicted lives shown above (20 years for unbonded overlay and reconstruction) and discount rate of 3 percent.

RECOMMENDED REHABILITATION (1989)

Technique	Quantity
Grinding	7040 sy
Full-depth repair of cracks	210 sy
Full-depth repair of joints	80 sy
Reseal transverse joints	4106 ft
Reseal lane/shoulder joint	10560 ft

Quantity per 2-lane mile and shoulders.

TABLE 9 RESULTS OF EXPEAR ANALYSIS OF NC 2

PAVEMENT DESIGN

Highway:	I-85 near Greensboro
Pavement type:	11-inch JPCP
Year constructed:	1982
Joint spacing:	19-18-25-23 feet
Dowels:	Doweled, 1.38-inch diameter
Base:	5-inch lean concrete
Subgrade:	A-4
Shoulders:	Tied PCC
Drains:	Drains present

TRAFFIC

Current 2-way ADT:	26,000
Percent trucks:	17.0
Lanes each direction:	2
Accumulated ESAL:	5.76 million (outer lane)

EXISTING PAVEMENT CONDITION (outer lane)

Year surveyed:	1987
PSR:	4.2
Deteriorated cracks:	0/mile
Deteriorated joints:	0/mile
Joint faulting:	0.02 inch
Longitudinal cracks:	0 feet/mile
Pumping:	High
PCC surface:	Tined, not polished
Joint sealant damage:	Low severity
"D" cracking:	None
Reactive aggregate:	None
Settlements/heaves:	None
Shoulder condition:	Excellent
Lane/shoulder joint:	Poor

Overall: Although drains are present, high-severity pumping indicates a drainage deficiency.

PHYSICAL TESTING RECOMMENDATIONS

Deflection test slab corners for void detection. Core at center of slab to obtain material samples. Examine stabilized base cores for erosion. Evaluate drainability (gradation, permeability) of subgrade.

FUTURE CONDITION WITHOUT REHABILITATION

Serviceability:	PSR = 3.0 in 20 years
Faulting:	< 0.10 inch for 20 years
Joint deterioration:	0/mile for 20 years
Cracking:	7/mile in 20 years

CONSEQUENCE OF DELAYING REHABILITATION

Subdrainage and slab support improvements are required now.

PREDICTED LIFE OF REHABILITATION

Alternative	Years	Unacceptable
Restoration	20+	

RESULTS OF LIFE-CYCLE COST ANALYSIS

Alternative	Initial Cost	Annual Cost
Restoration	29,300	1,900

Cost per 2-lane mile, based on predicted life shown above (20 years) and discount rate of 3 percent.

RECOMMENDED REHABILITATION (1989)

Technique	Quantity
Repair longitudinal subdrains	5280 ft
Subseal at joints	208 cf grout
Reseal lane/shoulder joints	10560 ft

Quantity per 2-lane mile and shoulders.

TABLE 10 RESULTS OF EXPEAR ANALYSIS OF NJ 2

PAVEMENT DESIGN

Highway:	Route 130 near Yardville
Pavement type:	10-inch JRCP
Year constructed:	1951
Joint spacing:	78 feet
Joint sealant:	Expansion
Dowel diameter:	1.25-inch stainless steel clad
Reinforcement:	0.168 in^2/ft
Base:	5-inch untreated aggregate
Subgrade:	A-4
Shoulders:	AC
Drains:	None

TRAFFIC

Current 2-way ADT:	24,650
Percent trucks:	22
Lanes each direction:	2
Accumulated ESAL:	34.8 million (outer lane)

EXISTING PAVEMENT CONDITION (outer lane)

Year surveyed:	1987
PSR:	3.8
Deteriorated cracks:	24/mile
Crack faulting:	0.02 inch
Deteriorated joints:	14/mile
Joint faulting:	0.06 inch
Longitudinal cracks:	10 feet/mile
Long. joint spall:	14 feet
Pumping:	None
PCC surface:	Not polished
Joint sealant damage:	High severity
"D" cracking:	None
Settlements/heaves:	None
Shoulder condition:	Good
Lane/shoulder joint:	Good

Overall: Some transverse crack and joint deterioration. Some faulting at joints and cracks. Shoulders are in good condition. Subdrainage deficiency indicated due to dense-graded aggregate base, A-4 subgrade, inadequate ditch depth and heavy traffic. Joint sealant is in poor condition.

PHYSICAL TESTING RECOMMENDATIONS

Deflection testing needed for structural analysis and void detection. Coring and materials testing needed for assessing extent of deterioration. Materials testing for base permeability.

FUTURE CONDITION WITHOUT REHABILITATION

Serviceability:	PSR < 3.0 in 2003
Deteriorated joints:	> 27/mile in 1990
Deteriorated cracks:	> 75/mile in 1989

CONSEQUENCE OF DELAYING REHABILITATION

This is a very old pavement that has carried a large amount of traffic and is now deteriorating (cracking, joint deterioration and faulting). The pavement has some potential for restoration if done soon.

PREDICTED LIFE OF REHABILITATION

Alternative	Years	Unacceptable
Restoration	8	Joint/crack deterioration
3-inch AC OL	6	Ref. cracking, rutting
5-inch crack/seat AC OL	10	Rutting
9-inch unbonded PCC OL	14	Jt deterioration, cracking
12-inch reconstruction	20	Jt deterioration, cracking

RESULTS OF LIFE-CYCLE COST ANALYSIS

Alternative	Initial Cost	Annual Cost
Restoration	182,000	24,400
3-inch AC OL	423,900	73,800
5-inch crack/seat AC OL	488,300	54,000
9-inch unbonded PCC OL	730,000	60,900
12-inch reconstruction	618,800	42,700

Cost per 2-lane mile, based on predicted lives and discount rate of 3 percent. Since shoulders are in good condition, shoulder removal and replacement not included in cost of reconstruction.

RECOMMENDED REHABILITATION (1990)

The restoration alternative is the most cost-effective. If a life of 8 years is acceptable, restoration is recommended. If not, reconstruction is recommended.

Restoration Techniques	Quantity
Full-depth repair joints	337 sy
Full-depth repair cracks	701 sy
Reseal transverse joints	1108 ft
Install subdrains (both lanes)	10,560 ft

carried about 35 million ESALs in the outer traffic lane since its construction in 1951. When surveyed in 1987, its PSR was 3.8, it had 24 deteriorated transverse cracks per mile, 14 deteriorated joints per mile, and some faulting at cracks and joints. High-severity joint sealant damage was also noted.

On the basis of the observed distress and heavy truck traffic, EXPEAR predicted that the pavement's condition would remain acceptable for only another few years. As Table 10 indicates, restoration in 1989 would have the lowest annual cost of all of the alternatives, and predicted life of 8 years. If rehabilitation were delayed beyond that time, overlay or reconstruction options would probably provide lower annual costs and better long-term performance.

CA 1–3, Poor Condition

Table 11 presents the results of the analysis of CA 1–3, a section of 8.4-in. JPCP located on I-5 near Tracy, California, in a dry, nonfreezing climatic zone. The pavement has carried about 7.6 million ESALs in the outer traffic lane since its construction in 1971. When surveyed in 1987, its PSR was 3.0, it had 30 cracks per mile, 10 spalled joints per mile, and 500 ft of longitudinal cracking per mile. Faulting at transverse joints averaged 0.10 in., the joints were not sealed, and medium-severity pumping was evident. The PCC slab exhibited low-severity reactive aggregate distress.

Because the condition of the project is already unacceptable, rehabilitation should not be delayed. As Table 11 indicates, the annual cost of restoration is similar to that of an unbonded overlay or reconstruction, but the predicted life of restoration is fairly short. A significant unknown is the rate of progression of reactive aggregate distress in the concrete. Coring, strength testing, and petrographic examination of the concrete were recommended by EXPEAR to assess the aggregate's reactivity. Restoration is recommended only if the reactive aggregate distress is not projected to progress further. Otherwise, an unbonded PCC overlay or reconstruction is recommended.

MI 4–1, Poor Condition

Table 12 presents the results of the analysis of MI 4–1, a section of 9-in. JRCP located on I-69 near Charlotte, Michigan, in a wet, freezing climatic zone. The pavement has carried about 4.4 million ESALs in the outer traffic lane since it construction in 1973. When surveyed in 1987, its PSR was 2.4, it had extensive transverse crack deterioration (222 per mile), moderate faulting (0.08 in. at cracks, 0.12 in. at joints), and medium-severity joint sealant damage.

The pavement needs immediate rehabilitation. As Table 12 indicates, restoration is a poor rehabilitation choice, in terms of both performance life and annual cost. The crack and seat AC overlay, saw and seal AC overlay, and bonded and unbonded PCC overlay options are all very close in predicted life and annual cost.

TABLE 11 RESULTS OF EXPEAR ANALYSIS OF CA 1–3

PAVEMENT DESIGN

Highway:	I-5 near Tracy
Pavement type:	8.4-inch JPCP
Year constructed:	1971
Joint spacing:	12-13-19-16 feet
Dowels:	Undoweled
Base:	5.4-inch cement-treated
Subgrade:	A-1
Shoulders:	AC
Drains:	No drains present

TRAFFIC

Current 2-way ADT:	13,000
Percent trucks:	19.0
Lanes each direction:	2
Accumulated ESAL:	7.62 million (outer lane)

EXISTING PAVEMENT CONDITION

Year surveyed:	1987
PSR:	3.0
Deteriorated cracks:	30/mile
Deteriorated joints:	10/mile
Joint faulting:	0.10 inch
Longitudinal cracks:	500 feet/mile
Pumping:	Medium
PCC surface:	Tined, not polished
Joint sealant damage:	High severity (not sealed)
"D" cracking:	None
Reactive aggregate:	Low severity
Settlements/heaves:	None
Shoulder condition:	Excellent
Lane/shoulder joint:	Poor

Overall: Significant joint deterioration, slab cracking and joint faulting causes roughness. Subdrainage deficiency exists.

PHYSICAL TESTING RECOMMENDATIONS

Deflection test for structure analysis and void detection. Core PCC surface and stabilized base at center of slab. Core representative deteriorated joints and cracks. Core longitudinal joint and crack. Test strength of PCC surface and stabilized base. Evaluate drainability (gradation, permeability) of subgrade. Petrographic exam of PCC for aggregate reactivity.

FUTURE CONDITION WITHOUT REHABILITATION

Serviceability:	PSR = 3.0 in 1987
Faulting:	0.10 inch in 1987
Pumping:	Medium in 1987

CONSEQUENCE OF DELAYING REHABILITATION

Condition is currently unacceptable.

PREDICTED LIFE OF REHABILITATION

Alternative	Years	Unacceptable
Restoration	5	Jt. deterioration
3-inch AC OL	8	Ref. cracking
5-inch crack/seat AC OL	10	Rutting
7-inch unbonded PCC OL	20+	
9-inch reconstruction	20+	

RESULTS OF LIFE-CYCLE COST ANALYSIS

Alternative	Initial Cost	Annual Cost
Restoration	180,000	37,100
3-inch AC OL	419,000	56,300
5-inch crack/seat AC OL	442,000	48,800
7-inch unbonded PCC OL	600,000	38,000
9-inch reconstruction	603,000	38,200

Cost per 2-lane mile, based on predicted lives shown above (20 years for unbonded overlay and reconstruction) and discount rate of 3 percent.

RECOMMENDED REHABILITATION (1989)

Restore only if petrographic analysis indicates low aggregate reactivity. Otherwise, overlay with unbonded PCC or reconstruct.

Rehabilitation Technique	Quantity
Full-depth repair deteriorated joints	207 sy
Full-depth repair deteriorated joints	634 sy
Reseal transverse joints	10440 ft
Seal longitudinal cracks	940 ft
Reseal lane/shoulder joint	10560 ft
Install subdrains	5280 ft

Quantity per 2-lane mile and shoulders.

TABLE 12 RESULTS OF EXPEAR ANALYSIS OF MI 4–1

PAVEMENT DESIGN

Highway:	I-69 near Charlotte
Pavement type:	9-inch JRCP
Year constructed:	1973
Joint spacing:	71 feet
Joint sealant:	Preformed
Dowel diameter:	1.25 in
Reinforcement:	0.162 in^2/ft
Base:	4-inch untreated aggregate
Subgrade:	A-4
Shoulders:	Tied PCC
Drains:	None

TRAFFIC

Current 2-way ADT:	13,700
Percent trucks:	11
Lanes each direction:	2
Accumulated ESAL:	4.37 million (outer lane)

EXISTING PAVEMENT CONDITION (outer lane)

Year surveyed:	1987
PSR:	2.4
Deteriorated cracks:	222/mile
Crack faulting:	0.08 inch
Deteriorated joints:	0/mile
Joint faulting:	0.12 inch
Longitudinal cracks:	0 feet/mile
Long. joint spall:	0 feet
Pumping:	None
PCC surface:	Tined
Joint sealant damage:	Medium severity
"D" cracking:	Low
Settlements/heaves:	None
Shoulder condition:	Good
Lane/shoulder joint:	Good

Overall: Traffic lanes show extensive transverse crack deterioration, but no joint deterioration. Some faulting exists at joints and cracks. Shoulders are in good condition. Subdrainage deficiency indicated by dense-graded aggregate base, A-4 subgrade, inadequate ditch depth and heavy traffic.

PHYSICAL TESTING RECOMMENDATIONS

Deflection testing needed for structural analysis and void detection. Coring and materials testing needed for assessing extent of deterioration from "D" cracking (both transverse and longitudinal joints). Materials testing for permeability.

FUTURE CONDITION WITHOUT REHABILITATION

Serviceability:	PSR < 3.0 in 1987
Deteriorated joints:	> 27/mile in 1997
Deteriorated cracks:	> 75/mile in 1987

CONSEQUENCE OF DELAYING REHABILITATION

Pavement is already very rough and needs immediate rehabilitation. All types of deterioration are predicted to increase in future. Pavement is too deteriorated for restoration now. AC overlay may not be feasible due to deterioration of PCC slab.

PREDICTED LIFE OF REHABILITATION

Alternative	Years	Unacceptable
Restoration	5	Jt. deterioration
3-inch AC OL	10	Ref. cracking
5-inch crack/seat AC OL	15	Rutting
3-inch saw/seal AC OL	13	Ref. cracking
3-inch bonded PCC OL	15	Ref. cracking
7-inch unbonded PCC OL	17	Jt deterioration, cracking

RESULTS OF LIFE-CYCLE COST ANALYSIS

Alternative	Initial Cost	Annual Cost
Restoration	718,200	143,500
3-inch AC OL	611,900	67,600
5-inch crack/seat AC OL	736,400	58,100
3-inch saw/seal AC OL	621,600	53,100
3-inch bonded PCC OL	706,100	55,800
7-inch unbonded PCC OL	708,200	55,200

Cost per 2-lane mile, based on predicted lives shown above and discount rate of 3 percent.

RECOMMENDED REHABILITATION (1989)

Three alternatives (3-inch saw/seal AC OL, 3-inch bonded PCC OL, 7-inch unbonded PCC OL) are very similar in performance and cost. Further analysis is needed for selection.

MI 1–10b, Poor Condition

Table 13 presents the results of the analysis of MI 1–10b, a section of 9-in. JPCP located on US-10 near Clare, Michigan, in a wet, freezing climatic zone. The pavement has carried about 0.9 million ESALs in the outer traffic lane since its construction in 1975. When surveyed in 1987, its PSR was 2.8, it had extensive joint deterioration (219 per mile), faulting of 0.19 in. at joints, extensive longitudinal joint spalling (1,395 ft per mile), low-severity pumping, medium-severity joint sealant damage, and medium-severity D cracking.

As Table 13 indicates, the pavement has too much deterioration for restoration to be cost-effective. An unbonded PCC overlay is the best rehabilitation choice in terms of performance and annual cost.

MN 1–8, Poor Condition

Table 14 presents the results of the analysis of MN 1–8, a section of 9-in. JRCP located on I-94 near Rothsay, Minnesota, in a dry, freezing climatic zone. The pavement has carried about 5.5 million ESALs in the outer traffic lane since its construction in 1970. When surveyed in 1987, its PSR was 3.4, it had extensive crack deterioration (102 per mile), joint deterioration (141 per mile), and longitudinal cracking (1,775 ft per mile). Faulting at transverse joints averaged 0.09 in. Low-severity D cracking and joint sealant damage were also noted.

The pavement's condition is currently unacceptable. As Table 14 indicates, the rehabilitation strategies with the lowest annual cost are reconstruction and unbonded PCC overlay. Because no preoverlay repair is involved (i.e., increases in distress quantities do not affect strategy cost), either reconstruction or an unbonded overlay could be delayed a few years. Despite the large amount of distress present, rideability is still acceptable, so some delay in rehabilitation could be tolerated.

SUMMARY

The pavements examined here that were in good condition had minor faulting (average of 0.02 in.), little or no joint spalling or load-related cracking, and good ride quality (PSR greater than 3.5). For these pavements, restoration was consistently the most cost-effective rehabilitation strategy.

Pavements in fair condition had greater faulting (average of 0.11 in.), moderate joint spalling (average of 5 joints per mile) and load-related cracking (average of 11 cracks per mile), and fair ride quality (PSR greater than 3.0). Restoration was the most cost-effective rehabilitation strategy for four of the five case studies in fair condition. The exception was a pavement that had joint deterioration because of reactive aggregate.

The pavements in poor condition had high levels of faulting (average of 0.13 in.), a large number of spalled joints (average of 92 per mile) and load-related cracks (average of 88 per mile), and poor ride quality (PSR of 3.0 or less). In every case examined, overlay or reconstruction was more cost-effective than restoration.

TABLE 13 RESULTS OF EXPEAR ANALYSIS OF MI 1–10b

PAVEMENT DESIGN

Highway:	US 10 near Clare
Pavement type:	9-inch JPCP
Year constructed:	1975
Joint spacing:	13-19-18-12 feet
Dowels:	Undoweled
Reinforcement:	None
Base:	4-inch asphalt-treated
Subgrade:	A-2
Shoulders:	AC
Drains:	None

TRAFFIC

Current 2-way ADT:	5,100
Percent trucks:	8
Lanes each direction:	2
Accumulated ESAL:	0.88 million (outer lane)

EXISTING PAVEMENT CONDITION (outer lane)

Year surveyed:	1987
PSR:	2.8
Deteriorated cracks:	0/mile
Crack faulting:	0.00 inch
Deteriorated joints:	219/mile
Joint faulting:	0.19 inch
Longitudinal cracks:	0 feet/mile
Long. joint spall:	1395 feet
Pumping:	Low
PCC surface:	Tined
Joint sealant damage:	Medium severity
"D" cracking:	Medium
Settlements/heaves:	None
Shoulder condition:	Good
Lane/shoulder joint:	Good

Overall: Traffic lanes show extensive joint deterioration from "D" cracking. Serious faulting exists. Shoulders are in good condition.

PHYSICAL TESTING RECOMMENDATIONS

Deflection testing needed for structural analysis and void detection. Coring and materials testing needed for assessing extent of deterioration from "D" cracking (both transverse and longitudinal joints). No roughness or skid testing needed.

FUTURE CONDITION WITHOUT REHABILITATION

Serviceability:	PSR < 3.0 in 1987
Faulting:	> 0.10 inch in 1987
Deteriorated joints:	> 55/mile in 1987

CONSEQUENCE OF DELAYING REHABILITATION

Pavement too deteriorated for restoration. Transverse and longitudinal joint deterioration will increase. AC overlay may not be feasible due to deterioration of PCC slab.

PREDICTED LIFE OF REHABILITATION

Alternative	Years	Unacceptable
Restoration	5	Jt deterioration
3-inch AC OL	17	Ref. cracking
7-inch unbonded PCC OL	20+	

RESULTS OF LIFE-CYCLE COST ANALYSIS

Alternative	Initial Cost	Annual Cost
Restoration	718,200	143,500
3-inch AC OL	929,500	64,600
7-inch unbonded PCC OL	567,400	34,900

Cost per 2-lane mile, based on predicted lives shown above and discount rate of 3 percent.

RECOMMENDED REHABILITATION (1991)

7-inch unbonded PCC overlay with no additional repair is the most cost-effective alternative, due to extensive repair needed for other alternatives.

Rehabilitation Techniques	Quantity
Unbonded PCC OL traffic lanes	14,080 sy
AC OL shoulders	8,800 sy

TABLE 14 RESULTS OF EXPEAR ANALYSIS OF MN 1–8

PAVEMENT DESIGN

Highway:	I-94 near Rothsay
Pavement type:	9-inch JRCP
Year constructed:	1970
Joint spacing:	27 feet
Dowels:	1-inch diameter
Reinforcement:	0.097 sq in / ft
Base:	5-inch asphalt-treated
Subgrade:	A-2
Shoulders:	AC
Drains:	None

TRAFFIC

Current 2-way ADT:	5,000
Percent trucks:	21
Lanes each direction:	2
Accumulated ESAL:	5.5 million (outer lane)

EXISTING PAVEMENT CONDITION (outer lane)

Year surveyed:	1987
PSR:	3.4
Deteriorated cracks:	102/mile
Crack faulting:	0.00 inch
Deteriorated joints:	141/mile
Joint faulting:	0.09 inch
Longitudinal cracks:	1775 feet/mile
Pumping:	None
PCC surface:	Tined
Joint sealant damage:	Low severity
"D" cracking:	Low severity
Settlements/heaves:	None
Shoulder condition:	Good
Lane/shoulder joint:	Good

Overall: Traffic lanes have a large amount of deteriorated transverse and longitudinal cracks and joints.

PHYSICAL TESTING RECOMMENDATIONS

Deflection testing for structural analysis and void detection. Coring at center slab, near trans. joints and longitudinal joints. Core examination and materials testing.

FUTURE CONDITION WITHOUT REHABILITATION

Serviceability:	PSR < 3.0 in 2004
Deteriorated joints:	> 27/mile in 1987
Deteriorated cracks:	> 75/mile in 1987

CONSEQUENCE OF DELAYING REHABILITATION

Joint deterioration and crack deterioration are already unacceptable. Further delay in rehabilitation would substantially increase maintenance cost and the cost of rehabilitation.

PREDICTED LIFE OF REHABILITATION (1992)

Alternative	Years	Unacceptable
Restoration	6	Faulting
3-inch AC OL	10	Rutting, ref. cracking
7-inch unbonded PCC OL	16	Jt. deterioration
9-inch reconstruction	20+	

RESULTS OF LIFE-CYCLE COST ANALYSIS

Alternative	Initial Cost	Annual Cost
Restoration	599,000	104,000
3-inch AC OL	748,000	83,000
9-inch reconstruction	633,600	42,600
7-inch unbonded PCC OL	704,000	52,900

Cost per 2-lane mile, based on predicted lives shown above (20 years for reconstruction) and discount rate of 3 percent.

RECOMMENDED REHABILITATION (1992)

Reconstruction has lowest annual cost; unbonded PCC overlay also provides acceptable life at low annual cost.

Rehabilitation Techniques	Quantity
Reconstruct both traffic lanes	14,080 sy
Reconstruct AC shoulders	9,387 sy

Quantity per 2-lane mile and shoulders.

The cost of rehabilitation is strongly tied to pavement condition, as follows:

Condition	*Average Initial Cost Per Lane-Mile ($)*	*Average Annual Cost Per Lane-Mile ($)*
Good	32,000	2,000
Fair	163,000	16,000
Poor	605,000	45,000

It pays, therefore, to maintain pavements in good condition and to rehabilitate them before they exhibit substantial distress.

In the case studies examined, an AC overlay with sawed and sealed joints was usually the most cost-effective AC overlay option. A 3-in. AC overlay with sawed and sealed joints was predicted to last longer and be more cost-effective than a conventional AC overlay of the same thickness. A 5-in. AC overlay of cracked and seated pavement typically was predicted to perform better than a conventional 3-in. AC overlay. However, the cost of cracking and seating and the cost of the additional 2 in. of AC resulted in a higher life cycle cost about half the time.

The unbonded PCC overlay provided the longest life of all overlay alternatives and was found to be cost-effective when the existing pavement was badly deteriorated. Reconstruction was cost-effective if the existing pavement exhibited extensive deterioration and the shoulders were in good enough condition that they did not need to be replaced.

Overall, the EXPEAR program provided realistic evaluations, future predictions, and selection of alternatives for the case studies.

ACKNOWLEDGMENTS

The research reported in this paper was part of a study entitled "Performance/Rehabilitation of Rigid Pavements" conducted for the FHWA by ERES Consultants, Inc., of Savoy, Illinois. The contract officer's technical representative for the study was Roger Larson. Kurt Smith and Sue James of ERES Consultants are gratefully acknowledged for their assistance.

REFERENCES

1. M. I. Darter, E. J. Barenberg, and W. A. Yrjanson. *NCHRP Report 281: Joint Repair Methods for Portland Cement Concrete Pavements.* TRB, National Research Council, Washington, D.C., 1985.
2. ERES Consultants, Inc. *Techniques for Pavement Rehabilitation.* Participants' Notebook, 4th ed., National Highway Institute and FHWA, U.S. Department of Transportation, 1987.
3. *Concrete Pavement Restoration—Performance Review.* Pavement Division and Demonstration Projects Division, FHWA, U.S. Department of Transportation, 1987.
4. M. B. Snyder, M. J. Reiter, K. T. Hall, and M. I. Darter. *Rehabilitation of Concrete Pavements, Volume I—Repair Rehabilitation Techniques.* Report FHWA-RD-88-071. FHWA, U.S. Department of Transportation, 1989.

5. M. I. Darter, J. M. Becker, M. B. Snyder, and R. E. Smith. *NCHRP Report 277: Concrete Pavement Evaluation System (COPES)*. TRB, National Research Council, Washington, D.C., 1985.
6. K. D. Smith, D. G. Peshkin, M. I. Darter, A. L. Mueller, and S. H. Carpenter. *Performance of Jointed Concrete Pavements, Volume I—Evaluation of Concrete Pavement Performance an Design Features*. Report FHWA-RD-89-136. FHWA, U.S. Department of Transportation, 1989.
7. K. T. Hall, J. M. Connor, M. I. Darter, S. H. Carpenter. *Rehabilitation of Concrete Pavements, Volume III—Concrete Pavement Evaluation and Rehabilitation System*. Report FHWA-RD-88-073. FHWA, U.S. Department of Transportation, 1989.
8. M. I. Darter, and K. T. Hall. *Structural Overlay Strategies for Jointed Concrete Pavements, Volume IV—Guidelines for the Selection of Rehabilitation Alternatives*. Report FHWA-RD-89-145. FHWA, U.S. Department of Transportation, 1989.
9. K. T. Hall, M. I. Darter, S. H. Carpenter, and J. M. Connor. Development of a Demonstration Prototype Concrete Pavement Evaluation System. In *Transportation Research Record 1117*, TRB, National Research Council, Washington, D.C., 1987.
10. K. T. Hall, J. M. Connor, M. I. Darter, and S. H. Carpenter. Development of an Expert System for Concrete Pavement Evaluation and Rehabilitation. *Proc., 2nd North American Conference on Managing Pavements*, Toronto, Ontario, Canada, Nov. 1987.
11. K. T. Hall, J. M. Connor, M. I. Darter, and S. H. Carpenter. Expert System for Concrete Pavement Evaluation and Rehabilitation. In *Transportation Research Record 1207*, TRB, National Research Council, Washington, D.C., 1988.

Publication of this paper sponsored by Committee on Pavement Rehabilitation.

Life-Cycle Cost Analysis of Ohio Pavement Rehabilitation Demonstration Projects

CHHOTE L. SARAF, JAMES C. KENNEDY, JR., KAMRAN MAJIDZADEH, AND S. WILLIAM DUDLEY*

A suitable life cycle cost analysis procedure for comparing the economics of eight different projects that were treated with five different rehabilitation methods generally used in Ohio is described. Because the initial condition of each pavement included in the study was different, it was necessary to adjust for this condition so that different pavements could be compared on an equitable basis. Initial salvage value was used for this purpose. Also, the daily traffic was different on each project. Therefore, service cost index, defined as the ratio of daily traffic to life cycle cost (in multiples of $1,000) was used for comparing the benefits and costs of each project or rehabilitation method used in this study. Analysis of data used in this study indicated that composite overlays were more cost-effective than unbonded rigid overlays for pavements subjected to high levels of daily traffic. Unbonded rigid overlays were also relatively less cost-effective than asphalt concrete (AC) overlays for low levels of daily traffic conditions. Crack and seat with AC overlay was more cost-effective under medium-to-high levels than under medium-to-low levels of traffic. Concrete pavement restoration was most expensive. Results of the analysis indicated that the procedure described is a reasonable method of comparing the life cycle costs of various rehabilitation methods used in Ohio.

Section 110 of the 1982 Surface Transportation Assistance Act reaffirms congressional intent that federal-aid projects including 4R work shall be constructed to preserve and extend the service life of highway systems. In the absence of another AASHO Road Test and with an emphasis on rehabilitation procedures, the Ohio Department of Transportation (ODOT) and the FHWA proposed to construct some full-scale rehabilitation road test sections on existing rigid pavements. Ten different sites, which were identified to be in need of rehabilitation, were selected for this purpose. These sites are shown on the county map of the state of Ohio (see Figure 1). A brief summary of the rehabilitation strategies used in each project is presented in Table 1. In Figure 1, the project number corresponds to the order listed in Table 1.

Several rehabilitation strategies were selected that would yield information suitable for evaluating the effectiveness of the following rehabilitation methods:

1. Concrete pavement restoration (CPR)—Project 4;
2. Conventional asphalt concrete (AC) overlay—Projects 6 and 10;
3. Unbonded jointed concrete overlay—Projects 1, 2, and 3;
4. Composite overlay—Project 5; and
5. Crack and Seat (C&S) with AC overlay—Projects 7, 8, and 9.

All pavements except those slated for C&S procedures included other repairs such as grout undersealing and full-depth joint repair as indicated in Table 1.

A suitable life cycle cost analysis procedure can be used for comparing the economics of various rehabilitation strategies included in the study. The data available for this purpose consisted of the pavement condition immediately before and after rehabilitation and the project cost along with its length and number of lanes. Because these projects were completed recently, long-term performance data will not be available for some time in the future. However, the method illustrated will be applicable when such data become available.

SELECTION OF PROJECTS

As stated earlier, 10 demonstration projects were selected by FHWA and ODOT for this study. Discussions with ODOT staff revealed that only a part of Project 8 (WYA-23-0.20) was given the listed treatment. Therefore, Project 8 is not included in the analysis. Also, Project 6 (MED-271-0.35/SUM-271-0.00), which included a 3-in. AC overlay, was not constructed according to plan (the project was readvertised for bids after it was terminated and was completed by the bonding company). As such, it was decided to exclude Project 6 from this analysis also. The remaining eight projects were selected for the cost analysis.

LIFE CYCLE COST ANALYSIS

Life cycle cost analysis is generally performed to evaluate alternative designs of rehabilitation strategies. Although there is no unique method of calculating the life cycle cost of a pavement rehabilitation action, most highway agencies include initial cost, future maintenance, and rehabilitation costs in similar analyses. Some agencies consider user cost as an important component of life cycle cost analysis, but it is generally difficult to estimate. Salvage value is another component of life cycle cost that should be included in the analysis if there is substantial difference in this value (because of various alternative strategies) at the end of the analysis period.

Available literature on life cycle cost analyses was reviewed to select a suitable method of analysis for this study. The

*Deceased.

C. L. Saraf and K. Majidzadeh, Resource International, Inc., 281 Enterprise Drive, Westerville, Ohio 43081. J. C. Kennedy, Jr., Battelle Laboratories, 505 King Avenue, Columbus, Ohio 43201.



FIGURE 1 Location of projects.

TABLE 1 OHIO PAVEMENT REHABILITATION DEMONSTRATION PROJECTS

Project Number	Project Identification	Rehabilitation Strategy	Start Date	Comp. Date
1	CLA-70-20.92	Undersealing and necessary joint repairs. 10-inch mesh-doweled PCC overlay with 60 foot joint spacing.	04/12/84	10/15/84
2	CLI-71-4.26	Undersealing all joints. 9-inch mesh-doweled PCC overlay with skewed joints spaced at 27 feet.	05/13/85	12/04/85
3	ATH-33-13.31	8-inch plain PCC with skewed joints at variable spacing.	04/02/85	10/15/85
4	ATH-33-10.41	CPR. Full-depth and bonded PCC repairs of failed areas. Adding tied PCC shoulders and resealing all joints and cracks.	09/04/84	05/31/85
5	FRA-70-0.02	Undersealing and joint repairs. Composite overlay, 3-inch AC on 9-inch plain PCC, slurry seal bond breaker and saw/seal joint in overlay EB.	04/02/85	11/01/85
6	MED-271-0.35/ SUM-271-0.00	Undersealing, joint repairs, tied PCC shoulder, 3-inch AC overlay. Saw/seal joints in overlay.	03/18/85	09/23/86
7	CLA-70-5.76	Crack and seat existing PCC, and 7-inch AC overlay.	08/06/84	07/31/85
8	WYA-23-0.20	Crack and seat existing PCC, and 6-inch AC overlay.	08/13/84	01/08/85
9	LIC-70-9.55 EB	Remove existing AC overlay, crack and seat PCC pavement, and 9-inch AC overlay.	08/21/85	10/11/86
10	HEN-24/6-9.61	Minimum joint repair, 6-inch AC overlay.	03/12/86	04/24/87

Alaska DOT, Pennsylvania DOT, and AASHTO analysis methods were reviewed for this purpose (1–3). Because of its simplicity, the Pennsylvania DOT analysis approach was used for this study. Figure 2 shows the use of this method for life cycle cost analysis of various rehabilitation strategies.

As indicated earlier, the life cycle cost of a given rehabilitation alternative generally consists of the following components:

1. Construction cost of rehabilitation,
2. Salvage value at the end of analysis period,
3. Routine maintenance cost during the analysis period, and
4. Rehabilitation cost (if required before the end of analysis period).

To estimate the life-cycle cost, these cost components are combined in the following manner:

Life cycle cost [Cost of major rehabilitation (initial)]

+ (Routine maintenance cost during the analysis period)

+ (Cost of any rehabilitation during the analysis period)

− (Salvage value of pavement at the end of the analysis period) (1)

Equation 1 is applicable to those cases for which life cycle costs of various alternatives are to be determined for the same pavement or project. In these cases, the initial condition of pavement and future traffic on the pavement are the same for all alternatives. Therefore, the total life cycle cost of each alternative represents its relative economics when compared with the life cycle costs of other alternatives. However, this comparability was not present for this study because different pavements were rehabilitated with different actions. The initial conditions of these pavements were not the same and the future traffic on these pavements will not be the same. Therefore, this study provided reasonable means of accounting for differences in the life cycle cost analyses so that costs could be compared on an equitable basis.

Two new terms that are specific to this study were introduced in this analysis to address these issues. Initial condition of each pavement was converted into its dollar value and called "initial salvage" of the pavement. By adding this value to the total cost estimated by Equation 1, all pavements were brought to a common starting point of so-called "zero value." The life cycle cost thus obtained represented the total amount of dollars spent on the pavement during the analysis period. Further, because each pavement was expected to serve a different amount of traffic [measured in terms of 18-kip equivalent single-axle loads (E–18s)] during the analysis period, it was assumed that the life cycle cost of each pavement was used to serve the traffic expected on the pavement during the analysis period. Therefore, an index called "service cost index" (SCI) was used to determine the relative benefits derived from each rehabilitation action. This index was defined as follows:

SCI = (Total number of E–18s served by the pavement during the analysis period)/(Total life cycle cost estimated for the pavement) (2)

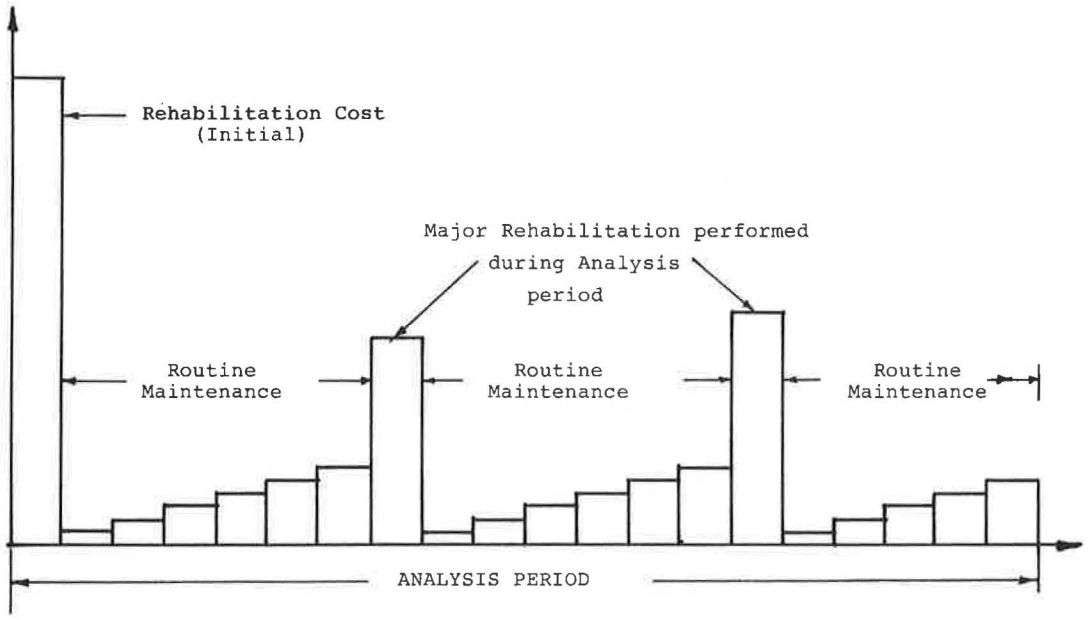


FIGURE 2 Typical distribution of yearly costs of maintenance and major maintenance during the analysis period.

If it is assumed that the traffic growth rates in the future of all pavements included in this analysis are the same, then the total number of E–18s served by each pavement is proportional to its daily E–18s. Therefore, daily E–18s were used in the numerator of Equation 2. Also, in order to limit SCI values to less than 100, the cost in the denominator was divided by 1,000.

Any period of analysis could have been used for the purpose of this analysis. However, a period of 20 years was selected and used in this analysis. Brief descriptions of each cost component are given in the following subsections.

Construction Cost of Rehabilitation

Construction costs for various rehabilitation actions were obtained from ODOT records. The costs of each project in terms of dollars per lane-mile are presented in Table 2 along with the year each project was completed. The data presented in Table 2 are important when comparing final project costs.

Projects 1, 2, and 3 used portland cement concrete (PCC) as the rehabilitation method. If all other factors were equal, Table 2 would imply that 10-in. PCC cost significantly less (per lane-mile) than 8-in. and 9-in. PCC. This conclusion is unreasonable; not all factors were equal between the projects. That is, each project was bid according to the specific requirements of the project so the contract price per lane-mile was peculiar to the project, the project's conditions, and the rehabilitation method.

The same sort of situation existed between Projects 7 and 10. A first look at Table 2 may imply that C&S and 7-in. AC overlay (of Project 7) generally is less costly per lane-mile than the conventional 6-in. AC overlay of Project 10. This conclusion is not correct generally, but is a result of the conditions involved in each project and not solely because of the rehabilitation method.

Salvage Value at the End of Analysis Period

Salvage value is the residual value of the pavement or its reusable material at the end of an analysis period (*3*). Because there are no well-defined formulas available to estimate the salvage value of a given pavement, it was proposed to use a simple method that was based on the remaining life of the pavement. For this purpose, it was assumed that a new pavement had a salvage value of 100 percent and a pavement with no remaining life had a salvage value of 0 percent. Thus, the salvage value at the end of the analysis period was estimated by the following relationship:

$$\text{Salvage value} = (\text{NR}/\text{ND}) \times (\text{Cost of new pavement}) \quad (3)$$

where

NR = remaining life of pavement in terms of E–18s, and
ND = design life of pavement in terms of E–18s.

After considering several alternatives, it was decided to use the AASHTO design equations for estimating the design life, ND (*3*). Remaining life, NR, was estimated by the following relationship:

$$\text{NR} = \text{ND} - [\text{Number of E–18s estimated for the analysis period (20 years) from traffic data collected at the beginning of the rehabilitation}] \quad (4)$$

The cost of new pavement is the average cost of new construction per lane-mile as determined by the Ohio DOT for the construction year 1988. A summary of salvage value estimates is presented in Table 3.

TABLE 2 INITIAL COST PER LANE-MILE

Project	Rehab.	Contract Cost per Lane-Mile ($)	Project Length (Miles)	No. of Lanes	Year Completed
1. CLA-70-2 .92	10 PCC	238,143	4.2	4	1984
2. CLI-71-4.26	9 PCC	321,057	3.0	4	1985
3. ATH-33-13.31	8 PCC	299,141	2.2	4	1985
4. ATH-33-10.41	CPR	70,478	2.8	4	1985
5. FRA-70-0.02	3AC/9PCC	254,913	3.4	6	1985
7. CLA-70-5.76	C&S*/7AC	167,976	5.2	4	1985
9. LIC-70-9.55EB	C&S*/9AC	213,649	6.4	2	1985
10. HEN-24/ 6-9.61/16/43	6" AC	168,743	4.9	4	1987

*C&S: Crack and Seat

TABLE 3 SUMMARY OF SALVAGE VALUE ESTIMATES AT THE END OF ANALYSIS PERIOD (COST PER LANE-MILE)

Project Number	PSI Measured Immediately After Rehab.	Design Life Estimated from AASHTO Equation, ND (10^6)	Number of E-18 Expected During 20 yrs., N (10^6)	**Salvage at the End of 20 yrs., (%)	**Salvage in 1988 Dollars ($)
RIGID PAVEMENTS					
1	3.6	62	45	27	111,375
2	3.9	43	37	14	57,750
3	4.3	10	6	40	165,000
4	3.4	5	5	0	0
5	4.2	88	65	26	107,250
FLEXIBLE PAVEMENTS					
7	4.6	21	14	33	136,125
9	4.2	35	35	0	0
10	3.9	7	13	0	0

* % Salvage = 100 (ND-N)/ND
** Based on cost of new pavement @ $412,500/lane-mile

Initial Salvage

As mentioned earlier, initial salvage is the dollar value of each pavement just before the major rehabilitation was applied to the pavement. A method similar to the mentioned method was used to estimate this value for all pavements. The design lives for these pavements were determined from the AASHTO (*3*) design equation using the original design thicknesses (before new overlays) and their material properties. Remaining lives for these pavements were determined by subtracting the estimated number, N, of E–18s to reach the PSI before rehabilitation from the design number, ND, of E–18s. A summary of initial salvage value calculations is presented in Table 4.

Routine Maintenance Cost

The routine maintenance cost for each pavement during the analysis period was estimated by the ODOT Bureau of Maintenance from its records. According to these estimates, routine maintenance cost increased from zero immediately after major rehabilitation repair to about $4,000 per lane-mile after 20 years. Thus, a stepwise increase of $200 per year was assumed for this purpose. For example, routine maintenance cost 1 year after rehabilitation is $200 per lane-mile, after 2 years it is $400 per lane-mile, and so on. Although these costs should differ for flexible and rigid pavements, it was decided to use the average values in this analysis; the results are not expected to be significantly affected by this assumption.

A maintenance schedule for each project was prepared by ODOT engineers using their previous experience in this area. These schedules are shown in Figure 3. Routine maintenance costs for each project were estimated from this schedule. Table 5 presents the yearly maintenance costs for Project 1. Similar tables were prepared for other projects.

Rehabilitation Cost

A schedule of routine maintenance and rehabilitation was developed for each project with the help of ODOT engineers

TABLE 4 SUMMARY OF ESTIMATES OF INITIAL SALVAGE VALUE BEFORE REHABILITATION (COST PER LANE-MILE)

Project Number	ND, 18K-ESAL, (10^6)	PSI before Rehab.	N, 18K-ESAL (10^6)	NR =ND-N (10^6)	Salvage NR/ND, (%)	*** Salvage Value (1988 dollars) ($)
1	5.7	3.1	2.5	3.2	56	231,000
2	5.7	1.9	4.9	0.8	14	57,750
3	2.5	2.6	1.7	0.8	32	132,000
4	5.7	3.2	2.2	3.5	61	251,625
5	5.7	2.5	3.7	2.0	35	144,375
7	5.7	2.7	3.3	2.4	42	173,250
9	NA*	NA*	NA*	NA*	30**	123,750
10	NA*	NA*	NA*	NA*	30**	123,750

* NA - not available
** Estimates based on condition of existing structure
*** Based on cost of new pavement @ $412,500/lane-mile

as shown in Figure 3. This schedule included a period of 20 years after rehabilitation for each project. Rehabilitation actions recommended for each project during this period represent the best estimates of ODOT engineers experienced in similar projects. Costs of proposed rehabilitation actions were estimated using current ODOT cost records. Actual costs for each type of rehabilitation used in this study are presented in Table 6.

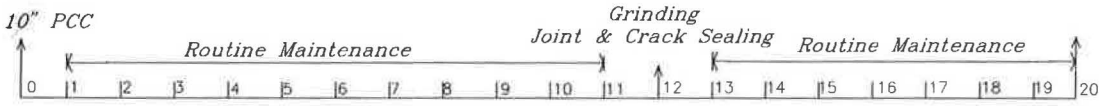
Inflation and Discount Rates

Because most of the costs were available in 1988 dollars, it was decided to convert each cost component into 1988 dollars. In order to convert the money spent in years other than 1988, an inflation rate of 4 percent was assumed. Two typical discount rates of 6 and 10 percent were used to estimate the present worth of future costs.

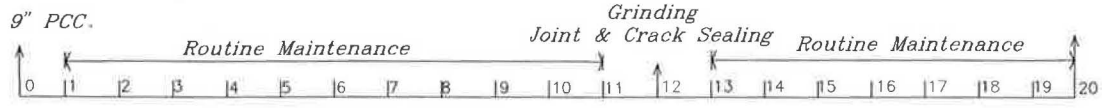
ANALYSIS OF DATA

Life cycle cost analysis of each project was performed with the help of Equation 1 and the data described in the previous sections. The cost of initial salvage, as described earlier, was added to Equation 1 for estimating the life cycle cost for the analysis period (20 years). An example of typical calculations performed for Project 1 is presented in Table 5. Similar calculations were performed for the remaining projects selected for this analysis and the results are summarized in Table 7.

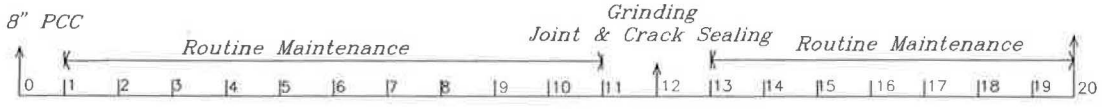
Estimates of E-18s per day, as calculated by the ODOT, were obtained for each project and are presented in Table 7. These values along with the life cycle cost estimates were used to calculate SCI values for each project with the help of Equation 2. The SCI values obtained are listed in Table 7. Using these values, each project was ranked from 1 to 8 (Rank 1 represented the highest SCI and Rank 8 represented the lowest). A summary of all calculations performed for this analysis is presented in Table 7.



PROJECT 1. CLA-70-20.92



PROJECT 2. CLI-71-4.26



PROJECT 3. ATH-33-13.31

FIGURE 3 (*continued on next page*)

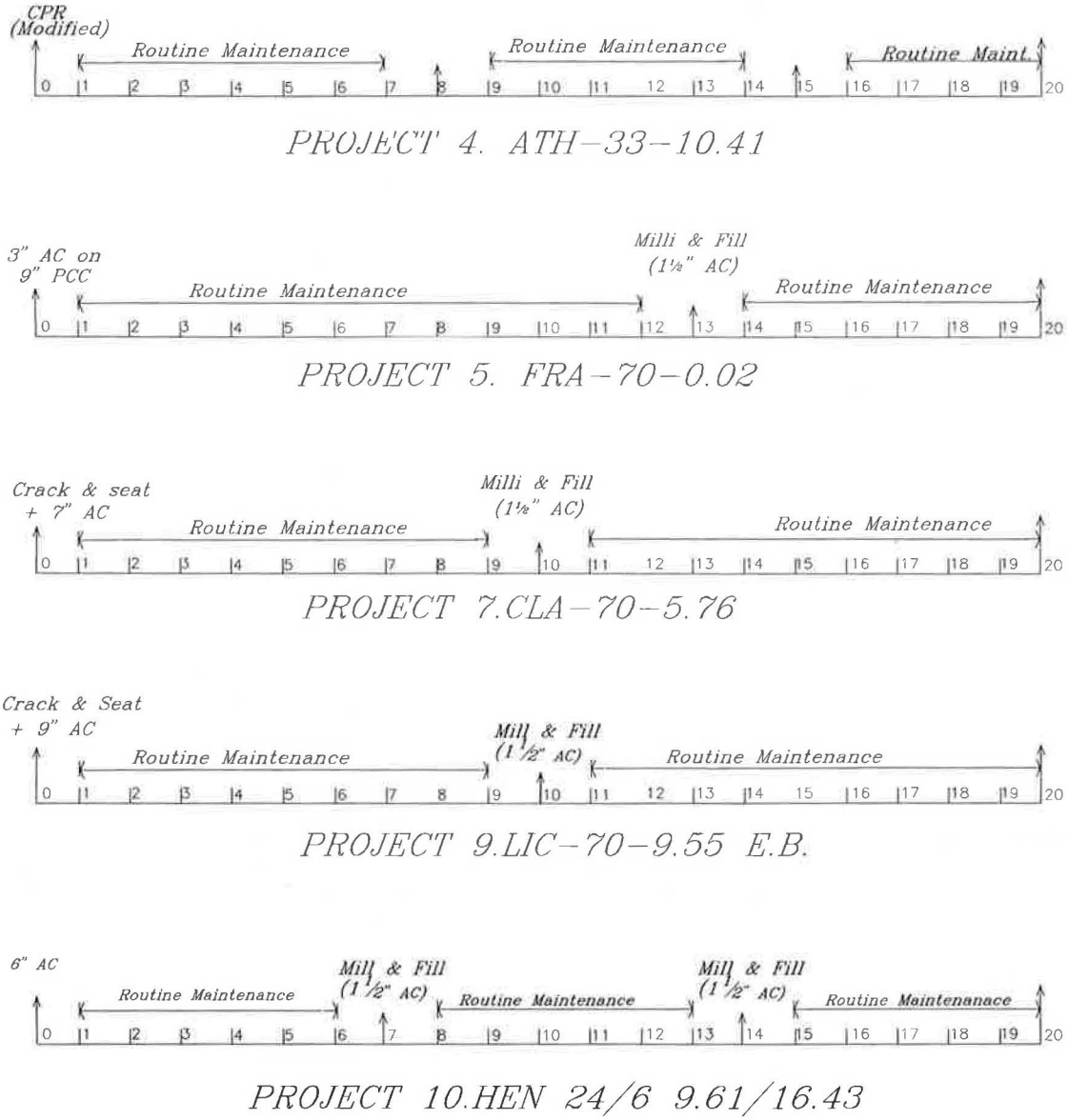


FIGURE 3 Schedule of routine maintenance and rehabilitation.

DISCUSSION OF RESULTS

A straightforward method for the life cycle cost analysis of various rehabilitation actions used in existing pavements has been described. However, data to verify the various assumptions used in this analysis will not be available for several years because the projects have been rehabilitated only recently. Keeping the limitations and the assumptions used in this analysis in mind, the results of this analysis are discussed in the following paragraphs. It is important to note here that the discount rates of 6 and 10 percent did not change the rankings of projects based on SCI; therefore, the following discussions will not mention this further.

Project 5 ranks first in cost-effectiveness (SCI) according to Table 7 although it was not lowest in its initial cost (see Table 2). Alternatively, Project 4, which used a CPR action because of its better initial condition and low daily traffic, was lowest in cost at the beginning of the period but it was last in cost-effectiveness at the end of the analysis period.

Project 1, which used 10-in. PCC overlay, was second behind Project 5 in cost-effectiveness at the end of the period. The results in Table 7 indicate that a savings in rehabilitation cost may be realized by using PCC overlays (either 9 or 10 in.) for pavements of high traffic volume.

Projects 7 and 9, which were rehabilitated with C&S plus AC layers, ranked 5th and 4th, respectively, according to Table 7. The 9 in. of overlay used in Project 9 served significantly more E-18s per $1,000 than the 7-in. overlay used in Project 7.

It is interesting to compare Projects 7 and 10. According to the SCI values of Table 7, the 6-in. overlay of Project 10 was not as economical as the treatment for Project 7. That is, although traffic was about the same for both projects, Project 7 was superior to Project 10 in daily service per $1,000.

TABLE 5 LIFE CYCLE COST ESTIMATE OF PROJECT 1, CLA-70-20.92

Year	Maintenance Actions	Cost per Lane-Mile (1988 dollars)	Cost Inflated @ 4%	Present Worth (1988 dollars)	
				Disc. @ 6%	Disc. @10%
0	10" PCC	398,220*	398,220	398,220	398,220
1	Routine Maint	220	208	196	189
2	Routine Maint	400	433	385	358
3	Routine Maint	600	675	567	507
4	Routine Maint	800	936	741	639
5	Routine Maint	1,000	1,217	909	755
6	Routine Maint	1,200	1,518	1,070	857
7	Routine Maint	1,400	1,842	1,225	945
8	Routine Maint	1,600	2,190	1,374	1,022
9	Routine Maint	1,800	2,562	1,516	1,087
10	Routine Maint	2,000	2,960	1,653	1,141
11	Routine Maint	2,200	3,387	1,784	1,187
12	Grinding J&C Seal	67,370	107,862	53,604	34,368
13	Routine Maint	200	333	156	96
14	Routine Maint	400	693	306	182
15	Routine Maint	600	1,081	451	259
16	Routine Maint	800	1,498	590	326
17	Routine Maint	1,000	1,948	723	385
18	Routine Maint	1,200	2,431	852	437
19	Routine Maint	1,400	2,950	975	482
20	Routine Maint	1,600	3,506	1,093	52
	Total	485,990	538,449	486,392	443,965

*Cost (1988 dollars) = Initial salvage + construction cost of rehabilitation - salvage at the end of analysis period
= (231,000 + 238,143 x 1.04^4 - 111,375)
= 398,219

TABLE 6 UNIT COST OF VARIOUS REHABILITATION ACTIONS USED IN THIS STUDY (1988 DOLLARS PER LANE-MILE)

ACTION	COST/Lane-Mile
1. Reconstruction with rigid	$ 412,500
2. CPR	$ 183,000
3. Joint and Crack Sealing	$ 46,250
4. Grinding	$ 21,120
5. AC Overlay (3" or less)	$ 71,750
6. Mill and Fill (1 1/2" Overlay)	$ 71,750
7. Routine Maintenance Calculated by the formula: cost = 200 n, where n is the number of years after rehabilitation and cost is the dollar amount per lane-mile.	$ 200n

This may suggest that the C&S action before overlay may have an influence on rehabilitation techniques under appropriate conditions in the future. However, this possibility must be considered in the context of the limitations under which this study was performed.

Project 3 was overlayed with 8-in. PCC. Projects 1 and 2 were overlayed with 10- and 9-in. PCC, respectively, because of expected higher traffic requirements compared with those of Project 3. The cost-effectiveness of Project 3 compared with that of either Project 1 or 2 is low and thus it appears that PCC overlay on pavements with light traffic may not be economical. An AC overlay may be more economical for low-trafficked pavements (compare Projects 3 and 10).

Finally, according to Table 7, Project 4, which used a modified CPR initially and an additional subsequent CPR with a nonstructural overlay during the analysis period, was estimated to be the least cost-effective among all rehabilitation strategies. Good original pavement condition (PCR = 64 and PSI = 2.6) and low traffic (700 daily 18-K ESALs) normally permits the use of such actions. Although such actions cost less initially, the cost of future repair and maintenance may lead to more expenses than are likely on other rehabilitation options that are more expensive initially.

In summary, the procedure used to estimate life cycle costs of various rehabilitation strategies seems to be reasonable but is only one of many methods currently used by others. The results obtained using this method appear acceptable within the context of current engineering practice. Future applicability will be established when field data become available.

CONCLUSIONS

On the basis of the information obtained in this study, the following conclusions can be drawn:

1. An estimate of pavement rehabilitation life cycle cost involving alternative actions can be obtained by combining the following cost components:

- Initial cost of the rehabilitation action,
- Rehabilitation cost during service life,
- Routine maintenance cost, and
- Salvage value before initial rehabilitation action and at the end of the service life period.

TABLE 7 SUMMARY OF LIFE CYCLE COST ANALYSIS

			Discounted @ 6%			Discounted @ 10%		
Proj. No.	Rehab. Action	Estimated E-18 per day	Life-Cycle Cost, $1,000 (in 1988 $)	SCI	Ranking Based on SCI	Life-Cycle Cost, $1,000 (in 1988 $)	SCI	Ranking Based on SCI
1	10" PCC	6,100	468.4	13.0	2	444.0	13.7	2
2	9" PCC	5,000	431.3	11.6	3	407.0	12.3	3
3	8" PCC	850	373.7	2.3	7	349.2	2.4	7
4	CPR	700	552.5	1.3	8	486.1	1.4	8
5	3" AC/ 9" PCC	8,950	397.2	22.9	1	370.1	24.2	1
7	C&S/ 7" AC	1,850	301.3	6.14	5	277.7	6.7	5
9	C&S/ 9" AC	4,800	439.3	10.9	4	415.7	11.5	4
10	6" AC	1,800	427.2	4.2	6	387.5	4.6	6

Suitable inflation and discount rates can be used for this analysis.

2. In order to compare life cycle costs of various rehabilitation actions, a service cost index (SCI) based on the number of E−18s served per $1,000 of life cycle cost per day can be used.

3. Using the SCI values obtained for this study, it was found that PCC overlays with or without AC overlay are cost-effective under conditions of high traffic (5,000 to 8,950 E−18s per day, see Projects 1, 2, and 5). For low traffic conditions, 8-in. PCC overlay was relatively expensive.

4. AC overlays with C&S are slightly less expensive (measured by SCI) than AC overlay without C&S (Projects 7 and 10).

5. Costs of AC overlays effectively decrease with increasing AC thicknesses for moderate-traffic (4,800 ESAL/day) compared with low-traffic (1,800 ESAL/day) conditions (Projects 7, 9, and 10).

6. CPR is least expensive in initial cost but most expensive in life cycle cost for the low-traffic conditions under which the project was built (see Project 4).

RECOMMENDATIONS

It is recommended that the ODOT continue to collect performance data every year for use in further evaluation of the maintenance and rehabilitation procedures that have been used in this study. Long-term performance of these pavements will enable them to determine the effectiveness of the rehabilitation techniques and develop guidelines for future actions.

ACKNOWLEDGMENTS

The study was sponsored by the Ohio Department of Transportation in cooperation with FHWA. The authors appreciate the support of the sponsoring agencies and the Resource International staff.

REFERENCES

1. R. B. Kulkarni, C. Saraf, C. J. Van Til, F. Finn and J. Hilliard. Life Cycle Costing of Paved Alaskan Highways. Report AK-RD-835. Alaska Department of Transportation and Public Facilities, Fairbanks, 1982.
2. W. Uddin, R. F. Carmichael, III, and W. R. Hudson. Life Cycle Analysis for Pavement Management Decision Making. Final Report, Pennsylvania Department of Transportation, Harrisburg, March 3, 1986.
3. *AASHTO Guide for Design of Pavement Structures*. AASHTO, Washington, D.C., 1986.

The contents of this paper reflect the views of the authors, who are responsible for the facts and validity of the developments presented herein. The contents do not necessarily reflect the views or policies of FHWA or ODOT. This paper does not constitute a standard, specification, or regulation.

Publication of this paper sponsored by Committee on Pavement Rehabilitation.

Concrete Slabs Stabilized by Subsealing: A Performance Report

SHIE-SHIN WU

Correcting concrete slab movement or pumping problems by subsealing is common practice. Subsealing fills voids beneath the slab, eliminating pumping and restoring uniform support to the slab, hence prolonging slab life. The North Carolina Department of Transportation has experienced accelerated slab cracking after subsealing operations in several projects. The problem has caused enough concern that a study was initiated to investigate the procedure of subsealing operation and the performance of slabs that were stabilized by subsealing. In order to compare reliability of different void detection techniques, several devices were used to locate voids beneath concrete slabs in a test road. Test results indicated that none of these devices produced compatible data. The test section was monitored for 4 years. Conditions of stabilized and unstabilized slabs were mapped and analyzed. Results indicated that, if not handled properly, subsealing can cause performance problems.

Concrete slabs move up and down constantly during their service life. There are two types of slab movements: (a) curling caused by temperature or moisture gradients in the slab, and (b) deflection caused by heavy loading. Curling causes slabs to move very slowly. Movements caused by loading normally have rapid action. When water is present under the slab, rapid slab movement causes ejection of water through joints, cracks, and slab edges. Yoder and Witczak (*1*) described this pumping action in great detail. They further indicated that four factors, namely, free water, voids, low-permeability soil, and loading, must be present for concrete pavement pumping to occur.

Water in pumping action can carry fines from the base or subgrade material if it is erodible. The pumping problem escalates as loss of fines creates greater voids, eventually causing loss of uniform support to the slab. Loss of uniform support leads to premature slab failure.

Darter's definition of subsealing is the insertion of material beneath the slab by pressure to fill voids and provide a thin layer to reduce deflection and resist pumping (*2*). Engineers usually perform subsealing operations to correct the pumping problem. The subsealing operation includes detecting the voids, drilling fill holes through the concrete slab, and filling the voids with nonerodible material. Subsealing is performed in order to achieve the following: (a) filling of voids to prevent the existence of free water, hence eliminating pumping; and (b) restoring of uniform support to the slab.

In the mid-1980s, the North Carolina Department of Transportation (NCDOT) completed several concrete pavement restoration (CPR) projects. Included as part of the CPR work was stabilization of slabs by subsealing with fly ash and cement grout. In those projects, division personnel observed an alarming increase in the rate of slab cracking. Therefore, they raised questions concerning the effectiveness of concrete slab subsealing. Their concerns included the technique for detecting voids under the slab, the threshold for subsealing, the hole pattern, procedures, equipment operation, etc. All of these could be summarized into one question: Was subsealing in fact solving problems or causing problems?

The division's concern was supported by the fact that stabilized slabs have broken faster than slabs that were not subsealed. This concern prompted a series of investigations to look into the subsealing operations and the performance of stabilized slabs.

This study was proposed to answer the following questions.

1. Does the rate of slab cracking change after subsealing? If so, what is the difference?
2. Is the technique of subsealing advanced enough to be used on a routine basis?

STUDY SECTION

A section of I-40 in Catawba County, North Carolina, was identified as the test section for this study. This section was selected because it had just been stabilized and no further CPR was scheduled. This selection provided a sample section with an ordinary subsealing operation. Slab performance observed in this section provided a set of unbiased data.

The evaluation section extended from the Catawba River bridge to just west of NC-16. Slabs were stabilized by means of subsealing with cement–fly ash grout in late 1984. Each lane of this four-lane divided highway contained 1,498 30-ft slabs. The number of slabs stabilized are presented in Table 1.

No work was performed to restore joint sealing in this section of highway. These old joints were mostly open. Wu and Hearne (*3*) found that a large quantity of water can infiltrate a tight, unsealed longitudinal joint. Although the purpose of subsealing is to fill voids under slabs and eliminate the free water reservoir, it cannot stop free water that moves by infiltration.

PAVEMENT PERFORMANCE SURVEY

During the first year beginning in April 1985, pavement condition surveys were performed once every 3 months. Field data were collected twice a year thereafter.

Pavement Management Unit, North Carolina Department of Transportation, P.O. Box 25201, Raleigh, N.C. 27611.

TABLE 1 SUMMARIZED SLAB STABILIZATION

Lane No *	Total Slab Number	Stabilized Slab Number	%
1	1498	399	26.6
2	1498	385	25.7
3	1498	5	0.3
4	1498	14	0.9
All	5189	803	13.4

* Lane number 1, eastbound outside lane
2, westbound outside lane
3, eastbound inside lane
4, westbound inside lane

Field surveys were done slab by slab. Both longitudinal and transverse cracks were carefully mapped. Growth of the crack was recorded. The numbers of total cracked slabs before subsealing operations are presented in Table 2.

The numbers of new cracks on stabilized slabs found in each survey, the accumulated cracked slabs for each lane, and the total cracked slabs for all lanes are presented in Table 3. The same information is presented in Table 4 for the unstabilized slabs.

The percent of additional slab cracking for every survey is presented in Table 5. Changes of the rate of slab cracking for different lanes are shown in Figures 1–5.

VOID DETECTION

In order to prove its effectiveness, the American Concrete Pavement Association with the help of the NCDOT put on a project to demonstrate subsealing procedures in August 1986. One of the objectives of this project was to illustrate the technique of detecting voids beneath slabs. Results of this demonstration project were provided by Oppermann (*4*).

Four different void-detecting devices were applied. These were the Benkelman beam (operated by NCDOT), falling weight deflectometer (FWD) (operated by NCDOT), Dynaflect deflectometer (operated by Austin Research Engineering), and a radar void detector (operated by Gulf Applied Technology).

All these devices were used to detect voids before and after the subsealing operation. The amount of grout taken at each location was recorded. A total of 34 joints were tested. After the subsealing and testing were completed, five slabs were cut with a concrete saw and raised to investigate the actual grout distribution.

Before-and-after test results and the acceptance of grout at all the joints are presented in Table 6. If acceptance of grout is used as an indicator of the presence of void, then comparing grout taken with results of the other void detection techniques will offer some indication of the effectiveness of that technique. Tables 7–10 indicate the relationship between these void detection technique test results and grout acceptance. These results indicate that, if grout acceptance demonstrates a void existing beneath the slab, the accuracy of detecting a void for any one of these methods is less than 70 percent.

Relative test results among the Benkelman beam, FWD, the radar, and grout taken are presented in Table 11. This table presents percent of matching results for both before and after testing.

After the subsealing operation, five slabs were sawed, raised, and removed carefully. Areas under these slabs were inspected and grout spreading was mapped. Results for the five slabs removed are as follows:

1. Joint 4. All methods indicated deflection decreased after subsealing. Very little grout was taken. A thin layer of grout was observed under the slab. Grout was also observed at the joint.
2. Joint 13. Again, all methods indicated deflection decreased after subsealing. A large amount of grout was taken. A large area of grout was found under the slab.
3. Joint 17. No void was detected by either radar or FWD, yet a large amount of grout was taken. Grout was apparent in the joint and a cone of grout was formed under the grout hole.
4. Joint 20. Both Benkelman beam and FWD indicated voids before and after subsealing; however, no grout was taken. Very little grout was spread under the slab. A cone was formed under a grout hole.

TABLE 2 NUMBER OF CRACKED SLABS BEFORE SUBSEAL

Date	Lane	Cracked Slab		% of Total Slab	
		Stabil.	Unstabil.	Stabil.	Unstabil.
04/84	1	2	12	0.5%	1.0%
04/84	2	7	10	1.8%	0.9%
04/84	3	0	7	0%	0.5%
04/84	4	1	7	7.1%	0.5%
04/84	All	10	36	1.2%	0.7%

TABLE 3 ADDITIONAL SLABS CRACKED (STABILIZED)

	New Cracks					Accumulate				
Lane	1	2	3	4	All	1	2	3	4	All
04/84	2	7	0	1	10	2	7	0	1	10
D 07/85	2	1	0	1	4	4	8	0	2	14
A 11/85	3	0	1	0	4	7	8	1	2	18
T 03/86	1	2	0	0	3	8	10	1	2	21
E 08/86	1	1	0	0	2	9	11	1	2	23
12/86	0	0	0	0	0	9	11	1	2	23
05/87	0	0	0	0	0	9	11	1	2	23
03/88	6	2	0	0	8	17	13	1	2	31

TABLE 4 ADDITIONAL SLABS CRACKED (UNSTABILIZED)

	New Cracks					Accumulate				
Lane	1	2	3	4	All	1	2	3	4	All
04/84	12	10	7	7	36	12	10	7	7	36
07/85	2	1	0	0	3	14	11	7	7	39
11/85	0	1	0	0	1	14	12	7	7	40
03/86	0	4	0	0	4	14	16	7	7	44
08/86	1	1	1	0	3	15	17	8	7	47
12/86	0	1	1	1	3	15	18	9	8	50
05/87	1	0	0	0	1	16	18	9	8	51
03/88	2	3	2	1	8	18	21	11	9	59

TABLE 5 SLAB CRACKING RATE

DATE	STABILIZED(%)	UNSTABILIZED(%)
04/84	1.25	0.69
07/85	0.49	0.06
11/85	0.49	0.02
03/86	0.37	0.08
08/86	0.25	0.06
12/86	0.0	0.06
05/87	0.0	0.02
03/88	1.0	0.15

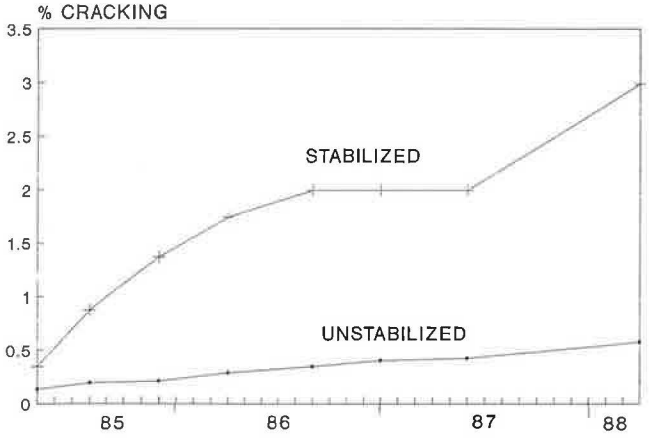


FIGURE 1 Transverse cracking (all lanes).

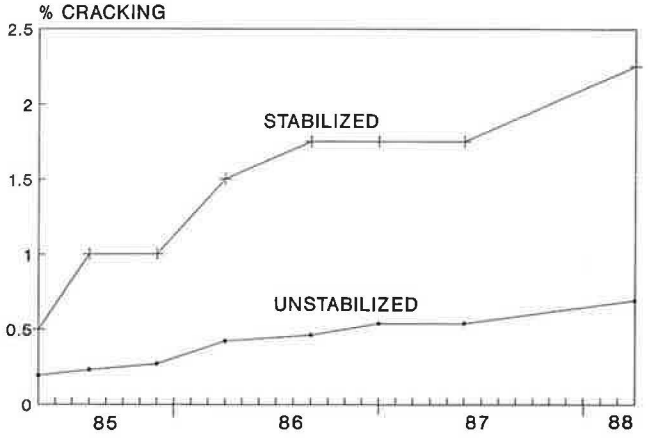


FIGURE 2 Transverse cracking (westbound, both lanes).

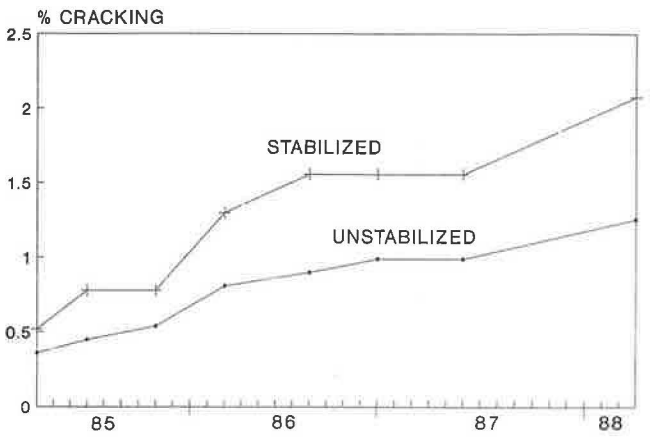


FIGURE 3 Transverse cracking (westbound, outside lane).

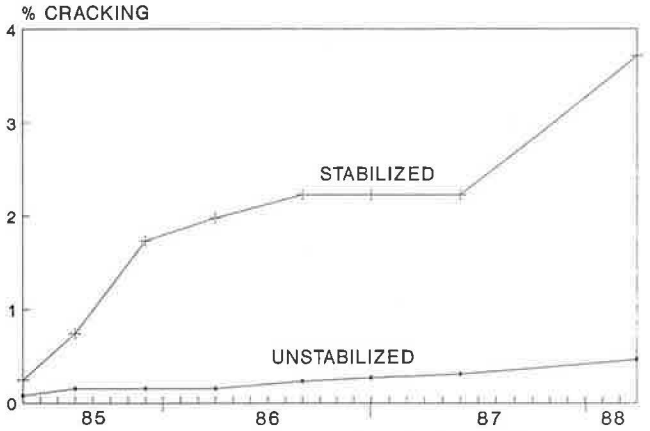


FIGURE 4 Transverse cracking (eastbound, both lanes).

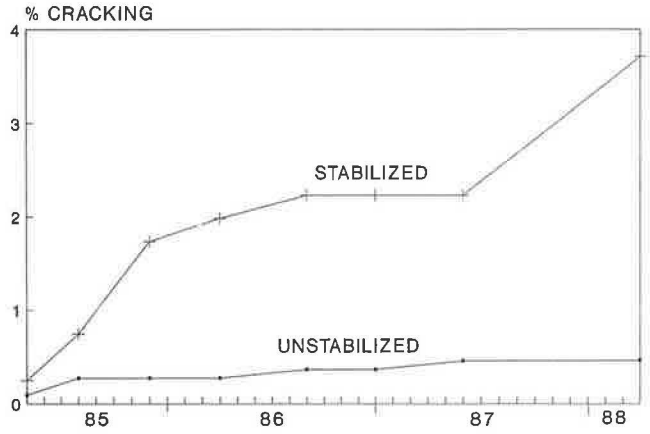


FIGURE 5 Transverse cracking (eastbound, outside lane).

5. Joint 22. Both radar and FWD indicated large voids on both sides of the joint; however, Benkelman beam indicated there is no need for subsealing. A large amount of grout was accepted. Under the slab, a large flow of grout was observed.

In all cases, when grout spread to the joint, some degree of grout penetration to the joint opening was observed.

To detect voids under slabs, a slab deflection reading is used for all these techniques except radar. The amount and shape of deflection determines if a joint needs to be stabilized. The field reading from another study (*3*) indicated that the magnitude of the deflection reading is a function of the degree of the slab curling movement. The deflection reading at the same joint varies depending on the time of day the testing is performed. The difference between maximum and minimum reading in a 24-hr period is greater than 10-fold.

RESULTS AND FINDINGS

Survey results indicated that the rate of cracking is greater in stabilized slabs than unstabilized slabs. The rate of cracking for the stabilized slabs increased rapidly soon after the subsealing operation. The rate of growth became steady a year later. However, in the last year of the monitoring period, a rapid growth rate was detected (see Figures 1–5).

This three-stage cracking phenomenon of the stabilized slabs can be explained by the following hypothesis.

- First Stage. After the slab was stabilized by filling the voids, the support conditions changed. Depending on the change, the new situation may be harmful to the slab. Filling the voids may induce stress caused by temperature change, uneven subgrade support, and restriction of deformation. This extra stress is in addition to the normal stress induced by traffic loading. The resulting stress can cause slab cracking in the first stage.
- Second Stage. After slabs that were disturbed by the subsealing operation cracked and subgrade support was reestablished, the cracking rates slowed down and followed the same pace as the unstabilized slabs.
- Third Stage. Slabs that were stabilized had been subject to poor support conditions for a period of time. Theoretically speaking, fatigue life of the slab is a function of the applied stress. The same wheel loading causes less stress in slabs with uniform support than in poorly supported slabs. Therefore the stabilized slabs have a shorter life expectancy. This hypothesis explains the rate of increase of the third stage.

Although every void detection technique was claimed to be capable of identifying voids beneath concrete slabs, it is not possible to prove that one technique is more reliable than the others from the results presented in Table 6. In fact, none of the five techniques participated in the study demonstrated consistent results.

During the subsealing operation, the operator stops grout injection when the slab starts moving upward or when grout spills from the joints, cracks, or grout holes. Usually, subsealing is performed in the fall and winter when joints are wide open. Grout under pressure may be forced into the opened joint. Observations of grouting operation and the following slab removal sustain this concern. Introducing incompressible material to the joint opening prevents slab expansion. Depending on the percentage of stabilized slabs, filling up joints will prevent them from functioning properly.

CONCLUSIONS

On the basis of this study, it is concluded that

1. Subsealing can fill the voids, thereby restoring slab support, if it is done properly.

TABLE 6 RESULTS OF DEFLECTION TESTING

Joint	Benkelman		FWD		Radar		Deflect	Grout
	B	A	B	A	B	A	*	Taken
1	N	N	Y	Y	Y	Y	- 8%	N
2	Y	Y	Y	Y	Y	Y		L
3	Y	N	Y	N	Y	Y	-48%	L
4	Y	N	Y	Y	Y	Y	-43%	N
5	Y	N	Y	N	Y	Y	-20%	G
6	Y	N	Y	N	Y	Y	-40%	G
7	Y	N	Y	N	Y	Y	+45%	G
8	Y	Y	Y	Y	Y	N	+40%	N
9	Y	N	Y	Y	Y	Y		G
10	Y	N	Y	N	Y	Y	-25%	G
11	Y	N	Y	Y	Y	Y	-20%	G
12	Y	N	Y	Y	Y	Y	-27%	G
13	Y	N	Y	N	Y	Y		G
14	Y	N	Y	Y	Y	Y	-15%	G
15	Y	Y	Y	N	Y	N	-17%	N
16	Y	N	Y	N	N	Y	-25%	G
17	Y	N	N	N	N	Y	-13%	G
18	Y	Y	Y	Y	Y	N	+ 7%	N
19	Y	Y	Y	Y	N	N	+20%	N
20	Y	Y	Y	Y	Y	N	+ 7%	N
21	N	N	Y	N	Y	N	0%	L
22	N	N	Y	N	Y	Y	+38%	G
23	Y	N	Y	N	Y	Y	-22%	G
24	Y	N	Y	N	N	Y	+13%	G
25	Y	N	Y	N	Y	Y	+ 7%	G
26	Y	Y	Y	Y	Y	N	+ 6%	N
27	Y	Y	Y	Y	Y	N	0%	N
28	Y	Y	Y	Y	Y	Y	0%	G
29	Y	Y	Y	Y	Y	Y	+60%	G
30	Y	N	Y	N	Y	Y	0%	G
31	Y	N	Y	Y	Y	Y	+25%	L
32	Y	Y	Y	Y	Y	Y	+25%	G
33	Y	N	N	N	Y	Y	-32%	G
34	Y	Y	Y	N	Y	Y	0%	G

Y: Void detected
N: No void detected
G: Grout taken
L: Low grout taken
N: No grout taken
* Percent change of deflection (before and after)

TABLE 7 BENKELMAN BEAM TEST RESULTS

Indicated Void		Grout	Number of
Before	After	Taken	Joints
Y	Y	Y	5
Y	Y	N	7
Y	N	Y	17
Y	N	N	2
N	N	Y	2
N	N	N	1
	TOTAL		34

TABLE 8 FWD TEST RESULTS

Indicated Void		Grout	Number of
Before	After	Taken	Joints
Y	Y	Y	9
Y	Y	N	8
Y	N	Y	14
Y	N	N	1
N	N	Y	2
	TOTAL		34

2. To eliminate free water effectively, all joints must be resealed following subsealing.

3. If it is not executed properly, subsealing can be harmful to the slab because it may result in raising of slabs and in uneven grout distribution.

4. While using deflection as an indicator in selecting slabs for stabilization, setting the threshold for such selection must also consider the time of day and the season in which testing is performed.

5. The timing of slab stabilization is important. Restoring support is too late if damage to the slab from loss of support has already occurred.

6. There is no reliable nondestructive testing method to detect voids underneath concrete slabs.

TABLE 9 RADAR TEST RESULTS

Change of Deflection	Grout Taken	Number of Joints
increase	Y	7
increase	N	5
no change	Y	4
no change	N	1
decrease	Y	11
decrease	N	3
total		31*

* No report at 3 joints

TABLE 10 DYNAFLECT DEFLECTOMETER TEST RESULTS

Indicated Void Before	After	Grout Taken	Number of Joints
Y	Y	Y	21
Y	Y	N	2
Y	N	Y	1
Y	N	N	6
N	N	N	1
N	Y	Y	3
total			34

TABLE 11 PERCENT OF MATCHING TEST RESULTS

	Benkelman	FWD	Radar
Benkelman	**	85 (74)	79 (18)
FWD	**	**	88 (38)
Grout Taken	67 (73)	67 (65)	73 (6)

Note: before (after)

7. The subsealing operation can introduce incompressible material to joint openings. Such filled joints will obstruct slab expansion.

REFERENCES

1. E. J. Yoder and M. W. Witczak. *Principles of Pavement Design*, 2nd ed., John Wiley, New York
2. M. I. Darter and S. H. Carpenter. *Techniques for Pavement Rehabilitation—A Training Course*, 3rd Revision, FHWA, U.S. Department of Transportation, 1987
3. S. S. Wu and T. M. Hearne, Jr. Performance of Concrete Pavement with Econocrete Base. *Proc., 4th International Conference on Concrete Pavement Design and Rehabilitation*, Purdue University, West Lafayette, Ind., 1989, pp. 683–695.
4. M. Oppermann. *Slab Stabilization Demonstration Project.* North Carolina Department of Transportation

The contents of this report reflect the views of the author. The contents do not necessarily reflect the official views or policy of the North Carolina Department of Transportation.

Publication of this paper sponsored by Committee on Pavement Rehabilitation.

Analysis of Three Concrete Restoration Techniques

B. F. McCullough, David W. Fowler, James R. Lundy, and Brock E. Hoskins

Three concrete pavement restoration techniques are described and the field performance of each is evaluated. Two of the three methods are used to restore the condition of continuously reinforced concrete pavements (CRCP) and the other was used to repair failed joints and broken slabs in an old plain jointed concrete pavement (JCP). Each of the techniques and the analysis results are described. A repair technique using polymer concrete to restore load transfer and seal surface cracks in several lane-miles of IH 610 in Houston, Texas, is described. This project, constructed in 1980, was surveyed in 1990. Results indicated that the majority of the repairs were intact after 10 years of heavy traffic. The area encompassing these polymer concrete repairs is currently being rehabilitated using a bonded overlay. One experimental section in the overlay project investigated the effectiveness of methyl methacrylate as a mop on pretreatment of the existing CRCP. Falling weight deflectometer (FWD) measurements taken before and after the treatment, as well as core analyses, indicated this technique to be only marginally effective in reducing deflection. A second technique used to repair longitudinal construction joints in CRCP before rehabilitation is described. Load transfer was reestablished by epoxying reinforcing steel in slots cut perpendicular to the joint. FWD measurements demonstrated this technique to be of significant benefit. Analyses indicated that the stress was reduced by as much as 40 percent through the use of this technique. The restoration of a two-lane JCP constructed in the 1930s was undertaken as part of an experimental test program to assess several rehabilitation options available for JCP. Deflection measurements were taken near transverse joints and longitudinal cracks before and after the repairs were made. Repairs were effected using precast joints and polymer concrete. Analyses indicated some reduction in deflection as the result of the restoration work.

Pavement repairs are often necessary to maintain a suitable riding quality. As traffic demands have increased substantially over the past several years and will continue to increase, it has become extremely important to implement effective pavement repairs. User costs escalate rapidly as delay increases. Therefore, the time required to implement a specific repair and the subsequent performance of the repair is of concern.

The University of Texas, Center for Transportation Research (CTR), and the Texas State Department of Highways and Public Transportation (SDHPT) have been working together to develop and implement effective repair procedures for PCC pavements. Several repair techniques have been investigated over the past years on distresses common in PCC pavements. Specific repair procedures implemented on continuously reinforced concrete pavements (CRCP) and jointed concrete pavements (JCP) are described and the effectiveness of each repair is evaluated.

The repair procedures discussed and evaluated in this article include the repair of uncontrolled longitudinal cracking on CRCP and JCP, the repair of failed longitudinal joints on CRCP, and the repair of transverse joints on JCP.

Center for Transportation Research, University of Texas, Austin, Tex. 78712.

POLYMER CRACK REPAIRS OF CRCP

Uncontrolled longitudinal cracking was a commonly observed distress in CRCP in the Houston, Texas, area in the late 1970s. Uncontrolled longitudinal cracking may be defined as any longitudinal cracking not occurring at a construction joint or sawed joint. An investigation indicated that the primary contributing factors to this type of cracking included inadequate saw-cut depth, pavement thickness in excess of planned values, and concrete strength variability (*1*). An analysis of several cores indicated that the cracking typically occurred around steel bars, because of a plane of weakness created by the bar itself and by poor consolidation of the concrete beneath the bar as shown schematically in Figure 1. The deterioration associated with these cracks prompted an investigation into possible repair methods.

The University of Texas at Austin, CTR, and the SDHPT developed and implemented a repair procedure for the uncontrolled longitudinal cracking that was present on IH-610 in Houston (see map shown in Figure 2). An example of this type of cracking is shown in Figure 3. The objective of the repair procedure was to seal the cracks to prevent water intrusion and further corrosion of the reinforcing steel.

The repair procedure is described as follows. The cracks were enlarged to a depth and width of approximately 1 in. using a single-piston pneumatic crack router (see Figures 4 and 5). The crack was filled with dry concrete sand. A methyl methacrylate (MMA) monomer system was then poured over the sand until it was completely saturated (see Figure 6). This polymer concrete bonded to and sealed the crack.

In 1980, a contract was let to repair approximately 100,000 linear feet of uncontrolled cracks using this technique. A visual examination of about 15 percent of the repaired cracks 1 year after the repairs were effected indicated that 56 percent were in good condition, 43 percent were in fair condition, and only 1 percent were in poor condition (*2*). Researchers reported that those areas rated fair or poor evidenced wear on the surface, apparently caused by evaporation of monomer from the surface or depletion of the monomer caused by leakage through the bottom of the crack (*2*). A second area

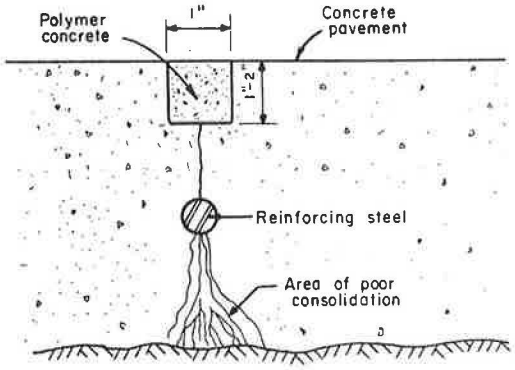


FIGURE 1 Cross section of distress and repair.

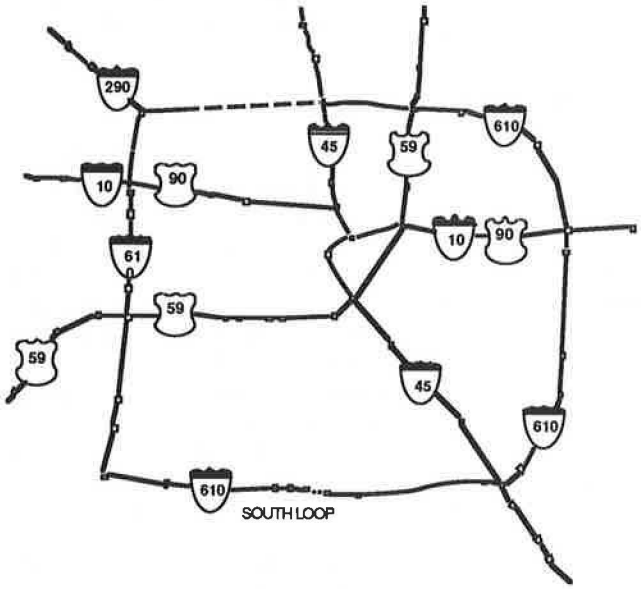


FIGURE 2 Map of Houston area showing location of repair sites.



FIGURE 3 Uncontrolled longitudinal cracking.

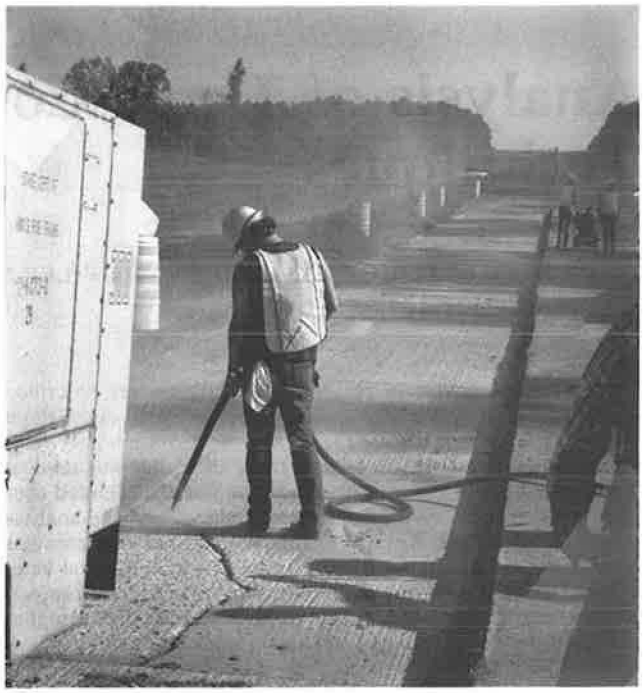


FIGURE 4 Crack router in operation.



FIGURE 5 Routed crack ready to receive polymer concrete filler.



FIGURE 6 Application of monomer.

was treated in 1985. An inspection of this area in 1987 indicated that 80 to 90 percent of the repairs were in good condition. In a few cases, continued lateral movement of the pavement caused longitudinal cracks to reopen either in the repaired areas or adjacent to them (*2*).

A followup survey was conducted in April 1990 to determine the long-term performance characteristics of the polymer concrete crack repairs. Five 200-ft sections were selected randomly. Three of these sections were located in the outside two lanes in the eastbound direction; the other two sections were located in the outside two lanes in the westbound direction. The repairs were again evaluated as being in good, fair, or poor condition. A rating of good required that the crack still be completely filled and sealed with the repair material. To be classified as fair, the majority of the repair material must be in place, but small infrequent cracks could be evident. A rating of poor required that all of the repair material had spalled out. Photos representing each rating condition are included in Figures 7–9. Rating quantities were based on linear feet of repair. The data obtained from the survey are presented in Table 1. Of the repaired longitudinal cracks surveyed, 85 percent were found to be in good condition, whereas only 10 and 5 percent were found to be in fair and poor condition, respectively.

An analysis of variance was performed on these data. The variance was checked between sections, between Lanes 3 and 4, and between ratings (good, fair, or poor). All two-way interactions were also checked for significance. The only parameter that indicated significance was that between ratings, as expected.

One of the westbound sections had transverse crack repairs as well as longitudinal crack repairs. The transverse crack repairs were evaluated in the same manner as the longitudinal crack repairs. However, the transverse crack repair data were not incorporated into the statistical analysis of the data. Within this section, 98 percent of the transverse crack repairs were in good condition, whereas the remaining 2 percent were in fair condition.

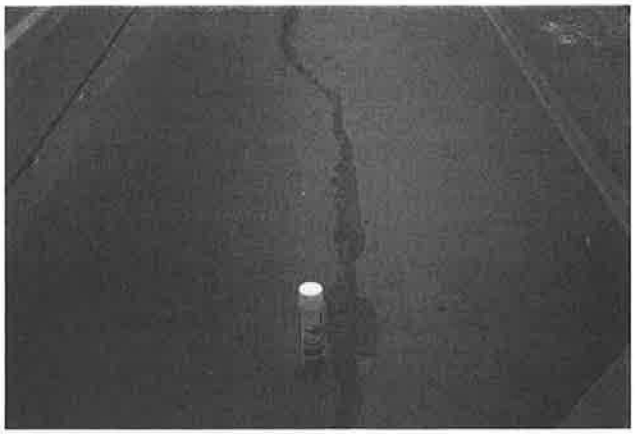


FIGURE 7 Repaired area typical of areas receiving a rating of good.



FIGURE 8 Repaired area typical of areas receiving a rating of fair.

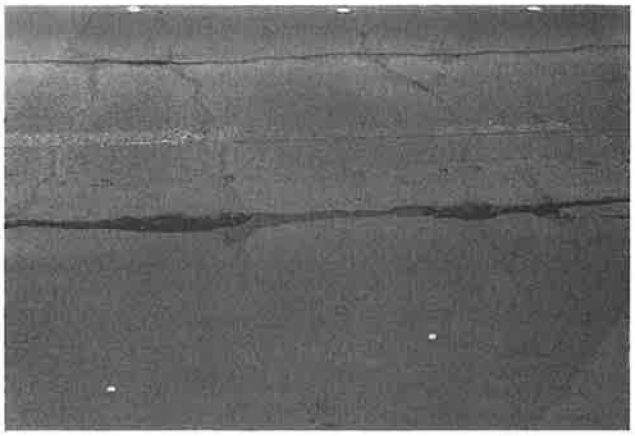


FIGURE 9 Repaired area typical of areas receiving a rating of poor.

TABLE 1 NUMBER OF LINEAR FEET OF REPAIRED CRACK IN EACH CATEGORY AS OF APRIL 1990

Section ID	Lane Number	Rating		
		Good	Fair	Poor
1	3	77	0	0
	4	143	0	0
2	3	58	15	36
	4	119	29	9
3	3	14	0	0
	4	140	0	0
4	3	31	7	0
	4	39	0	0
5	3	78	29	0
	4	0	0	0

The repairs have performed well overall and, based on performance, this technique is an effective means of repairing CRCP. However, the repair process is labor-intensive. Repairs on IH-610 were performed by several contractors. Investigators reported the cost for repairs ranged from \$6/ft to \$8/ft. The crack routing was performed at the rate of 25 ft/hr and bits had to be sharpened or replaced every 175 ft. The sand and monomer were placed manually and the sand was rewetted with monomer several times to maintain a saturated condition (*2*). If this technique is to considered viable, alternate procedures and techniques should be investigated to make the repair be more economical.

REESTABLISHING LOAD TRANSFER IN CRCP LONGITUDINAL JOINTS

Major repairs of CRCP longitudinal joints are increasingly becoming a necessary, though onerous, task for many highway agencies. When repair of longitudinal joints or cracks is required on major freeways, lane closures constitute a significant inconvenience to users. Fifty percent of the capacity of a four-lane facility may be lost if repair of the center longitudinal construction joint is required. Obviously, any effective method that expedites the procedure will result in a substantial savings to the public.

The preparation of an existing CRCP for rehabilitation using a bonded concrete overlay also requires repairs. In addition to the prerequisite surface cleaning using shot-blasting or cold milling, repairs are normally required to restore the structural integrity of the existing pavement. These repairs range from longitudinal joint routing and sealing to full-depth replacement of highly distressed areas. The discussion that follows is directed to the repair of longitudinal joints and cracks before the placement of a bonded concrete overlay. Similar techniques could be used on a CRC pavement that was not planned for immediate rehabilitation.

A common problem found in multilane facilities is the separation of lanes, particularly at the longitudinal construction joint shown in Figure 10. The parting of the adjacent lanes is particularly severe on horizontal curves where separation of 6 in. have been found. Uncontrolled longitudinal cracking may also be present on CRCP being considered for a bonded overlay. Although these cracks are narrow initially, with time they propagate and spall, resulting in a reduction in load transfer efficiency. The widths of these uncontrolled cracks are generally less than 1 in.



FIGURE 10 Separation of longitudinal construction joint.

These gaps, whether between lanes or midlane, represent a structural deficiency of the pavement. Transverse steel at these locations is deteriorated or nonexistent, thus eliminating load transfer. The opening allows the infiltration of water and incompressible fines, further aggravating the problem. Faulting and the associated traffic safety hazard eventually result if this problem is left untreated. Restoration of the structural integrity of the underlying slab is necessary before the placement of a bonded overlay.

Several types of repairs were performed on an existing CRCP in Houston, Texas, before the placement of the 4-in. bonded overlay. One form of repair attempts to reestablish load transfer across failed longitudinal joints and cracks by stitching the two sides of the crack together. In this context, stitching refers to cutting 1-in.-wide slots at 12-in. centers perpendicular to the joint. These slots are cut to a depth of 3 in. and an overall length of about 54 in., centered on the joint. After the slot is cleaned, a No. 5 tiebar is epoxied in the groove. Normal surface preparation follows after the specified curing time. A schematic of the repair is shown in Figure 11.

The majority of the stitching was done on longitudinal construction joint at the center of the four driving lanes in each direction. Some repairs of this type were necessary between Lanes 1 and 2, or Lanes 3 and 4, on the sawn longitudinal

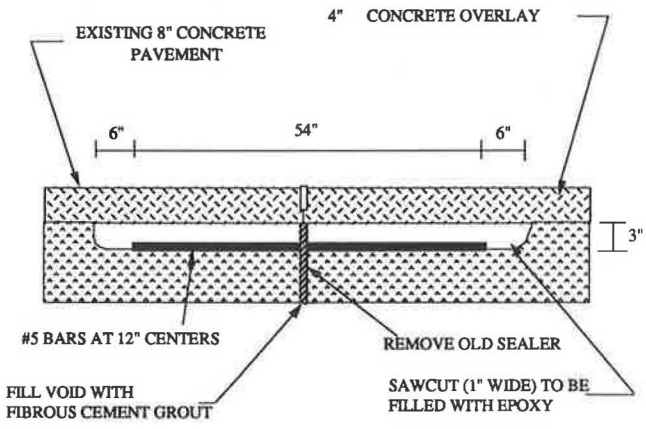


FIGURE 11 Schematic of longitudinal construction joint repair technique.

joint. The center construction joint could not be accessed because of the concrete median barriers used for traffic control during construction. Therefore two joints, each approximately 75 ft in length at the longitudinal sawn joint between Lanes 1 and 2, were selected for investigation.

Falling weight deflectometer (FWD) measurements were taken in each of these sections after the area had been closed to traffic. Before repair, FWD measurements were taken in February 1989 and, after repair, data were collected in June 1989. The general layout of the data collection at each site is shown in Figure 12. A summary of the influence of the repairs on the measured deflection is presented in Table 2. These results indicate that there has been a substantial decrease in the deflection as a result of the stitching repairs. However, because these measurements were taken at different times of the year under different environmental conditions, it is possible that some of the reduction in deflection could be attributed to seasonal effects rather than the repairs themselves.

Deflection measurements were taken at several (94) sites in February and June that were not repaired. These nonrepaired sites allow the influence of season and environment to be factored out of the repair site measurements. Thus, the true effect of the repair may be determined. Table 3 presents a summary of this work. Obviously a substantial decrease in deflection has occurred in the repair areas that may be attributed solely to the stitching. The deflection parameters most representative of the condition of the surface layer, namely the surface curvature index (SCI), basin slope (BS), and Sensor 1 deflection, have all decreased approximately 40 percent

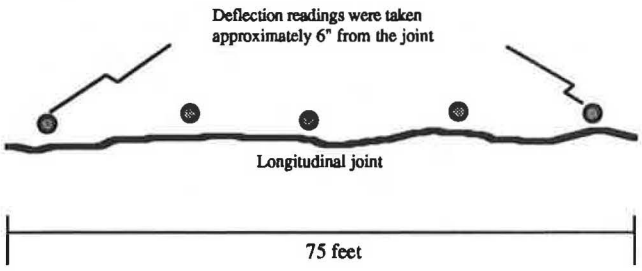


FIGURE 12 Plan view of deflection measurement locations.

TABLE 2 AVERAGE PERCENT CHANGE FOR ALL DROP HEIGHTS IN VARIOUS DEFLECTION PARAMETERS AFTER REPAIR

Site	Location	Load	DF1	SCI	BCI	BS
1	1	-8	-46	-72	-27	-55
	2	-10	-44	-69	-28	-54
	3	-12	-40	-23	-28	-48
	4	-12	-44	-42	-49	-51
	5	-11	-48	-76	-40	-59
2	6	-10	-45	-50	-28	-52
	7	-12	-36	-44	-29	-40
	8	-24	-34	-36	-45	-40
	9	-18	-42	-51	-31	-47
	10	-11	-39	-13	-30	-46

Notes: DF1= deflection sensor #1
SCI = Surface curvature index (sensor #1 - sensor #2)
BCI = Base curvature index (sensor #6 - sensor #7)
BS = Basin slope (sensor #1 - sensor #7)

TABLE 3 INFLUENCE OF SEASON (JUNE TO FEBRUARY) ON AVERAGE PERCENT DIFFERENCE OF VARIOUS DEFLECTION PARAMETERS

	Load	DF1	SCI	BCI	BS
Repaired	-13	-42	-56	-32	-49
Non-Repaired	-14	-8	-8	1	-5

as a result of the repairs. Although this is indicative of the effectiveness of the method, it does not establish fully the benefit received through the use of this repair technique.

The modulus values for a three-layer pavement structure were calculated using a backcalculation program for the before and after repair conditions. Average deflections for each of the four FWD drop heights were used as input to the program. The average modulus values for the three layers specified are presented in Table 4.

Using these modulus values and the equations of Westergaard, stresses in the concrete layer before and after repair can be calculated. The before-repair case was assumed to be best represented by the edge condition described by Westergaard caused by the large crack width and relative lack of load transfer. The after-repair condition was represented by an interior condition. The modulus of subgrade reaction required for the Westergaard analysis was obtained using the procedure described in the AASHTO Design Guide for determining a composite k-value. Table 5 presents the stresses calculated for each of the conditions.

Using the fatigue equation presented by Taute et al. and an assumed concrete strength of 650 psi, the expected life of the before-repair pavement was 880,000 18-kip ESALs, while the after-repair pavement should survive 3,900,000 ESALs repetitions without failure. These projections of fatigue life are provided for comparison purposes only.

From these analyses, it appears that a substantial reduction in deflection has occurred in those areas where the stitching repair technique was used. Although the exact benefit in terms of added life can not be determined, it is logical to assume that any reduction in pavement deflection on the order of 40 percent will substantially increase the life of the pavement. This reduction in deflection is of particular benefit when placing a thin, bonded concrete overlay.

JOINT AND CRACK REPAIR ON US-59

In 1989, repairs were made on a selected area on US-59 in District 11. This project served as a pilot study to determine the effectiveness of various types of concrete repairs. Repair techniques judged effective will be included in test sections to be constructed in 1991. These test sections are part of a research project undertaken by the Texas SDPHT to develop a long-range plan for the rehabilitation of 140 mi of US-59 in east Texas.

Approximately one-half of the total centerline mileage is rigid pavement and all of the rigid pavement has been overlaid with asphalt concrete. Reflective cracking and rutting are the most common distress manifestations throughout these overlaid sections. In the particular area selected for the pilot

TABLE 4 MODULUS VALUES BACKCALCULATED FROM FWD MEASUREMENTS

Pavement Layer	Modulus Values in psi	
	Before Repair	After Repair
CRC	4,300,000	6,500,000
Cement Treated Base	300,000	930,000
Roadbed Material	14,400	17,800

TABLE 5 CALCULATED STRESSES BEFORE AND AFTER REPAIR

	Composite k	Radius of relative stiffness	Stress (psi)
Before repair	1000	20.7	243
After repair	1500	20.8	148

study, the rigid pavement was constructed in the 1930s. The overlaid 9-7-9 thickened-edge jointed pavement was thought to be representative of the rigid pavements in the project.

The pilot study consisted of removing the existing asphalt concrete, effecting the repairs, and replacing the overlay. The effectiveness of the repairs would be judged by comparing the before- and after-repair FWD measurements and time for reflective cracks to develop repaired and non-repaired areas.

Figure 13 shows the repair site before milling. Approximately 7 in. of asphalt concrete was removed. After milling was completed, three joints were selected for replacement using the precast drop-in unit (see Figure 14). Sawing and subsequent removal required approximately 4.5 hr. The precast joint was placed on a graded bed of cement-stabilized sand. Set 45 was used as the filler material, or zipper, for two of the slabs and polymer concrete for the other.

Another joint was milled to a depth of about 3.5 in. and a width of 4 ft using the milling machine. On the following day, this joint received a prefabricated dowel basket assembly and Type III concrete. The milling operation required approximately 30 min (see Figure 15). Because both joint repair preparation techniques (sawing and milling) use water to lubricate the cutting heads, there was considerable water standing on the slab following joint preparation. Several hours were spent removing the water and cleaning the slab for monomer placement the following day.

Drying of the cracks and joints using propane burners and additional cleaning of these areas were required before implementing the crack repair procedure. Air-blasting of the cracks was followed by sand blasting in preparation for the monomer treatment. Most of the cracks were repaired using a monomer treatment. Others were treated with epoxy mortar. The monomer material was the same type as that used for the previously discussed repairs in Houston.

FWD measurements were taken on the concrete pavement before and after repairs. Analysis of the measurements in the entire repair section showed a 20 percent overall reduction in deflection because of the repairs. The precast slab showed a 22 percent reduction in deflection, on the basis of measure-



FIGURE 13 Repair site before construction.



FIGURE 14 Placement of precast joint section.

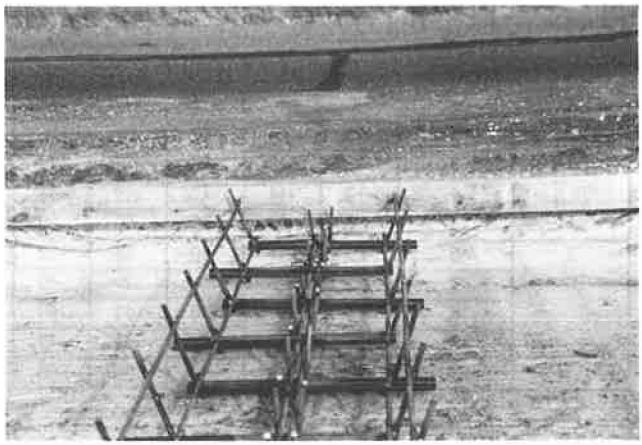


FIGURE 15 Milled joint and dowel basket assembly.

ments taken at the joint and adjacent to the slab on both sides of the joint. This reduction represents improved load transfer across the joint, which causes lower stress and subsequently increases pavement life. This reduction also reduces the probability that faulting will occur at the joint and subsequently reduces the severity of reflective cracking.

For the monomer crack repair, a 30 percent reduction in deflection was realized. Deflections were not measured on the dowel basket assembly joint replacement because the concrete needed time to cure. Deflections were compared before and after repairs at a location where no repairs occurred to realize differences in deflection caused by temperature. The change in deflection was insignificant and was, in fact, a slight increase.

A visual inspection of the pilot repair site was conducted in December 1989. No significant cracks had developed in the asphalt concrete. This short period, however, cannot be used to determine the performance of the repairs. The site should be monitored for several years to properly assess the effectiveness of the repairs. These repair techniques will also be implemented and subsequently monitored in a 1,000-ft test section on US-59 to be constructed this year.

On the basis of the FWD measurements taken, both the joint and crack repairs have proven effective. With regard to short-term performance, these repairs have performed well under traffic. However, both joint and crack repair techniques are labor-intensive. For the joint repair techniques to become more cost-effective, a better procedure for removing the concrete is needed. For the crack repairs, better procedures for routing and filling the cracks are needed. The estimated material costs for each repair procedure are as follows: (a) precast joint—$620 per joint lane, (b) milled joint—$150 per joint per lane, and (c) polymer concrete crack repair—$0.20 per linear foot.

CONCLUSIONS AND RECOMMENDATIONS

All of the repair procedures discussed have proven effective. The polymer concrete crack repairs in Houston have performed extremely well for 10 years under heavy traffic. The longitudinal joint repairs in Houston have been effective, as they have resulted in a 40 percent reduction in deflection. The polymer concrete crack and joint repairs in east Texas have resulted in a significant reduction in deflection and have performed well under traffic for several months.

However, further investigation is recommended for these repair procedures, as they have also proved to be labor-intensive. Alternative techniques should be investigated to make each repair procedure more economical. For the polymer concrete crack repair, a more rapid procedure for enlarging the cracks and a less labor-intensive method for filling the cracks are needed. For both the longitudinal and transverse joint repair, a more rapid method for removing the concrete is needed. It is anticipated that using larger bars at a larger spacing will result in a more cost-effective process.

The University of Texas at Austin, CTR, and SDHPT will continue to investigate the implementation and performance of these and other repair procedures for PCC pavements. It is expected that these repair procedures will be improved and that new techniques will be developed.

REFERENCES

1. B. F. McCullough. Longitudinal Cracking of CRCP in Houston Area. Technical Memorandum 388-2, Center for Transportation Research, The University of Texas at Austin, Dec. 1983.
2. W. D. Mangum, A. J. Bermudez-Goldman, D. Whitney, D. Fowler, and A. H. Meyer. Repairing Cracks in Portland Cement Concrete Using Polymers. Research Report 385-2F, Center for Transportation Research, The University of Texas at Austin, Nov. 1986.

Publication of this paper sponsored by Committee on Pavement Rehabilitation.

Development of Drainage Coefficients for the 1986 AASHTO Guide for Design of Pavement Structures

STEPHEN B. SEEDS AND R. GARY HICKS

A mechanistic-empirical methodology was applied to the procedure for considering the effects of drainage in the new AASHTO Guide pavement structural design process. The procedure considers the level of moisture exposure as well as the quality of drainage. Development of both rigid and flexible pavement models is covered. In addition, some of the general considerations associated with moisture effects and various drainage and subdrainage systems are discussed. Finally, recommendations are provided for future work to improve the methodology.

Generally speaking, most pavements fail because of a combination of three primary factors: traffic (cumulative wheel load applications), inadequate structural capacity (or loss of structural capacity), and poor support (or loss of support). Although some pavements have been known to fail because of various environmental effects, cumulative load applications are generally considered to be the number one cause of distress and deterioration. That is, if there were no traffic, there would be almost no distress. On the other hand, reduced capacity and inadequate support can also be important because, if the pavement is too thin or the support too weak, it would not take much traffic to result in failure.

Because engineers have little control over the ultimate traffic, their focus during the design stage is on the pavement structure and the support provided by the roadbed soil. If the support is strong, they tend to design relatively thin pavements. Conversely, if the support is weak, they must design relatively thick pavements. The strength of the support is dependent on the type of soil, its density, its permeability (or gradation), and its moisture content. Moisture content is perhaps the most critical factor related to support strength because it can make strong soils weak and weak soils weaker. In fact, it also weakens the strength of the layers that compose the pavement structure and, if present in sufficient quantities beneath a cut section of a sloping ground surface, can result in a severe slope failure. Recognition of the adverse effects of moisture on pavement performance led one famous pavement designer to observe that: "There are three important things to consider in the design of highway pavements, drainage, drainage, and drainage."

A considerable amount of work has been accomplished over the years in (a) identifying the sources of moisture that affect pavement performance, (b) developing design and construction procedures to drain or remove moisture, and (c) evaluating and predicting the effects of moisture. Following is a summary of several studies that are of pertinence to the subject. In 1974, Cedergren (*1*) prepared a textbook entitled *Drainage of Highway and Airfield Pavements* that describes the types of damage caused by poor drainage, provides techniques for estimating the influx of moisture, and reviews subsurface drainage design and construction methods that may be used to control moisture. With this work as a basis, Moulton (*2*) prepared a formal highway subdrainage design manual for the FHWA in 1980 that provided detailed procedures and guidance on the prediction of moisture inflow and on the design, construction, and maintenance of a variety of highway subdrainage systems. Ridgeway's report for NCHRP on pavement subsurface drainage systems (*3*) provided an excellent synthesis of design considerations and state practices through 1982. Carpenter et al. (*4*) completed a study for the FHWA in 1980 that provided a method for evaluating the potential for moisture accelerated (pavement) distress (MAD) to occur. It consists of a rating-indexing scheme both for the environment and for the characteristics of the pavement structure.

Recognition of the need to consider drainage in the pavement design process led the AASHTO Joint Task Force on Pavements to require the inclusion of drainage considerations in the new *AASHTO Guide for Design of Pavement Structures—1986* (*5*). Volume 1, Part I, of the Guide addresses the impacts of moisture, gives general design considerations, and references the work of Moulton (*2*) and Ridgeway (*3*). Volume 1, Part II, provides a subjective procedure for treating the moisture exposure level and the quality of drainage in the structural design process for both flexible and rigid pavements. Volume 2, Appendix AA, of the AASHTO Guide (*6*) contains an excerpt from a paper prepared originally by Benson (*7*) that, like Ridgeway (*3*), also provides guidelines for the design of highway internal drainage systems. This appendix is basically a summary documentation of the procedure that has been used extensively by the Illinois DOT in evaluating special moisture and drainage problems.

Overall, the AASHTO Guide provides procedures that can be used to evaluate the effects of drainage systems (and other important factors) on overall pavement performance and life cycle costs. In fact, the methodology has been incorporated into a user-friendly menu-driven computer program (*8*) that has made the process of evaluating alternative pavement designs much simpler.

S. B. Seeds, ARE Inc., 2600 Dellana Lane, Austin, Tex. 78746. R. G. Hicks, Department of Civil Engineering, Oregon State University, 106 Colvell Hall, Corvallis, Ore. 97331.

PURPOSES

One purpose is to discuss some of the key elements related to highway drainage as they are presented in the AASHTO Guide (*5*). The second (and more important) purpose is to describe the methodology that was used to treat the effects of moisture environment and quality of drainage in the pavement structural design process. Discussion of the first purpose is a recapitulation of Part I. Section 1.8, of the AASHTO Guide (*5*); the second purpose is essentially Volume 2, Appendix DD, of the Guide (*6*).

DRAINAGE DESIGN

Moisture Impacts

Drainage of water from pavements has always been an important consideration in road design; however, current methods of design that do not incorporate permeability into the design process have often resulted in base courses that do not drain well. This excess water combined with increased traffic volumes and loads often leads to early pavement distress in the pavement structure.

Water enters the pavement structure in many ways, such as through cracks, joints, or pavement infiltration, or as groundwater from an interrupted acquifer, high water table, or localized spring. Effects of this water (when trapped within the pavement structure) on pavements include

1. Reduced strength of unbound granular materials;
2. Reduced strength of roadbed soils;
3. Pumping of concrete pavements with subsequent faulting, cracking, and general shoulder deterioration; and
4. Pumping of fines in aggregate base under flexible pavements with resulting loss of support.

Less frequently noticed problems caused by entrapped water include (but are not limited to)

1. Stripping of asphaltic concrete,
2. Differential heaving over swelling soils, and
3. Frost heave.

The *AASHTO Interim Guide for Design of Pavement Structures* (*9*) did not treat the effects of drainage on pavement performance. In the new Guide, drainage effects were directly considered for the effect of moisture on roadbed soil and base strength (for flexible pavements) and for the effect of moisture on subgrade strength and base erodability (of concrete pavements). Although the effects of asphalt concrete stripping are not directly considered, those of swelling soils and frost heave are.

Moisture Treatment Methods

Methods for treating water in pavements have generally consisted of

1. Preventing water from entering the pavement,
2. Providing drainage to remove excess water quickly, and
3. Building the pavement strong enough to resist the combined effects of load and water.

When all possible sources of water are considered, protection of the pavement structural section from water entry requires interception of groundwater as well as sealing of the pavement surface. Considerable attention has generally been given to intercepting groundwater, whereas less attention has been given to sealing the surface to exclude infiltration from rain and snow melt. As a result, a considerable amount of water often enters the pavement substructure, resulting in a need for some type of drainage.

In order to obtain adequate pavement drainage, the designer should consider providing three types of drainage systems: (a) surface drainage, (b) groundwater drainage, and (c) structural drainage. Such systems, however, are only effective for free water. Water held by capillary forces in soils and in fine aggregate cannot be drained. The effects of this bound moisture must be considered in the design of pavement structures through its effect on the pavement material properties. Most existing pavements do not include drainage systems capable of quickly removing free water.

Most existing design methods have relied on the practice of building pavements strong enough to resist the combined effects of load and water. However, they do not always account for the potential destructive effects of water within the pavement structure. As a result, increased emphasis is needed to exclude water from the pavement and provide for rapid drainage. Although both approaches are extremely complex, the AASHTO Guide only emphasizes the treatment of drainage. However, maintenance policies should recognize the benefits and necessity of maintaining the joint and crack sealant and thus preventing water from leaking into the subbase layer.

Design Criteria for Pavement Subsurface Drainage

Two general types of pavement subsurface design criteria have been proposed for the use in pavements (*3*). These include

1. Criterion for the time of drainage of the base or subbase beginning with the flooded condition and continuing to an established acceptable level, and
2. An inflow-outflow criterion, by which drainage (outflow) occurs at a rate greater than or equal to the inflow rate, thus avoiding saturation.

Removal of the free water is often accomplished by draining the free water vertically into the subgrade, or laterally through a drainage layer into a system of pipe collectors. Generally, the actual purpose will be a combination of the two. Details of the design of subsurface drainage systems are important and are, therefore, addressed in Appendix AA, Volume 2, of the Guide (*6*).

Incorporation of Drainage Into the Guide

Drainage effects on pavement performance have been included in the new Guide by considering the effect of water

on the properties of the pavement layers and the consequences to the structural capacity of the pavement. Additional work is needed to document the actual effect of drainage on pavement life.

For new design (Part II), the effect of drainage is considered by modifying the structural layer coefficient (for flexible pavements) and the load transfer coefficient (for rigid pavements) as a function of

1. Quality of drainage (e.g., the time required for the pavement to drain), and
2. Percent of time the pavement structure is exposed to moisture levels approaching saturation.

The development of this methodology is described in the following section.

DEVELOPMENT OF COEFFICIENTS FOR TREATMENT OF DRAINAGE

This development of drainage coefficients used in flexible and rigid pavement design procedures was presented in Part II of the Guide. For flexible pavement design, the m value is used to reduce or increase the layer coefficient of the base and subbase layers. For rigid pavement design, the C_d value is used to modify stress conditions in the portland concrete cement (PCC) slab.

Effects of Water on Pavement Behavior

The Interim Guide (*9*) did not recognize the effect of positive drainage within the pavement structure on the life of the pavement. The introduction of the m and C_d values is intended to account for this important factor. Moisture in the pavement structure has a direct effect on the following:

1. Asphalt Concrete Surface. Water can lead to moisture damage, modulus reduction, and a loss of tensile strength. The experience of the authors indicates that saturation alone can reduce the dry modulus by 30 percent or more.
2. PCC Surface. Moisture has only a slight effect on the modulus and strength of PCC, but it can have an effect on curling and warping stresses in the slab.
3. Aggregate Base and Subbase. Added moisture will result in a loss of stiffness for all unbound aggregate materials. Reductions in modulus values of more than 50 percent have been reported in the literature (*10,11*).
4. Treated Bases. For asphalt-treated base (ATB), modulus reductions of up to 30 percent can be expected. For cement-treated base (CTB) and lime-treated base (LTB), modulus reductions caused by moisture would be slight; however, these materials are more susceptible to freeze-thaw damage.
5. Roadbed Soil. Free-draining soils should experience little modulus reduction, whereas those with low to very low permeability could experience modulus reductions of 50 percent or more.

The effect of moisture on roadbed soil is considered in the development of an "Effective Roadbed Soil Modulus," Appendix HH, Volume 2, of the new AASHTO Guide (*6*).

Quality of Drainage

The first issue addressed was the establishment of what constitutes good, fair, and poor drainage conditions. The method used to establish the quality of drainage was to calculate the time required to drain the base layer to 50 percent saturation (T_{50}). The actual approach followed is described by Moulton (*2*); T_{50} is determined for different combinations of permeability (k), length of drainage path (L), thickness of drainage layer (H), effective porosity (n), and slope (S). Results of the calculations are presented in Table 1. Because the permeability of the AASHO Road Test materials was 0.1 ft/day (or less), and the length of the drainage path (lane width in this case) was 12 ft, the time required to drain the unbound layers would be on the order of 5 to 10 days (approximately 1 week). If the length of the drainage path had been 24 ft, it would have taken 18 to 36 days (approximately 1 month) to drain. Using information provided by Moulton (*2*), the quality levels presented in Table 2 were established for drainage.

These criteria are recommended for use in both flexible and rigid pavement design.

Development of Flexible Pavement m Values

The approach used to evaluate the effect of drainage for flexible pavement design was to include adjustment factors (m values) to the structural number equation that modify the layer coefficients according to the anticipated moisture (drainage) conditions:

$$SN = a_1D_1 + a_2m_2D_2 + a_3m_3D_3 \quad (1)$$

where

SN = structural number,
a_1,a_2,a_3 = structural layer coefficients,
D_1,D_2,D_3 = layer thicknesses, and
m_2,m_3 = effect of water on the stiffness (strength) of each material.

In order to evaluate the effect of the m values on pavement thickness, three typical cross sections were evaluated (see Figure 1). It was assumed initially that the m values might vary from 0.5 to 1.4. This assumption resulted in new values of SN for each of the three cross sections shown in Figure 1. These values together with the incremental SN and D_1 values associated with each m value are given in Table 3. Note that an m value greater than 1.0 would result in a net decrease in required total SN or, if applied only to the surface layer, a decrease in surface thickness of about 1 to 2.5 in., depending on base thickness. Similarly, selection of an m value less than 1.0 would result in an increase in SN or in surface thickness. Because of its simplicity, this approach was selected for use in the Guide; however, additional evaluation was considered necessary to establish the m values for various qualities of drainage. Two approaches were considered in selecting m values:

1. Experience—based on field data, and
2. Theory—based on mechanistic analysis.

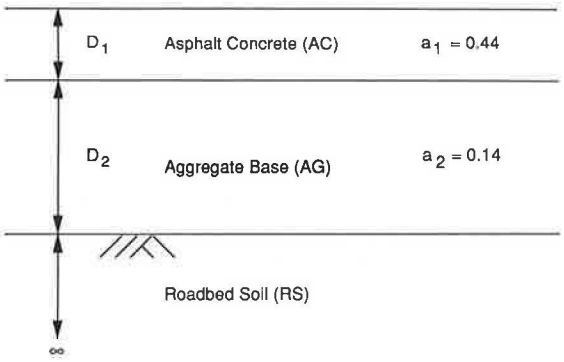
TABLE 1 TIME (DAYS) TO DRAIN BASE LAYER TO 50 PERCENT SATURATION (DAMP)

Permeability, k (ft/day)	Porosity, n	Slope, S	H = 1		H = 2	
			L=12	L=24	L=12	L=24
0.1	0.015	0.01	10	36	6	20
		0.02	9	29	5	18
1.0	0.027	0.01	2	6	5	18
		0.02	2	5	1	3
10.0	0.048	0.01	0.3	1	0.2	0.6
		0.02	0.3	1	0.2	0.6
100.	0.08	0.01	0.05	0.2	0.03	0.1
		0.02	0.05	0.2	0.03	0.1

Note: H refers to the thickness of the drainage layer (in feet) and L refers to the length of the drainage path (in feet).

TABLE 2 DRAINAGE QUALITY LEVELS

Quality of Drainage	Durations Required to Remove Water	
	Calculated	Recommended
Excellent	2–4 hr	2 hr
Good	½–1 day	1 day
Fair	3–6 days	7 days
Poor	18–36 days	1 month
Very poor	> 36 days	Does not drain



Case	Layer Thickness (inches)		SN
	D_1	D_2	
A	4	8	2.88
B	5	15	4.30
C	6	20	5.44

FIGURE 1 Pavement cross section (cases) evaluated in preliminary analysis.

TABLE 3 EFFECTS OF *m* VALUES ON SN AND SURFACE THICKNESS

m Value	m_2a_2	Cross Section (Case)		
		A	B	C
Calculated SN values				
1.4	0.196	3.33	5.14	6.56
1.0	0.140	2.88	4.30	5.44
0.7	0.098	2.54	3.67	4.60
0.5	0.070	2.32	3.25	4.04
Incremental SN values				
1.4	–	−0.45[a]	−0.84	−1.12
1.0	–	0.00	0.00	0.00
0.7	–	+0.34	+0.63	+0.84
0.5	–	+0.56	+1.05	+1.40
Incremental surface thicknesses (in.)				
1.4	–	−1.02[a]	−1.91	−2.55
1.0	–	0.00	0.00	0.00
0.7	–	+0.77	+1.43	+1.91
0.5	–	+1.27	+2.39	+3.18

[a]A minus sign indicates a reduction in cross sections as a result of improved drainage. A plus sign indicates an increase in cross section as a result of the lack of drainage.

As there were few field data to evaluate the effect of drainage on pavement life or pavement thickness, the theoretical approach was selected.

For the factorial of cross sections shown in Figure 2, the surface deflections (between the dual tires) were calculated using the ELSYM5 computer program (*12*). The modulus value for the surface was selected to represent an average condition at the AASHO Road Test. The modulus values selected for the aggregate base from experience demonstrate the potential effect of moisture (e.g., 40,000 psi corresponds to good drainage, whereas 10,000 psi is equivalent to very poor drainage). Modulus values used for the roadbed soil are typical of those found throughout the United States. The

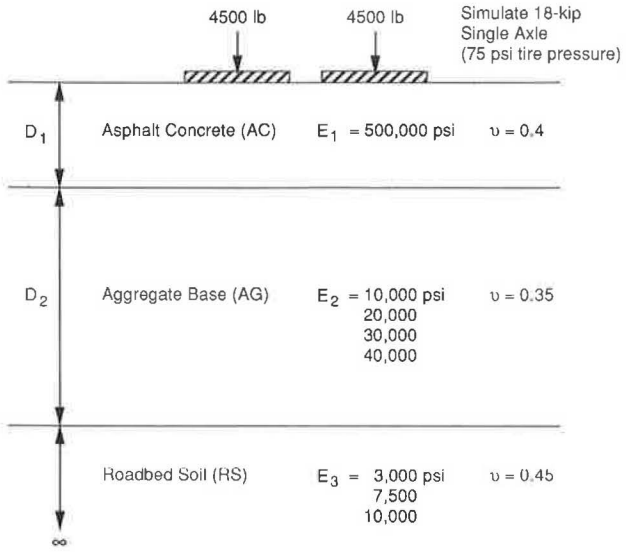


FIGURE 2 Pavement structural and material characteristics considered in ELSYM5 (elastic layer) analysis.

AASHO Road Test condition was assumed to have an aggregate base modulus of 30,000 psi and a roadbed soil modulus of 3,000 psi. Surface deflections for these conditions and for the three cases shown in Figure 2 are presented in Table 4. Surface deflections for the other modulus values are shown in Figure 3.

In order to quantify the effect of reducing base modulus on pavement thickness requirements, similar calculations were made, but with overlay thicknesses of 3, 5, and 6 in. over the sections shown in Figure 2. These results are presented in Table 5.

For E_2 equal to 10,000 psi (poor drainage), the surface deflections are plotted in Figure 4 versus overlay thickness. The added overlay thickness needed to maintain the surface deflection for the AASHO condition (E_2 = 30,000 psi) is also shown on the figure. Note that added surface thickness required increases with increasing base thickness. Figures 5 and 6 show similar results for E_2 to 20,000 and 40,000 psi, respectively.

In order to associate reduced modulus with m value, the incremental surface thicknesses summarized in Table 3 have been plotted in Figure 7. When these values are compared with the incremental thickness requirements on the basis of equal deflections, m values can be determined for the different base modulus values as presented in Table 6. This table indicates that a material having a base modulus of 10,000 psi would have an m value of about 0.4 whereas those with base moduli of 20,000 and 40,000 psi would have m values of about 0.7 and 1.2, respectively. Extrapolating these results yields an m value of 1.4 for an E_2 of 50,000 psi. On the basis of these results, the m values presented in Table 7 are recommended. However, it is recognized that these values would also vary with the percent of time the pavement structure is exposed to moisture levels approaching saturation. Figure 8 shows the approach for considering the variation in m value with percent of time the structure is in or near a saturated condition. This procedure was used for the development of the recommended m values presented in Table 8 [from Volume 1, Part II, Table 2.4 (*5*)].

These m values apply only to the effect of drainage on untreated base and subbase layers. Although improved drainage is certainly beneficial to stabilized or treated materials, the effects on performance of flexible pavements were not considered as profound as those indicated in Figure 8.

TABLE 4 SURFACE DEFLECTIONS FOR THREE CASES SHOWN IN FIGURE 2

Case	SN	Deflection (10^{-3} in.)
A	2.88	48
B	4.30	34
C	5.44	28

Development of Rigid Pavement C_d Values

The rigid pavement performance equation that has been modified to include a term C_d to account for the effects of drainage follows:

$$\log_{10}(W_{18}) = 7.35 * \log_{10}(D + 1) - 0.06 + \frac{\log_{10}\left(\frac{\Delta PSI}{4.5 - 1.5}\right)}{\left[1 + \frac{1.624 * 10^7}{(D + 1)^{8.46}}\right]} + (4.22 - 0.32 * p_t) * \log_{10}\left\{\frac{S_c' * C_d * (D^{0.75} - 1.132)}{215.63 * J\left[D^{0.75} - \frac{18.42}{(E_c/k)^{0.25}}\right]}\right\} \quad (2)$$

where

W_{18} = predicted number of 18-kip ESAL applications that can be carried by the pavement structure after construction,
D = pavement slab thickness (in.),
P_t = design terminal serviceabiliy index,
ΔPSI = difference between the initial design serviceability index (p_0) and the terminal design serviceability index (p_t),
S_c = PCC modulus of rupture (psi),
J = load transfer coefficient,
C_d = drainage coefficient,
E_c = PCC modulus of elasticity (psi), and
k = modulus of subgrade reaction (pci).

Because drainage condition influences slab support and therefore the overall stress condition in the slab, C_d was introduced into the portion of the performance Equation 2 that considers the slab's strength, stress, and support condition. In fact, C_d has the same relative impact on rigid pavement performance as both the modulus of rupture (S_c) and the load transfer

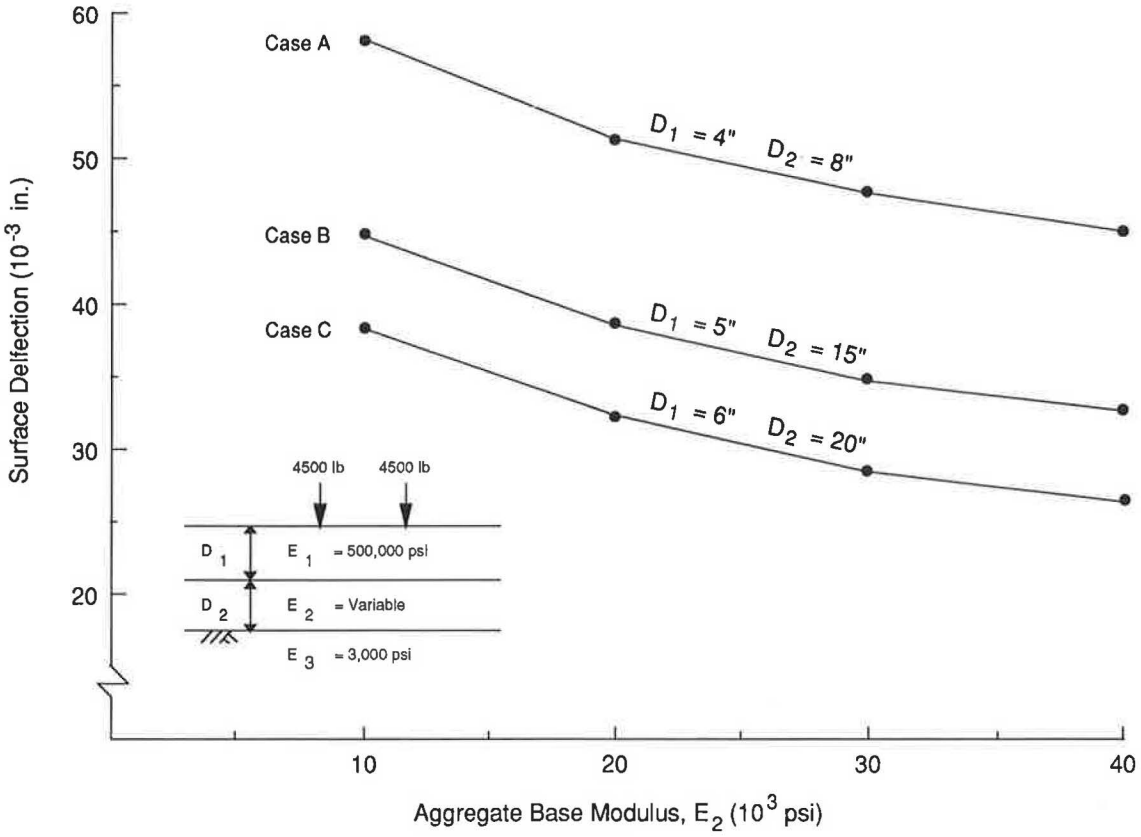


FIGURE 3 Variation in surface deflection with base modulus, AASHO road test conditions.

TABLE 5 VARIATION IN SURFACE DEFLECTION WITH OVERLAY THICKNESS (ROADBED SOIL MODULUS, E_3 = 3,000 psi)

Aggregate Base Modulus, E_2 (psi)	Case	Surface Deflection (10^{-3} in.) for Various Overlay Thicknesses, D_{ov} (in.)				
		-2.0	0.0	3.0	5.0	6.0
10,000	A	81.3	57.6	39.4	32.9	30.6
	B	58.2	44.9	33.6	29.0	27.2
	C	47.3	38.1	29.8	26.1	24.6
20,000	A	68.0	51.5	37.2	31.7	29.5
	B	46.7	38.5	30.5	26.8	25.3
	C	37.9	32.2	26.4	23.5	22.3
30,000	A	60.9	47.7	35.7	30.7	28.7
	B	41.1	34.9	28.4	25.3	23.9
	C	33.2	28.9	24.2	21.8	20.7
40,000	A	56.2	45.0	34.5	29.9	28.0
	B	37.6	32.4	26.9	24.1	22.8
	C	30.3	26.6	22.6	20.5	19.5

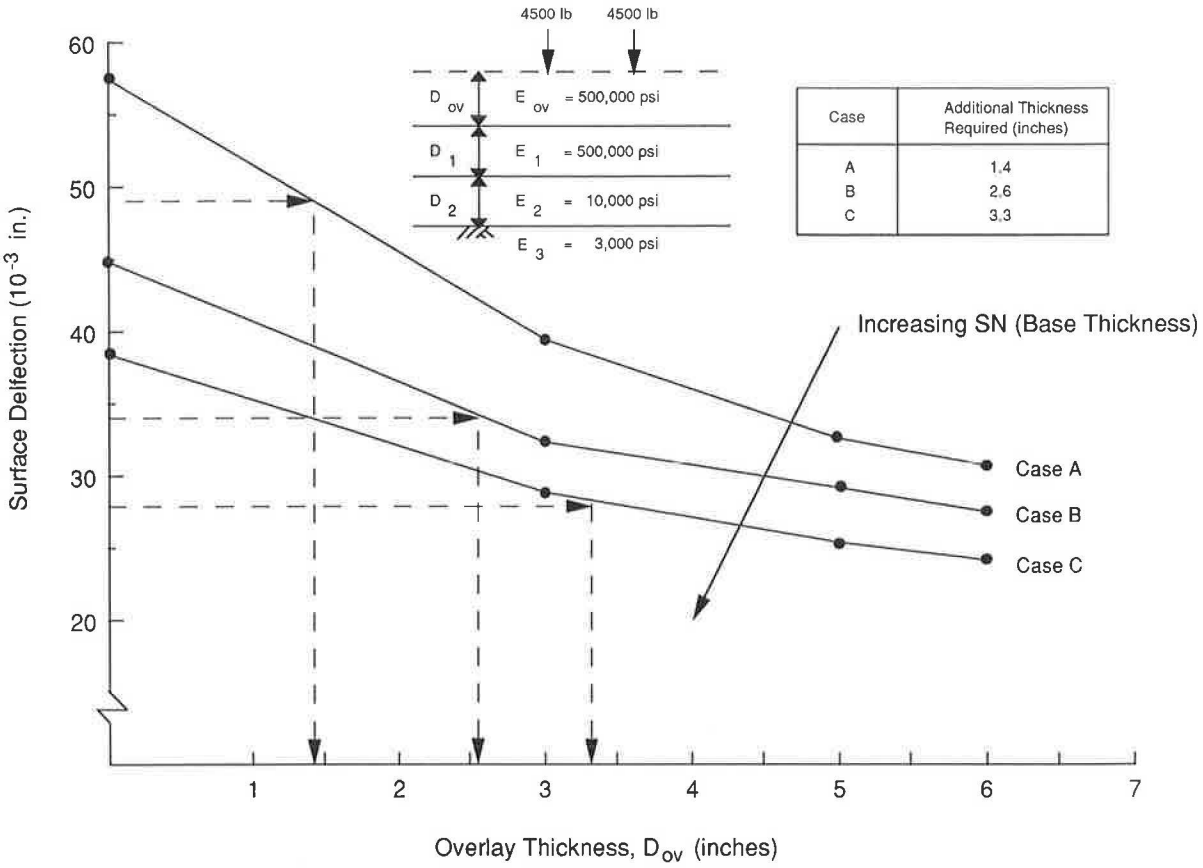


FIGURE 4 Variation in surface deflection with overlay thickness (E_3 = 3,000 psi, E_2 = 10,000 psi).

coefficient (J). For example, a 20 percent increase in C_d would have the same effect as a 20 percent increase in S_c or, because J is in the denominator, a 20 percent increase in $1/J$.

Unlike the approach used to develop m values for flexible pavement design, the consideration of drainage effects on base or subbase strength alone could not be used to derive C_d values that had a realistic impact on slab thickness; in other words, results of the approach did not pass the test for reasonableness. Consequently, an alternate approach was adopted whereby C_d values were backcalculated from Equation 2 using expected minimum effects of drainage condition on slab thickness. Figure 9 represents the results of these C_d calculations for a factorial of design combinations.

1. Original slab thicknesses (D) of 7, 10, and 13 in.;
2. Slab thickness variations (about the original thickness) of -1.5, -1.0, -0.5, $+0.5$, $+1.0$, and $+1.5$ in.;
3. PCC elastic moduli (E_c) of $3 * 10^6$, $5 * 10^6$, and $7 * 10^6$ psi; and
4. Modulus of subgrade reaction (k) values of 60, 100, 200, and 400 pci.

Variations in flexural strength (S_c) and load transfer coefficient (J) were not considered as they cancelled out of the equation. Other factors inherent in Figure 9 are (a) a fixed terminal serviceability (p_t) of 2.5, and (b) an average effect of PCC elastic modulus variation.

The curves shown in Figure 9 provide the basis for selection of the recommended ranges of C_d in Table 8 (from Volume 1, Part II, Table 2.5, of the Guide (*5*)). Basically, a 1-in. reduction in slab thickness was used to identify the maximum value of C_d (i.e., that corresponding to the excellent drainage class). Likewise, a 1.5-in. increase in slab thickness was used to identify the minimum value of C_d (i.e., that corresponding to the very poor drainage class). The other values in Table 9 were selected on the basis of an interpolation between these extreme values, considering (a) the percent of time the pavement structure is exposed to moisture levels approaching saturation, and (b) the intermediate levels of drainage quality or condition.

Figure 9 may also be helpful to some users who wish to apply their own experience in drainage effects on slab thickness to identify C_d values for their local conditions. In doing so, it should be recognized that the shaded regions for the three original slab thicknesses shown represent the effects of variation in slab support (i.e., modulus of subgrade reaction). For example, if the original slab thickness corresponding to conditions when drainage effects are not considered (i.e.,

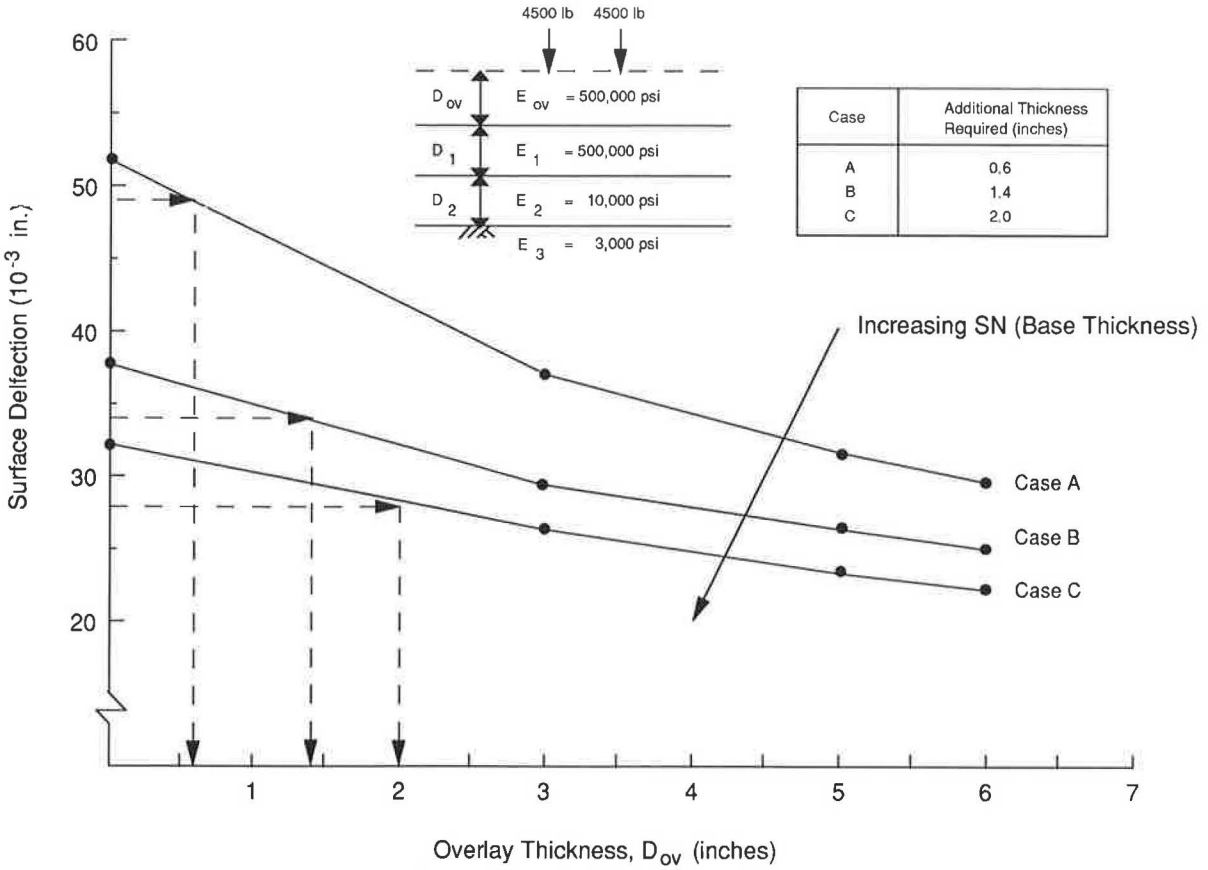


FIGURE 5 Variation in surface deflection with overlay thickness (E_3 = 3,000 psi, E_2 = 20,000 psi).

when C_d is equal to 1.0) is 7.0 in. and a C_d of 1.2 is used, the reduction in thickness would be about 0.75 in. for k to 60 pci and about 0.9 in. for k equal to 400 pci.

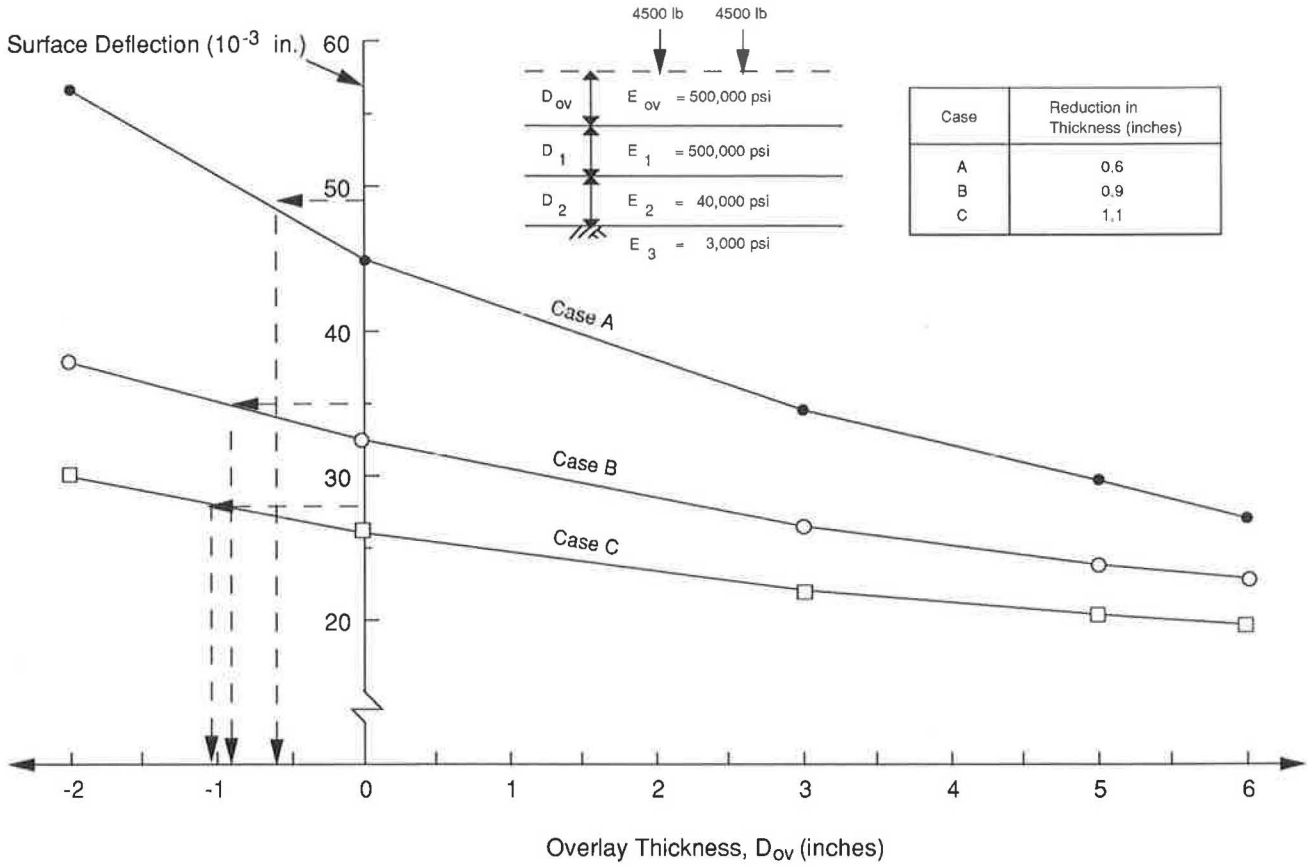
Table 10 presents the significance of the range of C_d values on how the slab support (k value) would vary to produce the same effect. It is based on a 10-in. PCC slab with an elastic modulus of $5 * 10^6$ psi. Because the range of k values is so wide compared to the associated range of C_d values, the obvious implication from this table is that the recommended C_d values account for more than just the effect of drainage condition on slab support. There may be some inherent recognition of the effect moisture environment has on curling and warping stresses in the slab. In any case, the recommended ranges of C_d do provide reasonable results for their effect on design slab thickness for different drainage conditions. However, data from field experiments and long-term pavement performance monitoring should be used to validate and improve these values.

FUTURE WORK

Some of the general considerations associated with the effects of moisture in pavements and how they have been treated have been addressed. More important, the methodology that was used to incorporate drainage considerations in the new *AASHTO Guide for Design of Pavement Structures—1986* has been described. In summary, a mechanistic approach combined with sound engineering judgment was applied to derive coefficients that could be used in the structural design process for both flexible and rigid pavements. The coefficients depend on the pavement's level of moisture exposure (environment) as well as the quality of drainage.

One of the problems with the methodology is that there are no well-defined procedures for translating the results of various drainage design procedures into the rather subjective inputs (coefficients) used in the Guide. In addition, there is no standard computer program that can be used by the highway pavement and subdrainage design engineers to assist them in evaluating moisture conditions and generating suitable drainage designs. Lastly, the process of determining appropriate drainage system unit costs for use in the Guide (and its related microcomputer program) is rather time-consuming and subject to error.

Therefore, improvements are needed to make the methodology less subjective and easier to use. It is anticipated that these improvements will be considered in a forthcoming FHWA project.



Case	Reduction in Thickness (inches)
A	0.6
B	0.9
C	1.1

FIGURE 6 Variation in surface deflection with overlay thickness (E_3 = 3,000 psi, E_2 = 40,000 psi).

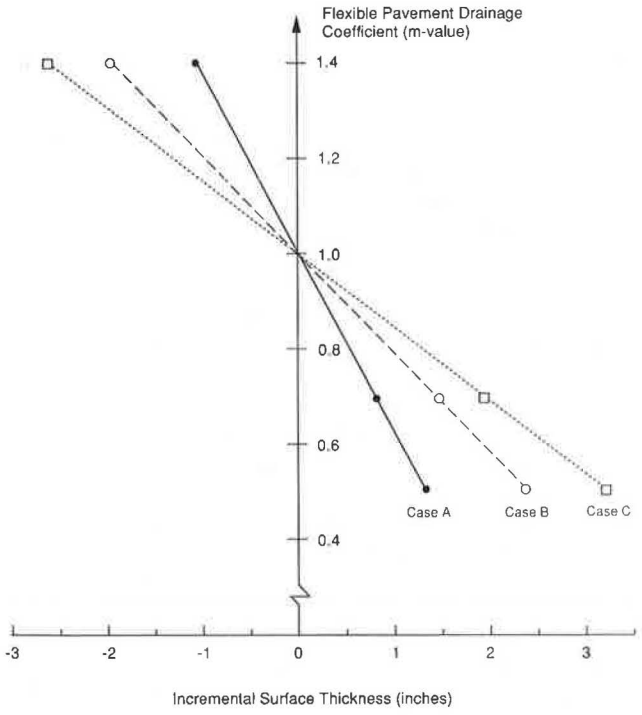


FIGURE 7 Variation in surface thickness requirements with *m* values from Table 3.

TABLE 6 ESTIMATED *m* VALUES FOR THREE CASES SHOWN IN FIGURE 7

Case	Aggregate Base Modulus (psi)	Incremental Thickness (in.)	Estimated *m* Value
A	10,000	+1.4	0.40
	20,000	+0.6	0.75
	40,000	−0.6	1.22
B	10,000	+2.6	0.40
	20,000	+1.4	0.72
	40,000	−0.9	1.20
C	10,000	+3.3	0.50
	20,000	+2.0	0.70
	40,000	−1.1	1.20

TABLE 7 RECOMMENDED *m* VALUES

Base Modulus E_2(psi)	Quality of Drainage	Recommended *m* Value
50,000	Excellent	1.4
40,000	Good	1.2
30,000	Fair	1.0
20,000	Poor	0.7
10,000	Very Poor	0.4

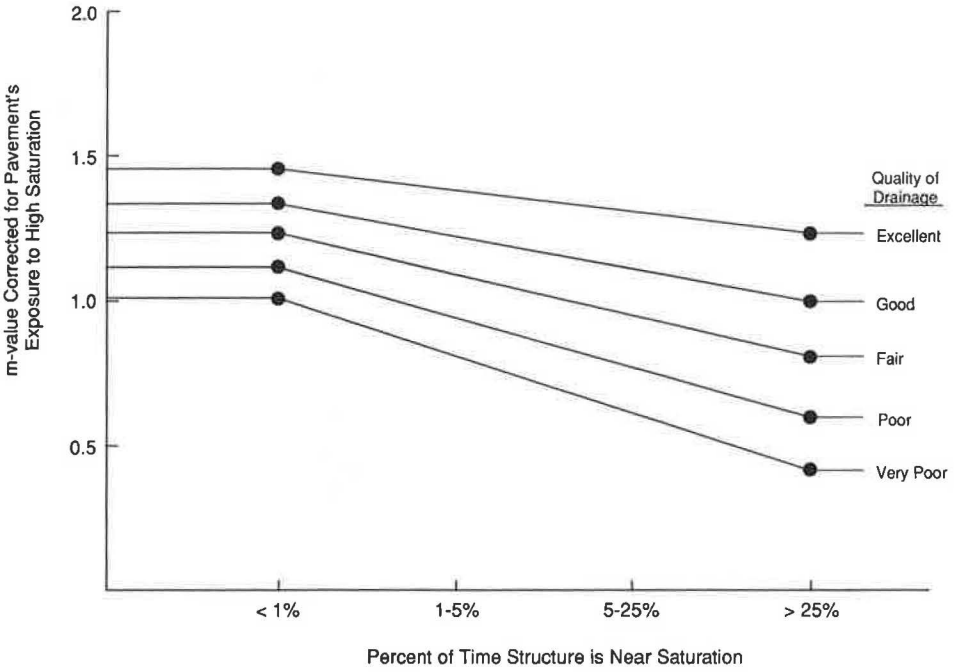


FIGURE 8 Recommended *m* values as a function of the quality of drainage and exposure to saturation.

TABLE 8 RECOMMENDED m_i VALUES FOR MODIFYING STRUCTURAL LAYER COEFFICIENTS OF UNTREATED BASE AND SUBBASE MATERIALS IN FLEXIBLE PAVEMENTS (*5*)

	Percent of Time Pavement Structure is Exposed to Moisture Levels Approaching Saturation			
Quality of Drainage	Less Than 1%	1-5%	5-25%	Greater Than 25%
Excellent	1.40-1.35	1.35-1.30	1.30-1.20	1.20
Good	1.35-1.25	1.25-1.15	1.15-1.00	1.00
Fair	1.25-1.15	1.15-1.05	1.00-0.80	0.80
Poor	1.15-1.05	1.05-0.80	0.80-0.60	0.60
Very Poor	1.05-0.95	0.95-0.75	0.75-0.40	0.40

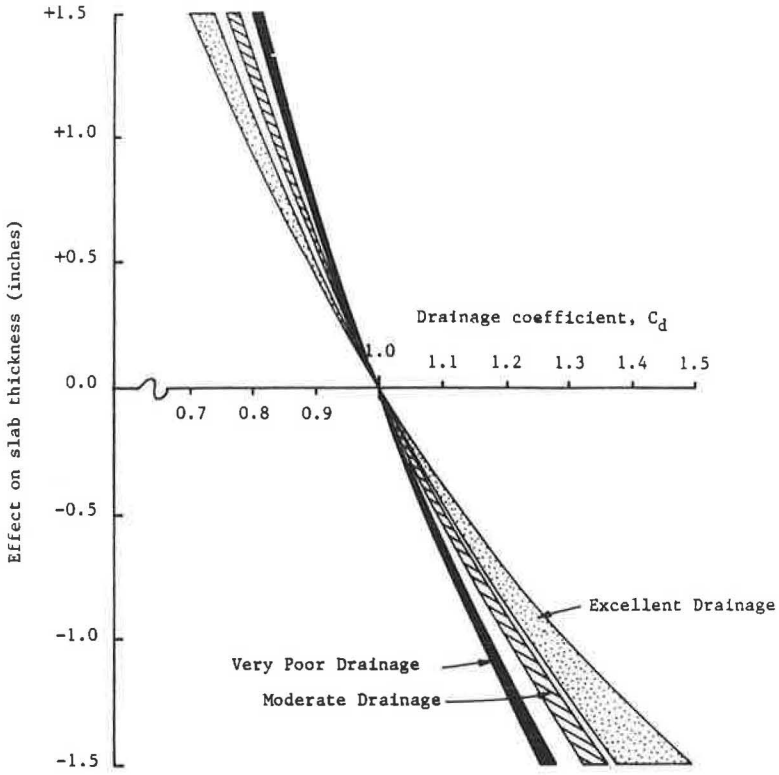


FIGURE 9 Effect of drainage coefficient on reducing or increasing original slab thickness.

TABLE 9 RECOMMENDED VALUES OF DRAINAGE COEFFICIENT C_d, FOR RIGID PAVEMENT DESIGN (5)

	Percent of Time Pavement Structure is Exposed to Moisture Levels Approaching Saturation			
Quality of Drainage	Less Than 1%	1-5%	5-25%	Greater Than 25%
Excellent	1.25-1.20	1.20-1.15	1.15-1.10	1.10
Good	1.20-1.15	1.15-1.10	1.10-1.00	1.00
Fair	1.15-1.10	1.10-1.00	1.00-0.90	0.90
Poor	1.10-1.00	1.00-0.90	0.90-0.80	0.80
Very Poor	1.00-0.90	0.90-0.80	0.80-0.70	0.70

TABLE 10 VALUES OF k PRODUCING SAME EFFECT AS CORRESPONDING VALUES OF C_d

Quality of Drainage	Selected C_d Value	Corresponding k-value (pci)
Excellent	1.2	942
Good	1.1	501
Fair	1.0	200
Poor	0.9	44
Very Poor	0.8	1

REFERENCES

1. H. R. Cedergren. *Drainage of Highway and Airfield Pavements*. John Wiley, New York, 1974.
2. L. K. Moulton. Highway Subdrainage Design. Report FHWA-TS-80-224. FHWA, U.S. Department of Transportation, 1980.
3. H. H. Ridgeway. *NCHRP Synthesis of Highway Practice 96: Pavement Subsurface Drainage System*. TRB, National Research Council, Washington, DC., Nov. 1982.
4. S. H. Carpenter, M. I. Darter, B. J. Dempsey, and S. Herrin. *A Pavement Moisture Accelerated Distress (MAD) Identification System*, Volume 1. Report FHWA-RD-81-079. FHWA, U.S. Department of Transportation, Sept. 1981.

5. *AASHTO Guide for Design of Pavement Structures*, Volume 1. AASHTO, Washington, D.C., 1986.
6. *AASHTO Guide for Design of Pavement Structures*, Volume 2. AASHTO, Washington, D.C., Aug. 1986.
7. G. R. Benson. *Guidelines for the Design of Highway Internal Drainage Systems*. Illinois Department of Transportation, Springfield, 1985.
8. *User's Manual for DNPS86, Design for New Pavement Structures Program (Version 2)*. AASHTO, Washington, D.C., April 1987.
9. *AASHTO Interim Guide for Design of Pavement Structures—1972*. AASHTO, Washington, D.C., 1972.
10. F. Finn, et al. *Development of Pavement Structural Subsystems*, Final Report, NCHRP Project 1-10B, TRB, National Research Council, Washington, D.C., Feb. 1977.
11. G. Rada and M. Witzcak. A Comprehensive Evaluation of Laboratory Resilient Moduli Results for Granular Materials. In *Transportation Research Record 810*, TRB, National Research Council, Washington D.C., 1981.
12. *ELSYM5, Elastic Layer Theory Computer Model (Version 3-72)*. Institute for Transportation Studies, Department of Civil Engineering, University of California, Berkeley, 1972.

Publication of this paper sponsored by Committee on Flexible Pavement Design.

Temperature and Suction Profiles Beneath Highway Pavements: Computed and Measured

D. E. PUFAHL AND R. L. LYTTON

A computer model has been developed that computes the temperature and suction profiles beneath highway pavements (or other similar covered areas) throughout a specified time period of simulation. The model is referred to as the "integrated computer model" because several modules that were developed for specific tasks have been brought together to form one complete package. Using 30 years of accumulated weather data as a basis, the model generates its own weather patterns that are representative of typical climatic conditions for a particular region of the United States. As the pavement structure and subgrade respond to the changing climatic conditions throughout the year, the model computes the corresponding changes in temperature and suction. Specific boundary conditions at three locations are required: (a) the top pavement surface, (b) the bottom boundary—an extended distance into the subgrade, (c) an intermediate boundary—the top of the subgrade. The pavement surface boundary uses a heat and moisture flux condition that depends on climate. The bottom boundary requires temperature and moisture conditions that are either constant or that may vary in a specific manner. The intermediate boundary requires an initial temperature and a moisture condition that may be either suction (head) or moisture flux. The concept of a transfer coefficient between the granular base and the fine-grained subgrade has been developed to describe the process by which water from the base course and subbase infiltrates the subgrade. This transfer coefficient cannot be measured experimentally, but the selection of an appropriate value controls not only the changes in moisture conditions, but also the temperature profile computed in the subgrade. Three instrumented sites in the United States with widely varying climatic and soil conditions are used to provide comparisons between measured and computed values of temperature and suction profiles.

Load response computer models have been used for a number of decades for highway pavement design and management. Although the importance of environmental influences on pavement performance has been recognized for the last 50 years or more, efforts to incorporate these factors into routine design have been less successful. Usually, the worst-case scenario, that being saturated conditions, was adopted for initial design. This approach was often justified by observing that saturation was the most severe condition, and that little or no information was available to perform and to verify other assumptions. Studies are now indicating that important climatic variables such as temperature, rainfall, wind speed, and solar radiation can be used to model more complex and thus more realistic temperature and moisture conditions characteristic of the more arid regions of the world. Moreover, instrumentation required to measure base course and subgrade temperatures and suctions are becoming increasingly reliable. These procedures coupled with powerful deterministic and stochastic analyses are providing meaningful results for climatic influences on highways over several years of computer simulation.

D. E. Pufahl, University of Saskatchewan, Saskatoon, Canada S7N OWO. R. L. Lytton; Materials, Pavement, and Construction Division; Texas Transportation Institute; College Station, Tex. 77843–3135.

The integrated computer model has been developed by the Texas Transportation Institute under contract with FHWA to simulate typical weather patterns and to assess their effects on the base course, subbase, and subgrade of highways throughout several years of operation. Although most emphasis has been placed on the continental United States, the program may be used in any part of the world where first-order weather data are available. The program has been described by Pufahl et al. (*1*) and in more detail by FHWA (*2*).

The model shown in Figure 1 is composed of four major components. They are the precipitation (precip) model (*1–3*); the infiltration and drainage (ID) model (*1,2,4*); the climatic-materials-structural (CMS) model (*1,2,5*); and the U.S. Army Cold Regions Research and Engineering Laboratory (CRREL) model (*1,2,6*). Those wishing to investigate the details of the program are referred to the original papers, reports, and user's guides concerning them (*1–6*).

Preliminary results (*1,2*) have indicated that the boundary conditions selected within the program have a major influence on the temperature and suction profiles that are generated during the course of simulation. One boundary in particular, that between the subbase and subgrade, is of particular significance. Two different moisture conditions that may be assumed at this boundary in the simulation are described. The effects of these assumptions on the computed values of suction and temperature are compared with measured values for three different sites in the United States.

BOUNDARY CONDITIONS

Figure 2, which is a schematic of a typical pavement structure, shows where each of the modules in the integrated model are used during the course of simulation. The figure is separated into two temperature divisions: above and below freezing. Additional divisions are based on temperature and moisture conditions.

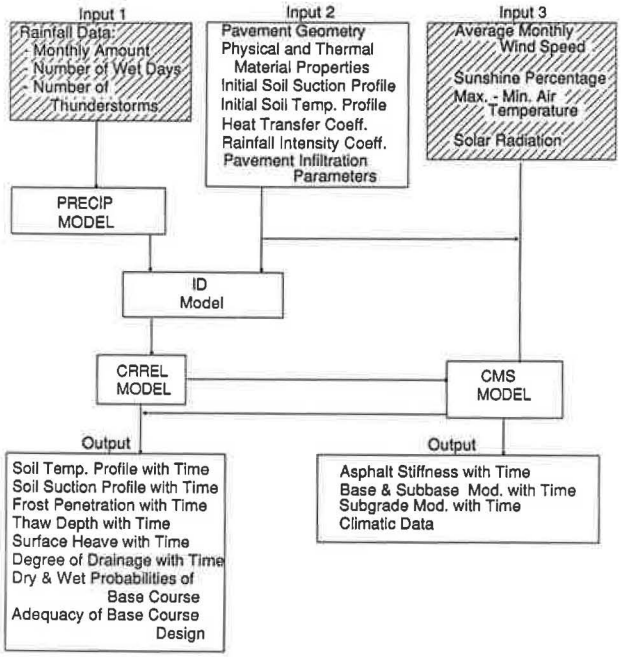


FIGURE 1 Integrated pavement model.

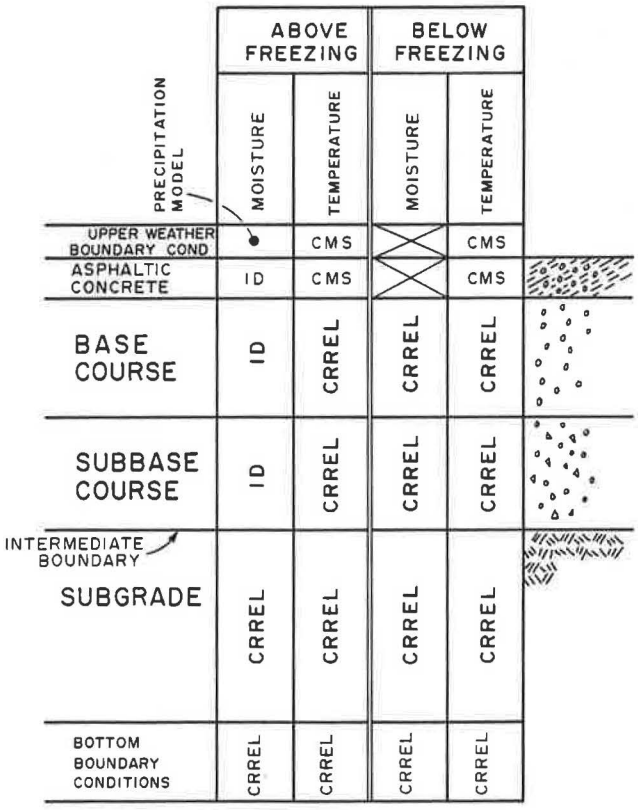


FIGURE 2 Pavement segments where component models are used.

The first boundary of moisture and temperature is encountered at the surface of the pavement, the second at the top of the subgrade, and the third (or bottom) boundary is in the order of 10 to 15 ft into the subgrade.

The pavement surface uses a heat and moisture flux condition that depends on climate. The heat flux is determined by establishing a heat balance at the surface by a combination of measurements and calculations that consider net radiation, average wind speed, and maximum and minimum mean air temperatures. These calculations are performed by the CMS model. The surface moisture influx condition uses the ID model to compute the amount of water infiltrating through the pavement and also handles the lateral drainage out of the base course. It also includes the precip model, which generates realistic rainfall patterns (*1–5*).

The bottom boundary requires temperature and suction values that are either constant during the course of simulation or that vary in a specified manner. If data from the site being considered are not available, techniques based simply on geographical location and soil type may be used as a first approximation (*1,2*).

The intermediate boundary requires initial temperature and suction conditions to be specified. These values must be provided as part of the initial input data. The original CRREL model uses a numerical solution of coupled heat and moisture transport to compute the changes in temperature and suction with time. For the most part, moisture movement occurred from the bottom upwards. Downward vertical drainage could occur when the ice lenses thawed, but no moisture was assumed to infiltrate through the pavement surface; this condition represented a zero-gradient boundary condition. Although this assumption is convenient, it is not often realistic (*2,6*).

MOISTURE FLUX AT THE SUBGRADE BOUNDARY

In many regions west of the Mississippi River, in the southern United States, in southern Canada and in other semiarid and arid regions of the world, highway subgrades are frequently composed of fine-grained, low-permeability soils that remain unsaturated throughout the year.

Infiltration of water through the pavement during or after a rainstorm will often produce free water in the base course and subbase (Figure 3). Thus, an abrupt boundary between

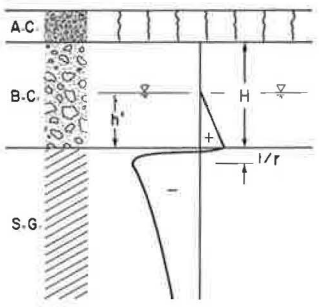


FIGURE 3 Schematic sketch of pavement structure.

a positive water pressure in the subbase and a negative water pressure or suction in the subgrade will exist at the interface. The gradient at this boundary equals the sum of the positive pressure in the subbase plus the suction in the subgrade times a pore pressure transfer coefficient, r. The transfer coefficient has units of inverse distance.

The concept has been adopted from the theory of an insulated, heated steel rod of initial uniform temperature with one end radiating heat to the air at a constant, lower temperature. The physical and thermal properties of the rod in comparison to the air are different and the formulation reveals that the transfer coefficient in the case of the heated rod is a function of the Steffan-Boltzmann constant of heat transfer, the absolute temperature of the rod, and the thermal conductivity of the rod. The unit of this transfer coefficient is also inverse distance.

Mitchell (*7*), using this analogy, found that a cylinder of soil of known constant suction enclosed on all sides, but open on one end to the atmosphere at a higher suction, underwent increases in suction at the exposed surface and along its entire length in general accordance with the theory used to predict the cooling of the steel rod. Using a value of 0.54/mm as a transfer coefficient for a column of soil 68 mm long, Mitchell was able to model the changes in suction with time throughout the length of the sample with acceptable accuracy. It is postulated here that changes in suction in the subgrade will occur because of changes in water pressure in the base and subbase in general accordance with the theory of the cooling steel rod or with the changes in suction along the column of unsaturated soil with one end exposed to the atmosphere.

The appropriate range of values for r in the integrated model appears to lie between 1.0×10^{-6}/in. and 1.0/in. and is controlled by the magnitude of the permeabilities on each side of the interface. Present indications suggest that a maximum value for r is numerically equal to the computed velocity of the water into the subgrade under a unit hydraulic gradient.

The gradient at the base course-subgrade interface is represented as

$$\frac{\delta h}{\delta z} = -r\left(\frac{p}{\gamma_w} - h_s\right) \tag{1}$$

where

$\delta h/\delta z$ = gradient,
r = pore pressure transfer coefficient,
γ_w = density of water
h' = height of water in the base course,
p = $\gamma_w h'$, and
h_s = negative pore water pressure in the subgrade at the interface.

As the water builds up in the base course to a height, h', above the interface with the subgrade, the positive pore water pressure head in the base course at the interface is described as

$$\frac{p}{\gamma_w} = h'\left[\frac{1 - \frac{k_s}{k_b}(1 - rh_s)}{1 + \frac{k_s}{k_b}rh'}\right] \tag{2}$$

where k_s is the permeability of the subgrade and k_b is that of the base course.

The velocity of flow into the subgrade is found by equating the velocity of vertical flow in the base course to the velocity in the subgrade. The velocity in the subgrade, v_s is

$$v_s = -k_s\left[-r\frac{h'\left(1 - \frac{k_s}{k_b}\right) - h_s}{1 + \frac{k_s}{k_b}rh'} - 1\right] \tag{3}$$

Substituting Equation 2 into Equation 1 yields the following:

$$\frac{\delta h}{\delta z} = -r\frac{h'\left(1 - \frac{k_s}{k_b}\right) - h_s}{1 + \frac{k_s}{k_b}rh'} \tag{4}$$

The size of the gradient and thus the velocity of flow into the subgrade is controlled by the size of the transfer coefficient, r.

The flux boundary condition has been programmed in the integrated model to allow the flux to be set either at the base course subgrade interface (the intermediate boundary) or at the bottom boundary of the problem (lower boundary). The velocity at either boundary may be set independently of the other.

When the pore water pressures in the base and the subgrade are fairly close together, the flux boundary condition will perform just like a suction boundary condition. The farther apart the two pore water pressures are, the more active the flux boundary condition will be in controlling the rate of flow of water into or out of the subgrade.

The flux boundary condition with a positive r value imposes a velocity of flow from the base course into the subgrade that carries heat with it. This connection results in a cooling of the surface layer and base course. A negative value of the r imposes a velocity that flows upward and results in higher temperatures in the base and the surface courses. Thus, the measured temperatures are useful in adjusting the r values to fit the measured temperature and suction field data.

COMPARISON OF RESULTS

The integrated model has been used at three sites in the United States with widely varying climatic conditions.

1. College Station, Texas: a wet, nonfreeze climate with a clay subgrade.
2. Amarillo, Texas: a dry, freeze-thaw climate with a clay subgrade.
3. Deland, Piatt County, Illinois: a wet, hard-freeze climate with a silty subgrade.

The data from the first two sites were measured in a National Science Foundation study at Texas Tech University in collaboration with Texas A&M University. Data at the Illinois site were obtained by University of Illinois personnel.

The saturated permeability and the Gardner constants were selected from a compendium of data determined and collated by CRREL. This information is contained in the user's manual that accompanies the integrated model.

The soils classifications from the three sites reported here were matched with similar soils in the CRREL document. The properties used to identify and compare the soils were based mainly on density, water content, gradation, and the Unified Classification.

The measured and calculated suction and temperature values are compared on the dates when the measurements were taken.

College Station, Texas

The test site is a covered area 24 × 40 ft (7.3 × 12.2 m) placed on an expansive clay with a 6-in.-deep (15-cm) sand cushion topped by a layer of polyethylene plastic. Surface elevations, suctions, and temperatures were measured monthly, with the latter two measurements being made to a depth of 8 ft (2.4 m). Changes in suction were more pronounced near the edge of the covered area than near the center so that the suction measurements which are used for comparison purposes were those in the center, 10 ft (3.0 m) from the closest edge, and corresponding to the moisture conditions expected beneath the inner wheel path of a pavement with a 4-ft (1.2-m) shoulder.

The soil layers at the College Station site are shown in Figure 4 along with some measured and assumed soil properties. Figure 5 shows the initial suction and temperature

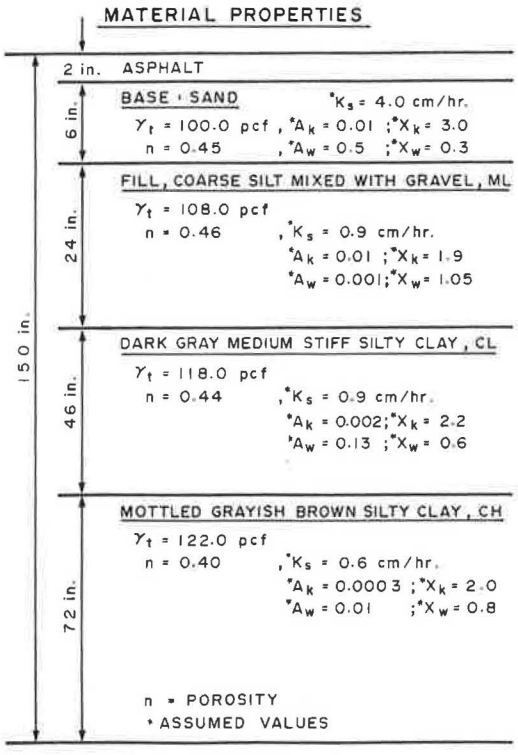


FIGURE 4 College Station, Texas: Soil profile and properties.

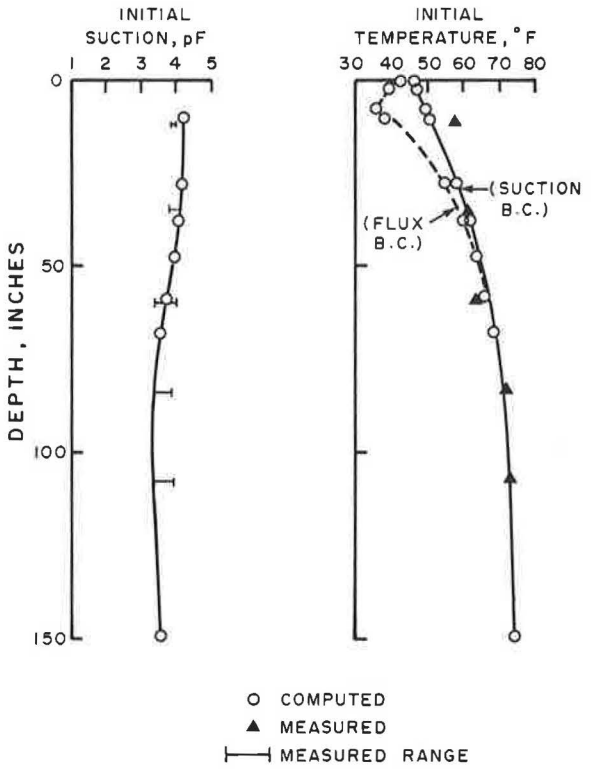


FIGURE 5 College Station, Texas: Assumed and actual suction and temperature conditions on a typical January 1.

conditions assumed for a typical January 1 date. The computed temperature and suction values are reported at 8:00 a.m. in the morning of the date noted. Calculations are begun at midnight on January 1 and the initial conditions shown in Figure 5 represent 8 hr of stepping forward in time. The boundary condition imposed between the base course and the subgrade makes a substantial difference in both the suction and temperature values computed in the base and the upper levels of the subgrade. For the flux boundary condition, an r value of 0.01 was used in all of the runs reported here. The flux boundary condition resulted in an initial temperature profile that was considerably colder than the profile derived from the suction boundary condition and also colder than the actual measured values of the temperature.

Figure 6 shows the measured and computed suction profiles at several different times of the year. Figure 7 shows the measured and computed temperature profiles at the same times of the year. For the flux boundary condition, an r value of 0.01 was used in all of the runs reported here. The flux boundary condition resulted in an initial temperature profile that was considerably colder than the profile derived from the suction boundary condition and also colder than the actual measured values of the temperature. The flux boundary condition with a positive r value imposes a velocity of flow from the base course into the subgrade that carries heat with it. This results in a cooling of the surface layer and base course. A negative value of r imposes a velocity that flows upward and will result in higher temperatures in the base and the surface courses. Thus, the measured temperatures are useful in adjusting the r value to fit the measured temperature and

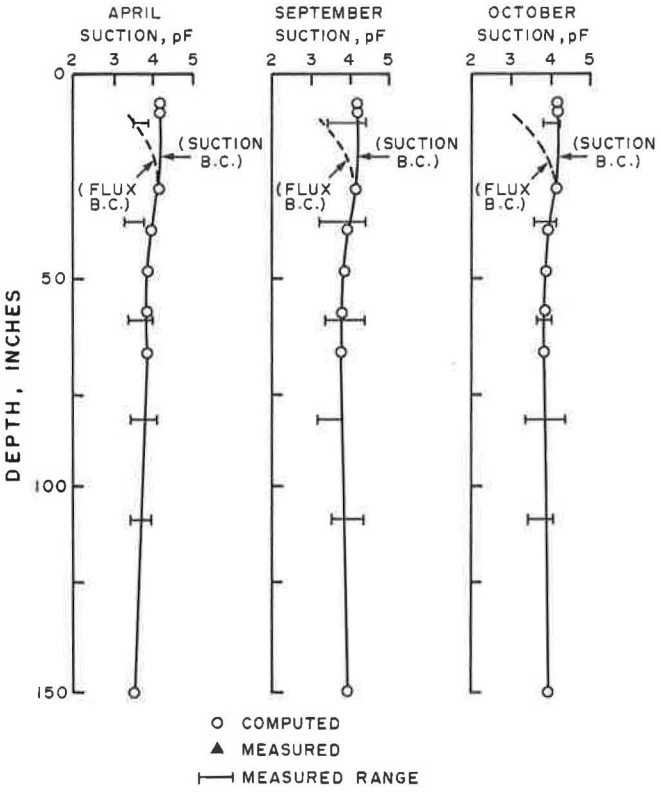


FIGURE 6 College Station, Texas: Computed and measured suction profiles at different times of the year.

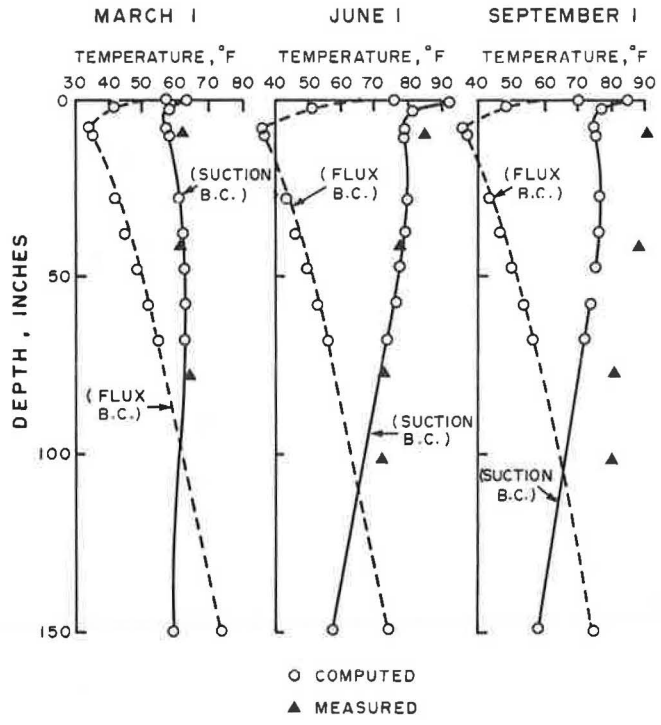


FIGURE 7 College Station, Texas: Computed and measured profiles at different times of the year.

suction field data. Additional simulations will establish more precisely the role of the selected r values. The effect of the flux boundary condition with a positive r value of 0.01 is evident in both Figures 6 and 7. The effect on suction diminishes rapidly with depth. Figure 8 shows the computed variation of suction throughout the year at a depth of 3 ft (0.9 m) together with the total simulated rainfall that fell during each month of the year. The measured suctions at the same depth are shown on the same figure. Suction measurements were taken with psychrometers and temperatures were measured with thermocouples.

Amarillo, Texas

The site at Amarillo, Texas, is similar to the College Station site. It is a covered area analogous to a slab on an expansive clay subgrade with the same 6-in. (15-cm) sand layer beneath a polyethylene plastic sheet 24 × 40 ft (7.3 × 12.2 m) in plan dimensions. Suction and temperature measurements to a depth of 8 ft (2.4 m) were made each month. Surface elevations were also determined. Suction and temperatures were measured with psychrometers and thermocouples, respectively.

The soil layers at Amarillo are shown in Figure 9, along with the total unit weight, porosity, and permeability properties. Figure 10 shows the initial suction and temperature profiles assumed for a typical January 1 date along with measured values of the same profiles made in January. The difference in temperature profiles generated by the flux and suction boundary conditions is not as strikingly different as was the case in College Station, Texas. This is probably because the difference in suction level at the boundary between the base course and the subgrade is lower than was the case in College Station, and this implies a lower velocity of flow

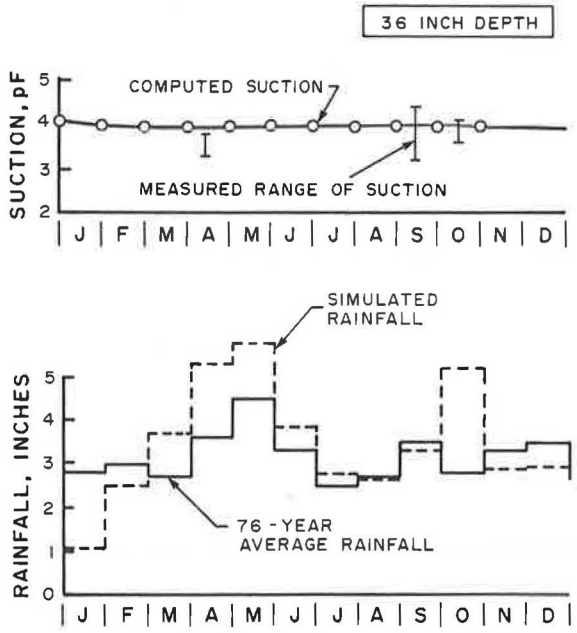


FIGURE 8 College Station, Texas: Computed and measured suctions at 36-in. depth below the surface and monthly rainfall.

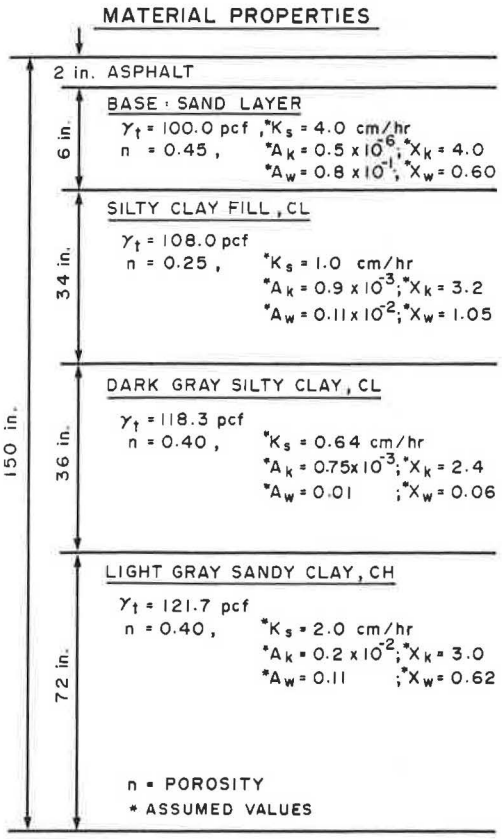


FIGURE 9 Amarillo, Texas: Soil profile and properties.

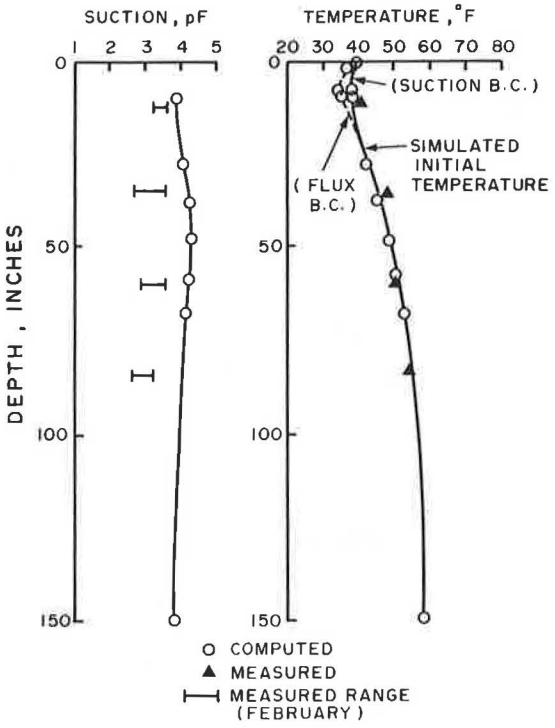


FIGURE 10 Amarillo, Texas: Initial measured and simulated suction and temperature profiles on January 1.

of both water and heat into the subgrade. Figure 11 shows the measured and computed suction profiles at several times during the year. Figure 12 shows the measured and computed temperature profiles at the same times of the year. The difference in temperature profiles between the flux and suction boundary condition cases brackets the actual measured temperatures, indicating perhaps that a different r value for the flux boundary condition may be able to match the field temperature data well while, at the same time, falling within the measured suction range consistently. Figure 13 shows the computed variation of suction throughout the year at the 1-ft (0.3-m) depth in the silty clay layers together with the simulated rainfall that fell during each month, and the 44-year average monthly rainfall in Amarillo, Texas. The simulated rainfall was 82 percent higher than the normal average rainfall accounting for the computed suctions falling toward the wetter side of the measured range of suctions. The years during which the site was monitored were all wetter than the average year. The range of suctions that were measured at the same depth are also shown in Figure 13.

Deland, Piatt County, Illinois

The instrumented site in Piatt County, Illinois, near Deland is on a rural road, FAS Route 537. The pavement consisting of a double bituminous surface treatment on an 8-in. (20-cm) aggregate base course, is 24 ft (7.3 m) wide with 6-ft (1.8-m) unpaved shoulders. Suction, temperature, and frost depth measurements were made periodically with the measurement dates spaced at 3 to 4 months apart. Suction was measured with tensiometers, moisture cells, and psychrometers. Temperatures were measured with thermocouples. At this site mainly because of the low suctions, the tensiometer readings were considered to be most reliable.

The soil profile is shown in Figure 14, along with assumed soil properties for each layer. The water table fluctuated throughout the year from a high elevation of 46 in. (1.2 m) below subgrade level to a low of 105 in. (2.7 m) below the subgrade.

Figure 15 shows the assumed initial suction and temperature profiles for January 1 of the simulated year. In this case, both the flux and the suction boundary condition between the base course and subgrade provide practically the same pore water pressures as an initial condition. This is because of the small difference of negative pore water pressures at the interface between the base course and the subgrade. The initial-temperature profile is virtually the same with both boundary conditions.

Figure 16 shows the measured and computed pore water pressure profiles at two different times during the year. The computed pore water pressures are practically the same for both boundary conditions. Both have the same profile pattern and are nearly the same as the values measured with tensiometers.

Figure 17 shows the measured and computed temperature profiles at three different times during the year. The computed temperature profiles are the same to three significant figures for the two boundary conditions, unlike the two previous cases. In the present case, both boundary conditions predict

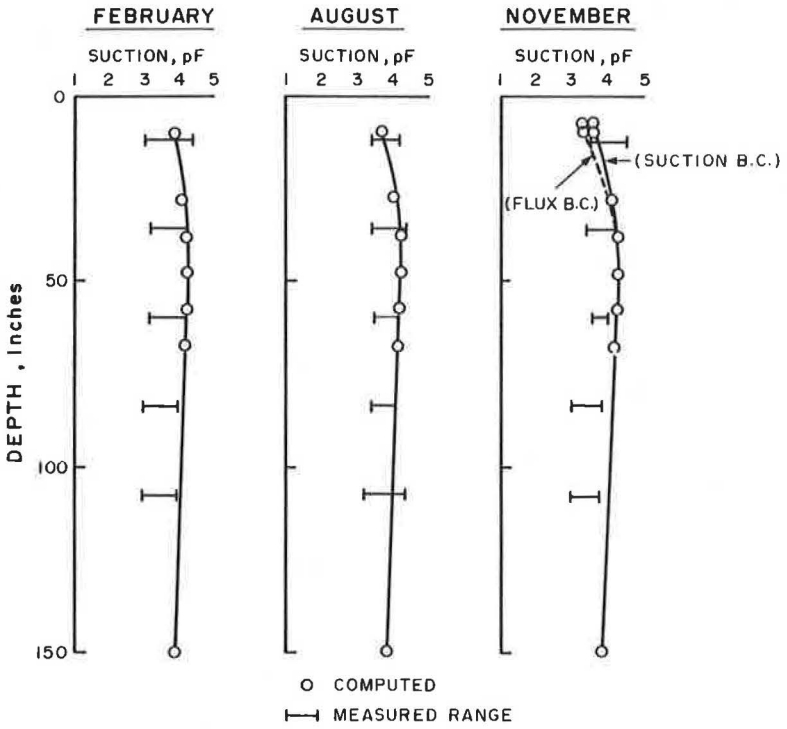


FIGURE 11 Amarillo, Texas: measured ranges and computed suction profiles at different times of the year.

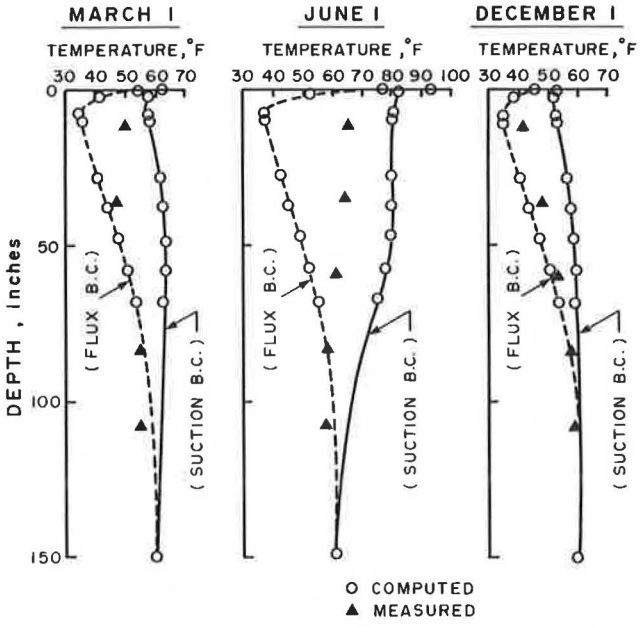


FIGURE 12 Amarillo, Texas: measured ranges and computed temperature profiles at different times of the year.

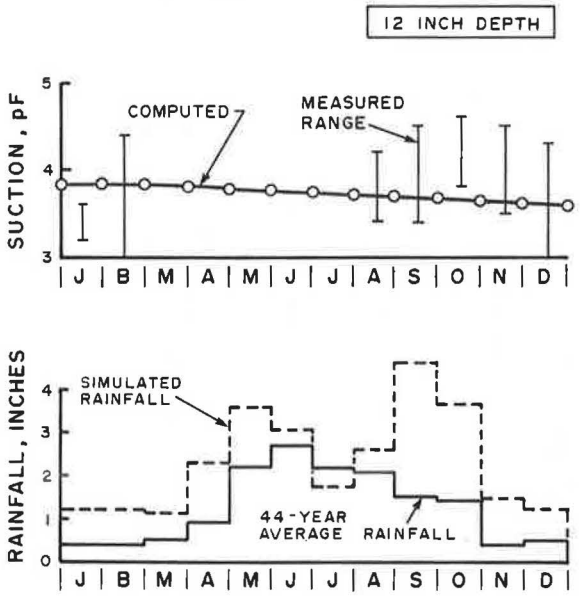


FIGURE 13 Amarillo, Texas: Computed and measured suction at a 12-in. depth below the surface and monthly rainfall.

a temperature profile that is fairly close to the values measured in the field.

Figure 18 shows the computed variation of pore water pressure throughout the year at a depth of 28 in. (0.7 m) below the subgrade level (which is in the brown silty clay soil layers), together with the simulated rainfall that fell during each month and the simulated snow melt. The measured pore water pressures at the same depth are also shown. The calculated negative pore water pressures at that depth change rapidly with time, particularly at the end of January when the ground freezes and at the beginning of February when the snow begins to melt. The computed patterns match the measured rise and fall of pore water pressure although the magnitudes are slightly different.

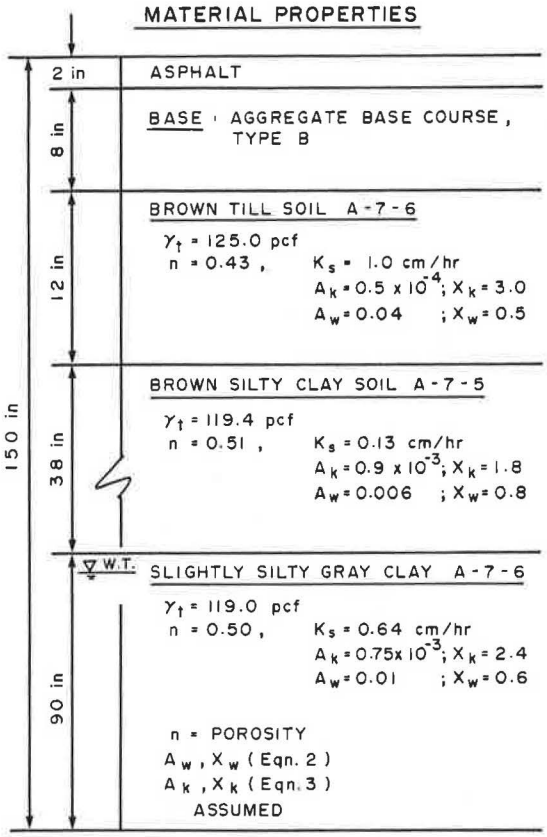


FIGURE 14 Deland, Piatt County, Illinois: Soil profile and properties.

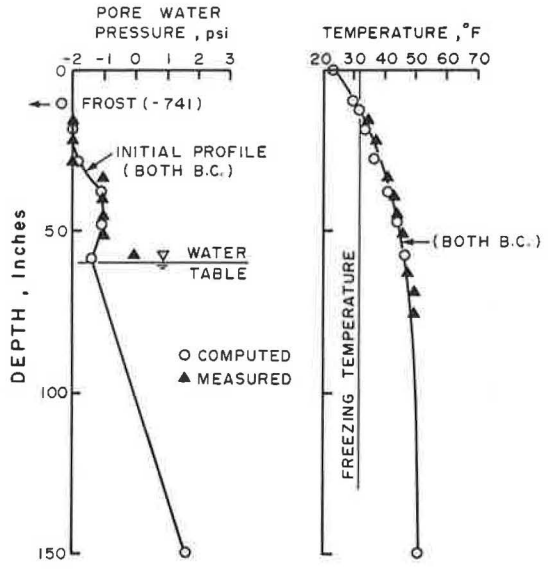


FIGURE 15 Deland, Piatt County, Illinois: Initial measured and assumed pore water pressure and temperature profiles, January 1.

Figure 19 shows the depth of frost penetration, both observed and computed, together with the computed frost heave and the period of time during which either snow or freezing temperatures sealed off the penetration of water from the surface into the sublayers. The depth of the frost zone observed in the field is matched better using the suction boundary condition than using the flux boundary condition. The largest mean frost heave is nearly the same using both boundary conditions but is more realistic when using the suction boundary condition because of the shallower depth of frost penetration.

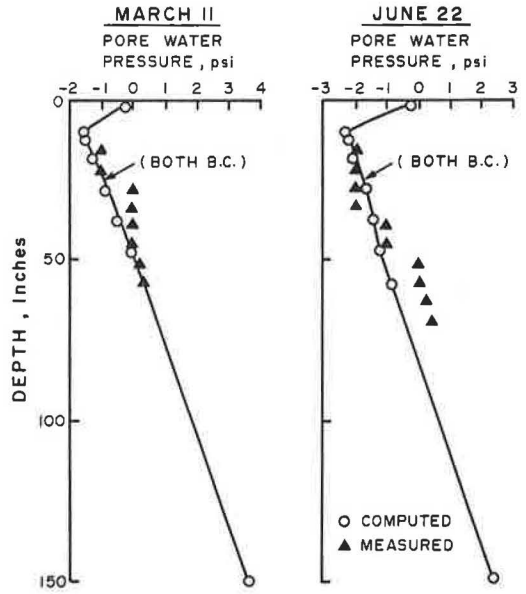


FIGURE 16 Deland, Piatt County, Illinois: Measured and computed pore water pressure profiles at different times of the year.

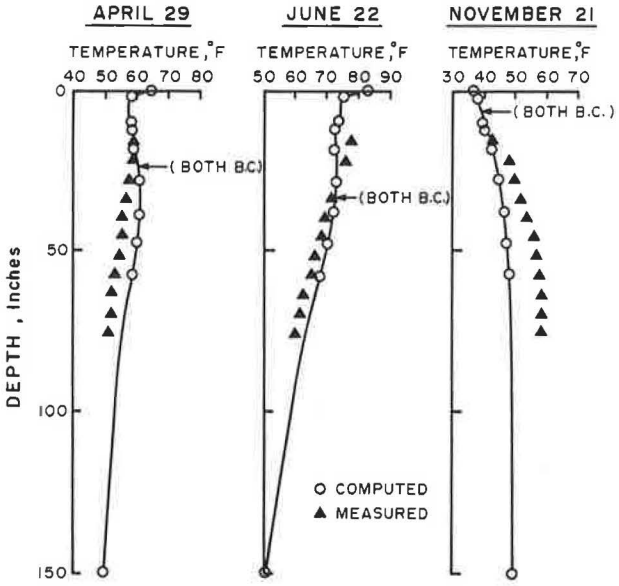


FIGURE 17 Deland, Piatt County, Illinois: Measured and computed temperature profiles at different times of the year.

EVALUATION AND CONCLUSIONS

The simulated temperatures using the two boundary conditions, flux and suction, commonly bracketed the measured values. The simulated suctions and pore water pressures followed the same patterns as in the measured data and were

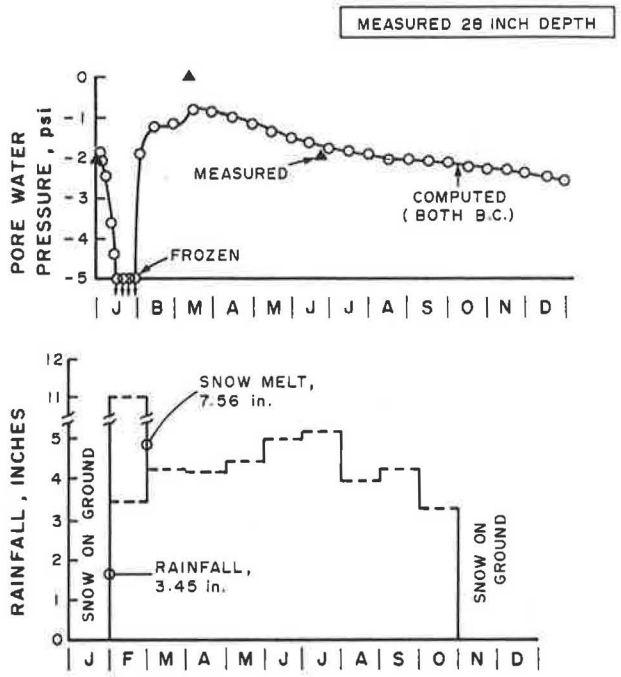


FIGURE 18 Deland, Piatt County, Illinois: Computed and measured pore water pressures and simulated rainfall and snowmelt.

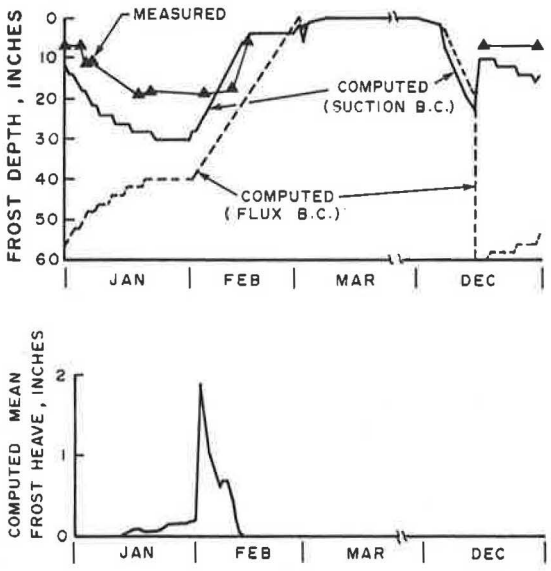


FIGURE 19 Deland, Piatt County, Illinois: Computed and measured frost depths and frost heaves.

generally within the measured ranges. The temperature profiles were particularly sensitive to the base course subgrade boundary condition. Because of this sensitivity, it is possible, by adjusting the flux by trial and error, to get the measured and computed temperatures to match as closely as desired, but there is no guarantee that the same boundary conditions and soil properties will provide as good a match to the temperature values observed in the following year. The suction values in College Station, Texas, and in Amarillo, Texas, had a much broader range at any given depth and time than the computed values. This is undoubtedly caused by the cracks in the clay soil subgrade, which transmit water faster along specific paths than is estimated by the program. There is a tendency for the computed subgrade suction beneath pavements in these areas to become irreversibly wetter with time.

Reliable suction measurements extending over significant periods of time are not easily obtained in the field. Temperatures can be measured much more easily and reliably. Relatively high suctions such as those at the Amarillo site can be measured quite accurately with psychrometers. Low suctions such as those at the Deland site can be monitored reasonably well with tensiometers. Intermediate values may be more difficult to determine. Perhaps the greatest difficulty is to maintain the instrumentation and to keep it calibrated for more than a year. Areas of significant frost penetration represent even greater problems. To obtain field suction data of the extent and quality described in this paper is truly remarkable. Monitoring field suctions over long periods of time in a variety of soil climatic conditions remains an ongoing challenge.

Both the positive and negative pore water pressures in Deland, Illinois, were predicted with reasonable accuracy.

Although it is not the objective of the simulation to duplicate field measurements exactly, it is reasonable to assume that adjusting the transfer coefficient r at the base course subgrade boundary will have a significant effect on the values of temperature and suction that are computed in the subgrade. The transfer coefficient r controls the magnitude and direction of the flux at the upper boundary. This flux carries heat along with it. Thus, both the temperature and suction profiles will be affected by the value of r selected for the analysis. This effect was described at the College Station site. It is hoped that ongoing simulations will establish a relationship between subbase and subgrade properties and the transfer coefficient.

REFERENCES

1. D. E. Pufahl, R. L. Lytton, and H. S. Liang. An Integrated Computer Model to Estimate Moisture and Temperature Effects Beneath Pavements. In *Transportation Research Record 1286*, TRB, National Research Council, Washington, D.C., 1990.
2. *An Integrated Model of the Climatic Effects on Pavements*. Final Report, FHWA, U.S. Department of Transportation, 1990.
3. H. S. Liang and R. L. Lytton. Rainfall Estimation for Pavement Analysis and Design. In *Transportation Research Record 1252*, TRB, National Research Council, Washington, D.C., 1989.
4. S. J. Lui and R. L. Lytton. 1985. *Environmental Effects on Pavement Drainage*, Volume 4. FHWA, U.S. Department of Transportation, 1985.
5. B. J. Dempsey, W. A. Herlach, and A. J. Patel. *The Climatic-Materials-Structural Pavement Analysis Program*. Final Report, FHWA, U.S. Department of Transportation, 1984.
6. G. L. Guymon, R. L. Berg, and T. C. Johnson. *Mathematical Model of Frost Heave and Thaw Settlement in Pavements*. U.S. Army Cold Regions Research and Engineering Laboratory, Hanover, N.H. 1986.
7. P. W. Mitchell. *The Structural Analysis of Footings on Expansive Soil*, (2nd ed.). Research Report 1. K. W. G. Smith and Associates, Adelaide, South Australia, March 1980.

Publication of this paper sponsored by Committee on Environmental Factors Except Frost.

Abridgment

Wave Model of Mat Foundation Movement on Expansive Clays

L. D. JOHNSON AND A. L. BRANCH, JR.

Soil differential movement patterns from soil moisture changes cause considerable damages to all types of structures and pavements. Such damage may be assessed by modeling foundation movements with wave patterns. Angular distortion, an indicator of the degree of damage, may be readily evaluated from wave patterns of elevation profiles obtained with close spacings between measuring points, such as 1 ft (0.3 m). Preliminary data based on total deformations from elevation profiles taken in four facilities indicate that the performance of mat foundations for resisting wall cracks may be quantified by simple rating systems. The maximum relative thickness D_{rel_m} derived as part of this study was found consistent in rating the performance of these four facilities and also indicated the location of the most serious distortion in a given facility. The concept of D_{rel_m} also has potential as a design aid for foundations. Other potentially useful rating systems include the wave index.

Soil differential movement patterns cause considerable damages to all types of structures and pavements such as military facilities, commercial buildings, houses, pavements, and parking lots. Differential soil movement may accumulate almost immediately after construction and continue to increase over many years. Moisture changes in expansive clay soils are a common cause of destructive differential movements. These patterns are hypothesized as being representative of wave motion with relatively long wavelengths exceeding 4 ft.

DAMAGE ASSESSMENT BY SOIL AND FOUNDATION WAVE PATTERNS

Differential soil movement may be described with wave motion by using angular distortion, as shown in Figure 1.

$$\beta = \frac{2A}{l/2} = \frac{4A}{l} \tag{1}$$

where

- β = average angular distortion bounded by crest and trough of wave;
- A = amplitude of the wave pattern as restrained by the foundation, ft (m); and
- l = wavelength of the movement pattern, ft (m).

Damage such as from cracks in walls, distorted floors, and misaligned door and window frames may be correlated with angular distortion (*1*,*2*). A slight degree of damage is expected if $\beta > 0.0015$ (*2*).

A reduction factor R_f relates restrained heave or amplitude A of soil beneath the mat with unrestrained amplitude A_u of the soil-foundation wave pattern.

$$R_f = \frac{A}{A_u} \tag{2}$$

The soil wavelength is assumed to remain unaltered when restrained by the foundation and the foundation is assumed to remain in complete contact with the soil. A_u is a measure of potential soil heave. R_f is analogous to a reduction factor that is the differential settlement beneath the mat restrained by mat stiffness divided by unrestrained differential settlement of a fully flexible mat; it is a function of relative stiffness K_s, shown in Figure 2, defined as (*3*,*4*)

$$K_s = \frac{E_c}{E_s} \cdot \frac{D_e^3}{\left(r \cdot \frac{l}{2}\right)^3} \cdot (1 - \nu_s^2) \tag{3}$$

where

- E_c = modulus of concrete or foundation elasticity, ksf;
- D_e = equivalent mat thickness, ft;
- ν_s = soil Poisson's ratio, 0.4;
- E_s = modulus of soil elasticity, ksf;
- l = wavelength of soil movement, ft;
- L = length of the mat, ft (m);
- B = width of the mat, ft (m);
- R = equivalent radius, $(LB/\pi)^{1/2}$ ft (m); and
- r = ratio of mat diameter to the wavelength, $2R/l$.

The equivalent mat thickness D_e is the thickness of a flat mat or may be a measure of the thickness of ribbed mats when the stiffness contributed by stiffening beams is included.

The effective mat diameter $2R_c$ equals l when $2R$ exceeds the wavelength l because a mat with $2R > l$ can ride on top or span the wave, whereas a mat with $2R < l$ may tilt into the depression of the wave. The critical case occurs when D_e is maximum, i.e., $2R_c = l$ and $r = 1$.

A new term, relative thickness D_{rel}, may be defined from Equation 3

$$D_{rel} = D_e \left[\frac{E_c}{E_s} \cdot (1 - \nu_s^2)\right]^{1/3} = R_c(K_s)^{1/3} \tag{4}$$

L. D. Johnson, Waterways Experiment Station, 3909 Halls Ferry Road, Vicksburg, Miss. 39180. A. L. Branch, Jr., Superconducting Super Collider Project Office, U.S. Department of Energy, 1801 North Hampton, Suite 310, DeSoto, Tex. 75115.

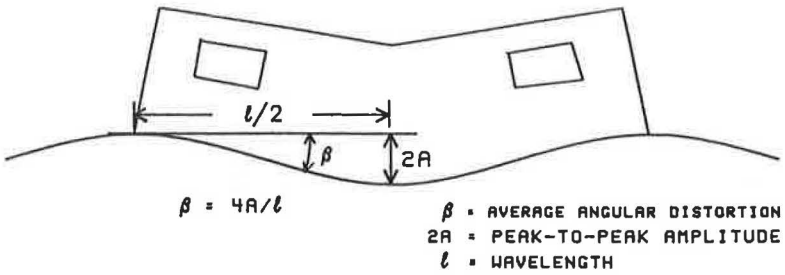


FIGURE 1 Angular distortion related to wave motion.

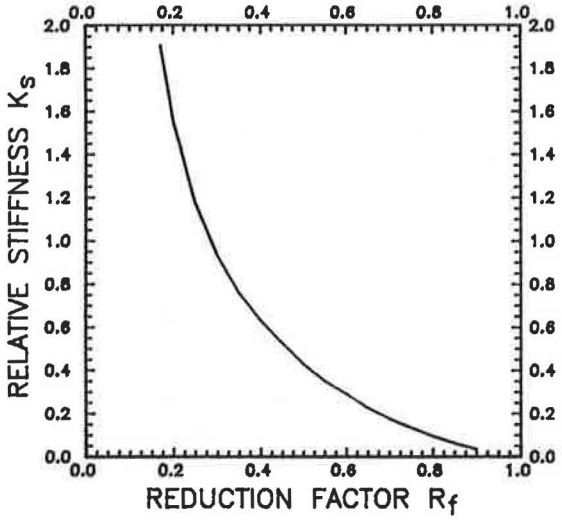


FIGURE 2 Relationship between reduction factor R_f and relative stiffness K_s (3,4).

where D_{rel} is in ft (m). D_{rel} is dependent only on R_c (= $l/2$) and K_s and may be calculated from given elevation profiles without knowledge of soil or foundation elastic parameters. D_{relm}, the maximum value of D_{rel} calculated for an elevation profile, is determined for a specific location and is expected to have the most potential for damage. D_{relm} may therefore be useful for rating performance of foundations while indicating the location of the most damaging distortion in the profile. D_{relm} is calculated from measured elevation profiles using the ADATG computer program.

For example, the full-loop elevation profile of line ATC1 of the Automated Technology Center, Figure 3, exhibits a large dip between 200 and 246 ft with a peak-to-peak (relatively) unrestrained amplitude $2A_u$ of about 1 in. and span length l of about 46 ft. The restrained amplitude $2A = \beta \cdot l/2$ from Equation 1 is (0.0015)(46)(12/2) = 0.4 in. Therefore, from Equation 2, $R_f = 2A/2A_u = 0.4$. For $R_f = 0.5$, K_s from Figure 2 is about 0.6. D_{rel} from Equation 4 is $(46/2)(0.4)^{1/3}$, or about 19 ft, which is the maximum value D_{relm} for this profile.

Relative thickness, calculated from Equation 4 using Equation 2, may be plotted versus $1/2R_c$ (or frequency $1/l$) for different angular distortions to determine how critical frequencies change depending on tolerable angular distortions β. The results of this type of analysis indicate that the relative thickness will be a maximum, D_{relmax}, at a particular frequency f_c, defined as follows:

$$D_{relmax} = \frac{0.066A_u}{\beta} \tag{5a}$$

$$f_c = \frac{4.8\beta}{A_u} \tag{5b}$$

in which A_u is in inches. If mat dimension $2R < 2R_c = l_c$, then relative thickness may be less than D_{relm} and may be calculated from Equation 4 setting $R_c = R$. Equations 5 may also be applied to pavements.

PERFORMANCE RATING SYSTEMS

Systems to quantify deformation patterns are useful to determine a way of rating foundation performance. The method of quantifying distortion should be independent of the length of the floor used to determine the elevation profile for a given spacing between measurement points Δx. This provision provides flexibility in making comparisons between elevation profile measurements obtained from different size structures. Three systems that are independent of the length of the elevation

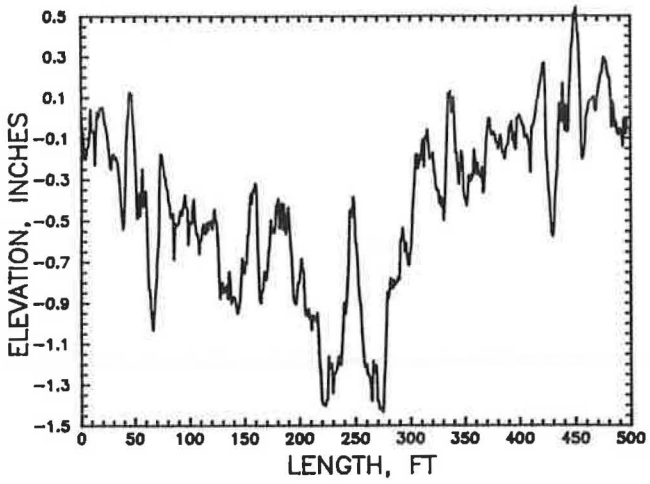


FIGURE 3 Elevation profile of line ATC1 of the Automated Technology Center for a full loop.

profile in addition to D_{relm} and may be useful to quantify damage to structures from foundation distortion are *F*-numbers FL and FF (ASTM E1155M-87), wave index WI (*5*), and a microrelief index MIF (*6*). FF is associated with floor flatness, whereas FL is associated with floor levelness. WI was evaluated over a spacing from 1 to 50 ft; therefore, WI = WI50. These systems provide a measure of average floor distortion over the length of the profile, whereas D_{relm} is a measure of extreme distortion in the profile.

The four rating systems are applied to four facilities briefly described in Table 1 with a description of damage. The Coastal Engineering Research Center (CERC) and Automated Technology Center (ATC) facilities are located in the Waterways Experiment Station, Vicksburg, Mississippi, whereas the Troop Medical Clinic (TMC) and Troop Dental Clinic (TDC) are located in Fort Sam Houston, Texas. These facilities are single-story, masonry structures constructed with initially horizontal floors. Several elevation full-loop profiles using an automated dipstick floor profiler with spacing Δx = 1 ft (0.3 m) were conducted along straight lines in hallways of each facility. These profiles include total deformations. Additional future surveys are required to deterine foundation distortion caused entirely by soil deformations; however, these preliminary surveys should indicate gross trends and provide a basis for analysis of future readings.

Analysis of the floor profiles using the rating systems are shown in Table 2 using the full loop. Walls adjacent to survey lines with the least *F*-numbers and the largest WI50, D_{relm}, and MIF values of a particular facility should be associated with the most damage. D_{relm} consistently provides the largest values associated with the most damage of all the survey lines of a given facility. WI50 is nearly consistent with the data.

CONCLUSIONS

Soil deformation may be modeled by waves. Angular distortion, an indicator of potential damage, is readily evaluated from wave patterns. The thickness of mat foundations required to accommodate a given unrestrained soil deformation may be calculated for a limiting angular distortion.

Preliminary data based on total deformations of some mat foundations indicate that the performance of structures relative to cracking in walls may be rated by simple systems. D_{relm} was consistent with cracking observed in the facilities, has the advantage of indicating the location of potential damage of walls from mat distortions, and may also assist in estimating the thickness of mat foundations required to reduce

TABLE 1 DESCRIPTION OF FACILITIES

Facility	Foundation	Performance
Coastal Engineering Research Center	4-inch slab-on-grade with spread footings	Large fractures 0.2 inch (5 mm) wide top of exterior walls at the middle adjacent and parallel with lines CERC4 and CERC5; performance near remaining survey lines satisfactory; elevation profiles vary in length from 100 to 200 ft (30 to 61 m); constructed in stages from 1965 to the present
Automated Technology Center (ATC)	8-inch slab-on-grade with spread footings	Jagged fracture in dry wall up to 0.2 inch (5 mm) wide and 8 ft (2.4 m) high adjacent and parallel with survey line ATC1 225 ft (67 m) from the initial point about 28 December 1989; constructed August 1989
Troop Medical Clinic (TMC)	Stiffened ribbed mat	Dry wall adjacent and parallel with line TMC5 contains several cracks near top of the wall up to 0.13 inch (3 mm) wide; elevation profiles vary from 80 to 200 ft (24 to 61 m); constructed during 1980 and 1981
Troop Dental Clinic (TDC)	Stiffened ribbed mat	Dry wall adjacent and parallel with line TDC7 contains minor cracking up to 0.06 inch (2 mm) wide; remaining walls less affected by distortions; overall performance satisfactory; elevation profiles varied from 150 to 200 ft (46 to 61 m); constructed during 1980 and 1981

TABLE 2 PERFORMANCE RATINGS OF FACILITIES

Facility	Date of Survey	Survey Line	F-Numbers FL	F-Numbers FF	Wave Index WI50, in.	Maximum Relative Thickness D_{relm}, ft	Microrelief Index MIF
CERC	07/20/89	CERC1	20.71	20.73	0.1061	5.7944	0.3131
		CERC2	16.82	17.64	0.1172	6.4958	0.2276
		CERC3	23.79	23.37	0.1020	6.8294	0.1630
		•CERC4	22.20	24.20	0.2261	7.7983	0.2604
		•CERC5	23.40	25.28	0.2160	13.7278	0.2103
ATC	12/12/89	• ATC1	14.75	14.25	0.2029	18.7418	0.5627
		ATC6	16.63	17.73	0.1289	2.8157	0.2413
		ATC7	15.22	14.34	0.2638	7.6883	0.1488
		ATC8	16.66	18.46	0.1257	8.6827	0.2144
		ATC9	16.30	17.94	0.1353	11.4439	0.2305
		ATC10A	19.51	19.05	0.1454	5.5272	0.2071
		ATC11	13.76	13.70	0.1499	9.5875	0.2319
TMC	02/01/90	TMC3	22.43	23.73	0.2027	12.0680	0.5148
		TMC4	27.19	26.11	0.0982	5.3678	0.1828
		• TMC5	18.91	21.73	0.2856	23.6370	0.4685
TDC	02/01/90	TDC6	17.43	18.64	0.1353	8.8534	0.2013
		• TDC7	16.42	18.07	0.2709	10.6759	0.3256
		TDC8	14.40	20.21	0.2610	8.6779	0.2069

Note: • indicates survey line adjacent to wall with most damage

a given soil deformation. WI50 was nearly consistent with all of the data.

ACKNOWLEDGMENT

This study was supported by the Office of the U.S. Army Chief of Engineers, Washington, D.C. Permission was granted by the Chief of Engineers to publish this information.

REFERENCES

1. H. E. Wahls. Tolerable Settlement of Buildings. *Journal of Geotechnical Engineering*, Vol. 107, No. 11, 1981, pp. 1489–1504.
2. M. D. Boscardin and E. J. Cording. Building Response to Excavation Induced Settlement. *Journal of Geotechnical Engineering*, Vol. 115, No. 1, 1989, pp. 1–21.
3. J. N. Kay and R. L. Cavagnaro. Settlement of Raft Foundations. *Journal of Geotechnical Engineering*, Vol. 109, No. 11, 1983, pp. 1367–1382.
4. P. T. Brown. Numerical Analysis of Uniformly Loaded Circular Rafts on Deep Elastic Foundations. *Geotechnique*, Vol. 19, No. 3, 1969, pp. 399–404.
5. Concrete Surfaces: Elevation, Slope and Wavincss. *Concrete Materials and Methods of Construction*, Appendix E. Canadian Standards Association, Rexdale, Ontario, Canada, 1990, pp. 107–112.
6. M. J. M. Römkens and J. Y. Wang. Effect of Tillage on Surface Roughness. *Transactions, American Society of Agricultural Engineers*, Vol. 29, 1986, pp. 429–433.

The views of the authors do not purport to reflect the views of the Department of the Army or the Department of Defense.

Publication of this paper sponsored by Committee on Environmental Factors Except Frost.

Simulation of Climatic and Vegetation Effects on Pavements on Expansive Clays

M. PICORNELL AND MOHD ASRI B. ABD RAHIM

The flow of moisture through a continuum cannot explain the very wet conditions present under pavements in semiarid and arid climates. A possible major cause is the presence of shrinkage cracks. In this manner, the water infiltrates through the cracks where it is slowly absorbed on the crack walls. This water is, then, effectively trapped within the soil mass because the prevailing suction gradients are not large enough or do not act for sufficiently long times to remove significant amounts of moisture. A simplified model to simulate the infiltration of rainfall through the crack fabric and the removal of soil moisture by soil evaporation and plant transpiration along the sides of a pavement is described. The moisture movement through the crack fabric is simulated as an open channel flow. The moisture transfer from the cracks to the soil on the crack walls is assumed to be one-dimensional absorption. The results of simulations for several climatic regions of Texas are presented. For all these regions, the model predicts steady closing of the crack fabric under the pavement. The time to closing ranges from less than 1 year for the climatic conditions of Houston to more than 8 years for the climatic conditions of El Paso. In contrast, the shrinkage cracks under the edge of the pavement and within the soil adjacent to the pavement close during wet periods and then reopen again during extended dry periods. For the wetter climates, the cracks are generally closed and only open during periods of consistent dry weather. For the drier climates, the cracks remain open at all times.

Pavements build on expansive soils are known to develop roughness not associated with traffic. This type of pavement roughness has been attributed to the presence of shrinkage cracks in the subgrade soils (*1*). Rainfall can penetrate very fast through the crack fabric. The water, impelled by gravity and under positive pressures, goes where the crack directs it. The water in the cracks has little exposure to the atmosphere, which allows ponding time for the water to seep into the soil matrix on the crack walls. This seepage causes concentrated surface heaving along the trace of the crack and consequently the development of roughness.

Pavement roughness reduces the serviceability index significantly and thus requires periodic maintenance, such as releveling and overlays, to restore riding quality. The Texas State Department of Highways and Public Transportation has been trying for some time to reduce the expenses associated with this periodic maintenance by installing vertical moisture barriers. Field test sections have been implemented in San Antonio, Texas, on IH-37 (*2*) and along IH-30 in Greenville, Texas (*3*). Additional test sections have been recently established and are being monitored.

M. Picornell, Civil Engineering Department, University of Texas at El Paso, El Paso, Tex. 79968. M. A. B. Abd Rahim, Univeristi Sains Malaysia, Minden, 11800 Panang, Malaysia.

The purpose of the moisture barrier is to isolate the subgrade soils from seasonal climate changes. In the first trials (*2*), the moisture barrier was placed to a depth of 8 ft, on the basis of moisture content monitoring data for the region. Later on, it was recognized (*4*) that one of the main functions to be performed by a vertical moisture barrier is to prevent rainwater from accessing the crack fabric within the subgrade soils. This need led to choosing the depth of the barrier on the basis of the expected maximum possible depth of shrinkage cracks at the site.

Field monitoring data obtained on several test sections indicated that the role of the vertical moisture barrier can be different at different sites. In the test sections of IH-37 in San Antonio, Texas, suction measurements on both sides of the barrier indicated (*5*) that the soils enclosed by the barrier remained at a nearly constant suction during more than 2 years. Meanwhile, the soils outside the barrier were experiencing significant suction changes. Field measurements also indicated lack of roughness development in the test sections, whereas in the adjacent control section roughness was developing at a steady rate. In this case, the moisture barrier had protected the soils under the pavement of the moisture changes observed in the soils on the side of the pavement. In contrast, pavement roughness measurements at the trial sections on IH-30 have indicated (*3*) that the test sections experienced higher rates of roughness development than adjacent control sections. At this site, the barrier actually retained moisture inside rather than keeping it outside.

These results suggest that the barrier can play different roles depending on site-related conditions. Among the most influential factors are the climate, pavement surface conditions, initial moisture conditions of the subgrade soils, and moisture barrier depth. Furthermore, the site location, such as on a hill, on a slope, or in a cut, will also affect the role played by a moisture barrier.

These considerations illustrate the need of a physically based model that would account for the movement of moisture through the shrinkage cracks, and the seepage of this moisture into the soil matrix, together with realistic models for the replenishment and removal of moisture from the subgrade soils.

REVIEW OF EXISTING LITERATURE

Infiltration into expansive soil deposits has long been considered to be affected by the presence of shrinkage cracks. There is ample evidence (*6,7*) in the literature that rainfall percolates through cracks and then slowly seeps into soil peds. As the

soil matrix gains moisture, it swells and progressively closes the cracks.

The presence of shrinkage cracks in expansive soil deposits is apparent. In very dry soils, profuse surface cracks form on the ground surface. Cracks with openings on the ground surface up to about 1 in. and several feet deep (*8*) have been reported. Furthermore, the crack patterns and frequency have been observed (*8,9*) to depend on the vegetative cover. The crack opening decreases from a maximum at the soil surface to zero at the crack tip. The variation of the crack opening with depth has been described with curves of linear shrinkage versus depth (*9*). Morphological studies (*10*) have revealed the presence of approximately rectangular blocks of soil formed by aggregation of soil peds. These studies also revealed that infiltration of rainwater into the crack fabric is determined by the soil surface microrelief. The water is directed towards the cracks through surface depressions. Then the water runs down the crack faces, wetting only a small fraction of the exposed crack surface. This effect causes the bulk of rainwater that is penetrating the cracks to move directly to the tip of the cracks.

The presence of cracks in aquifer-bearing formations results in two distinctive flows taking place: one through the cracks and the other through the porous medium between cracks. The water inside the cracks is more mobile than the water within the matrix of the porous medium. Traditionally, the modeling of this type of flow has been approached with Barenblatt's (*11*) double porosity concept. However, this approach is not appropriate in the present application under unsaturated conditions. An additional complication is the fact that cracks in expansive soil deposits close as the soil matrix gains moisture; thus the porosities do not remain constant.

The first known attempt to include the effect of shrinkage cracks on infiltration was by Richards (*12*). In this work, the subsoil was divided into blocks and two permeability coefficients were used, one along the cracks and the other through the soil matrix. This model did not account for changes caused by the swelling and shrinkage of the soil.

The moisture accumulated inside the crack fabric and in the soil blocks can be depleted as a result of evaporation at the soil surface and plant transpiration. Soil evaporation has been proved to be an ineffective mechanism of moisture removal from the soil by a number of investigators (*13–15*). The consensus is that even a small amount of soil evaporation forms a dry soil crust at the soil surface that prevents further evaporation from taking place. Existing field monitoring data (*15*) suggest that soil evaporation might affect only the soil within the upper foot of the soil deposit.

Plant transpiration, by way of contrast, is a much more effective mechanism of moisture removal from the soil. The native vegetation, such as roadside grasses, removes water from the soil through the root system. Nevertheless, when the soil suction reaches the wilting point of the vegetation, all transpiration ceases. Because of the extremely small permeabilities of expansive soils, the removal of water by the root system is confined to the rooting depth of the vegetation (*16*).

These considerations suggest that a model that could approximate field behavior would have to consider the following:

1. The infiltration of rainfall into an expansive soil deposit takes place primarily through the crack fabric,
2. The soil mass is divided into approximately parallelepipedic blocks by the crack fabric,
3. The moisture transfers from the cracks to the soil blocks,
4. The gain in moisture causes swelling of the soil blocks and thus modifies the crack fabric, and
5. The removal of water from the soil mass is primarily determined by the transpiration of the native vegetative cover.

MAIN FEATURES OF THE MODEL

The model considers a fixed length of highway. The subgrade soils are considered divided into parallelepipedic blocks. The model formulates several water balances within this section, when subjected to a sequence of climatic conditions.

The rainfall on the pavement is subdivided into infiltration through the pavement and runoff to the side drainage ditch. The model adds the rainfall infiltration to the volumes of water stored in the cracks. For this purpose, the model keeps track of two total volumes of water stored in the crack fabric of the subgrade soils: one for the soils under the pavement and inside the barrier, and the other for the soils outside the vertical moisture barrier.

The water stored in the crack fabric is lost to seepage into the soil blocks, to transfers of water under the barrier, or to transpiration through the root systems of roadside vegetation. The water balances for the soils on both sides of the barrier are formulated on a daily basis, except during rainfall events when the water balances are formulated every minute.

Every time that the water balance is formulated, the volume of water transferred to the soil blocks is used to reconsider the block sizes and, thus, the geometry of the crack fabric.

Climatic Conditions

The regional climatic conditions are summarized in two daily parameters: rainfall depth and potential evapotranspiration. On days with rainfall larger than trace, a third parameter is needed: rainfall duration. The daily time series with these parameters can be actual weather data or based on stochastic simulation for the regional climatic conditions. A more thorough description of the weather data and analysis needed has been provided by Abd Rahim and Picornell (*17*).

Rainfall Depth Assignment

The rainfall depth on the pavement surface is subdivided into two parts. The first part corresponds to the infiltration through cracks and fissures of the pavement. The second part is the remaining rainfall depth that is assigned to runoff to the side drainage ditch.

The infiltration through the pavement is added to the water stored in the crack fabric beneath the pavement. If the crack fabric within the subgrade fills with water, the remaining rainfall depth is assigned to runoff to the side drainage ditch.

The infiltration into the soil outside the barrier is the result of direct rainfall in the area plus the runoff coming from the pavement surface. The runoff from the pavement surface is multiplied by a factor selected by the user, to account for runoff coming from higher areas of the pavement and drainage ditch.

The infiltration into soils adjacent to the pavement is assumed to replenish the water within the crack fabric. The maximum depth of water that the model allows to pond within the drainage ditch can be arbitrarily selected. If the water level within the crack fabric accumulates to this limit, the rest of the potential infiltration is lost.

The combined possibilities offered by the depth of water ponding within the drainage ditch and the multiplying factor of the runoff from the pavement cover all possible cases of drainage conditions.

Cross Section Definition

Input for the model includes the characteristics of the pavement surface, the moisture barrier, and the crack fabric within the subgrade soils. The model only contemplates one-half of the pavement surface split along the centerline of the highway. A typical cross section is shown in Figure 1.

The surface of the paved subgrade is considered to be horizontal. The program starts by fitting a series of soil blocks of specified dimensions from the subgrade surface down to the actual crack depth for the three soil regions labeled *Uncovered*, *Pavement*, and *Edge* in Figure 1. All the distances and slopes labeled in this figure can be arbitrarily specified. The thickness of the base and subbase, the depth and width of the vertical moisture barrier, and the rooting depth of the roadside vegetation can also be specified. On the basis of the relative depth of the barrier and the rooting depth of the roadside vegetation, the cross section is subdivided into the three zones: *Pavement*, *Edge*, and *Uncovered* indicated in Figure 1. The zone *Edge* consists of the soils enclosed within the barrier near the edge of the pavement. The width of the *Edge* zone is selected to be equal to the distance from the bottom of the barrier to the bottom of the root zone of the roadside vegetation. The model then considers that the roadside vegetation can develop roots within this zone, and thus, evapotranspiration can remove soil water from the cracks and from the soil blocks within this soil region.

SHRINKAGE CRACK FABRIC

The geometry of the crack fabric is specified by a list of block sizes with depth. Morphological observations (*10*) in dry clayey soils indicate that the soil mass is divided into parallelepipedic blocks of increasing sizes with depth. Figure 2 shows some of the block sizes typical for several soil conditions.

The model can accept a user supplied sequence of blocks from the subgrade surface to the crack depth. The model uses this sequence to divide the subgrade soils into blocks. Then the model shrinks these blocks on the basis of the initial moisture conditions specified. During the simulation, the model keeps track of the position of the centroid and the sizes of each block. On the basis of the positions of all blocks and their sizes, the crack volume available for storage of rainfall can be calculated.

Initial Subsurface Conditions

The properties of each soil block in the size list can be specified. Thus, it is possible to define as many soil layers as block sizes are included in the set of soil blocks. The input needed

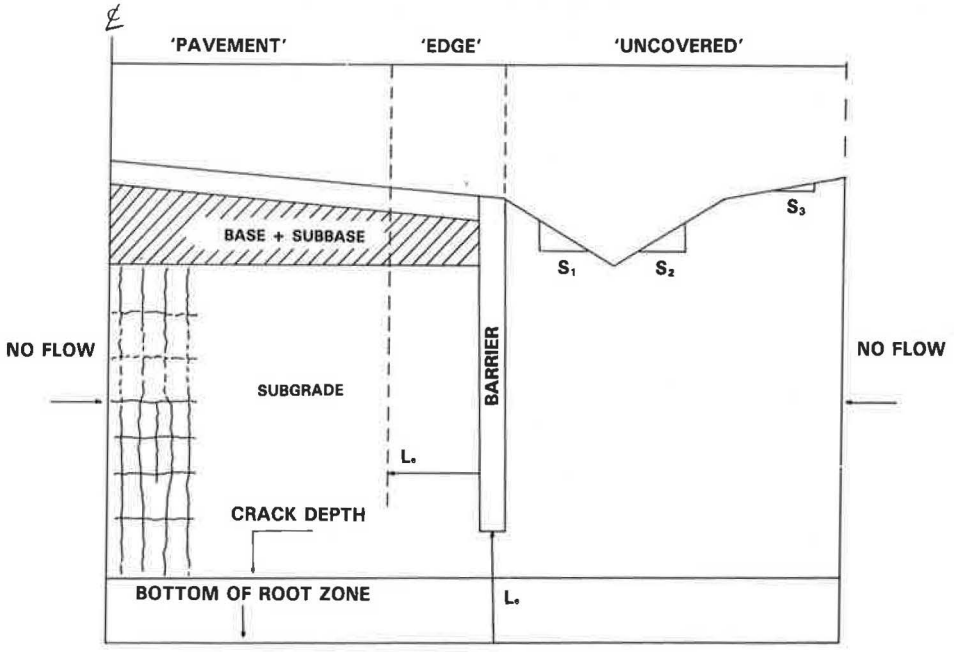


FIGURE 1 Main features of highway cross section.

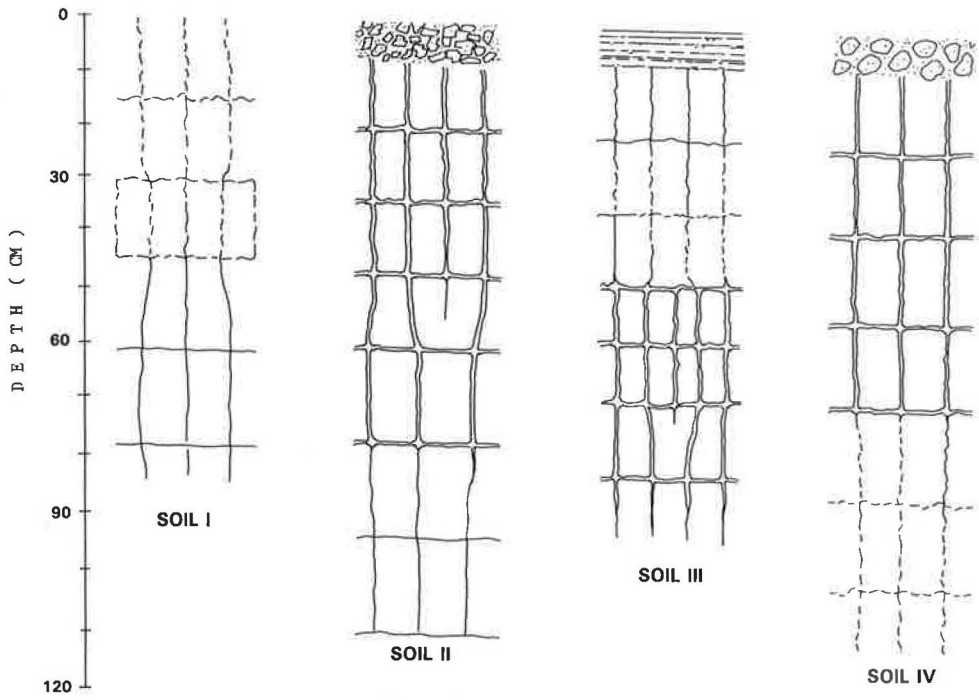


FIGURE 2 Soil block sizes for several different soils.

includes the initial state of the subsurface soils and the flow properties of each soil type specified. The initial state of the subsoil can be described by the shrinkage and suction profiles with depth.

Holmes (*18*) has shown that clayey soils remained essentially saturated to very high suctions, such as 100 bars. For the subgrade soils, the soil suctions of interest range from a field capacity of 0.3 bar to the wilting point of the vegetation around 15 bars. Thus it is reasonable to assume that the volume change of a soil block is identical to the volume of moisture gained or lost by the soil block. This volume of water is controlled by the specific moisture capacity, that is, the slope of the moisture characteristic curve of the soil.

The flow properties of the soil matrix can be specified independently for each block. In this sense, the specific moisture capacity and the permeability for each soil type have to be specified for a range of suction from 0 to over 15 bars.

Development of Block Curves

The rate of moisture transfer from the cracks to the soil blocks is approximated with a master block curve developed for each block size and soil type. This curve is derived by modeling a one-dimensional unsaturated water flow within the soil block. The soil inside the block is assumed to be at a constant suction initially. The water flow is assumed to take place along the smallest side of the block. The full master curve is developed in two steps: a wetting and a drying phase.

In the wetting phase, the soil block is subjected to a zero suction at the two exposed faces. For every time step, the volume of water flowing into the block is calculated for both exposed faces. The volume of water absorbed by the block is assumed to be equal to the volume heaved by the block; thus allowing to calculate the variation of the block's volume with time.

In the drying phase, the block at the same initial suction is exposed to a soil suction of 15 bars at both exposed faces. The volume of moisture extracted from the block at each time step is calculated using the same one-dimensional water flow. Again, the volume change of the block is assumed to be equal to the volume of water lost through both exposed faces. The simulation proceeds until the flow (intake or release) at the two exposed surfaces is smaller than 0.01 cm^3/day.

The results of the two phases are incorporated into a single master curve for each block. Examples of master curves for several block sizes are shown in Figure 3. These curves are used during the simulation to determine the rate of moisture transfer from the crack fabric to the blocks and the change in sizes of the soil blocks on gaining or releasing soil water.

Pavement Surface Conditions

Rainfall infiltration through the pavement surface is estimated with the same procedure outlined by Liu and Lytton (*19*). This procedure allows two alternative ways to estimate the infiltration rate through the pavement surface depending on the information available. When there is no information about the type of pavement or the length of cracks and joints on the pavement surface, the infiltration is estimated on the basis of the worst of several published cases (*20*). If the pavement surface conditions are known, then the infiltration through the pavement surface is determined on the basis of the pavement type and length of cracks and joints as proposed by Ridgeway (*21*).

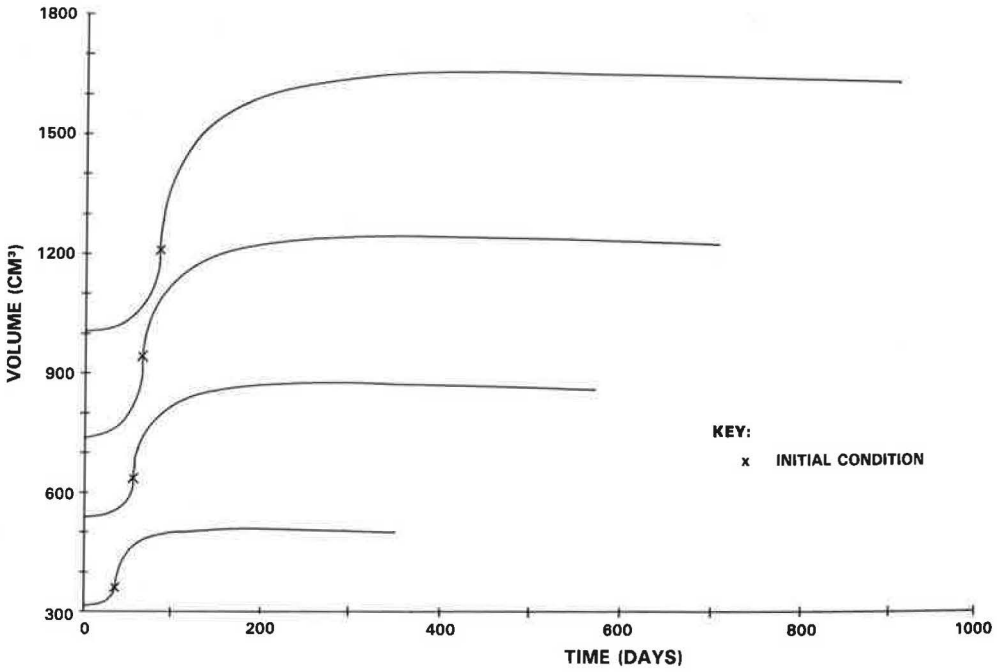


FIGURE 3 Examples of master block curves for several block sizes.

Roadside Vegetation

The native vegetation growing along the roadside provides the most effective mechanism for removing moisture from the subsurface soil within the rooting depth of the vegetation. The amount of water removed by the plants is determined by the environmental demand imposed on the plants, the potential evapotranspiration, and to some degree the exposure of the plants to the environment. This exposure is measured by the leaf area index (LAI). This index measures the leaf surface area exposed per unit of ground surface area.

The taller the vegetation, the larger is the LAI. Mowing roadside grasses is a common practice. The result of mowing is a large sudden decrease of the LAI, which reduces exposure of the vegetation to the environment and, thus, reduces the water removal from the soil mass. Any desired sequence of LAI for a 365-day year can be used by the model to assess the actual evapotranspiration.

Moisture Removal Assignment

The actual removal of water from the subgrade soils is determined by the potential evapotranspiration and the storage of moisture in the soil profile. The actual evapotranspiration is estimated using a simplified procedure (*22*) verified for the climatic conditions of central Texas. The difference between the water depth stored in each block from field capacity to the wilting point is taken as the total storage possible in the block. The sum of the storage for all the blocks in the block sequence is the maximum storage for the soil profile.

The potential evapotranspiration is subdivided into potential soil evaporation and plant transpiration on the basis of the LAI. The effect of the stage of drying is then evaluated independently for the two components. Soil evaporation is evaluated from the matrix properties of the soil as summarized in a diffusion parameter. Plant transpiration passes through several stages, but in all cases the actual plant transpiration is estimated on the basis of the LAI and monthly averages of actual evapotranspiration. After the two components have been evaluated, they are added together to determine the actual evapotranspiration.

After the actual evapotranspiration is known, it has to be determined from where the water has to be removed. The first choice is whether the water has to be removed from the cracks or from inside the soil blocks. A second choice has to be considered: whether the water should come from the soil mass adjacent to the pavement or from the soil mass under the pavement. The evaporation from the soil surface can take place only at the *Uncovered* soil surface outside the pavement area. However, plant transpiration removes water from the soil inside the rooting depth of the vegetation. Thus, if the vegetation can spread roots under the pavement, plant transpiration can be supplied by soil water stored in the soils under the pavement.

For this purpose, the soil mass has been subdivided into the three regions shown in Figure 1. The soil region *Pavement* is not accessible to the roots of the roadside vegetation, implying that the moisture in these soil blocks cannot be removed. In this sense, the soil blocks in this region can only swell, but there is no mechanism to permit shrinkage or removal of moisture from these blocks. In contrast, the moisture in the crack fabric can flow from the *Pavement* to the *Edge* and to the *Uncovered* soil region in response to differences in water levels. The soil region *Edge* is assumed to be accessible to the root system of the roadside side vegetation, and thus, soil water can be removed from this region. The *Uncovered* soil region is the most exposed, and soil water can be removed from this region by the two mechanisms soil evaporation and plant transpiration.

In summary, the actual evapotranspiration is removed from the soil in the *Edge* and *Uncovered* regions. Therefore, the soil blocks in these two regions can experience swelling and shrinking, implying that the cracks could close during wet periods and open again during consistently dry periods. This process contrasts with that of the cracks in the *Pavement* region that are only allowed to close.

The rooting depth of the roadside vegetation has a large influence because the shrinking under the edge will open cracks allowing rainfall water to bypass the barrier, if the barrier did not extend to the rooting depth of the roadside vegetation. Most commonly, the roadside vegetation is grass. There is a wealth of information (*16*) indicating that grasses have maximum rooting depths of 8 to 9 ft. However, when shrubs or trees grow in the vicinity of the pavement, much larger rooting depths should be expected.

The actual evapotranspiration depth is taken from the water stored in the cracks. When the cracks do not hold enough water to satisfy all the actual evapotranspiration, the remaining is taken from the soil blocks in the *Edge* and *Uncovered* regions. The water stored in the crack fabric of the *Uncovered* region is the first source of water, followed by the *Edge* region. When the water in the crack fabric has been depleted, the actual evapotranspiration is taken from the soil blocks. The moisture from the blocks is removed from the soil block that is under the wettest conditions. The decision of which block is the wettest is based on the relative positions of the blocks along the master block curves.

Block Absorption and Desorption

The model keeps track of three sets of blocks; one on each of the three soil regions: *Pavement*, *Edge*, and *Uncovered*. For each block, and at every time step, the coordinates of the center of the block, the width, length, and height of the block, and the total volume of each block are recorded.

The total volume of the soil block at any time indicates the position of the soil block along the master block curve. This position also determines the rate of volume increase for any period of time that the soil block is submerged. This increase is obtained from the master block curve, increasing the time step desired and finding the corresponding new volume of the block.

The rate of desorption of the soil blocks subject to water removal by the root system of the vegetation is determined by the actual evapotranspiration. The water removal will cause the blocks to slide down along the master block curve. On rewetting, the block will start from a lower position along the master block curve.

Crack Fabric Reconsideration

The crack fabric depth is evaluated and tracked for each of the three soil regions: *Pavement*, *Edge*, and *Uncovered*. The program keeps track of one set of soil blocks for each region. Each set consists of the number of soil blocks of different sizes at increasing depths specified by the user. The changes occurring in this set of blocks times the number of soil blocks fitted within the corresponding region are used to calculate crack opening changes within the region.

The soil within the second and third soil regions are subject to drying by the root system of the vegetation. Thus the crack depth in these zones is subjected to closing during wet spells and crack opening during dry spells. The program keeps track of one set of blocks for each region and assumes that the rest of the blocks within each region behave identically to the set of blocks tracked. Thus the changes recorded for the set of blocks times the number of blocks fitted inside the region are used to calculate crack openings within the regions.

Water Transfer Underneath the Barrier

The program considers one water level on each side of the barrier. The transfer of water from one side to the other is assumed to take place through the shrinkage cracks in the soil underneath the vertical moisture barrier. If these cracks close, all transfer of water between the two sides is stopped.

The water transfer when the cracks are opened is impelled by the difference in elevation between water levels. The flow of water through the cracks is estimated using Manning's formula. The hydraulic radius is calculated at every time step taking into account the wetted perimeter of all shrinkage cracks included in the highway section being analyzed.

RESULTS OF TRIAL RUNS AND DISCUSSION

The model has been used in several trial runs to illustrate the effects of the more relevant parameters on the infiltration of rainfall into the subgrade soils. The first few runs were intended to illustrate the effect of the climatic conditions. Stochastically generated weather data for Houston, San Antonio, Dallas-Fort Worth, and El Paso, Texas, were used for these runs. Several extra runs were performed for the climatic conditions of San Antonio for different moisture barriers to illustrate the effect that the barrier has on the wetting process of the subgrade soils. Thorough documentation of all the results of these runs has been provided by Abd Rahim and Picornell (*17*).

Effects of Climate

The first set of runs was performed for the same subsurface soil and pavement conditions. Specifically, the crack fabric was assumed opened to 1.20 m below the subgrade surface and the moisture barrier extended 0.70 m below the subgrade surface. The initial subgrade moisture conditions, the block sequence, and the flow properties of the soil used have been provided by Abd Rahim and Picornell (*17*). The period of simulation was 5 years for the climatic conditions of Houston, Dallas-Fort Worth, and San Antonio; for El Paso the simulation extended over 10 years. The results of the simulation at each site are summarized in annual plots of water levels within the crack fabric and elevations of the crack tips in the *Pavement*, *Edge*, and *Uncovered* soil regions.

The plots obtained from the first year of the simulation for Houston, Texas, are shown in Figure 4. The crack tip at the beginning of the simulation has been used as the reference point for the elevations shown in all figures. Figure 4 shows

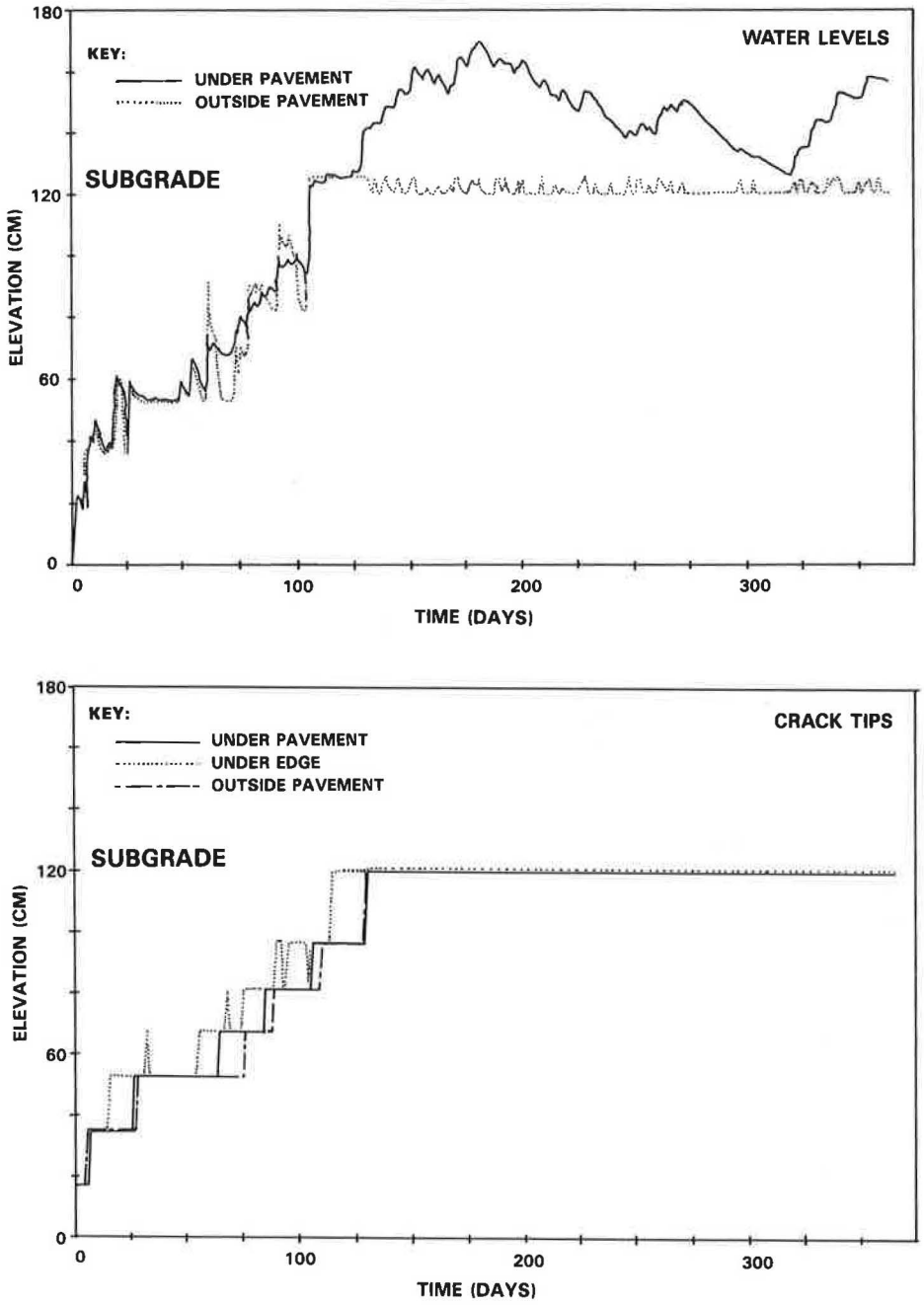


FIGURE 4 Results of simulation for first year in Houston, Texas.

that the water levels in the crack fabric fill the cracks on both sides of the barrier in about 4 months. Thereafter, the cracks remain full during the rest of the simulation, with the exception of a few short summer periods. The cracks under the moisture barrier close in a month and never open again. In the three soil zones, all the cracks close to the subgrade surface in about 4 months. Thereafter, the cracks open annually for periods of 1 to 2 months, and then close again for the rest of the year.

The results of the simulation for San Antonio, Texas, exhibit similar patterns. The plots for the first and second years of the simulation are presented in Figures 5 and 6. The water levels in the crack fabric exhibit a general increasing trend with occasional fluctuations during the first 2 years. In general, the water level in the *Uncovered* region lags behind the water level within the *Pavement* region. The crack tip elevations indicate that about 2 months after the beginning of the simulation the cracks under the barrier close, and about 18 months from the beginning, the cracks in the *Pavement* region have closed to the subgrade surface. During the first 2 years, all crack tips exhibit a general increasing elevation trend with the cracks in the region *Uncovered* lagging somewhat. After the first 2 years, the cracks in the *Edge* and *Uncovered* regions have closed and only open occasionally during the summer months.

The results of the simulations for Dallas-Fort Worth are similar to the results for San Antonio. The water level in the *Pavement* soil region reach the top of the subgrade in less

the period of the simulation. The results of these simulations indicate that when the pavement is cra ked or fissured, a large fraction of the rainfall infiltrates through the pavement and into the subgrade. The result is that the subgrade soils in the *Pavement* region can swell faster than the soils in the *Uncovered* region. These results could explain the observed behavior (*3*) in IH-30 that exhibited faster roughness development in the sections with moisture barrier than in control sections.

SUMMARY AND CONCLUSIONS

A computer program has been assembled to simulate the movement of water under a pavement on a cracked swelling soil subgrade. Specifically, it was desired that the program could account for the infiltration of rainfall through cracks and joints on the pavement surface and the horizontal water flow through the shrinkage crack fabric.

The basic assumption has been that the crack fabric displays a simple geometric configuration of superimposed parallelepipeds. The water is assumed to flow through the cracks under positive pressure, and then is slowly absorbed by the soil blocks. As the water is absorbed, the blocks swell and the geometry of the crack fabric changes. The water absorbed by the blocks is assumed to be immobilized unless the road side vegetation has established roots within the blocks.

Trial runs for some climatic conditions of Texas exhibit a wide range of possible behavior; under the wetter conditions of Houston the cracks close in a matter of a few months, while for the drier conditions of El Paso the cracks remain open during the 10 years of simulation.

These results have shown that the shrinkage crack fabric under the pavement steadily closes even under the dry conditions of the El Paso climate. The wetter the climate, the faster the cracks close; from a minimum of 4 months in Houston to a maximum of 7 years in El Paso.

Trial runs performed with several moisture barrier depths have indicated hat if the pavement surface has cracks and joints that allow water infiltration, the moisture barrier can cause faster swelling under the pavement than the surrounding soils.

REFERENCES

1. M. O. Velasco and R. L. Lytton. Pavement Roughness on Expansive Clays. *Research Report 284-2*. Texas Transportation Institute, Texas A&M University, College Station, 1981.
2. M. L. Steinberg. Deep Vertical Fabric Moisture Seals. *Proc., 4th International Conference on Expansive Soils* (D. Snethen, ed.), ASCE, New York, 1980.
3. D. A. Gay and R. L. Lytton. Moisture Barrier Effects on Pavement Roughness. In *Measured Performance of Shallow Foundations*, Geotechnical Special Publication 15, ASCE, New York, 1988.
4. M. Picornell. The Development of Design Criteria to Select the Depth of a Vertical Moisture Barrier. Dissertation. Texas A&M University, College Station, 1985.
5. M. Picornell, R. L. Lytton, and M. L. Steinberg. Matrix Suction Instrumentation of a Vertical Moisture Barrier. In *Transportation Research Record 945*, TRB, National Research Council, Washington, D.C., 1983.
6. D. E. Kissel, J. T. Ritchie, and E. Burnett. Chloride Movement in Undisturbed Swelling Clay Soil. *Proc., Soil Science Society of America*, Vol. 37, 1973, pp. 21–24.
7. G. Blake, E. Schlichting, and U. Zimmermann. Water Recharge in a Soil with Shrinkage Cracks. *Proc., Soil Science Society of America*, Vol. 37, 1973, pp. 669–672.
8. J. R. Johnston and H. O. Hill. A Study of the Shrinking and Swelling Properties of Rendzina Soils. *Proc., Soil Science Society of America*, Vol. 9, pp. 24–29.
9. A. Z. El Abedine and G. H. Robinson. A Study on Cracking in Some Vertisols of the Sudan. *Geoderma*, Vol. 5, 1971, pp. 229–241.
10. J. Bouma and L. W. Dekker. A Case Study on Infiltration Into Dry Clay Soil. I. Morphological Observations. *Geoderma*, Vol. 20, 1978, pp. 27–40.
11. G. I. Barenblatt, Y. P. Zheltov, and I. N. Kochina. Basic Concepts in the Theory of Seepage of Homogeneous Liquids in Fissured Rocks. *Prikladnaya Matematika i Mekhanika*, Vol. 24, 1960, pp. 1286–1303.
12. B. G. Richards. A Mathematical Model for Moisture Flow in Horsham Clay. *Civil Engineering Transactions, Institution of Engineers*, Australia, Vol. CE10, No. 2, 1968, pp. 220–224.
13. J. T. Ritchie and J. E. Adams. 1974, Field Measurements of Evaporation from Soil Shrinkage Cracks. *Proc., Soil Science Society of America*, Vol. 38, pp. 131–134.
14. A. A. B. Williams and J. T. Pidgeon. Evapo-Transpiration and Heaving Clays in South Africa. *Geotechnique*, Vol. 23, No. 2, 1983, pp. 141–150.
15. B. J. Richards. Moisture Flow and Equilibria in Unsaturated Soils for Shallow Foundations. ASTM STP 417. *Permeability and Capillarity of Soils*, 1967, pp. 4–34.
16. M. Picornell and R. L. Lytton. Behavior and Design of Vertical Moisture Barriers. In *Transportation Research Record 1137*, TRB, National Research Council, Washington, D.C., 1987, pp. 71–82.
17. M. A. B. Abd Rahim and M. Picornell. Moisture Movement Under the Pavement Structure. Research Report 1165-1. Center for Geotechnical and Highway Materials Research, University of Texas at El Paso, 1989.
18. J. W. Holmes. Water Sorption and Swelling of Clay Blocks. *Journal of Soil Science*, Vol 6, No. 2, 1955, pp. 200–208.
19. S. J. Liu and R. L. Lytton. Environmental Effects on Pavements—Drainage Manual. Report FHWA/RD-84/116. Texas Transportation Institute, Texas A&M University, College Station, 1985.
20. B. J. Dempsey and Q. L. Robnett. Influence of Precipitation, Joints, and Sealing on Pavements Drainage. In *Transportation Research Record, 705*, TRB, National Research Council, Washington, D.C., 1979, pp. 13–23.
21. H. H. Ridgeway. Infiltration of Water Through the Pavement Surface. Transportation Research Record 616, TRB, National Research Council, Washington, D.C., 1976, pp. 98–100.
22. C. W. Richardson and J. T. Ritchie. Soil Water Balance for Small Watersheds. *Transactions of the American Society of Agricultural Engineers*, 1973, pp. 72–77.

Publication of this paper sponsored by Committee on Environmental Factors Except Frost.

Measuring Negative Pore Water Pressures in a Freezing Environment

D. G. FREDLUND, J. K. GAN, AND H. RAHARDJO

The measurement of negative pore water pressures is essential to the study of soil behavior in a freezing environment. Various devices are now available for suction measurements in unfrozen, unsaturated soils. The possibility of using these devices in the measurement of negative pore water pressures under freezing conditions is discussed. The thermal conductivity sensor appears to be a promising device for suction measurement. The thermal conductivity method of suction measurement in a freezing environment is examined. The theory of freezing soil and the thermal properties of soil are presented. Suction measurements in a freezing environment using thermal conductivity sensors from recent tests conducted at the University of Saskatchewan are also presented. The results are interpreted using the theory of freezing soil and the thermal properties of soil. The latent heat of fusion associated with the water phase transformation of water has significant influence on the thermal conductivity reading of the sensor during freezing and thawing. The formation of ice on freezing makes the interpretation of sensor reading difficult because of the significantly higher thermal conductivity of ice than that of water.

The negative pore water pressures in a soil or soil suctions affect the moisture flow, volume change, shear strength, and frost-heaving characteristics of a soil as it freezes. There is therefore a need for reliable techniques to measure negative pore water pressures in a freezing environment. Various techniques are now available for measuring soil suction in unfrozen soils. Of these techniques, the thermal conductivity sensor appears to be one of the most promising devices. The suitability of the thermal conductivity sensor for in situ suction measurements in a freezing environment is evaluated.

PHYSICS OF THE PROBLEM

As temperature drops below 0°C, some soil waters freeze producing ice in the soil. Consider the situation of a thermal gradient with the coldest temperature at the ground surface. Figure 1 (*1*) shows a typical temperature gradient in a soil under freezing conditions. Water moves from the unfrozen zone to the frozen zone through a thin partially frozen fringe. The frozen zone slowly advances to a greater depth below the ground surface.

The ability of water to move upward to the freezing fringe is attributed to the development of a negative pore water pressure (suction) gradient through the frozen fringe as shown in Figure 1 (*1*). The suction can be negligible in sands, but more significant in silts and clays depending on the temperature gradients and the rate of freezing (*2*). The suction just below the frost front can range from 6 kPa in silt to 400 kPa in Leda clay (*3*). The suction values in the frozen zone increase with decreasing temperatures below 0°C.

Water can exist in three phases as shown by a phase diagram (Figure 2). The fusion curve, *OC*, is associated with the freezing and thawing processes. At a given temperature, T, ice and water can coexist under a specified pressure as determined by the fusion curve, *OC*. The slopes of the curves on the phase diagram in Figure 2 are described by the Clausius-Clapeyron equation (*4*). For the fusion curve, *OC*, the slope has the following relation:

$$\frac{dP}{dT} = -\frac{L}{Tv_w} \tag{1}$$

where

dP = change in pressure;
dT = change in temperature;
L = latent heat of fusion, which is the heat liberated when water turns to ice or the heat absorbed when ice turns to water (i.e., 333 kJ/kg);
T = temperature (°Kelvin); and
v_w = specific volume of water [i.e., $1/\rho_w$ where ρ_w is the water density (1,000 kg/m³)].

Equation 1 has commonly been used to calculate the suction developed in the freezing fringe. Williams (*2*) defined the suction in the frozen soil as the difference between the ice and the pore water pressures ($u_i - u_w$), where u_i = ice pressure and u_w = pore water pressure. The ice pressure, u_i, is usually assumed to be constant (e.g., atmospheric pressure, or $u_i = 0$ gauge). This definition of suction is analogous to the matric suction definition in an unsaturated soil. The presence of suction results in a lower freezing temperature from that of the normal freezing temperature of 0°C or 273.15°K (*5*). The suction in the frozen soil can be related to the lowering of the freezing temperature below 0°C (i.e., dT_0) using Equation 1.

$$\frac{d(u_i - u_w)}{dT_0} = -\frac{L}{T_0 v_w} \tag{2}$$

where

T_0 = normal freezing temperature in Kelvin (i.e., 273.15°K or point O in Figure 2); and
dT_0 = freezing point depression, either in degrees Celsius or Kelvin.

D. G. Fredlund and J. K. Gan, Department of Civil Engineering, University of Saskatchewan, Saskatoon, Saskatchewan, Canada S7N 0W0. H. Rahardjo, School of Civil and Structural Engineering, Nanyang Technological Institute, Singapore 2263.

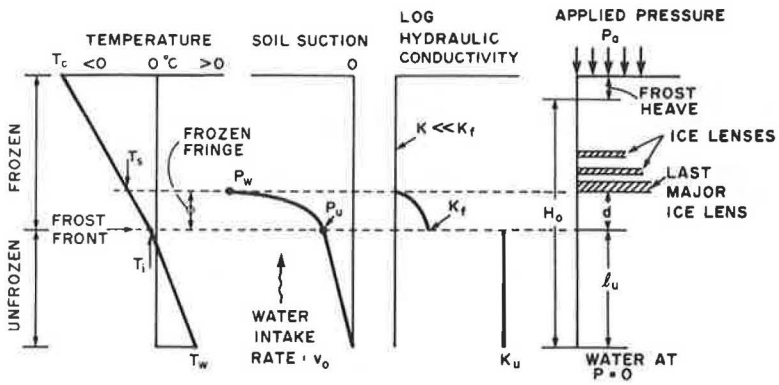


FIGURE 1 Schematic description of a freezing system (*1*).

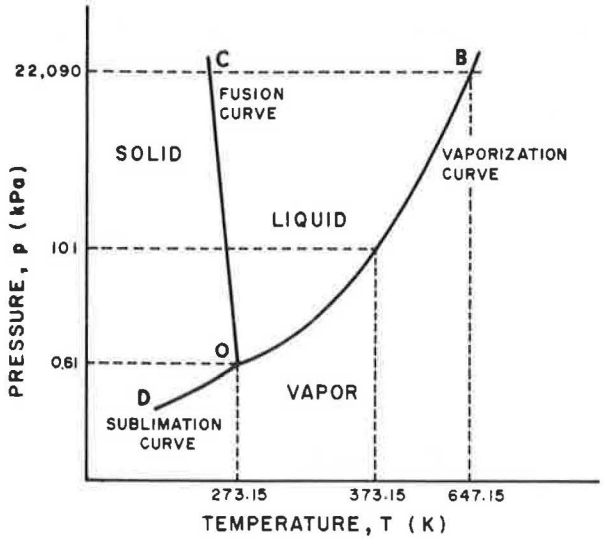


FIGURE 2 Phase diagram for water (not to scale).

Considering a constant ice pressure (i.e. $u_i = 0$) and rearranging Equation 2 yields an equation for the suction in the frozen soil:

$$d(-u_w) = -\frac{L}{T_0 v_w} dT_0 \tag{3}$$

The $d(-u_w)$ term in Equation 3 refers to an increase in suction as the freezing temperature is lowered by dT_0 from 0°C. In other words, the suction increases as the temperature decreases below 0°C. Equation 3 is plotted in Figure 3 together with typical experimental data (*2*).

RELEVANT PROPERTIES OF PARTIALLY FROZEN SOILS

Water in a porous medium, such as soil, does not all freeze at a single freezing temperature (Figure 4) (*6*). The freezing characteristics of the pore water are dependent on many factors. Among these factors are (a) mineralogical composition, (b) specific surface area of soil solids, (c) surface forces, (d) osmotic potential of soil solution, (e) grain size and grain size distribution, and (f) surface charged density. Generally, the smaller the particles, the greater the amount of unfrozen water present at any temperature below freezing (Figure 4). As freezing progresses, it becomes increasingly more difficult to freeze the remaining water. The freezing point depression is caused by the increasing surface forces on the water as the freezing advances closer to the particle surface.

Thermal Conductivity

In a soil, heat is transferred by direct thermal conductivity, k, which is defined as the amount of heat that is transferred in a unit time through a unit length of the soil with a unit cross-sectional area under a unit temperature gradient. The thermal conductivities of the various constituents in a soil are different and must be combined to give the apparent thermal conductivity of the soil. As the proportions of the constituents are changed, the apparent thermal conductivity of the soil will also change. Typical values of thermal conductivities of various constituents of a partially frozen soil are given in Tables 1–3 (*7*). For a given soil, the bulk density of the soil particles remains fairly constant. However, there are significant changes in the proportion of the frozen and unfrozen water contents as the water freezes.

The thermal conductivity of ice is approximately four times greater than that of water (Figure 5). As the ice content in a soil increases, the unfrozen water content decreases. During freezing, it is anticipated that the apparent thermal conductivity of the soil will increase.

Heat Capacity

The heat capacity of a soil refers to the quantity of heat that is required to raise the temperature of a unit mass of the soil by 1°C. The heat capacity of a partly frozen soil is simply the sum of the heat capacities of its constituents. When freezing occurs, the heat capacity appears to increase significantly because of the latent heat of fusion that is required in the water-ice phase transformation. The specific heat capacity, c, is the heat capacity of the soil per unit weight. Typical values of specific heat capacities of soil constituents are presented in Tables 1–3 (*7*).

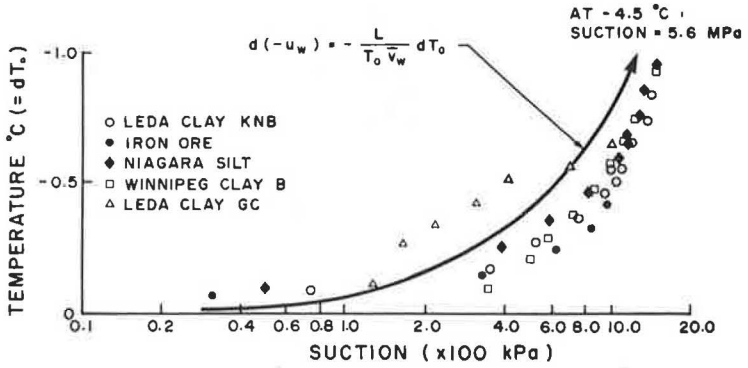


FIGURE 3 Theoretical and experimental relationships between temperature and suction at atmospheric pressure (*2*).

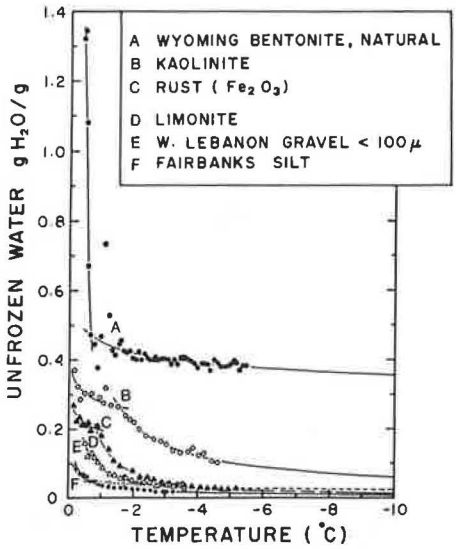


FIGURE 4 Variation of unfrozen water content with temperature for six representative soils and soils constituents (*6*).

TABLE 1 THERMAL PROPERTIES OF SOIL CONSTITUENTS AT 20°C AND 1 atm (*7*)

Material	Density ρ (kg/m3)	Specific Heat c (kJ/kg°C)	Thermal Conductivity k (W/m K)	Thermal Diffusivity α (10-7 m2/s)
Quartz	2650	0.732	8.4	43
Many soil minerals*	2650	0.732	2.9	43
Soil organic matter*	1300	1.925	0.25	15
Water	1000	4.184	0.6	1.42
Air	1.2	1.004	0.026	0.21

* Approximate average values

Latent Heat

The latent heat of fusion is the heat or energy that is required in a phase change (e.g., from a liquid to a solid phase, or vice versa). For water, the latent heat of fusion, L, is 333 kJ/kg. This means that 333 kJ of heat is liberated when 1 kg of water turns to ice, or is absorbed when 1 kg of ice turns to water.

TABLE 2 PHYSICAL PROPERTIES OF LIQUID WATER (*7*)

Temp (° C)	Density (kg/m3)	Specific Heat (kJ/kg° C)	Thermal Conductivity (W/m K)	Latent Heat of Evaporation (kJ/kg)
-10	997.94	4.268	-	2523
-5	999.18	-	-	-
0	999.87	4.2150	0.561	2499
4	100.00	-	-	-
5	999.99	4.1995	0.574	2487
10	999.73	4.1894	0.596	2476
15	999.13	4.1832	0.595	2464
20	998.23	4.1790	0.603	2452
25	997.08	4.1769	0.611	2440
30	995.68	4.1756	0.620	2428
35	994.06	4.1752	0.628	2417
40	992.25	4.1756	0.632	2405
45	990.24	4.1765	0.605	2393
50	988.07	4.1777	0.645	2381

The phase transformation takes place without any change in temperature.

Thermal Diffusivity

The thermal diffusivity, α, of a soil is given by

$$\alpha = \frac{k}{\rho c} \tag{4}$$

where

k = thermal conductivity,
c = specific heat capacity, and
ρ = density.

Thermal diffusivity controls the rate at which a temperature change spreads through a mass. The thermal conductivity of ice is approximately four times that of water. The specific heat capacity of ice is approximately half that of water. Consequently, the diffusivity of ice is about eight times the diffusivity of water. Therefore, in a frozen soil, temperatures can change faster and to a greater extent than in an unfrozen soil.

TABLE 3 PHYSICAL PROPERTIES OF ICE (*7*)

Temp (°C)	Density (kg/cm^3)	Specific Heat c (kJ/kg°C)	Thermal Conductivity (cal/cm s °C) (W/m K)	Latent Heat of Sublimation (kJ/kg)	Latent Heat of Fusion (kJ/kg)
-20	920	1.958	2.433	2836	289
-10	919	2.029	2.319	2835	312
0	917	2.105	2.240	2833	333

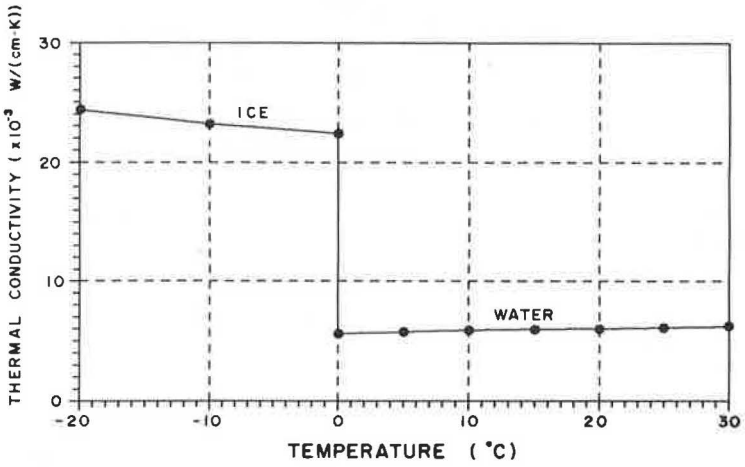


FIGURE 5 Thermal conductivity of ice and water at various temperatures.

In a fine-grained soil, the water in the pores freezes gradually. Its latent heat is therefore released in stages (Figure 6) (*8*). The rate of the heat released reduces with decreasing temperatures. The result of a release in latent heat is a sudden change in the specific heat immediately below the temperature at which freezing begins (Figure 7) (*9*). The latent heat acts similar to a large sink in which heat is released or absorbed without any change in temperature. This sudden change in the specific heat causes a corresponding sudden change in the diffusivity (e.g., Figure 8) (*10*).

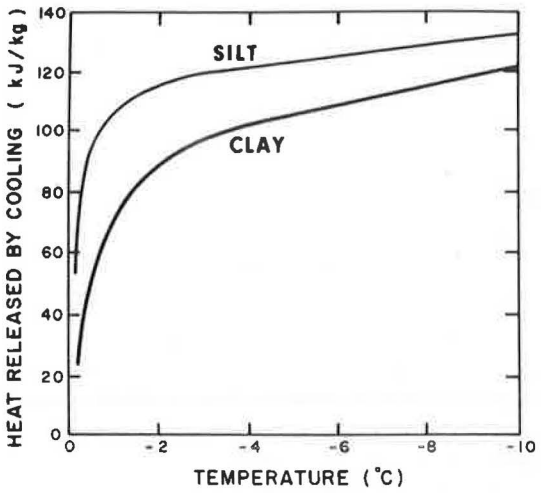


FIGURE 6 Latent heat released on cooling below 0°C (*8*).

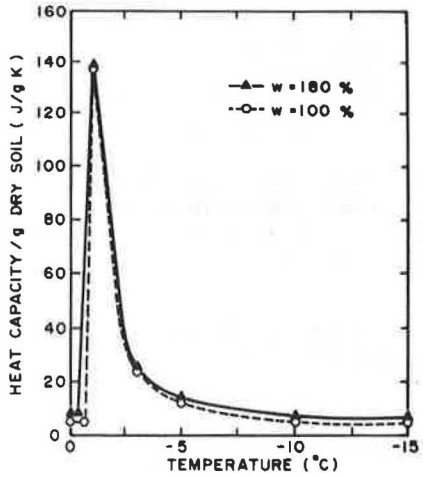


FIGURE 7 Relationship between heat capacity and temperature of a partially frozen bentonite (*9*).

SUCTION MEASUREMENT TECHNIQUES

Several techniques are available for suction measurements in an unfrozen soil. These techniques include (a) tensiometers, (b) psychrometers, (c) filter paper methods, and (d) thermal conductivity sensors. Some of these techniques have also been used for frozen solids. The psychometric and filter paper techniques do not require intimate contact with the soil. The other techniques require the use of a porous medium in intimate contact with the soil and allowing the suction in the medium

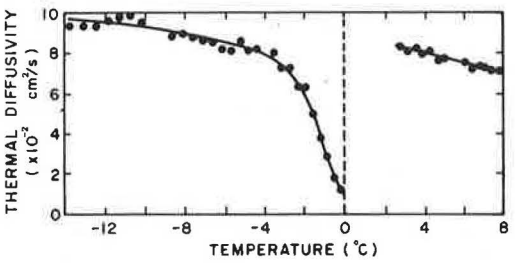


FIGURE 8 Variation of thermal diffusivity with temperatures for a kaolinite suspension (*10*).

to come to equilibrium with the suction in the soil. Water in the porous medium has different freezing characteristics from the water in the soil. Under subzero temperatures, the different freezing characteristics may present some problems in obtaining accurate suction measurement.

Tensiometers

Tensiometers have commonly been used to measure the negative pore water pressures in an unsaturated soil. The tensiometer consists of a porous ceramic, high air entry cup connected to a pressure-measuring device through a small-bore capillary tube. The tube and the cup are filled with deaired water. The cup can be inserted into a precored hole until there is intimate contact with the soil. After equilibrium has been achieved, the water in the tensiometer will have the same negative pressure as the pore water in the soil. The water pressure that can be measured using a tensiometer is limited to approximately −90 kPa because of cavitation of water in the tensiometer.

Ingersoll and Berg (*11*) have used tensiometers for measuring negative pore water pressures under freezing conditions. The tensiometer cups were installed along a cylindrical soil column 1 m long and 14 cm in diameter. The tensiometer tube was filled in with a solution of ethylene glycol and water to lower the freezing point of the tensiometer fluid. The soil suctions increased as the temperature decreased below 0°C. Typical results are plotted in Figure 9 along with the corresponding temperatures. As freezing progresses, the measured suctions decreased abruptly, indicating a breakdown in the measuring system.

Psychrometers

Thermocouple psychrometers are used to measure soil suction by measuring the relative humidity in the soil. Soil suction results in a decrease in the relative humidity. Measurements of soil suction are commonly conducted in the laboratory by placing a small soil specimen in a chamber together with the psychrometer. The relative humidity is then measured after equilibrium is attained between the air near the psychrometer and the pore air in the soil. The suction range that can be reliably measured by psychrometers in a controlled temperature environment is from 100 to 8,000 kPa.

Use of psychrometers in the measurements of soil suction in a freezing environment have not been cited. However, psychrometers have been used to measure relative humidity (and therefore suction) in snow (*12*). The results indicate a

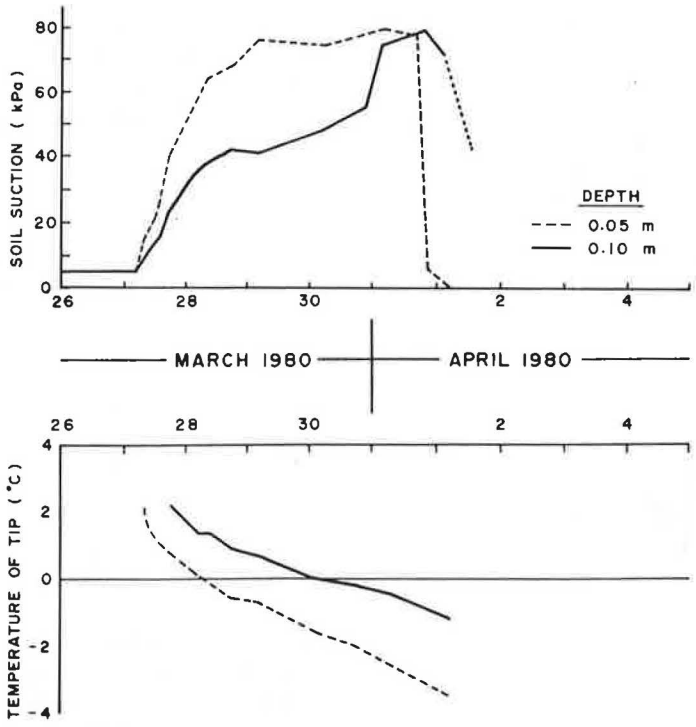


FIGURE 9 Suction measurements using tensiometers in a freezing environment (*11*).

reduction in the relative humidity with decreasing temperatures below 0°C.

Filter Paper Technique

The filter paper technique has not been used to measure soil suction under frozen conditions. The vapor pressure associated with ice implies that there may be some possibility in using this technique for frozen soils. Research is needed in this area.

Thermal Conductivity Sensor

The operation of a thermal conductivity sensor is based on the principle of heat dissipation in a porous material. The rate of heat dissipation is dependent on (a) the thermal conductivity of the solid material and of the water, and (b) the mass of the solid and the water. The thermal conductivity of air can be considered negligible. For a particular sensor, the mass of the solid is a constant and the rate of heat dissipated in the solid will be constant. Therefore, changes in the rate of heat dissipated in a sensor are directly related to the water content of the sensor.

When a sensor is inserted into a soil, water will move between the sensor and the soil. The movement of water takes place until stress equilibrium is attained between the soil and the sensor. The equilibrium water content of the sensor is an indication of the suction in the sensor and in the soil. The water content of the sensor can be calibrated against the applied suction using a modified pressure plate apparatus (*13*).

A typical sensor is made up of two parts, (a) a heating and heat sensing device enclosed within, (b) a porous block (Figure 10). The heater and the sensing devices are embedded within a porous ceramic of low thermal conductivity. The porous ceramic should be relatively small to ensure a rapid response. However, the porous ceramic must be sufficiently large so that the heat pulse generated is fully contained within the ceramic block. Otherwise, the thermal conductivity reading will be affected by the type of surrounding soil.

The reading operation consists of measuring the electrical output (current or voltage) before the heat pulse and the electrical output after a 60-sec heat pulse was applied. The heat pulse was then ended. The heat pulse is a precisely controlled amount of heat applied at a fixed rate. The change in voltage output is a function of the electrical resistance, which in turn is a function of the temperature rise. The voltage outputs varies linearly with temperature and therefore the difference is not affected by the temperature of the sensor. A single calibration is therefore adequate for all temperatures.

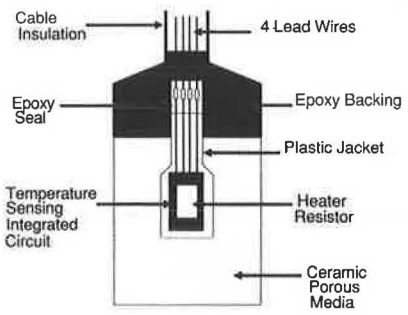


FIGURE 10 A cross-sectional diagram of the AGWA–II thermal conductivity sensor.

In an unfrozen soil, a low water content in the sensor, or high soil suction, would result in a high temperature increase in the thermal conductivity sensor. This high temperature increase indicates a low apparent thermal conductivity of the sensor because of its low water content. In a frozen or partially frozen soil, the thermal conductivity of the sensor is not only a function of the unfrozen water content, but it also depends on the ice content. Thus, in a frozen soil at a low unfrozen water content, the temperature increase recorded by the sensor would be expected to be low because of the high thermal conductivity of ice.

RESULTS OF SUCTION MEASUREMENTS USING THERMAL CONDUCTIVITY SENSORS

Lee (*14*) used heat dissipation sensors (MCS 6000) sensors both for in situ and for laboratory suction measurements. MCS 6000 sensors were manufactured by Moisture Control System Corporation, Findlay, Ohio. The results of in situ suction measurements conducted in a glacial till are shown in Figure 11. The results indicate that suction variations followed closely the daily temperature variation. The soil suction increased as the temperature approached 0°C. When the temperatures dropped below 0°C, the sensor was not able to record any suction reading.

Van der Raadt et al. (*15*) used AGWA–II thermal conductivity sensors for monitoring suction changes below railway subgrades. AGWA–II sensors were manufactured by Agwatronics Incorporated, Merced, California. Results of suction measurements using the AGWA–II sensors from one site are shown in Figure 12. The results also show that the suction readings increased as the temperature decreased below freezing. Several suction measurements were obtained for the soil in the frozen state.

RECENT EXPERIENCE WITH THE AGWA–II SENSOR IN A FREEZING ENVIRONMENT

Suction measurements have been recently made in a freezing environment at the University of Saskatchewan. The measurements were made using AGWA–II thermal conductivity sensors. A soil column was prepared by compacting a glacial till into a PVC cylinder.

The cylinder had a height of 300 mm and a diameter of 150 mm. A thermal conductivity sensor together with a thermocouple were embedded near the top, middle, and bottom sections of the soil column (Figure 13). The thermocouple was used to measure the temperature in the soil at the proximity of each thermal conductivity sensor. The column was insulated on all sides except for the top face. The top of the column was subjected to temperatures ranging from 22°C down to −20°C inside a freezing chamber.

The suction and temperature measurements with respect to time are shown in Figures 14–16. All three sensors ap-

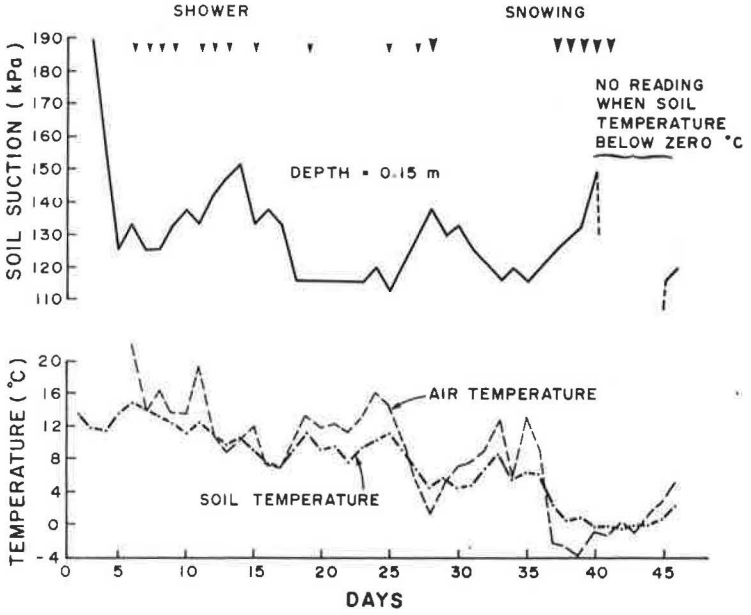


FIGURE 11 Field measurements of matric suction in a glacial till using the MCS 6000 thermal conductivity sensors (*14*).

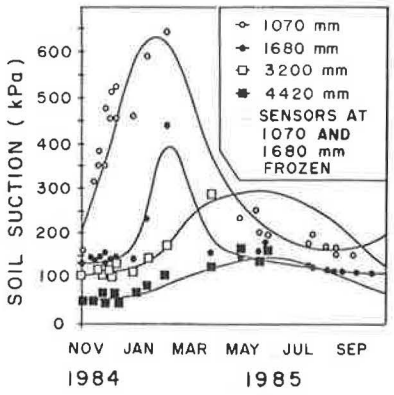


FIGURE 12 Variation of soil suction with time of year for various depths of Regina clay in Saskatchewan (*15*).

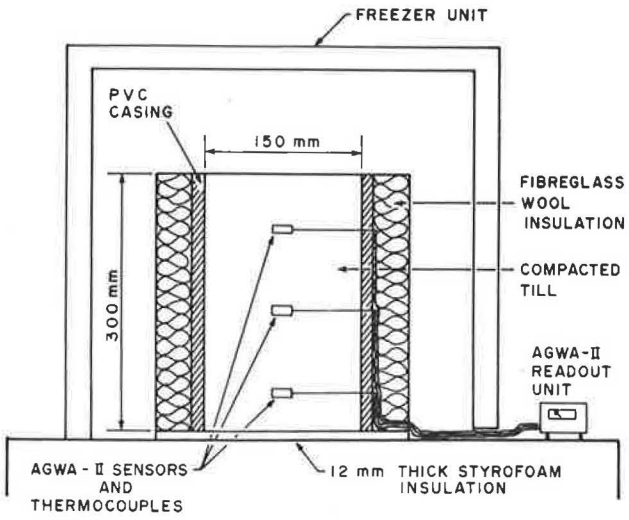


FIGURE 13 Setup for soil suction measurements using the AGWA–II sensor in a freezing test.

peared to respond in a similar manner. As the temperature decreased from above freezing to below freezing, the sensor readings dropped sharply. As freezing progresses, the sensor readings increased rapidly to approximately the same readings before freezing occurs. The same behavior was observed as the temperature was increased from below freezing to above freezing. All three sensors showed that after thawing, the soil suctions dropped to a range of 0 to 40 kPa.

INTERPRETATION OF TEST RESULTS

As the water in the sensor begins to freeze, the apparent thermal conductivity of the sensor is affected by the latent heat of fusion. During the freezing process, the latent heat of fusion is released at a constant temperature. However, the water in the sensor does not freeze simultaneously, but rather it freezes in a gradual manner. As a result, the temperature increase produced by the heat pulse will be smaller in a freezing sensor as compared to that registered in a nonfreezing sensor. This phenomenon could be attributed to the tendency of the water to maintain a constant temperature during the phase transformation. The reduced temperature increase in a freezing sensor would then be interpreted from the calibration curve as a decreasing soil suction. This situation is demonstrated by the drops in soil suction readings as the temperature decreases to 0°C.

After a major portion of the water in the sensor has frozen, the temperature increase measured because of the heat pulse depends on the proportion of ice and unfrozen water, and also on the quantity of air bubbles present. The higher sensor readings in the frozen state are probably because of the re-

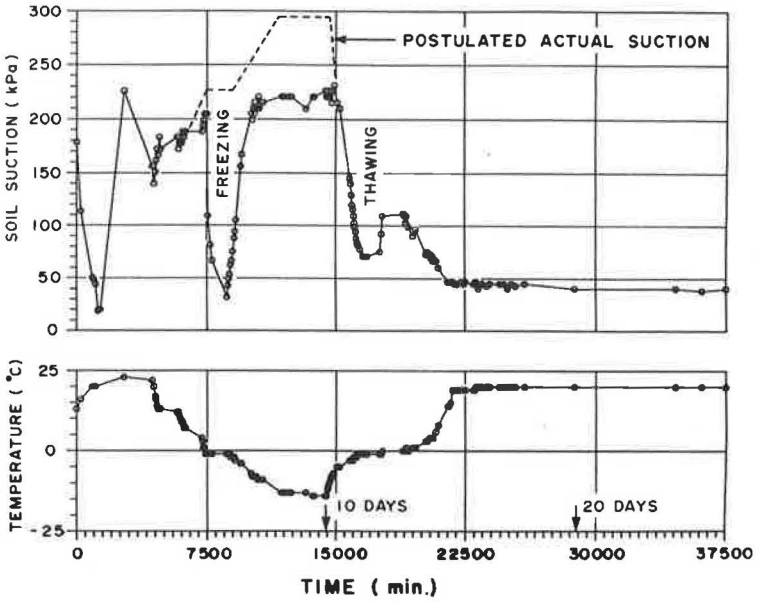


FIGURE 14 Suction and temperature measurements at the top section of the soil column.

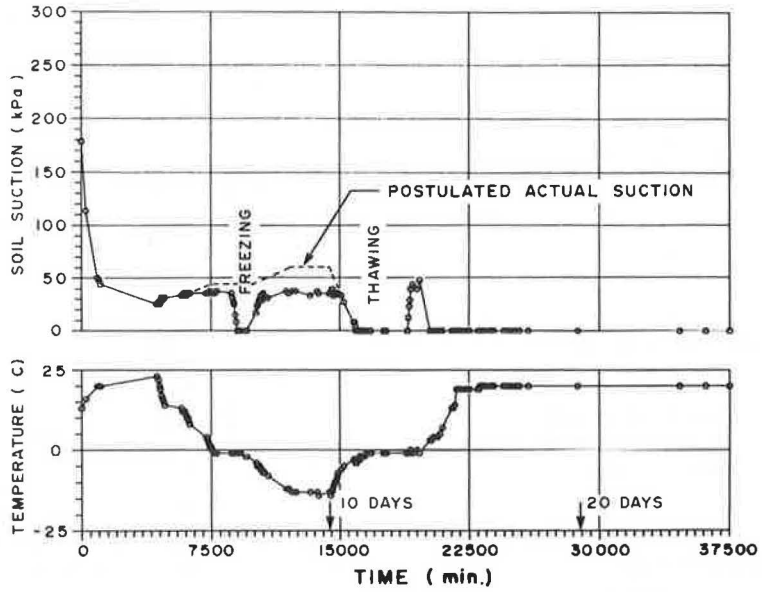


FIGURE 15 Suction and temperature measurements at the middle section of the soil column.

duced thermal conductivity caused by the presence of air bubbles.

As the water in the sensor begins to thaw, the heat pulse released in the sensor is again affected by the latent heat of fusion. During the thawing process, the latent heat of fusion is adsorbed at a constant temperature. The thawing process also occurs gradually within the sensor. The tendency to maintain a constant temperature will again reduce the temperature increase generated by the heat pulse. As a result, the suction readings will drop again as the temperature increases toward 0°C.

The reduction in the sensor reading after a complete thawing of the ice, is probably caused by the overwetting of the sensor, which is followed by separation from the soil. The separation of the sensor from the soil could be caused by the expansion of the frozen soil water and the migration of melting water upon thawing. In fact, the soil column was found to have expanded vertically by approximately 5 mm at the end of the test. When the water at the contact between the sensor and the soil thaws, a portion of the water may migrate into the sensor pores. As a result, a gap develops between the sensor and the soil. Once the sensor has separated from the

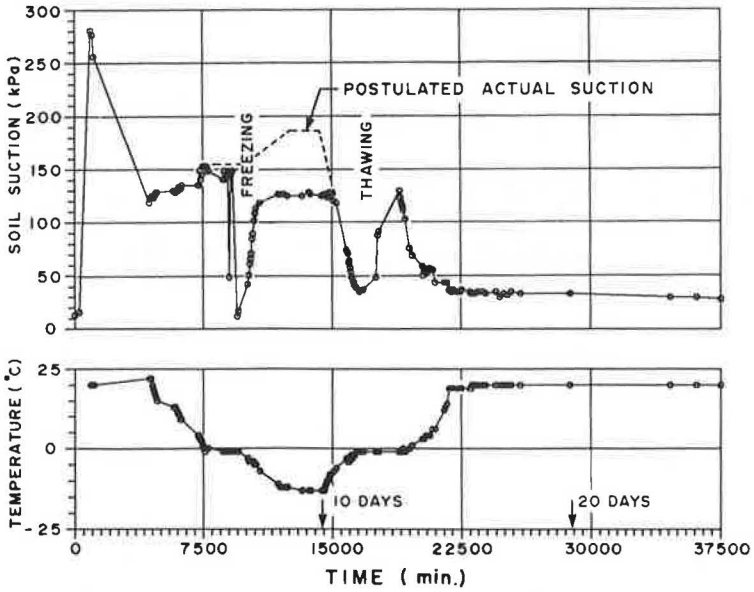


FIGURE 16 Suction and temperature measurements at the bottom section of the soil column.

soil, the sensor registers a suction reading depending on the remaining water content of the sensor.

CONCLUSION

Experimental evidence has identified the difficulties associated with the measurement of negative pore water pressures in freezing soils. In particular, the use of thermal conductivity sensors in freezing environment is emphasized. Distinct drops in suction readings have been observed during the freezing and thawing processes. These drops are attributed to the effect of the latent heat of fusion on the thermal conductivity measurements. Also, as soil freezes, the proportions of unfrozen and frozen water change. Ice and water have different thermal conductivities. As a result, the sensor readings are difficult to interpret and to convert to soil suctions. In addition, the rigid, brittle ceramic used for the thermal conductivity sensors is susceptible to cracking caused by the expansion on freezing, especially under high water content conditions.

REFERENCES

1. J. M. Konrad. Segregation Potential–Pressure–Salinity Relationships near Thermal Steady State for a Clayey Silt. *Canadian Geotechnical Journal*, Vol. 27, No. 2, 1990, pp. 203–215.
2. P. J. Williams. *The Surface of the Earth: An Introduction to Geotechnical Science*. Longman, New York, 1982, 212 pp.
3. P. J. Williams. *Properties and Behavior of Freezing Soils*. Publication 72. Norwegian Geotechnical Institute, 1967, 120 pp.
4. B. P. Van Haveren, and R. W. Brown. The Properties and Behavior of Water in the Soil–Plant–Atmosphere Continuum. In *Psychrometry in Water Relations Research* (R. W. Brown and B. P. Van Haveren, eds.), *Proc., Symposium on Thermocouple Psychrometers*, Utah State University, Logan, 1972, pp. 1–27.
5. N. E. Edlefsen, and A. B. C. Anderson. Thermodynamics of Soil Moisture. *Hilgardia*, Vol. 15, No. 2, 1943, pp. 31–298.
6. D. M. Anderson and N. R. Morgenstern. Physics, Chemistry and Mechanics of Frozen Ground: A Review. *Proc., 2nd International Conference on Permafrost*, Yakutsk, U.S.S.R., North American Contribution, National Academy of Sciences, Washington, D.C., 1973, pp. 257–288.
7. W. R. Van Wijk (ed.). Physics of Plant Environment, 2nd ed. North Holland, Amsterdam, The Netherlands, 1963, 382 pp.
8. O. Johansen. *Thermal Conductivity of Soils*. Ph.D. Dissertation, Trondheim, Norway, 1976.
9. P. F. Low, D. M. Anderson, and P. Hoekstra. Some Thermodynamic Relationships for Soils at or below the Freezing Point. 1. Freezing Point Depression and Heat Capacity. *Water Resources Research*, Vol. 4, No. 2, 1968, pp. 379–394.
10. P. Hoekstra. *Special Report 103: The Physics and Chemistry of Frozen Soils*. Effects of Temperature and Heat on Engineering Behavior of Soils, HRB, National Research Council, Washington, D.C., 1969, pp. 78–90.
11. J. Ingersoll and R. Berg. Simulating Frost Action by using an Instrumented Soil Column. Frost Action and Risk Assessment in Soil Mechanics. In *Transportation Research Record 809*, TRB, National Research Council, Washington, D.C., 1981, pp. 34–42.
12. B. P. Van Haveren. Measurement of Relative Vapor Pressure in Snow with Thermocouple Psychrometers. In *Psychrometry in Water Relations Research*, R. W. Brown and B. P. Van Haveren (eds.), *Proc., Symposium on Thermocouple Psychrometers*, Utah State University, Logan, 1972, pp. 178–185.
13. D. G. Fredlund, and D. K. H. Wong. Calibration of Thermal Conductivity Sensors for Measuring Soil Suction. *Geotechnical Testing Journal*, Vol. 12, No. 3, Sept. 1989, pp. 188–194.
14. R. K. C. Lee. *Measurement of Soil Suction using the MCS 6000 Sensor*. M.Sc. thesis. University of Saskatchewan, Saskatoon, 1983.
15. P. van der Raadt. *Field Measurement of Soil Suction using Thermal Conductivity Matric Potential Sensors*. M.Sc. thesis. University of Saskatchewan, Saskatoon, 1988.

Publication of this paper sponsored by Committee on Frost Action.

Field Testing of a Model for Water Flow and Heat Transport in Variably Saturated, Variably Frozen Soil

XIA XU, JOHN L. NIEBER, JOHN M. BAKER, AND DAVID E. NEWCOMB

The simultaneous heat and water (SHAW) model was tested with soil water content and temperature profile data for a soil located near Rosemount, Minnesota. The predicted frost-thaw depth, soil water content, and temperature at depths of 10, 20, and 80 cm are compared with measured values. The results indicate that the prediction of frost depth and temperature profile agrees well with measured field data, whereas agreement between measured and predicted liquid soil water content is fair. The model was applied to a hypothetical case of a paved soil to assess the impact of the presence of the pavement on frost penetration into the soil profile. It was found that the frost front penetrates deeper into the underlying soil in the case of a paved soil surface in contrast to the case of an unpaved soil.

Seasonal freezing and thawing of soil occurs in a large part of the earth's land mass. Freezing-thawing phenomena affect many natural processes and have a significant influence on many human activities. The study of heat and water transfer, freezing, and thawing has been involved in many disciplines including agriculture, hydrology, civil engineering, environment, and geology. Extensive reviews of current knowledge associated with heat and mass transfer and the effects on soil physical properties were prepared by Czurda (*1*), Kay and Perfect (*2*), and Lundin (*3*). Since the early 1970s, numerous papers have been written on the modeling of simultaneous transport of heat and water in soils subjected to freezing and thawing (*3–18*).

The freezing-thawing process influences many soil properties including hydraulic, thermal, and physical strength properties, and therefore the process affects not only the transport of heat and water but also the strength of the soil. In the natural environment, the freezing-thawing process affects the partitioning between infiltration and runoff of snowmelt and rainfall (*3*), and therefore it has a major impact on runoff generation and soil erosion (*15,19*). The process also influences the redistribution of soil water (*20,21*) during the winter months and will thereby affect the magnitude and temporal distribution of groundwater recharge.

The processes of soil freezing and thawing can dramatically affect the stability of manmade structures such as building foundations, retaining walls, and highway pavements (*22,23*). Although the freezing of the soil can increase the mechanical strength of the soil, frost heaving might accompany the freezing process resulting in severe structural damage (*24*). Even when frost heaving does not occur, the thawing of a previously frozen soil can drastically reduce the mechanical strength of the soil during the thawing period.

The modeling of simultaneous heat and water transport in soils subjected to cycles of freezing and thawing temperatures can improve the understanding of the effects of soil and climate parameters on the water and temperature status of soils. The modeling process facilitates the prediction of trends in the outcome for the system prior to construction of the system and therefore can provide alternative strategies for establishing design criteria (*25*).

One model of simultaneous water and heat transport that incorporates freezing/thawing conditions is the SHAW model presented by Flerchinger and Saxton (*15*). This model is a physically based model originally designed for application in an agricultural field, soil-crop, residue-snow system, and is capable of predicing soil temperature, liquid soil water content, ice content, soil solutes distribution, and freezing and thawing depth. Because of its physical basis and flexibility for model input parameters, the model may be applied to other conditions like highway pavement.

The objectives of the study are to (a) test and evaluate the SHAW model with measured field data and (b) apply the model to the condition in which a pavement is present to assess the effect of the pavement on the frost and thaw depth in soil.

GOVERNING EQUATIONS FOR MASS AND HEAT TRANSPORT

For an unsaturated soil under freezing conditions, three phases are present in the system, including solid (soil particles and ice), liquid (unfrozen water), and gas (air and water vapor). The time-dependent status of each of the phases can be described by equations for conservation of mass and energy along with constitutive relations describing fluxes of heat and mass. The flow of water occurs in two phases, the liquid and vapor phases. For the flow of water in each of the two phases, the driving forces consist of both the hydraulic gradient and the temperature gradient (*26,27*). The temperature gradient induces the flow of water both in liquid water and in vapor phases. The flowing liquid water and water vapor carry heat and thereby affect the temperature gradient.

X. Xu and J. L. Nieber, Department of Agricultural Engineering, University of Minnesota, 1390 Eckles Avenue, St. Paul, Minn. 55108. J. M. Baker, USDA-ARS and Soil Science Department, University of Minnesota, 1991 Upper Buford Circle, St. Paul, Minn. 55108. D. E. Newcomb, Civil and Mineral Engineering Department, University of Minnesota, 18 East 49th Street, Minneapolis, Minn. 55414.

Early work regarding the mathematical description of coupled flux laws for water and heat was done by Philip and de Vries (*26*), de Vries (*27*), and Taylor and Cary (*28*). These works have led to the definition of two distinct approaches for deriving the constitutive relations for coupled water flow and heat transport in porous media. Hillel (*29*) refers to these approaches as the mechanistic approach represented by Philip and de Vries (*26*), and the irreversible thermodynamic approach represented by Taylor and Cary (*28*). The main difference between these two approaches lies in the definition of the coefficients appearing in the constitutive relations.

The SHAW model has essentially adopted the mechanistic approach to simulate heat and water transport in freezing soil. In deriving the governing equations, it is assumed that the change in fluid storage because of the compressibility of the soil and water is negligible compared to that because of the change in saturation of the soil (which is true for natural flow conditions), and that liquid water transport in response to thermal and osmotic gradient is negligible. The water balance equation for a variably saturated, variably frozen, vertical soil profile is Equation 1, and the heat balance is Equation 2, after neglecting the heat content change caused by the sensible heat flux by vapor flow (*14*).

$$\frac{\partial \theta_l}{\partial t} + \frac{\rho_i}{\rho_l}\frac{\partial \theta_i}{\partial t} = \frac{\partial}{\partial z}\left[k\left(\frac{\partial \Psi_m}{\partial z} - 1\right)\right] - \frac{1}{\rho_l}\frac{\partial q_v}{\partial z} + \frac{1}{\rho_l}S_w \qquad (1)$$

$$C\frac{\partial T}{\partial t} - \rho_i L_f \frac{\partial \theta_i}{\partial t} + L_v\left(\frac{\partial \rho_v}{\partial t} + \frac{\partial q_v}{\partial z}\right) = \frac{\partial}{\partial z}\left(\lambda \frac{\partial T}{\partial z}\right) - c_l\frac{\partial (q_l T)}{\partial z} + S_h \qquad (2)$$

where

θ_l = volumetric liquid water content, m^3/m^3;
t = time, sec;
ρ_i = density of ice, kg/m^3;
ρ_l = density of liquid water, kg/m^3;
θ_i = volumetric ice fraction, m^3/m^3;
k = unsaturated hydraulic conductivity, m/sec;
Ψ_m = soil matric potential, m;
z = depth from soil surface, m;
q_v = flux of water vapor in the z direction, kg/m^2-sec;
S_w = source or sink term for liquid water, kg/m^3-sec;
C = apparent volumetric heat capacity of soil, J/m^3-°C;
T = soil temperature, °C;
L_f = latent heat of fusion, J/kg;
L_v = latent heat of vaporization, J/kg;
ρ_v = density of ice, kg/m^3;
λ = thermal conductivity of the soil, W/m-°C;
c_l = heat capacity of liquid water, J/kg-°C;
q_l = flux of liquid water in z direction, kg/m^2 sec; and
S_h = heat source or sink term, W/m^3.

Flerchinger (*14*) used the finite difference method with the Newton-Raphson iterative technique to solve the simultaneous heat and water equations given by Equations 1 and 2 for the soil. Similarly, the governing equations for water flow and heat transport in the snowpack and in the crop residue layer were developed and solved using the same numerical method.

Boundary and Initial Conditions

The conditions at the upper boundary drive the flow of water and transport of heat within the soil profile. The heat and water fluxes between the atmosphere and the soil system are calculated on the basis of energy and mass balance between the atmosphere and the soil system. The heat balance at the upper boundary is composed of heat conduction into the surface, latent heat, and sensible heat transfer into the atmosphere. The water balance for the upper boundary is composed of precipitation, snowmelt, water flux into the surface by infiltration, evaporation, and surface runoff. Therefore, the heat and water balance at the upper boundary contains the coupled processes of water flow and heat transport. The heat and water balance can be derived with commonly available weather data.

For a paved surface, the vapor flux from the surface to the air or water flux from the air into the surface is small because of the low hydraulic conductivity of the pavement. Because of this low flux rate, the energy consumption by the latent heat flux will be insignificant.

In the SHAW model, the lower boundary conditions for the heat and water equations are taken to be specified temperature and soil water content, respectively. These specified values can be either a constant with time or varying with time. The initial conditions for the SHAW model are specified temperature and soil water content in the soil profile for the heat equation and water equation, respectively. Weather variables are applied on hourly basis.

SHAW MODEL INPUT-OUTPUT FILES

Because of model availability and its physical basis, the SHAW model was selected for testing with the measured field data in this study. The model requires input data for the following five files: (a) the description of input and output data files; (b) hourly weather data including air temperature, wind speed, relative humidity, solar radiation, and precipitation; (c) soil temperature profile; (d) the soil water content profile; and (e) description of the site characteristics. For the third and fourth files, at least two profiles are required for the initial profile and for the profile at the end of the simulated period.

The site characteristic file requires information including the simulation period, location, slope, and aspect of the study site, albedo of dry soil, and some aerodynamic roughness parameters. It also facilitates specification of up to 20 layers for the soil, and corresponding soil texture and other physical properties for each layer. If snow, crop-residue, or a solute are present in the system, additional information is required for each of their corresponding properties.

Output of the SHAW model yields nine files including (a) general output information and hourly or daily temperature, soil water, and solute profiles; (b) side-by-side predicted and measured soil water and temperature profiles; (c) predicted temperature profiles; (d) predicted soil water profiles; (e)

water balance summary; (f) frost/thaw depth and ice content profile; (g) summary of energy flux at the upper boundary; (h) total solute concentration profiles; and (i) solute concentration of soil solution.

SHAW MODEL TESTING

In this study, the SHAW model was tested using a set of measured field data including weather data, soil property data, and measured liquid soil water content and temperature profiles for an agricultural experimental field located in Rosemount, Minnesota. Then using the same weather data and soil profile data, two simulations were performed, one for a paved surface and the other for an unpaved surface. Results are presented in the form of three simulation runs. Run 1 is for an instrumented agricultural field with a bare soil surface; this run is referred to as the unpaved field site. The lower boundary conditions for soil temperaure and soil water content in Run 1 are measured soil temperature and measured soil water content at a depth of 1 m. The simulation results in Run 1 were used to compare profiles of soil temperature, liquid soil water content, and frost-thaw depth predicted with the SHAW model with field measurements of the same variables.

All information for Run 2 was the same as in Run 1 except the lower boundary was defined at a depth of 10 m, where soil temperature was considered as constant over a year. Soil water content was also specified to be a constant throughout the period of simulation at this depth. Run 3 is for the hypothetical highway pavement profile, which differs from Run 2 in replacing the top 40 cm of soil in the unpaved soil profile with 25 cm of concrete and 15 cm of base coarse material. The pavement and subsurface conditions in Run 3 are similar to the conditions at an instrumented field site near Faribault, Minnesota. The simulated results presented by Runs 2 and 3 are used to assess the effect of the paved surface on frost-thaw depth.

Unpaved Field Site Description

The data acquisition site for the field testing of the SHAW model is located at the Agricultural Experiment Station in Rosemount, Minnesota. The slope of the land is essentially zero. The land is cultivated and the top 20 cm was considered as the tilled layer. There was no crop residue cover on the soil surface during the period of data acquisition. A plan view of the site is shown in Figure 1. A weather station at the site measured incoming solar radiation, precipitation, air temperature, relative humidity, and wind speed. Total soil water content was measured with the neutron scattering method, while liquid soil water content was measured with the method of time domain reflectometry (TDR) (*30,31*). Soil temperature was measured with copper-constantan thermocouples. The sensors for measuring temperature and liquid soil water content were installed at depths of 2.5, 5, 10, 20, 30, 40, 60, 80, and 100 cm.

The required initial soil water content and temperature profiles for Run 1 were measured and are shown in Figure 2. The required lower boundary conditions at 1-m depth for

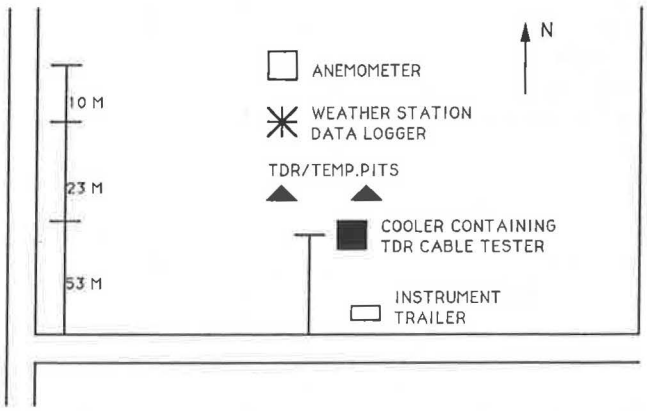


FIGURE 1 Plan view of the site for acquisition of weather data, soil temperature profile data, and soil water content profile data located at the Rosemount Experiment Station.

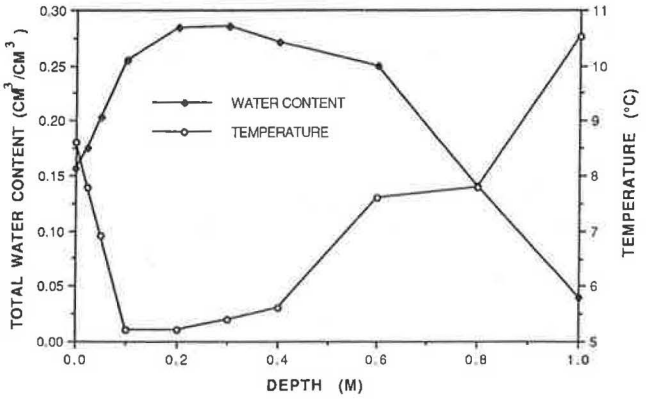


FIGURE 2 Initial water content and temperature profile on November 5, 1989, at the field site.

temperature and soil water content for Run 1 are shown in Figure 3.

Soil properties data required by the SHAW model are profiles of properties including soil texture, dry bulk density, water retention curve parameters, and saturated hydraulic conductivity. Soil texture data and soil bulk density data were measured directly from soil samples. The procedures for estimating soil hydraulic and thermal properties from texture and bulk density data are described in the following paragraphs.

The total porosity of the soil was estimated by assuming a particle density of 2.65 g/cm^3. The soil hydraulic parameters including pore size distribution index b, air entry potential Ψ_e, and saturated hydraulic conductivity K_S were estimated from soil bulk density and soil texture. Campbell (*32*) presented empirical equations for calculating b, Ψ_e, and K_S on the basis of the geometric mean particle size, d_g (mm), and geometric standard deviation, σ_g (mm). These geometric properties were calculated from the following equations.

$$d_g = \exp(x) \tag{3}$$

and

$$\sigma_g = \exp(y) \tag{4}$$

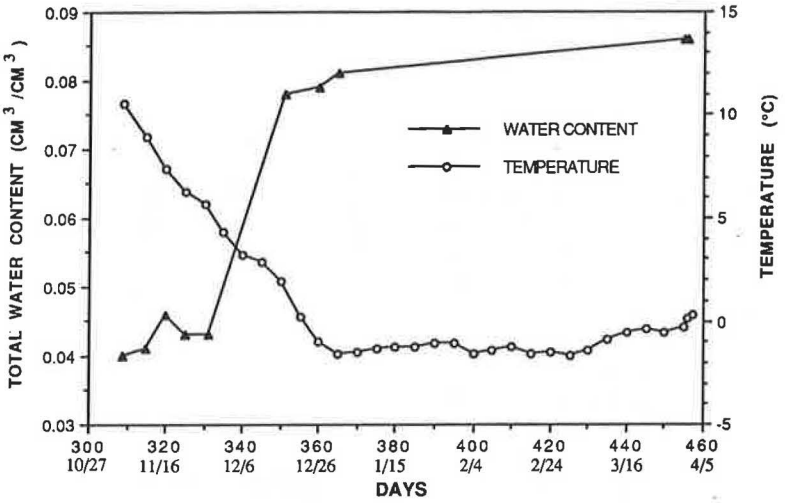


FIGURE 3 Temperature and total water content specified at the lower boundary of 1-m depth for the SHAW model simulations.

in which

$$x = m_c \ln(0.001) + m_{si} \ln(0.026) + m_{sa} \ln(1.025) \quad (5)$$

$$y = [m_c(\ln 0.001)^2 + m_{si}(\ln 0.026)^2 + m_{sa}(\ln 1.025)^2 - x^2]^{1/2} \quad (6)$$

and m_c, m_{si}, and m_{sa} are the mass fractions of clay, silt, and sand, respectively.

With these parameters, the pore size distribution index b can be calculated from

$$b = -2\Psi_{es} + 0.2\sigma_g \quad (7)$$

where

$$\Psi_{es} = -0.5 d_g^{-1/2} \quad (8)$$

The equations from Campbell (*32*) for estimating air entry value and saturated hydraulic conductivity are as follows:

$$\Psi_e = \frac{\Psi_{es}}{g}\left(\frac{\rho_b}{1.3}\right)^{0.67b} \quad (9)$$

$$k_s = 14.4\left(\frac{1.3}{\rho_b}\right)^{1.3b} \exp[-(6.9m_c + 3.7m_{si})] \quad (10)$$

where

Ψ_e = air entry value, m;
ρ_b = bulk density, g/cm³;
g = acceleration of gravity, 9.8 m/sec²; and
K_s = saturated hydraulic conductivity, cm/hr.

On the basis of these equations, the soil parameters for hydraulic properties were calculated and are presented in Table 1. This table includes two sets of parameters for pore size distribution, air entry potential, and saturated hydraulic conductivity. One set was calculated from Equation 8, which has a coefficient of −0.5. The other set was calculated from the same equation but with a coefficient of −0.2, which was used by Flerchinger (*14*). Both sets of soil parameters were used for input to the SHAW model.

TABLE 1 MEASURED AND ESTIMATED PROPERTIES FOR THE SOIL AT THE EXPERIMENTAL SITE LOCATED AT THE ROSEMOUNT EXPERIMENT STATION

Depth (cm)	ρ_b (g/cm³)	Sand	Silt	Clay	b*	Ψ_e^* (cm)	K_s^* (cm/h)	b#	$\Psi_e^\#$ (cm)	$K_s^\#$ (cm/hr)
2.5	1.016	0.19	0.58	0.23	8.24	-8	4.82	4.42	-6	1.42
5.0	1.012	0.19	0.58	0.23	8.24	-8	5.03	4.42	-6	1.45
10.0	1.112	0.19	0.58	0.23	8.24	-14	1.83	4.42	-8	0.84
20.0	1.204	0.19	0.58	0.24	8.44	-22	0.75	4.49	-11	0.50
30.0	1.270	0.15	0.64	0.22	8.41	-31	0.38	4.29	-13	0.34
40.0	1.261	0.15	0.64	0.22	8.41	-29	0.41	4.29	-13	0.35
60.0	1.275	0.19	0.59	0.22	8.09	-29	0.44	4.33	-12	0.40
80.0	1.345	0.31	0.50	0.19	7.07	-29	0.45	4.20	-11	0.51
100.0	1.536	0.25	0.57	0.18	7.20	-60	0.11	4.05	-17	0.21

The SHAW model evaluates the thermal conductivity of the soil on the basis of the de Vries (*32*) equation, which can be written as,

$$\lambda = \frac{\sum \zeta_j \lambda_j V_j}{\sum \zeta_j V_j} \quad (11)$$

where

ζ_j = weighting factor for the jth soil constituent,
λ_j = thermal conductivity of the jth soil constituent, and
V_j = volumetric fraction of the jth soil constituent.

For the thermal conductivity of soil minerals, the value of 7.5 was used on the basis of a weighted average of approximately 78 percent quartz (sand and silt) with a thermal conductivity of 8.8 W/m-°C, and 22 percent clay minerals with a thermal conductivity of 2.9 W/m-°C. The thermal conductivity of water, ice, and air were taken as 0.57, 2.2, and 0.025 W/m-°C, respectively (*29*). The weighting factors were determined as 0.20 for soil solids, 1.0 for water, 0.51 for ice, and

1.47 for air, based on de Vries (*33*), by assuming spherical solid particles.

Hypothetical Paved Condition

The only difference between the paved and the unpaved soil condition is the presence of the base coarse material and the pavement. For the pavement condition, the concrete pavement is 25 cm thick and the base coarse material is 15 cm thick. The soil below the base coarse material is the same soil present in the unpaved soil at the depth of 40 cm and below. The bulk density of the concrete is taken as 2.30 g/cm^3 and the saturated hydraulic conductivity is assumed to be 0.001 cm/hr. The albedo of the concrete is prescribed as 0.20. For the base coarse material, the bulk density is prescribed as 1.8 g/cm^3 and the saturated hydraulic conductivity is 1.8 cm/hr. The temperature at the lower boundary of 10-m depth is specified as 5.6°C and the soil water content is specified as 0.3.

RESULTS AND DISCUSSION

The primary interest of the current modeling exercise is in testing the ability of the SHAW model to predict observed liquid soil water content and soil temperature profiles. Therefore, solute transport in the soil is not considered although the SHAW model has the facility to predict solute transport. The simulation was started at the date of November 5, 1989, and ended on March 31, 1990, the period of measured data. Simulations were performed using both soil parameter data sets presented in Table 1, but only the simulated results from the soil parameter set derived with the Flerchinger (*14*) coefficient are presented because these were in best agreement with field observations.

Run 1

Temperature Profile

The comparison between the measured and predicted field temperature at a depth of 10 cm is shown in Figure 4. Except for large disagreements on Days 318 to 328 and 345 to 358, the measured and predicted temperatures are in good agreement. The lowest temperature is about −14°C for both measured and predicted values. The measured minimum occurs on Day 356, whereas the predicted minimum occurs on Day 351. The predicted temperature values appear to be more responsive to variations in air temperature than the measured temperature, at least for the first part of the period of observation. Fluctuations in both the observed and predicted temperatures appear to be similar after Day 350.

Figure 5 shows the predicted and measured temperature for the 20-cm depth. The overall trend of the temperature variation at the 20-cm depth is similar to that of the 10-cm depth. However, the curves for both predicted and measured temperature have been smoothed and the magnitude of the peaks observed at the 10-cm depth have been reduced at the 20-cm depth. The minimum measured temperature is about

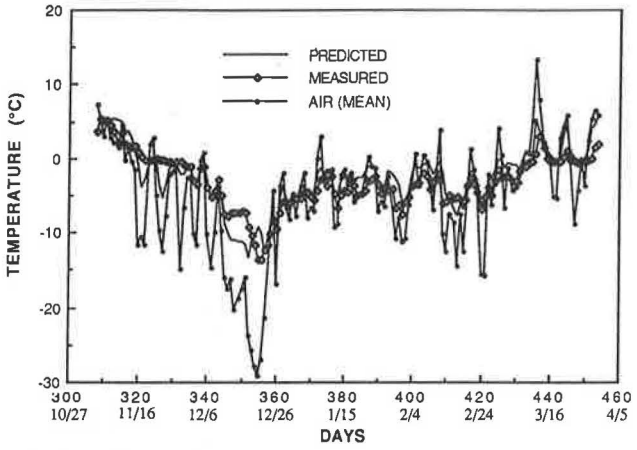


FIGURE 4 Comparison of temperature predicted by the SHAW model with measured temperature at the 10-cm depth.

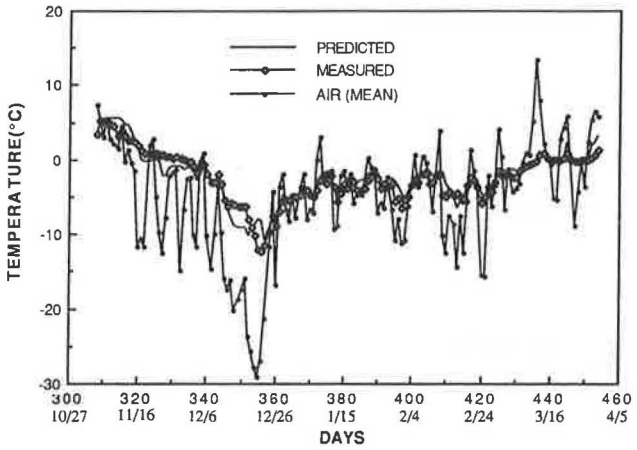


FIGURE 5 Comparison of temperature predicted by the SHAW model with measured temperature at the 20-cm depth.

−12.5°C, which occurs about 2 days later than at the 10-cm depth. The minimum predicted temperature is about −11°C. For the period following the minimum temperature, the predicted and measured temperatures are in good agreement.

The predicted and measured temperatures for the 80-cm depth are shown in Figure 6. Both the predicted and measured temperature variations are smooth. The lowest predicted and measured temperatures are each about −2.8°C. The overall agreement between measured and observed values is good for the entire period of observation. The single low temperature point at Day 365 appears to be an error in the temperature measurement.

Using the SHAW model, Flerchinger (*14*) simulated soil temperature profiles for a conventionally tilled soil with a bare surface, and a no-till soil having a heavy crop residue cover. He compared his predicted results with measured temperatures at the soil surface and at depths of 7.5 and 15 cm. The comparison indicated that the soil temperature predicted at the soil surface and at the two depths agreed well with the measured temperatures. The results presented from this study confirm the results given by Flerchinger (*14*) and demonstrate that the SHAW model has a good capability for predicting soil temperature profiles.

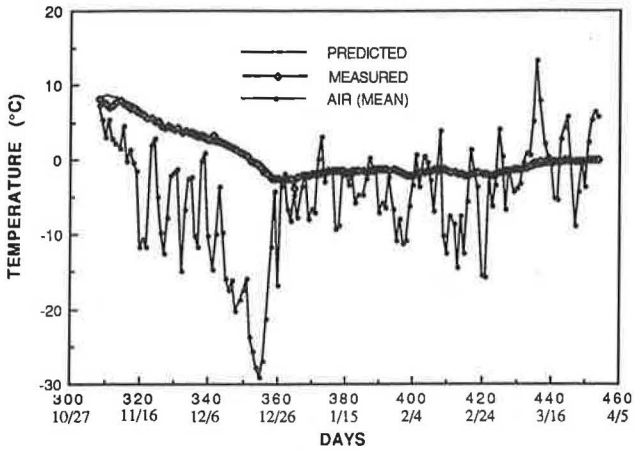


FIGURE 6 Comparison of temperature predicted by the SHAW model with measured temperature at the 80-cm depth.

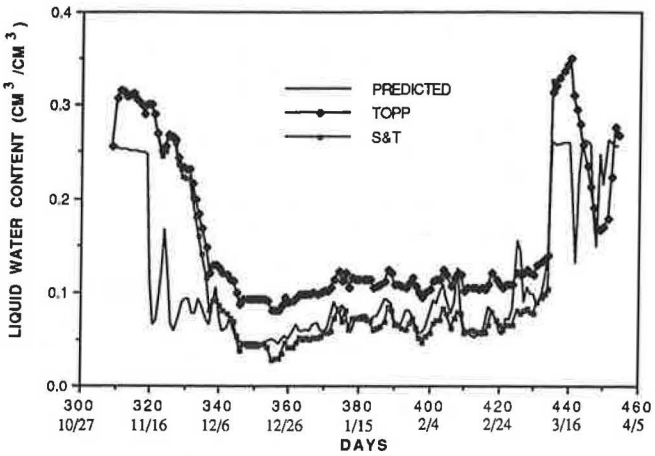


FIGURE 7 Comparison of liquid soil water content predicted by the SHAW model with measured liquid soil water content at the 10-cm depth.

Liquid Soil Water Content Profile

The model output results give the total water content and ice content. For comparison with the measured liquid soil water content data, the predicted liquid soil water content was obtained by subtracting the predicted ice content from the predicted total water content. The predicted liquid soil water content at depths of 10, 20, and 80 cm are plotted with the measured field data in Figures 7–9, in which the measured data are shown as sets labeled TOPP and S&T. The TOPP data were derived using the calibration equation from Topp et al. (*30*) to convert measured TDR dielectric constant with liquid soil water content. The Topp et al. calibration was developed for unfrozen soils but was assumed here to apply for frozen soil conditions. The S&T data were derived using the calibration equation from Smith and Tice (*31*) developed for frozen soil conditions. The largest difference between the two calibration equations occurs for liquid soil water contents below 0.10.

For the liquid soil water content at the 10-cm depth, Figure 7 shows that the predicted liquid soil water content agrees very well with the S&T data from Day 336 to Day 435 when most soil water is frozen. The TOPP data are underpredicted for this same period. The predicted liquid soil water content is lower than the measured content right after the beginning of the simulation. This difference may have been caused by an error in the precipitation record at the site. The precipitation record for the second two days of the simulation were missing. The observed soil water content indicates that a precipitation event may have occurred on the second day of the simulation. It can be seen that the predicted freezing for the 10-cm depth occurs around Day 316 and the measured data show freezing occurs around Day 320. The delay in observed initial freezing is because of the higher liquid soil water content.

The time of thawing observed is similar to the predicted time of thawing in which liquid soil water content suddenly increased a significant amount. However, for the time after Day 435 the measured liquid soil water content is increased to about 0.36, whereas predicted liquid soil water content is increased to 0.26. Several freezing and thawing cycles can be

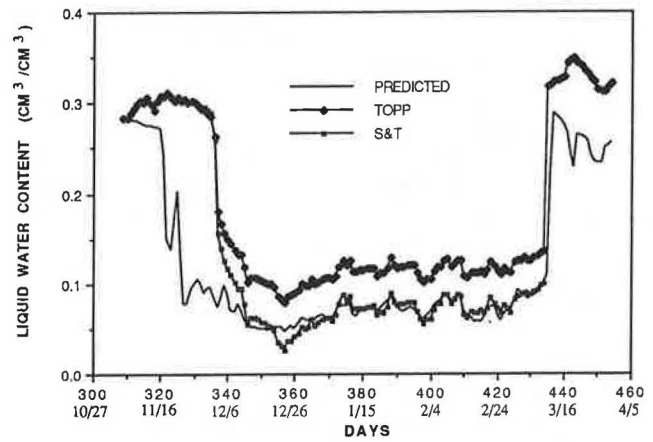


FIGURE 8 Comparison of liquid soil water content predicted by the SHAW model with measured liquid soil water content at the 20-cm depth.

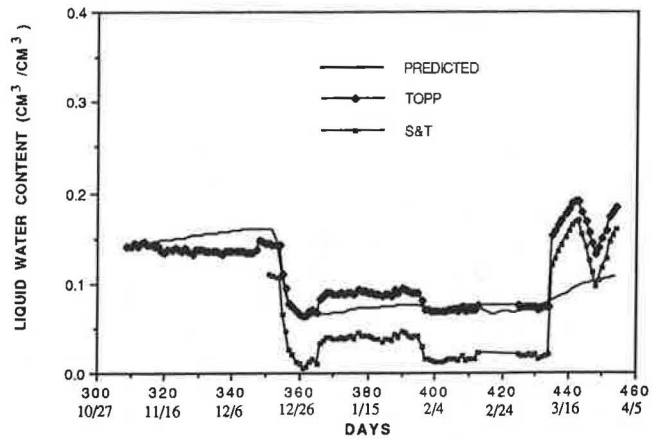


FIGURE 9 Comparison of liquid soil water content predicted by the SHAW model with measured liquid soil water content at the 80-cm depth.

clearly seen from predicted liquid soil water contents, which correspond to the change of air temperature. The measured data seem less sensitive to the fluctuation of the air temperature. This is probably caused by the additional heat capacitance and latent heat associated with the higher water content for the observed data.

Similar to the results for the 10-cm depth, Figure 8 shows that the predicted liquid soil water content at the 20-cm depth agrees very well with the S&T data from Day 340 to Day 435, whereas the TOPP data again lie above the predicted. The predicted liquid soil water content underpredicts the measured liquid soil water content before freezing, probably for the same reasons given earlier for the 10-cm depth. The predicted freezing occurs about 18 days earlier than the measured, again because of the additional liquid soil water in the profile. The time of thawing occurs about the same day for predicted and measured. However, for the time after Day 435 the predicted liquid soil water content is again lower than the measured content.

Figure 9 shows the predicted and measured liquid soil water content at 80 cm. The predicted liquid soil water content agrees fairly well with the TOPP data, but overpredicts the S&T data. A slight increase of water content is observed for the predicted liquid soil water content before freezing, whereas the measured liquid soil water content remained fairly constant for the same time period. The predicted freezing of the soil water at the 80-cm depth occurs at about the same time as the measured. The thawing times for the predicted and the measured are close, but the predicted thawing process is much slower than the measured process. The difference leads to a large difference in liquid soil water content after thawing begins. The fluctuation in the measured liquid soil water content after Day 442 corresponds to the observed air temperature fluctuations.

Flerchinger (*14*) compared the total soil water content predicted with the SHAW model to measured data total soil water content data for a soil profile up to a 170-cm depth. The comparisons were made for selected days, not for the entire period as done here. For those selected days, most of the predicted total soil water content profiles were observed to agree well with the measured data. However, significant differences between predicted and measured total soil water contents were also found on some of the selected days.

Frost and Thaw Depth

Because no direct measurement of frost and thaw depth was made, the actual frost and thaw depth was estimated from the measured liquid soil water content and temperature profile data. The soil was considered frozen at a given depth when the temperature at that depth fell below 0°C and the liquid soil water content at that depth exhibited a sudden drop. An exact measure of the maximum depth of frost penetration could not be made because the temperature and soil water content sensors were not closely spaced, and only existed down to the 1-m depth. Based on this field data, it is estimated that the maximum frost depth over the entire winter period was about 1 m. The predicted maximum depth is 92 cm.

The comparison of predicted and measured frost and thaw depth can be seen from Figure 10. It is seen that the predicted

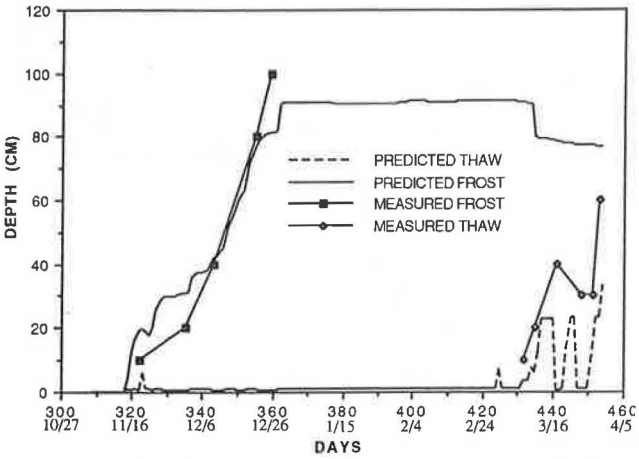


FIGURE 10 Comparison of frost-thaw depth predicted by the SHAW model with measured frost-thaw depth.

frost depth agrees well with measured data up to Day 355. The largest difference between predicted and measured frost depth occurs between Days 320 and 342 when the predicted frost depth advances faster than the measured frost depth over the depth from 10 to 20 cm. On day 360, both the predicted and the measured frost depths reached maximum values. However, the predicted maximum frost depth is about 8 cm less than the measured maximum frost depth.

The predicted thawing started from Day 430, which is about the same time as the initiation of thawing estimated from the measured data. Because of the cycling between the cold and warm weather, there are several thaw and freezing cycles. The measured data indicate that the whole soil profile thawed completely on Day 455. However, model prediction indicated that thawing was not complete until about 4 days later.

Flerchinger (*14*) simulated the frost depth for six field plots for two winter periods. Surface cover conditions applied to the plots included bare, light, medium, and heavy crop residue amounts. The simulated results were compared to the frost depth estimated by electrical resistance blocks and frost tube methods. For most of these stimulations, the predicted frost depths were generally midway between the frost depths estimated by the resistance block and frost tube data. This indicated a reasonable agreement between predicted and measured frost depth. However, disagreement was found in some cases. For instance, the predicted frost depths were slightly larger than the measured frost depth for two of the plots having a medium and heavy residue cover, whereas the predicted frost depth was lower than measured frost depth for one of the plots having light residue cover.

Flerchinger and Hanson (*34*) applied the SHAW model to a rangeland watershed. The simulation was performed for three sites through the 1986–1987 winter, and one site through the two-winter period of 1985–1987. The results exhibited good agreement between predicted and measured temperatures at depths of 2.5, 5, and 10 cm. The predicted maximum frost depth generally agreed with measured values within less than a 10 percent error. For one site, a 14 percent difference between the predicted and measured maximum frost depth was found. Soil water content prediction results were not provided.

Runs 2 and 3

Effect of Pavement

For the comparison of frost-thaw depth between the unpaved and paved soil profile, the results of Runs 2 and 3 are plotted in Figure 11. The frost and thaw depth for the paved surface is measured relative to the surface of the pavement. The frost penetration is deeper in the paved profile than in the unpaved profile for the winter period examined here. Initiation of soil freezing occurs on Day 318 for both the paved and unpaved soil profiles. However, the frost penetration advances rapidly in the paved profile in contrast to the unpaved profile. It only takes 4 or 5 days for the top 40 cm of the paved soil to freeze (concrete and base coarse), whereas it requires about 30 days for the same depth of soil freezing to occur in the unpaved soil profile. This is because the concrete and base coarse material in the paved site have larger thermal conductivity than the top 40 cm of soil and because the concrete and the coarse material freezing release less latent heat because of the low moisture content in the concrete and low soil water content of the coarse base.

There is a short period of about 20 days after the top 40-cm depth freezes in the paved profile in which the freezing depth remains relatively constant while the advancement of frost depth continues in the unpaved profile. This is because of relatively high initial soil water content around 0.26 at the depth of 40 to 60 cm in the paved profile and because freezing induces the upward flow of water to the freezing front. Then the frost depth advances consistently to the maximum depth of 80.2 cm in the paved profile near Day 357. A similar trend in frost penetration is seen for the unpaved profile after Day 340; however, the maximum frost depth is 61 cm on Day 360.

The simulation results of thaw depth response indicate that the thaw depth in the paved profile is significantly larger than that in the unpaved profile for several warm periods. The reason for the higher thaw depth response for the paved soil profile in comparison to the unpaved profile is the same given earlier for frost depth response.

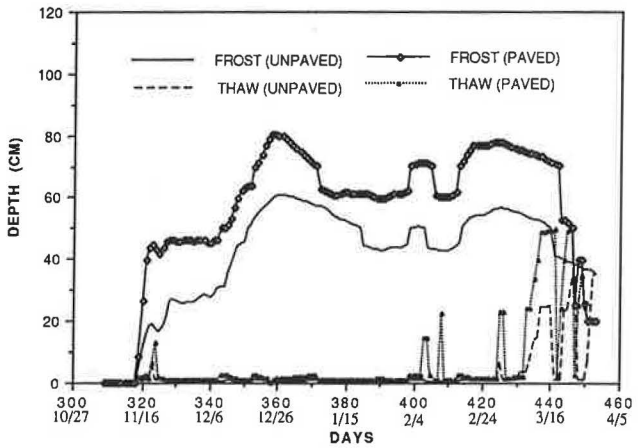


FIGURE 11 Comparison of frost-thaw depth predicted by the SHAW model for two hypothetical cases; the case of a bare soil surface and the case of a paved soil surface. (For both cases, the lower boundary conditions were specified as constant temperature and constant total water content at a depth of 10 m.)

SUMMARY AND CONCLUSION

The SHAW model has been tested with measured liquid soil water content and temperature data acquired over the winter of 1989 for a field site located at Rosemount, Minnesota. Very good agreement was observed between the predicted and measured soil temperature profiles, and good agreement was found between the frost depth estimated from the field data and the frost depth predicted by the model. Observed thaw depth response was predicted somewhat less satisfactorily by the SHAW model, although the model did accurately predict the initiation of the major thaw event.

Good agreement between measured and predicted liquid soil water content depended on the calibration equation used to convert TDR dielectric measurements to liquid soil water content values. The calibration equation of Smith and Tice (*31*) yielded better agreement for depth less than 80 cm, while the calibration equation of Topp et al. (*30*) yielded better agreement for a depth of 80 cm. Additional future work is needed to assess the calibration equation for TDR measurements for variably saturated, variably frozen soils.

In addition to needing more accurate liquid soil water content measurements, improving agreement between predicted and measured liquid soil water content requires having better-defined soil hydraulic properties for variably saturated, variably frozen soil conditions. In this study, these properties were not measured directly for either unfrozen or frozen soil conditions, but were instead derived from estimates using equations based on measured grain size distribution and bulk density of the soil. Additional work is needed to measure these properties directly.

It is unlikely that disparities between measured and predicted liquid soil water content can be attributed to limitations of the mathematical equations on which the SHAW model is based. However, this possible source of inaccuracy will be assessed in future studies.

After testing the SHAW model with measured field data, the effects of concrete pavement and a layer of base coarse on frost and thaw penetration into the soil profile were assessed. This assessment was done by comparing frost-thaw response for a paved soil and an unpaved soil. Results indicated that the frost-thaw response is more rapid and of greater magnitude for the paved soil case than for the unpaved case.

The SHAW model was originally intended to solve coupled water flow and heat transport problems for conditions commonly found in agricultural, forested, and range lands. These conditions typically have a soil surface covered with vegetation and residue in addition to snow. However, the SHAW model facilitates the simulation of layered media by allowing the assignment of appropriate hydraulic and thermal properties to each layer. It was therefore possible to simulate the presence of a paved surface by assigning hydraulic and thermal properties for concrete to the top layer of the profile. Preliminary analysis indicates that the SHAW model has the potential to be a useful tool to adequately predict the status of soil water and soil heat beneath pavements.

ACKNOWLEDGMENT

The authors wish to thank the Center for Transportation Studies at the University of Minnesota and the Minnesota De-

partment of Transportation for financial support of this study, which was published as Paper 18,769 of the scientific journal series of the Minnesota Agricultural Experiment Station on research conducted under Minnesota Agricultural Experiment Station Project 12-48. The authors also wish to thank Gerald N. Flerchinger for providing the SHAW model and for suggestions on running the model.

REFERENCES

1. K. A. Czurda. Freezing Effects on Soils: Comprehensive Summary of the ISGF 82. *Cold Regions Science and Technology*, Vol. 8, 1983, pp. 93–107.
2. B. D. Kay and E. Perfect. *5th International Symposium on Ground Freezing: State of the Art: Heat and Mass Transfer in Freezing Soils*, Jones and Holden (eds.), Balkema, Rotterdam, 1988, pp. 3–21.
3. L. C. Lundin, *Water and Heat Flows in Frozen Soils: Basic Theory and Operational Modeling*. Ph.D. dissertation, Uppsala University, Uppsala, Sweden, 1989.
4. R. L. Harlan. Analysis of Coupled Heat-Fluid Transport in Partially Frozen Soil. *Water Resources Research*, Vol. 9, No. 5, 1973, pp. 1314–1323.
5. G. F. Kennedy and J. Lielmezs. Heat and Mass Transfer of Freezing Water-Soil System. *Water Resources Research*, Vol. 9, No. 2, 1973, pp. 395–400.
6. B. D. Kay and P. H. Groenevelt. On the Interaction of Water and Heat Transport in Frozen and Unfrozen Soils, I. Basic Theory: The Vapor Phase. *Soil Science Society of America Proceedings*, Vol. 38, 1974, pp. 395–400.
7. P. H. Groenevelt and B. D. Kay. On the Interaction of Water and Heat Transport in Frozen and Unfrozen Soils, II. The Liquid Phase. *Soil Science Society of America Proceedings*, Vol. 38, 1974, pp. 400–404.
8. G. L. Guymon and J. L. Luthin. A Coupled Heat and Moisture Transport Model for Arctic Soils. *Water Resources Research*, Vol. 10, 1974, pp. 995–1001.
9. Y. W. Jame and D. I. Norum. Heat and Mass Transfer in a Freezing Unsaturated Porous Medium. *Water Resources Research*. Vol. 16, 1980, pp. 811–819.
10. T. V. Hromadka II, G. L. Guymon, and R. L. Berg. Some Approaches to Modeling Phase Change in Freezing Soils. *Cold Regions Science and Technology*, Vol. 4, 1981, pp. 137–145.
11. G. L. Guymon, T. V. Hromadka, II, and R. L. Berg. A One Dimensional Frost Heave Model Based Upon Simultaneous Heat and Water Flux. *Cold Regions Science and Technology*, Vol. 3, 1980, pp. 253–262.
12. S. K. J. Kung and T. S. Steenhuis. Heat and Moisture Transfer in A Partly Frozen Nonheaving Soil. *Soil Science Society of America Journal*, Vol. 50, 1986, pp. 1114–1122.
13. S. Mu and B. Ladanyi. Modeling of Coupled Heat, Moisture and Stress Field in Freezing Soil. *Cold Regions Science and Technology*, Vol. 14, 1987, pp. 237–246.
14. G. N. Flerchinger, *Simultaneous Heat and Water Model of A Snow-Residue-Soil System*. Ph.D. dissertation, Washington State University, Pullman, 1987.
15. G. N. Flerchinger and K. E. Saxton. Simultaneous Heat and Water Model of A Freezing Snow-Residue-Soil System. 1. Theory and Development. *Transactions of the ASAE*, Vol. 32, 1989, pp. 573–578.
17. J. L. Pikul, L. Boersma, and R. W. Rickman. Temperature and Water Profiles During Diurnal Soil Freezing and Thawing: Field Measurements and Simulation. *Soil Science Society of America Journal*, Vol. 53, 1989, pp. 3–10.
18. J. L. Pikul and J. F. Zuzel. Heat and Water Flux in A Diurnally Freezing and Thawing Soil. In *Proc., International Symposium on Frozen Soil Impacts on Agricultural, Range, and Forest Lands*, K. R. Cooley (ed.), Spokane, Wash., 1990, pp. 113–119.
19. J. L. Pikul and R. R. Allmaras. A Field Comparison of Null-Aligned and Mechanistic Soil Heat Flux. *Soil Science Society of America Proceedings*, Vol. 48, 1984, pp. 1207–1214.
20. A. R. Jumikis. Some Concepts Pertaining to Freezing Soil Systems, In *Special Report* 40: *Water and Its Conduction in Soils*, H. F. Winkerhorn (ed.), National Research Council, Washington, D. C., 1958, pp. 178–190.
21. A. C. Palmer. Ice Lensing, Thermal Diffusion and Water Migration in Freezing Soils. *Journal of Glaciology*, Vol. 6, 1967, pp. 681–694.
22. A. I. Wallace and P. J. Williams. Problems of Building Roads in the North. *Canadian Geography Journal*, Vol. 89, No. 1–2, 1974, pp. 40–47.
23. R. L. Berg, G. L. Guymon, and T. C. Johnson. *Mathematical Model to Correlate Frost Heave of Pavements With Laboratory Predictions*. Report 80-110. U.S. Army Cold Regions Research and Engineering Laboratory, Hanover, N.H., 1980.
24. R. D. Miller, Freezing Phenomena in Soils. In *Applications of Soil Physics*, D. Hillel (ed.), Academic Press, New York, 1980, pp. 254–299.
25. M. W. Smith and A. Tvede. The Computer Simulation of Frost Penetration Beneath Highways. *Canadian Geotechnical Journal*, Vol. 14, 1977, pp. 167–179.
26. J. R. Philip and D. A. de Vries. Moisture Movement in Porous Materials Under Temperature Gradients. *Transaction of the American Geophysical Union*, Vol. 38, 1957, pp. 222–232.
27. D. A. de Vries. Simultaneous Transfer of Heat and Moisture in Porous Media. *Transactions of the American Geophysical Union*, Vol. 39, 1958, pp. 909–916.
28. S. A. Taylor and J. W. Cary. Linear Equations for Simultaneous Flow of Matter and Energy in a Continuous Soil System. *Soil Science Society of America Proceedings*, Vol. 28, 1964, pp. 167–172.
29. D. Hillel. *Fundamentals of Soil Physics*, Academic Press, New York, 1980, pp. 287–317.
30. G. C. Topp, J. L. Davis, and A. P. Annan. Electromagnetic Determination of Soil Water Content: Measurements in Coaxial Transmission Lines. *Water Resources Research*, Vol. 16, No. 3, 1980, pp. 574–582.
31. M. W. Smith and A. R. Tice. Measurement of the Unfrozen Water Content of Soils: Comparison of NMR and TDR Methods. Report 88-18. U.S. Army Cold Region Research and Engineering Laboratory, Hanover, N.H., 1988.
32. D. S. Campbell. *Soil Physics With Basic: Transport Models for Soil-Plant Systems*. Elsevier Soil Publishing Co., Amsterdam, The Netherlands, 1985.
33. D. A. de Vries. Thermal Properties of Soils. In *Physics of Plant Environment*, W. R. van Wijk (ed.), North-Holland, Amsterdam, The Netherlands, 1963, pp. 210–235.
34. G. N. Flerchinger and C. L. Hanson. Modeling Soil Freezing and Thawing on a Rangeland Watershed. *Transactions of the ASAE*, Vol. 32, 1989, pp. 1551–1554.

Publication of this paper sponsored by Committee on Frost Action.

Effect of a Geotextile on Water Migration and Frost Heave in a Large-Scale Test Basin

SALLY A. SHOOP AND KAREN S. HENRY

The objective of this study was to examine the effect of a needle-punched polyester geotextile on moisture migration and frost heave during freezing and thawing in a large test basin. In the past, nonwoven polypropylene geotextiles have been effective in reducing frost heave in laboratory tests. In this case, a needle-punched polyester geotextile separator was monitored for its influence on frost heave and soil moisture tension for four freeze–thaw cycles in a large test basin. Results from freezing tests in the test basin without a water table and with a water table present 12.7 cm below the fabric suggest that use of the fabric results in greater frost heave. When the water table was above the fabric, the fabric had no influence on frost heave or water distribution in the soil. Laboratory tests indicate that the separator had no effect on frost heave. Tensiometer data in the test basin indicate that lateral transmission of water through the fabric may have occurred, so transmission of water from thawed soil to freezing soil may have contributed to increased frost heave. It is concluded that if a geotextile is used in frost-susceptible soil, proper drainage and the correct fabric type must be used to prevent increased frost heave. The role of geotextile surface properties is important and their influence on moisture migration should be investigated further.

The objective of this study was to determine the effect of a needle-punched polyester geotextile separator on moisture migration during freezing in a large-scale test basin. The capillary breaking action of polypropylene geotextiles has recently been found effective for reducing frost heave in the laboratory (*1*). Testing geotextiles for this purpose on a larger scale was desirable and, therefore, implemented as an adjunct study of a project evaluating vehicle mobility on thawing soils (*2*). The geotextile that was used as a soil separator was also monitored for its effect on frost heave.

SOIL MOISTURE AND CAPILLARY BARRIERS IN FREEZING SOILS

Moisture Migration in Freezing Soils

When a frost-susceptible soil freezes in the presence of an adequate water supply, soil water will migrate from warmer regions to the location of the freezing front and form ice lenses. Ice lens formation, also called ice segregation, is the primary cause of frost heave. As water freezes and becomes depleted adjacent to the ice, water pressure in that vicinity drops (tension increases) and water migrates to this location.

U.S. Army Cold Regions Research and Engineering Laboratory, 72 Lyme Road, Hanover, N.H. 03755-1290.

If a soil is not saturated, frost heave can still occur. In this case, water moves in adsorbed films and capillary spaces to the freezing front. Hence, the water available in the capillary fringe of a water table has always been a concern of geotechnical engineers when designing to prevent frost heave. U.S. Army Corps of Engineers guidance states that a water table within 2 m of the surface at any time of the year constitutes an adequate water supply for frost heaving to be troublesome (*3*).

Geotextiles as Capillary Barriers

Scandinavian countries have used capillary barriers consisting of coarse granular material (i.e., sands and gravels) to break the capillary rise of water in roads built on frost-susceptible subgrades (*4,5*). The capillary barrier layer is placed above the water table and below the maximum depth of frost. It then reduces water availability to the freezing front and thus reduces frost heave.

Laboratory research has indicated that geotextiles can reduce frost heave in soils when placed above the water table and below the freezing front (*1,6,7*). Results from an instrumented soil column subjected to freezing from the top down indicated that a needle-punched polypropylene geotextile interrupted a constant soil moisture tension gradient (i.e., moisture content gradient); also, the soil above the fabric progressively dried during freezing, indicating that the geotextile layer restricted upward water migration (*6,8*).

Geotextile properties used in capillary barriers include relatively large pore sizes and hydrophobic fibers. The equation for the height of capillary rise in a cylinder demonstrates the importance of these parameters, even though the pore space in a soil is very complex (*9*):

$$h = \frac{2T \cos \alpha}{R\gamma} \quad (1)$$

where

h = height of capillary rise,
T = surface tension of liquid,
R = radius of the tube,
γ = unit weight of the liquid, and
α = contact angle between the liquid and the tube (wetting angle).

If a geotextile has larger pores than the surrounding soil or a higher wetting angle, it will have a lower height of capillary rise, as well as lower hydraulic conductivity when the soil is not saturated.

Soil Moisture Measurement in Freezing Soils

The total soil-water potential consists of the sum of the matric potential, the osmotic potential, the gravitational potential, and other effects that may influence the energy status of soil water (*10*). The matric potential of soil water depicts the tenacity with which soil water is held by the soil matrix and is related to the soil wetness through the soil-moisture characteristic curve. Thus, measurement of the soil matric potential, also called soil-moisture tension, can be converted to soil water content through use of the soil-moisture characteristic curve.

The soil-moisture characteristic is determined in the laboratory; there is a hysteresis effect for wetting and drying processes. The density of the soil also affects the soil-moisture characteristic. Because of hysteresis and the dependence of soil density, the in situ measurement of soil moisture tension and its conversion to moisture content by use of the soil-moisture characteristic provide only an estimate of soil wetness.

When a soil is not frozen or saturated, its matric potential can be measured with soil-moisture tensiometers. A tensiometer is composed of a porous ceramic tip connected to a manometer through a tube (see Figure 1). Normally, all parts of the tensiometer are filled with water. When the tensiometers were subjected to freeze–thaw cycles, they were filled with propylene glycol to avoid damage from freezing. McKim et al. (*11*) found that the tensiometer response is the same whether filled with glycol or water. When the porous cup is placed in the soil, the fluid inside the cup equilibrates with the soil water through the pores in the ceramic tip. When the soil is not saturated, the soil water is at less-than-atmospheric pressure, and it will draw fluid from the tensiometer. The resulting drop in pressure (rise in tension) is indicated on the tensiometer gage.

EXPERIMENTAL METHOD

The experimental program was conducted as an adjunct to an off-road vehicle mobility test program in thawing soils (*2*).

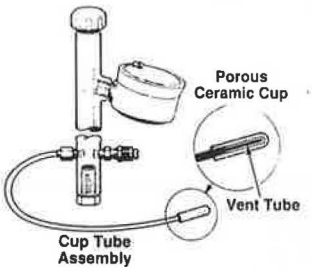


FIGURE 1 Construction and components of a soil moisture probe tensiometer.

It was designed to determine how a needle-punched polyester geotextile separator affected frost heave and moisture migration during freezing. Open-system freezing tests (i.e., freezing tests with water freely available to the soil) were also conducted in the laboratory on specimens containing the test basin soils, with and without the geotextile as a separator, in order to examine its influence on frost heave.

Freezing and thawing in the test basin were controlled using refrigeration panels placed on the soil surface. Moisture content in the soil was varied by changing the water table depth or by adding surface water to simulate rain or snow melt. The soil moisture tension and temperature profile were recorded throughout freezing and the amount of frost heave was measured by surface elevation surveys.

FERF Test Basin

The large-scale experimental work was done in the Frost Effects Research Facility (FERF) of the U.S. Army Cold Regions Research and Engineering Laboratory (CRREL) in Hanover, New Hampshire. The unique capabilities of the FERF allow large-scale experimental conditions to be carefully controlled. The conditions varied were freeze rate, depth of frost, water table elevation, and soil moisture content. The test basin used was 36.6 m long and 12.3 m across, as shown in Figure 2. For freezing and testing, it was only used one-half at a time; vehicle mobility testing occurred on one-half of the test basin during the thaw while the other half of the test basin was being frozen.

Soils

The test section consisted of a bottom layer of fill and a top layer of test soil, separated by a geotextile (Figure 3). The purpose of the fill material was to simulate a natural environment (i.e., having no rigid, impermeable layer directly below the layer of test soil) and to allow for a water table to be added and varied relatively quickly. The test soil was chosen to simulate an off-road condition for vehicle mobility testing. It is a typical subgrade or off-road material in this part of New England. The fill soil was a bank run gravelly sand from Pompy Pit, Thetford, Vermont, and the test soil was a silty sand from Lebanon, New Hampshire. The grain size distribution curves and moisture characteristics for both soils are shown in Figures 4 and 5. The height of saturated capillary rise can be estimated from the moisture-tension curves. Examination of the drying curves (arrow toward increasing tension) in Figure 5 indicates that the breakthrough pressure (nearly 100 percent saturation) for the Lebanon sand is approximately 6 kPa; it is approximately 3 kPa for the Pompy pit sand. Dividing by the unit weight of water yields the height of capillary rise—0.6 m for the Lebanon sand and 0.3 m for the Pompy pit sand.

The frost susceptibility of the base material (gravelly sand) is classified as low, on the basis of the standard CRREL frost heave test and the Corps of Engineers classification scheme (*3,12*). The silty sand test soil is highly frost susceptible, having a frost heave rate of 7.4 mm/day when subjected to the

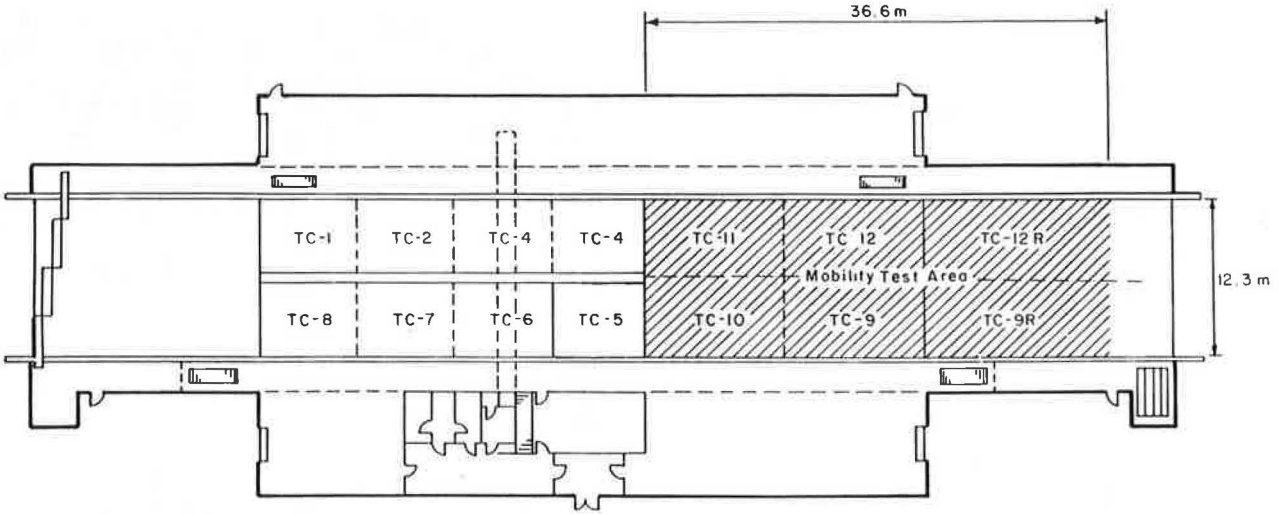


FIGURE 2 Plan view of the soil test basin (hatched area) in the Frost Effects Research Facility.

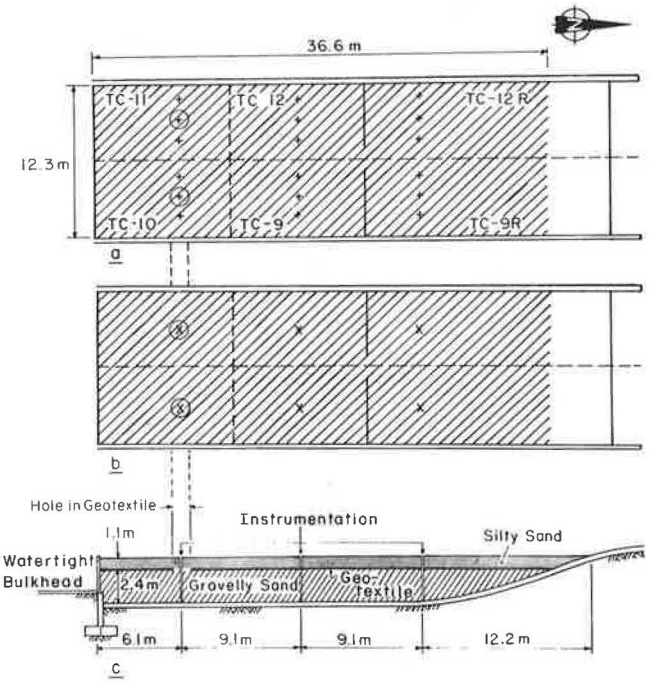


FIGURE 3 Plan view and cross section of the test basin: (a) location of frost heave survey stations, (b) instrumentation locations, and (c) cross section of the soil basin showing configuration of test soil, base fill, and geotextile as well as location of instrumentation.

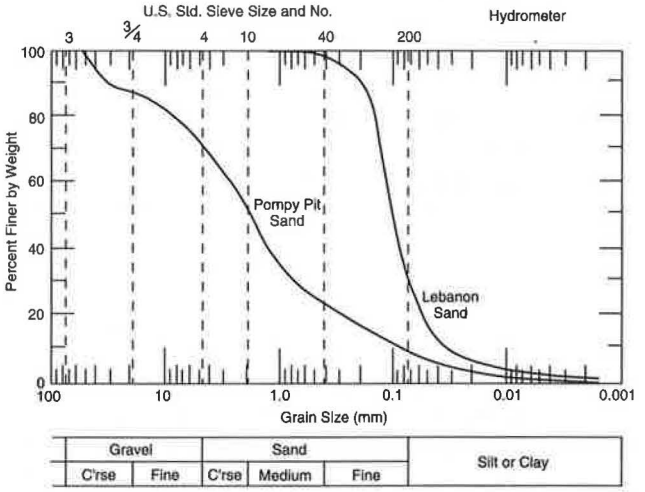


FIGURE 4 Grain size distribution curves of the bank run gravelly sand used for the base fill (below the fabric) and the silty sand used as the test soil (above the fabric).

standard CRREL frost heave test. Frost heave test data and additional soil properties have been provided by Shoop (*13*).

Geotextile

The geotextile used was a needle-punched polyester. It was chosen as a separator for the two soils on the basis of the Corps of Engineers Civil Works Guide Specification, #CW-02215, March 1986, using Filter Design Criteria. Specifications are as follows:

Characteristic	*Specification*
Thickness	3.3 mm
Weight	0.34 kg/m^2
Equivalent opening size	70 to 100 mm
Permittivity	300 sec^{-1}
Puncture	578 N
Mullen burst	2700 kPa
Grab tensile/Elongation	1156/100 N per percent

On the basis of past work, polypropylene would have been chosen for a capillary barrier material owing to its hydrophobic nature (e.g., *1*). However, a polyester fabric was selected so that water could easily move across the layer of the fabric. Polyester is less hydrophobic than polypropylene (adsorbing and absorbing water more readily). It may still act as a cap-

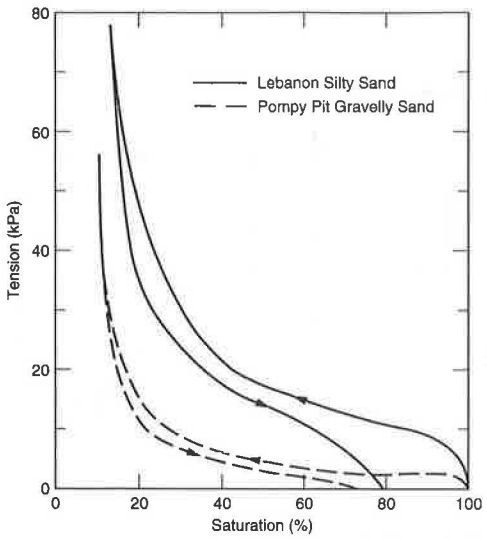


FIGURE 5 Moisture tension curves for the Pompy Pit bank run (gravelly sand) and Lebanon sand (silty sand).

illary barrier because, on average, it had larger pore sizes than the surrounding soil, and possibly was somewhat more hydrophobic than the soil. Specifying that the fabric be made of polyester did not guarantee the wetting behavior because surface finishes can change the wetting properties of the fibers (*14*).

The fabric separated the test soil and the base fill at a depth of 107 cm. It was placed over the entire test basin with the exception of two circular holes, of 1.2-m (4-ft) diameter, cut into the fabric as shown in Figures 3 and 6. Each circle had a vertical string of tensiometers and thermistors located in its center; these sections were used as reference sections. Entire sections were not left without the geotextile separator because the separator was necessary for maintaining the test sections for vehicle mobility testing. The fabric was present at the other four instrumentation locations (Figure 3).

Instrumentation

Thermistors and tensiometers were used to monitor soil temperature and moisture tension throughout each freeze–thaw cycle. The soil instrumentation was concentrated in the upper 30 cm because this is the area of most concern for vehicle mobility. Near the fabric, the thermistors were placed symmetrically at 2.5 and 30.5 cm above and below the fabric. Figure 7 shows the vertical configuration and location of the instrumentation.

Water Table

Water was added to the basin through four standpipes, one in each corner of the basin. These pipes were connected to horizontal pipes located 0.3 m from the bottom of the test cell in the base fill. The lower pipes were perforated to allow water seepage, and the water level was measured at each of the standpipes. To lower the water table, water was drained through four drains in the test basin floor.

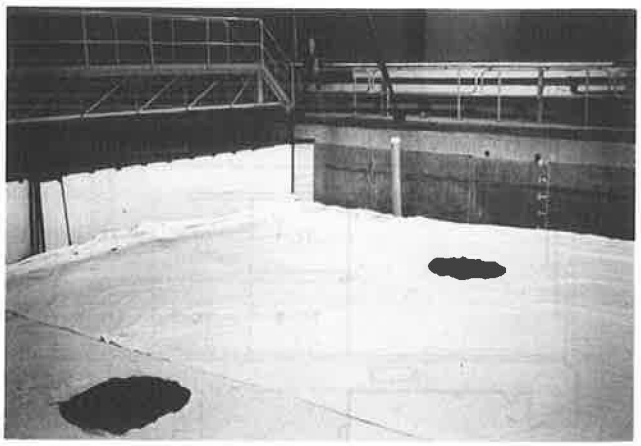


FIGURE 6 Geotextile being installed and the 1.2-m-diameter hole in the geotextile around the instrumentation in Test Cells 10 and 11.

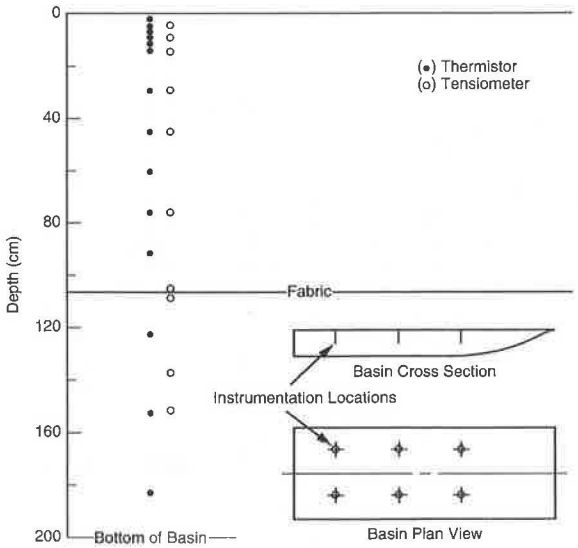


FIGURE 7 Instrumentation configuration in the test basin.

Test Basin Procedure

The soil was placed in the basin in 15-cm lifts, tilled, then compacted to 95 percent of maximum density as determined using modified Proctor compaction tests (ASTM D 1557); compaction curves were provided by Shoop (*13*). If desired, water was added and allowed to equilibrate. The soil surface elevation was then surveyed (Figure 3a). Freezing panels were placed on the soil surface and the soil was frozen from the top down. The freezing rate was controlled by adjusting the temperature of the coolant in the refrigeration panels. The soil was frozen to depths ranging from 43 to 66 cm. When the desired frost depth was obtained, the panels were removed.

While the soil was still frozen, the soil surface was surveyed to determine the amount of frost heaving. The soil was then allowed to thaw by maintaining spring-like conditions within the building (7°C to 13°C). Vehicle mobility was tested during thawing. After the soil was thoroughly thawed, it was tilled and compacted for the next frost cycle.

Laboratory Freezing Tests

Standard CRREL frost susceptibility tests were conducted on four specimens prepared from the test basin soils. The details of the procedure were provided by Chamberlain (*12*). Usually, cylindrical soil specimens, 150 mm in diameter by 150 mm in height, are compacted to a specified uniform density and subjected to two freeze-thaw cycles. Before freezing, the samples are saturated for 24 hr, then the water table is lowered to 1 cm above the base of the sample. Water is freely available through porous base plates during the test, and each freeze or thaw cycle lasts for 24 hr.

For this test program, a few modifications were made to the standard procedure. Four specimens were prepared, and each one consisted of one-half Pompy Pit gravelly sand, placed in the bottom of the cylinder, and one-half of Lebanon fine sand, placed in the top of the cylinder. Two of the specimens contained disks of the geotextile separating the soil layers. The fabric was glued to the edge of the container with silicone adhesive. In addition, the specimens were subjected to five freeze-thaw cycles.

For the laboratory freezing tests, the Pompy Pit bank run gravel was compacted to 2.00 Mg/m^3 (125 lb/ft^3) dry density, which is 93 percent of maximum dry density, and the silty sand was compacted to 1.68 Mg/m^3 (105 lb/ft^3), which is also 93 percent of maximum dry density.

CONDITIONS TESTED AND RESULTS

Frost heave, soil moisture tension, and temperature were monitored for the freeze cycles and conditions presented in Table 1. The soil moisture tension profiles during freezing were studied to determine the influence of the geotextile on moisture in the soil. The surface of the soil was surveyed before and after each freeze to measure the total amount of frost heave. The results of tests are discussed for three different water tables: no (or deep) water table, a water table 12.7 cm below the geotextile, and a water table 11.4 cm above the geotextile. Data from the test sections in the ramp area of the test basin were not consistent with the other test data and were believed to be influenced by outside conditions. Therefore, they are not included.

No Water Table

The first two freeze cycles on the test basin were done without a water table. Water was added to the soil surface to aid soil compaction when preparing the test section and this surface water quickly drained into the soil. The initial moisture conditions, the length of the freeze, and the frost depth were different for the two tests as indicated in Table 1 and Figure 8.

The soil tension porfiles before each of the freeze cycles are shown in Figure 8. The drying portion of the soil-moisture characteristic (Figure 5) was used with the tensiometer data to estimate the soil-moisture contents. The drying portion of the curve was used because the soil had been wetted to field capacity (specific retention) during compaction. Tensiometer data before freezing (Figures 8a and 8b) indicate that the soil immediately above the interface between the fine sand and gravelly sand was near saturation regardless of whether the fabric was present. Both cases indicate that the soil below the fabric was drier than the soil at the same depth when no fabric is present. Before the first freeze test began, the soil below the fabric was at 14 percent saturation compared to 48 percent for the soil below the hole in the fabric. Before the second freeze, this difference was smaller—25 percent saturation below the fabric versus 44 percent saturation when no fabric was present.

During freezing, all of the unfrozen soil below the depth of frost became drier (soil tension increased) as the soil moisture was drawn to the freezing front. Figures 9 and 10 show selected soil tension profiles throughout Freeze Cycles 1 and 2, respectively. Only the data below the frost line are shown because tensiometers do not work reliably in frozen soils. When the fabric was present, there was a significant break in the soil-moisture tension gradient (approximately 12 kPa), and the soil below the fabric is drier than that above the fabric.

TABLE 1 FROST HEAVE, FROST DEPTH, AND WATER LEVEL FOR EACH OF THE FREEZE CYCLES

				Frost heave (cm)		
					Above fabric	
Freeze cycle	*Julian days*	*Frost depth (cm)*	*Water level (cm)*	*Above hole*	*Ave.*	*(Std. dev.)*
1	120–138	56	no water table	0.61	1.45	(0.95)
2	160–201	43	no water table	0.91	2.67	(1.89)
3	63–311	66	12.7 cm below fabric	4.88	7.01	(2.68)
4	313–361	52	1.4 cm above fabric	7.93	7.77	(0.88)

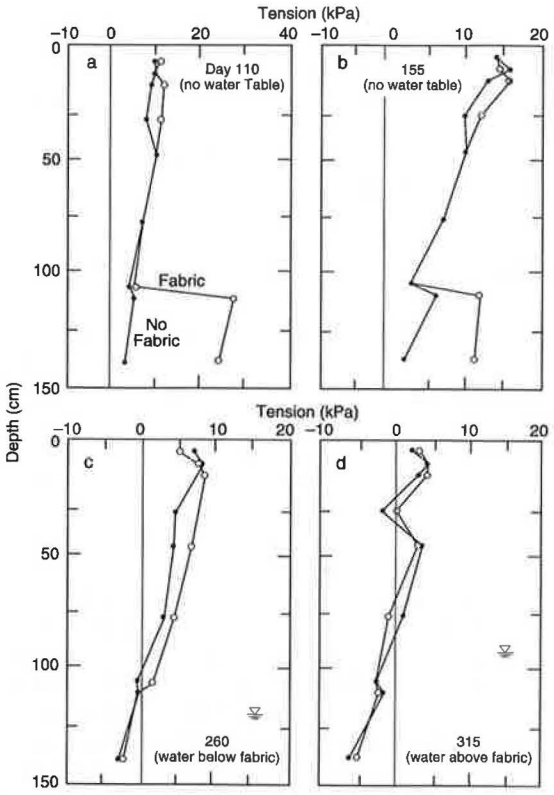


FIGURE 8 Tension profiles before each freeze cycle (a) tension measured on Julian Day 110, no water table; (b) tension measured on Julian Day 155, no water table; (c) tension profiles on Julian Day 260, water below fabric; and (d) tension profile on Julian Day 315, water above fabric.

However, the soil moisture tension gradient is essentially constant on either side of this discontinuity. Furthermore, throughout the test, the soil above the interface between the base fill and test soil is at about the same degree of wetness (90 to 100 percent saturated) regardless of whether the fabric is present.

During the first freeze cycle (Julian Days 120 to 138, Figure 9), the soil both above and below the fabric, as well as the soil without fabric, continually dried as freezing progressed. Furthermore, the fabric did not appear to restrict the moisture movement because the soil above the fabric did not dry out any faster than the soil below (Figure 9b).

During the second freeze cycle (Julian Days 160 to 210, Figure 10), when no fabric was present, the tension profiles indicate increased moisture in both the upper and lower soils after Day 175. When fabric was present, tension profiles exhibited progressively wetter conditions above the fabric whereas the soil below the fabric continued to dry. When no fabric was present, both the silty sand and the gravelly sand became wetter as freezing progressed. Because water was added to Test Cells 11 and 12 for compaction while freezing was occurring in Test Cells 9 and 10, the water added during compaction (or released during the thaw of Test Cells 11, 12, and 12R) may have migrated through the fabric to the east side of the basin where the soil was freezing, being drawn into the soil above by the capillarity of the fine sand.

The frost heave calculated from the elevation surveys for all freeze cycles are presented in Table 1. For the no-water-table condition (Cycles 1 and 2), the data suggest that frost heave above the hole is less than the frost heave above the fabric. However, the frost heave above the hole in the fabric falls within one standard deviation of the mean, leaving some doubt as to the statistical significance of the lower frost heave value.

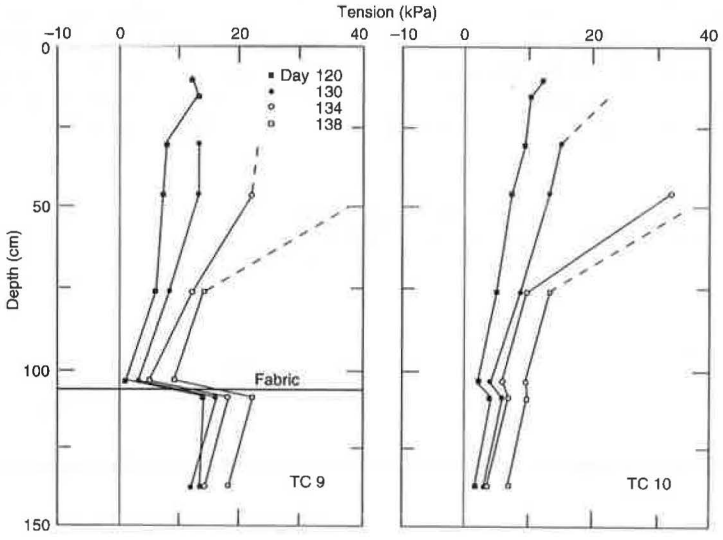


FIGURE 9 Representative tension profiles throughout the freeze cycle during Julian Days 120 to 138 (no water table).

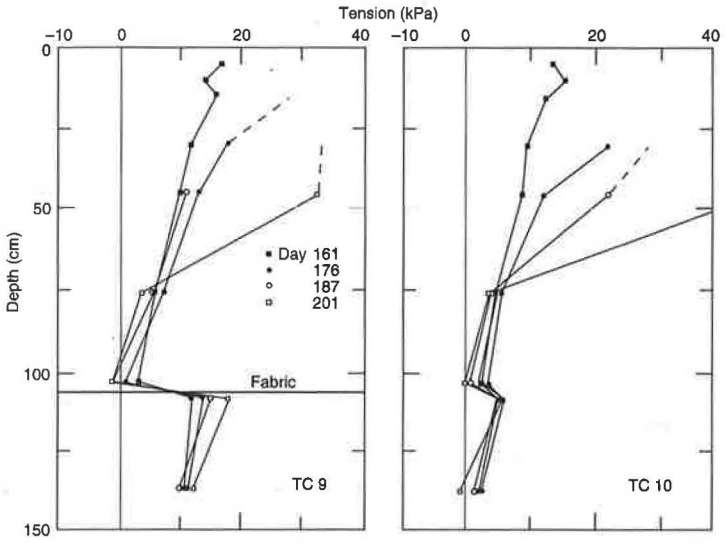


FIGURE 10 Tension profiles for the freeze cycle during Julian Days 160 to 201 (no water table).

Water Table Below Fabric

The third freeze test was conducted to examine the influence of the geotextile on water migration and frost heave when a water table was present below the fabric. The water level was initially raised to 2.5 cm below the fabric and then allowed to fluctuate between 2.5 and 20.0 cm below the fabric to simulate natural fluctuations in a water table. The average water table elevation was 12.7 cm below the fabric.

Before freezing, the soil tension profiles indicate that the depth of the water table was immediately below the fabric (Figure 8c), and this agrees with the water levels measured in the wells. The soil above the fabric was slightly drier than the soil above the hole in the fabric. The tension data also indicate that the water level was about 12 cm higher when there was no fabric. The capillary fringe may have extended up into the silty fine sand, and when the fabric was present, the fabric may have prevented the capillary rise of water.

The soil moisture tension profiles during freezing for this test are shown in Figure 11. For both the fabric and no-fabric locations, the tension gradient, and thus the moisture conditions, did not change much during freezing. Below the fabric, the tensiometers indicate a positive pressure of 1 to 4 kPa (when corrected for elevation), reflecting that they are below the water table. There was little or no change in the tension gradient at the soil interface whether or not the fabric was present.

The heave measured above the hole in the fabric is 4.9 cm and the average of the heave measured at stations above the fabric is 7.0 cm. These frost heave data again suggest that the

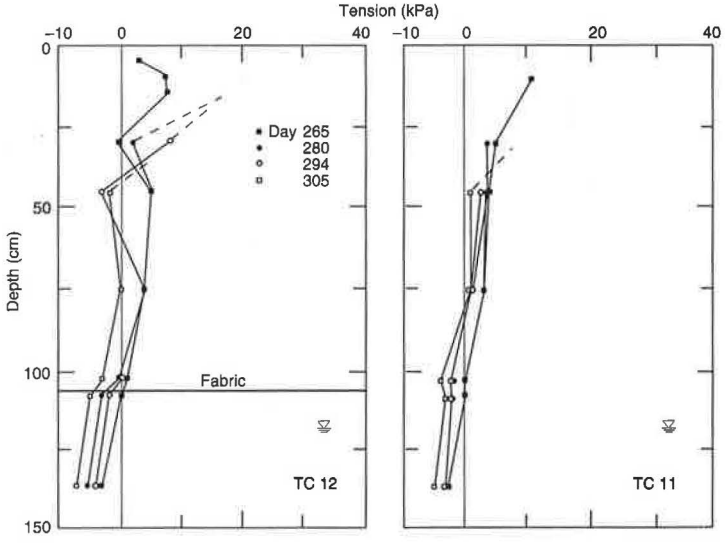


FIGURE 11 Tension profiles for the freeze cycle during Julian Days 263 to 311. The water level averages 12.7 cm below the level of the fabric.

use of the fabric resulted in more frost heave; but the heave above the hole in the fabric falls well within one standard deviation of the average of the heave above the fabric. Again, the effect of fabric on frost heave cannot be stated with certainty.

Water Table Above Fabric

During the fourth freeze cycle on Julian Days 313 to 361, the water table was held an average of 11.4 cm above the fabric (fluctuating between 3 and 18 cm above the fabric). The soil moisture tension profiles shown in Figure 12 exhibit little change with the progression of freezing. The small fluctuations seen were related to the changes in the water table level. As expected, the fabric had no significant influence on the soil moisture tension. Furthermore, there is no offset in the soil moisture tension profile at the change in soil type, regardless of whether fabric is present. There was no difference in frost heave above the reference and fabric sections (Table 1).

Laboratory Test Results

The results of the laboratory freezing tests, in terms of frost heave as a function of time for the first and fifth (last) freezing cycles are shown in Figures 13a and 13b. Table 2 presents the frost heave rates during the sixth to eighth hour of freezing [the dependent variable recommended by Chamberlain (*12*)]. The fabric had no significant influence on the rate of frost heave in these freezing tests. Neither the shape of the frost heave curve, nor the rates of frost heave are significantly different for the tests with fabric compared to the tests without fabric. Differences in overall heave at the end of the first freeze cycle most likely originate from the time in which ice began nucleating in the soil.

DISCUSSION OF RESULTS

In the test basin, the soil above the fabric was nearly always close to saturation (90 to 100 percent saturated before freezing), even when no water table was present. This condition indicates that the fabric may be preventing or retarding the downward, gravity-driven flow of water that had been added to the soil surface during test basin construction and soil preparation. This process is supported by the observation that the base soil is considerably drier below the fabric during Freeze Cycles 1 and 2 (ranging from 14 to 25 percent saturation), whereas the base soil below the hole in the fabric is significantly wetter (starting at about 50 percent saturation for both cycles and drying to approximately 30 percent in Cycle 1). Additional information suggesting that the fabric affects soil moisture distribution is the tensiometer data during the third freeze cycle when the water table was added below the fabric. Here, the test soil above the hole in the fabric is wetter than the test soil above the fabric. It reflects the same type of conditions as the first two freeze cycles, only now the water is available from below the fabric instead of draining from above, and the source of greater moisture above the hole in the fabric is the capillary fringe above the water table (rather than gravity drainage), which is apparently restricted by the fabric.

During all tests, the tension gradient with depth was constant although interrupted by the presence of the fabric. The gradient offset attributable to the fabric was greatest during Freeze Cycles 1 and 2 when no water table was present. For these cases, the tension gradient was offset by 10 to 20 kPa at the fabric, with the soil below being drier. Normally, water will flow from an area of low soil moisture tension to high soil moisture tension. Thus, the individual curves of Figures 9b and 10b may indicate that soil water moves from the region just above the fabric to the region just below the fabric. If this were true, the soil above the fabric would exhibit increased soil moisture tension with time, whereas the soil below

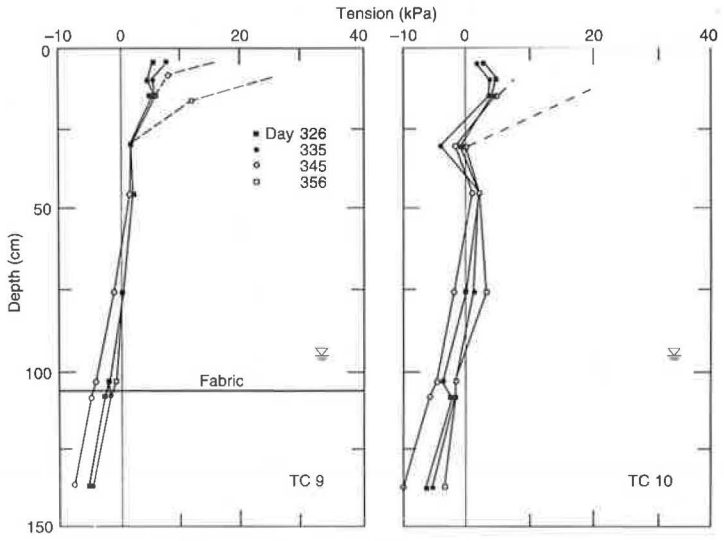


FIGURE 12 Tension profiles for the freeze cycle during Julian Days 313 to 361. The water level averages 11.4 cm above the fabric level.

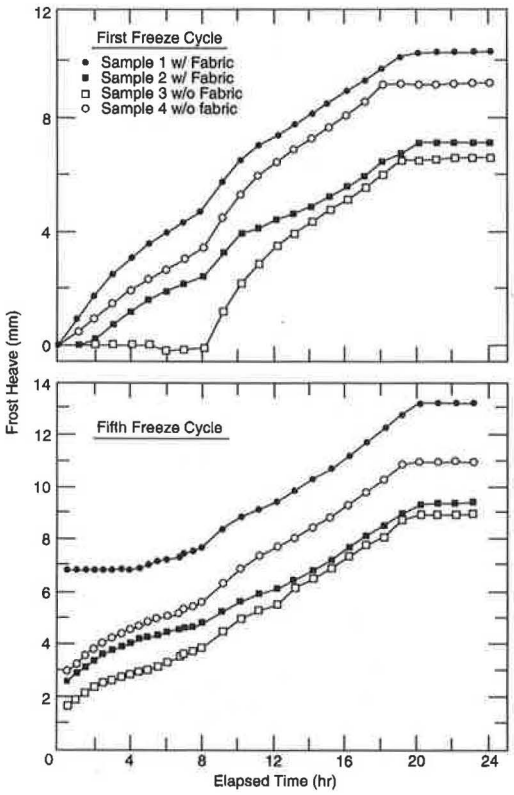


FIGURE 13 Laboratory frost heave test data—frost heave versus time for the first and fifth freeze cycles.

the fabric would exhibit decreased soil moisture tension. This trend did not occur in the data. Furthermore, it is not prudent to project what is known about soil moisture movement in soils onto soil movement across the geotextile layer. In the analysis, the tensiometer data were considered to be providing information about soil moisture in the soils only, and not in the geotextile.

The tension profiles remained essentially the same shape during Freeze Cycle 1, i.e., the soils both above and below the fabric were drying at the same rate, indicating that water was moving through the fabric. However, during Freeze Cycle 2, the moisture increased during freezing directly above the fabric while the soil below continued to dry (Figure 10). This additional moisture must have migrated through the fabric from the other side of the test basin where the soil was thawing and water had been added for reprocessing the soil. This behavior was unexpected but laboratory tests indicated that the fabric readily transported or siphoned moisture laterally even when no pressure differential was applied. Syphoning behavior of geotextiles has also been reported by Zerfass (*15*).

Frost heave measurements indicated that when the water table was below the fabric or absent, the frost heave above the fabric was greater than the frost heave when fabric is absent. However, because the magnitude of the difference is within one standard deviation of the mean, the significance of the difference is questionable. (The relatively high standard deviation of the frost heave measurements is ascribable to the roughness of the frozen ground.)

Open-system freezing tests of the soil-geotextile system in the laboratory indicated that the fabric did not affect frost heave. The difference between freezing in the test basin and the laboratory procedure was that the water in the laboratory freezing tests must flow vertically to cause frost heave, whereas in the test basin water was not constrained to flow only vertically. In addition, the laboratory tests were performed by first fully saturating the sample and then lowering the water table before freezing began. Freezing took place with a constant-head water supply, again not the same conditions as the large-scale basin tests.

Past work has indicated that nonwoven polypropylene (i.e., hydrophobic) geotextiles reduce frost heave up to 75 percent in open-system laboratory freezing tests (*1,7*). The most significant difference in the experimental parameters between past work and the laboratory tests conducted for this program is the nature of the polymer from which the fabric is manufactured. The polymer significantly influences the wetting properties of the geotextile. There are no standard tests for determining fiber wettability; however, a simple measurement was made of the relative performance of two geotextiles by placing the bottom 1 mm of a strip of geotextile into a dish of water. The observations were that the polyester geotextile used in this study wetted easily and displayed a capillary rise of 9 mm, which occurred in less than 2 min, whereas a similar geotextile made of polypropylene did not wet even after 48 hr. This result demonstrates the need for more work to define the role of fiber surface properties in geotextiles acting as capillary barriers.

SUMMARY AND CONCLUSIONS

The results of freezing tests conducted in the large test basin suggest that the use of the geotextile separator resulted in greater frost heave when the water level was either quite deep or just below the fabric. As expected, the fabric had no influence on frost heave when the water level was above it. An

TABLE 2 LABORATORY FREEZING TEST FROST HEAVE RATES (mm/hr) FOR THE SIXTH TO EIGHTH HOUR OF FREEZING

	With fabric		*Without fabric*	
	Sample 1	*Sample 2*	*Sample 3*	*Sample 4*
Cycle 1	0.45	0.30	—	0.40
Cycle 5	0.20	0.20	0.33	0.15

interesting result of the tests is the apparent lateral transmission of water through the fabric from the thawed section to the freezing section in the second freeze cycle.

The test results indicate that caution should be exercised when selecting a geotextile for any function that would place frost-susceptible soil above it in a frost prone region. Until more research is conducted, if a fabric is selected for use as a separator in frost-susceptible soils, it appears prudent to include drainage at the level of the geotextile if it is desirable to minimize frost heave.

ACKNOWLEDGMENTS

Many thanks to Rosanne Stoops and Andrew Sundelin. Rosanne dutifully installed the tensiometers, took all the readings and entered the data into the computer. Both Rosanne and Andrew spent many hours manipulating and graphing the tensiometer and temperature data. Richard Guyer was the expert behind the temperature measurements and data acquisition system who faithfully checked the acquisition equipment and changed the data collection tapes weekly over the years. The instrumentation was carefully and proficiently built, installed, and repaired (often) by Steve Decato, Chris Berini, and Tommy Hall. The refrigeration personnel at CRREL did a superb job of project support and were a pleasure to work with. Last, thanks to the thoughtful technical reviews provided by Richard Berg, Frederick Crory, and Edwin Chamberlain, and by the four anonymous TRB reviewers.

REFERENCES

1. K. Henry. Use of Geotextiles to Mitigate Frost Heave in Soils. In *Proc., 5th International Conference on Permafrost*, Trondheim, Norway, 1988, pp. 1096–1101.
2. S. Shoop. *Vehicle Mobility on Thawing Soils: Interim Report on CRREL's Test Program*. Special Report 89-31. U.S. Army Cold Regions Research and Engineering Laboratory, Hanover, N.H., 1989.
3. R. Berg and T. Johnson. *Revised Procedure for Pavement Design under Seasonal Frost Conditions*. Special Report 83-27. U.S. Army Cold Regions Research and Engineering Laboratory, Hanover, N.H., 1983.
4. F. Rengmark. Highway Pavement Design in Frost Areas in Sweden. In *Highway Research Record 33*, HRB, National Research Council, Washington, D.C., 1963, pp. 137–150.
5. O. A. Taivainen. Preventive Measures to Reduce Frost Heave in Finland. In *Highway Research Record 33*, HRB, National Research Council, Washington, D.C., 1963, pp. 202–216.
6. K. Henry. Geotextiles as Capillary Barriers. Geotechnical Fabrics Report, March–April, 1990, pp. 30–36.
7. T. Allen, J. R. Bell and T. S. Vinson. *Properties of Geotextiles in Cold Regions Application*. Transportation Research Report 83-6. Transportation Research Institute, Oregon State University, Corvallis, 1983.
8. K. Henry. Effect of Geotextiles on Water Migration in Freezing Soils and the Influence of Freezing on Performance. *Proc., Geosynthetics '91 Conference*, Vol. 1, Atlanta, Ga., 26–28 February 1991, pp. 469–484.
9. R. D. Holtz and W. D. Kovacs. *An Introduction to Geotechnical Engineering*. Prentice-Hall, Englewood Cliffs, N.J., 1981.
10. D. Hillel. *Introduction to Soil Physics*. Academic Press, New York, 1982.
11. H. L. McKim, R. L. Berg, R. W. McGaw, R. T. Atkins, and J. Ingersoll. Development of a Remote-Reading Tensiometer/Transducer System for Use in Subfreezing Temperatures. *Proc., 2nd Conference on Soil-Water Problems in Cold Regions*, Edmonton, Alberta, Canada, Sept., 1976, pp. 31–45.
12. E. J. Chamberlain. *A Freeze-Thaw Test to Determine the Frost Susceptibility of Soils*. Special Report 87-1, U.S. Army Cold Regions Research and Engineering Laboratory, Hanover, N.H., 1987.
13. S. Shoop. *Research Plan and Experimental Design for the Study of Vehicle Mobility in Thawing Soils*. Internal Report 1001, U.S. Army Cold Regions Research and Engineering Laboratory, Hanover, N.H., 1988.
14. J. R. Bell et al. *Evaluation of Test Methods and Use Criteria for Geotechnical Fabrics in Highway Applications*. Report FHWA/RD-80/021. FHWA, U.S. Department of Transportation, 1980.
15. K.-Ch. Zerfass. Syphoning Effect of Geotextiles. *Proc., 3rd International Conference on Geotextiles*, Vienna, Austria, 1986, pp. 1197–1202.

Publication of this paper sponsored by Committee on Frost Action.